NASA CR 66178

PUBLICATION NO. U-3556

RE-ENTRY AND SPACE SYSTEMS PROGRAMS

FINAL REPORT

RESEARCH, DEVELOPMENT, AND PRELIMINARY DESIGN FOR THE LUNAR PENETROMETER SYSTEM APPLICABLE TO THE APOLLO PROGRAM

PHILCO

A SUBSIDIARY OF Ford Motor Company

AERONUTRONIC DIVISION

FORD ROAD/NEWPORT BEACH, CALIFORNIA

27 APRIL 1966

Publication No. U-3556

RE-ENTRY AND SPACE SYSTEMS PROGRAMS

FINAL REPORT
RESEARCH, DEVELOPMENT, AND PRELIMINARY DESIGN FOR THE LUNAR PENETROMETER SYSTEM APPLICABLE TO THE APOLLO PROGRAM

Prepared for:

National Aeronautics and Space Administration
Langely Research Center
Hampton, Virginia

Contract No. NASI-4923

Approved: R. S. Kraemer
R. S. Kraemer, Program Engineer

V. Skoro
V. Skoro, Program Supervisor

W. Hostetler
W. Hostetler, Manager, Space Programs

27 April 1966

AERONUTRONIC
DIVISION OF PHILCO CORPORATION
A SUBSIDIARY OF Ford Motor Company,
FORD ROAD NEWPORT BEACH, CALIFORNIA

CONTENTS

CONTENTS (Continued)

CONTENTS (Continued)

CONTENTS (Continued)

SECTION 1

INTRODUCTION

This report presents the results of the Lunar Penetrometer System (LPS) Program conducted by Aeronutronic for the Langley Research Center, National Aeronautics and Space Administration, under Contract NAS1-4293. This effort covered a period from April 1965 through March 1966. The basic program objective was to conduct the necessary research, development, and preliminary design required to establish the design parameters for a flight penetrometer system. Three major areas of activity were defined in support of the program objective. An impact research task was established to investigate thoroughly the impact characteristics exhibited by target materials simulating several physical models of the lunar surface. The second task comprised the preliminary design, development, and testing of engineering prototype omnidirectional penetrometers. The third major task was the preliminary design and testing of a data relay link required for Apollo application of the penetrometer system. This report presents the design approaches followed, tradeoff studies made, and results obtained in these activities.

SECTION 2

SUMMARY

The Lunar Penetrometer System Program was initiated with a state-of-the-art review of existing technology pertinent to the penetrometer system. The results of this review were reported in Aeronutronic Report No. U-3132, "State-of-the-Art Review, Research, Development and Preliminary Design for the Lunar Penetrometer System Applicable to the Apollo Program," dated 10 June 1965. New technological developments required for the penetrometer system included a miniaturized but accurate omnidirectional accelerometer, telemetry which was stable during high energy impact shocks up to 7000 g, an isotropic transmitting antenna operating with good efficiency even though drastically subscale and immersed in a magnetic soil medium, and the low-noise recording of impact accelerations over a hard line with negligible zero shift at velocities up to 250 ft/sec. These problems yielded to concentrated development effort, and all major objectives of the program were accomplished.

More than 200 impact tests were conducted with accelerometer-instrumented spherical projectiles in an extensive parametric impact research test effort to investigate soil penetration characteristics. Accurate impact acceleration signatures were obtained for velocities of 20, 150, and 250 ft/sec; off-normal angles of 0, 30, and 60 degrees; ambient pressures of 1 atmosphere and 10^{-5} Torr; penetrometer diameters of 4, 8.5, and 12 inches; and penetrometer weights of 2.2, 4, 5, and 8 pounds. The crushing effects of balsa impact limiters of 7 and 11 lb/ft^3 density were also investigated. Including among ten target materials were very low bearing strength flocculent cabosil (0.8 psi penetration resistance at a depth of 18 inches), basalt silt, a variety of alluvial and ground basalt sands, cellular foam cobbles and pebbles, and a rigid steel plate. Results are summarized in Section 4 of this report.

A LEM landing simulator facility was constructed to investigate the surface penetrating characteristics of the LEM landing gear under simulated lunar landing conditions. Landing simulations with a single landing gear strut and pad were conducted at a surface impact velocity of 10 ft/sec and under mass inertial loadings of 4000, 8000, and 16,000 pounds. Three sand materials and a cellular foam were employed as target materials. It is significant to note that the depth of LEM pad penetration increased rapidly as the surface bearing strength was decreased below 20 psi (see Figure 4-67).

Several promising data correlation methods were developed. Good correlation of the penetrometer data was achieved with an analytical model which permits the direct derivation of surface density and static bearing strength. Tests with the more dense penetrometers also showed excellent correlation between surface static bearing strength and penetrometer depth of penetration (second integration of the acceleration versus time trace). The LEM landing data showed reasonable agreement with the analytical model for compacted and cohesive materials but indicated the need for a "jack hammer" correction factor to account for the increased penetration into loose particulate materials caused by strut vibration.

The development of the omnidirectional telemetering penetrometer assembly is summarized in Section 5 of this report. A substantial portion of the effort was devoted to the development of impact-insensitive electronics, especially in the transmitter oscillator module. Prototype transmitters demonstrated a frequency shift of only one part in 10^4 under extreme impact conditions (200 ft/sec against a rigid steel plate), which is well below the data distortion threshold. Prototype omnidirectional accelerometers demonstrated less than ± 7 percent isotropic deviation from a linear calibration characteristic. Three complete prototype penetrometers were assembled and tested. The spherical assemblies were 8.5 inches in diameter and weighed approximately 4.7 pounds. The first prototype penetrometer had a faulty battery and was only partially successful. Prototypes No. 2 and 3 were completely functional, demonstrating good dynamic response and a high degree of ruggedness. Field impact tests demonstrated the expected characteristic impact signatures and demonstrated excellent isotropic reproducibility.

An engineering model of the data relay subsystem required for the Apollo Lunar Survey Probe mission was assembled and functionally tested. A simulation test was successfully conducted of the complete communications link from multiple impacting penetrometers to the data relay to receiving equipment aboard the Apollo CSM. The data relay equipment and associated communication analyses are described in Section 6, while the communication link systems tests results are summarized in Section 7.

A reliability program was conducted in support of the penetrometer system design. Unqualified components were subjected to impact evaluation tests, including measurement of transients during impact in addition to impact

survival. The reliability analyses and predictions for the major portions of the lunar penetrometer system are summarized in Section 8 of this report.

A preliminary design was completed of a flight model lunar penetrometer system compatible with the proposed Apollo Lunar Survey Probe mission. Performance specifications were prepared for all subassemblies of this flight design. These are contained in a comprehensive Program Plan, which is presented under separate cover as Aeronutronic Publication No. U-3557.

Major accomplishments under the Lunar Penetrometer System Program include the following:

(1) Development of the first workable omnidirectional accelerometer.

(2) Development of omnidirectional impact-insensitive telemetry.

(3) Accumulation of a comprehensive file of accurate impact signatures characteristic of a wide range of material properties.

(4) Simulation of LEM lunar landings.

(5) Demonstration of working prototype penetrometers with repeatable, accurate output signals and good isotropic characteristics.

(6) Demonstration of a complete communications link from multiple penetrometers through a data relay to the Apollo CSM.

From the overall program results it is concluded that the lunar penetrometer system constitutes a promising means for measuring lunar surface characteristics with a high degree of accuracy and for certifying the lunar surface to be adequately strong for the first Apollo landing on the moon.

SECTION 3

SYSTEM DESCRIPTION

3.1 MISSION DEFINITION

The lunar penetrometer system has been designed to make direct measurements of the lunar surface characteristics to fulfill the objectives of:

(1) Certifying a safe landing site for the Apollo Lunar Excursion Module (LEM).

(2) Extending man's fundamental knowledge of the moon.

The site certification mission defined during the course of the Lunar Penetrometer Program is illustrated in Figure 3-1. This mission features the use of Apollo spacecraft orbiting the moon for reconnaissance purposes prior to the first Apollo mission to land a LEM on the moon. The LEM assembly carried on this mission does not carry landing gear and is not intended for lunar descent. Eight Lunar Survey Probe (LSP) packages are mounted on four sides of the LEM descent stage. During the orbital reconnaissance mission, the probes are selectively launched to place site certification payloads onto potential LEM landing sites.

As illustrated in Figure 3-1, two retro firings bring the LSP package out of orbit to a nominally zero velocity relative to the lunar surface at an altitude of between 943 and 3770 feet. The payload deployed at this point includes a camera-carrying survivable capsule and the lunar penetrometer system. The penetrometers and the survivable capsule are deployed simultaneously so that the relative landing positions of the survivable capsule and the penetrometers are not influenced by any residual lateral velocity

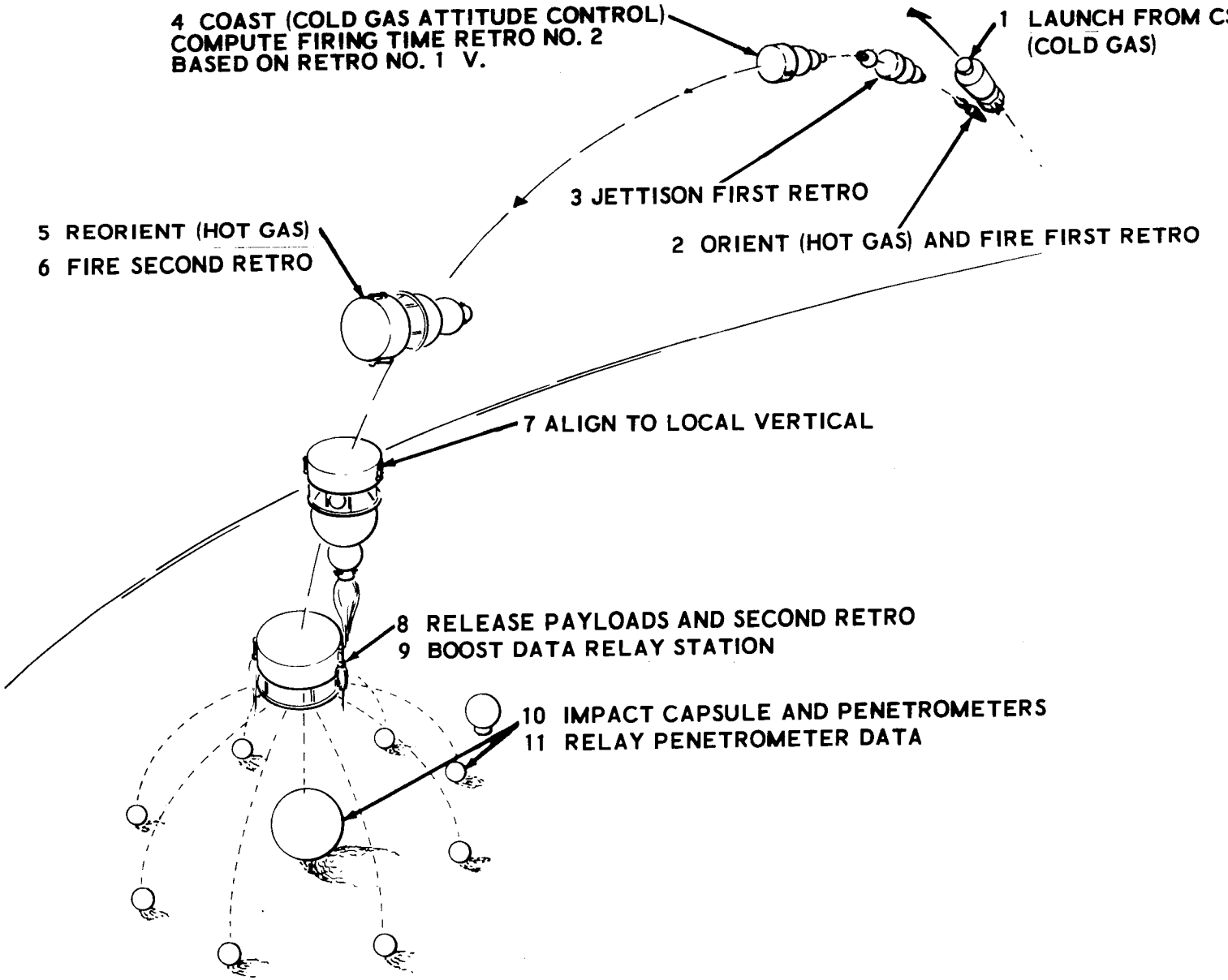
4 COAST (COLD GAS ATTITUDE CONTROL)
COMPUTE FIRING TIME RETRO NO. 2
BASED ON RETRO NO. 1 V.
1 LAUNCH FROM CSM
(COLD GAS)
3 JETTISON FIRST RETRO
2 ORIENT (HOT GAS) AND FIRE FIRST RETRO
5 REORIENT (HOT GAS)
6 FIRE SECOND RETRO
7 ALIGN TO LOCAL VERTICAL
8 RELEASE PAYLOADS AND SECOND RETRO
9 BOOST DATA RELAY STATION
10 IMPACT CAPSULE AND PENETROMETERS
11 RELAY PENETROMETER DATA

of the probe package. The penetrometers impact the lunar surface at a vertical velocity of between 100 to 200 ft/sec and a horizontal velocity of less than 30 ft/sec. In order to impact within the high-resolution viewing range of the camera and the survivable capsule, the penetrometers are to impact the surface at a nominal distance of from 200 to 500 feet from the landed survivable capsule, with the specific target distance to be selected at a later date when the camera design becomes firm.

Design requirements imposed on a lunar penetrometer system by the LSP site certification mission are summarized in Table 3.1. The system is required to deploy eight spherical penetrometers of nominally 8.5 inches diameter. The penetrometers are to be capable of transmitting acceleration versus time signatures upon impact on surfaces ranging from very high bearing strengths (e.g., rock) down to appreciably less than the 12 psi LEM bearing strength requirement. It is a design objective to keep all sensing and transmitting errors in the signal from the penetrometer to less than 10 percent, independent of the direction of impact of the penetrometer spheres on the surface.

The data relay portion of the lunar penetrometer system hovers above the surface and is required to receive signals from the eight impacting penetrometers, including a worst-case condition when all eight penetrometers impact simultaneously, and to amplify the signals and transmit them to receiving and recording equipment aboard the orbiting Apollo CSM spacecraft. (In addition to the previously mentioned LEM assembly, the spacecraft includes a combined command module and service module, designated the CSM.) The maximum communication ranges required of the lunar penetrometer system are 2 nm from the impacting penetrometer to the data relay and 100 nm from the data relay to the orbiting CSM. There must be sufficient power margins in the penetrometer signal to overcome signal attenuation as the penetrometer buries itself into the surface.

To be compatible with the LSP package, the entire lunar penetrometer system was targeted to be contained within a cylindrical volume 26 inches in diameter by 15.3 inches high. This requirement is expected to be modified as the LSP vehicle becomes better defined. It is a firm design objective that the total weight for the lunar penetrometer system assembly not exceed 100 pounds.

3.2 SYSTEM FUNCTIONAL DESCRIPTION

Figure 3-2 illustrates in block diagram form the overall lunar penetrometer system, consisting of the Penetrometer, Data Relay, and CSM Receiving subsystems. The Penetrometer subsystems perform the function of measuring the dynamic acceleration versus time signature generated upon impact with the lunar surface and telemetering this signature to the hovering Data Relay. The Data Relay receives the signals from each of the eight penetrometers, demodulates the signals, and multiplexes the data using eight

TABLE 3.1

LUNAR PENETROMETER DESIGN REQUIREMENTS

Penetrometers	
Number	8
Diameter (Nominal)	8.5 in.
Impact Velocity, Vertical	100 to 200 ft/sec
Lateral	0 to 30 ft/sec
Lunar Surface, Density (ρ)	10 to ∞ lb/ft^3
Bearing Strength (σ)	$<$ 12 to ∞ lb/in.^{2}
Sensing and Transmitter Error	$\pm$10 percent
Data Relay	
Range, from Penetrometer	2 nm
from Apollo CSM	100 nm
Total Assembly	
Diameter	26 in.
Height	15.3 in.
Weight	$\lesssim$ 100 lb

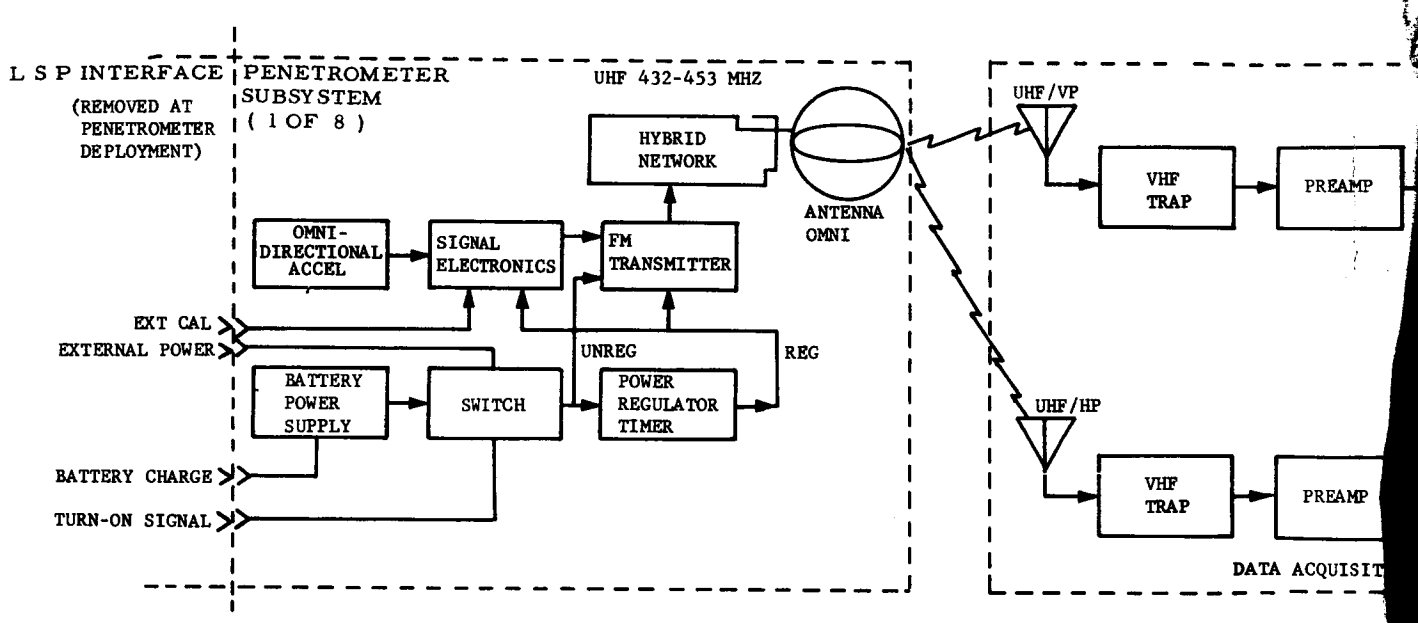
L S P INTERFACE
(REMOVED AT PENETROMETER DEPLOYMENT)
PENETROMETER SUBSYSTEM (1 OF 8)
UHF 432-453 MHZ
HYBRID NETWORK
ANTENNA OMNI
OMNI-DIRECTIONAL ACCEL
SIGNAL ELECTRONICS
FM TRANSMITTER
EXT CAL
EXTERNAL POWER
UNREG
REG
BATTERY POWER SUPPLY
SWITCH
POWER REGULATOR TIMER
BATTERY CHARGE
TURN-ON SIGNAL
UHF/VP
VHF TRAP
PREAMP
UHF/HP
VHF TRAP
PREAMP
DATA ACQUISIT

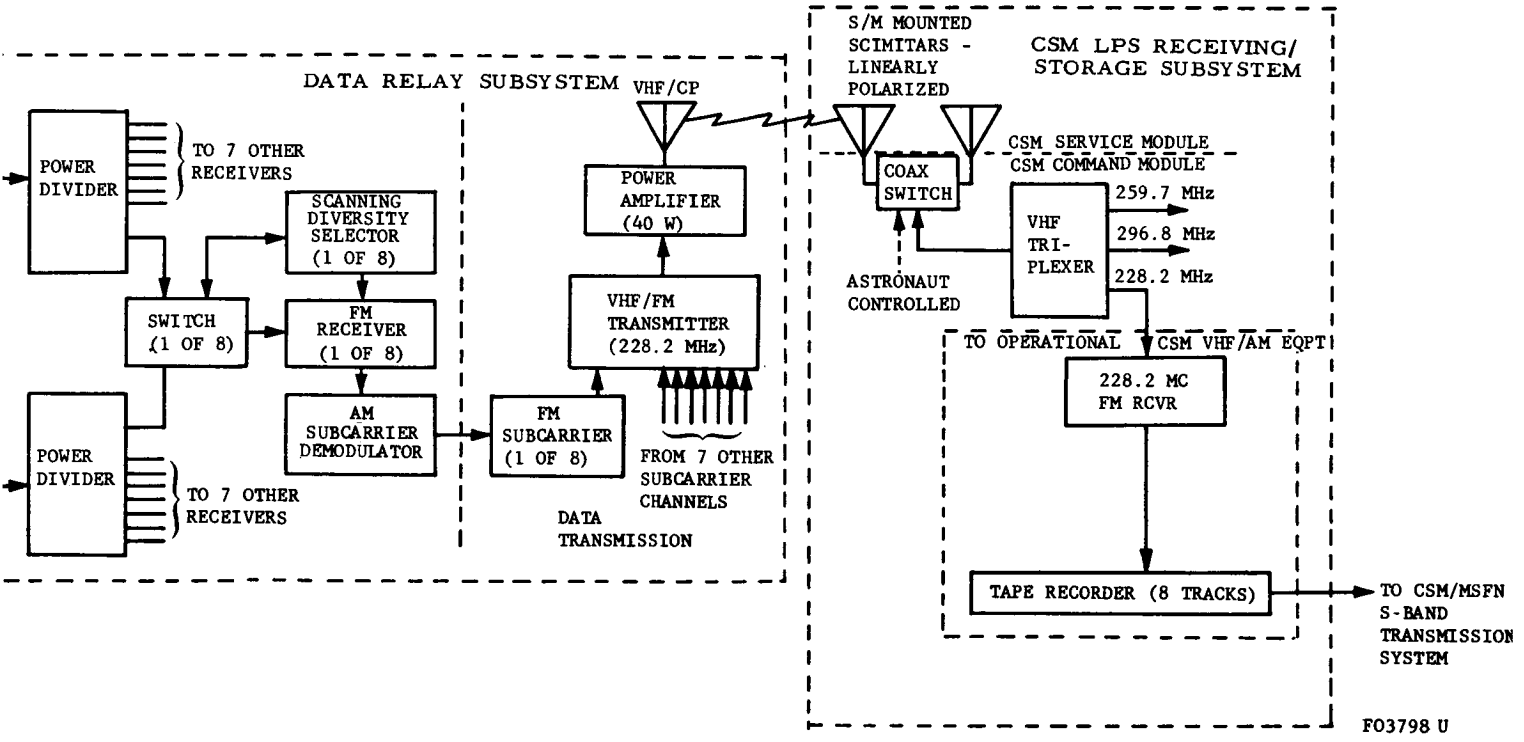

FIGURE 3-2. LUNAR PENETROMETER SYSTEM BLOCK DIAGRAM

[redacted]

constant bandwidth subcarriers for transmission to the orbiting CSM. The functions of each of the three major subsystems are described in the succeeding paragraphs.

3.2.1 PENETROMETER SUBSYSTEM

Each of the eight penetrometers contains complete sensing, signal conditioning, and telemetering capabilities to transmit the measured impact data to the hovering Data Relay. Each penetrometer subsystem contains an omnidirectional accelerometer, signal-processing electronics, a transmitter, a near isotropic transmitting antenna, a battery power supply, and a power regulator/timer. These functional subassemblies are mounted in a metallic sphere surrounded by a spherical layer of balsa wood which performs the functions of absorbing excess energy during impact upon rigid surfaces and increasing measurement accuracy by lowering the density of the penetrometer subsystem during impact on soft surfaces.

a. Acceleration Sensing. The ommidirectional accelerometer is designed to sense impact accelerations in the range of 50 to 7000 earth g, regardless of penetrometer orientation at impact. The design objective of the complete penetrometer subsystem is to measure and transmit the dynamic impact acceleration with an error of less than 10 percent.

b. Signal-Processing Electronics. The signal-processing electronics receive the impact acceleration signature from the accelerometer, condition the signal in accordance with a predetermined transfer function, and amplitude-modulate a subcarrier with the conditioned signal. The transfer function provided by the signal electronics is a two-step linear function designed to place maximum accuracy in the lower portion of the acceleration range.

c. Transmitter. The AM subcarrier from the signal-processing electronics frequency-modulates a nominal 432-450 MHz transmitted carrier; the individual carrier frequencies of the eight penetrometers are spaced at 3 MHz intervals over this band. The solid-state transmitter delivers a nominal 0.5 watt carrier power to the antenna subassembly.

d. Antenna. The antenna subassembly, consisting of two slow-wave loops fed in quadrature via a hybrid network, provides near-isotropic radiation patterns with all possible states of polarization. The structural design details of the antenna, as with the other penetrometer subassemblies, are included in Aeronutronic Publication U-3557.

e. Battery Power Supply. The battery power supply provides a minimum 22-volt unregulated output over the mission life-time of the penetrometer subsystem (from LSP deployment until lunar impact). The battery power supply consists of a string of rechargable cells maintained at their nominal charge capacity by the LSP power supply until penetrometer subsystem deployment.

f. Power Regulator/Timer. The power regulator/timer subassembly performs two functions. The power regulator provides a regulated +17 volts and -3.3 volts power supply to the using subassemblies throughout the penetrometer subsystem mission lifetime. The timer subassembly switches the penetrometer subsystem to internal power for a fixed, preset interval of time upon deployment from the LSP.

3.2.2 DATA RELAY SUBSYSTEM

The Data Relay is an integral portion of the Lunar Survey Probe vehicle which is designated to the lunar penetrometer system. It consists of:

(1) The necessary structure to contain and deploy the penetrometers;

(2) The necessary receiving equipment to receive the UHF rf signals radiated by the penetrometers;

(3) The equipment to retransmit the combined data at a specific VHF rf frequency for reception by the orbiting CSM; and

(4) A self-contained source of electrical power.

a. Data Reception. Two polarization diverse receiving antennas are utilized because the penetrometers are not attitude stabilized and, therefore, can furnish radiated signals with various polarization states. Signals from the two receiving antennas are fed to rf amplifiers and then to two power dividers. The power dividers allow a total of eight receivers to be used with either antenna. At the input to each FM receiver is an rf switch to automatically switch to the unused antenna at any time the received signal drops below a preset threshold value. Each of the eight receivers is tuned to receive the transmission from one of the specific eight penetrometers.

The FM receivers, operating in the 432-453 MHz range, each contain wideband discriminators. Output signals from the eight receivers go to 40 KHz AM demodulators, which produce analog output signals corresponding to the accelerations measured by the penetrometer.

The overall receiving system noise figure is less than 6 db. VHF signal rejection is provided in the receiving transmission line to minimize effects of the high power emanating from the relay transmitting antenna. Mission geometry relative to Data Relay receiving antenna aspect angle coverage requirements is currently undefined; consequently, antenna coverage details remain unspecified until probe vehicle configuration and deployment profiles receive definition.

b. Data Transmission. The Data Relay is required to transmit the multichannel measured acceleration data a distance of 100 nm to the orbiting CSM. The relay radio link employs an FM/FM VHF transmission system with a nominal 40-watt FM transmitter output power operating at an rf frequency in the 225-260 MHz band. An eight-channel constant bandwidth subcarrier modulation will be applied to the rf carrier. The individual penetrometer measured acceleration data (i.e., output of the data acquisition section) frequency modulate the eight subcarrier channels. The block diagram of Figure 3-2 shows the conventional VHF data transmission functional elements. Transmitting antenna aspect angle coverage requirements remain unspecified for reasons explained in the preceding paragraph.

3.2.3 CSM RECEIVING SUBSYSTEM

a. Data Reception. A detailed description of the Block II CSM operational communication system is given in Appendix F. As shown in Figure 3-2, the CSM contains two service-module mounted VHF scimitar antennas. Selection between the two antennas is manually controlled by the CSM crew using a remotely controlled coax switch. The selected antenna is connected through this switch to a three-part VHF multiplexer. Two of the ports, 296.8 MHz and 259.7 MHz, are required for operational CSM voice communications. A third port with an assigned frequency of 228.2 MHz is reserved for scientific and R&D purposes. It is likely that this frequency would be used for the Data Relay--CSM transmission link.

Those additional equipments required for reception and processing of the Data Relay transmitted signals are indicated by the dashed lines in Figure 3-2. The FM receiver contains a wideband carrier discriminator. The discriminator output is fed to the wide band analog tape recorder.

b. Data Processing and Storage. The existing CSM recorder does not have the capability for recording of the eight data subcarriers; consequently, a separate recorder is required for this purpose. This recorder must also have a playback capability for subsequent retransmission of the penetrometer data to earth via the CSM-Manned Space Flight Network S-band transmission system.

3.3 SYSTEM PRELIMINARY DESIGN

3.3.1 PENETROMETER

A preliminary design of the omnidirectional impact sensing lunar penetrometer is presented in Figure 3-3. The design locates the omnidirectional accelerometer at the center of the 3-1/2 inch diameter payload assembly. Beneath this is the power supply, voltage regulator, and electronic initiation switch; above are the signal-processing electronics and transmitter. The antenna consists of two orthogonal great circle loops located in the equatorial and polar planes. They are spaced 1/2 inch from the inner sphere by means of polypropylene plastic spacers. The transmitter output is inductively coupled to the antenna elements by an orthogonal pair of metal feed loops which extend through the equatorial region of the aforementioned spacer. The entire assembly is protected from failure due to impact upon rigid surfaces by the presence of a spherical balsa wood impact limiter extending to a diameter of 8.5 inches.

The central structural housing is fabricated of aluminum in three pieces. The center section forms the backbone of the structure and is provided with a web upon which the accelerometer is mounted and the electronic modules are assembled. The lower structure is retained by a peripheral equatorial coupling nut to allow replacement of the critical power supply section following assembly, checkout, and potting. The upper structure is threaded directly into position with no provision for removal, since this portion of the electronics is considered to be not amenable to repair.

All critical circuit electronic components are bonded to rigid surfaces, but are not allowed to be fully potted. This minimizes the loads, consequently minimizing deformations imposed upon them at impact, and thereby reduces the frequency shifts to a minimum. As an additional aid to the minimization of frequency shift, the extremely critical oscillator area is provided with a thin outer wall (to bridge externally imposed loads) and a thick inner wall (supporting only its own weight). This minimizes the deflection of the latter which severely affects circuit tuning.

All voids between the electronic modules and the primary spherical structure are fully potted to provide distributed, uniform load paths regardless of the direction of impact. An exception is the accelerometer mounted in the center structure,which is provided with a slight void about its pressure-sensitive case to minimize the coupling of any sonic resonances which may be excited upon impact.

Access to two eight-pin electrical connectors located in the equatorial plane of the structure is provided by two 1/2-inch-diameter holes through

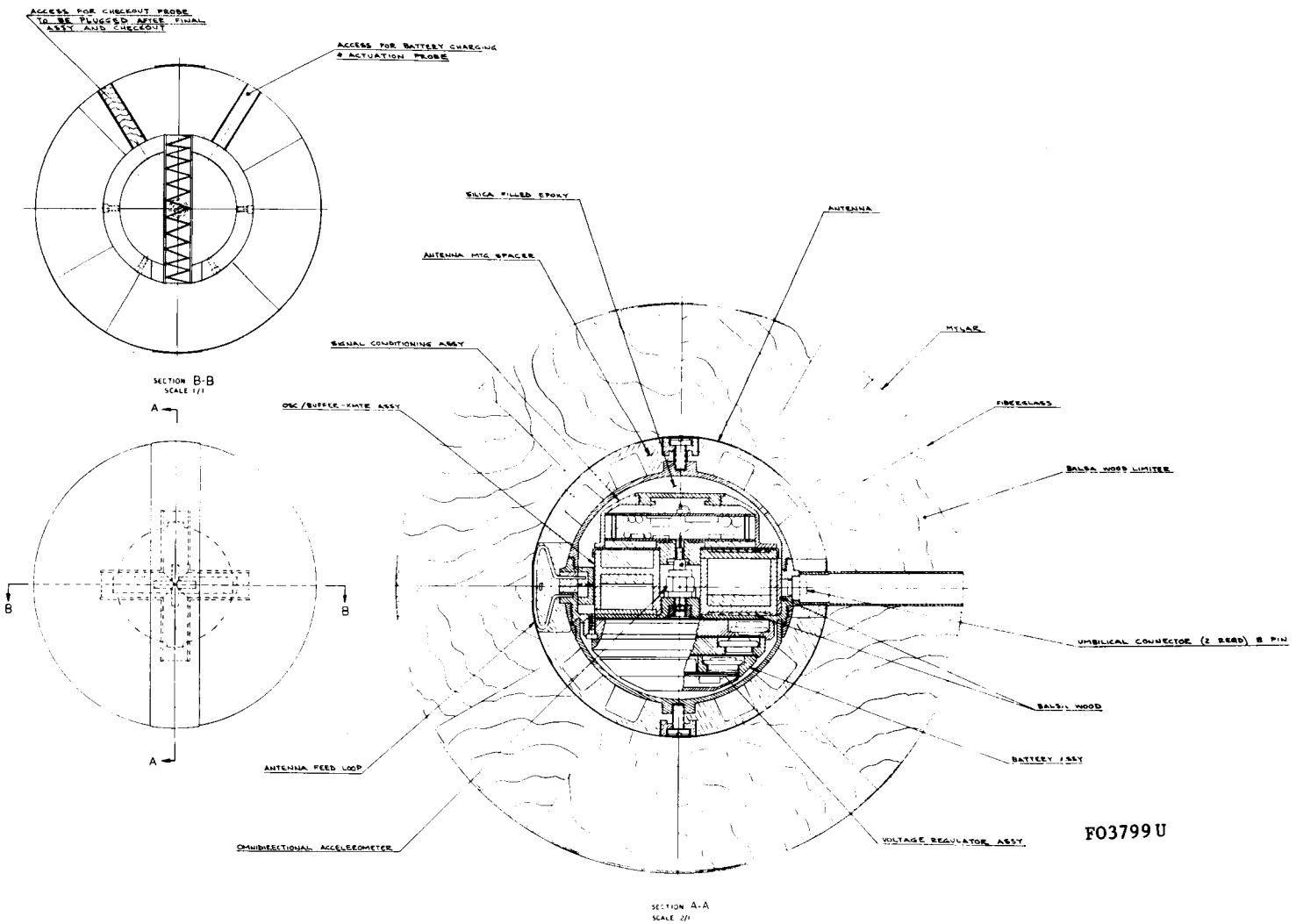

FIGURE 3-3. PRELIMINARY LAYOUT--FLIGHT PENETROMETER

the limiter. The purpose of these connectors is twofold. One is used for electrical checkout and calibration; its access hole will be filled with a plug of balsa limiter material prior to flight. The other plug is for charge of the battery power supply and for power turn-on via an electronic switch prior to launch. Access to this plug is provided throughout translunar flight by a removable probe connected to the Data Relay System power and sequencing assembly.

3.3.2 DATA RELAY

A preliminary layout of the Data Relay System is presented in Figures 3-4 and 3-5. The configuration shown packages the data relay electronics and eight 8-1/2-inch-diameter penetrometers with ejection mechanisms into an envelope 26 inches in diameter and 13.8 inches high. Figure 3-6 gives an expanded view of the electronics packaging.

The primary structural element of the assembly is a central octagonal parallel piped tube approximately 9 inches across. This tube forms the structural housing for the data relay electronics subassembly. The latter is built up from separate electronic modules which are then mounted into position on properly damped aluminum honeycomb shelves provided with appropriate spacers. The entire subassembly will thus be wired and checked out as a separate, readily accessible unit and then installed into position within the primary structure.

The transmitting and receiving antennas consist of identical element arrays differing only with respect to their length and operational frequency. Each array consists of four identical telescoping elements; these are positioned one above the other at two locations 90 degrees apart. Each antenna system provides full hemispherical coverage.

The eight penetrometers are positioned around the periphery of the structure in a staggered array. This approach maintains the payload diameter within the specified 26-inch-diameter envelope restriction. Each layer of four penetrometer balls (spaced 90 degrees apart) is provided with four "cupped" brackets mounted between adjacent spheres; these act to provide axial support during thrust. Lateral support and retention is provided by two straps extending peripherally around each set of four balls. Each strap is provided with two bolt cutters and appropriate fittings 180 degrees apart to allow for redundant release and deployment of the omnidirectional impact-sensing penetrometers.

The energy required for ejection is provided by springs located directly behind each penetrometer sphere. These spring packs are installed into the octagonal structure following installation of the electronics assembly. Coincident with the location of these ejection springs an electrical probe is provided from within the electronics assembly. This probe mates with the penetrometer during flight via the previously mentioned limiter access hole and allows for a trickle battery charge plus power turn-on prior to launch.

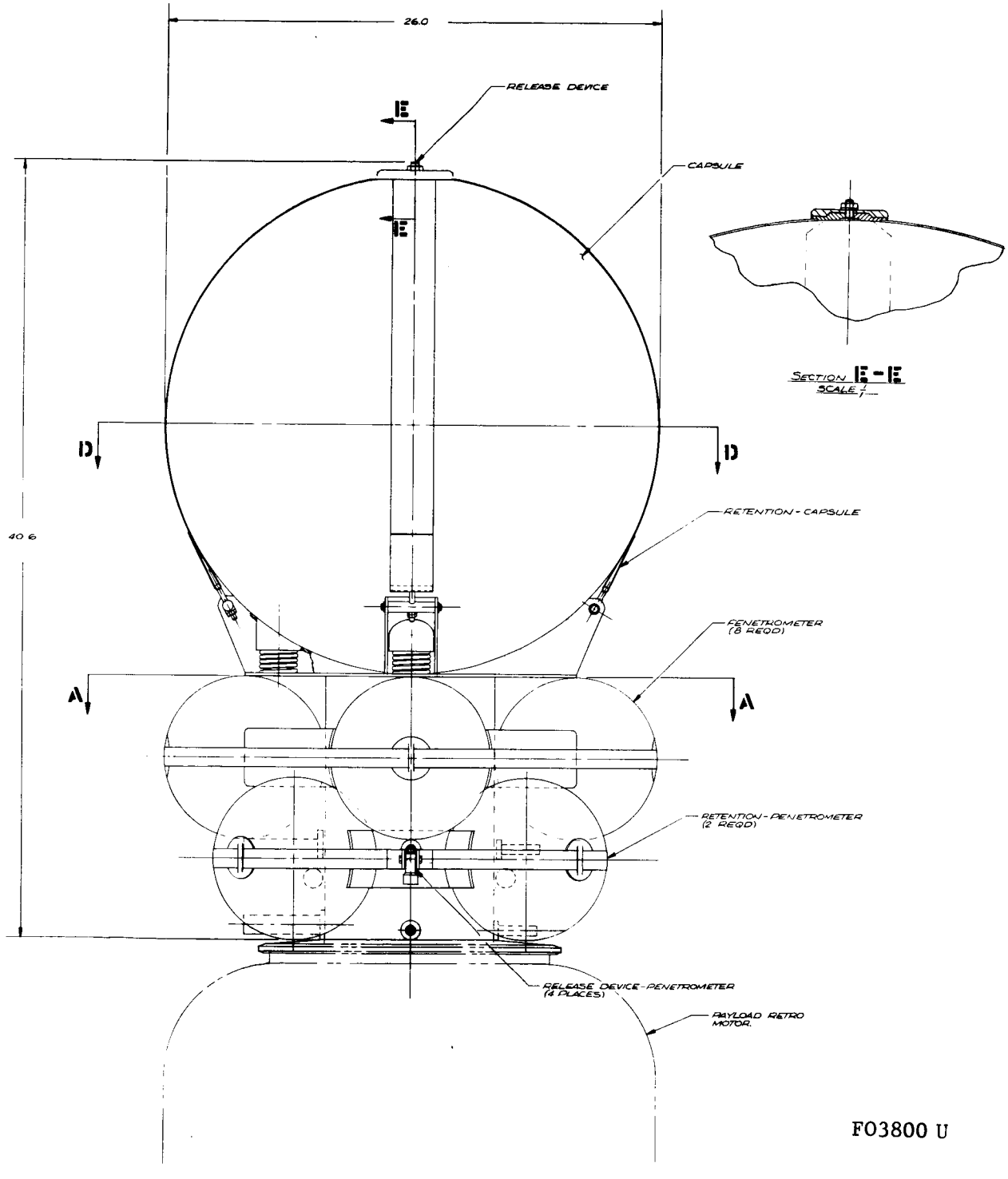

FIGURE 3-4. DATA RELAY PRELIMINARY LAYOUT

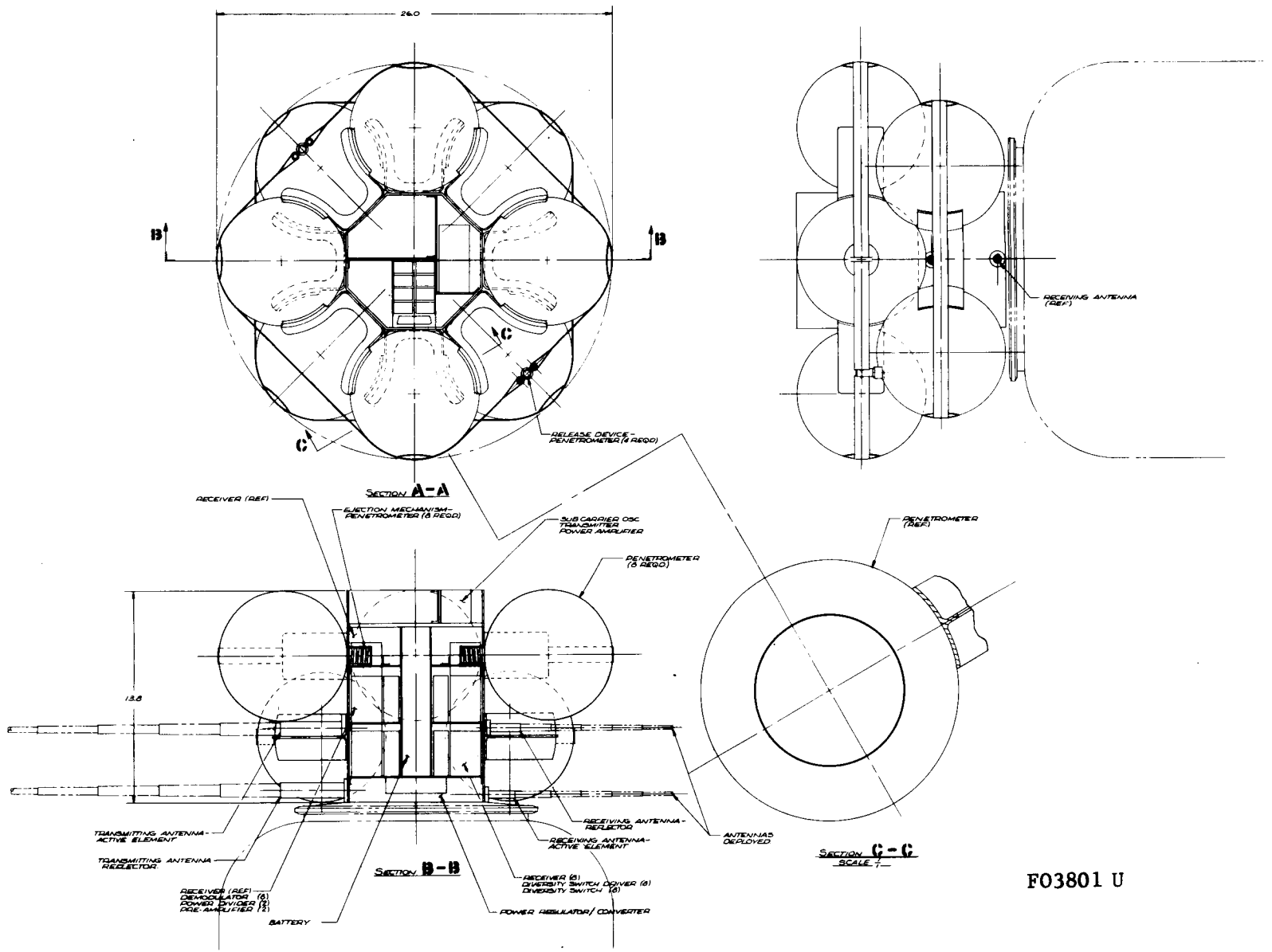

FIGURE 3-5. DATA RELAY PRELIMINARY MECHANICAL DESIGN DETAILS

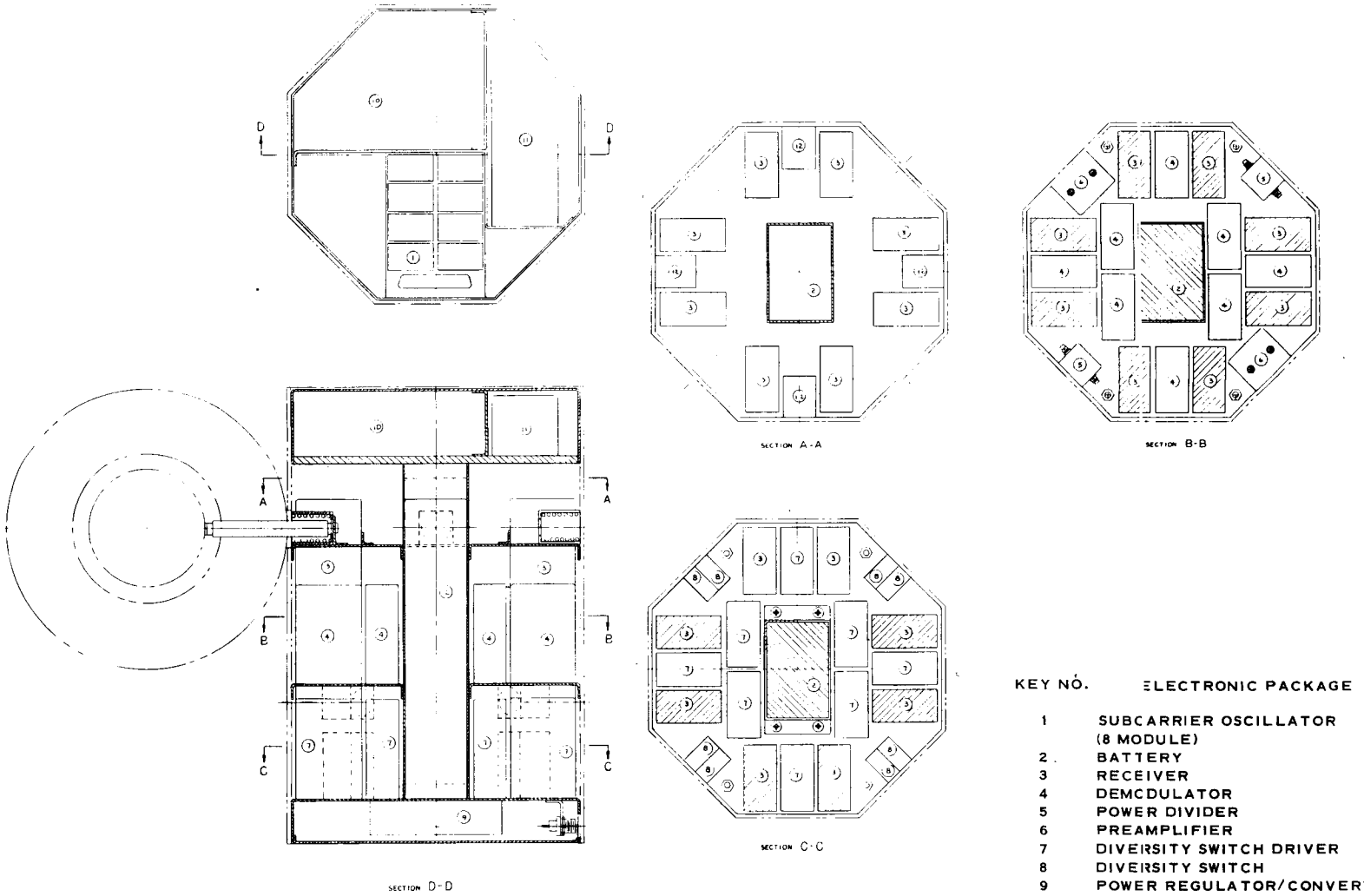

FO3802 U

FIGURE 3-6. DATA RELAY PRELIMINARY ELECTRONIC PACKAGING LAYOUT

SECTION 4

IMPACT RESEARCH PROGRAM

4.1. INTRODUCTION

The impact research program conducted a parametric study of low velocity impact phenomena resulting from the impingement of accelerometer-equipped penetrometers on target materials carefully chosen to represent a broad range of physical characteristics. These phenomena were studied by testing a series of accelerometer-equipped spherical penetrometers having varied diameter, mass, and density characteristics delivered at velocities of from 20 to 250 fps into target materials representing lunar surface models, and spanning the range of engineering requirements set up for LEM landing specifications. Tests were conducted under atmosperic and vacuum environments to evaluate the effect of vacuum on soil characteristics.

The LEM test program complemented the impact research tests in evaluating several of the target materials. The LEM test facility simulated the LEM mass and landing gear configuration, including the landing pad and crushable honeycomb strut. Data were obtained for depth of penetration into the target materials under simulated LEM lunar landing conditions. These data were then compared with the impact research test data for the same target materials in order to correlate penetration depths with the acceleration-time curves obtained with the penetrometers.

The impact research and LEM pad testing programs have successfully demonstrated that:

(a) Acceleration-time signatures are unique to the specific materials tested

(b) From the acceleration-time signatures, approximations of the density and bearing strength of these specific materials can be ascertained and the depths of penetration of a penetrometer predicted

(c) Knowledge of these material characteristics can, in turn, be utilized to predict the depths to which a LEM pad will penetrate regardless of landing geometry.

4.2 TARGET MATERIALS

The target materials utilized for impact research testing were defined by mutual agreement between LRC and Aeronutronic. The group of 10 materials is listed and their physical characteristics described in Table 4.1. These materials were specifically selected to represent:

(1) Effective geological models of lunar surface materials, as follows:

Model	Simulating Material
Suspended dust	Loosely packed Cab-O-Sil
Noncohesive particulate material	Porous mixtures of cobble to dust-sized particles
Cohesive froths	Brittle organic foam

(2) A range of solid mechanics properties defined by engineering limits to the LEM landing capability that encompasses a rigid model with infinite bearing strength of 0.8 psi at 18 inches.

TABLE 4-1

PHYSICAL CHARACTERISTICS OF TARGET MATERIALS

MATERIAL DESIGNATION	COMPOSITION	GRAIN SIZE RANGE MAX	GRAIN SIZE RANGE MEAN	GRAIN SIZE RANGE MIN.	DENSITY IN LB/FT^3	ANGLE OF REPOSE IN DEGREES	DEGREE OF ROUNDING	SOURCE OF MATERIAL	PREPARATION OF MATERIAL
1. RIGID MATERIAL	STEEL PLATE BACKED BY REINFORCED CONCRETE								
2. BASALT AGGLOMERATE (COBBLE-PEBBLE MIXTURE)	OLIVINE BASALT: PLAGIOCLASE 40%, PYROXENE 40%, OLIVINE 15%, MAGNETITE 5%	21.6CM	3.7MM	2 MM	≈117		EXTREMELY ANGULAR	RECENT LAVA FLOW, PISGAH CRATER, SAN BERNARDINO COUNTY, CALIFORNIA	HAND SORTING AND MECHANICAL CRUSHING AND SIEVING
3. BASALT SAND	OLIVINE BASALT	500μ	340μ	63μ	90.0	46°	VERY ANGULAR	RECENT LAVA FLOW	MECHANICAL CRUSHING AND SIEVING
4. NEVADA NO. 60 SAND	QUARTZ 100%	420μ	160μ	105μ	97.3	36°	WELL ROUNDED	DESERT DUNE SAND, CLARK COUNTY, NEVADA	MECHANICAL SIEVING
5. NEVADA 120 NO. 1 SAND (DENSELY PACKED)	QUARTZ 100%	120μ	70μ	53μ	94.0	36°	WELL ROUNDED	DESERT DUNE SAND	MECHANICAL SIEVING
6. NEVADA 120 NO. 2 SAND (LOOSELY PACKED-AERATED)	QUARTZ 100%	120μ	70μ	53μ	87.6	36°	WELL ROUNDED	DESERT DUNE SAND	MECHANICAL SIEVING
7. BASALT SILT	OLIVINE BASALT	325μ	32μ	20μ	81.0	51°	VERY ANGULAR	RECENT LAVA FLOW	MECHANICAL CURSHING AND SIEVING
8. CABOSIL NO. 1 POWDER (DENSELY PACKED)	SILICA 100%	0.015μ			5.2	48°[1]	SPHERES	CABOT CORPORATION	VAPOR PHASE HYDROLYSIS OF $SiCl_4$
9. CABOSIL NO. 2 POWER (LOOSELY PACKED-AERATED)	SILICA 100%	0.015μ			4.7	48°[1]	SPHERES	CABOT CORPORATION	VAPOR PHASE HYDROLYSIS OF $SiCl_4$
10. FOAM	URETHANE				2.0			CPR DIVISION OF UPJOHN COMPANY	SAW INTO 48 INCH DIAMETER X 10 INCH BILLETS

[1] ANGLE OF REPOSE MEASURED WITH CABOSIL IN SAME FLOCCULATED STATE AS WHEN IMPACT TESTED.

(3) Materials capable of being prepared in dense and loose packing states as follows:

Material	Packing State	Density (lb/ft^3)	Bearing Strength (psi)
Nevada 120-1 sand	Dense	94	108
Nevada 120-2 sand	Loose	87.6	26
Cab-O-Sil No. 1 powder	Dense	5.2	2.5
Cab-O-Sil No. 2 powder	Loose	4.7	0.8

(4) A foam material that simulates both a low density, cohesive, vacuum-welded particulate material, and a cellular rock froth.

(5) A cobble-pebble mixture that investigates the signature of a surface having individual particles corresponding to the dimensions of the penetrometer.

(6) Particulate materials, composed of well rounded grains and very angular grains; as follows:

Material	Grain Roundness	Angle of Repose (degrees)
Basalt sand	Very angular	46
Nevada No. 60 sand	Well rounded	36
Nevada No. 120 sand	Well rounded	36
Basalt silt	Very angular	51

The grain size distribution of the particulate target materials is denoted on Figure 4-1. The cobble-pebble mixture is skewed to the coarse end of the size spectrum, the crushed basalt materials are skewed to the fine end, the natural dune sands are fairly uniform in distribution, and Cab-O-Sil is essentially unidimensional. In the case of Cab-O-Sil, flocculation into ring-shaped clusters of particles caused by humidity and electrostatic effects creates the high degree of porosity ($\approx$ 97 percent) necessary to achieve the low bearing strength (0.8 psi at a depth of 18 inches) exhibited by this material in the fluffed form. Figure 4-2 portrays the shape and size distribution of the individual grains comprising the particulate target materials. The rigid, agglomerate, and foam materials are depicted in Figure 4-3.

The Nevada No. 60 and No. 120 sands are naturally occurring pure quartz dune sands from southern Nevada. They were obtained from the Brumley-Donaldson Company, Los Angeles; dealers in glass and foundry sands. The olivine basalt was collected by Aeronutronic personnel from the Pisgah Crater lava flow and

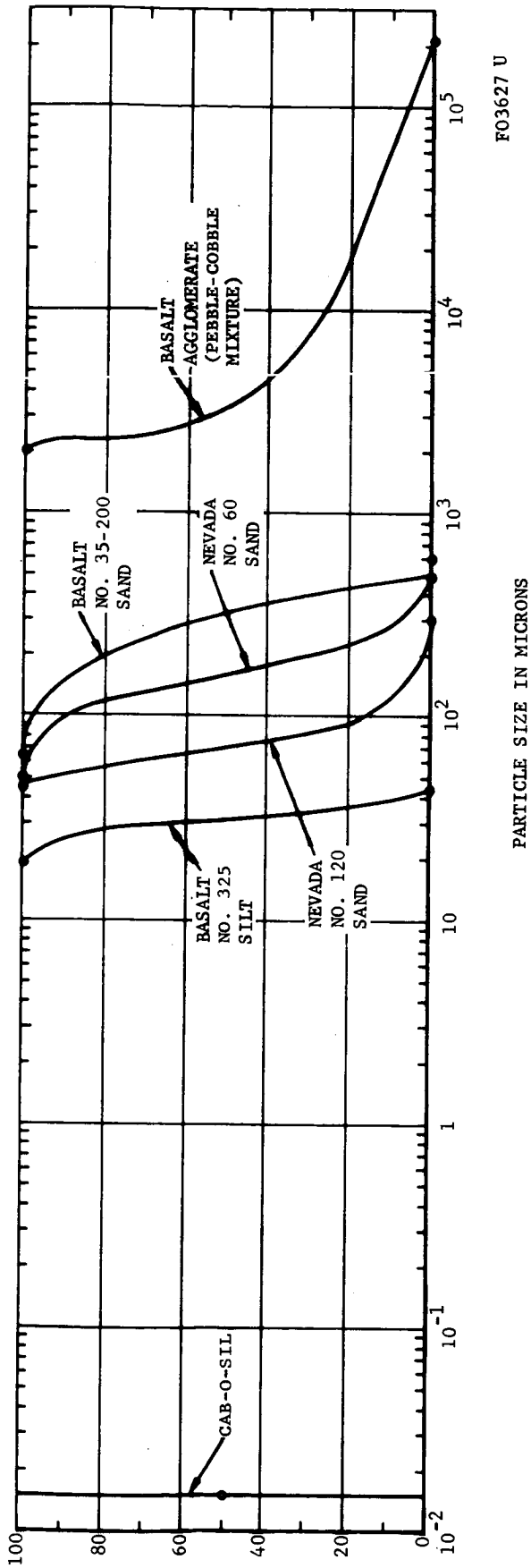

FIGURE 4-1. GRAIN SIZE DISTRIBUTION OF PARTICLE TARGET MATERIALS

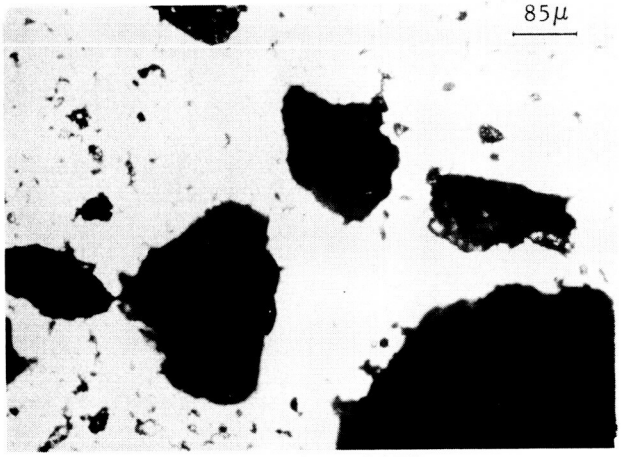

a. BASALT SAND

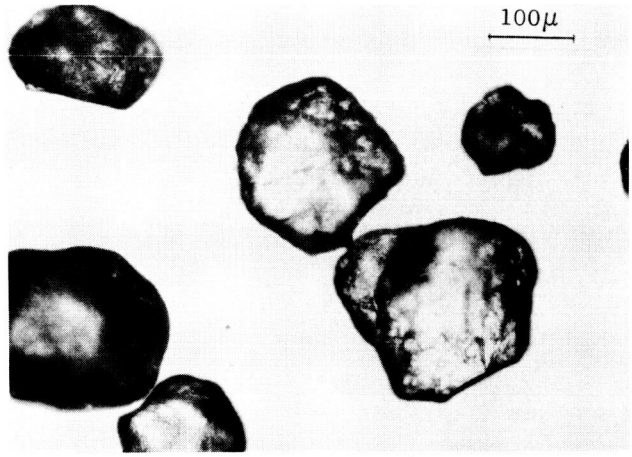

b. NEVADA NO. 60 SAND

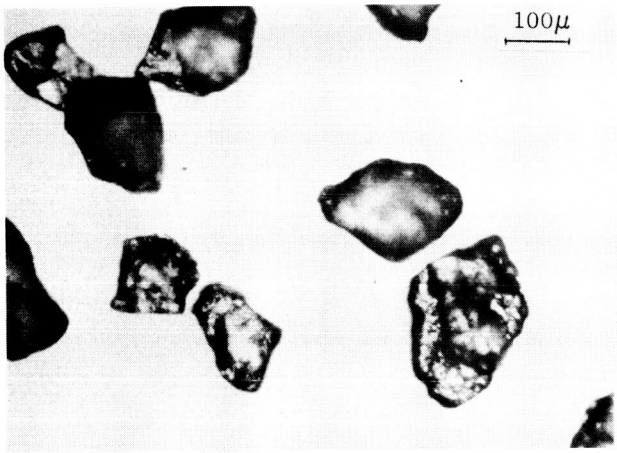

c. NEVADA NO. 120 SAND

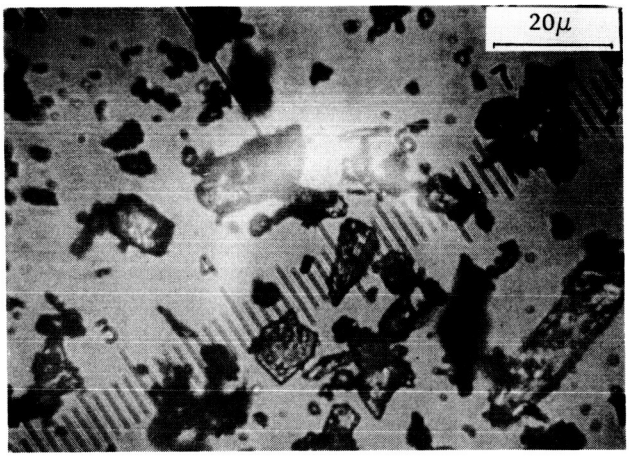

d. BASALT SILT

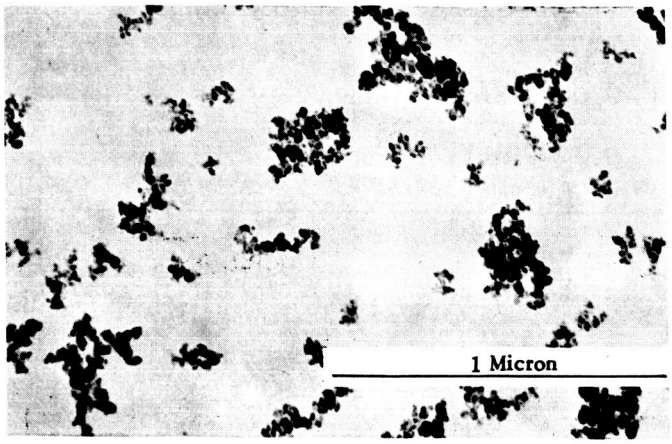

e. CABOSIL

FO3628 U

FIGURE 4-2. PHOTOMICROGRAPHS OF PARTICULATE TARGET MATERIALS

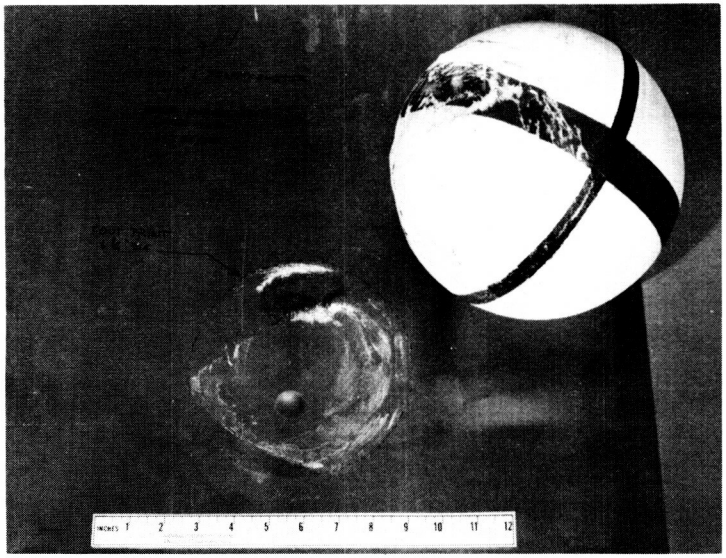

a. RIGID TARGET

b. BASALT AGGLOMERATE TARGET (COBBLE-PEBBLE MIXTURE)

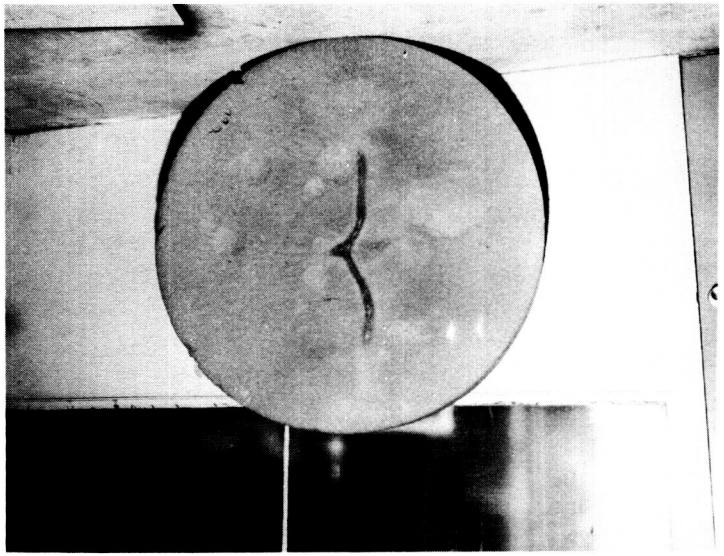

c. FOAM DISKS

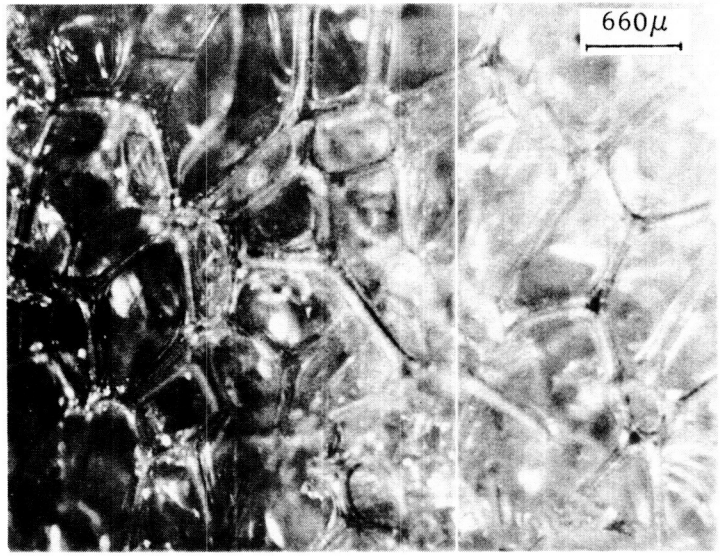

d. CLOSEUP OF FOAM SHOWING CELLULAR STRUCTURE AND DIMENSIONS

FO3629 U

FIGURE 4-3. RIGID, FOAM, AND BASALT AGGLOMERATE TARGETS

crushed and sized by the L. A. Chemical Company, Los Angeles. The Cab-O-Sil and urethane foam materials were obtained directly from the respective manufacturers.

Pisgah Crater olivine basalt is a remarkably homogeneous material. Primary voids occupy from 10 to 25 percent of the volume of surface samples. The flow is relatively recent and that factor coupled to the desert climate has completely retarded weathering so that all of the material collected is unaltered. The vesicles are almost wholly unfilled; those that are open to the atmosphere are limonite stained, the remainder unstained and open. One of the basic reasons this type of material was selected lay with the preponderant microcrystalline ground mass making up over 80 percent of the rock. The approximate mineralogical composition of the rock, including phenocrysts, is as follows:

Mineral	Max Crystal Dimensions (mm) Groundmass	Phenocrysts	Approx Amount Present (percent)
Plagioclase	0.2	1.5	40
Pyroxene	0.2	1.0	40
Olivine	0.2	2.0	15
Magnetite	0.05	None	5

The plagiosclase minerals are lath-like but, when crushed to less than 200μ material, the amount of persistent laths are considerably reduced from 40 percent. The remaining minerals have essentially equidimensional crystal geometries both in free and fractured form

4.2.1 CONDITIONING TECHNIQUES, ATMOSPHERIC

Because of the parametric nature of the impact research program, it was necessary to insure repeatable target characteristics from test to test. Materials No. 1, 2 and 10 of Table 4.1 posed no problems of repeatability and required no special handling or conditioning techniques. However, the particulate materials (No. 3 through No. 9) did require development of special conditioning techniques to obtain repeatable bearing strengths and densities from test to test.

a. Loosely Packed. To obtain a loosely packed (sometimes referred to as fluffed) condition, several techniques were applied to the full scale containers (42-inch diameter by 4 feet high) of test materials.

(1) Tumbling and Rolling. Tumbling and rolling of these large containers (Figure 4-4) resulted in nonuniform samples with bearing strengths varying by as much as a factor of 2 at different positions in each sample. This condition was deemed unacceptable.

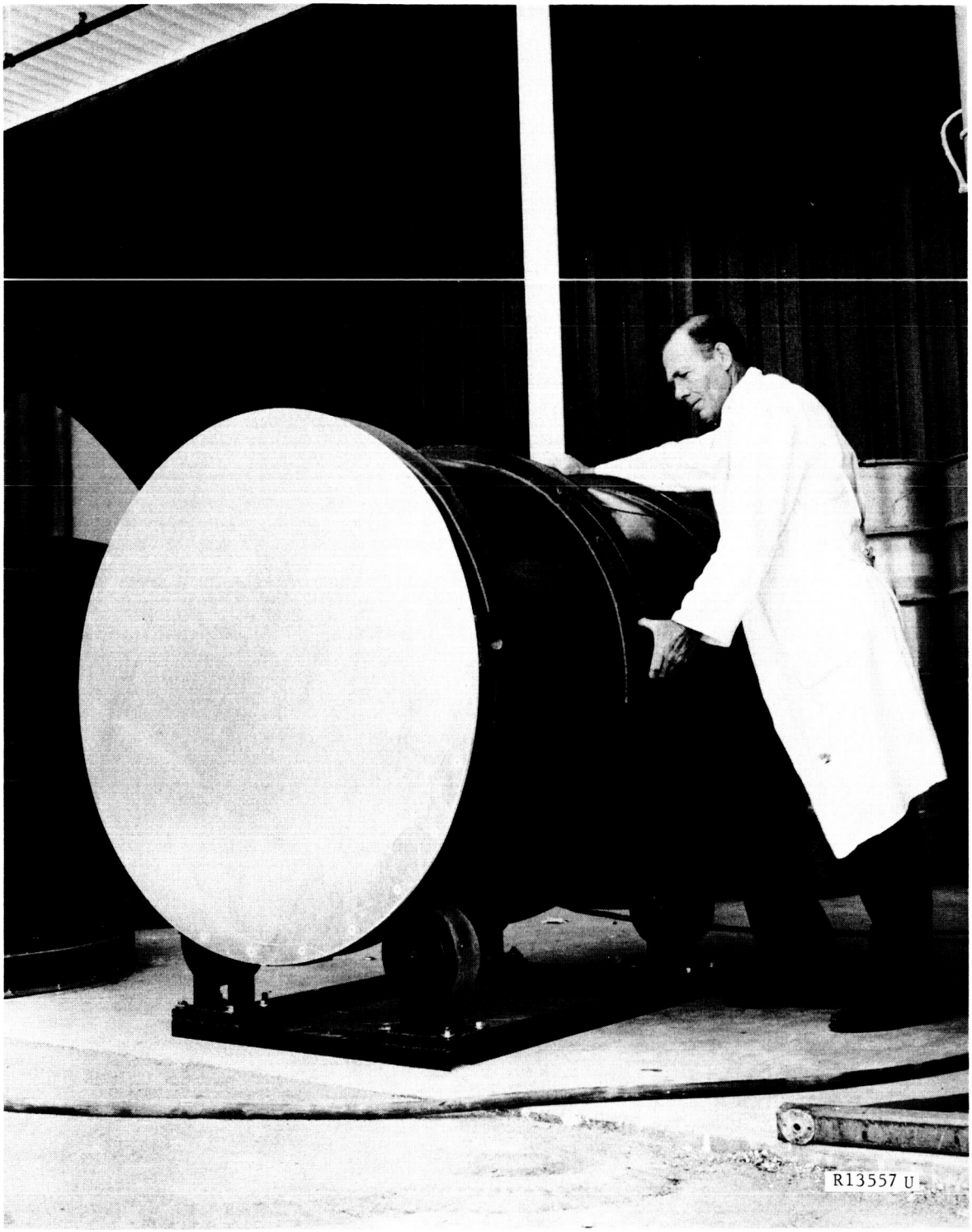

FIGURE 4-4. TARGET MATERIAL CONDITIONING WITH A DRUM ROLLER

(2) Uniform Pour. As a result of the failure in mechanical rolling to provide a uniform sample, a new technique was devised which was called the Uniform Pour conditioning method. This consisted of pouring the material from one container to another through a hopper and hose assembly. The material was uniformly poured layer on layer with a minimum of drop height. It was effective in producing a uniform sample, but presented a time consuming, formidable handling task.

(3) Aeration. In the aeration technique, pressurized gaseous nitrogen was blown through the test material from jets in the bottom on the container. Aeration experiments with two early devices were failures. Venting of the gas through small jets produced a mixing effect limited to a few localized areas. Langley Research Center had been successful in utilizing the aeration method on smaller scale samples and discussions were held with Langley to determine paths of action to improve our technique. Several major suggestions were received.

(a) Increase gas flow through larger distribution system

(b) Increase orifice size and number of orifices

(c) Provide a full sheet of felt over the orifices sealed around the edges to act as a diffuser.

These suggestions were incorporated in a new aeration manifold, shown in Figure 4-5.

After an initial failure, which was corrected with improved sealing, it was used successfully throughout the impact research program for the preparation of all particulate materials.

The complete aeration system, shown in Figure 4-6 consists of the distribution manifold plate at the bottom of the target material container, a filter on the top of the container, and a pressure regulated nitrogen supply. The distribution manifold contains 1/8-inch orifices spaced 4 inches apart and covered by a 1/16-inch felt pad which acts as a diffuser and prevents clogging of the orifices. Commercial fiberglass furnace filters are utilized to prevent dust from blowing out of the containers. The aeration process is controlled by adjustment of the nitrogen pressure regulators and the time duration of aeration. Each material required a slightly different process for optimum results. Those processes are specified below:

(a) Nevada No. 60 Sand. Aerate material at 400 psig for one minute. Wait 15 minutes for the material to settle before performing tests.

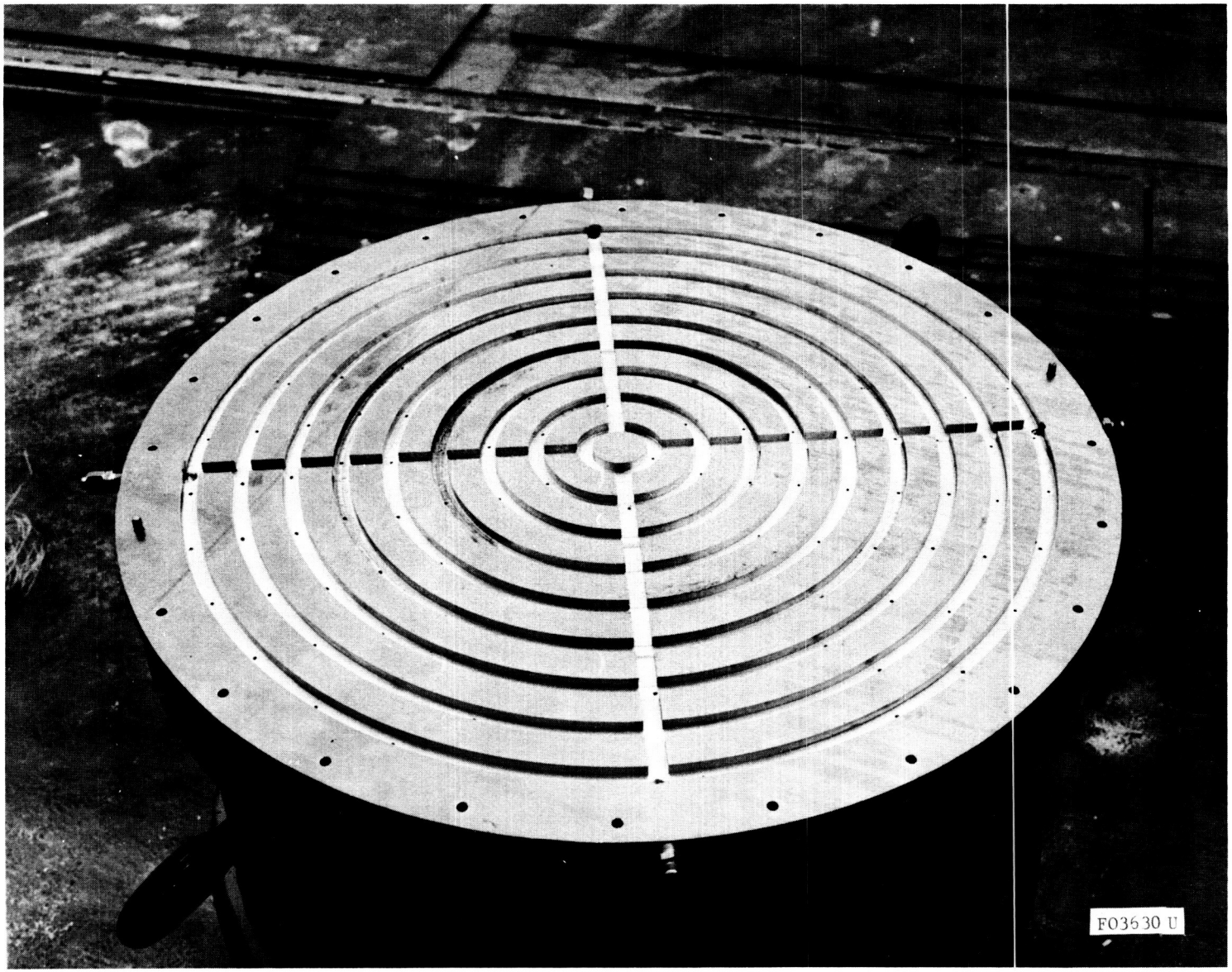

FIGURE 4-5. AERATION MANIFORD, INVERTED, WITHOUT SEALING LID

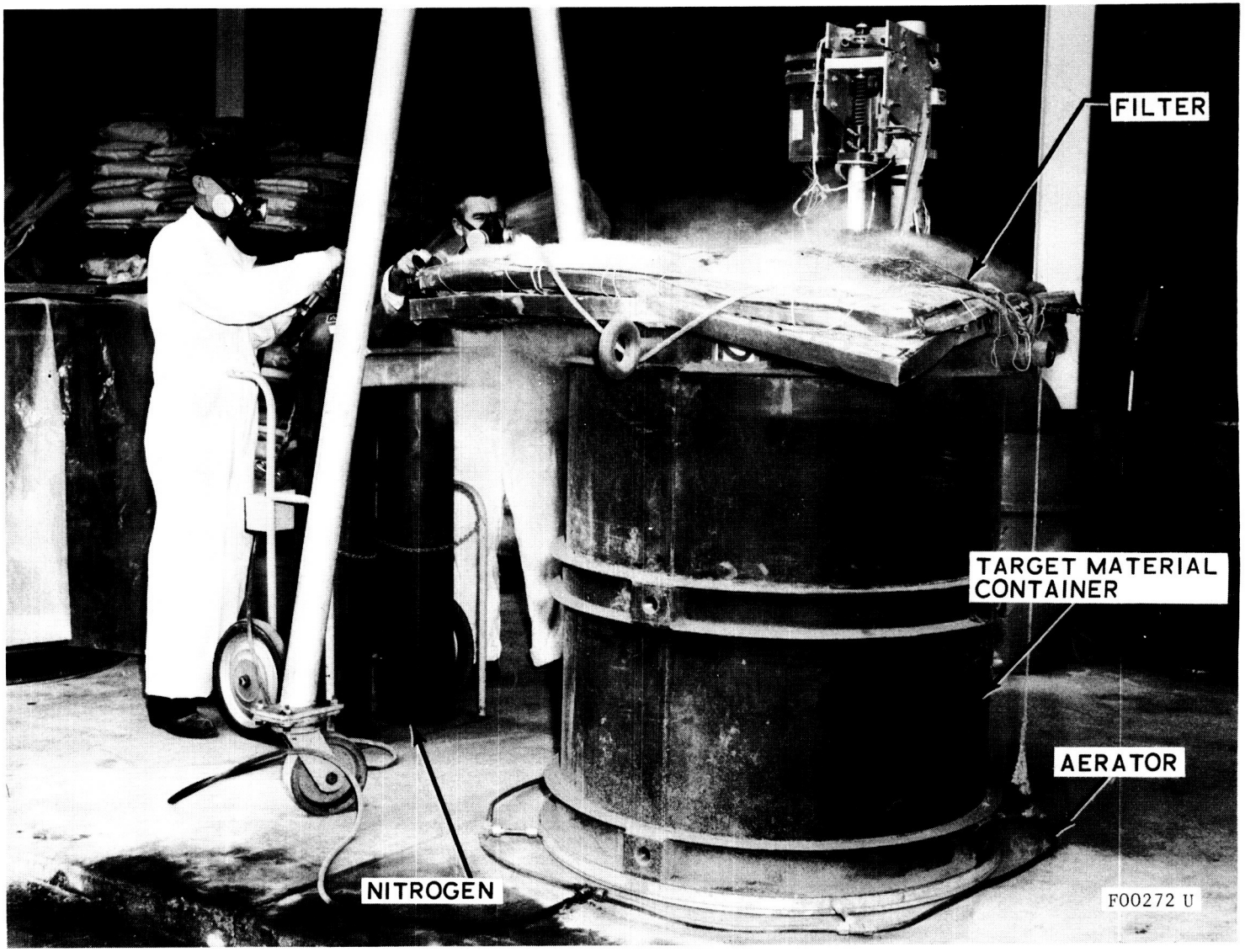

FIGURE 4-6. COMPLETE AERATION SETUP

(b) Basalt Sand. Aerate at 400 psig for 15 seconds. Lower pressure to 200 psig and hold for 15 seconds, then lower pressure to 40 psig and maintain for 4.5 minutes. Shut off the gas supply and wait 15 minutes before performing tests.

(c) Nevada 120 No. 2 Sand. Same as Nevada 60.

(d) Basalt Silt. Aerate at 60 psig for 5 minutes. Wait 15 minutes before performing tests.

(e) Cab-O-Sil No. 2 Powder. Use low pressure aeration (2 to 5 psig) while stirring until the depth of the material increases about 20 percent. Wait 20 minutes for the material to settle under its own weight before performing tests.

b. Densely Packed. To obtain densely packed conditions (compacted), several techniques of compressing the test materials were investigated. Attempts to compact material with a weighted lid proved cumbersome with negligible results. An alternate method of compression by vacuum pumping from within the container was also tried. This resulted in a slight increase of density. Experiments with combinations and variations of the above two techniques also failed. Ultimately, good results were obtained by use of a commercial vibrator of a type used to settle concrete: the Viber Company Model 31 vibrator equipped with a 3-foot stiff shaft and a 3-inch diameter head. Subsequent experiments with variation of operation time and location of the vibrating probe were made to determine an optimum procedure for each material.

The following processes were developed for preparing compacted target materials of repeatable bearing strength and density:

(1) Nevada 120 No. 1 Sand. Aerate with nitrogen gas at 400 psig for one minute. Then, compact the material by pushing the vibrator from the target surface to the bottom and back up, all in about 15 seconds. Execute four such vibrations at each corner of a square pattern, the vertices of which lie about eight inches from the container wall.

(2) Cab-O-Sil No. 1 Powder. Apply persistent vibration until its volume stops decreasing. Start the vibrator at the bottom of the container moving it in circular and criss-cross patterns while slowly withdrawing it out of the material.

4.2.2 BEARING STRENGTH TESTS, ATMOSPHERIC

Data obtained from bearing strength probe tests were used to verify the uniformity and repeatability of the prepared target samples. All target materials except the rigid material and the pebble-cobble mixture were subjected to bearing strength tests. The test device (see Figure 4-7) measured the target material resisting force against various diameter spheres and discs adapted to a motorized probe. The probe penetrated test materials at a constant velocity of 0.5 inch per second to a maximum depth of two feet. The loads were measured by strain gages and the displacement by a potentiometer. The strain gage and potentiometer signals were recorded on an X-Y plotter resulting in a load versus deflection curve.

The tester utilizes a ball-bearing screw driven from a 1/4 horsepower, 60 rpm gear-head motor. It is portable, can be readily attached to any of the target material containers, can be operated remotely, and will function in a vacuum environment. The latter factor was significant in evaluating the effects of vacuum on target materials.

a. Test Procedures. After experimental conditioning techniques with the new aerator proved successful, a series of bearing strength tests in each of the particulate materials were conducted to determine the statistical repeatability of the conditioning technique and to discover the effects of the probe geometry on the data. The procedures were as follows:

(1) Prepare the specimen target material in accordance with Paragraph 4.2.1.

(2) Make probe penetration tests 90 degrees apart around the material container to show uniformity and repeatability of the sample. Precede each penetration test with the specified conditioning process.

(3) Perform a probe-shape effects test to compare penetration resistance of the 2-1/2 inch diameter sphere, 4-inch diameter spheres, and 4-inch diameter disc.

(4) Establish average and standard deviation curves of penetration resistance versus depth for each of the particulate target materials. (When conducting impact research tests, penetration resistance tests of the target material before and after a series of impacts must yield data within the standard deviation bounds previously established.)

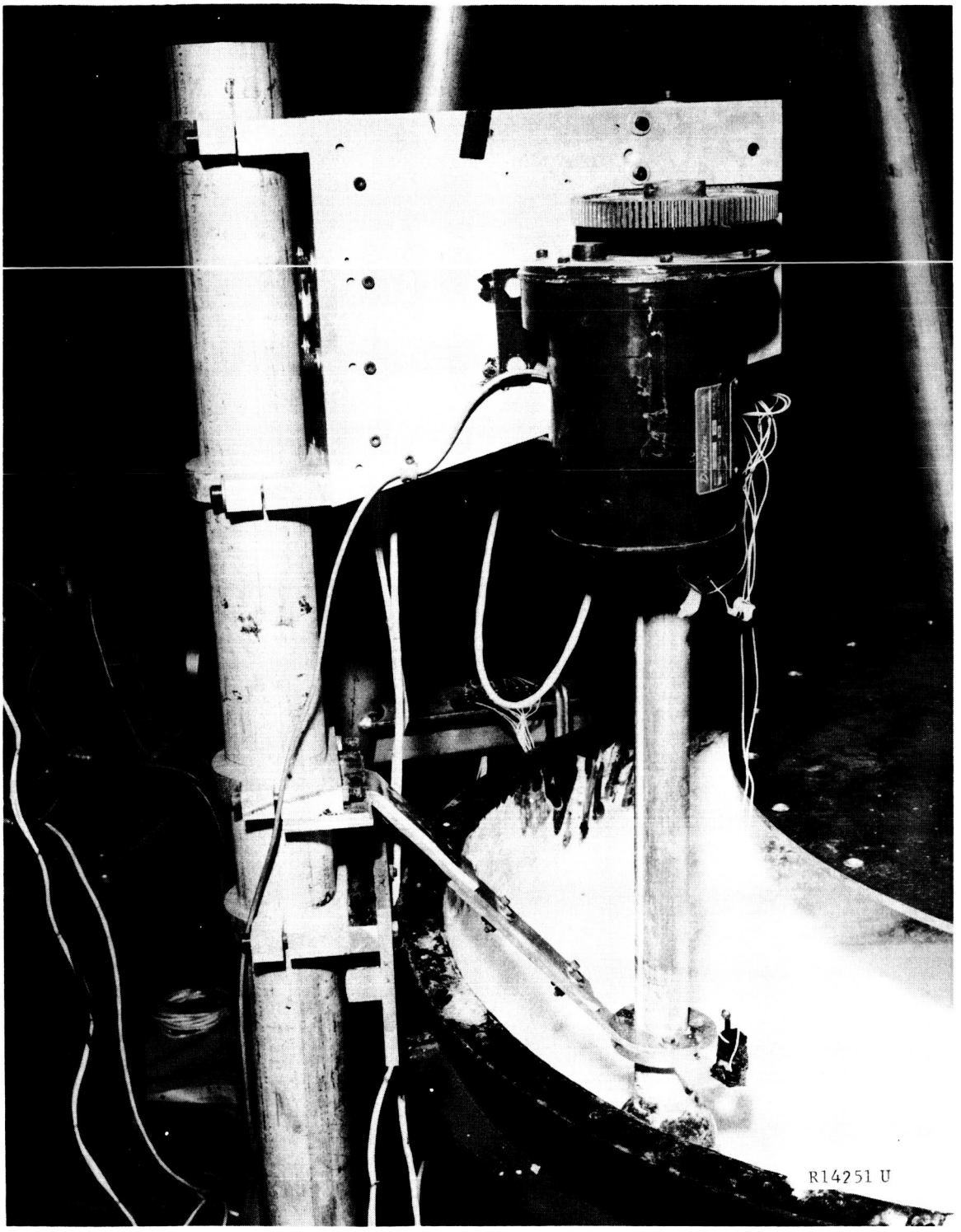

FIGURE 4-7. TARGET MATERIAL BEARING STRENGTH TESTER

b. Test Results.

(1) Nevada No. 60 Sand. Seven penetration resistance tests were conducted to obtain the average curve of Figure 4-8. Figure 4-9 illustrates the data from three probe geometries in terms of bearing pressure for the three probes. Table 4.2 tabulates the probe effects data for three depths of penetration.

TABLE 4.2

PROBE SHAPE EFFECTS, NEVADA 60 SAND

Depth of Penetration (inches)	6	12	18
Bearing strength, 2.5 in. sphere (psi)	14.6	26.0	32.0
Bearing strength, 4 in. sphere (psi)	15.6	32.6	46.8
Bearing strength, 4 in. flat (psi)	18.2	34.8	47.6

(2) Basalt Sand. Soil bearing strength tests were performed on olivine basalt sand, 35/200 mesh. Nine probe tests to determine repeatability were made. See Figure 4-10 for derived average and standard deviation curves. Nine other probe tests were made, four with a 4-inch sphere and five with a 4-inch diameter disc. The tests were made to investigate probe shape effects on basalt sand. See Figure 4-11 for resultant curves.

(3) Nevada 120 No. 2 (Sand). Nevada No. 120 sand was tested extensively in its aerated state. The average curve and standard deviation were constructed. During a rain storm, the Nevada No. 120 sand became damp and was later baked to eliminate the moisture. Subsequent tests showed that the bearing strength had increased and a new average curve was determined as shown in Figure 4-12. All impact tests were conducted in this later material.

Probe shape effects tests are shown in Figure 4-13. The results are also shown below in Table 4.3.

TABLE 4.3

PROBE SHAPE EFFECTS, NEVADA NO. 120-2 SAND

Depth of Penetration (inches)	6	12	18
Bearing strength, 2.5 in. sphere (psi)	8.9	19.0	25.2
Bearing strength, 4 in. sphere (psi)	10.3	23.3	34.6
Bearing strength, 4 in. flat (psi)	15.8	29.1	40.0

(4) Basalt Silt. The olivine basalt 325 mesh produced very uniform and repeatable samples. The average curve and one-sigma deviation curves are shown in Figure 4-14. At a 6-inch penetration, the average bearing pressure was 3.1 psi with a standard deviation of 0.24 psi.

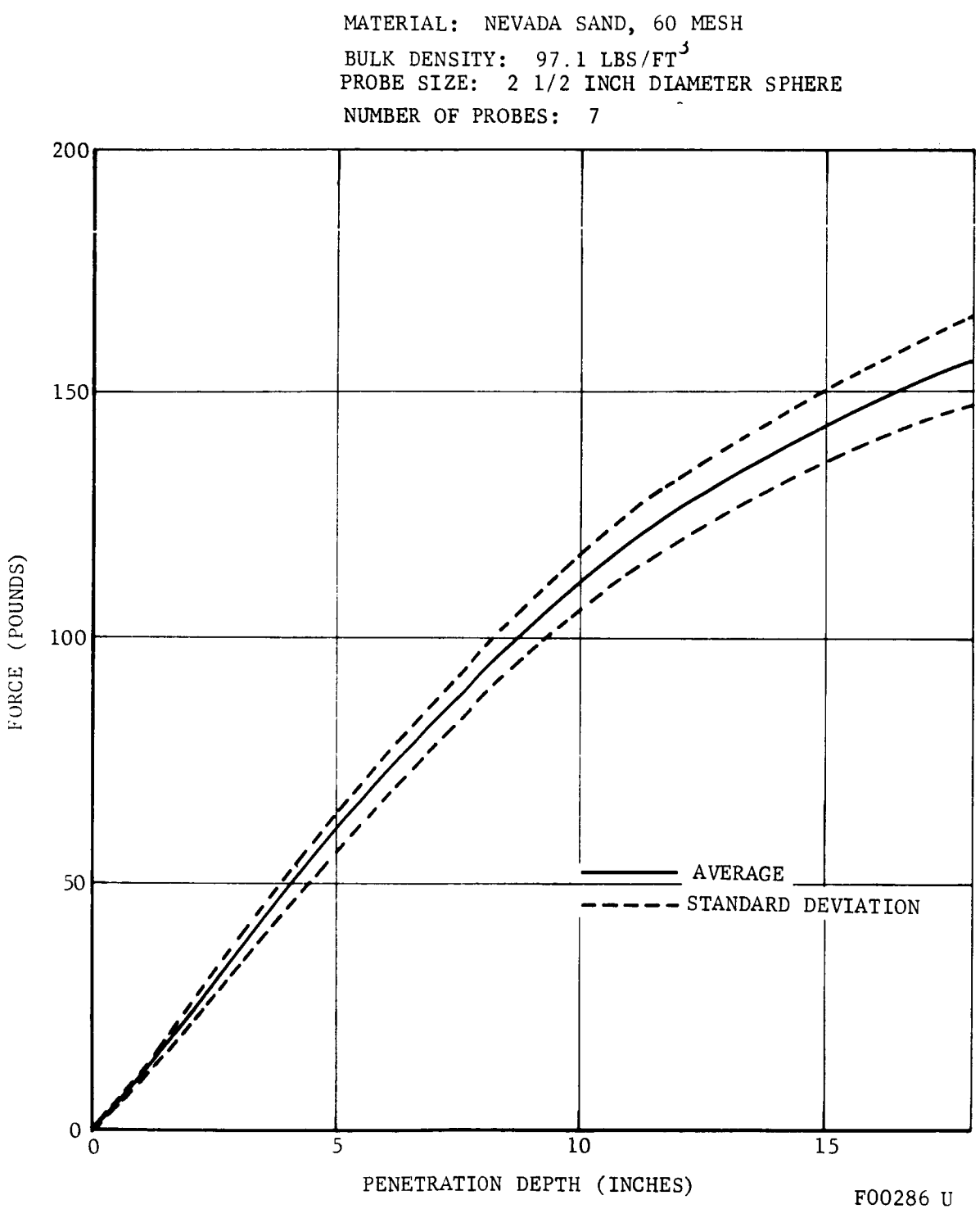

FIGURE 4-8. BEARING STRENGTH TESTS OF NEVADA 60 SAND

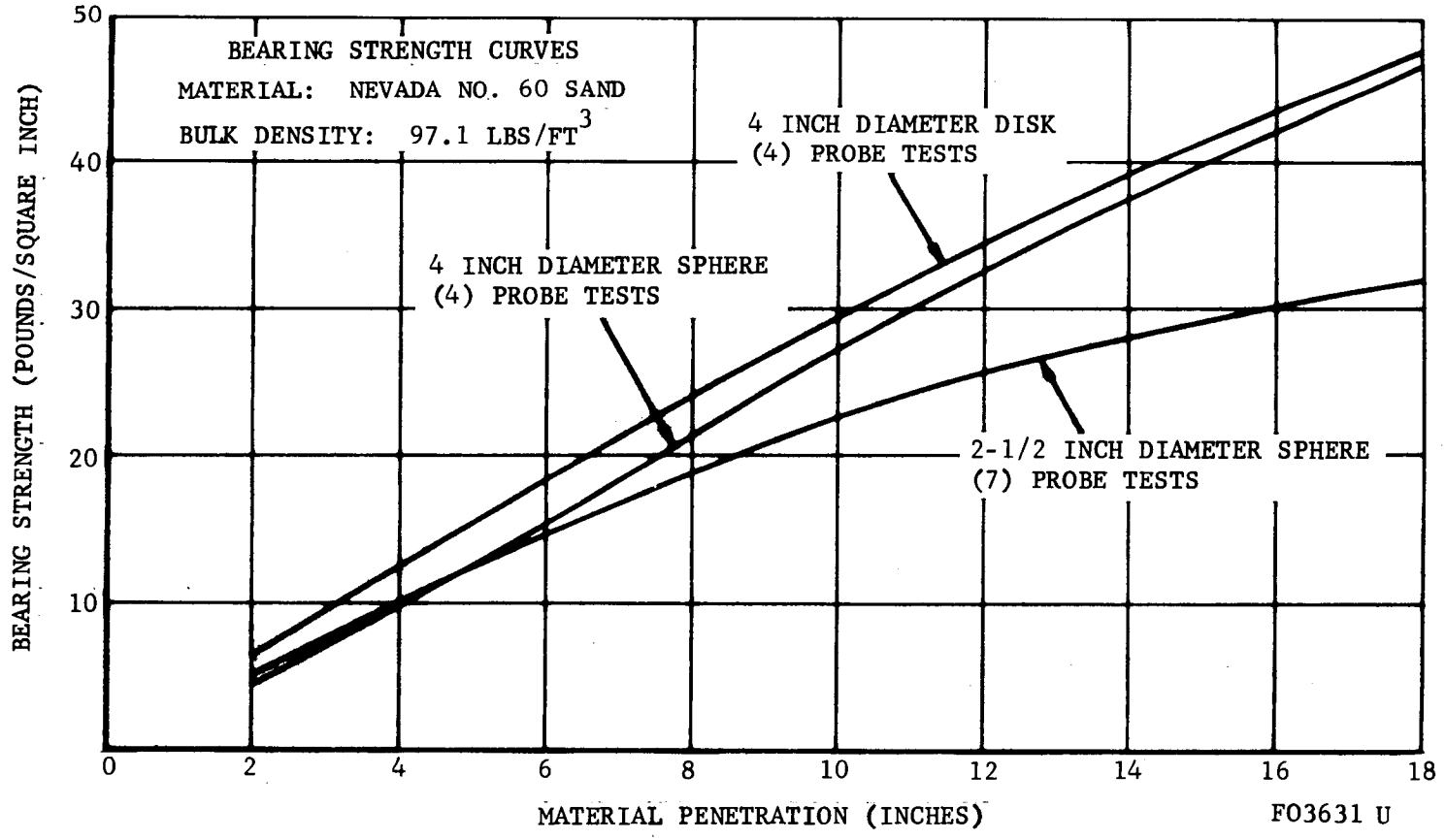

FIGURE 4-9. PROBE SHAPE EFFECTS IN NEVADA 60 SAND

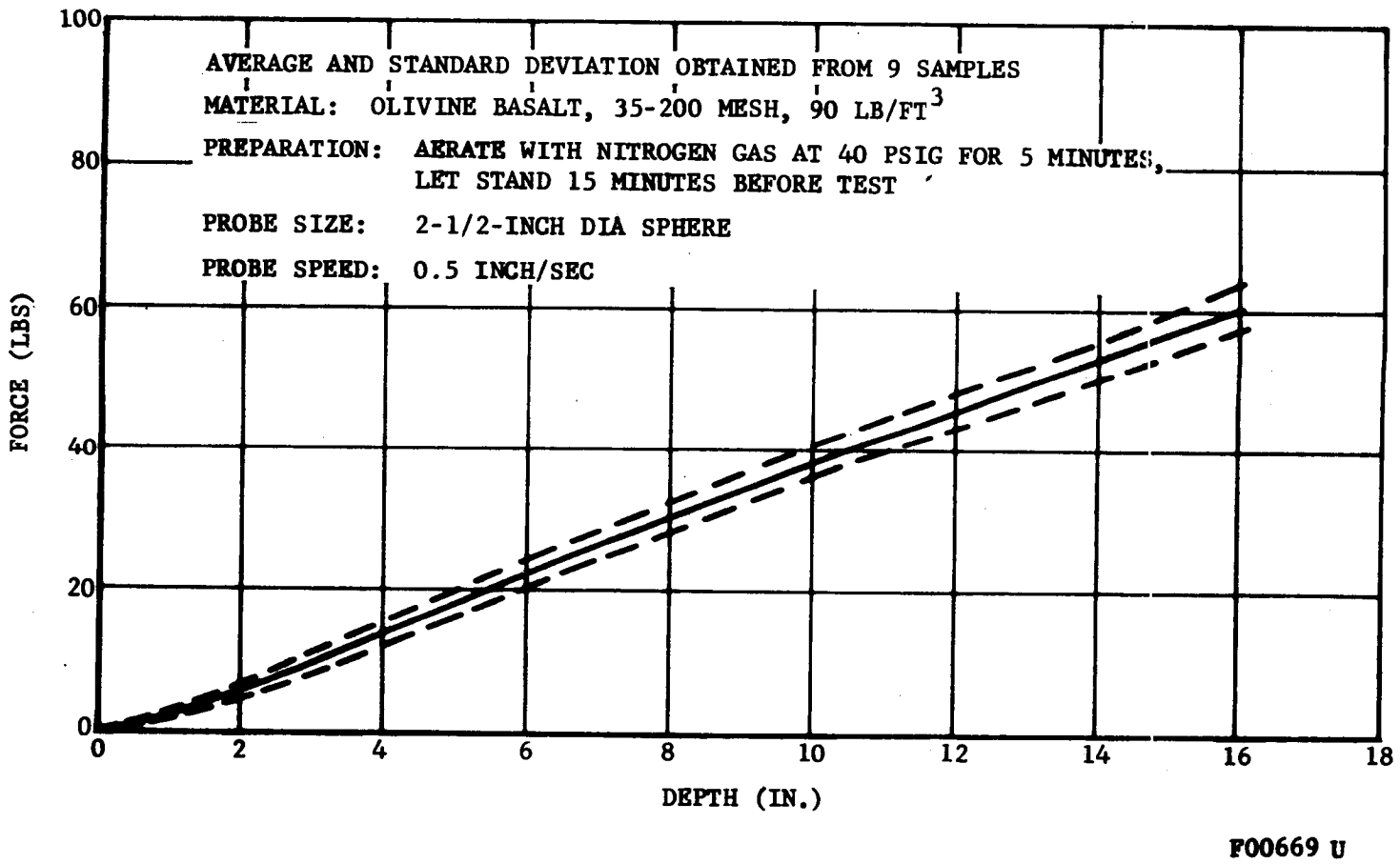

FIGURE 4-10. BASALT SAND STANDARD BEARING STRENGTH CURVE

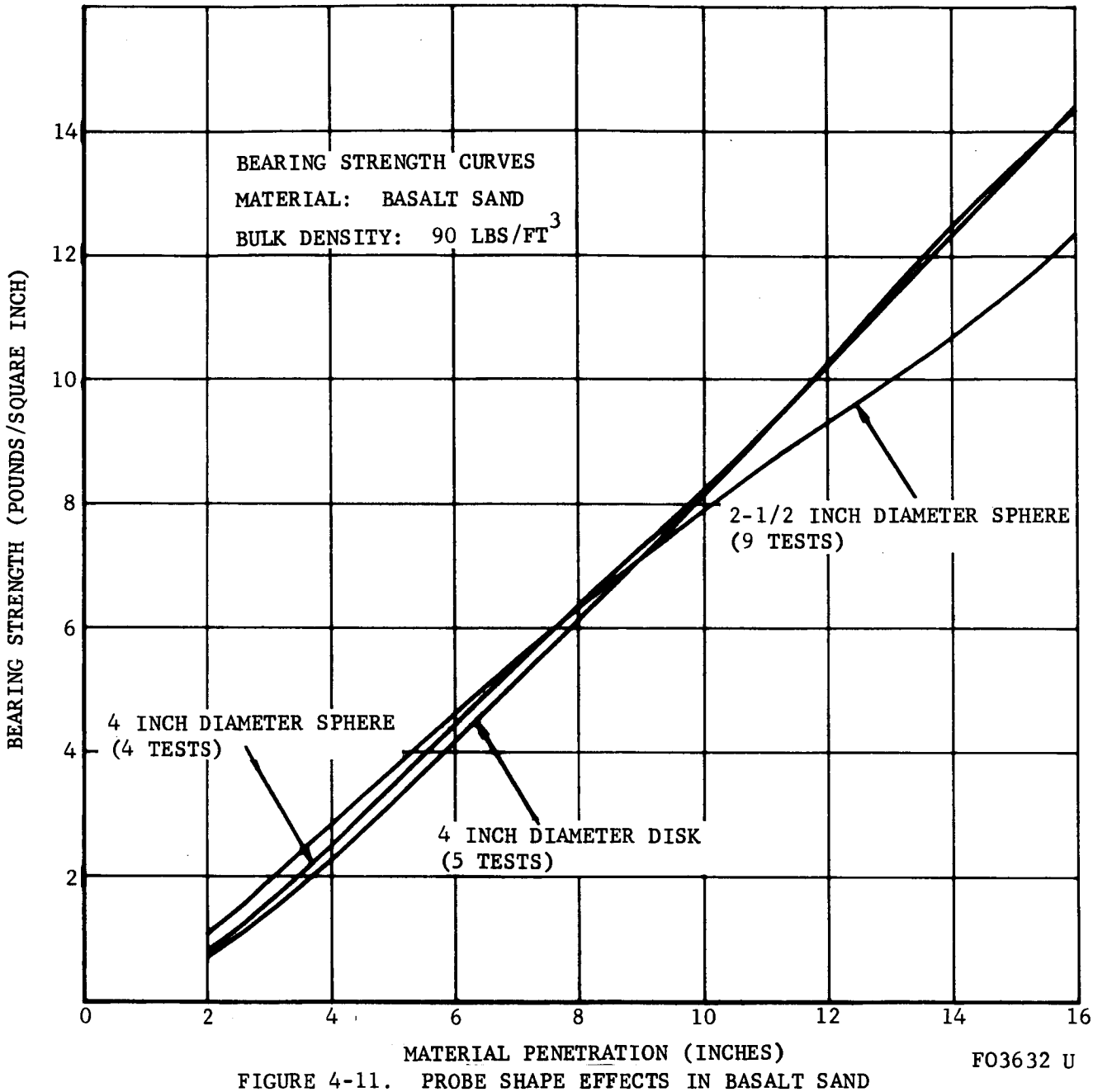

FO3632 U

FIGURE 4-11. PROBE SHAPE EFFECTS IN BASALT SAND

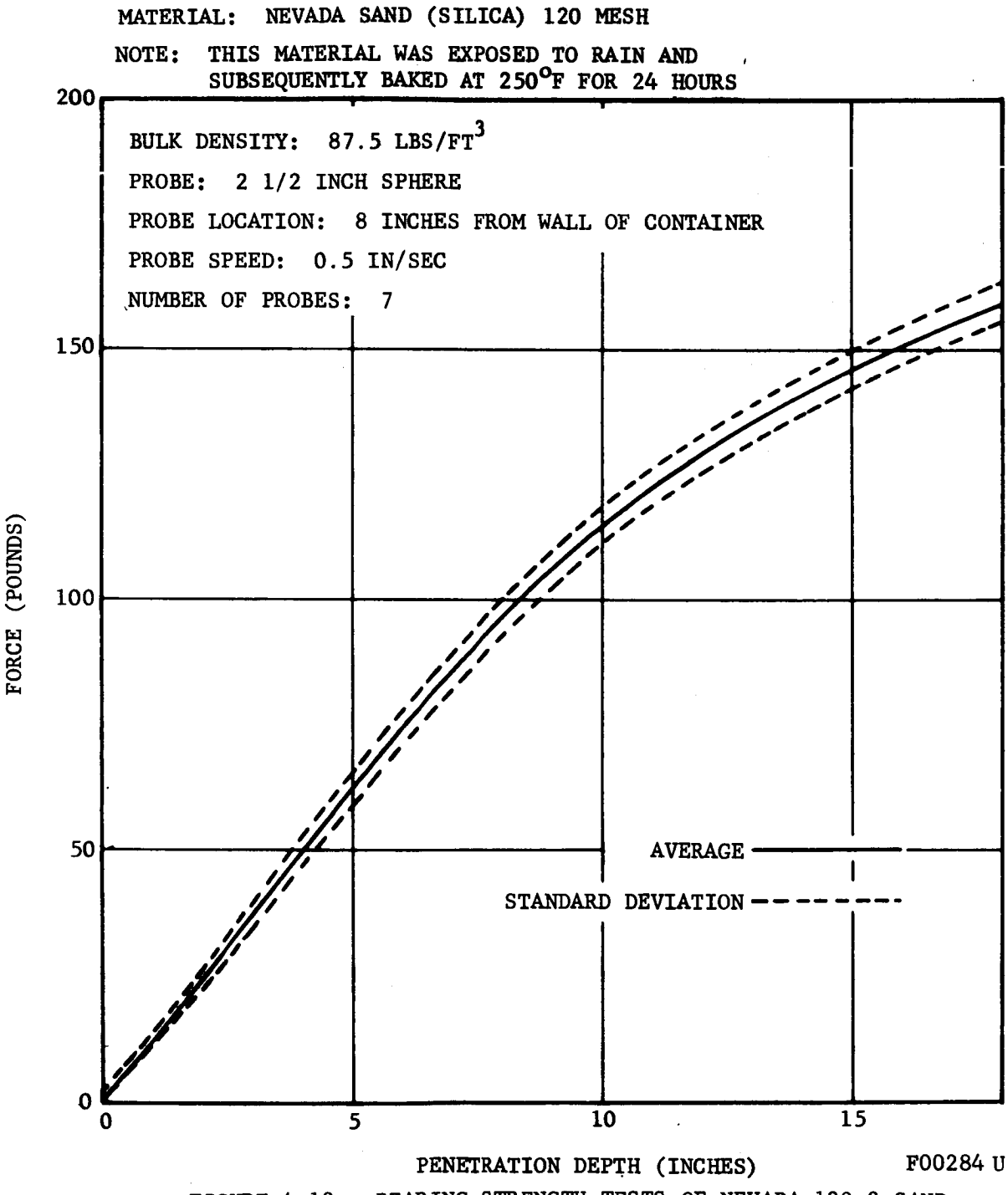

FIGURE 4-12. BEARING STRENGTH TESTS OF NEVADA 120-2 SAND

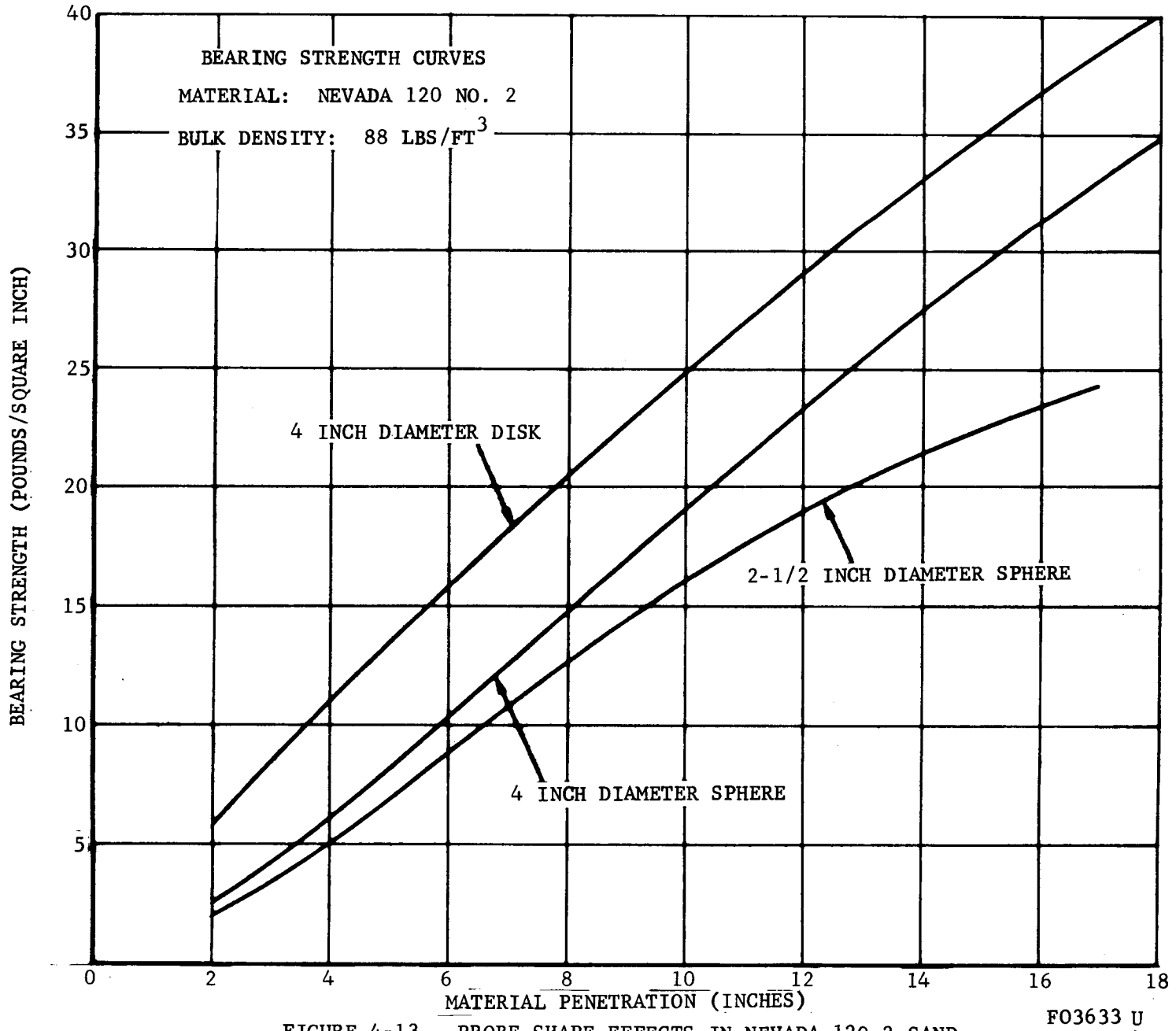

FO3633 U

FIGURE 4-13. PROBE SHAPE EFFECTS IN NEVADA 120-2 SAND

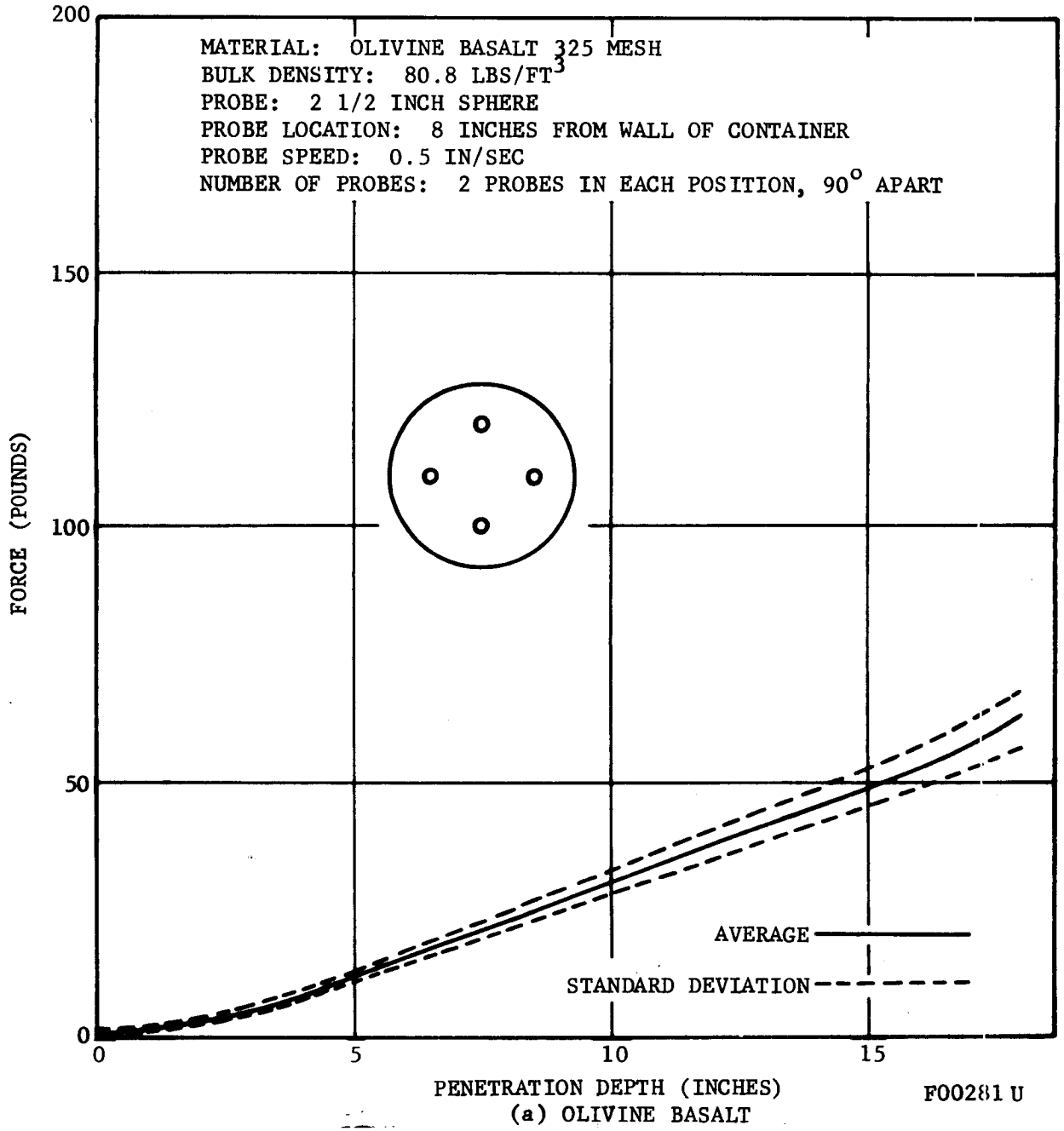

(a) OLIVINE BASALT

FIGURE 4-14. A BASALT SILT STANDARD BEARING STRENGTH CURVE

Probe shape effects are shown in Figure 4-15. Table 4.4 makes a comparison of bearing pressure at various depths.

TABLE 4.4

PROBE SHAPE EFFECTS, BASALT SILT

Penetration (inches)	6	12	18
Bearing strength, 2.5 in. probe (psi)	3.1	7.64	12.6
Bearing strength, 4 in. probe (psi)	2.28	6.31	12.5
Bearing strength, 4 in. flat probe (psi)	2.40	7.88	14.7

(5) Cab-O-Sil No. 2 Powder. Probe tests were made in aerated Cab-O-Sil. The results are illustrated in the average and probe shape effects curves of Figures 4-16 and 4-17. Note that a 4-inch rather than a 2-1/2-inch probe was used in obtaining the standard bearing strength curve for loose Cab-O-Sil. This was necessitated because the very low strength of the material resulted in the 2-1/2-inch probe yielding a signal too low for adequate resolution.

(6) Nevada 120 No. 1 Sand. Densely packed Nevada 120 sand was prepared in the fashion indicated previously in Paragraph 4.2.1 b.(1). Results of the bearing test probes are shown in Figure 4-18.

(7) Cab-O-Sil No. 1 Powder. Compacted Cab-O-Sil samples were subjected to bearing strength tests. The results are illustrated in Figure 4-19.

(8) Urethane Foam. No special material preparations were performed on the foam except for cutting the bulk material into 42-inch diameter by 10-inch thick discs to fit existing test containers. Bearing strength tests were made in the target material after each impact test. These data are included in a separate document along with the impact research data.

4.2.3 BEARING STRENGTH TESTS, VACUUM

In the early work with vacuum conditioning of Cab-O-Sil, several important characteristics were observed. The air and vapor in the material would produce a boiling, bubbling action on the powdered material. With rapid pump down, a substantial amount of material would erupt from the container into the vacuum chamber. This problem was previously handled by heating the material to remove volatiles and maintaining a very slow or intermittent pumping rate to prevent rapid boiling and eruption. The process required several work shifts with constant vigilance but could be accomplished.

Improved methods to reduce pump down time were investigated. One important step was to limit exposure of the material to atmosphere and maintain it primarily in vacuum environment. Another step was to place a felt filter

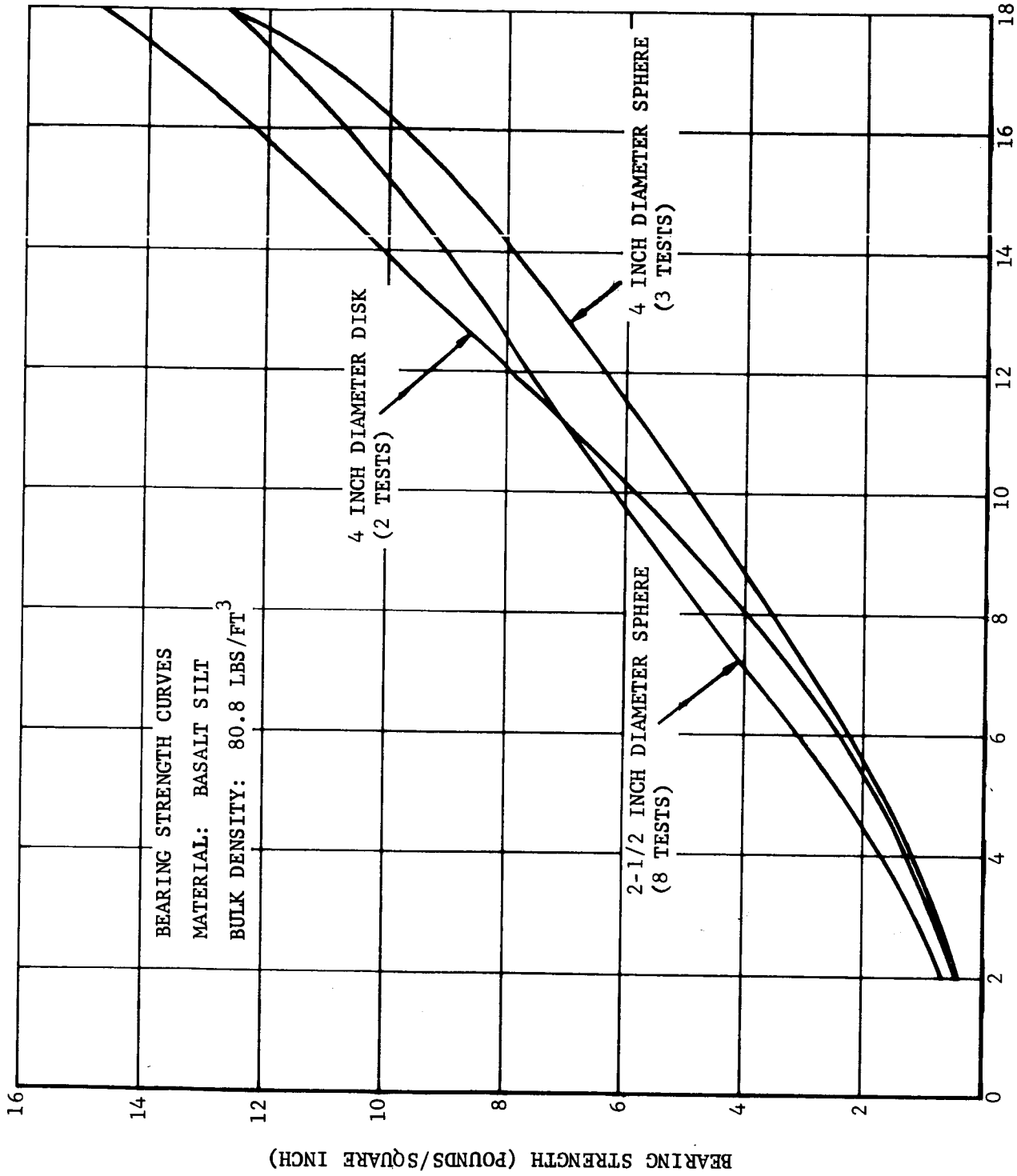

FIGURE 4-15. PROBE SHAPE EFFECTS IN BASALT SILT

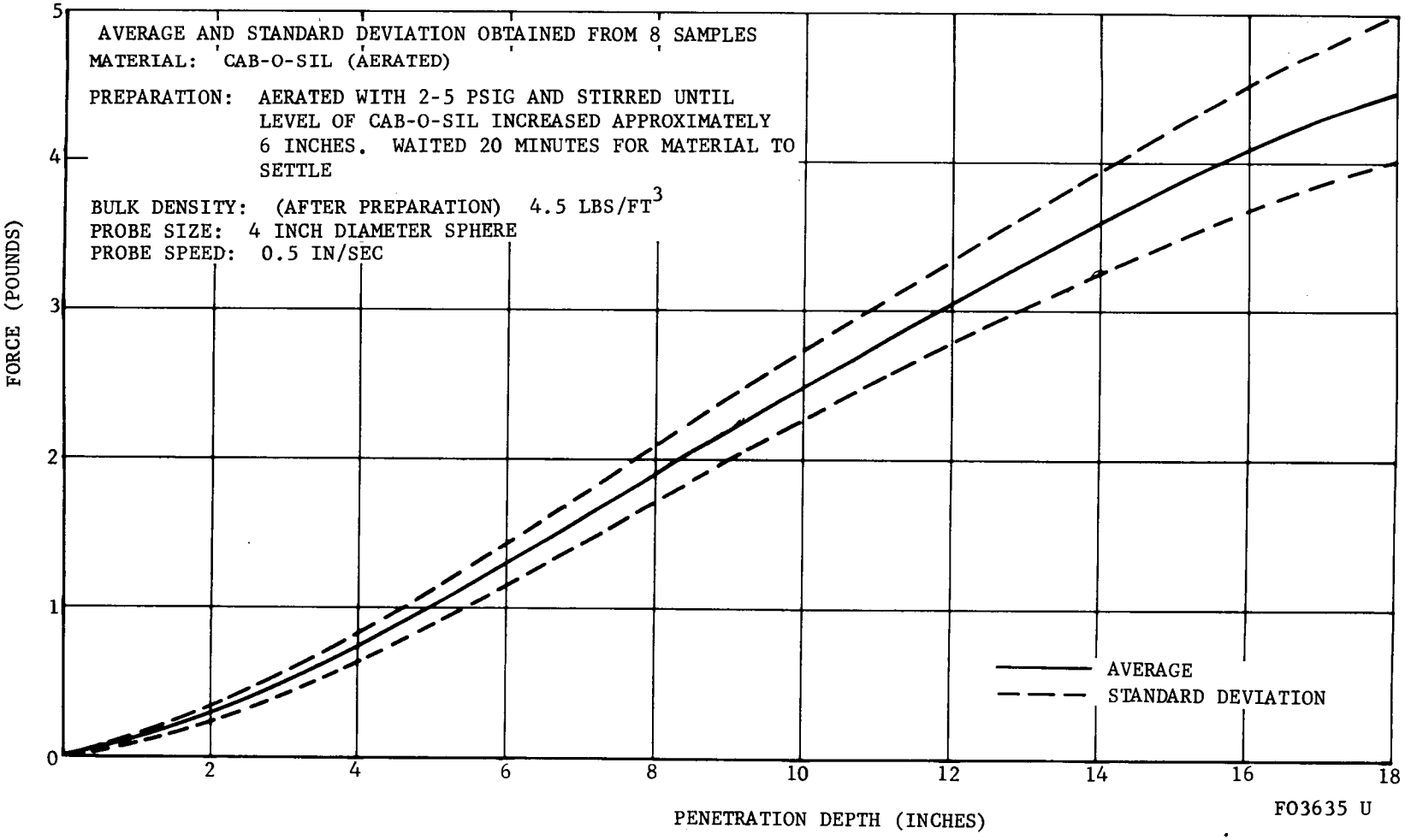

FIGURE 4-16. CAB-O-SIL NO.2 STANDARD BEARING STRENGTH CURVE

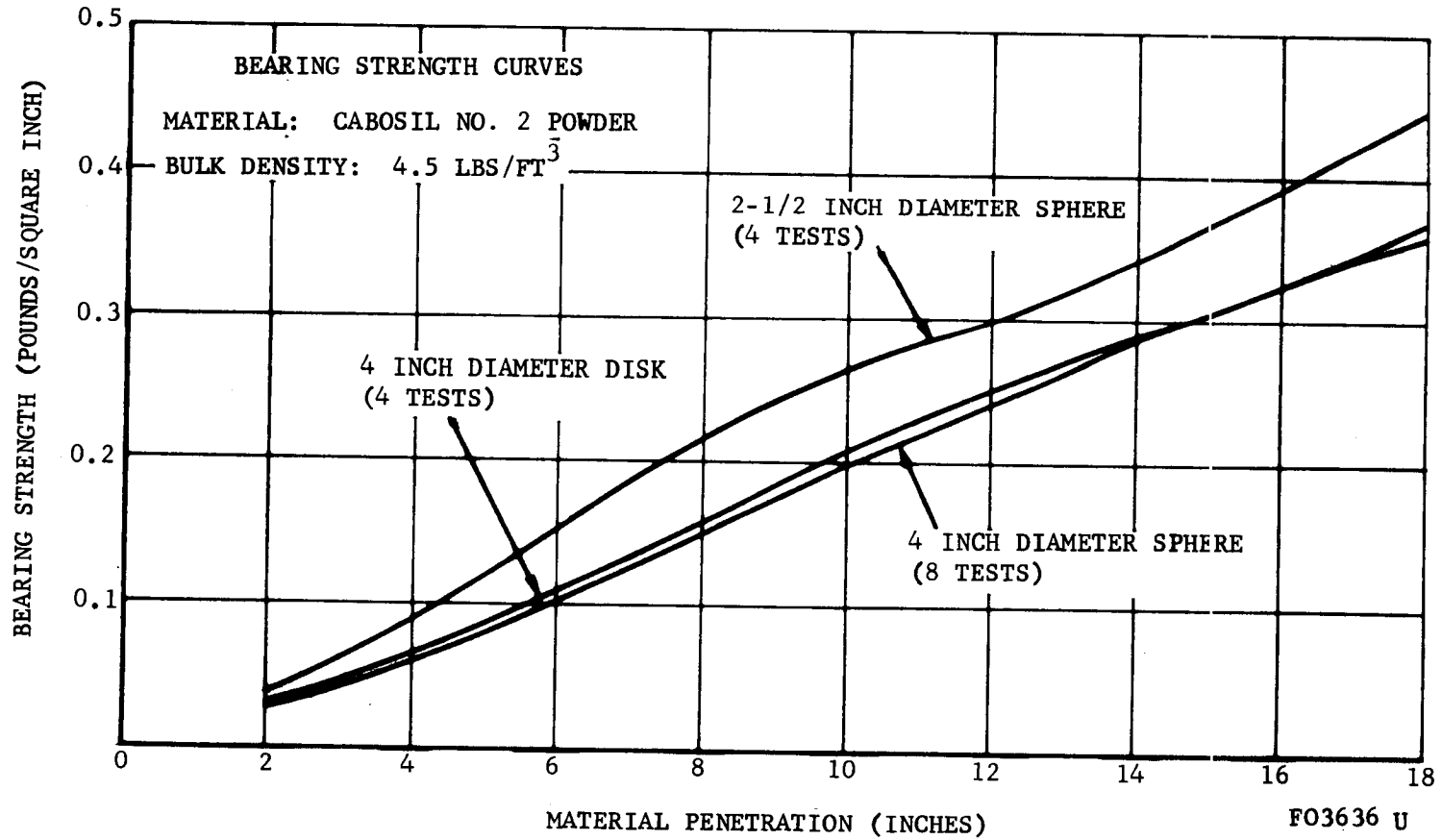

FIGURE 4-17. PROBE SHAPE EFFECTS IN CAB-O-SIL NO. 2

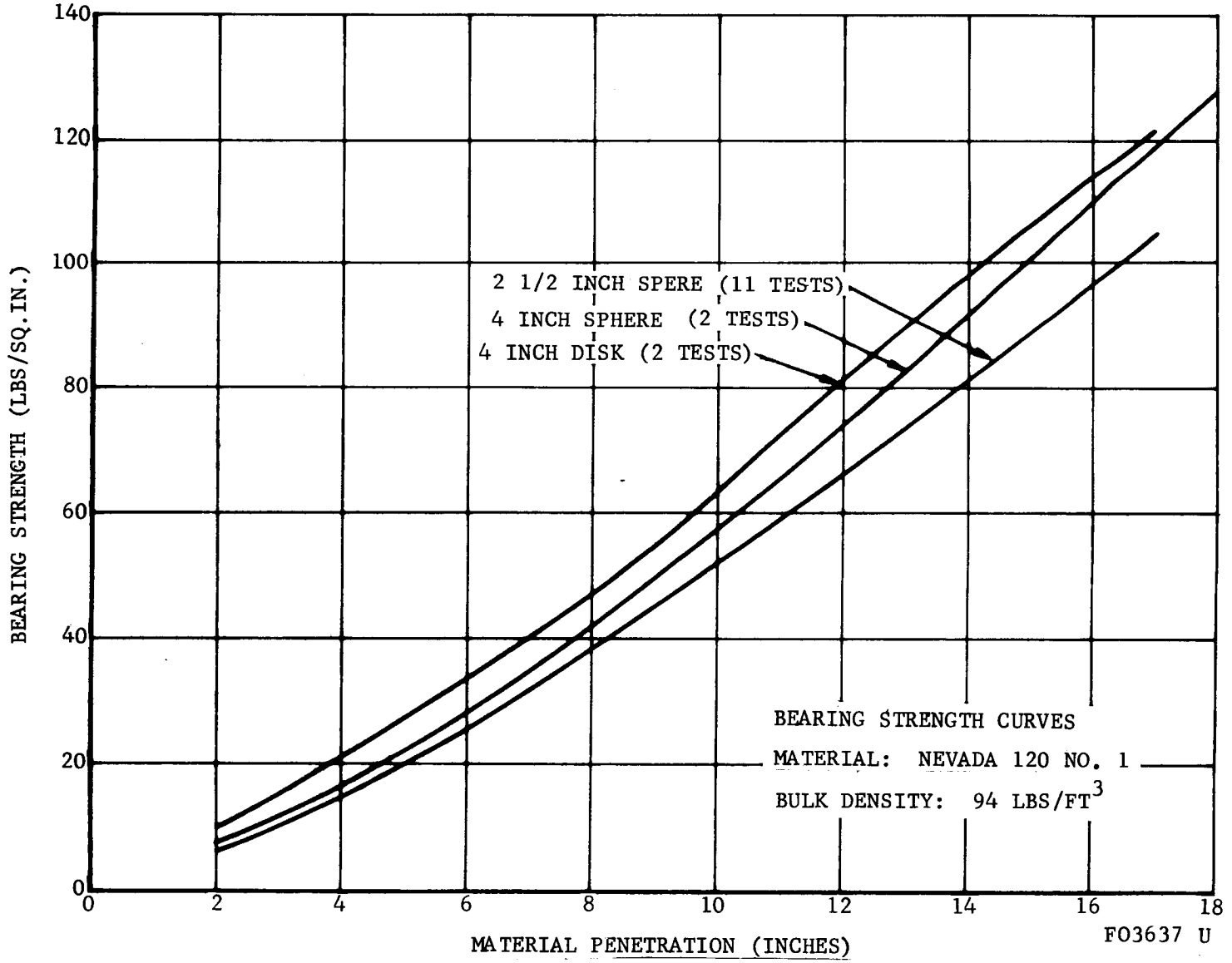

FIGURE 4-18. PROBE SHAPE EFFECTS IN COMPACTED NEVADA 120-1 SAND

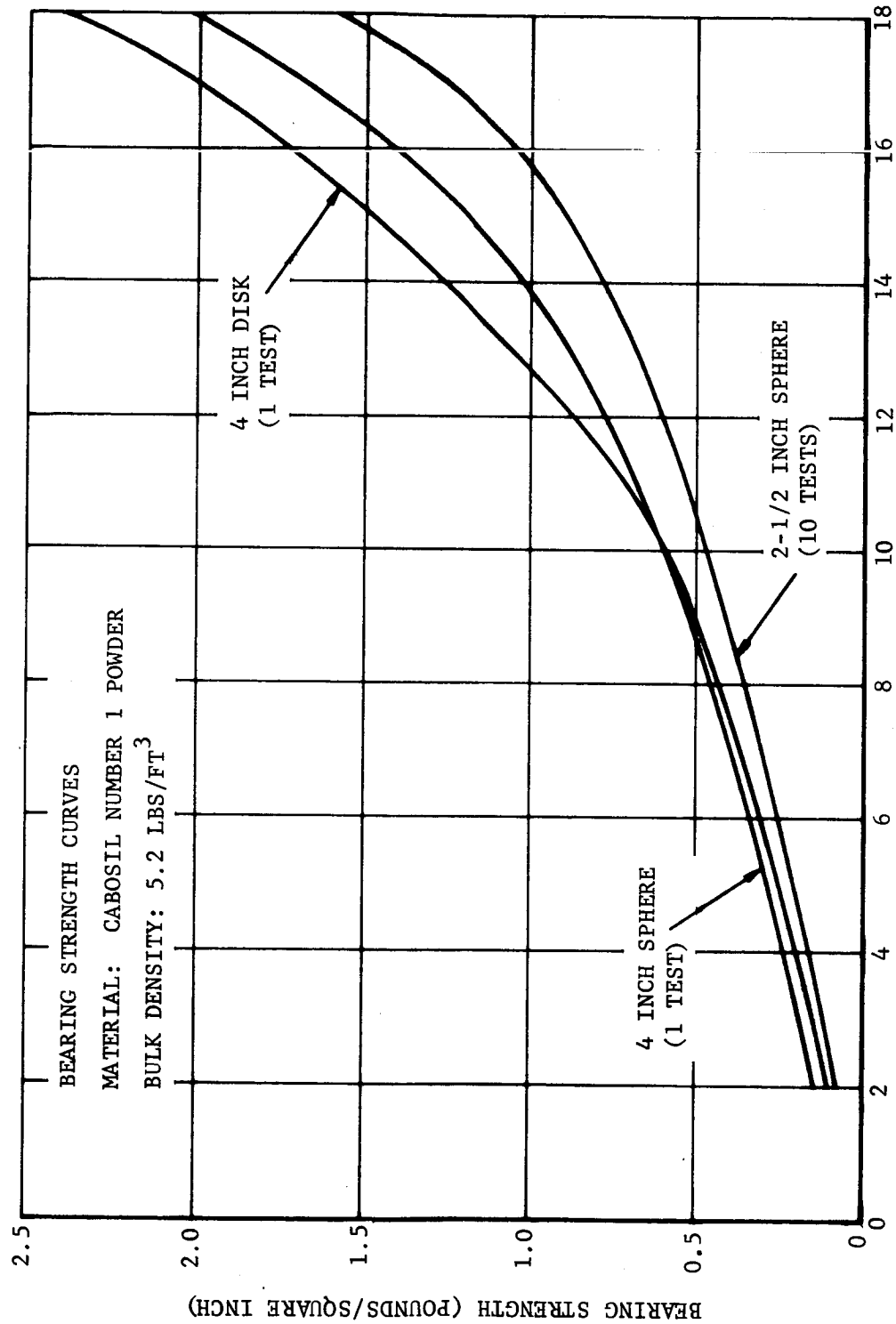

FIGURE 4-19. PROBE SHAPE EFFECTS IN COMPACTED CAB-O-SIL

on the container to prevent eruption of material into the chamber. This allowed rapid pump down of the material without eruption into the chamber. After an initial period with internal eruptions occurring, the material settled down to where all boiling ceased and was stable. This procedure was developed to where Cab-O-Sil could be vacuum conditioned in five to six hours at the maximum pumping rate of the facility. Chamber pressures of 2×10^{-5} Torr were obtained and pressures within the material of less than 700 microns were achieved. The above pumping time was further reduced by first rough pumping the chamber and then allowing an overnight soak.

Bearing strength tests were performed to demonstrate the uniformity and repeatability of this process. Uniformity within the container was demonstrated by mounting the bearing tester on a traverse and probing in three locations across the barrel. Figure 4-20 illustrates uniformity of the material while Figure 4-21 indicates the repeatability of the material for three tests.

Larger diameter probes were adapted to the bearing tester and additional bearing tests under vacuum in Cab-O-Sil were made. The recorded results, as shown in Figure 4-22, exhibited a wide range of probe shape effects. Figure 4-23 compares bearing strengths obtained in vacuum with those of the atmospheric cases.

Vacuum probe tests were performed also in Nevada 120-2 samples. This was done before and after dynamic impact tests. Comparative results are shown in Figure 4-24 with associated atmospheric bearing strength tests.

The material exploded during the vacuum impact test on urethane foam, which is of a cellular nature. Therefore, no vacuum bearing strength tests in this target material were attempted.

PROBE SEQUENCE:
1. POS. 3, 8 IN. FROM BARREL WALL, CHAMBER AT 4×10^{-5} TORR, CABOSIL AT 600 MICRONS
2. CENTER OF BARREL, CHAMBER AT 6.2×10^{-5} TORR, CABOSIL AT 600 MICRONS
3. POS. 1, 8 IN. FROM BARREL WALL, CHAMBER AT 1.2×10^{-4} TORR, CABOSIL AT 600 MICRONS

CABOSIL PREPROBE PREPARATION

1. (12-27-65 1500) AERATED TILL SOIL 4 IN. FROM TOP OF BARREL (AERATED TWICE WITH SETTLING OF 20 MIN.)
2. (12-27-65 1600) START EVACUATING CHAMBER
3. (12-27-65 1700) STOP EVACUATING CHAMBER
4. (12-28-65 0730) START EVACUATING CHAMBER
5. (12-28-65 0940) STOP EVACUATING CHAMBER (CHAMBER AT 4×10^{-5} TORR. CABOSIL AT 600 MICRONS)

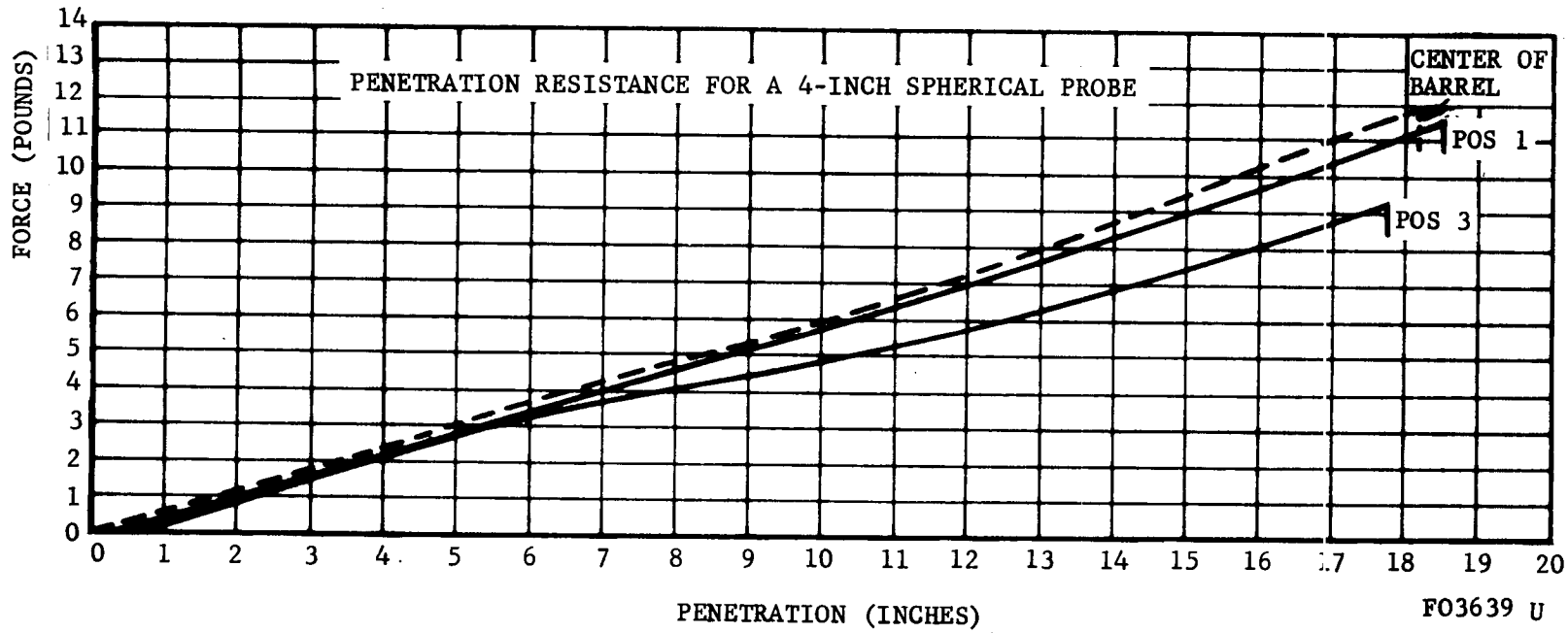

FIGURE 4-20. CAB-O-SIL UNIFORMITY IN VACUUM CHAMBER

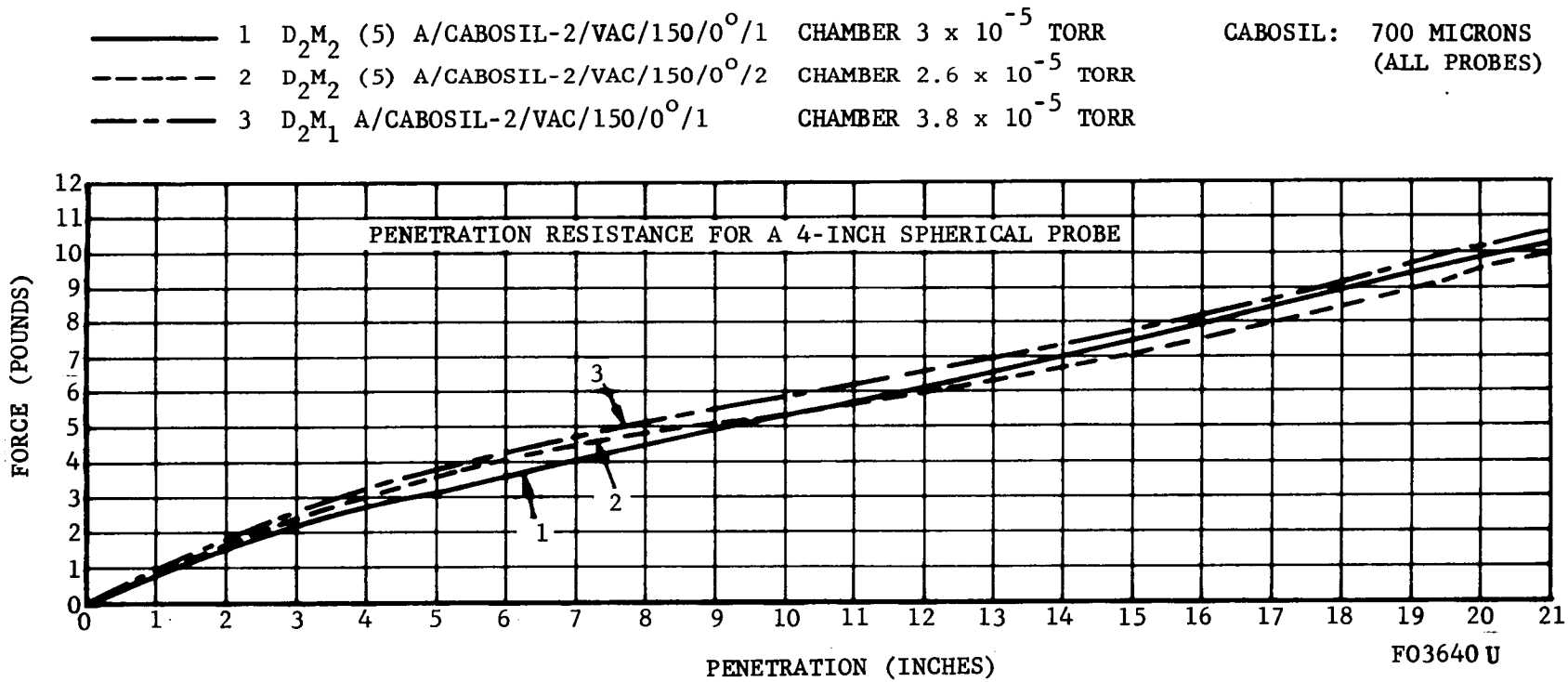

FIGURE 4-21. CAB-O-SIL REPEATABILITY IN VACUUM CHAMBER

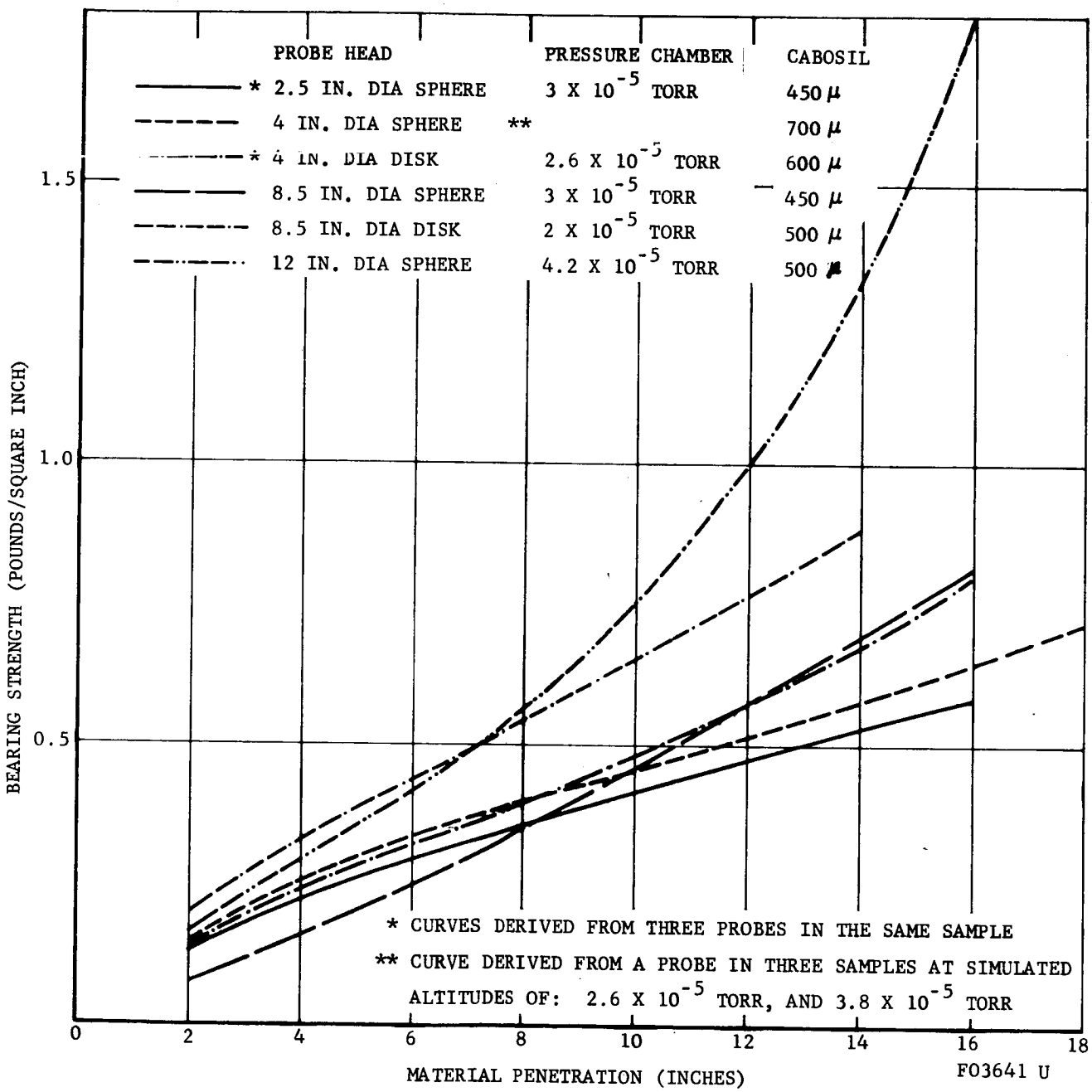

FIGURE 4-22. VACUUM PROBE SHAPE EFFECTS IN COMPACTED CAB-O-SIL

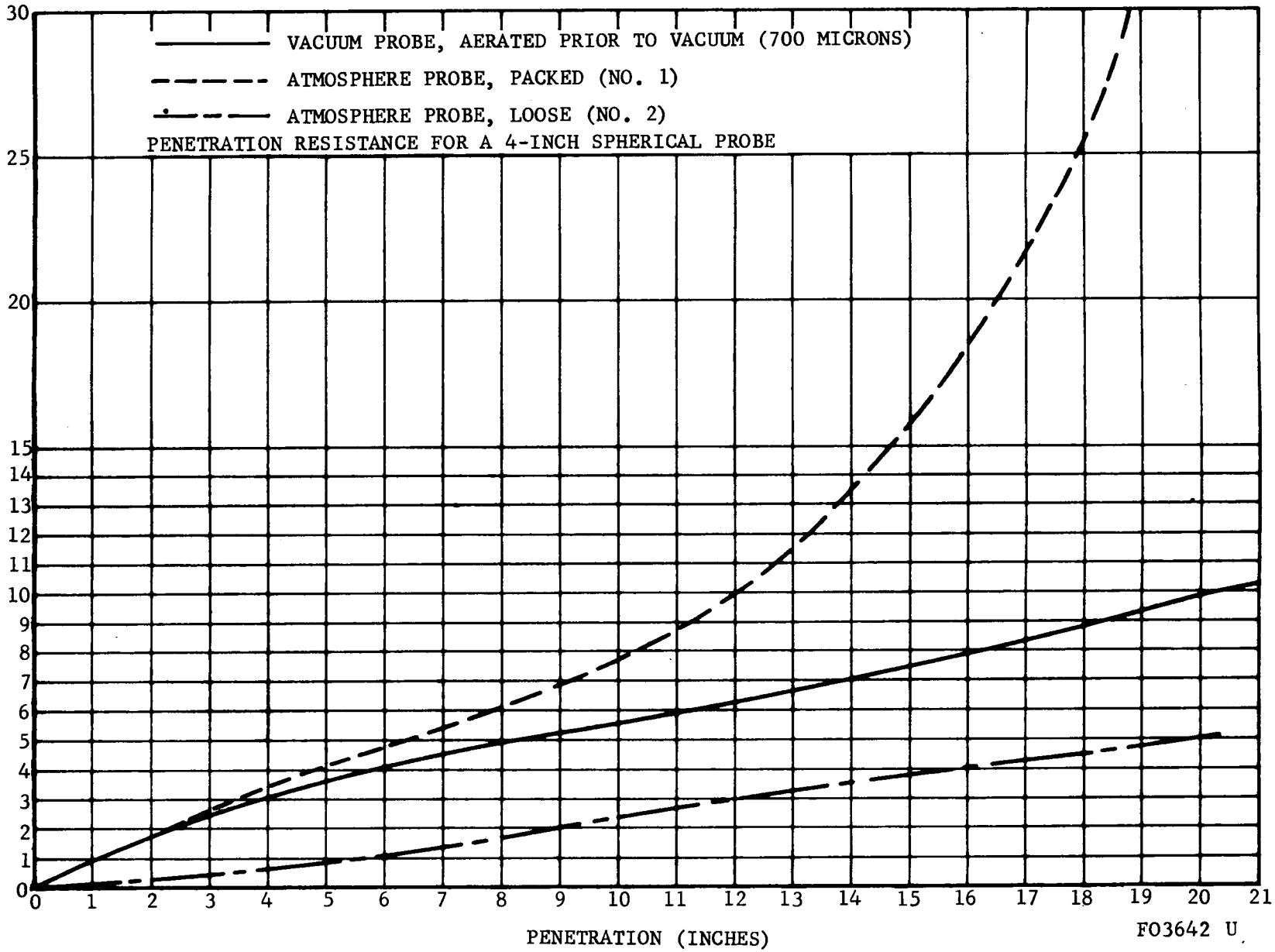

FIGURE 4-23. CAB-O-SIL CHARACTERISTICS IN VACUUM AND ATMOSPHERE

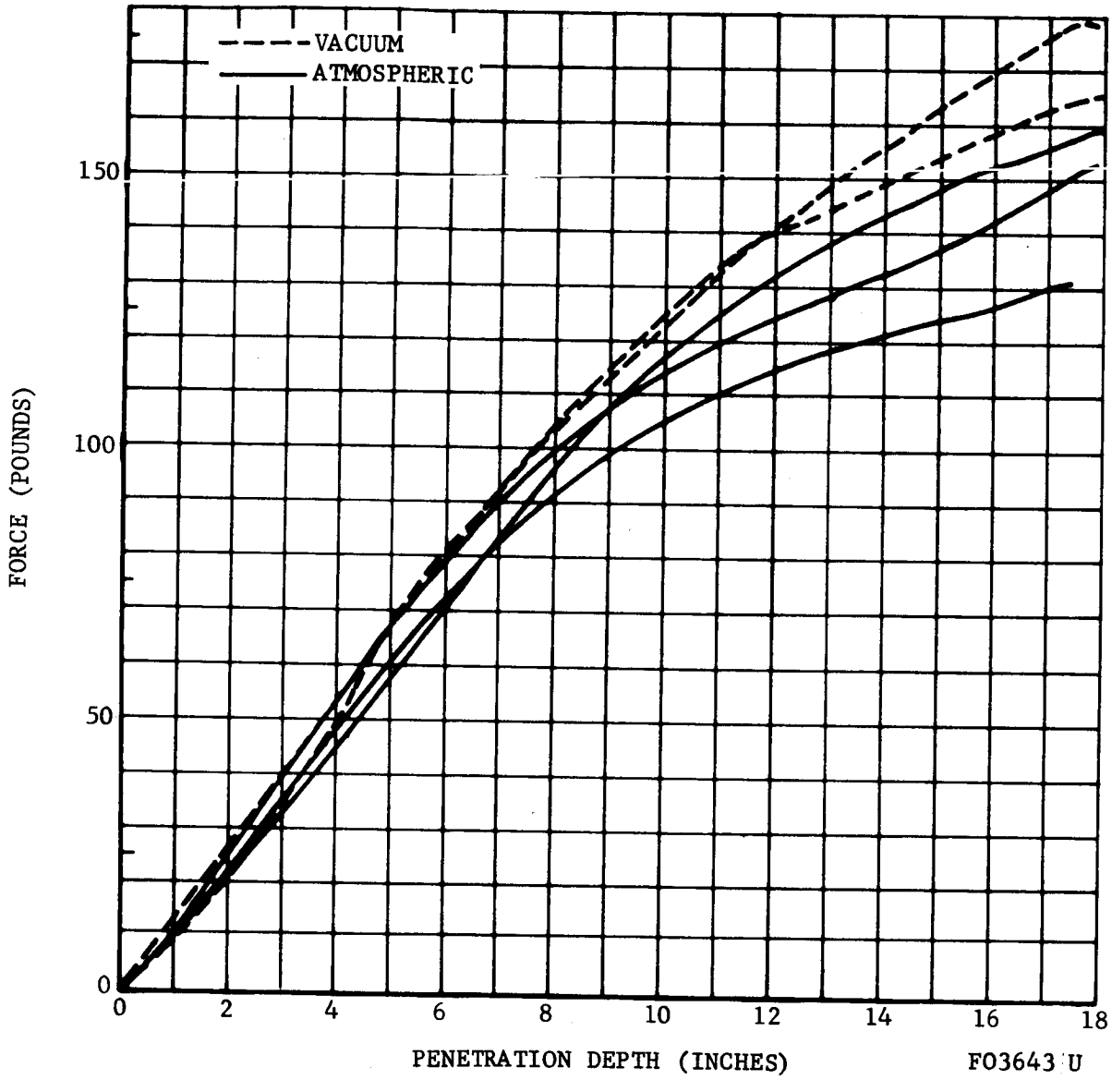

FIGURE 4-24. ATMOSPHERIC AND VACUUM BEARING STRENGTH TESTS, NEVADA 120-2 SAND

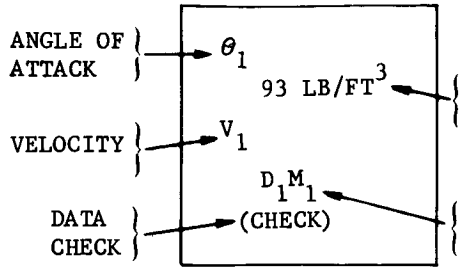

EXPLANATION

ANGLE OF ATTACK (IN DEGREES FROM VERTICAL)

$\theta_1 = 0^\circ$

$\theta_2 = 30^\circ$

$\theta_3 = 60^\circ$

VELOCITY (IN FPS)

$V_1 = 20$

$V_2 = 150$

$V_3 = 200$

(OD, IN INCHES) DIAMETER \ MASS (IN.LB)	M_1 2.2	M_2 5.0	M_3 8.0
D_1 4	θ_1 113 LB/FT^3 V_2 D_1M_1 (CHECK)	θ_1 258 LB/FT^3 V_2 D_1M_2	
D_2 8.5	θ_1 13 LB/FT^3 V_2 D_2M_1	$\theta_{1,2,3}$ 29 LB/FT^3 $V_{1,2,3}$ D_2M_2-P (WITH LIMITER) D_2M_2 (RIGID SPHERE)	θ_1 V_2 47 LB/FT^3 D_2M_3
D_3 12		θ_1 9.6 LB/FT^3 V_2 D_3M_2	

FO3644 U

FIGURE 4-25. PARAMETRIC STUDY MATRIX

4.3 IMPACT TESTING

4.3.1 TEST OBJECTIVES AND DESCRIPTION

The impact research testing program was based upon testing a range of target materials in relation to a parametric study matrix. This matrix is illustrated by Figure 4-25. The test variables were considerable in number and could permutate into a very large number of test matrix points. As a result the variables were considered in order of effectiveness to the overall objectives and a modified test matrix was formulated during the conduct of the program which provided broad information but remained within the limits of the contract scope.

The basic test variables were combined to provide the parameters for the test matrix data points. Projectile configuration was an important consideration. The ultimate size of the penetrometer was not established; therefore, 6 projectiles were chosen encompassing three masses and 3 diameters. The nominal design goal of the penetrometer was an 8.5-inch diameter sphere weighing five pounds. Diameters of 4- and 12-inch, and weights of 2.2 and 8.0 pounds were selected as extreme values to encompass possible diameters and weights. Ten target materials were selected to encompass a range of bearing strength and physical characteristics. Trajectory considerations of velocity and angle were incorporated into the matrix; also, environmental conditions of atmosphere and vacuum were included.

The resultant impact matrix is shown in Table 4.5. The material variable is indicated along the top of the table, while velocity variable is shown vertically on the side of the table and also includes angle variables.

Since target material No. 6 (Nevada 120-2 sand) used in the LEM correlation tests did not duplicate the bearing strength characteristics of the similar material used in the impact research tests, it was necessary to add the LEM material to the test matrix, redesignating it as target material No. 11, Nevada 120-2L sand.

Test projectiles identified by diameter and mass are located in the table. Both rigid test spheres and balsa limiter test spheres were included in the program. The balsa sphere is identified by a suffix P with the density the next digit, e.g. D2M2-P11.

4.3.2 TEST EQUIPMENT

The basic equipment required to conduct the test program included target material, velocity generator, vacuum equipment and adapters, test spheres,

TABLE 4.5 IMPACT RESEARCH TEST MATRIX

TARGET NO.		1	2	3	4	5	6		7	8	9		10		11
MATERIAL		RIGID MODEL	COBBLE-PEBBLE MIXTURE	NEVADA NO. 60 SAND	BASALT SAND	NEVADA 120 NO. 1 SAND	NEVADA 120 NO. 2 SAND		BASALT SILT	CABOSIL NO. 1 POWDER	CABOSIL NO. 2 POWDER		FOAM		NEVADA 120 NO. 2L
θ	V	ATM	ATM	ATM	ATM	ATM	VAC	ATM	ATM	ATM	VAC	ATM	VAC	ATM	ATM
θ_1 0°	V_1 20 FPS			D_2M_2	D_2M_2	D_2M_2		D_2M_2	D_2M_2	D_2M_2	D_2M_2	D_2M_2		D_2M_2	D_2M_2
θ_1	V_2			D_1M_1	D_1M_1	D_1M_1		D_1M_1	D_1M_1		D_1M_1			D_1M_1	D_2M_2P-11**
				D_1M_2	D_1M_2	D_1M_2		D_1M_2	D_1M_2		D_1M_2			D_1M_2	(50, 100, 150)
		D_2M_1*-P7		D_2M_1		D_2M_1		D_2M_1	D_2M_1		D_2M_1			D_2M_1	
0°	150	D_2M_2-P11		D_2M_2		D_2M_2	D_2M_2	D_2M_2	D_2M_2	D_2M_2	D_2M_2	D_2M_2	D_2M_2	D_2M_2	
				D_2M_3		D_2M_3		D_2M_3	D_2M_3		D_2M_3			D_2M_3	D_2M_3
				D_3M_2		D_3M_2		D_3M_2 NOTE	D_3M_2		D_3M_2			D_3M_2	
θ_1 0°	V_3 250	D_2M_2-P11 (200)	D_2M_2-P11 (200)	D_2M_2	D_2M_2	D_2M_2		D_2M_2	D_2M_2		D_2M_2 (75)			D_2M_2	
θ_2 30°	V_2 150			D_2M_2		D_2M_2		D_2M_2						D_2M_2	
θ_3 60°	V_2 150°	D_2M_2-P11												D_2M_2	

MATERIALS:

NEVADA 120 NO. 1 SAND CABOSIL NO. 1 POWDER	COMPACTED STATE
NEVADA 120 NO. 2 SAND CABOSIL NO. 2 POWDER	LOOSE STATE (AERATED)
NEVADA 120 NO. 2L	MATERIAL OBTAINED FROM LEM TEST FACILITY, COMPACTED STATE

IMPACT LIMITER EQUIPPED TEST SPHERES

SPHERE	DIAMETER	WEIGHT	DENSITY OF BALSA
D_2M_1*-P7	8.5 IN.	4 LB	7 LB/FT^3
D_2M_2-P11	8.5 IN.	5 LB	11 LB/FT^3
D_2M_3-P16	8.5 IN.	8 LB	16 LB/FT^3

NOTE: D_2M_1*-P7**(50, 85, 100, 125)
D_2M_2-P11**(50, 85, 100, 125, 150)

RIGID PROJECTILES

	M_1 2.2 LB	M_2 5.0 LB	M_3 8.0 LB
D_1 4.0 IN.	●	●	
D_2 8.5 IN.	●	●	●
D_3 12.0 IN.		●	

FO3653 U

and instrumentation. The equipment and techniques for target material were discussed in previous sections so are not included here.

a. Velocity Generator Equipment

(1) Aeronutronic Hyge. Aeronutronic possessed, prior to this contract, a horizontal pneumatic accelerator which was used on Ranger hard landing capsules. This facility is a pneumatic cylinder containing a 12-inch bore and a 10-foot stroke. It has the capability to accelerate several hundred pounds to 200 feet per second. It was readily adaptable for rigid impacts. A large concrete block with a plate on the impact face was set into the Hyge pit to provide the rigid target. A ball adapter cup was mounted on the end of Hyge rod. A net rebound trap, triggered by the ball passing through was placed near the rigid target. This test setup is shown in Figure 4-26 as viewed from the target.

(2) Pneumatic Accelerator Facility. In order to throw projectiles into particulate materials, a vertical test configuration was highly desirable. A special vertical facility was designed to accomplish this. The test facility is shown in Figure 4-27. Basically, it consists of a pneumatic accelerator, a support stand, test sphere adapter, and a target material reservoir.

The pneumatic accelerator consists of an 8-inch diameter cylinder with a 3-foot stroke. With a maximum thrust of 100,000 pounds, the machine is capable of accelerating projectiles weighing less than 10 pounds to 250 feet per second. The machine consists of a high pressure reservoir located above an air cylinder containing a light weight piston and rod. A quick opening valve releases the high pressure nitrogen into the active cylinder, thus accelerating the piston. The chamber under the piston acts as a snubbing cushion with stroke and acts to decelerate the piston rod after the ball has been fired. The piston and rod will make several decaying oscillations and come to rest. After some minor corrections, the accelerator proved to be very useful, providing over 500 shots. The machine is readily adjustable to any speed by varying reservoir pressure and is very repeatable for any established velocity setting.

The support stand provided a flange mounting for the pneumatic accelerator and provided the function of elevating the accelerator 10 feet above the ground. It is constructed of steel pipe columns and a welded upper truss of steel pipe. The reaction loads of 100,000 pounds are transmitted through the structure into the concrete floor to which it is anchored. The test sphere adapter is a spherical adapter which screws into the end of the accelerator rod. Three sizes are available to accommodate the test spheres.

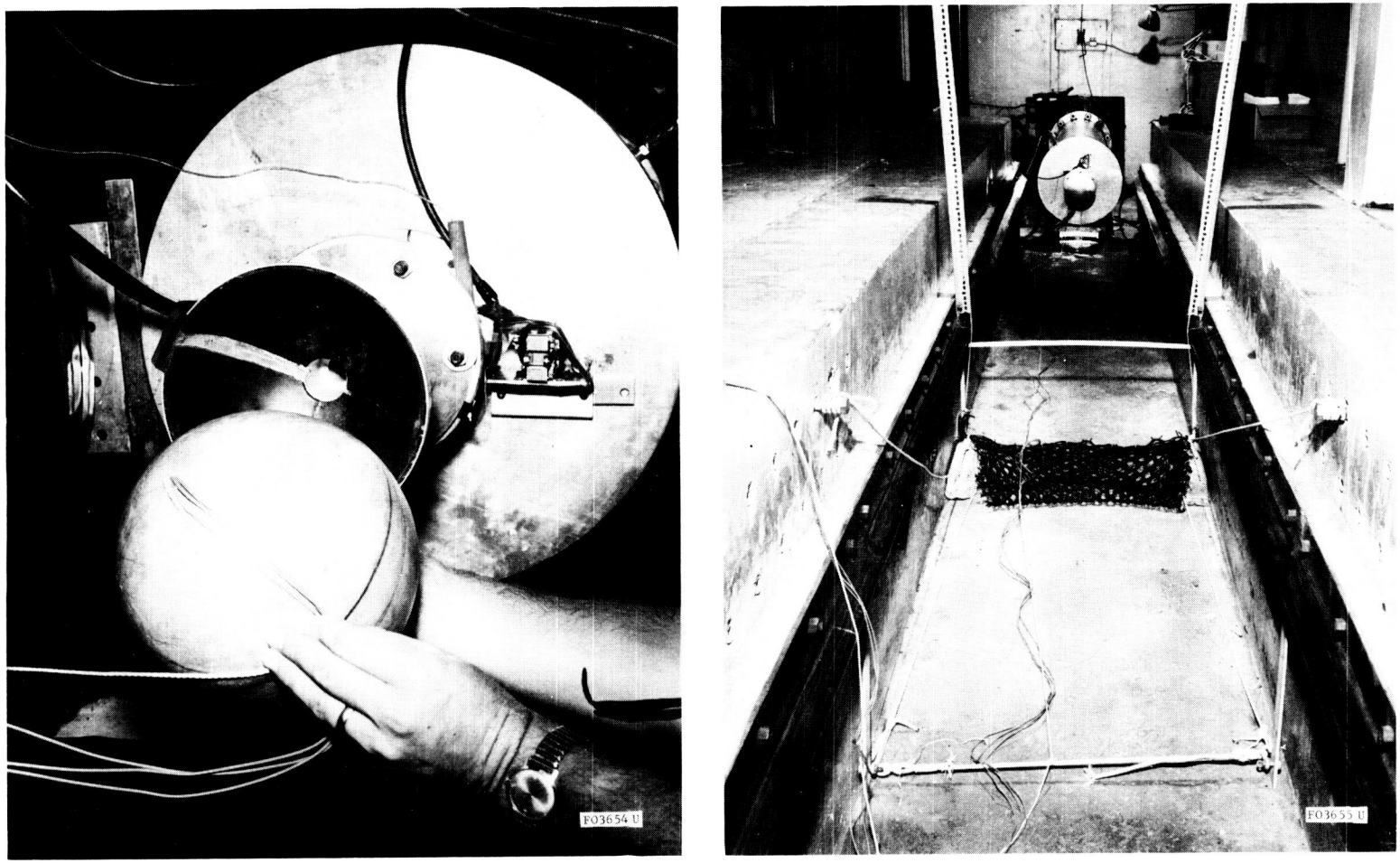

FIGURE 4-26. HYGE TESTING SETUP

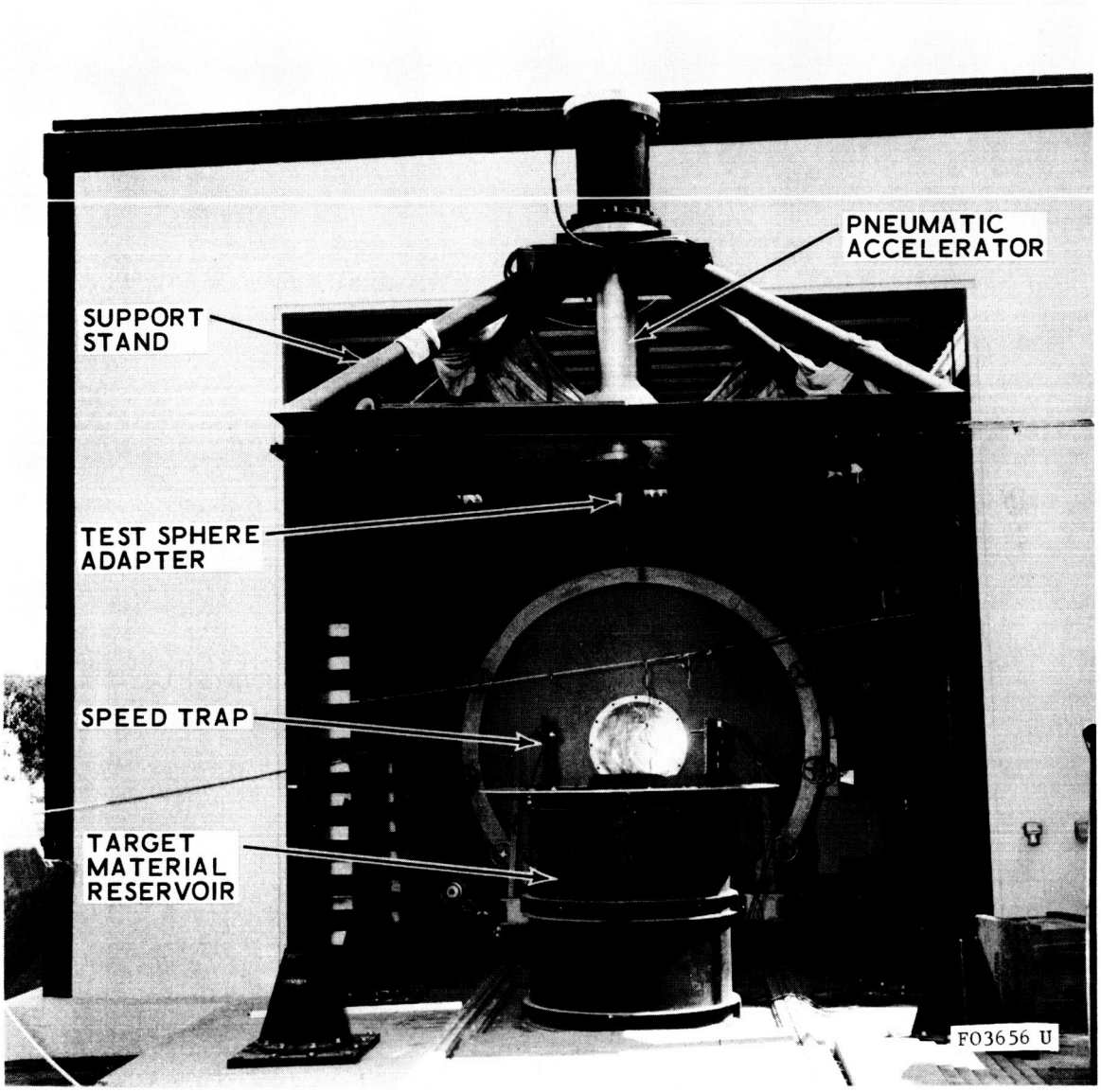

FIGURE 4-27. IMPACT RESEARCH TEST SETUP

b. Vacuum Test Facility. Aeronutronic has a high-vacuum facility 8 feet in diameter by 30 feet long. This facility has the capability to pump down to 10^{-6} torr. The vacuum facility was specially adapted to accommodate the impact research experiment. The penumatic accelerator support stand was designed to straddle the vacuum chamber so that the accelerator would be mounted above it. The acceleration rod was adapted to the chamber with a combination bellows and sliding seal. The bellows protected the chamber from structural loading while the sliding seal allowed the rod to stroke without breaking the vacuum. The target material container was mounted from the floor through a similar bellows arrangement on a solid shaft. Again, the chamber was isolated from structural loading with impact loads going directly to the floor. The seals and the load isolators were highly successful and presented no problem. All instrumentation and operations were controlled outside the chamber through vacuum feed-through ports.

c. Test Projectiles. Eight test sphere configurations have been used to obtain valid impact research data. All are modifications of the original devices. Table 4.6 lists the design parameters. The specified weights in the table are total weights including accelerometers, cable anchors, etc.

TABLE 4.6

IMPACT RESEARCH PROJECTILES

Projectile	Diameter (in)	Weight (lb)	Material	Aluminum Inner Sphere Wt (lb)	Aluminum Inner Sphere Dia (in)
D1M1	4.0	2.2	Aluminum	---	---
D1M2(5)	4.0	5.0	Al and Steel	---	---
D2M1A	8.5	2.2	Mag and 2 lb/ft^3 Foam	---	---
D2M1-P7	8.5	4	7 $\pm$ 0.25 lb/ft^3 Balsa	2.2	3.50
D2M2(5)A	8.5	5.0	Mag and 2 lb/ft^3 Foam	---	---
D2M2-P11	8.5	5	10.6 $\pm$ 0.4 lb/ft^3 Balsa	2.8	3.78
D2M3A	8.5	8.0	Mag and 2 lb/ft^3 Foam	---	---
D3M2(5)A	12.0	5.0	Mag and 2 lb/ft^3 Foam	---	---

(1) Four-Inch Spheres. Figure 4-28 is a photograph of a partially assembled D1M2(5) projectile. The accelerometer block is an aluminum cube, 1.5 inch on each side, bored out for mounting Endevco 2225 accelerometers on orthogonal axes. This triaxial assembly bolts to the aluminum base of the sphere. Particular attention must be given to assuring intimate contact and flat surfaces at the accelerometer-block interfaces and block-sphere interface. Otherwise, waveform distortion and ringing can occur, particularly with short rise-time shocks. The upper hemisphere is stainless steel, and, contrary to the photo, uses 10-32 thread Microdot feed-through connectors. Short cables connect each accelerometer to a feed-through connector on the upper hemisphere.

D1M1 uses the same geometry, but an aluminum upper hemisphere is used instead of stainless steel. In this way, a lighter projectile is obtained.

(2) 8-1/2-Inch Balsa Projectiles. D2M1-P7 and D2M2-P11 have inner spheres of the same geometry described in the preceding paragraph except that the diameters are altered per Table 4.6. Balsa wood hemispheres of prototype LPS geometry are bonded over the inner sphere. Cables are routed through a half-inch hole at one of the poles and then potted with RTV foam. Two layers of fiberglass and resin over the entire sphere and then a reinforcing band of fiberglass around the equatorial joint complete the assembly.

(3) 8-1/2 x 12-Inch Foam Spheres. Figure 4-29 illustrates the construction techniques used for the 8-1/2 and 12-inch foam projectiles. The major difference between these spheres and those designs reported in the seventh monthly progress report is that here an aluminum tube is used to line the accelerometer access hole, and a stiffer magnesium base is used, both in order to stiffen the projectile and raise its lowest resonance frequency.

d. Instrumentation

(1) System Description. Throughout the impact testing program, independent measurements of projectile acceleration, initial projectile speed and depth of penetration of the projectile into the target material were made. Depth of penetration measurements required no instrumentation in the sense the term is used here, but simply involved a physical measurement of the final position of the projectile several minutes after an impact test.

Figure 4-30 is a block diagram of the instrumentation system used to obtain acceleration and speed data. Figure 4-31 is a photograph of the

FIGURE 4-28. IMPACT RESEARCH PROJECTILE, D1M2(5)

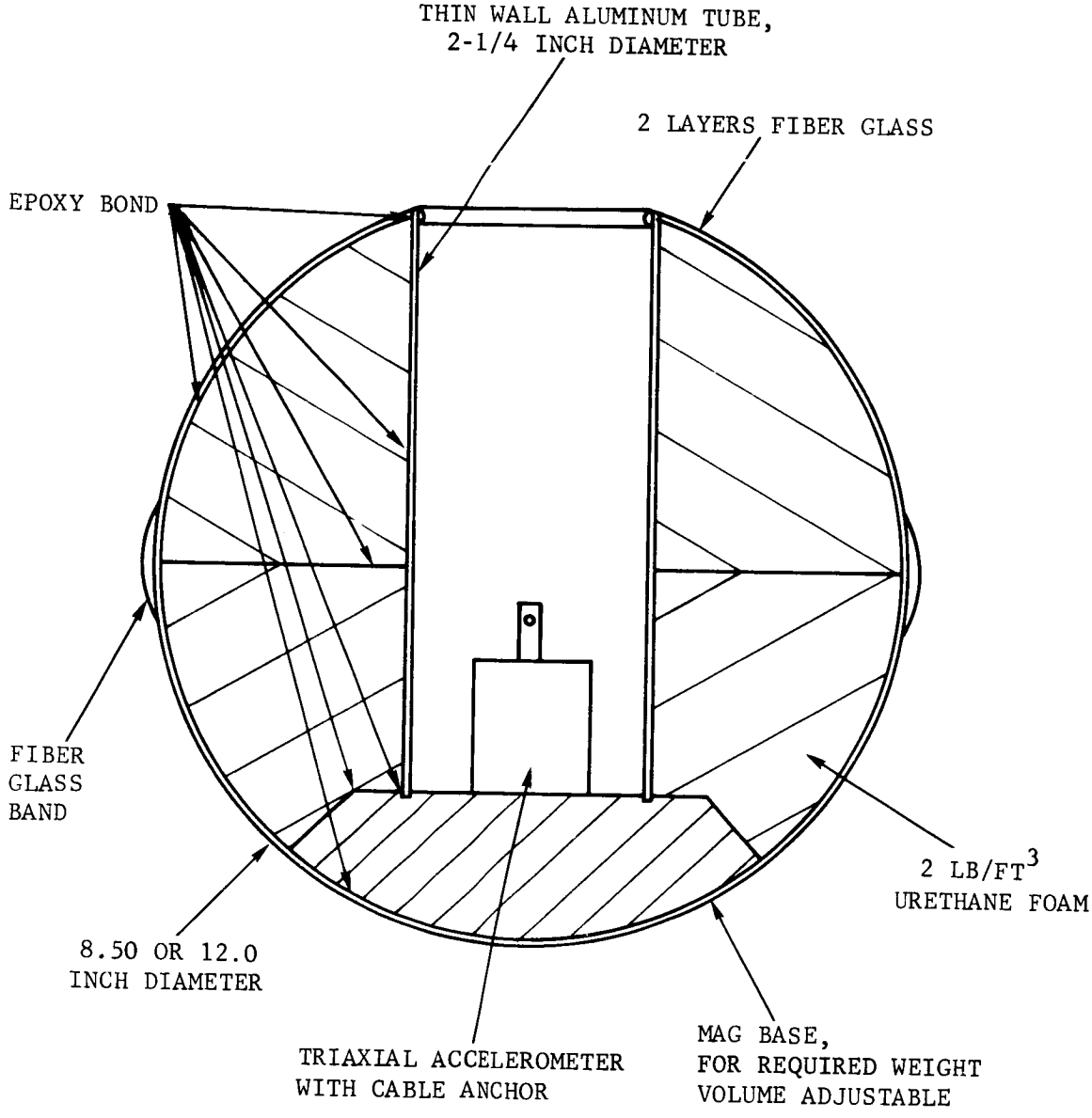

FIGURE 4-29. IMPACT RESEARCH FOAM PROJECTILE

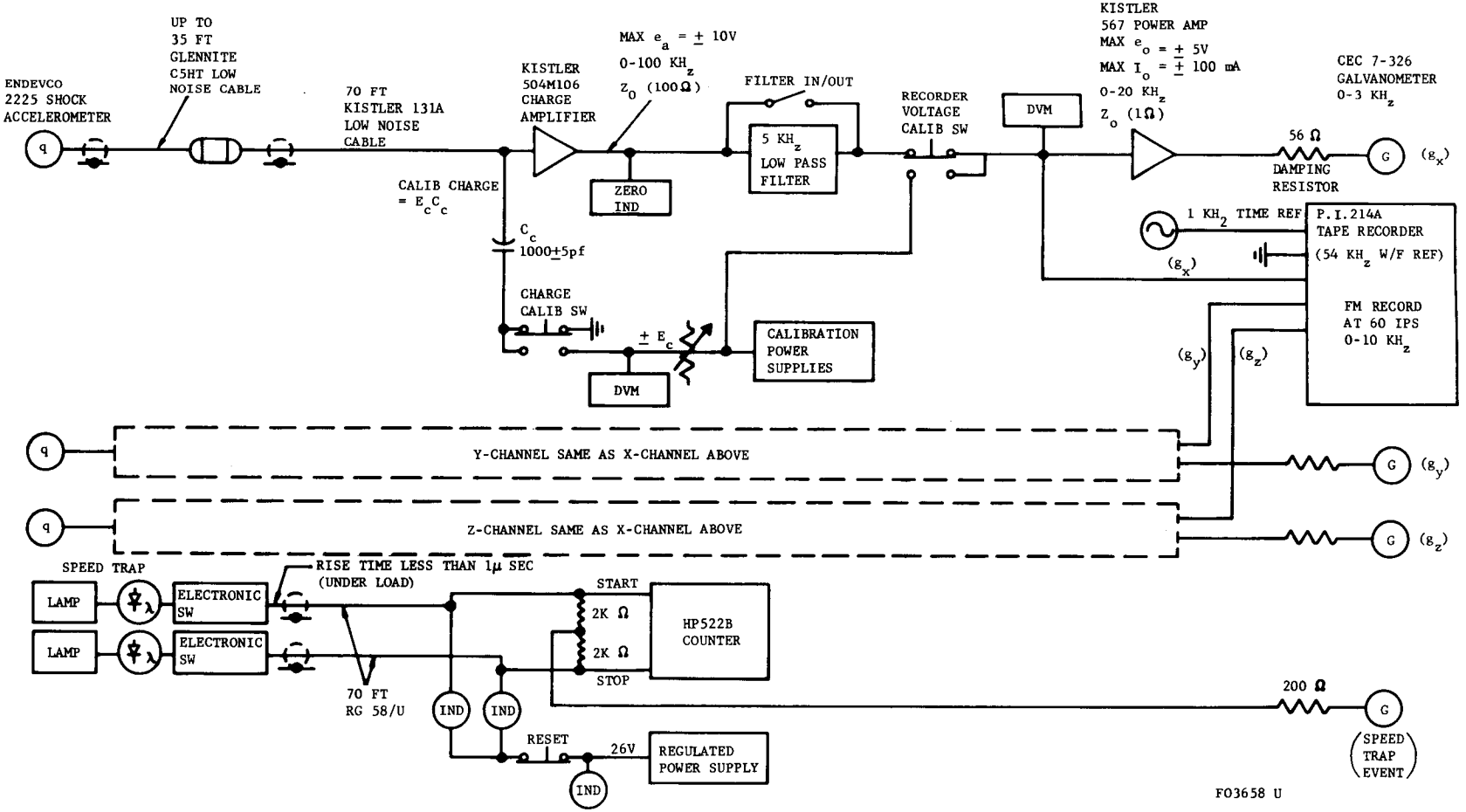

FIGURE 4-30. IMPACT RESEARCH ACCELERATION & SPEED DATA ACQUISITION

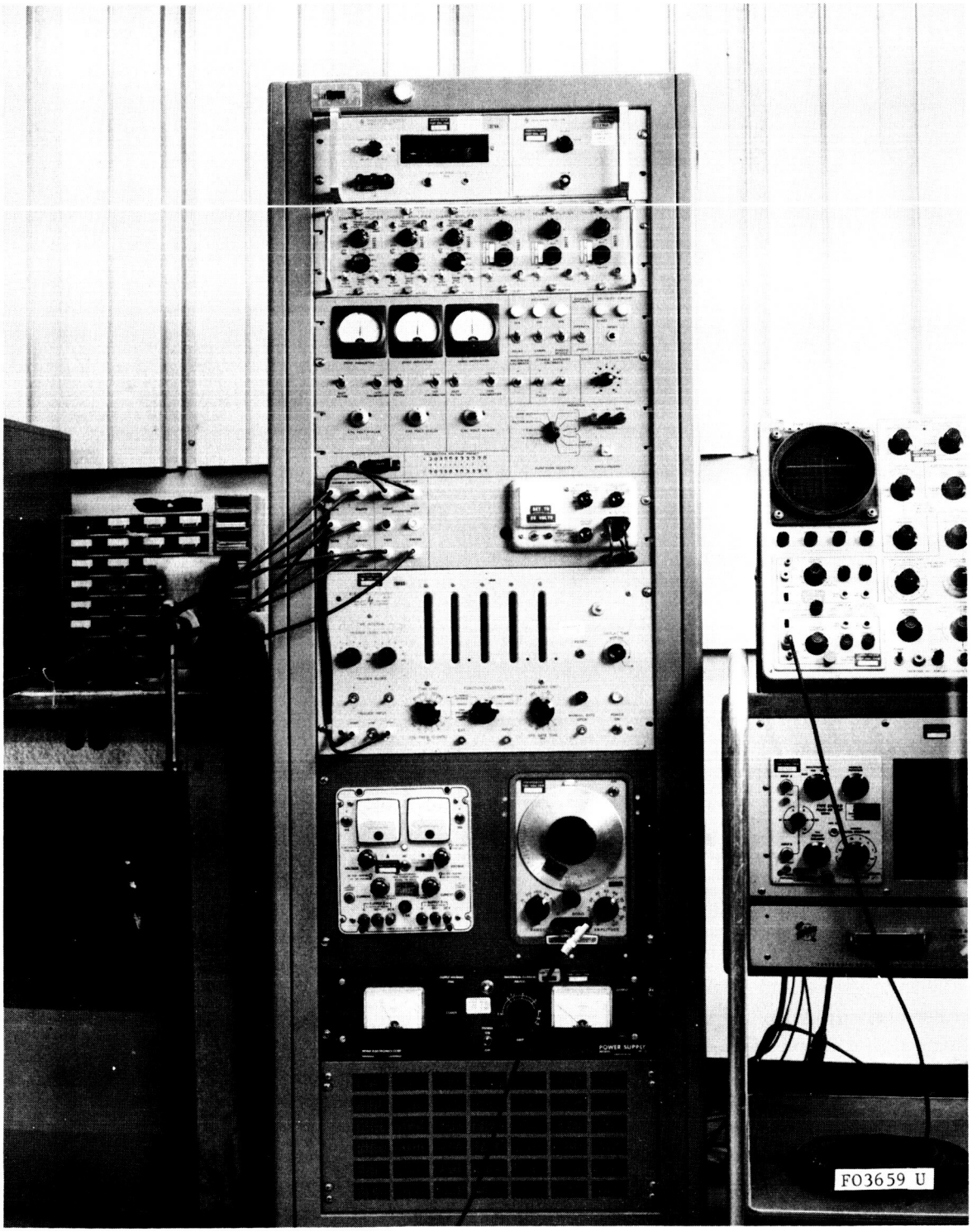

FIGURE 4-31. IMPACT RESEARCH TEST CONSOLE

test console which housed all of that system except for the transducers, speed trap switches, and recorders.

Starting at the upper left of Figure 4-30, acceleration is sensed by piezoelectric accelerometers in the test sphere. The type used here (Endevco 2225) are particularly suitable for this application by virtue of their ability to monitor high energy shocks with little or no zero-shift, less than two percent non-linearity and low cross axis sensitivity.

The accelerometer-generated charge signals are routed through low noise coaxial cables to the test console. Early in the program, it became evident that those cables which trail the projectile (flying cables) can be insidious generators of spurious charge. Great care must be exercised in selecting the cables for low noise properties and in physically arranging them for a minimum amount of whipping and contact with foreign objects during high speed tests.

The sixth monthly progress report discusses an intensive diagnostic test program, wherein several sources of noise were discovered including the original accelerometers, sphere construction, and flying cables. Table 4.7 summarizes those studies and the corrective actions taken.

Charge amplifiers are used to convert the accelerometer charge signals to high level voltage signals. The Kistler 504 charge amplifier can be described as an operational amplifier with capacitive feedback. The input charge signal appears across the feedback capacitor which is the scale-factor determining component. Low frequency response of the charge amplifier, and therefore the entire system, is limited by a controlled resistive leakage path around the feedback capacitor. Typical low frequency cut-off values used in this program are of the order 10^{-4} cps resulting in no droop or tilt of flat topped pulses lasting several hundred milliseconds. Calibration of the system utilizes injection of known charge signals at the input of the charge amplifier in parallel with the transducer. The charge calibration signal is adjusted to any desired level by varying the voltage of a dc power supply to the desired level which satisfies the relationship: $q = CE$, where C is a 1000 pf precision capacitor between the power supply and amplifier input and q is the desired charge to be inserted.

A zero indicator consisting of a zero-center microammeter and appropriate buffering is provided at the output of the charge amplifier. This allows zero adjustment readout of the charge amplifier during setup and provides immediate fault indications for all preceding circuitry.

SUBJECT	TEST	RESULTS	CONCLUSIONS
SIGNAL CONDITIONING ELECTRONICS	500% IMPULSIVE OVERLOAD	NO NOISE OR ZERO SHIFT, INSTANT RECOVERY	OK AS IS
STANDING CABLES	MECHANICAL MOTION	NO NOISE	OK AS IS
FLYING CABLES	CRUSH AND SLAP		USE GLENNITE C5 HT OR KISTLER 870 M2
ENDEVCO 3060A		1600 pC PULSE; 224 pC SHIFT	
KISTLER 121		>80 pC PULSE; 25 pC SHIFT	
KISTLER 870 M2		3 pC PULSE; NO SHIFT	
MICRODOT 250-3849		1600 pC PULSE; 160 pC SHIFT	
GLENNITE C5 HT		2 pC PULSE; NO SHIFT	
EPOXY PROJECTILE	3000 LB SQUEEZE	128 pC SIGNAL	DO NOT ENCAPSULATE ACCELEROMETER
ACCELEROMETER	TRANSVERSE SHOCK		USE ENDEVCO 2225
KISTLER 808 M101(TRIAX)		ZERO SHIFT	
KISTLER 808A		ZERO SHIFT	
KISTLER 805		ZERO SHIFT	
ENDEVCO 2223C(TRIAX)		ZERO SHIFT	
ENDEVCO 2225		NO ZERO SHIFT	
ELECTRA SCIENTIFIC ES 6041		NO ZERO SHIFT	
NEW PROJECTILE	150 FPS, FOAM TARGET	NO ZERO SHIFTS SMALL NOISE BEFORE IMPACT	RE-RIG FLYING CABLE
RE-RIG FLYING CABLE	150 FPS, FOAM TARGET	NO ZERO SHIFTS NO PRE-IMPACT NOISE	USE THIS SETUP

TABLE 4.7 IMPACT RESEARCH DIAGNOSTIC TESTS SUMMARY

Next a second-order low pass filter is provided to attenuate noise above 5 KH_Z. A switched short circuit path around the filter is provided for cases in which filtering is not desired.

The signal is then routed simultaneously through a galvanometer driver amplifier and to a tape recorder. The galvanometers are used to provide a quick-look display on direct readout oscillograph paper. If the quick-look record indicates a satisfactory test, then the tape recorded data are scheduled for computer processing.

All acceleration data and a 1 KHz time reference signal are FM recorded on magnetic tape with a 54 KHz subcarrier. Each acceleration channel is connected to two tracks on the recorder. One of the two tracks has a lower modulation sensitivity and will accommodate signal levels up to two times the predicted level. This over-range capability has prevented the need for retesting in more than a few cases. One track on each of the two head stacks is used for wow and flutter reference when the data are ultimately played into the computer.

A speed trap mounted near the target surface consists of two light beams effectively spaced 12 inches apart. Spacing is adjusted prior to each impact test by placing a shadow mask at the position of the projectile path and then adjusting the lamp spacing until both photoelectric switches just trigger. Each switch contains a photo-diode in the base circuit of an overdriven direct-coupled amplifier with an SCR output. As the light beams are interrupted, the switches operate, placing a low impedance across the output leads. Voltage on the output leads from a high impedance voltage source drops to near zero, operating the time interval section of an electronic counter. The sum of the voltage on the two signal leads is also applied to a galvanometer on the oscillograph recorder and serves as a back-up time interval display. The speed trap accuracy is limited by the precision with which the effective light beam spacing can be set ($\pm$0.05 inch), the simultaneity of the two switches (0.0001 second) and the resolution of the electronic counter (0.00500 $\pm$ 0.00001 second), at 200 feet per second. This yields a maximum possible timing error of 0.02 milliseconds corresponding to less than $\pm$ two feet per second error at 200 feet per second projectile speed.

(2) Data Processing and Display. Magnetic tape recordings of impact research data are re-recorded onto continuous loop tape at a speed reduction of 32:1. Figure 4-32 illustrates the gross process.

A tape loop containing calibration signals, for the impact data to follow, is played into the computer at 30 inches per second, thereby achieving an

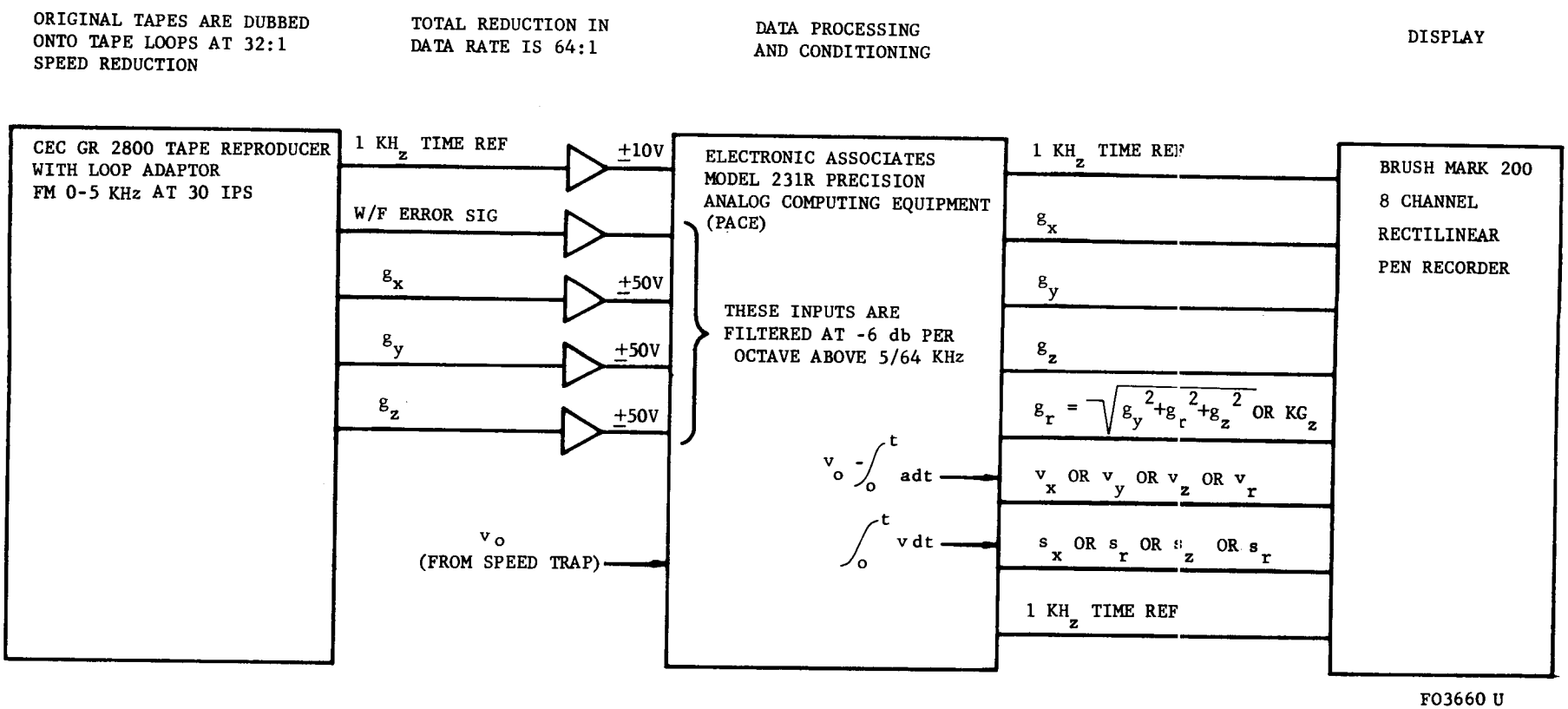

FIGURE 4-32. IMPACT RESEARCH DATA PROCESSING

overall data rate reduction of 64:1. Using the calibration signals, the computer is adjusted for the following results: (a) maximum wow and flutter tape noise cancellation, (b) cancellation of data zero offset due to non-precise subcarrier center frequency, (c) correct scale factors for the pen recorder, (d) correct integration rates to obtain velocity and distance outputs, and (e) sufficient 1 KH_Z signal amplitude. Next, a tape loop containing the shock data is played into the computer. The wow and flutter compensation and zero offsets are trimmed if required.

An initial-condition voltage corresponding to the speed-trap value of initial projectile speed is applied to the first integrator so that the output will be: $v = v_o - \int_o^t a\,dt$. This allows the display to show the projectile coming to a full stop or rebounding at a constant velocity as the case may be. Furthermore, it allows computation of depth of penetration with respect to a stationary reference. Without the initial condition information, velocity would be computed as an incremental change and distance would be computed with respect to a coordinate system moving in space with a velocity of v_o.

Iterative computer solution is provided by control circuits synchronized with the motion of the data tape loop. The integrators are turned on just before the leading edge of the shock data and reset occurs after the data have passed. Referring to Figure 4-33, we see a typical display of computer output.

In the upper right-hand corner is identified the magnetic tape and event where the calibration and impact data for this test are stored (LPS-023-12). The date of the computer run is also noted there. Lower down, below the sinusoidal time reference trace, is the title of the test and pertinent data about the projectile, initial velocity, etc. In this case, the projectile was a 5.26-pound, 8.5-inch diameter sphere including an 11 lb/ft^3 balsa limiter. The target material was aerated 120 mesh Nevada sand from the LEM test site. The test was performed in atmosphere at 108 ft/sec. The trajectory was zero degrees off the target normal and this was the first test using that combination of parameters.

There is very little output in the g_x and g_y channels indicating that the projectile hit the sand squarely with the z-axis parallel to the trajectory. For this reason, $|g_r|$ was not computed, i.e., $g_r = g_z$. The g_z trace indicates: (1) there was no discernible ringing of the projectile, (2) the peak acceleration was 1300 g, (3) the time to peak was about 0.8 millisecond, (4) acceleration dropped off to a plateau of less than 40 g, and (5) decreased to zero at some time that is not evident by inspection of the g_z curve alone.

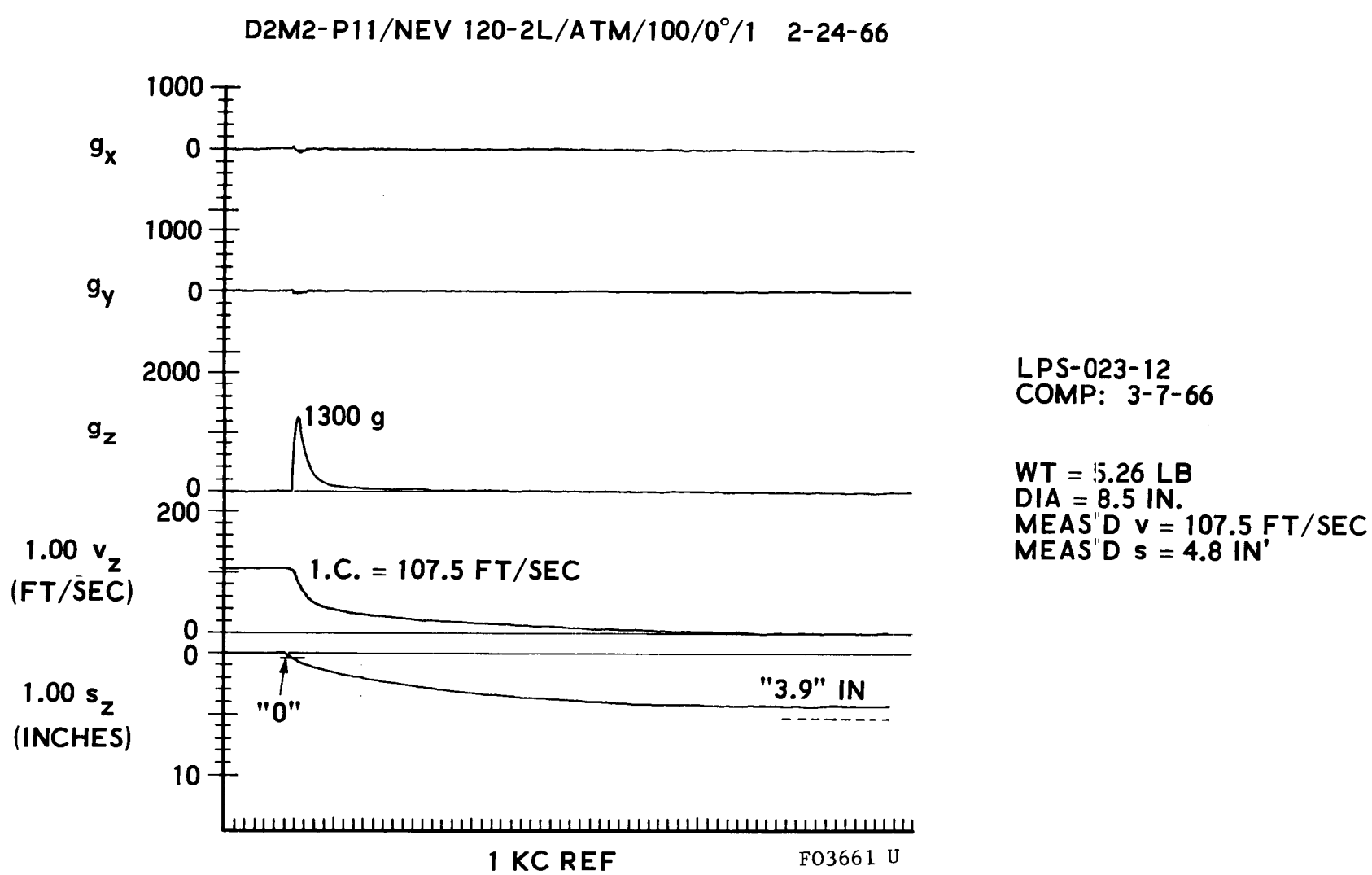

FIGURE 4-33. TYPICAL DATA FROM COMPUTER

For purposes of integrating g_z to obtain velocity, zero-g was defined in the computer as that value of g_z for time greater than 60 milliseconds past the leading edge of the data. Using the speed-trap reported value of initial velocity as a computer initial condition resulted in a final computer velocity that was both constant and zero. That correlation constitutes a statement of validity concerning the entire g_z information channel. A second piece of information obtained from the velocity trace is the time at which g_z actually reached zero. We see in this case that the velocity became constant (zero-g) about 48 milliseconds past the leading edge of the data.

The depth of penetration curve starts downward at the instant the computer is switched from "i.c." to "operate." The cross on the curve (s_z) indicates the location of first contact of the projectile with the target material. Measurements of depth of penetration from the curve are referenced to that origin. The computed depth of penetration is 3.9 inches which is 0.7 inch short of the independently measured value. The reason for the discrepancy is not known but may be due to any combination of the following factors.

(1) The position of the projectile five minutes after impact may indeed have been different than its position 50 milliseconds after impact.

(2) There may have been a rate error in the second integrator.

(3) There may have been some rebound not allowed by the computer. In that case, the final velocity would be indicated as a constant negative value and the depth of penetration curve would have a markedly different shape.

(4) A constant error of 1.45 g (0.07 percent of full scale) in the computer definition of zero g would yield the 0.7-inch displacement error in 50 milliseconds.

The coefficient "1.00" in front of the v_z and s_z labels indicate that no adulterations to the acceleration scale factor were made in order to force the computed velocity change to equal the speed-trap value.

Much interest has been shown lately concerning the long tail, or pedestal, or plateau, following the main pulse of impact acceleration. In order to demonstrate the existence of such a phenomenon in particulate target materials without resorting to computer integration, the impact test just illustrated was repeated using eight-times greater sensitivity in the charge amplifier. The quick-look oscillogram has been reproduced in Figure 4-34. A plateau of about 25 g and a total pulsewidth of about 49 milliseconds are clearly indicated.

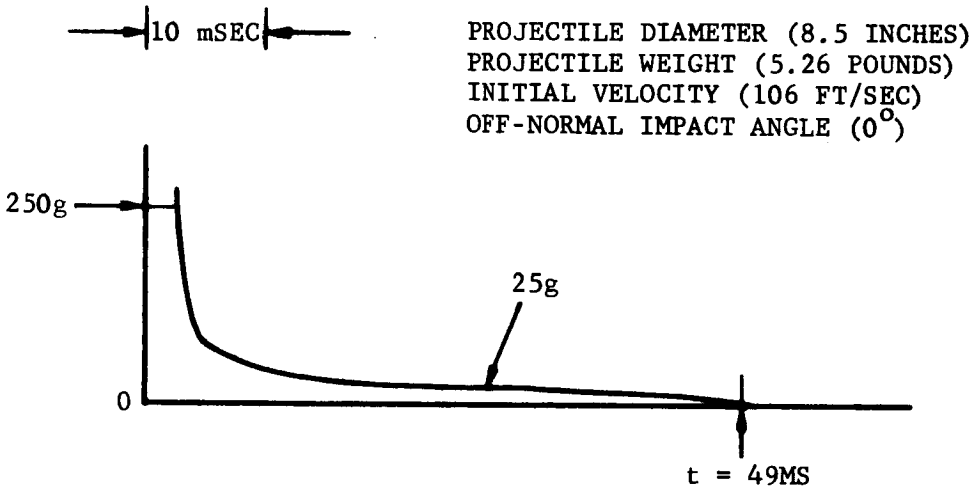

FIGURE 4-34. ACCELERATION TAIL-OFF FOR IMPACT INTO NEVADA 120-2L SAND

4.3.3 TEST RESULTS

a. Balsa Sphere Impact Tests. Some seventeen impact tests, using the balsa limiter equipped projectiles D2M1*-P7 and D2M2-P11, were conducted to obtain data for assessing limiter properties. Tests at several velocities into Nevada 120-2 sand indicated that both projectiles sustained limiter crushing damage for initial speeds greater than 125 feet per second. The maximum payload peak shock during a rigid impact was 5000 g for the eleven lb/ft^3 limiter. Table 4.8 tabulates the significant data from all of the tests.

b. Impact Research Data. The entire collection of impact research acceleration-time histories is published under separate cover. However, several of the data have been reduced for convenient presentation here in the form of comparative results. Figure 4-35 illustrates some typical waveforms obtained from impacts against a wide range of materials. It is complemented by Figure 4-36 which shows in bar chart form, the peak accelerations obtained from thirteen combinations of target material and atmospheric pressure for constant projectile parameters. Figure 4-37 compares bearing strength and acceleration curves for two materials in vacuum and at atmospheric conditions. Figures 4-38 through 4-40 are graphs illustrating the effects of velocity, projectile diameter, and projectile weight respectively. And, finally, Table 4.9 compares projectile trajectory angle data.

TABLE 4.8

BALSA LIMITER IMPACT TESTS

Test	Proj Wt (lb)	Initial Speed (ft/sec)	Peak Accel (g)	Time to peak (ms)	Total Duration (ms)	Depth of Penetration (in.)	Balsa Crush (in.)
D2M1-P7/Rigid/0°	3.94	143	4800	1.1	2.2	0	1-1/4
D2M2-P11/Rigid/0°	5.15	153	5000	1.1	2.1	0	1
D2M2-P11/Rigid/0°	5.17	196	5100	1.1	3.3	0	1-5/8
D2M2-P11/Rigid/60°	5.05	150	2500	0.9	2.5	0	9/16
D2M2-P11/Cobble/0°	5.26	208	4300	0.9	9.0	1.0	1
D2M1-P7/Nev 120-2/0°	4.02	72	1400	0.9	22	3.8	0
D2M1-P7/Nev 120-2/0°	4.02	85	2250	0.7	26	3.8	0
D2M1-P7/Nev 120-2/0°	4.02	101				3.8	0
D2M1-P7/Nev 120-2/0°	4.02	126	2600	0.4	11	3.6	1/2
D2M2-P11/Nev 120-2/0°	5.01	52	395	1.0	56	3.8	0
D2M-P111/Nev 120-2/0°	5.01	87	1200	0.3	48	4.5	0
D2M2-P11/Nev 120-2/0°	5.01	102	1700	0.3	40	4.5	0
D2M2-P11/Nev 120-2/0°	5.01	127	2500	0.3	40	4.0	Superficial Damage
D2M2-P11/Nev 120-2/0°	5.01	152	7400	0.5	44	4.3	1/4
D2M2-P11/Nev 120-2L/0°	5.26	52	370	0.9	59	4.3	0
D2M2-P11/Nev 120-2L/0°	5.26	108	1300	0.6	48	4.8	0
D2M2-P11/Nev 120-2L/0°	5.26	148	2700	0.6	42	4.3	0

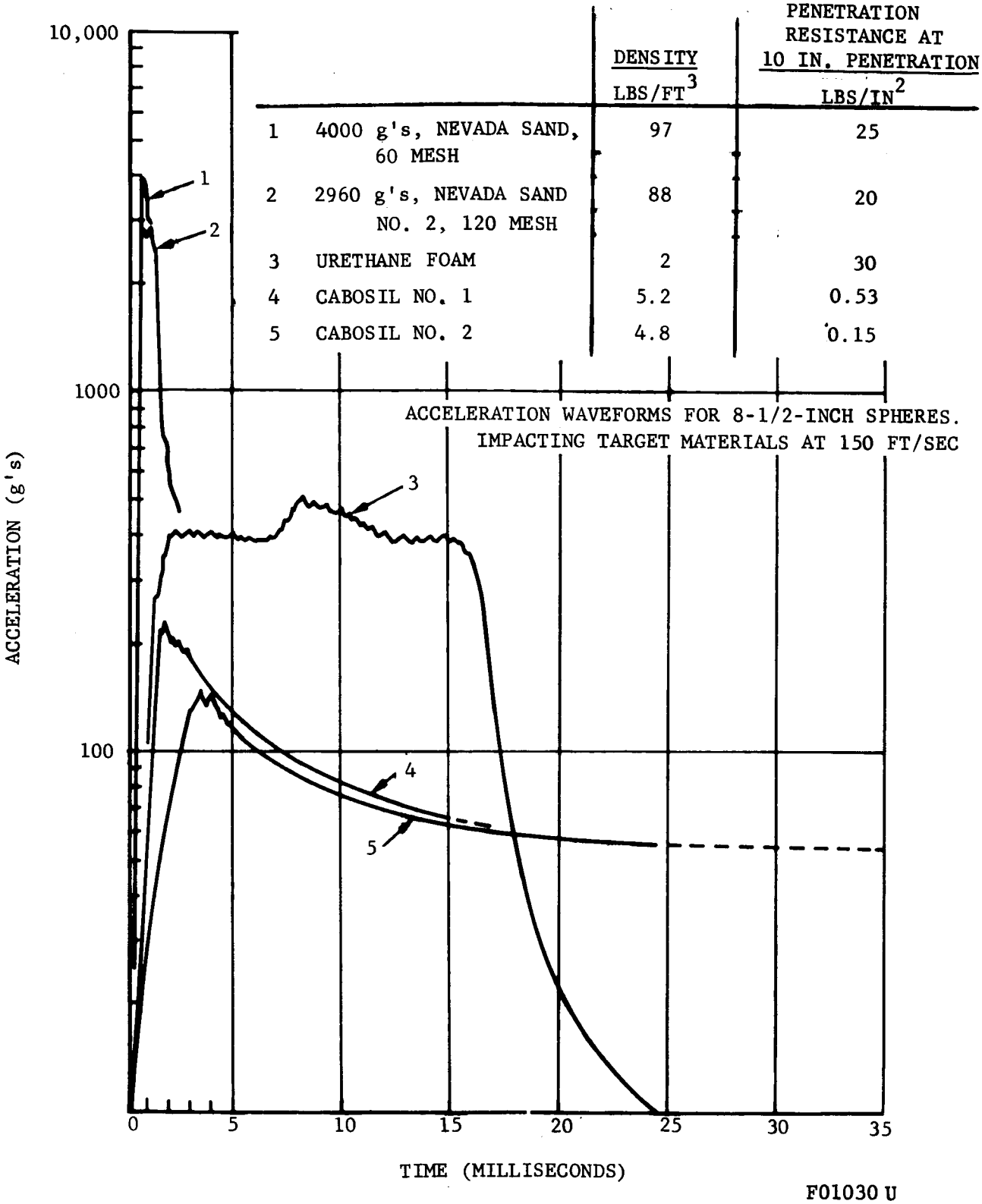

		DENSITY LBS/FT^3	PENETRATION RESISTANCE AT 10 IN. PENETRATION LBS/IN^2
1	4000 g's, NEVADA SAND, 60 MESH	97	25
2	2960 g's, NEVADA SAND NO. 2, 120 MESH	88	20
3	URETHANE FOAM	2	30
4	CABOSIL NO. 1	5.2	0.53
5	CABOSIL NO. 2	4.8	0.15

FIGURE 4-35. IMPACT ACCELERATION CURVES

FOR 8.5 INCH DIAMETER, 5 POUND PROJECTILES AT 150 FT/SEC

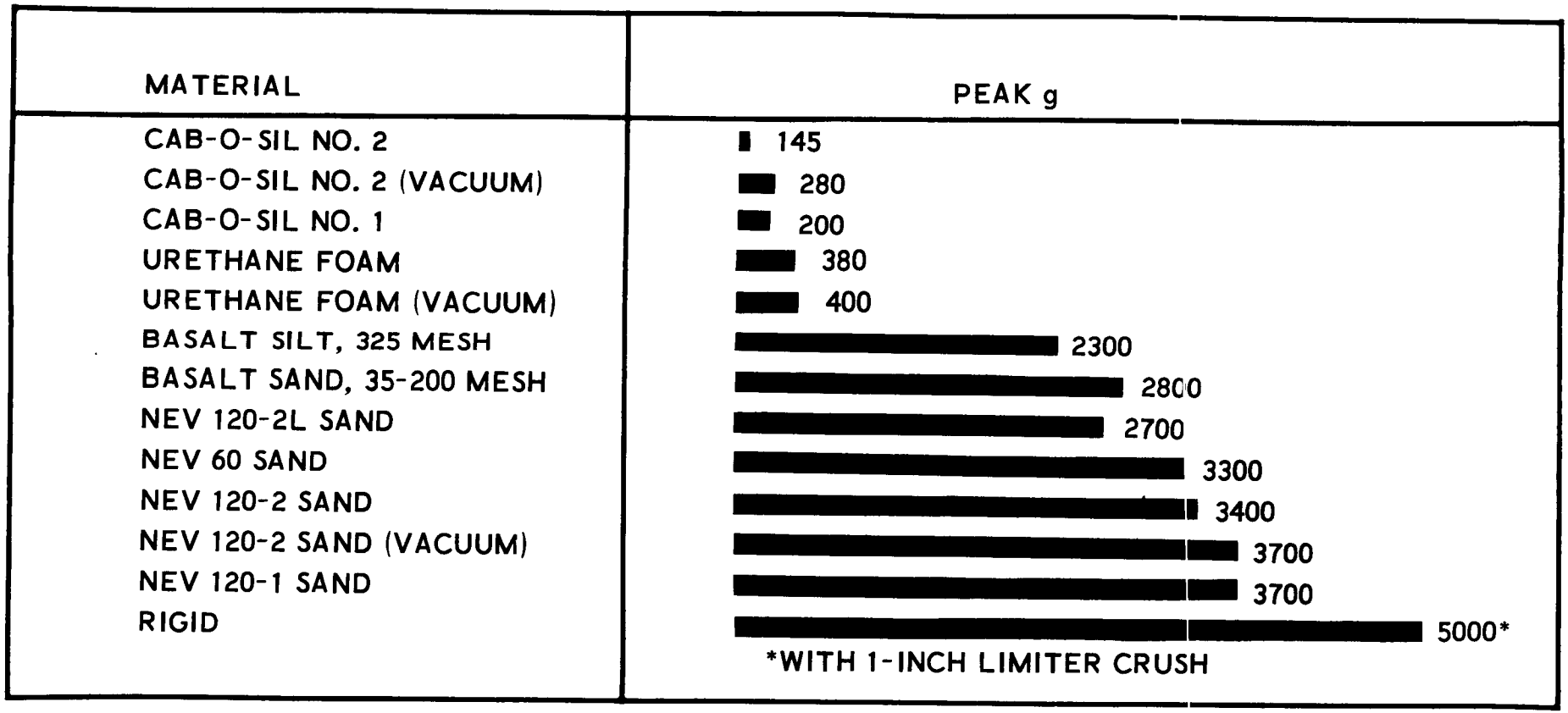

F03663 U

FIGURE 4-36. PEAK ACCELERATIONS IN TARGET MATERIALS

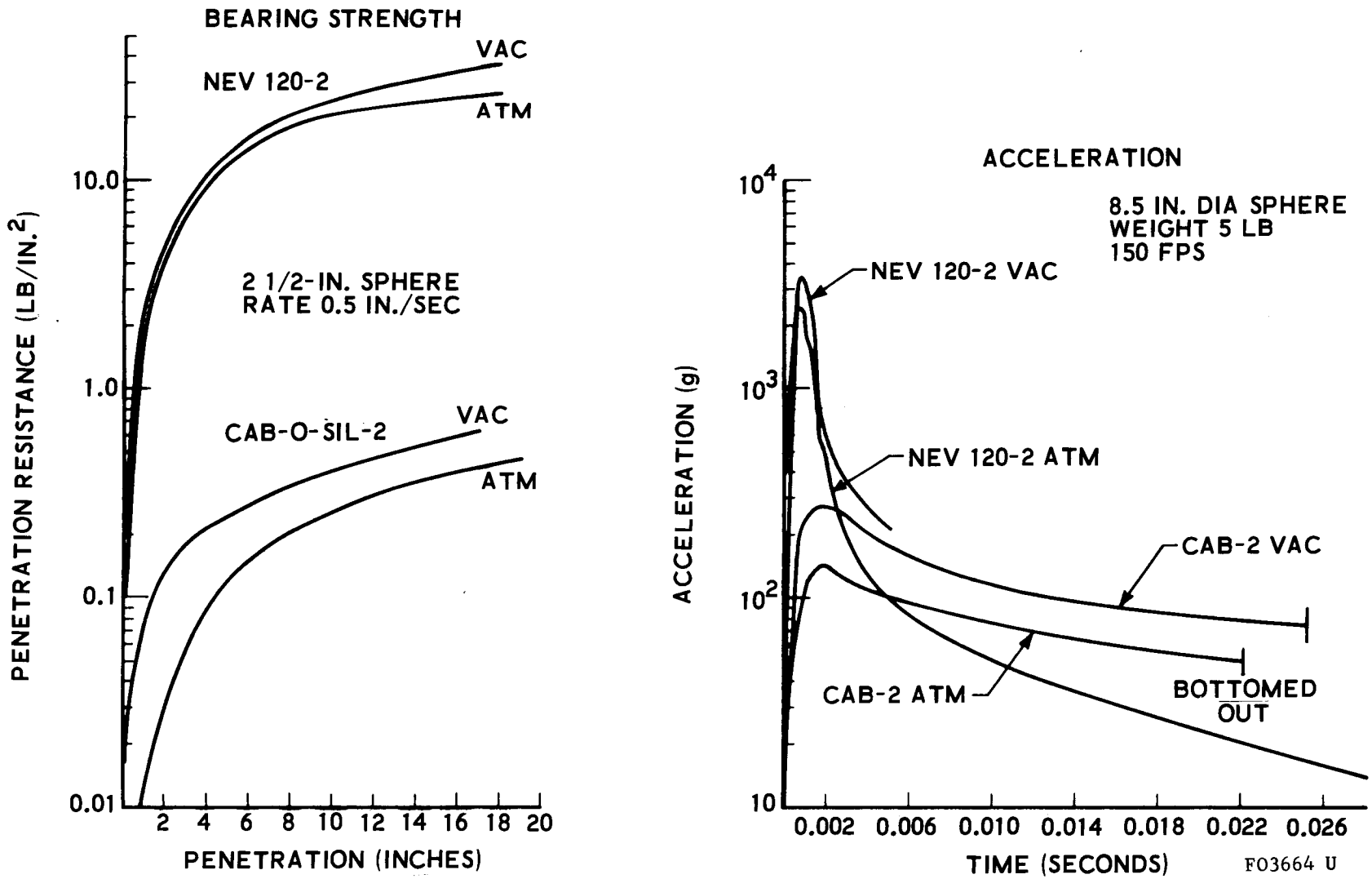

FIGURE 4-37. TYPICAL VACUUM EFFECTS

EFFECTS OF VELOCITY

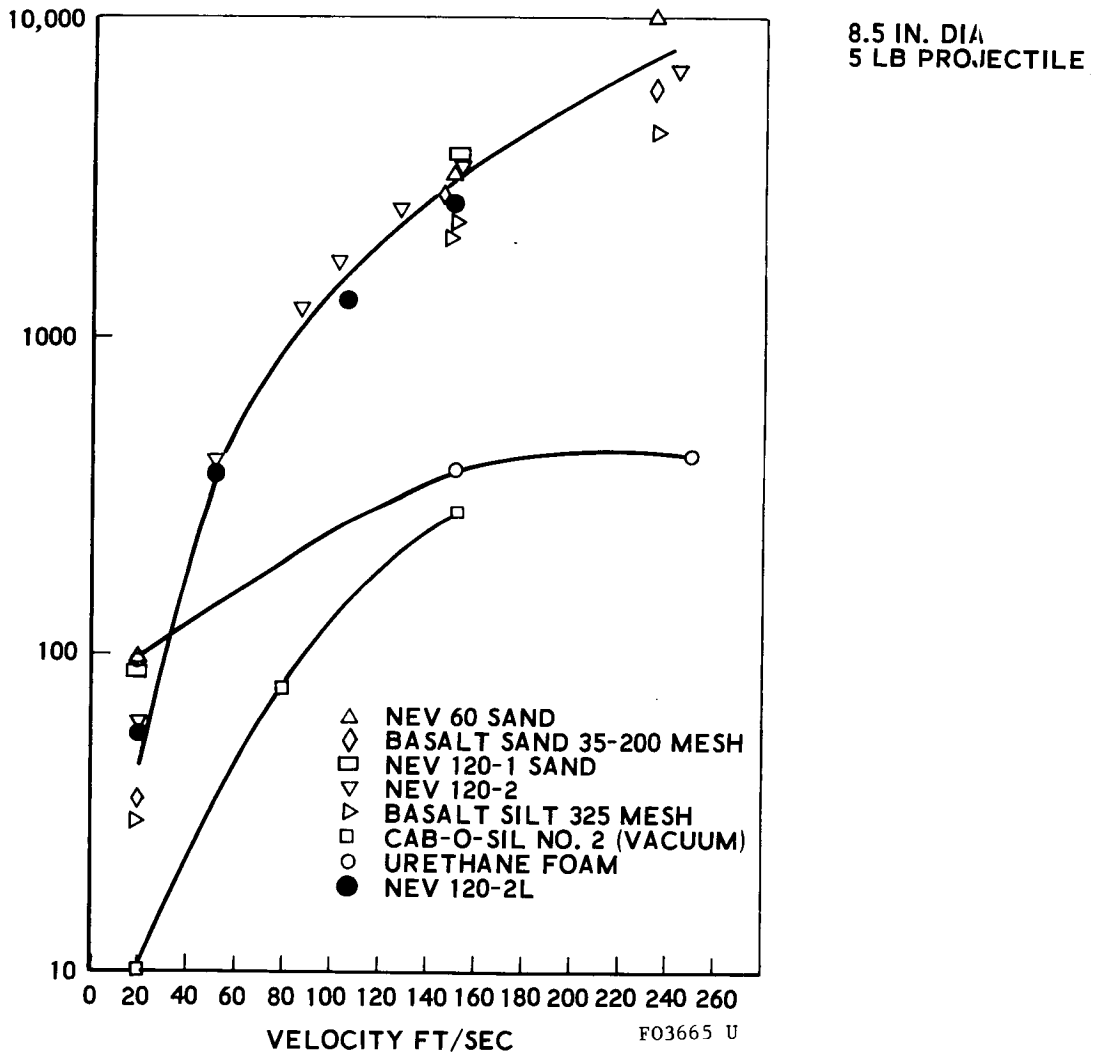

FIGURE 4-38. EFFECTS OF VELOCITY

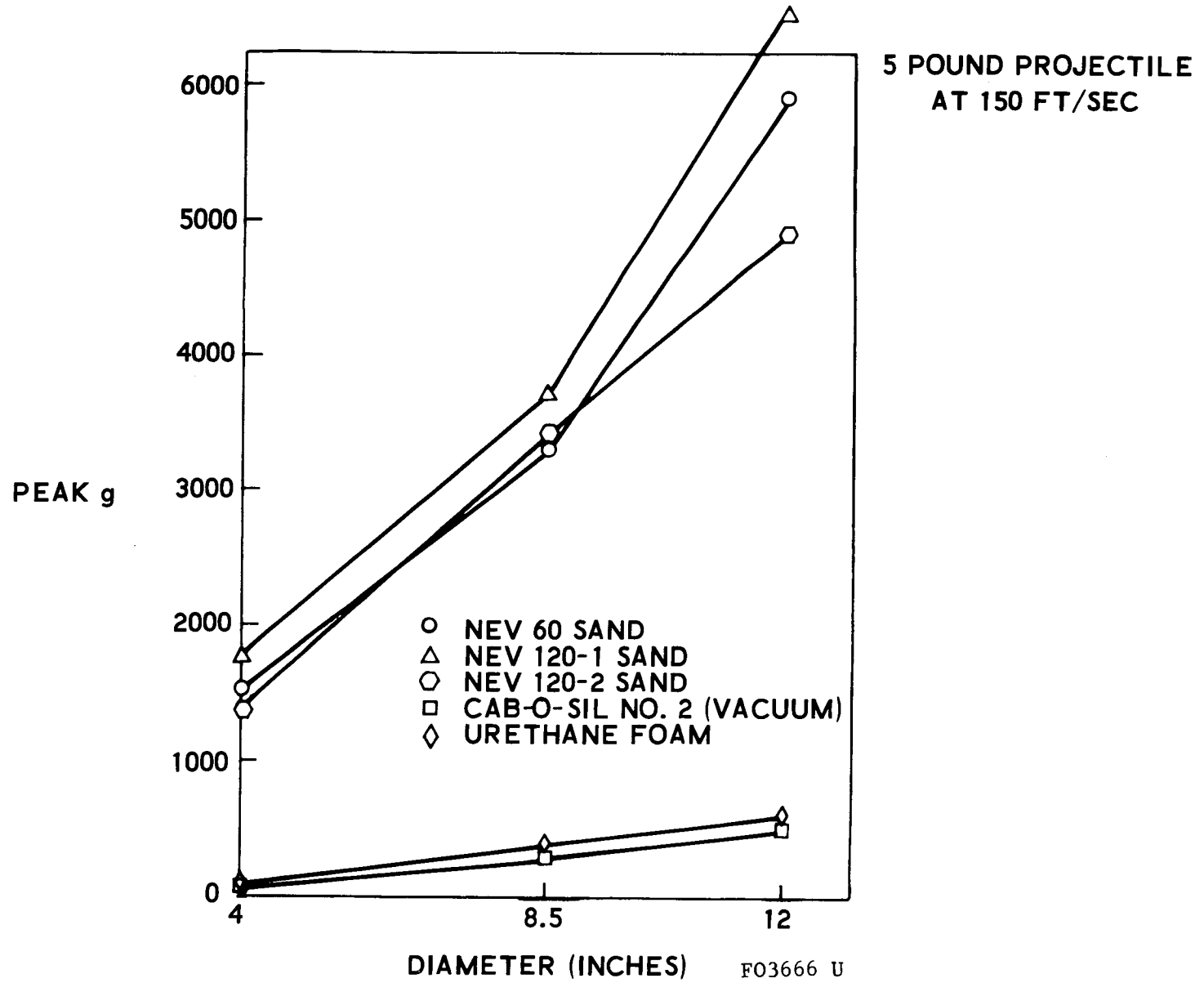

FIGURE 4-39. EFFECT OF DIAMETER

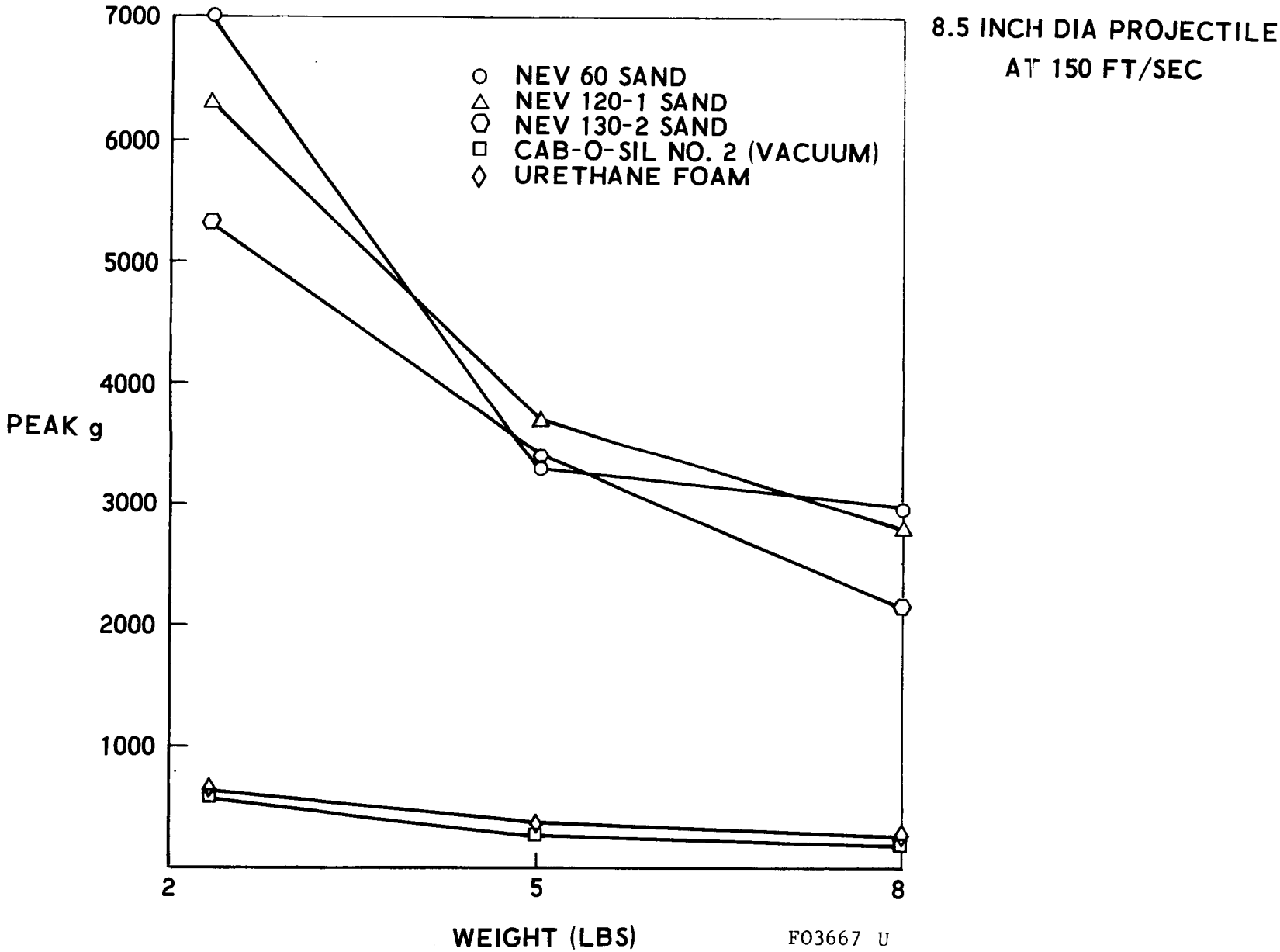

FIGURE 4-40. EFFECT OF WEIGHT

TABLE 4.9

EFFECTS OF ANGLE BETWEEN TRAJECTORY AND NORMAL TO TARGET SURFACE

8-1/2 DIA, 5LB PROJECTILE AT 150 FT/SEC

TARGET	PEAK g 0°	PEAK g 30°	PEAK g 60°	RATIO $\frac{g}{g_{0^\circ}}$
RIGID	5000		2500	0.50
NEV 120-1 SAND	3700	3100		0.84
NEV 120-2 SAND	3400	2700		0.79
NEV 60 SAND	3300	2600		0.79
URETHANE FOAM	380	375	335	> 0.88

4.4 LEM IMPACT TESTING

4.4.1 TEST OBJECTIVES AND DESCRIPTION

The test objectives were to simulate LEM landing conditions in lunar surface models and establish:

(1) Impact characteristics of the LEM on a range of selected target materials.

(2) Correlation factors with penetrometer impact test data and simulated LEM landing conditions.

A vertical test configuration was selected with a free fall velocity of 10 feet per second. The LEM landing gear was simulated by utilizing a boiler plate strut and pad with the strut honeycomb load stroke characteristics and pad configuration duplicated. The LEM mass was duplicated to 25, 50, and 100 percent of the vehicle landing weight. This coincided with a one, two, or four-legged landing condition. A constant force pneumatic device was provided to account for lunar gravity effects in earth gravity testing.

Four target materials were selected ranging from soft to hard sand and included a foam material. These materials were conditioned and controlled to provide a duplication of that utilized in the penetrometer impact research program. Static bearing strength tests were accomplished with several probe sizes (8.5 inch spherical, 8.5 inch flat, 12 inch spherical, and LEM pad) to establish material properties. In addition to providing gross information on total pad penetration and strut compression, the test system was instrumented to provide dynamic information of displacement-time, acceleration-time and force-time histories of the tested configuration.

The LEM test matrix shown in Figure 4-41 defines the test program conducted.

4.4.2 LEM LANDING TEST FACILITY DESCRIPTION

The LEM Landing Test Facility is shown in schematic form in Figure 4-42. The major elements are the LEM strut simulator, crushable honeycomb, LEM equivalent mass, explosive bolt release, constant force gravity simulator, test gantry, static bearing tester, target material reservoir, target material aeration system, and dynamic instrumentation system.

The basic test sequence is as follows:

(1) The target material is conditioned by the aeration system and evaluated for bearing strength properties by the static bearing tester.

M	3 NEVADA NO. 60 SAND	5 NEVADA 120 NO. 1 SAND	6 NEVADA 120 NO. 2 SAND	10 FOAM
25% LEM VEHICLE WEIGHT	X	X	X	X
50%	X	X	X	X
100%	X	X	X	X

EXPLANATION

ALL TESTS CONDUCTED IN ATMOSPHERE

FOR ALL TESTS:
ANGLE = 0° FROM VERTICAL
V = 10 FPS

TARGET MATERIALS TESTED IN RESERVOIRS MEASURING 15 x 15 x 6 FT:

3. NEVADA NO. 60 SAND
5. NEVADA 120 NO. 1 SAND
6. NEVADA 120 NO. 2 SAND

TARGET MATERIAL TESTED IN BIN MEASURING 5 FT DIA x 4 FT DEEP:

10. FOAM

F03668 U

FIGURE 4-41. LEM CORRELATION TEST MATRIX

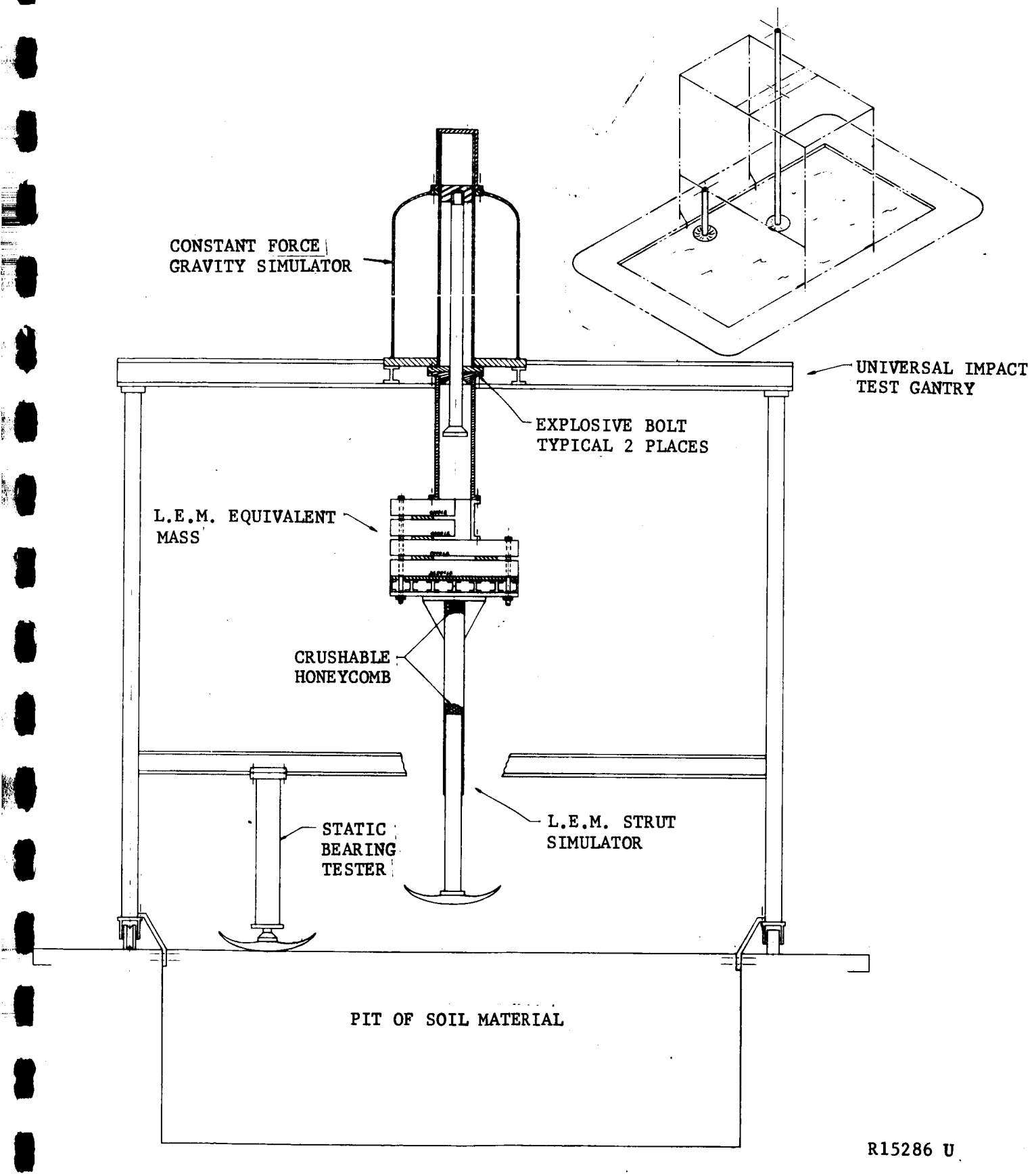

FIGURE 4-42. LEM STRUT DROP TEST ASSEMBLY

(2) The LEM mass system is released by explosive bolts and allowed to free-fall to a velocity of 10 ft/sec.

(3) The gravity simulator is engaged just prior to contact with the target material by the LEM pad. The simulator will provide a constant force of 5/6 the earth weight for the remainder of the system motion.

(4) The LEM strikes the target material and a combination of pad penetration and strut compression occurs.

(5) The instrumentation system provides dynamic data of displacement, acceleration and force. The major elements of the facility are described below:

a. LEM Test Gantry. The LEM test gantry is shown in Figure 4-43. It consists of a 25 foot long x 10 foot wide x 28 foot high steel structure which straddles the target material reservoir. The gantry is mounted on wheels and is moved by means of a motor driven winch on angle rails. The gantry provides the mounting for the gravity simulator and LEM mass at a top interface plate adapter. The gantry also provides the mounting for the static bearing tester at the lower cross beam.

b. LEM Landing Pad. The LEM landing pad is a duplicate of the LEM dimensional configuration, but is constructed of cast aluminum instead of fiberglass and honeycomb. The major diameter of the pad is 37 inches.

c. LEM Equivalent Weight. The LEM equivalent weight consists of 4 steel blocks each 6 inches thick x 4 feet square weighing approximately 4000 pounds. The mass is attached rigidly to the LEM strut below and hung from the gravity simulator.

d. LEM Strut and Honeycomb. The LEM strut assembly construction is similar to an aircraft landing cylinder with concentric tubes. The cylinder is 7.0 inches I.D. and the strut is 6.0 inches O.D. with nylon bushing guides. Two crushable honeycomb cartridges are installed in the cylinder. The strut assembly with the honeycomb cartridges is shown in Figure 4-44. The honeycomb cartridges each have a different constant load characteristic. The first unit is 17.15 inches long and designed to crush at a constant 6000 pound force for 70 percent of its original length, while the other is designed to crush at a constant 12,000 pound force for 70 percent of its original length. A static test, configured as shown in Figure 4-45, was conducted to demonstrate load stroke characteristics. The results are shown in Figure 4-46.

e. Target Material Reservoir. The target material pit consists of two 15-foot square by 6 foot deep reservoirs for the sand target materials

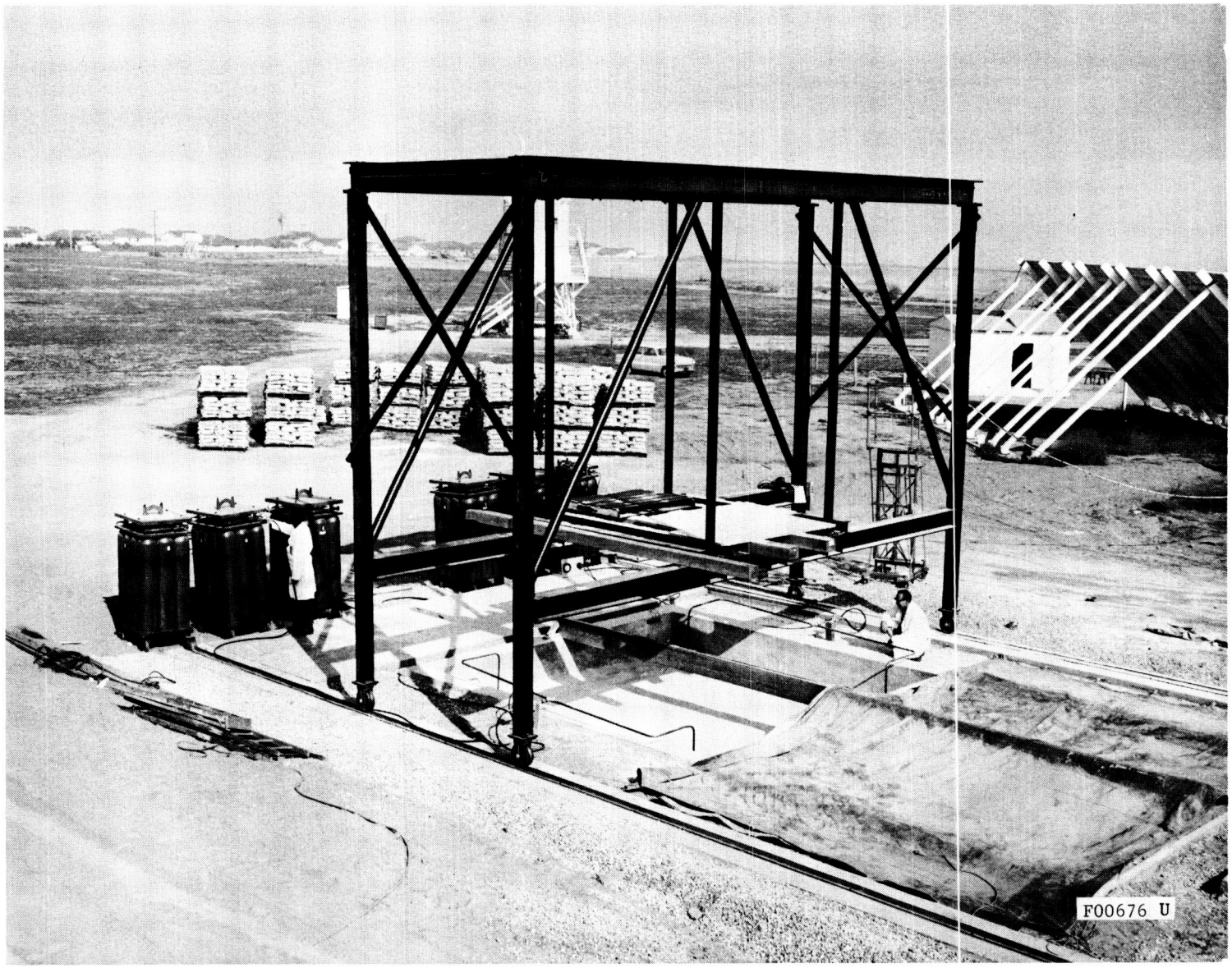

FIGURE 4-43. LEM DYNAMIC LANDING TEST FACILITY

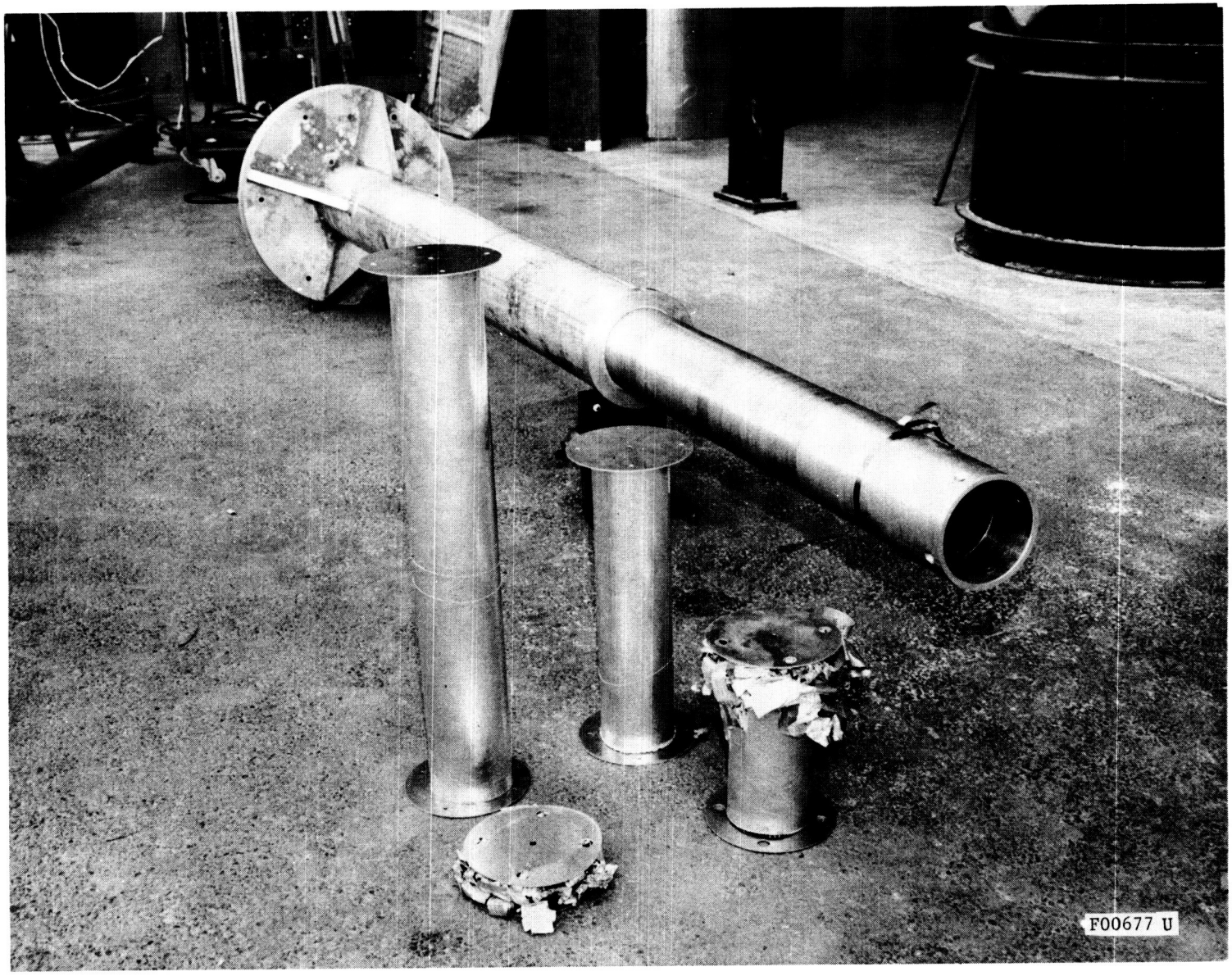

FIGURE 4-44. BOILER PLATE LEM STRUT WITH CRUSHED AND UNCHUSHED PIECES OF HONEYCOMB

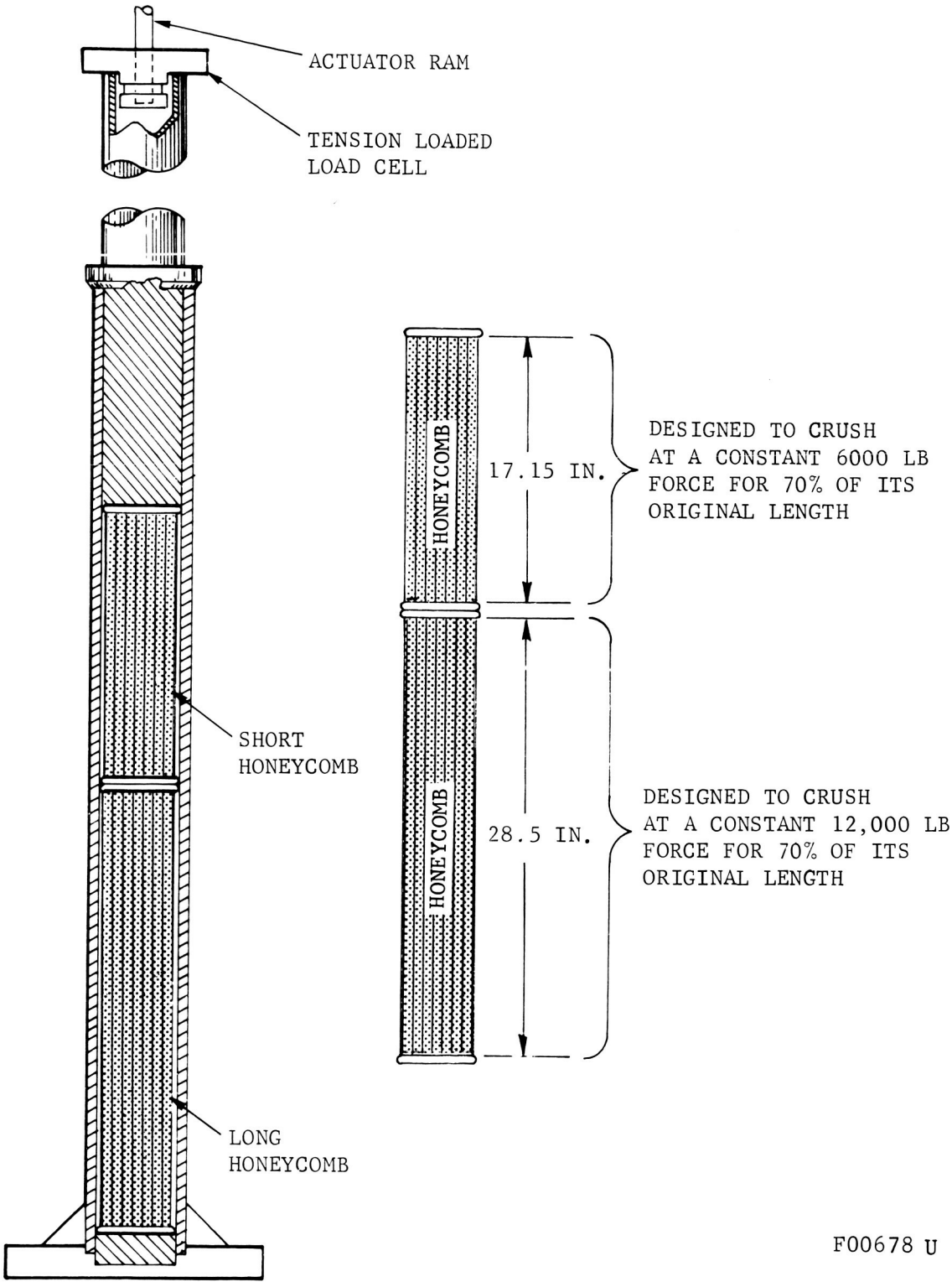

FIGURE 4-45. LEM HONEYCOMB CRUSH TEST

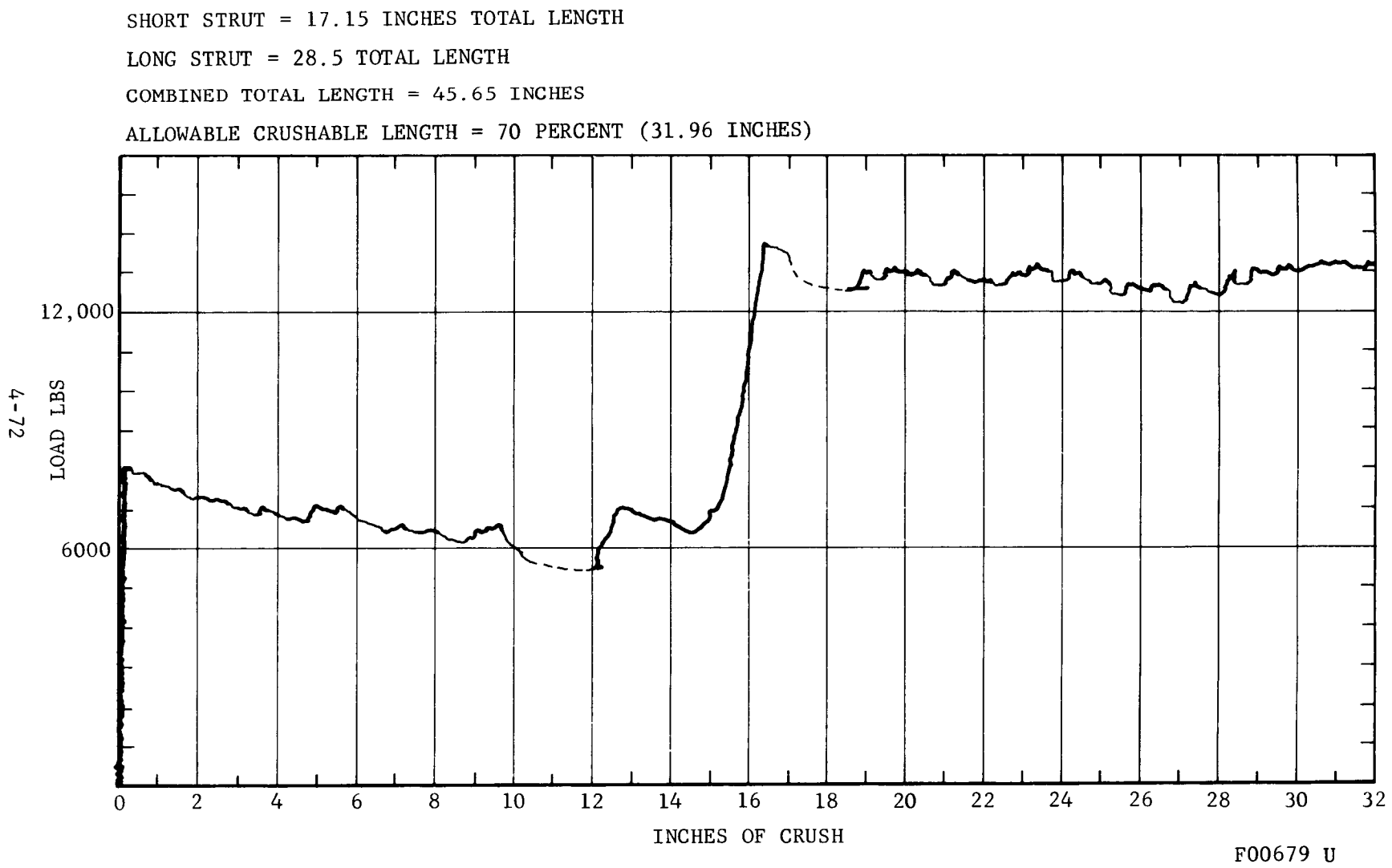

FIGURE 4-46. LEM STRUT LOAD-STROKE CURVE

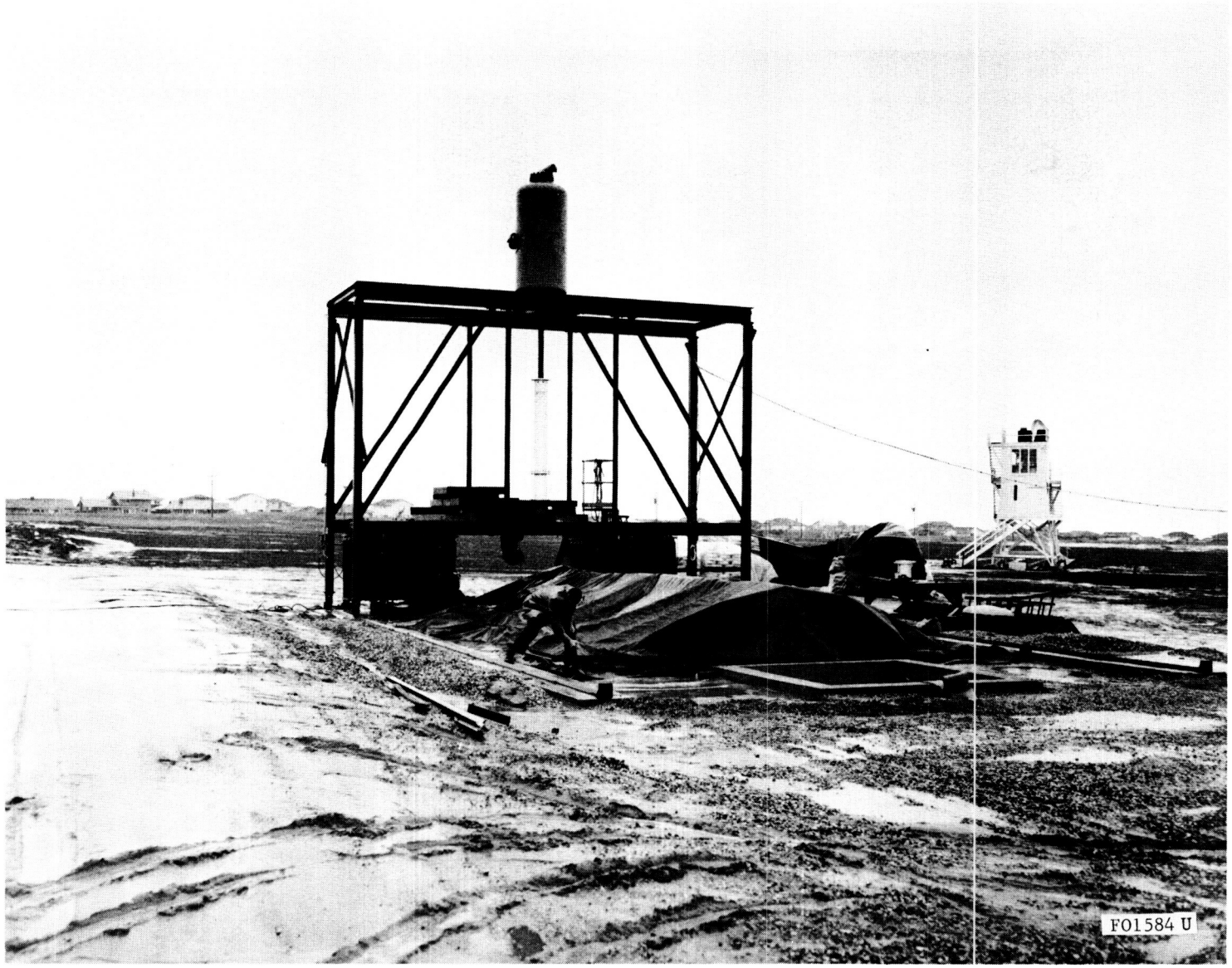

FIGURE 4-47. LEM CORRELATION TEST FACILITY

and a 5-foot square by 4-foot deep reservoir for the foam material. The reservoir was constructed by excavating the required volume and lining the walls with steel reinforced gunnite. The gunnite provided the protection barrier from water and soil contamination. A plastic coated nylon cover mounted on a portable tubular frame provided protection from rain and evening fog. The cover is shown in Figure 4-47. Included in the reservoir construction are two concrete runways to allow the gantry to traverse from one material area to the other. Sixty tons of Nevada 60 and Nevada 120 sands are installed in the reservoirs.

f. Aeration System. The aeration method of material conditioning was implemented for the LEM facility to duplicate methods utilized in the Impact Research Program. The aerator (Figure 4-48) consists of a 12 x 12 foot square manifold of 2-1/2 inch pipe with an array of parallel 1 inch pipe spaced on 6 inch centers. Spaced on 6 inch staggered centers are 1/8 inch orifices. The grid is covered with a felt pad bonded to the manifold. The felt pad serves as a diffuser for the gas and prevents sand from clogging the orifices. The aerator is placed on the bottom of the target material pit. The aerator is fed nitrogen gas from a bank of 72 bottles through two dome loader regulator valves. The aeration process consists of supplying an input at 100 psi for a period of two minutes. The present bank of N_2 cylinders is adequate for four aerations.

g. Lunar Gravity Simulator. The lunar gravity simulator is a constant force air cylinder which is preset to a resistance of 5/6 of the earth weight of the LEM assembly. As the pad enters the soil, its weight is reduced to 1/6 of earth value (lunar gravity) while retaining its full mass inertia properties. The pneumatic gravity simulator is shown in Figure 4-49. The gravity simulator consists of a 12-inch diameter air cylinder surrounded by a tank. The volume of the tank is large compared to the cylinder. The bottom of the cylinder is vented into the tank. The tank and lower part of the cylinder are charged to the same pressure. Normally, as an air cylinder operates, compression of the trapped air occurs rapidly with stroke. However, with the large tank to vent into, relatively little change in pressure occurs with stroke. Thereby, a constant force characteristic can be maintained.

A check was made to determine the percent increase in load pressure characteristics with piston stroke. The data are tabulated as follows:

Feet Traveled by Payload	Percent Increase in Tank Pressure
0	0
1	1.4
2	2.9
3	3.6
4	5.0
5	5.7
6	7.1

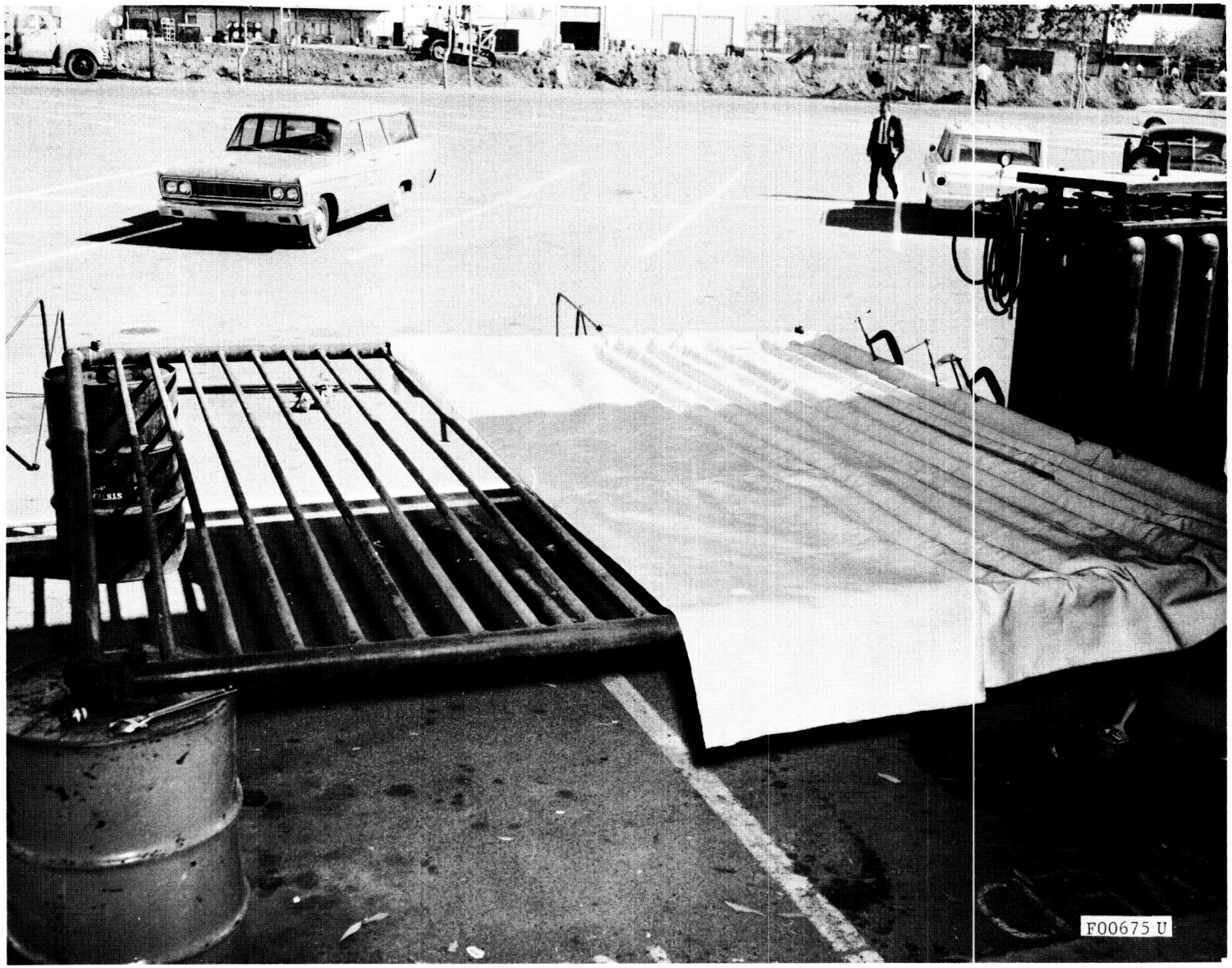

FIGURE 4-48. AERATOR FOR THE LEM TARGET MATERIAL RESERVOIR

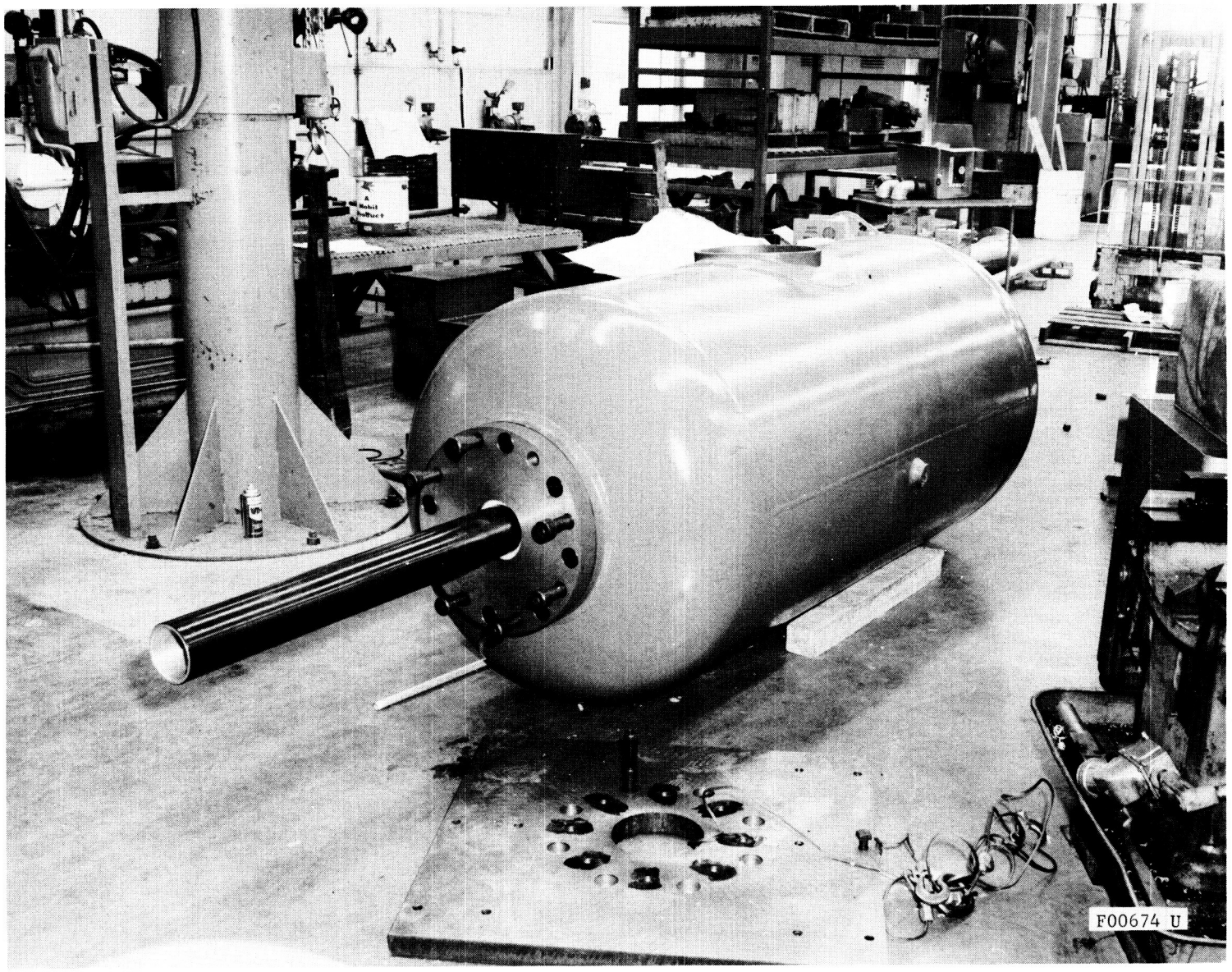

FIGURE 4-49. PHEUMATIC GRAVITY SIMULATOR FOR THE LEM TEST FACILITY

The gravity simulator is capable of greater than 6 feet of stroke and can handle up to 16,000 pounds. In addition to providing the constant force device, the gravity simulator provided other useful test system functions. The cylinder rod served as the free fall guide and also housed a stop and load cell. The LEM mass system always remained engaged to the simulator rod and, after a test, could be quickly retrieved by increasing the internal air pressure.

h. Static Bearing Tester. The static bearing tester primary operation characteristics provide a constant rate of one-inch per minute to a two-foot depth with a load capability of 16,000 pounds. A hydraulic cylinder pressurized by a controlled rate pump system was used to implement the requirement. The cylinder was hung from the gantry on an I-beam traverse. With the gantry mobility and the traverse, the bearing tester could be rapidly positioned to any place in the material. The bearing tester was instrumented with a load cell and displacement potentiometers whose outputs were recorded on an X-Y plotter. Readily adaptable to the cylinder load cell were 8 1/2-inch spherical, 8 1/2-inch flat, 12-inch flat and LEM pad probe sizes.

In addition to the large hydraulic bearing tester, the motor driven unit with the 2-1/2 inch spherical probe was utilized as a standard. This allowed a direct comparison to the impact research program.

i. LEM Dynamic Test Instrumentation. The instrumentation for monitoring the test consists of two load cells, two displacement sensors, two accelerometers, signal conditioning and recording. The LEM dynamic instrumentation sensor configuration is shown in Figure 4-50. Both the LEM mass and LEM pad are instrumented with a displacement sensor and accelerometer. The gravity simulator and the LEM strut are instrumented with load cells. With these sensors the following important dynamic parameters can be obtained:

(1) Displacement - Time History
Mass Displacement
Strut Compression
Target Material Penetration

(2) Mass Acceleration - Time History

(3) LEM Pad Acceleration - Time History

(4) Strut Compression Load - Time History

(5) Gravity Simulator Load - Time History

A photograph of the LEM Strut sensors is shown in Figure 4-51. A photograph of the location of mass sensors is shown in Figure 4-52. The

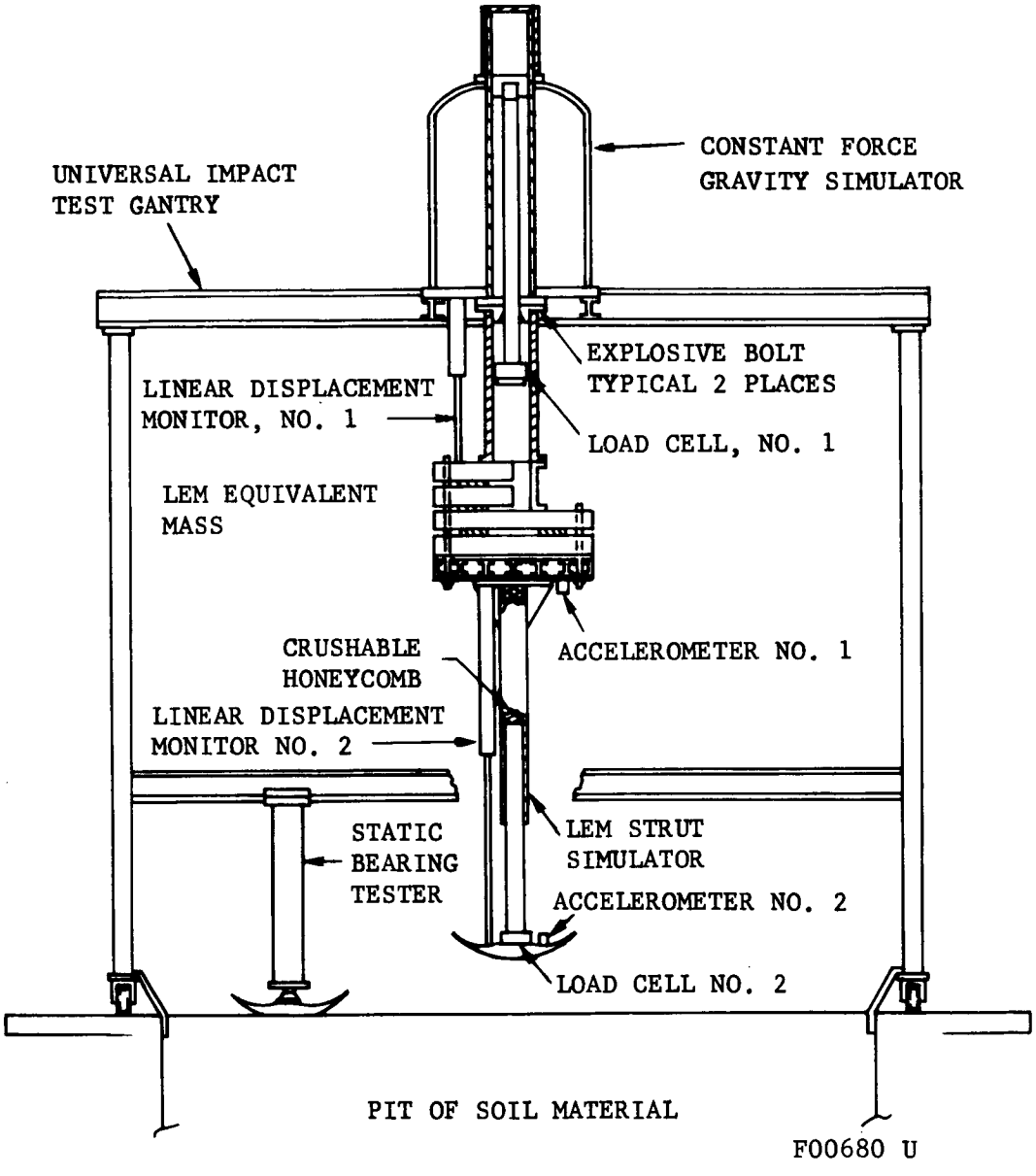

FIGURE 4-50. LEM DYNAMIC INSTRUMENTATION SENSOR CONFIGURATION

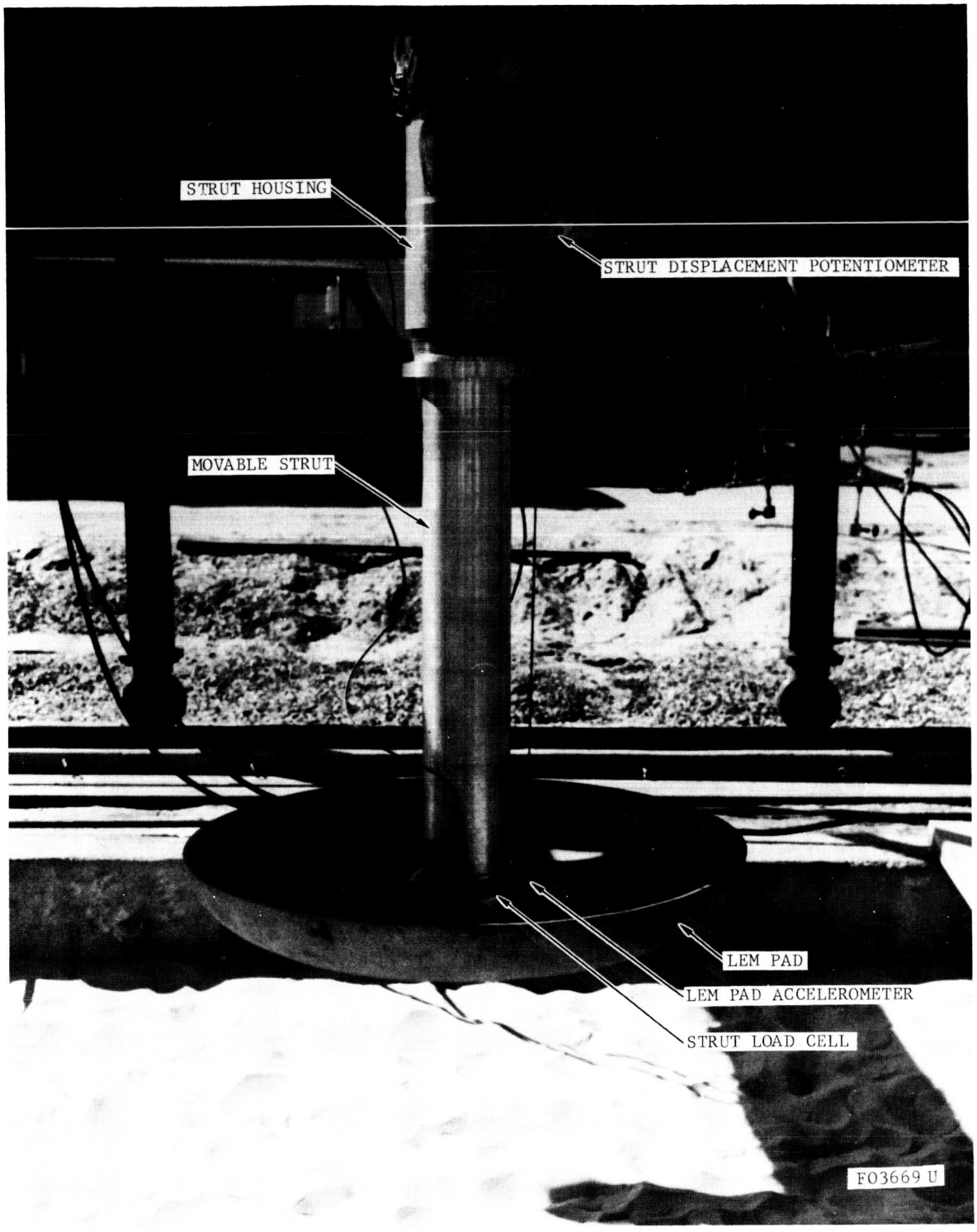

FIGURE 4-51. LEM STRUT SENSORS

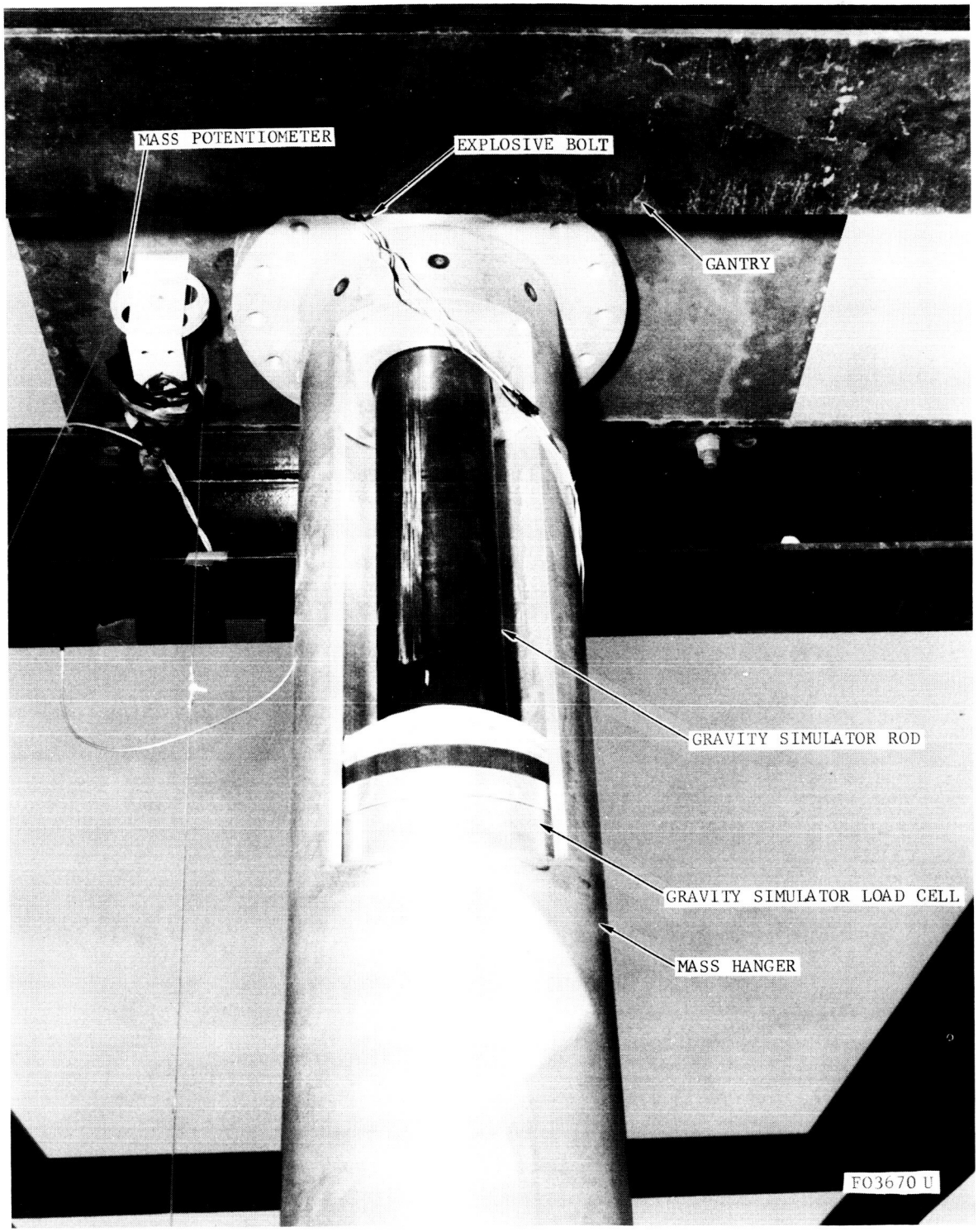

FIGURE 4-52. LEM MASS SENSOR

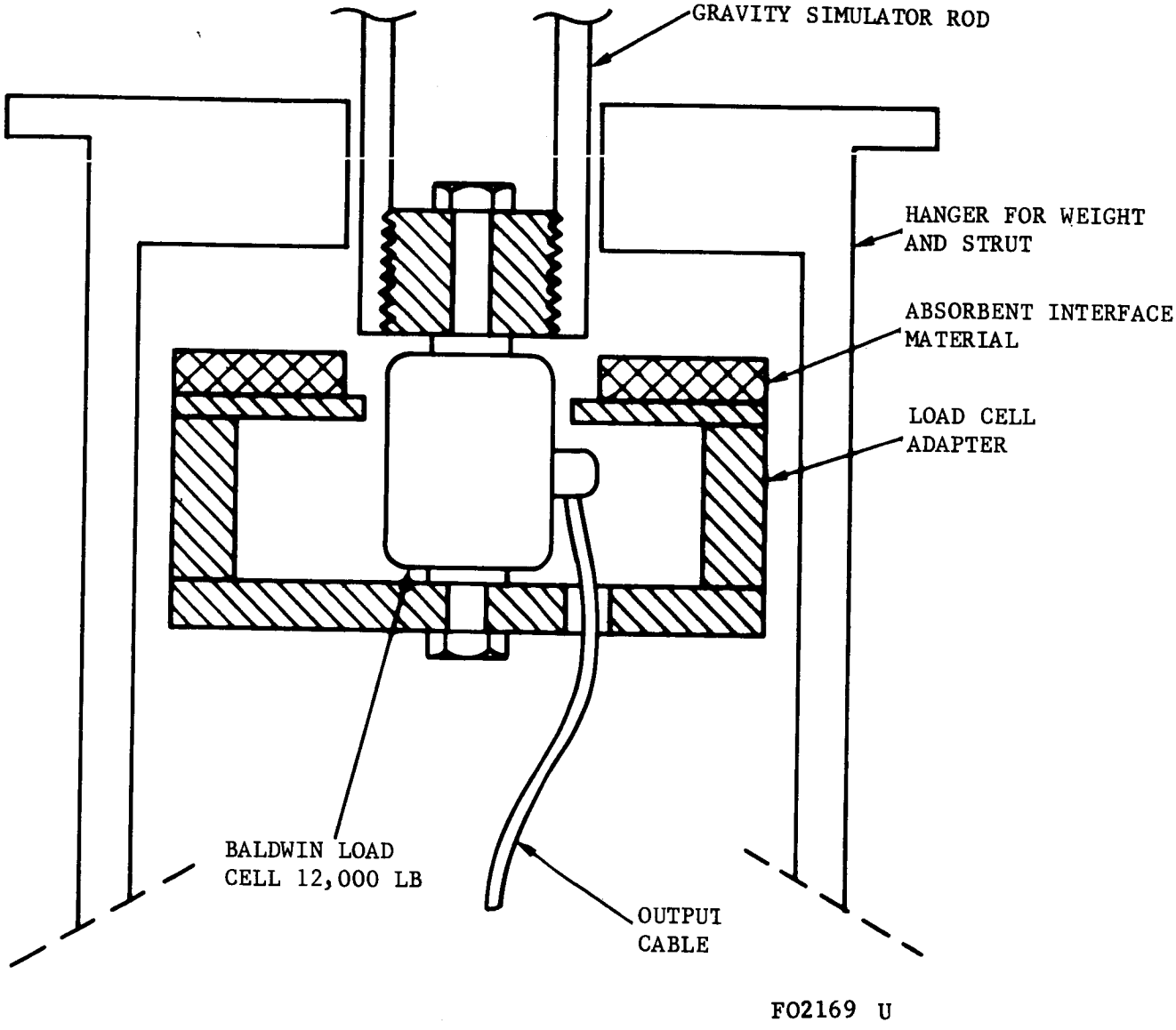

FIGURE 4-53. GRAVITY SIMULATOR LOAD CELL ADAPTATION

gravity simulator load cell assembly is further defined in a sketch in Figure 4-53.

A block diagram for the dynamic instrumentation is shown in Figure 4-54. The strain gage instruments input into a CEC bridge amplifier, while the potentiometers input into balance and signal conditioning networks. These signals are fed into galvanometers of a CEC type 5-124 oscillograph which displays the traces on direct write paper. Calibration of the sensor recording system was accomplished prior to each test and is part of the display record. Calibration of the load cells was accomplished by the shunt resistor method, which provides signals equal to those of known loads. Turning the accelerometers over 180 degrees gives accurate 2 g signals. The displacement potentiometers, which are driven by pulley and cable systems, are calibrated by direct movement of the cables. Scale factors are set with the use of precision attenuators and gain adjustments.

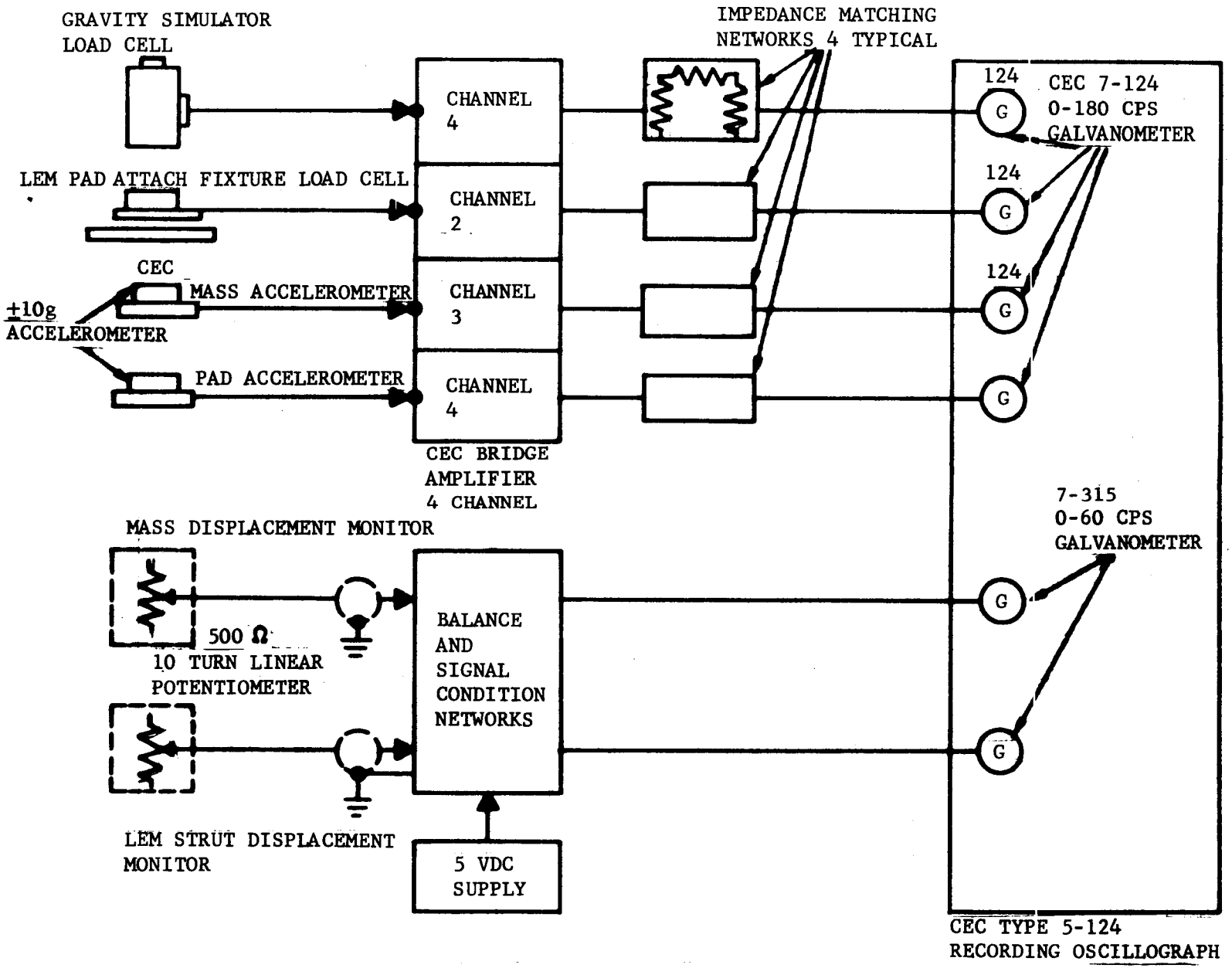

FIGURE 4-54. LEM DYNAMIC INSTRUMENTATION

4.4.3 LEM STATIC TEST RESULTS

a. Material and Soil Conditioning. Four materials were selected for the LEM facility tests. They were Nevada 120-2 sand (aerated), Nevada 120-1 sand (compacted), Nevada 60-2 sand (aerated) and polyeurethane foam (2 lb/ft^3). Seventy tons of the Nevada 120 sand and the Nevada 60 sand were procured. The 15-foot square reservoirs were filled to a 5-foot level. The objective in soil conditioning was to duplicate the state of material achieved in the impact research program. The methods were similar with scaled up equipment. The sand was fluffed with the aeration technique but instead of two nitrogen bottles, a bank of 72 was required. The aeration process in both Nevada 120-2L and Nevada 60-2 was identical with 100 psi at the dome loader valve for 2 minutes.

Compaction of the Nevada 120 to a -1 condition was achieved with the concrete vibrator utilized in the impact research program. The technique was also similar with the vibrator placed in the soil on a pattern of 2 foot centers. The vibrator was sunk in the sand to a depth of 3 feet and retracted within 1 minute.

b. Bearing Test Summary.

(1) Comparative testing, Impact Research versus LEM. In order to compare the impact research and the LEM static bearing strength directly, the motor driven static tester with the 2-1/2 inch spherical diameter probe was used. This has a constant rate drive at 1/2 inch per second.

Comparative curves for the four materials are shown in Figure 4-55, 4-56, 4-57, and 4-58. The LEM data compares very favorably with the impact research data with the exception of the Nevada 120-2 which was supplemented by the Nevada 120-2L. The LEM and impact research Nevada 120-2L vary from one another by a maximum of 7 percent with the characteristic shape very similar. The Nevada 60-2 exhibits a slightly higher characteristic in the LEM pit than the impact research program. The maximum difference is approximately 8 percent. The polyurethane foam characteristic shape was the same; the difference in bearing strength varied 6 to 19 percent along the flat pulse. The Nevada 120-1 average curve compares very closely with the impact research data. Although the average bearing strengths are close, this is deceptive because the compaction process was not completely homogeneous and a data spread occurs in relation to distance from compaction probe position. However, this is not critical since in the compacted soil very little penetration occurs.

(2) Probe Shape Curves. Each material was static tested with the hydraulic tester at 1 inch per minute with various probe shapes. An 8-1/2 inch diameter spherical, 8-1/2 inch diameter flat, 12-inch diameter spherical, and a LEM pad shape were used as probes to a depth of 2 feet or a maximum load of 16,000 pounds. The LEM pad shape and area are defined in

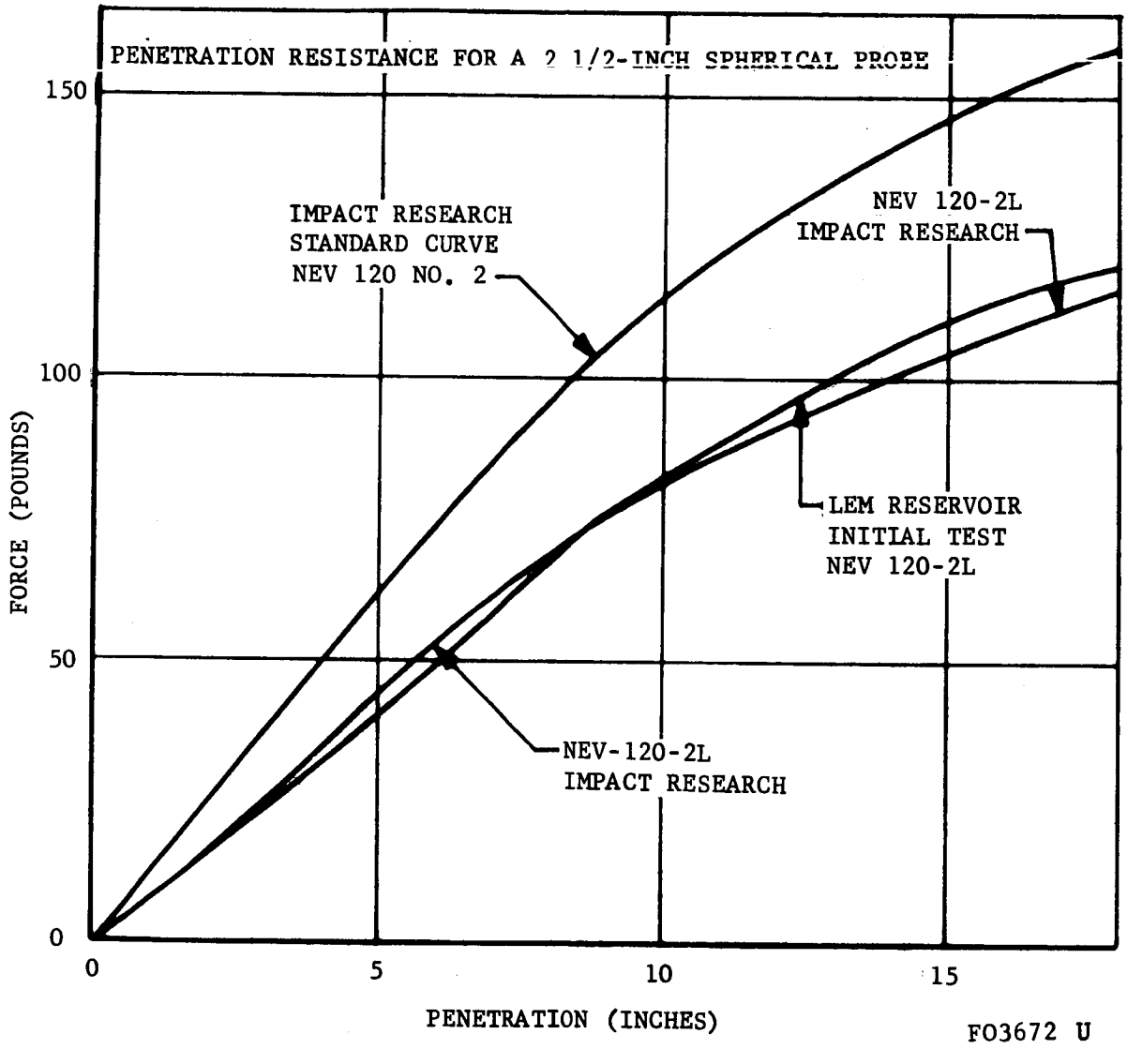

FIGURE 4-55. COMPARATIVE BEARING STRENGTH CURVES FOR NEVADA 120 NO. 2 SAND AND NEVADA 120-2L SAND, LEM VERSUS IMPACT RESEARCH

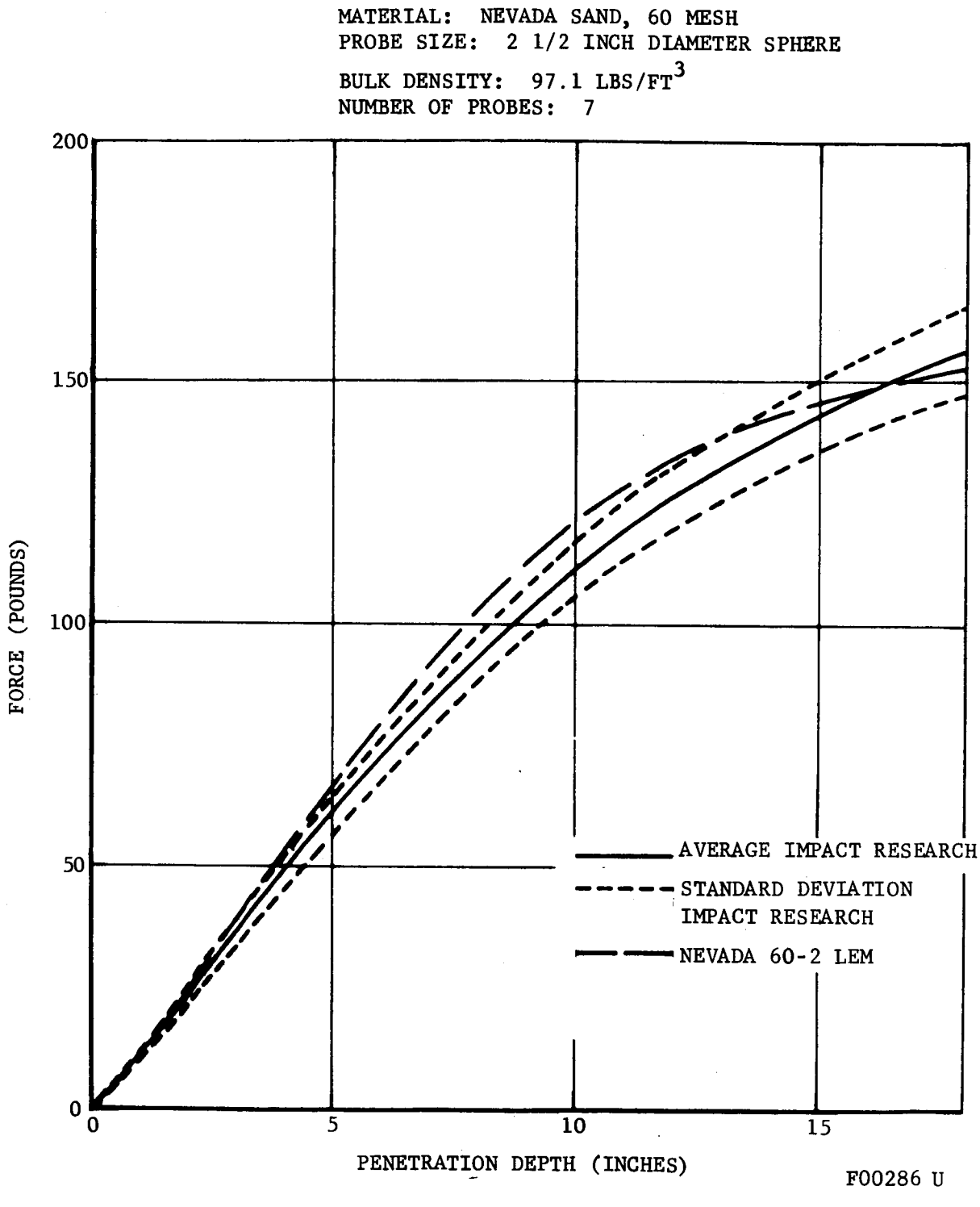

FIGURE 4-56. COMPARATIVE BEARING STRENGTH TESTS OF NEVADA 60-2 SAND, LEM VERSUS IMPACT RESEARCH

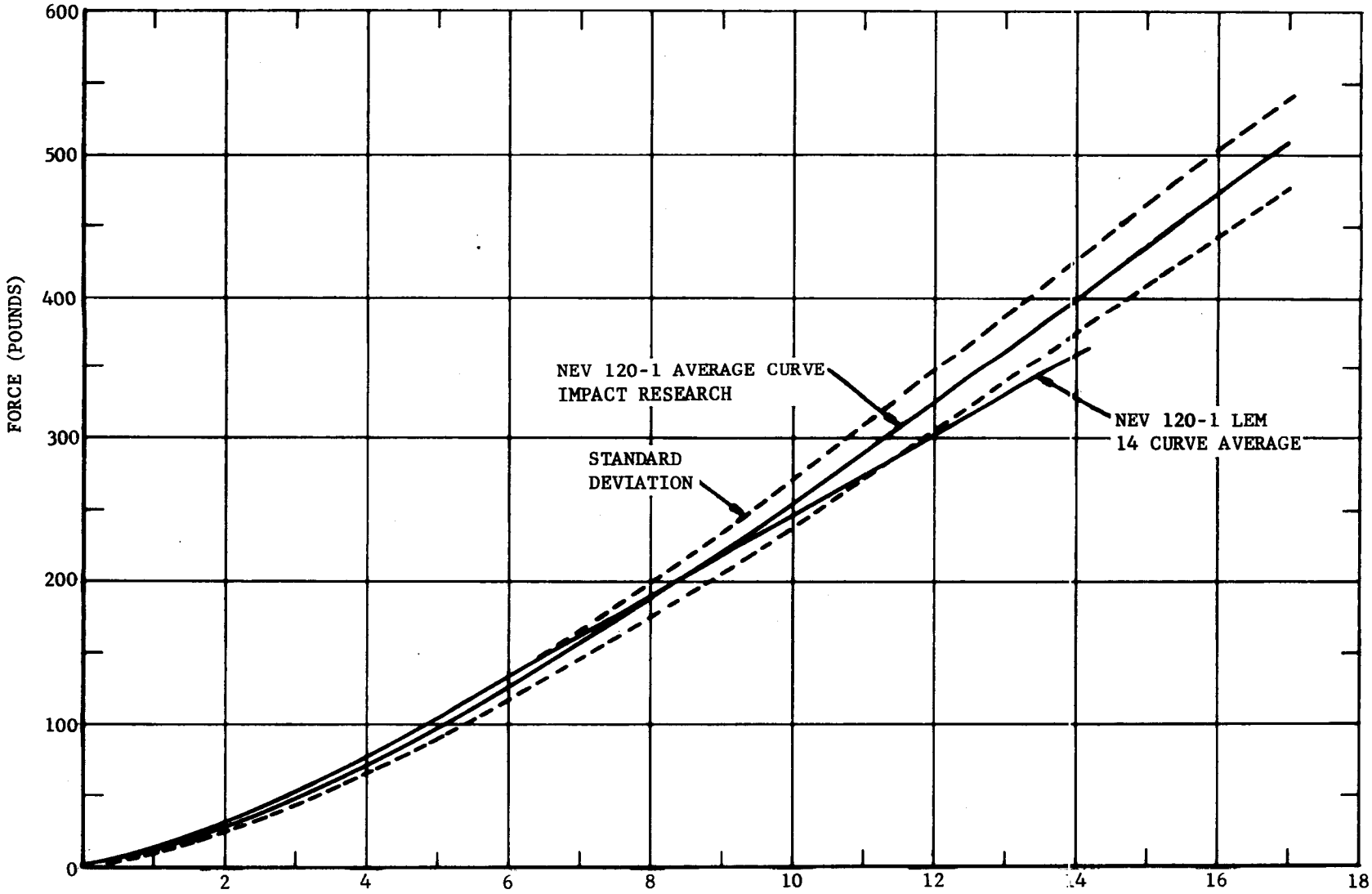

FIGURE 4-57. COMPARATIVE BEARING STRENGTH CURVE FOR NEVADA 120-1 SAND

FO3673 U

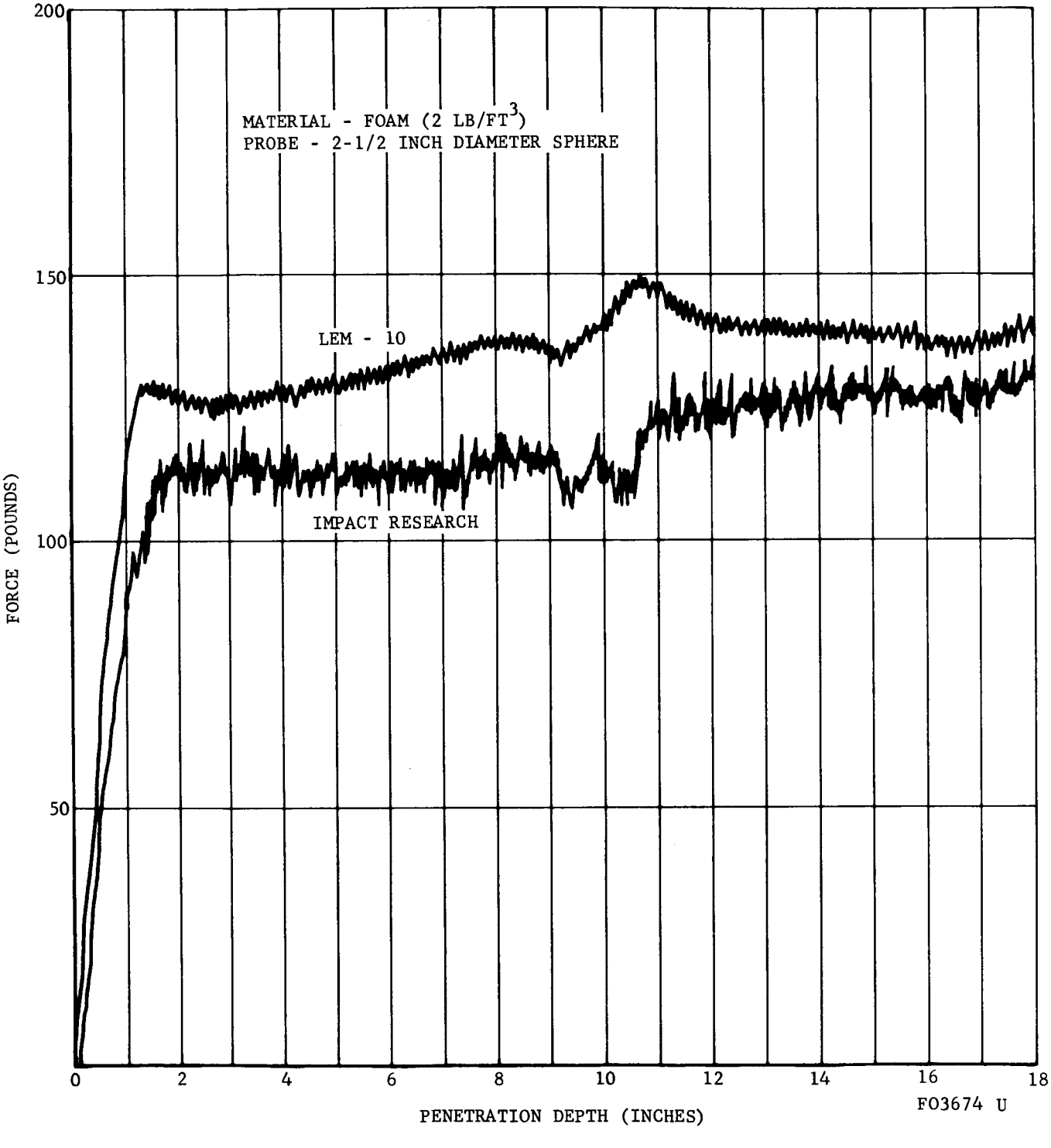

FIGURE 4-58. COMPARATIVE BEARING STRENGTH CURVE FOR FOAM

Figure 4-59. The results for each material are plotted on a single force-penetration curve. This is called a probe shape family curve. These curves are exhibited in Figures 4-60 through 4-63 for the Nevada 60-2, Nevada 120-2L, Nevada 120-1, and foam materials. The sand materials exhibited identical linear characteristics after probe penetrated to full dimension.

Comparative LEM pad static curve in Figure 4-59 shows the bearing strength range of the four materials. The Nevada 120-2L sand was the softest of the materials while Nevada 120-1 sand was the hardest. It is interesting to note that within the 3-inch penetration measured, the Nevada 120-1 was identical to the foam material.

In order to determine probe shape effects, the information in each of the family curves must be normalized with respect to area.

This normalized information was utilized to form a dimensionless parameter the probe shape factor (Kp)

$$K_p = \frac{\text{Bearing strength (any probe) at a specific penetration}}{\text{Bearing strength (2.5 inch sphere probe) at the specific penetration}}$$

Curves plotted for the probe shape factor on each of the materials against penetration are given in Figure 4-64. The base line is for the 2.5 inch probe and the probe shape factor 1.0. The other curves indicate the variance from the 2.5-inch probe.

Trends shown in the curves in Figure 4-64 are:

(a) Probe shape effects are significant in all materials. The effects occur in an orderly fashion in each material but not consistently from material to material.

(b) In the loose materials, the bearing strength measurement increases with diameter up to a probe factor of 2. The flat plate produced a higher probe factor than the spheres.

(c) In the hard materials Nevada 120-1 and foam, the probe factors are smaller, approximately 1.25 through most of the penetration.

(d) The LEM pad tests exhibit characteristics within the range of the other probe shapes but are not consistent from material to material. Because of the high area of the pad, the penetration was too shallow to obtain a full trend. In the loose material, the 8.5 inch sphere and the LEM probe factors tend to approach to within 25 percent of each other.

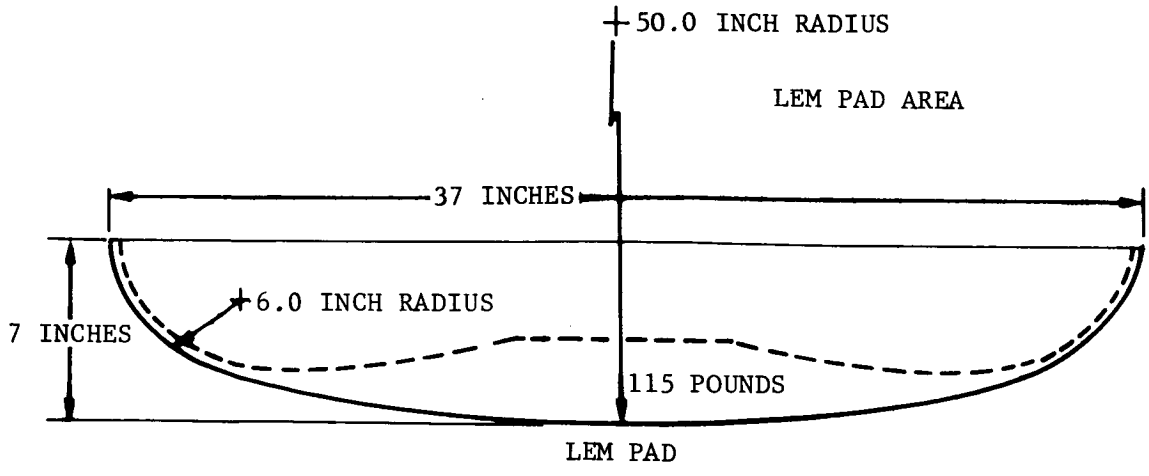

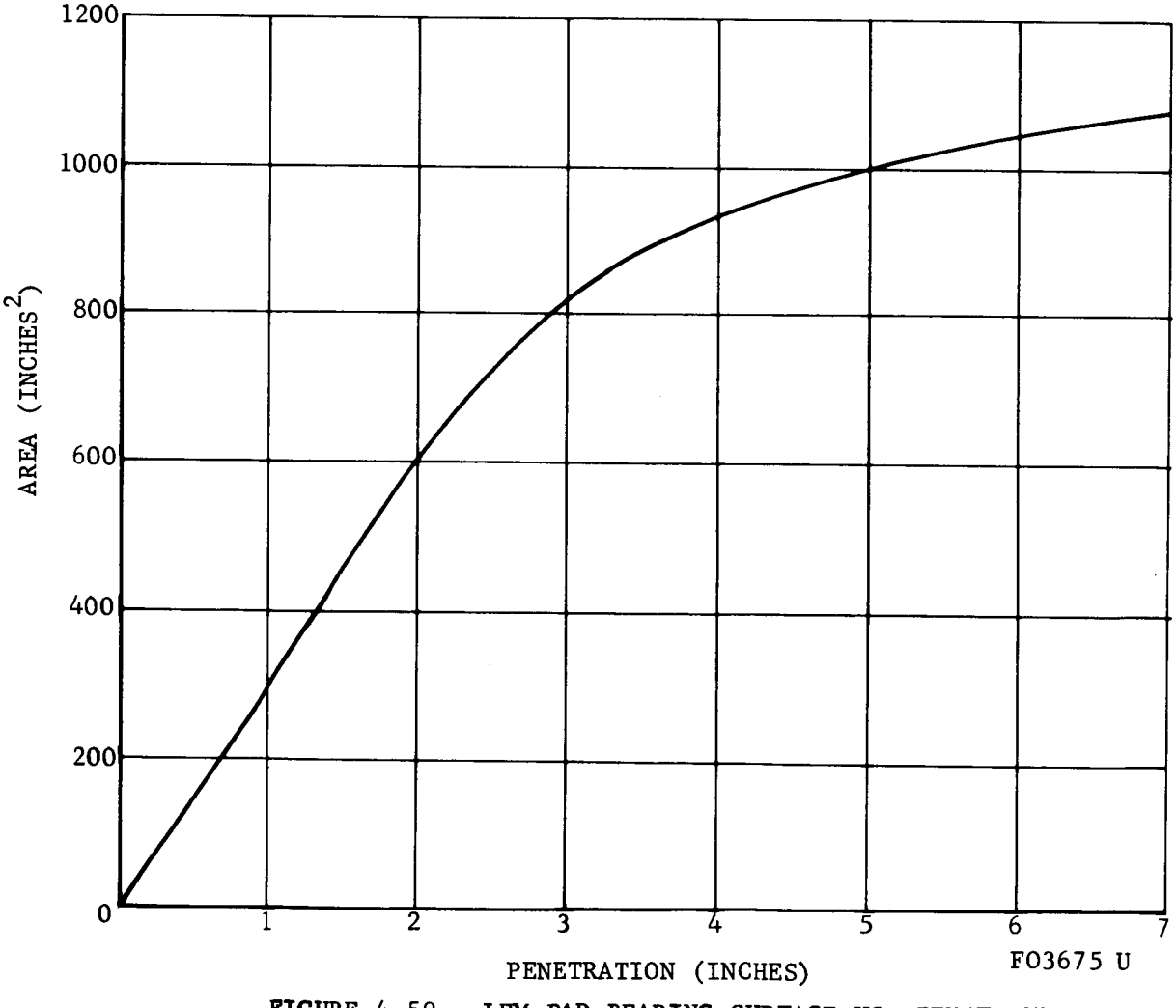

FIGURE 4-59. LEM PAD BEARING SURFACE VS. PENETRATION

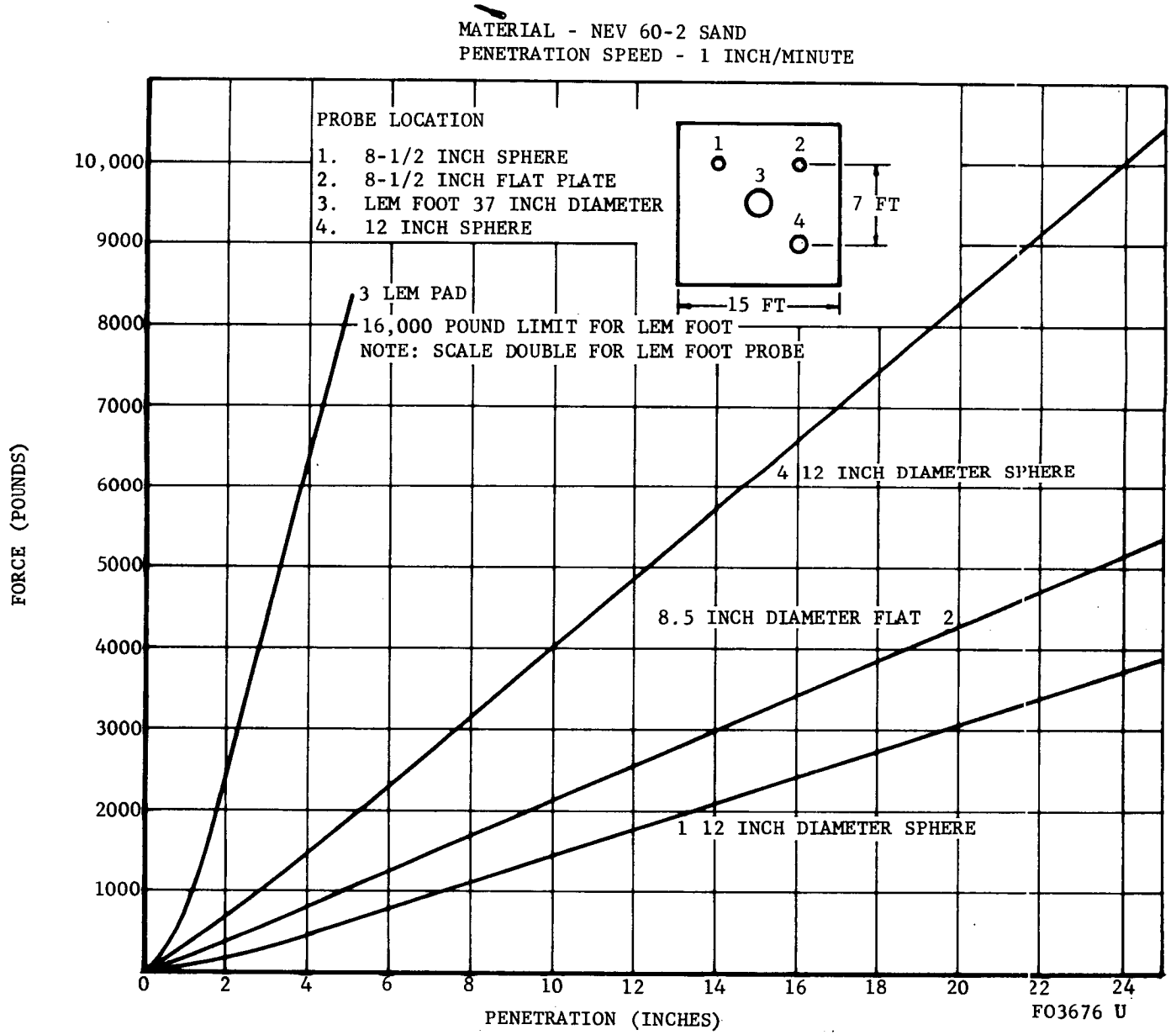

FIGURE 4-60. LEM PROBE SHAPE EFFECTS IN NEVADA 60-2 SAND

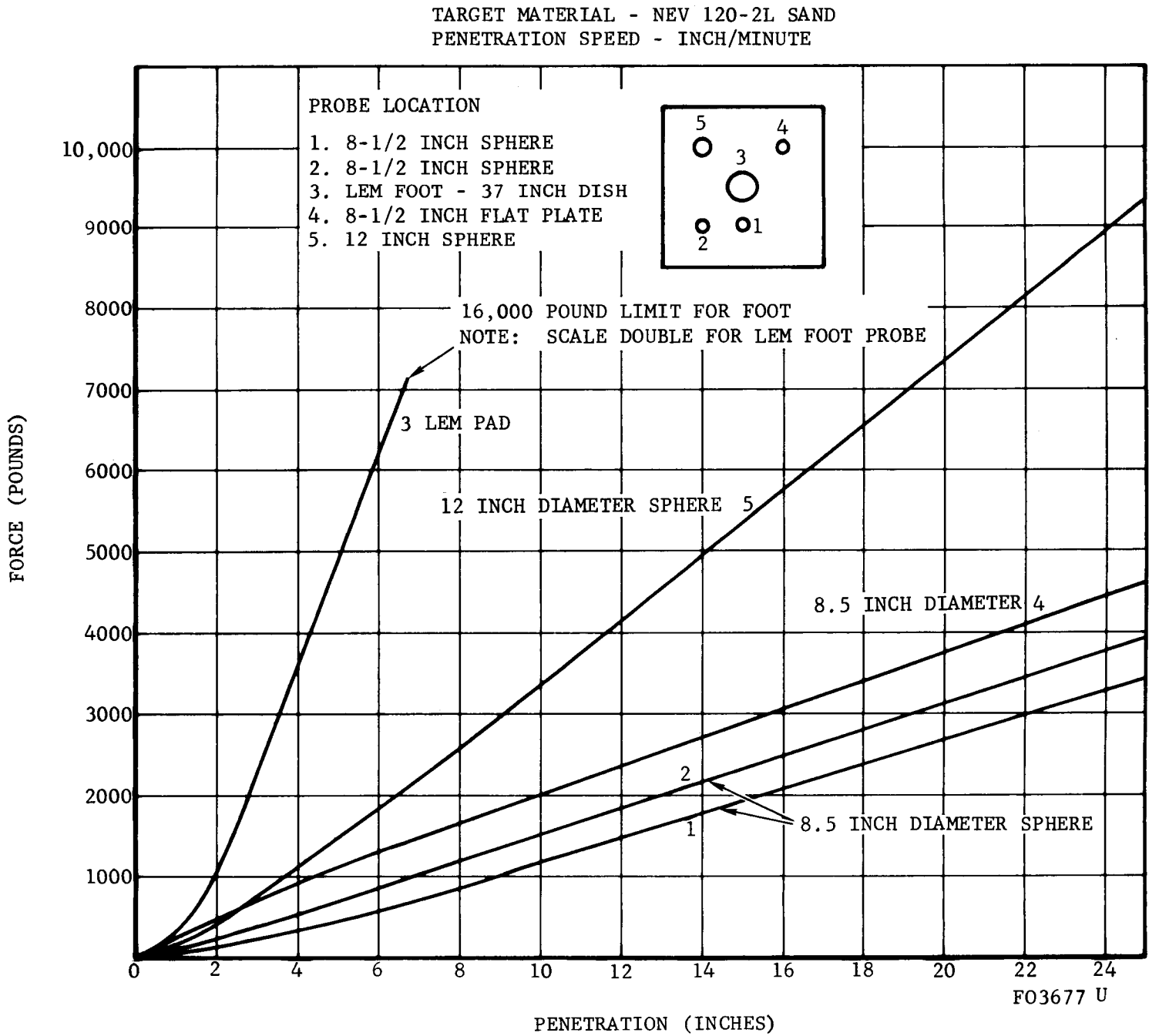

FIGURE 4-61. LEM PROBE SHAPE EFFECTS IN NEVADA 120-2L SAND

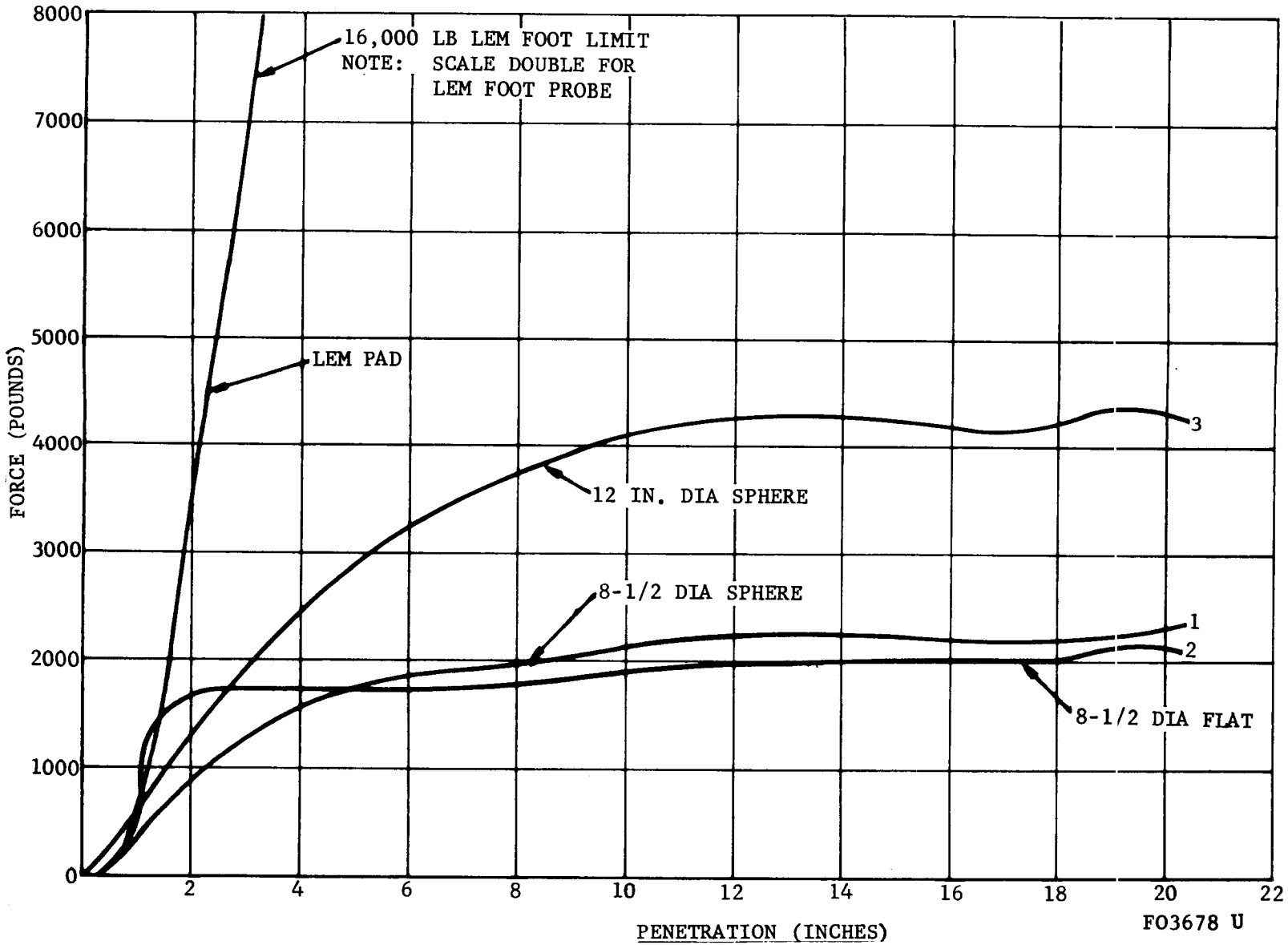

FIGURE 4-62. LEM PROBE SHAPE EFFECTS IN FOAM

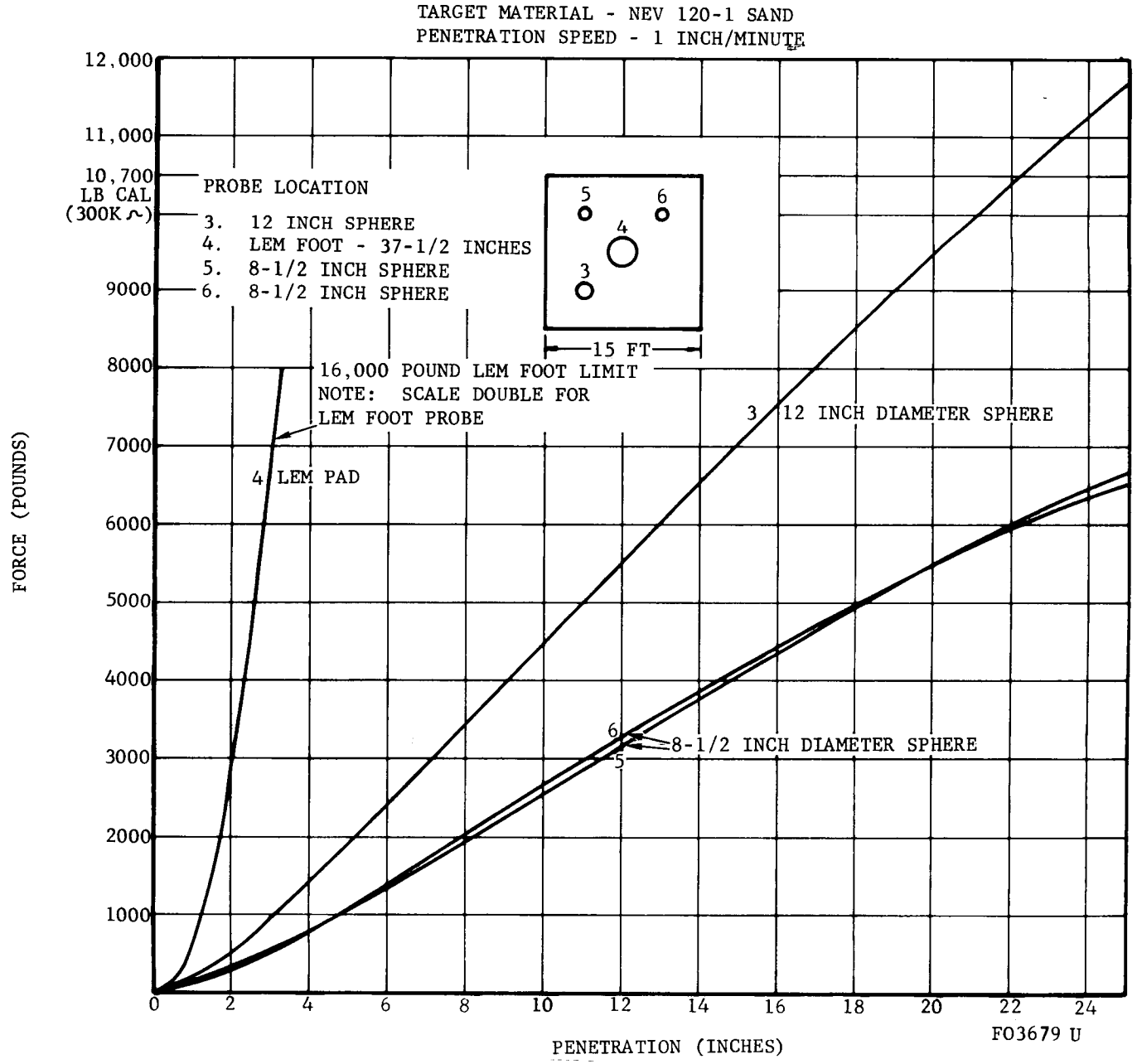

FIGURE 4-63. LEM PROBE SHAPE EFFECTS IN NEVADA 120-1 SAND

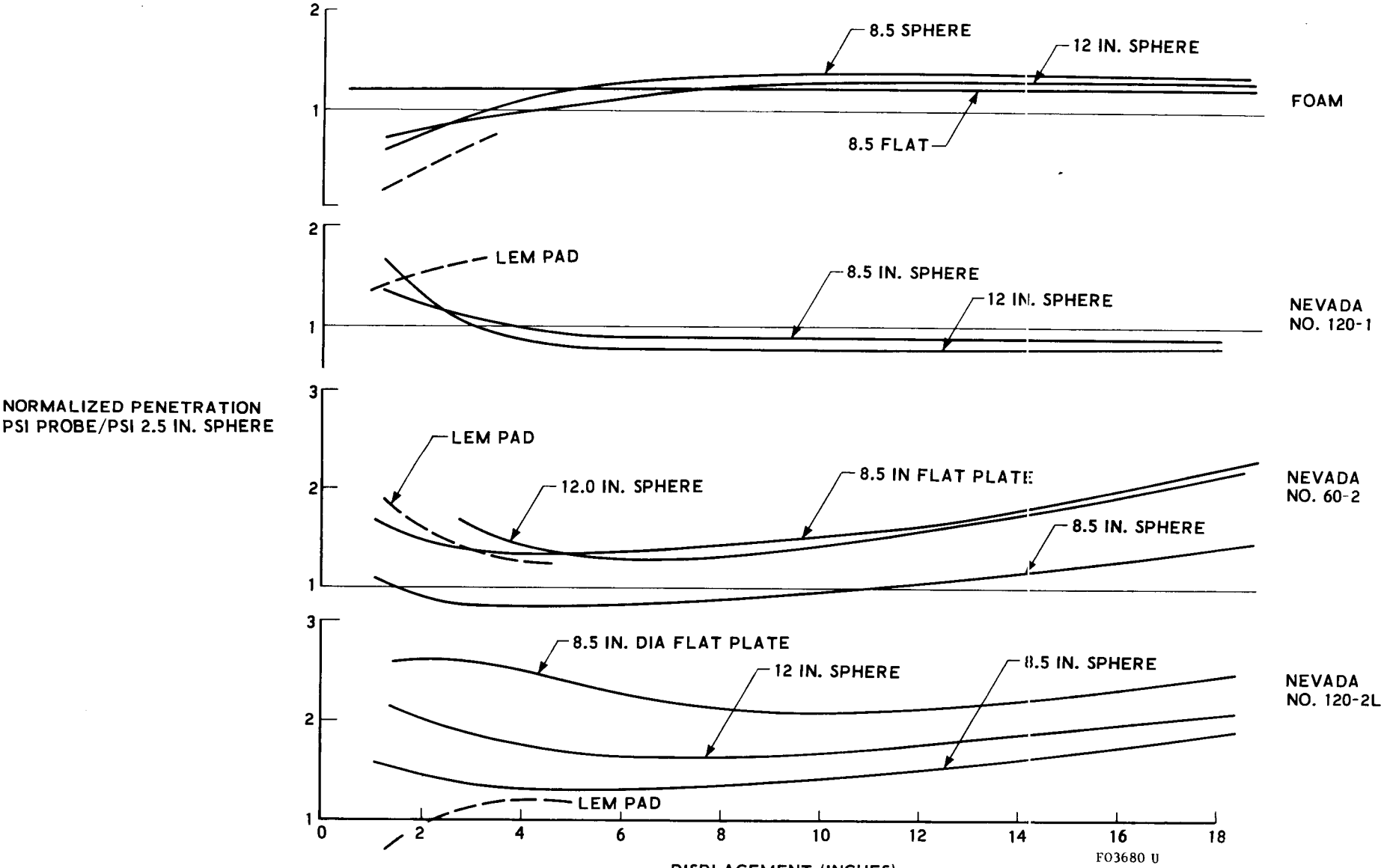

FIGURE 4-64. EFFECT OF STATIC PROBE SHAPE

4.4.4 LEM DYNAMIC TEST RESULTS

a. Typical Data Trace. The instrumentation scheme was described in previous sections. The data display from the dynamic test require some explanation in regards to interpretation. Basically, there are two sources of data, which are shown in Figures 4-65 and 4-66.

(1) The data sheet which contains physical measurements made prior to and after the test.

(2) The oscillograph record, which provides the dynamic information of the six sensors versus time.

In examining the LEM data sheets in Figure 4-65, the information in relation to measured test results is contained in 7C-strut compression and 8-pad penetration. Also contained on the data sheet is the system weight as measured through the instrumentation. The measured fall heights are indicated in items 1 and 2. The scale factors are indicated in item 5. The upper load cell, accelerometer and potentiometer describe dynamic properties of mass while the lower load cell, accelerometer and potentiometer describe dynamic properties of the strut.

The dynamic information is shown in Figure 4-64. There are six traces, the first plotted against a uniform time scale.

(1) Mass Displacement

(2) Mass Accelerometer

(3) LEM Pad Accelerometer

(4) Honeycomb Crush (Strut Displacement)

(5) Gravity Simulator load cell

(6) LEM Pad Load cell

The mass displacement curve provides an absolute displacement (inches) versus time (milisecond) curve for the mass. The honeycomb crush (strut displacement curve) provides a relative displacement time curve between the pad and the mass, which is the absolute strut compression curve. If the event of hitting the target material is taken as zero; subtracting the honeycomb crush displacement will provide the displacement time curve of target material penetration. The data on the displacement curves can be cross checked directly with measured values of free fall distance, strut compression, total travel on the data sheet.

1.	HEIGHT FROM PAD TO SAND	31-3/4 IN.
2.	FREE FALL TO FELT PAD	18-3/4 IN.
3.	TOTAL HUNG WEIGHT	7764 LB
4.	BEARING STRENGTH CURVE	NONE
5.	SCALE FACTORS	
	A. UPPER LOAD CELL	4080 LB/IN.
	B. UPPER ACCELEROMETER	4.87 g/IN.
	C. UPPER POTENTIOMETER	20 IN./IN.
	D. LOWER LOAD CELL	4000 LB/IN.
	E. LOWER ACCELEROMETER	5.06 g/IN.
	F. LOWER POTENTIOMETER	10 IN./IN.
6.	GRAVITY SIMULATOR PRESSURE	
	A. EQUILIBRIUM PRESSURE	NOT MEASURED
	B. SET PRESSURE	48 PSI
7.	STRUT	
	A. INITIAL LENGTH	33-5/8 IN.
	B. FINAL LENGTH	17.0 IN.
	C. COMPRESSION	16-5/8 IN.
8.	PAD PENETRATION DEPTH	13-3/8 IN.
9.	POST TEST WEIGHT	8000 LB
10.	POST TEST EQUILIBRIUM PRESSURE	75 PSI

FO3681 U

FIGURE 4-65. TYPICAL LEM DYNAMIC TEST DATA SHEET

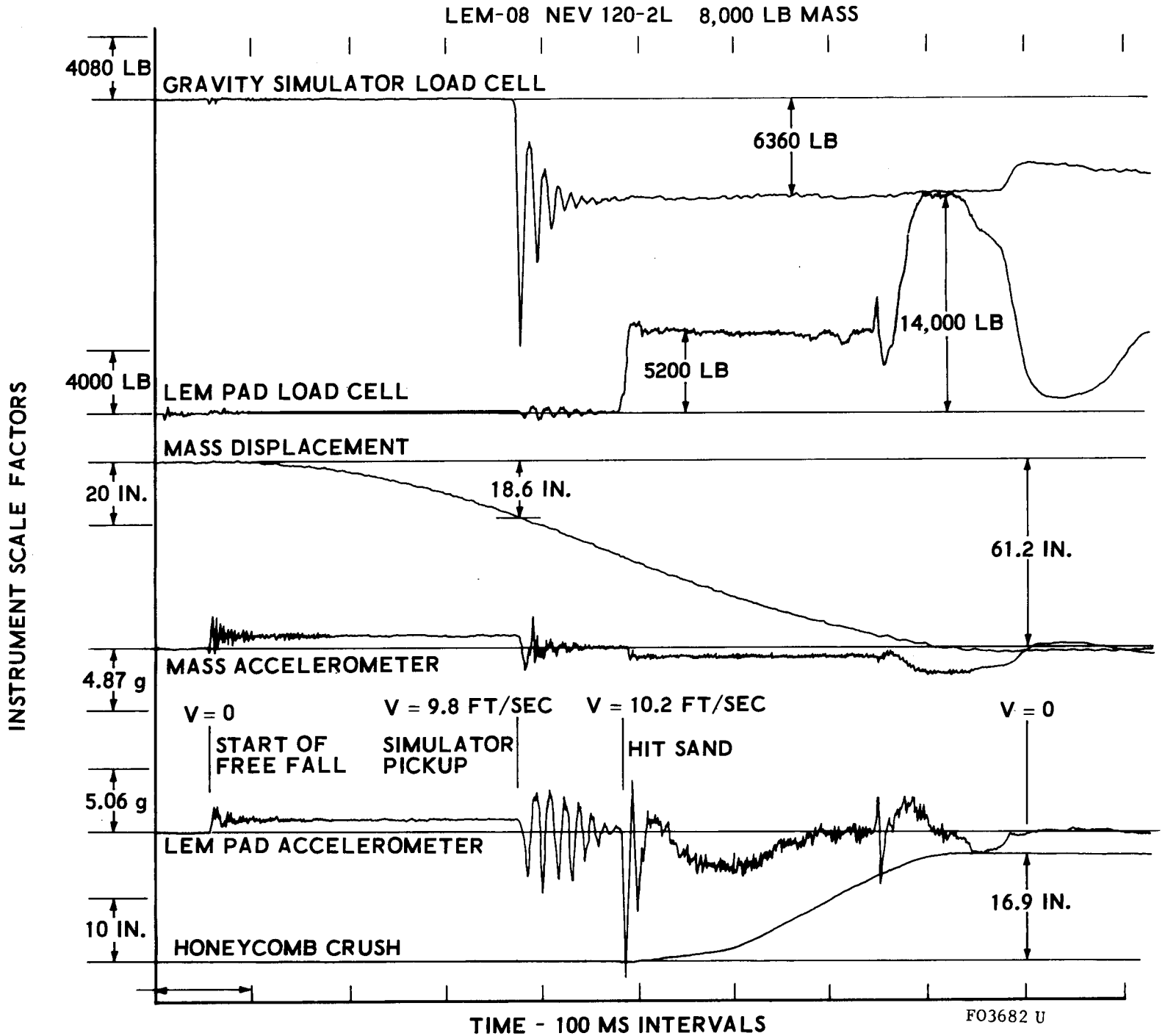

FIGURE 4-66. LEM DYNAMIC TEST - TYPICAL DATA

The mass accelerometer curve describes the absolute deceleration of the mass, while the LEM pad accelerometer curve describes the absolute deceleration of the pad. If no strut motion occurs the two readings should be identical. Normally with strut motion occurring, the pad accelerometer will read considerably higher than the mass accelerometer. The mass accelerometer exhibits a positive 1 g during free fall, a negative spike on gravity simulator engagement, a positive 1/6 g until hitting the target material, a negative acceleration during material entry and 6000 pound strut compression, and a larger negative acceleration upon 12,000 pound strut compression. The LEM pad accelerometer duplicates the sequence but with greater excursions.

The gravity simulator load cell provides a direct measurement of the gravity simulator restraining load. Upon engagement of the mass with the simulator a sharp load spike occurs which damps out. A constant load characteristic is exhibited at the end of system motion. The objective is to have the constant load equal to 5/6 the measured load.

The dynamic data can be interpreted to identify experiment events. The following events are significant:

(1) Start of free fall.

(2) Engagement of gravity simulator.

(3) Impact with target material.

The start of free fall is indicated by accelerometers increasing sharply to 1 g and the mass displacement curve increasing from a zero point. The engagement of the gravity simulator is indicated by a sharp negative spike of the accelerometers and a sharp loading on the gravity simulator load cell. The hitting of the target material is identified by a sharp rise in the LEM pad load cell, spike in the accelerometer cubes and usually start of displacement on the strut displacement curve.

b. Composite Data Table. A composite data table is presented in Table 4.10. Included in this table are the values of the controlled parameters of the test system. These parameters are velocity, honeycomb load output, and gravity simulator factor. These values are presented for each test and the percent deviation from the nominal indicated. It is highly desirable that the control parameters be constant from test to test. With statistical reduction, the following are observed:

Honeycomb (6000 lb) Average Value - 5,667
Percent from Nominal - 5.7
Standard Deviation
from Average - 6.1 percent

TABLE 4.10 COMPOSITE LEM TEST DATA TABLE

	FOAM									NEVADA 120-1 SAND								
	4,000 lb LEM-06			8,000 lb LEM-10			16,000 lb LEM-15			4,000 lb LEM-18			8,000 lb LEM-11			16,000 lb LEM-16		
	Nom or Meas	Dyn Data	% Diff	Nom or Meas	Dyn Data	% Diff	Nom or Meas	Dyn Data	% Diff	Nom or Meas	Dyn Data	% Diff	Nom or Meas	Dyn Data	% Diff	Nom or Meas	Dyn Data	% Diff
A. Velocity	10	10.1	1.0	10	9.25	7.5	10	11.03	10.03	10	9.7	3	10	10.5	5	10	10.15	1.5
B. Depth of Penetration	2	1.8	10.0	3.3	3.3	0	6.2	6.7	8.1	2.5	2.3	8.0	3.6	1.9	47.2	6.5	6.2	4.6
C. Strut Characteristics																		
1. Compression Load 6,000 lb	6,000	5,517	8.5	6,000	5,140	14.5	6,000	5,611	6.5	6,000	5,300	11.9	6,000	5,778	3.7	6,000	5,621	6.3
2. Compression Load 12,000 lb	12,000	--	--	12,000	13,035	8.6	12,000	12,023	0.2	12,000	--	--	12,000	12,433	7.2	12,000	12,045	0.4
3. Crushed Length 6,000 lb	10.0	10.5	0.5	15.9	16.2	1.0	15.5	16.5	6.4	12.1	13.05	7.5	15.5	15.2	1.9	15.7	15.8	0.6
4. Crushed Length 12,000 lb	--	--	--	3.8	3.5	8.0	16.3	16.4	0.6	--	--	--	11.2	12.1	9.8	16.2	15.9	1.8
D. Gravity Simulator Characteristics																		
1. Gravity Simulator Load	--	3,470	--	--	5,893	--	--	12,942	--	--	3,050	--	--	4,842	--	--	12,795	--
2. Weight	3,825	--	--	7,844	--	--	15,055	--	--	3,825	--	--	7,844	--	--	15,055	--	--
3. Gravity Factor	0.833	0.907	8.9	0.833	0.751	9.8	0.833	0.859	3.1	0.833	0.796	4.4	0.833	0.617	27.1	0.833	0.849	1.9

TABLE 4.10 (CONTINUED)

	NEVADA 60-2									NEVADA 120-2L								
	4,000 lb LEM-07			8,000 lb LEM-09			16,000 lb LEM-14			4,000 lb LEM-05			8,000 lb LEM-08			16,000 lb LEM-13		
	Nom or Meas	Dyn Data	% Diff	Nom or Meas	Dyn Data	% Diff	Nom or Meas	Dyn Data	% Diff	Nom or Meas	Dyn Data	% Diff	Nom or Meas	Dyn Data	% Diff	Nom or Meas	Dyn Data	% Diff
A. Velocity	10	9.23	7.7	10	9.90	1	10	9.75	2.5	10	9.80	2	10	9.95	0.5	10	9.94	0.6
B. Depth of Penetration	7.4	7.9	6.7	8.44	6.3	25.3	10.9	10.2	6.4	12.1	12.8	5.8	13.4	13.0	3.0	15.3	12.3	19.6
C. Strut Characteristics																		
1. Compression Load 6,000 lb	6,000	5,802	3.3	6,000	5,659	5.7	6,000	6,376	6.2	6,000	5,975	0.4	6,000	5,200	13.3	6,000	6,048	0.8
2. Compression Load 12,000 lb	12,000	--	--	12,000	10,959	8.7	12,000	13,000	8.0	12,000	--	--	12,000	14,000	16.6	12,000	12,700	5.8
3. Crushed Length 6,000 lb	7.3	6.7	8.2	15.3	16.4	7.2	15.5	16.0	3.2	2.7	2.0	25.8	15.5	16.7	7.7	15.8	15.2	3.8
4. Crushed Length 12,000 lb	--	--	--	4.48	4.6	2.6	16.4	17.0	3.6	0	0	0	0.9	0.3	66.0	15.2	15.4	1.3
D. Gravity Simulator Characteristics																		
1. Gravity Simulator Load	--	2,892	--	--	5,720	--	--	12,580	--	--	3,250	--	--	6,365	--	--	12,943	--
2. Weight	3,825	--	--	7,884	--	--	15,055	--	--	3,825	--	--	7,844	--	--	15,055	--	--
3. Gravity Factor	0.833	0.750	10	0.833	0.73	12.0	0.833	0.835	0.24	0.833	0.871	4.6	0.833	0.811	2.5	0.833	0.859	3.1

Honeycomb (12,000 lb)	Average Value - 12,525 Percent from Nominal - 4.4 Standard Deviation from Average - 5.3 percent
Gravity Factor (5/6)	Average Value - 0.8198 Percent from Nominal - 1.2 Standard Deviation from Average - 6.6 percent
Velocity (10 ft/sec)	Average Value - 9.94 Percent from Nominal - 0.60 Standard Deviation from Average - 4.75 percent

In examining data on a gross trend basis, the fixed test parameters are controlled accurately enough to observe trends without large scatter of data points. In solving absolute or individual test problems, the specific values can be used rather than the nominal or average.

Also included in the table are the test results penetrations in the target material and strut compression. These values are obtained by two methods; one by direct measurement after the test and the other from the dynamic data of the displacement potentiometers.

c. LEM Landing Pad Penetration-Time Data. A summary of the LEM Landing Pad; measured penetrations is shown graphically in Figure 4-67. The presentation has penetration as an abscissa and bearing strength (7-inch depth with 12-inch sphere) as ordinate. It is not an absolute curve of penetration versus bearing strength but a graphic display. Some trends indicated from this curve are:

(1) A rapid increase in penetration occurs in materials of lower bearing strength than the Nevada 60-2 sand.

(2) Materials in the range of bearing strength greater from that of 60-2 exhibit high resistance to penetration.

(3) The LEM landing mass only slightly affects depth of penetration in the loose materials.

A dynamic pad penetration-time curve gives a display of pad penetration characteristics. Three composite curves are presented and provide some insight into the penetration mechanism. Figure 4-68 shows LEM Pad penetration versus time for four materials with a nominal 4000 pound mass and velocity of 10 ft/sec. Some dynamic trends indicated are:

(1) The penetration rise time occurs within 50 milliseconds (20 percent of the pulse duration) in the harder materials and is increasingly longer in the softer materials.

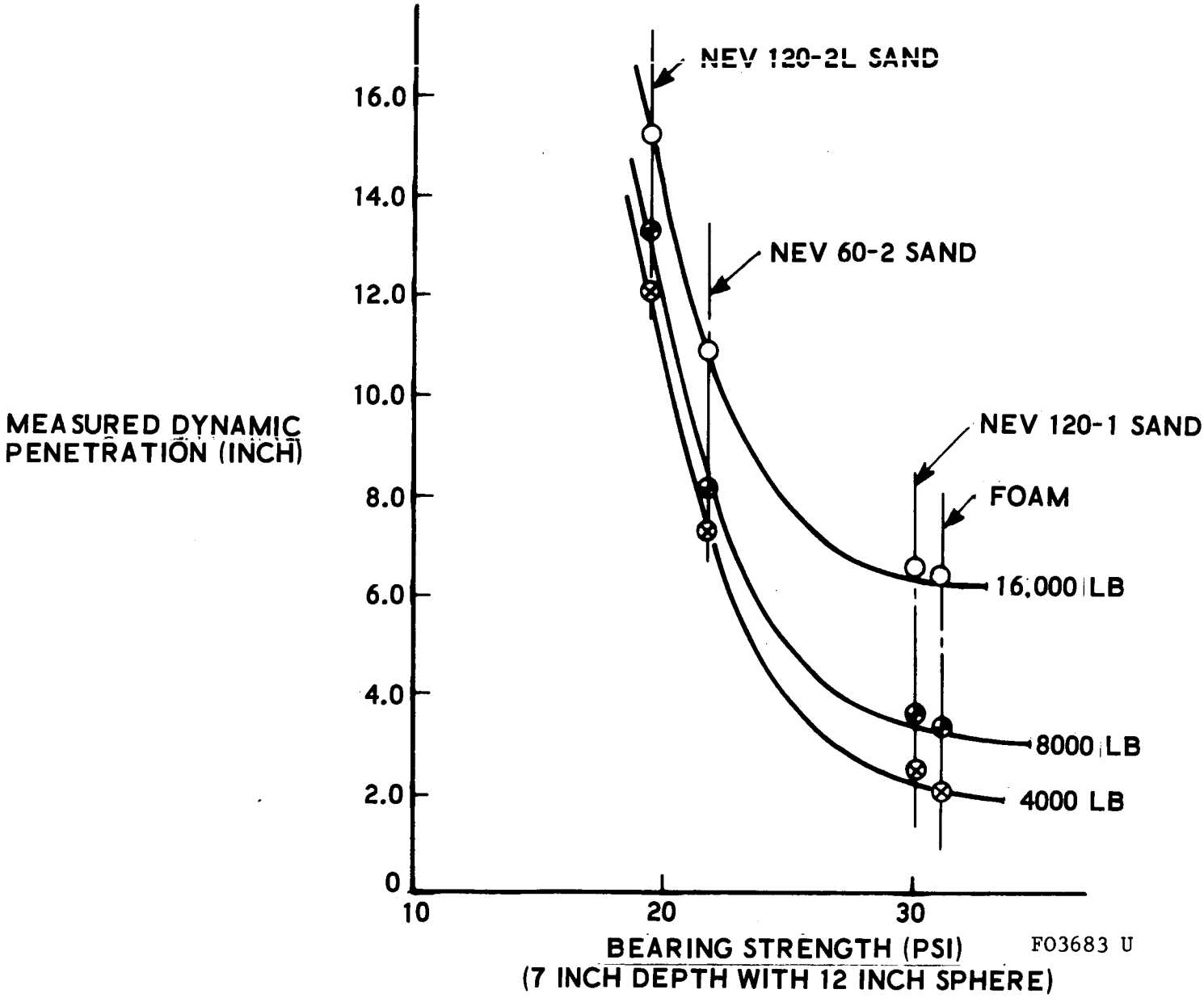

FIGURE 4-67. LEM LANDING PAD PENETRATION SUMMARY

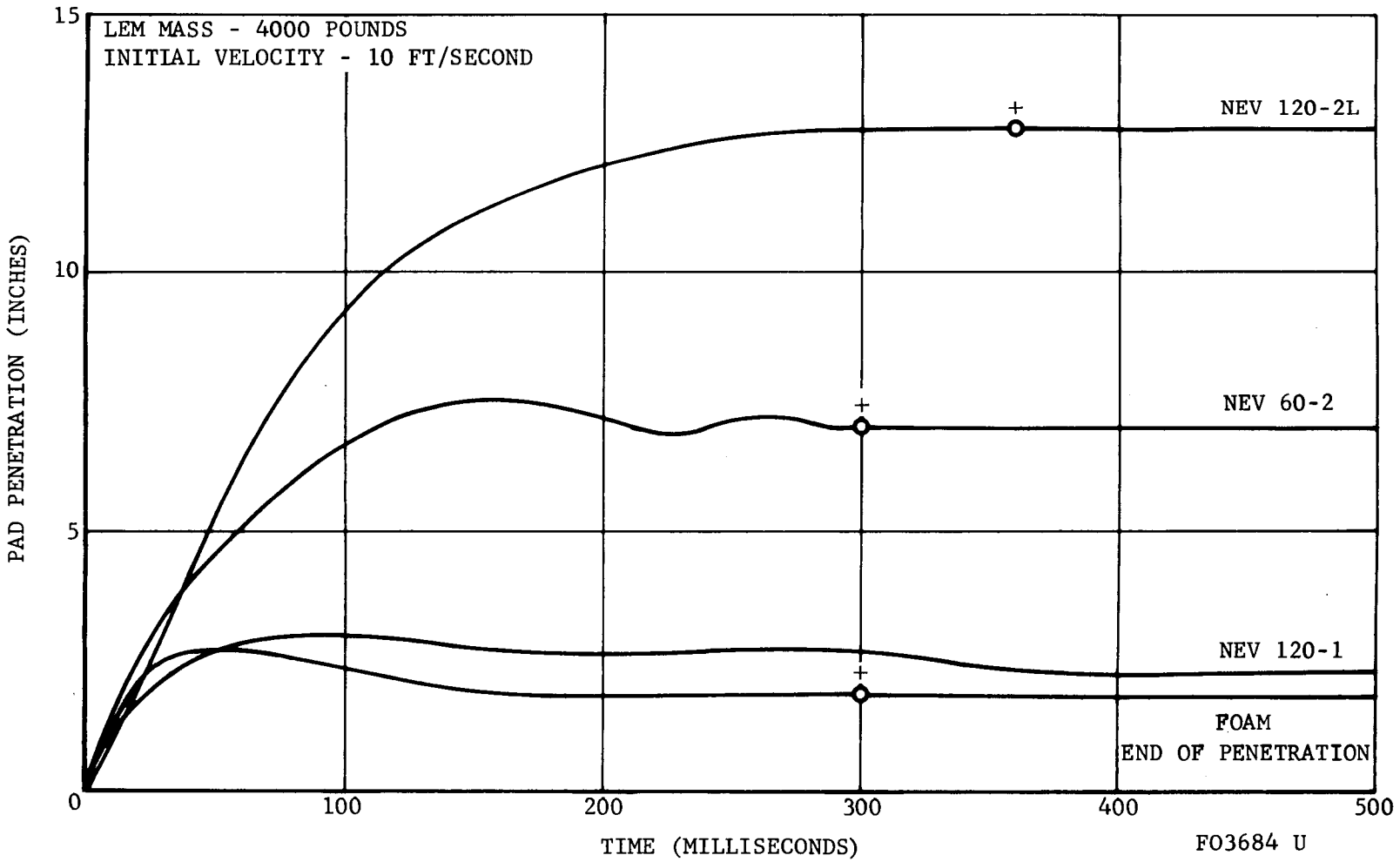

FIGURE 4-68. LEM PAD PENETRATION VERSUS TIME

(2) Dynamic penetration exhibits elasticity with an initial penetration greater than that at final rest.

(3) Penetration and rise time of penetration are related to bearing strength of the target materials.

Figures 4-69 and 4-70 show penetration time curves in the Nevada 60-2 sand and Nevada 120-2L with a family of weights. Trends exhibited by these curves are:

(1) Mass effects on penetration are minor.

(2) Three distinct rise times (humps) are exhibited at the beginning of 6000 pound honeycomb, 12,000 pound honeycomb and the strut bottom out events.

(3) Pad penetration occurs primarily at initial contact.

These curves summarize the dynamic penetration results. Penetration-time curves for each run are included in the LEM test data book submitted as a separate document.

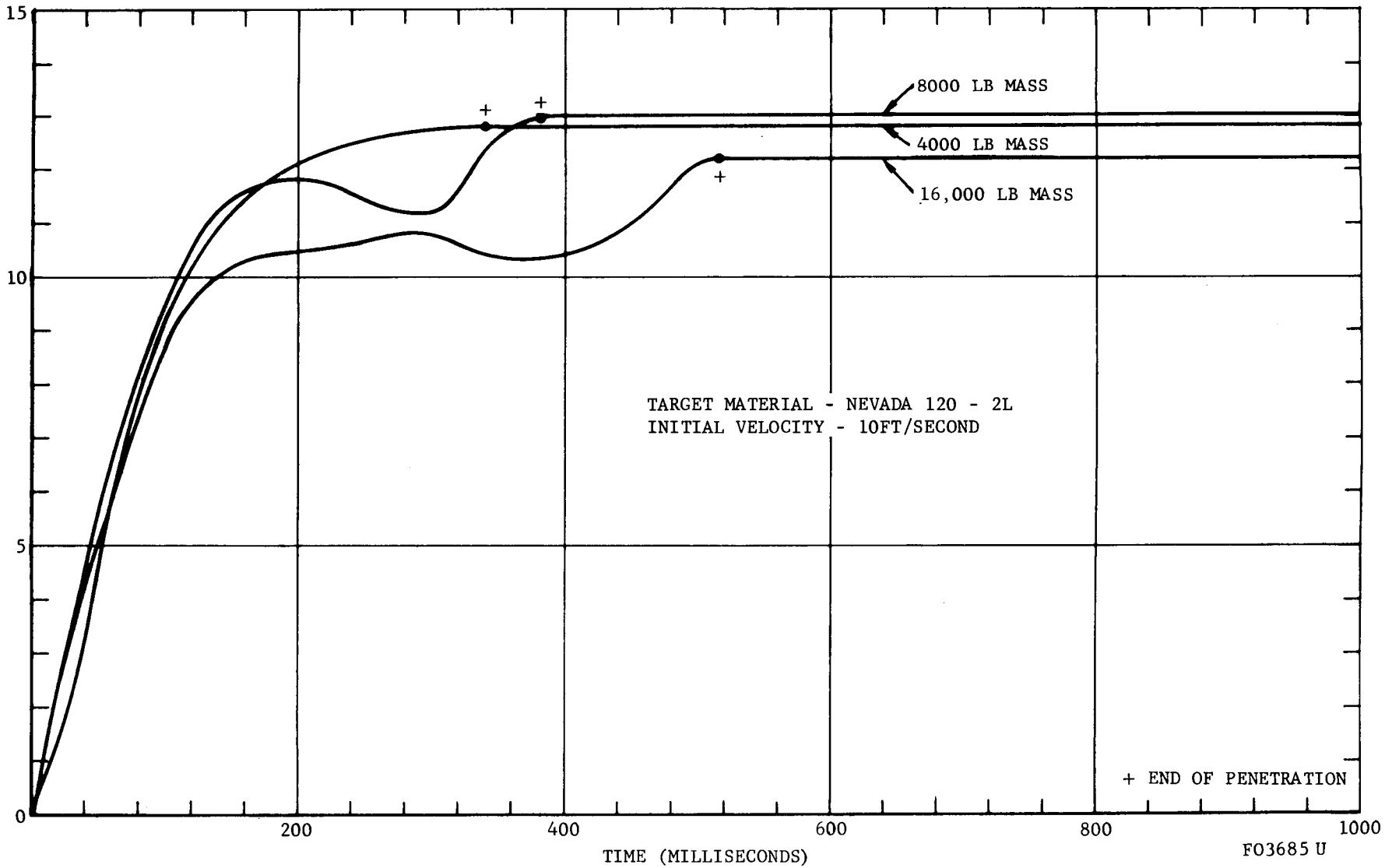

FIGURE 4-69. LEM PAD PENETRATION FAMILY CURVES IN NEVADA 120-2L SAND

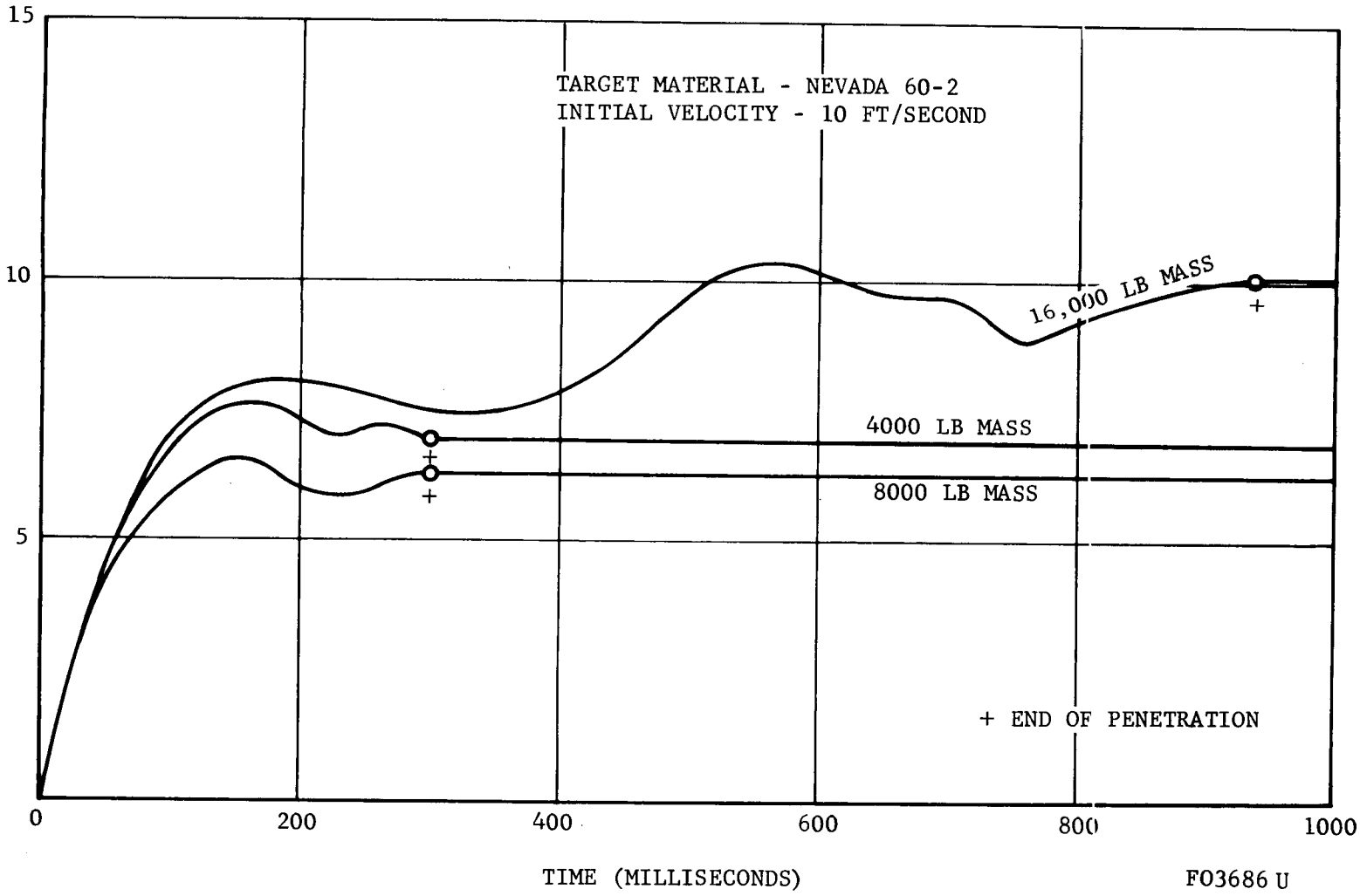

FIGURE 4-70. LEM PAD PENETRATION FAMILY CURVES IN NEVADA 60-2 SAND

4.5 DATA CORRELATION AND ANALYTICAL MODELS

4.5.1 DYNAMIC PENETROMETER DATA

For particulate (granular) earth media target materials in Figure 4-71, dimensionless penetration (depth of penetration relative to projectile radius) is plotted versus a density parameter which is target density relative to projectile average density (weight divided by volume). For the data at hand it is seen that for the higher values of the density parameter the total depth of penetration is seen to be one projectile diameter or less. Therefore, it is to be expected that the target static penetration resistance, which for these particulate materials increases from zero with increasing depth, should play a negligible role at such shallow penetrations. For lower values of the relative density parameter, however, the penetration is seen to increase and become large relative to the projectile diameter, so that target static resistance characteristics could then be expected to be important in determining penetration. It is seen that at lower values of target density relative to projectile density, the relative penetration appears to be ordered according to target material type, and indeed the order is such that the deeper penetrations (for a specified relative density) correspond to the target materials with the lower static penetration resistance characteristics. For data points representing penetrations greater than one projectile diameter, the relative penetration is plotted versus a dimensionless strength parameter in Figure 4-72. The particular strength parameter selected is suggested by the following simple theoretical consideration. For very low values of the target density relative to projectile density (γ_p) and for penetrations which are large compared to projectile diameter, target inertial resistance can be expected to play a small role relative to the target static penetration resistance in determining the penetration behavior. If inertial effects are neglected, and if the target static resistance characteristic is assumed to be approximately linear with slope K (lb/in^2 per inch), it can easily be shown from energy considerations that, for a given projectile radius and initial velocity, the relative penetration parameter is proportional to $(K_\sigma/\gamma_p)^{-1/2}$. The penetration depths calculated from such simple energy considerations, neglecting target material inertial resistance effects, are considerably greater than the experimental values shown in Figure 4-72. But within the inherent scatter (around 20 or 25 percent) of the data, the correlation with the selected strength parameter is quite good. This is possibly explained by the fact that for the particulate target materials under consideration here, the densities did not vary by more than about 25 percent. (Note that the data in Figure 4-72 corresponds to a single nominal value for both projectile radius and initial velocity.)* For increasing values of the relative density parameter, deviations from this correlation can be expected to increase.

*Experimental data available for particulate cohensionless materials at other velocities and projectile radii correspond to sufficiently high values of the relative density parameter that relatively shallow penetrations occur and strength effects are not dominant.

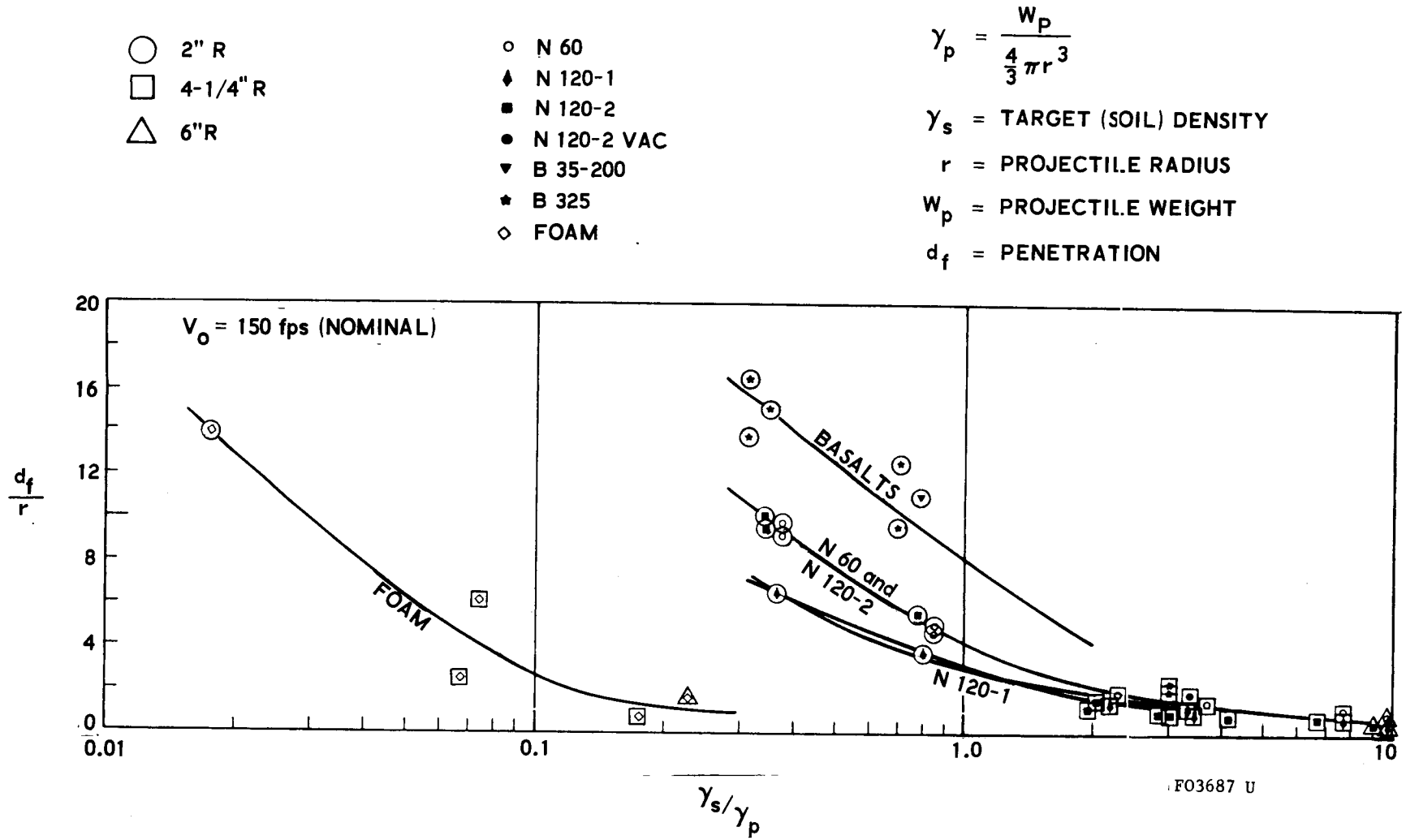

FIGURE 4-71. PENETRATION VERSUS DENSITY

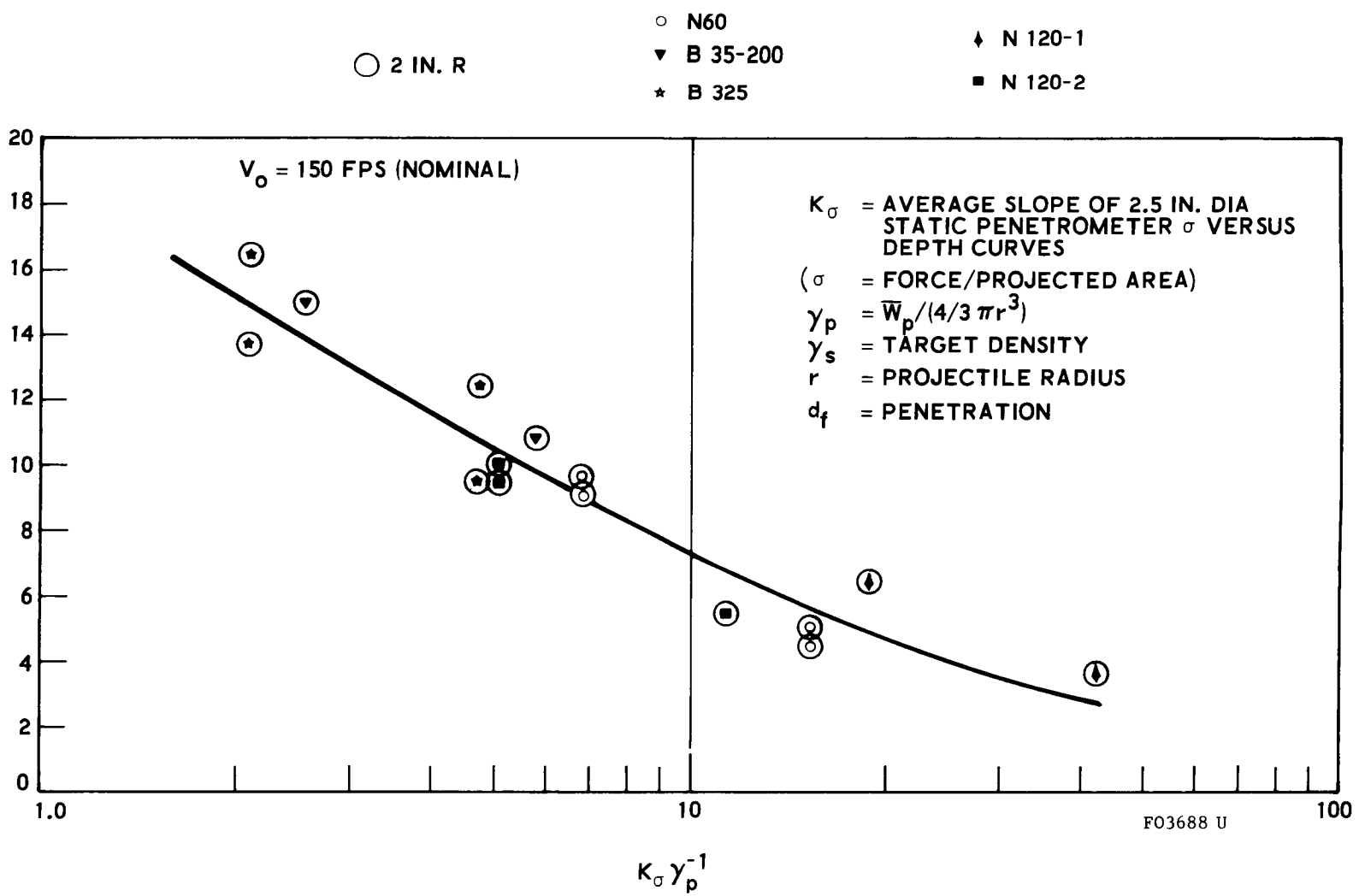

FIGURE 4-72. PENETRATION VERSUS BEARING STRENGTH

Trends in the peak acceleration data are displayed in terms of dimensionless parameters in Figure 4-73. The peak acceleration data are plotted versus the ratio of target material density to average projectile density because the peak acceleration tends to occur at such shallow penetration depths that target material inertial effects can be expected to dominate strength effects.

4.5.2 ANALYTICAL MODELS FOR PENETROMETER IMPACT ANALYSES

a. Original Model. Prior to the beginning of the present lunar penetrometer system contract, Aeronutronic had developed a method of analysis for a rigid body penetrating a deformable media.[1,2,3] In this work, the target material properties σ and ρ, bearing strength and density, respectively, were assumed to be constant, i.e., not varying with depth of penetration.

The capability of considering variable target strength and density parameter has been incorporated into the existing penetration mechanics analysis during the present program. This required a considerable amount of additional analytical development as well as revision of the constant-material-properties computer program.

The compressive strength parameter (σ), previously assumed to be constant, is now expressed as a function of depth of penetration into the target material (x) in the form

$$\sigma = a_0 + a_1 x + a_2 x^2 + a_3 x^3 \qquad (1)$$

The mass density ρ of the target material, also assumed to be constant in the previous solution is now expressed as

$$\rho = b_0 + b_1 x + b_2 x^2 \qquad (2)$$

---

1. Adams, D. F. and Tsai, S. W., A Mechanics Analysis of Armor Penetration, Philco Research Laboratories, Publication No. U-2600, May 1964.

2. Study of Mechanisms of Armor Penetration Resistance - Final Technical Report, Philco Research Laboratories, Publication No. U-2500, January, 1964.

3. Adams, D. F. and Doner, D. R., "Determining the Material Properties of a Remote Target by Analyzing Acceleration-Time Impact Data," Journal of Spacecraft and Rockets (to be published in Spring 1966).

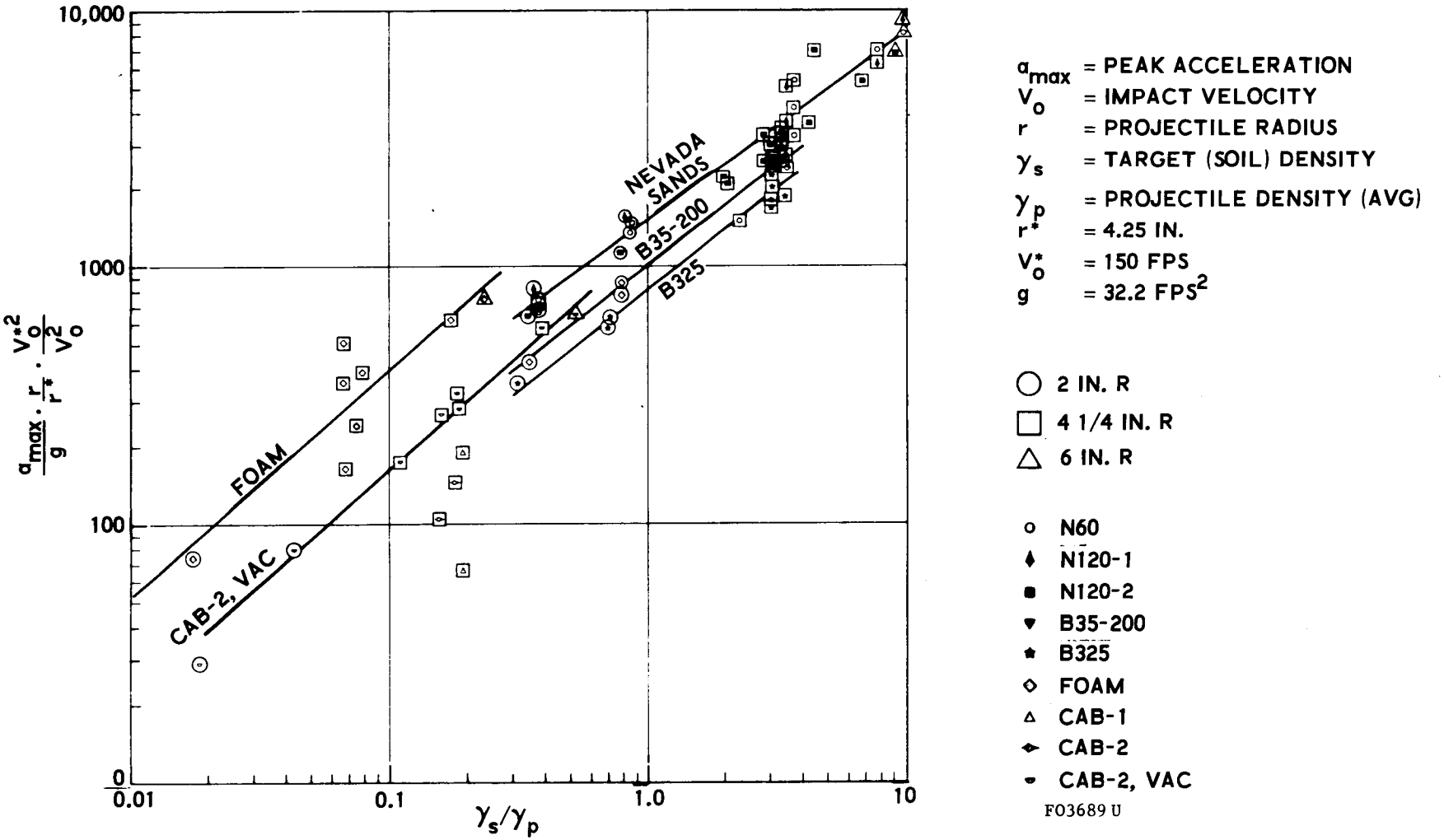

FIGURE 4-73. PEAK DECELERATION VERSUS DENSITY

Since both σ and ρ vary with depth of penetration, it is necessary to integrate these effects over the spherical surface of contact between penetrometer and target. During the entrance phase, i.e., for penetration depths less than the radius of the penetrometer, the contact area is also varying as a function of x.

Although the detailed mathematics of the method of solution become somewhat involved, the resulting relationships reduce to a very usable form.

A detailed derivation of the penetration equations for constant material properties is contained in Reference 3. The basic method of analysis remains unchanged for variable properties. A brief description of the method will be given here in order to point out the assumptions used and the applicability of the theory to the present program.

The motion of the penetrometer is assumed to be resisted primarily by two types of forces as it penetrates the lunar surface; the resistance of the lunar material to penetration because of its compressive resistance, and the inertial resistance of the material as it is displaced by the penetrometer.

The inertial resistance force per unit area, being a function of the velocity at which the lunar material at any particular point on the interface is being displaced, is dependent upon the geometry of the penetrometer and varies over the contact surface. This force per unit area can be obtained at a particular point by writing a work-energy relation for the differential element of mass of lunar material at that point. The total resisting force is then obtained by integrating over the entire contact surface.

Having defined the forces resisting penetration of the penetrometer, the equation of motion can be written as

$$mv \frac{dv}{dx} = -\int_{A_s} \sigma \cos\theta \, dA_s - \int_{A_s} 1/2 \, \rho \, (\cos^3\theta) \, v^2 \, dA_s \qquad (3)$$

where the component of each force per unit area in the direction of penetrometer motion is integrated over the surface area of the penetrometer in contact with the lunar material. The terms m and v represent penetrometer mass and velocity, respectively, σ and ρ are the lunar material compressive strength and mass density, x is the depth of penetration measured to the tip of the penetrometer, A_s is the surface area of contact corresponding to x, and θ is the angle measured from the direction of motion to the differential element of surface area dA_s, cos θ being used to obtain the component of the resisting force per unit area (which acts normal to the surface) in the direction of motion. In the present program, both σ and ρ are assumed to be functions of x, as indicated in Equations (1) and (2), respectively.

The frontal surface area of the penetrometer in contact with the lunar material (A_s) increases from zero to a maximum as the depth of penetration (x) increases from zero to complete submersion and then remains constant. Thus, two differential equations are obtained from Equation (3) when limits are substituted into the integrated expressions. One equation represents penetrometer motion during the entrance phase and the other the motion from then on.

The method of analysis is applicable to a penetrometer of any shape. To evaluate the integrals in Equation (3) for a particular geometry, relations between θ, A_s, and x are obtained using appropriate geometrical relations.

In the original formulation (constant material properties), the solution of Equation (3), a nonlinear differential equation, was obtained analytically, Taylor series expansion being utilized in integrating an exponential function in the solution of the first phase equation. In the variable material properties solution, Equation (3) has been solved numerically using a digital computer. In either case, values of velocity are obtained for specified values of displacement. When both sides of Equation (3) are divided by m, an expression for acceleration, i.e., $a = v\,(dv/dx)$, is obtained as a function of both v and x. Hence, accelerations can be obtained, since v is known for specified values of x.

Numerical integration of the velocity-displacement relationship to obtain the elapsed time of penetration is accomplished by using six-point Lagrangian integration coefficients with the same choice of velocity values as used in determining the acceleration.

Based upon this method of analysis, four digital computer programs have been developed to handle various aspects of the problems of analyzing experimental data. These programs are described in the following paragraphs.

(1) LPS-1 Material Properties Determination. This program is used to determine the variable material properties of the impacted target by analyzing experimental acceleration-time impact data. The unknown target material strength is assumed to vary with depth of penetration as $\sigma = a_0 + a_1x + a_2x^2 + a_3x^3$, where a_0 through a_3 are coefficients to be determined. For the present, target material density has been assumed to be independent of depth of penetration. Thus, target density (ρ) is a fifth unknown to be evaluated.

Equations of motion have been derived, involving the terms acceleration, velocity, displacement, σ, ρ, projectile diameter, and projectile weight, all of which are known except σ (expressed in the above polynomial form) and ρ. Selecting five sets of values of acceleration, velocity, and displacement from the experimental acceleration-time curve and the corresponding velocity-time and displacement-time curves, and substituting into

the derived equations of motion, a system of five linear algebraic equations is obtained involving the five unknowns, a_0, a_1, a_2, a_3, and ρ. This system of equations is solved simultaneously on a digital computer, using Gaussian elimination with row interchange. The computer prints out the values of the coefficients a_0 through a_3, ρ (both as mass density - lb-sec^2/in.^{4} and weight density - lb/ft^3), computes values of σ for each of the five input values of displacement, and tabulates computed values of σ for 1 inch increments of penetration from 0 to 50 inches.

(2) LPS-2 Integration of Acceleration-Time Data. In the event that experimental acceleration-time data are obtained without corresponding velocity-time and displacement-time data being available (in the present program, these auxiliary curves have been obtained by analog integration while summing up the components of the three uniaxial acceleration traces), this program digitally integrates the experimental acceleration-time data. Thus, this program is used to support Program LPS-1 when necessary.

(3) LPS-3 Determination of Acceleration-Time Curves. This program is used to determine theoretical acceleration-time curves when target material properties are either known or assumed. The program is capable of assuming variable target strength and density of the forms $\sigma = a_0 + a_1x + a_2x^2 + a_3x^3$ and $\rho = b_0 + b_1x + b_2x^2$, respectively.

The equations of motion are solved on a digital computer using Aeronutronic Library Subroutine RKS3 in the fixed interval mode. The computer prints out, in tabular form, for any specified increments of displacement, the following quantities: displacement (inches), velocity (ft/sec), acceleration (earth g), time (milliseconds), target strength (lb/in.^{2}), and target density (lb/ft^3).

(4) LPS-4 Evaluation of Target Strength Coefficients. Experimental static penetration test data are obtained in the form of force-displacement curves. Program LPS-4 fits the polynomial, $\sigma = a_0 + a_1x + a_2x^2 + a_3x^3$, to these data for use as input in Program LPS-3 or for comparison with calculated output values from Program LPS-1.

The program solves a system of four linear algebraic equations containing the four unknowns, a_0, a_1, a_2, and a_3 in a manner similar to that of Program LPS-1. The computer outputs the computed values of a_0 through a_3, computed values of σ (lb/in.^{2}) for each of the four input values of x (inches), and tabulates values of σ for any specified increment of x from zero to any specified upper limit.

b. Revised Penetrometer Model. As indicated in the previous section, the original analytical model was developed before experimental data were obtained. For the foam material used in the test program, the agreement between predicted acceleration-time and depth of penetration values and experimental data was excellent. The foam is a solid, i.e., nonparticulate, material and the analytical model was originally developed for such materials.

The agreement between this theory and experimental data for the particulate materials tested was not satisfactory, however. Four typical experimental acceleration-time plots are shown in Figures 4-74 through 4-77, representing various particulate target materials, velocities, and penetrometer configurations. Also indicated in each figure is the corresponding predicted curve, labeled original theory. As can be seen, the predicted curves range from having correct general shape characteristics but insufficient peak amplitude, as in Figure 4-74, to what appears to be a completely different response than measured, as in Figure 4-75. It is obvious that the response for particulate target materials is considerably different than for solid materials, for which the original theory was first developed.

After sufficient experimental data became available and a better interpretation of the penetration phenomena could be established, refinements in the analytical solution were made and the digital computer program was modified accordingly. One such revision was the assumption that a zone of target soil material directly ahead of the penetrometer becomes accelerated to the velocity of the penetrometer and subsequently moves with it, as indicated in Figure 4-78. This additional mass (m_2) is assumed to increase linearly with depth of penetration (x) and to be a function of the diameter (D) of the penetrometer, i.e., $m_2 = K_1 (\pi D^2/4) \rho x$. The term ρ represents target mass density and K_1 is a constant factor representing the volume of material assumed to be moving with the penetrometer. The value of K_1 has been determined by comparisons with experimental data, as will be shown.

One other revision has been in the assumption of the zone of target soil material contributing to the inertial resistance effect. In the original analysis (developed for solid materials), only that volume of material directly displaced by the penetrometer at any instant was assumed to be associated with inertia effects. However, as indicated in Figure 4-78, a much larger volume of material is apparently being influenced by the penetrating body in particulate materials. Thus, the inertial resistance term originally assumed in the model, which is a function of target density, depth of penetration, velocity, and geometry, has been increased by a constant factor K_2.

The values of K_1 and K_2 to be used in the revised theory have been evaluated by comparing the theory with available experimental data. The revised theory is also shown in Figures 4-74 through 4-77. In general, values of K_1 and K_2 of approximately 2 and 7, respectively, provide reasonable agreement between theory and experiment. However, certain apparent deviations have been observed. For example, the predicted depth of penetration of the 250 ft/sec shots is somewhat greater than measured, although excellent agreement has been obtained for most of the 20 and 150 ft/sec data. Also, the values of K_1 and K_2 required to match the experimental Cab-O-Sil penetration data are somewhat lower than

D1M1/BAS 35-200/ATM/150/0°/2

MEASURED INITIAL VELOCITY: 152 FPS

MAXIMUM PENETRATION:

EXPERIMENT = 21.8 INCH

ANALOG = 18.5 INCH

ORIGINAL THEORY = 17.3 INCH

REVISED THEORY = 21.12 INCH

PROJECTILE: 4 INCH DIAMETER , 2.2 POUNDS

TARGET: BASALT SAND

ATMOSPHERIC IMPACT ANGLE: 0°

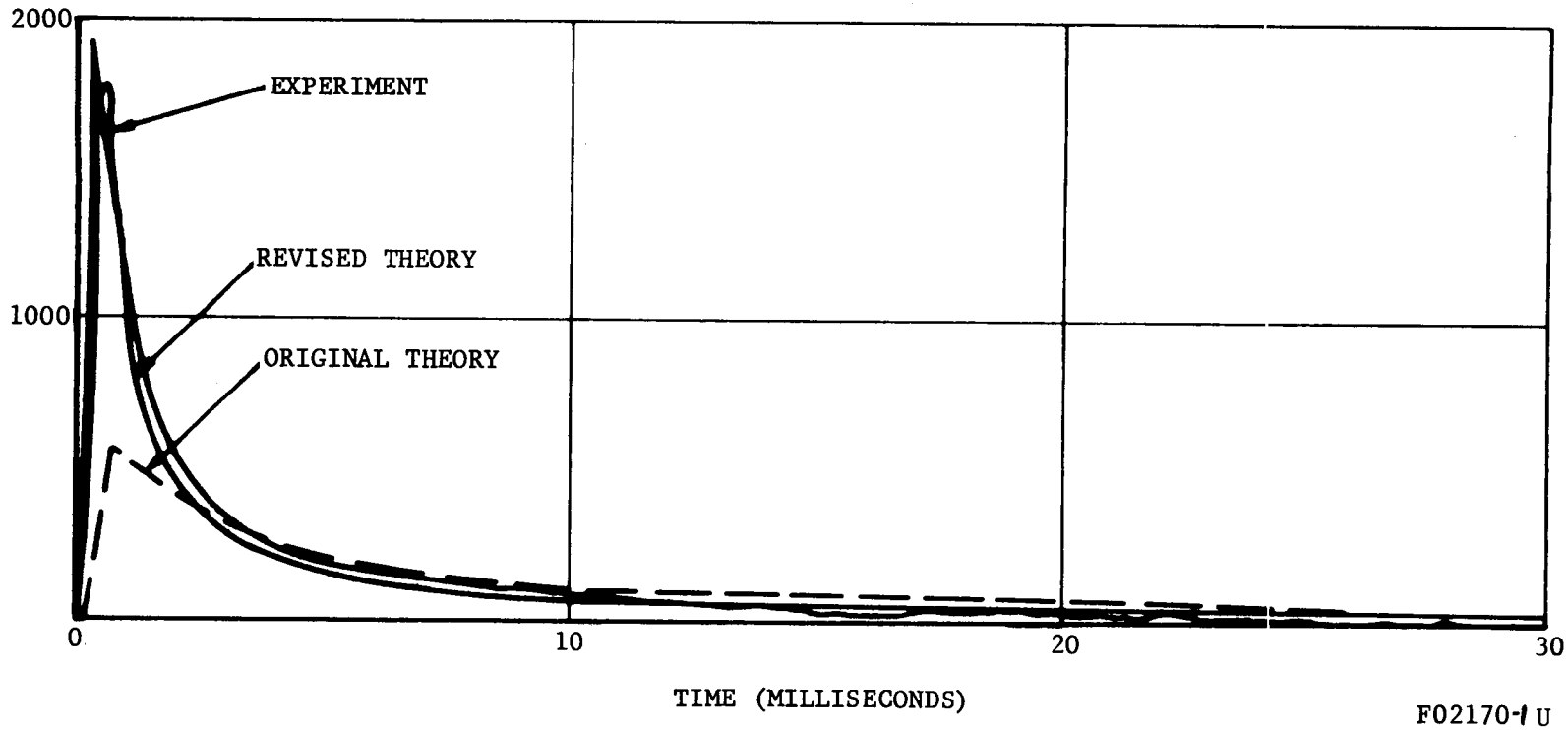

FIGURE 4-74. COMPARISON OF ACCELERATION WAVEFORMS FOR IMPACT INTO BASALT SAND

D2M2(5)A/BAS-325/ATM/20/0°/4

MEASURED INITIAL VELOCITY: 20 FPS

MAXIMUM PENETRATION:

EXPERIMENT = 6.8 INCH

ANALOG = 5.0 INCH

ORIGINAL THEORY = 5.4 INCH

REVISED THEORY = 6.16 INCH

PROJECTILE: 8 1/2 INCH DIAMETER , 5 POUNDS

TARGET: BASALT SILT

ATMOSPHERIC IMPACT ANGLE: 0°

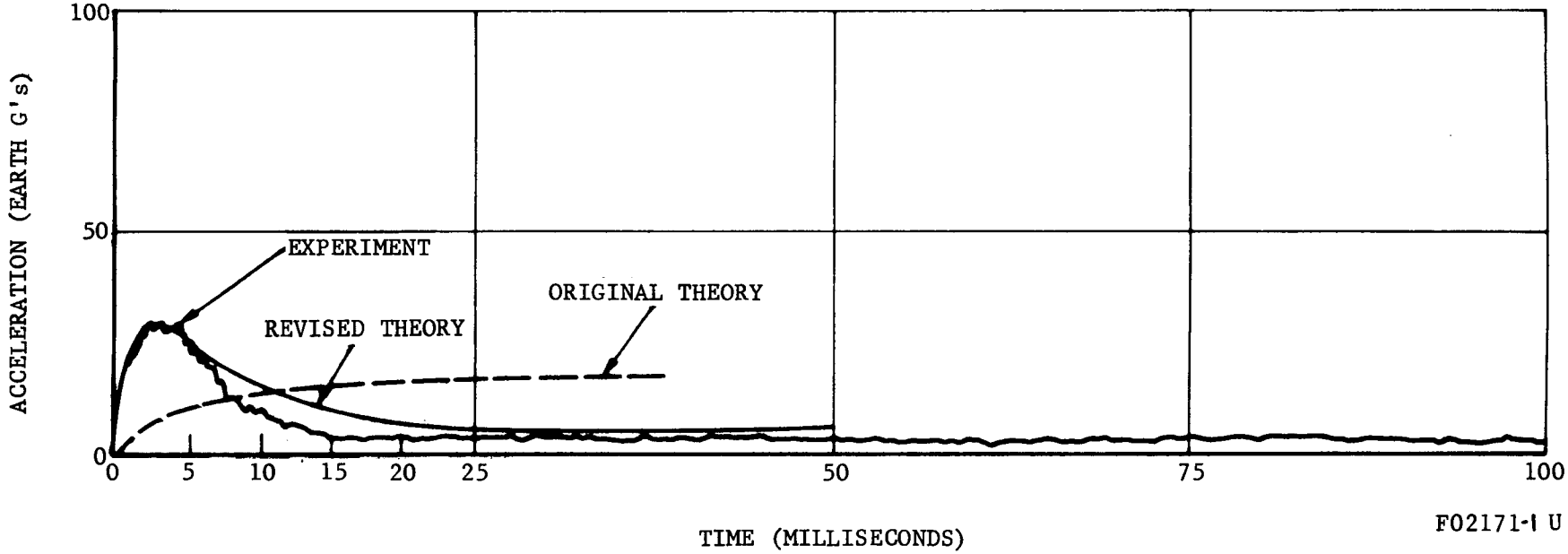

FIGURE 4-75. COMPARISON OF ACCELERATION WAVEFORMS FOR IMPACT INTO BASALT SILT

D2M2(5)A/CAB-1/ATM/150/0°/1

MEASURED INITIAL VELOCITY: 152 FPS

MAX PENETRATION:

EXPERIMENT	=	*	INCH
ANALOG	=	*	INCH
ORIGINAL THEORY	=	59.0	INCH
REVISED THEORY	=	60.82	INCH

PROJECTILE: 8 1/2 INCH DIAMETER , 5 POUNDS

TARGET: CABOSIL NO. 1

ATMOSPHERIC IMPACT ANGLE: 0°

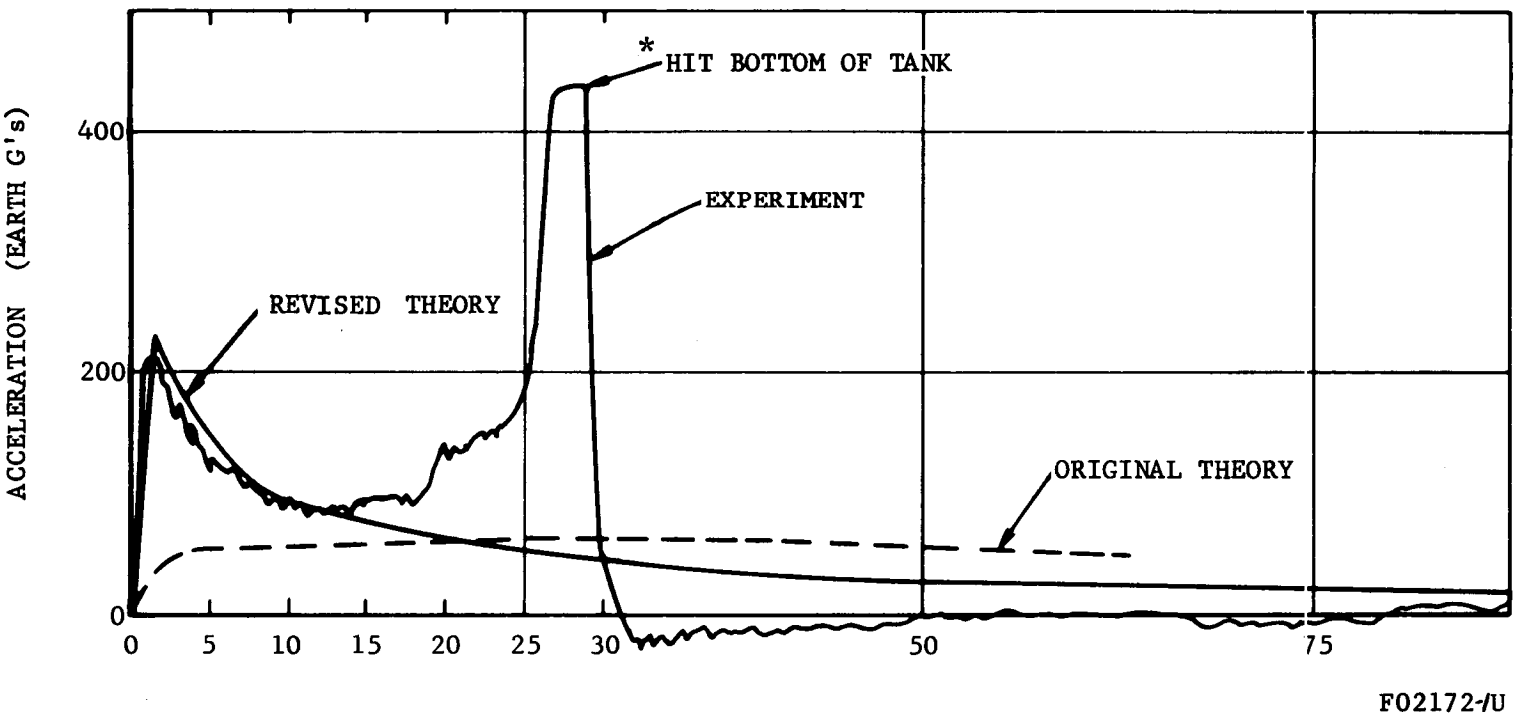

FIGURE 4-76. COMPARISON OF ACCELERATION WAVEFORMS FOR IMPACT INTO CAB-O-SIL .

D1M2(5)/NEV 60/ATM/150/0°/1

MEASURED INITIAL VELOCITY: 149 FPS

MAXIMUM PENETRATION:

EXPERIMENT	= 18.5	INCH
ANALOG	= 21	INCH
ORIGINAL THEORY	= 23	INCH
REVISED THEORY	= 19.70	INCH

PROJECTILE: 4 INCH DIAMETER , 5 POUNDS

TARGET: NEVADA 60 SAND

ATMOSPHERIC IMPACT ANGLE: 0°

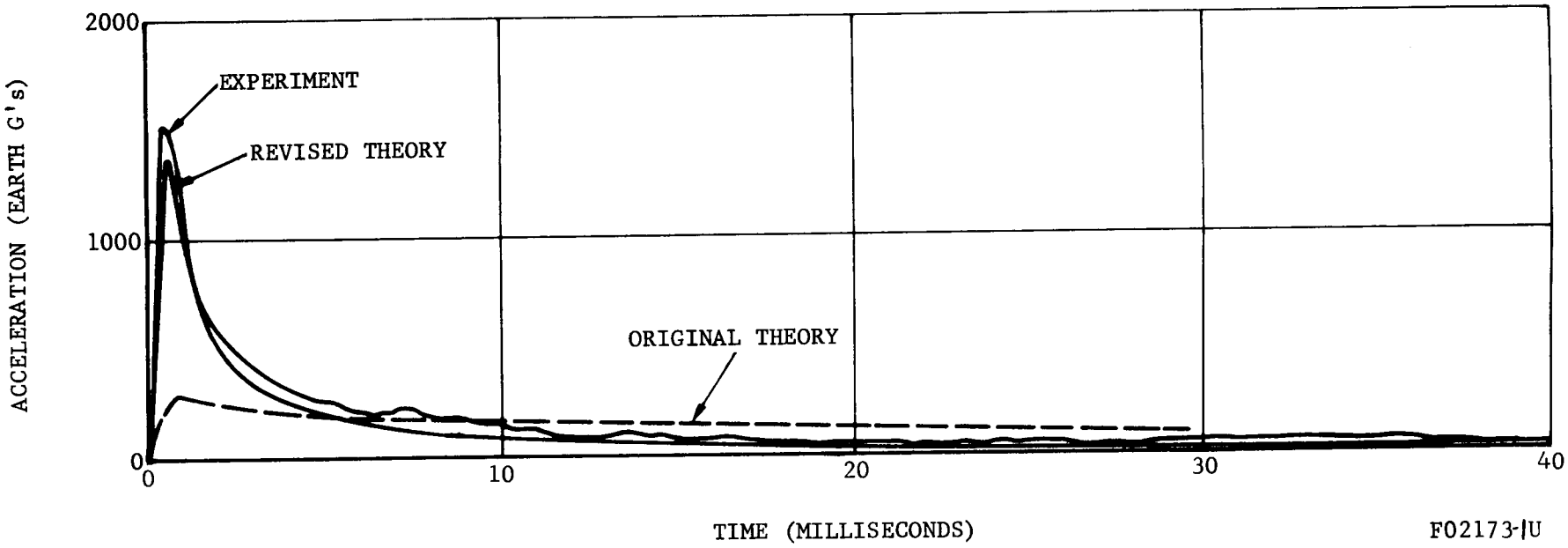

FIGURE 4-77. COMPARISON OF ACCELERATION WAVEFORMS FOR IMPACT INTO NEVADA 60 SAND

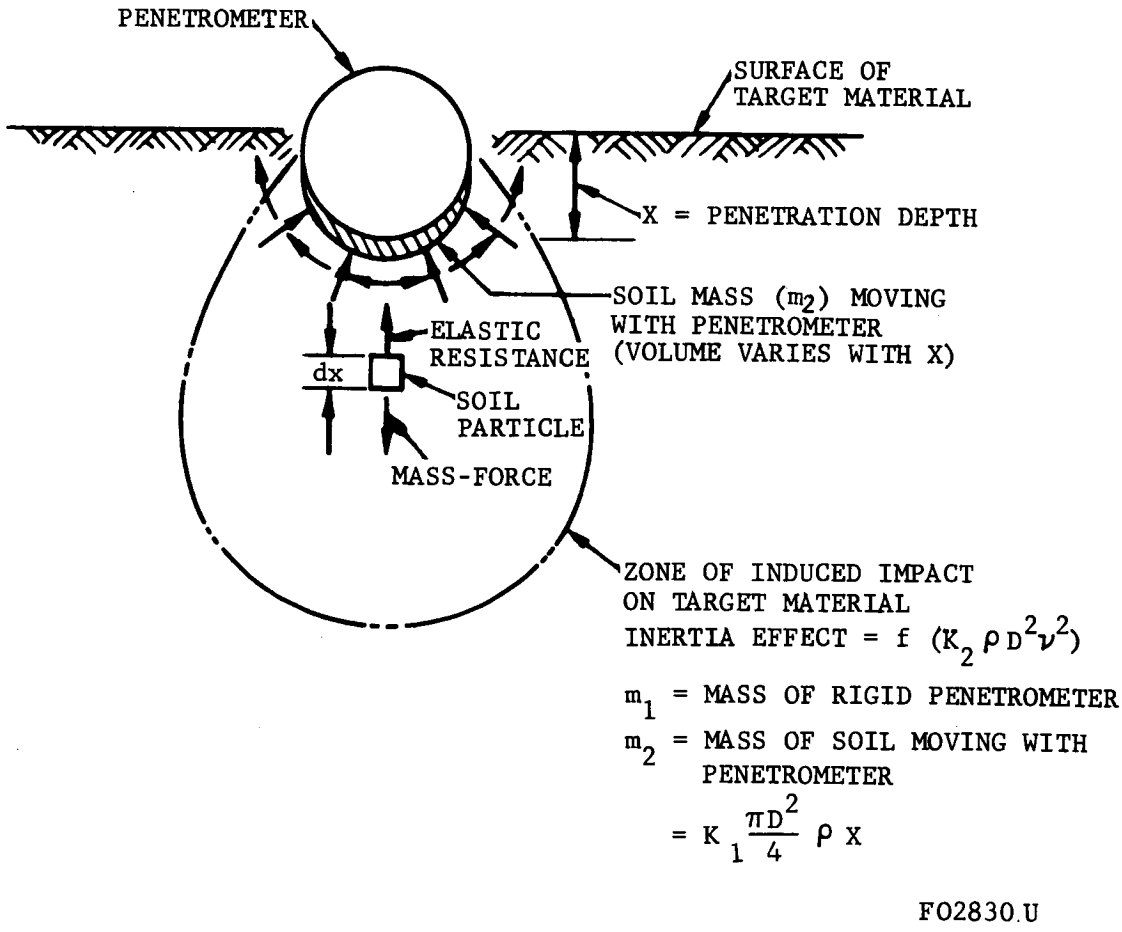

FIGURE 4-78. ZONE OF MATERIAL AFFECTED BY PENETROMETER IMPACT

$K_1 = 2$, $K_2 = 7$. However, because all but the 20 ft/sec tests into Cab-O-Sil struck bottom, experimental verification of predicted penetrations has not been possible in general. Figure 4-76 does indicate good agreement in the initial part of the curve, however,

The good agreement obtained by making the relatively simple modifications indicated demonstrates the general validity of the basic method of approach. However, it is not intended to imply that the present, relatively simple theory will provide excellent agreement for all test configurations and target materials. A more detailed analytical investigation must still be made now that experimental data are available. Only such an investigation, which considers characteristic soil material properties directly, can lead to a general soil penetration theory.

4.5.3 ANALYTICAL MODELS FOR LEM PAD IMPACT ANALYSIS

a. Lem Mechanical Model. The mechanical model utilized to describe the dynamics of LEM pad penetration is illustrated in Figure 4-79 and is analogous to a rigid-plastic structural model. Elastic modes of the structure are not treated. The honeycomb strut is assumed to crush at a constant load. Before the load in the honeycomb strut rises to a level sufficient to initiate crushing, the mechanics of penetration is treated as that of a rigid single degree of freedom system with a total mass equal to the payload mass (W/g) plus the mass (w/g) of the pad, together with the effective or "stagnation" mass (w*/g) of target material adjacent to and in motion with the pad. The motion is opposed by the resisting force of the target material consisting of "static" and dynamic components. The differential equation for this phase of the motion (including a term for the simulated reduced gravity) is:

$$\left(\frac{W + w + w^*}{g}\right) \cdot \left(\frac{dv}{dt} - \frac{g}{6}\right) = -F_{stat} - F_{dyn} \qquad (4)$$

v = velocity of the pad (equal to the velocity of the payload for this phase of the motion)

t = time

$g = 32.2\ fps^2$

F_{stat} = the soil static resistance given as a function of penetration depth

F_{dyn} = the dynamic target material resistance force and is represented by the following analytical expression:*

$$F_{dyn} = k_2 \frac{\gamma}{g} \frac{\pi r^2}{4} \left[1 - \left(1 - \frac{x}{r}\right)^4\right] v^2 \quad \text{for } x < \bar{x} \qquad (4a)$$

$$= k_2 \frac{\gamma}{g} \frac{\pi r^2}{4} \left[1 - \left(1 - \frac{\bar{x}}{r}\right)^4\right] v^2 \quad \text{for } x > \bar{x} \qquad (4b)$$

*See Paragraph 4.5.2

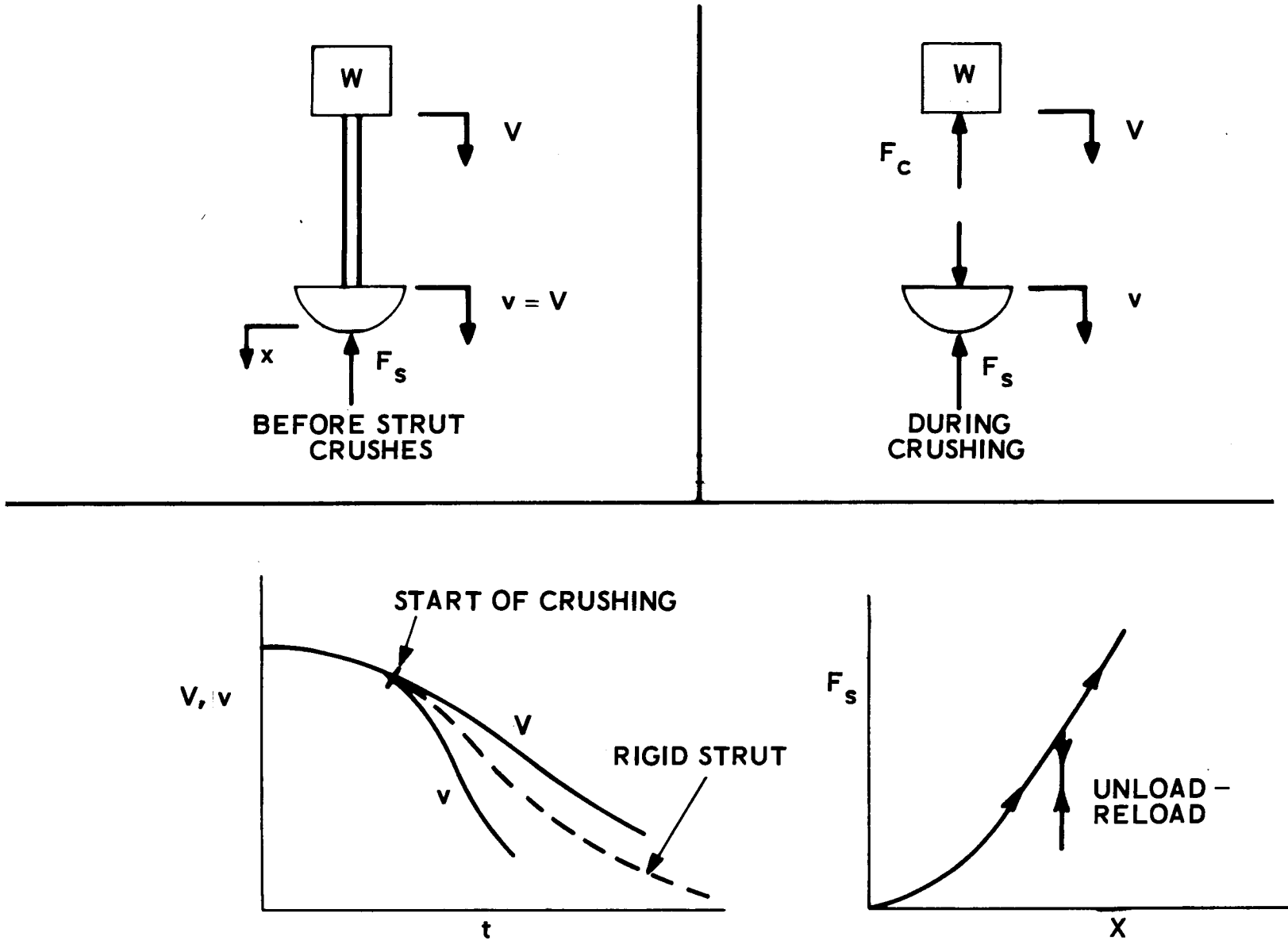

FIGURE 4-79. LEM MODEL

in which

k_2 = an empirical coefficient

γ = weight density of the target material

r = radius of curvature of the LEM pad

x = depth of penetration

$\bar{x}$ = the depth beyond which there is not significant veriation in pad area.

Since $\frac{\bar{x}}{r} < 0.075 \ll 1$,* the following approximate relation for F_{dyn} can be employed:

$$F_{dyn} \cong k_2 \frac{\gamma}{g} (\pi r x) v^2 \quad \text{for } x \leq \bar{x} \tag{5a}$$

$$\cong k_2 \frac{\gamma}{g} (\pi r \bar{x}) v^2 \quad \text{for } x > \bar{x} \tag{5b}$$

The stagnation mass of soil in motion with the pad is represented as a function of x by the following analytical expression:**

$$\frac{w^*}{g} = k_1 \frac{\gamma}{g} \left[2\pi r x \left(1 - \frac{x}{2r} \right) \right] x \quad \text{for } x \leq \bar{x} \tag{6a}$$

$$= k_1 \frac{\gamma}{g} \left[2\pi r \bar{x} \left(1 - \frac{\bar{x}}{2r} \right) \right] x \quad \text{for } x > \bar{x} \tag{6b}$$

As in the case of the dynamic resistance force component, the following approximation is valid (since $\bar{x}/r$ is small relative to unity):

$$\frac{w^*}{g} \cong k_1 \frac{\gamma}{g} (2\pi r x^2) \quad \text{for } x \leq \bar{x} \tag{7a}$$

$$\cong k_1 \frac{\gamma}{g} (2 r \bar{x} x) \quad \text{for } x > \bar{x} \tag{7b}$$

Noting that (8)

$$\frac{dv}{dt} = v \frac{dv}{dx} = \frac{1}{2} \frac{d(v^2)}{dx}$$

*r = 50 inches, $\bar{x} \cong 3.6$ inches

**The basis for this representation is discussed in Paragraph 4.5.2

Equation (4) can be written

$$\frac{d(v^2)}{dx} + f(x) \cdot v^2 = R(x) \tag{9}$$

where

$$f(x) = \frac{2k_2\gamma(\pi rx)}{W + w + 2k_1\gamma\pi rx^2} \quad \text{for } x \leq \bar{x} \tag{10a}$$

$$= \frac{2k_2\gamma(\pi r\bar{x})}{W + w + 2k_1\gamma\pi r\bar{x}x} \quad \text{for } x > \bar{x} \tag{10b}$$

and

$$R(x) = 2g\left(\frac{1}{6} - \frac{F_{stat}}{W + w + 2k_1\gamma\pi rx^2}\right) \quad \text{for } x \leq \bar{x} \tag{11a}$$

$$= 2g\left(\frac{1}{6} - \frac{F_{stat}}{W + w + 2k_1\gamma\pi r\bar{x}x}\right) \quad \text{for } x > \bar{x} \tag{11b}$$

The solution to Equation (9) can be shown to be given by the following expressions ($k_1 \neq 0$):

For $x \leq \bar{x}$

$$v^2 = \left(1 + \frac{2k_1\gamma\pi rx^2}{W + w}\right)^{-\frac{k_2}{2k_1}} \left\{ v_o^2 + \int_o^x R(u) \cdot \left(1 + \frac{2k_1\gamma\pi ru^2}{W + w}\right)^{\frac{k_2}{2k_1}} \cdot du \right\} \tag{12a}$$

where v_o is the impact velocity

For $x > \bar{x}$,

$$v^2 = \left\{ \left(1 + \frac{2k_1 \gamma \pi r \bar{x} x}{W + w} \right) - \frac{k_2}{k_1} \right\} \bar{v}^2 \left(1 + \frac{2k_1 \gamma \pi r \bar{x}^2}{W + w} \right)^{\frac{k_2}{k_1}}$$

$$+ \int_{\bar{x}}^{x} R(u) \cdot \left(1 + \frac{2k_1 \gamma \pi r \bar{x} u}{W + w} \right)^{\frac{k_2}{k_1}} \cdot du \Bigg\} \qquad (12b)$$

where $\bar{v}$ is the velocity given by Equation (12a) evaluated at $x = \bar{x}$.

Since F_{stat}, and therefore R, is a known function of the penetration depth (x or u), Equation (13) can be integrated, by numerical techniques, if necessary, to give velocity v as a function of x.

The depth at which crushing is initiated can be determined as follows: When the load in the honeycomb strut reaches the crushing level, F_c, the acceleration of the payload is

$$\frac{W}{g} \left(\frac{dV}{dt} - \frac{g}{6} \right) = -F_c \qquad (13)$$

Where V is the velocity of the payload. But, during this initial phase of the motion; that is, up to the initiation of honeycomb crushing

$$V = v \qquad (14)$$

so that at the instant the honeycomb strut starts to crush

$$\frac{dv}{dt} - \frac{g}{6} = - \frac{F_c}{W} g \qquad (15)$$

Substituting Equation (15) in Equation (3) it is seen that honeycomb crushing commences when the following relation is satisfied:

$$\left(\frac{W + w + w^*}{W} \right) \cdot F_c = -F_{stat} - F_{dyn} \qquad (16)$$

where F_{dyn} is given by Equation (5) and w* is given as a function of x by Equation (7). Since F_{stat} and v are now known as functions of x, the depth x_c at which crushing commences can be determined numerically with the use of Equation (16).

After the initiation of crushing of the honeycomb strut (that is for $x > x_c$), the differential equation of motion of the payload mass is:

$$\frac{W}{g}\left(\frac{dV}{dt} - \frac{g}{6}\right) = - F_c \tag{17a}$$

or

$$\frac{W}{g}\ \frac{dV}{dt} = \frac{W}{6} - F_c \tag{17b}$$

This is simply the trivial problem of a constant mass accelerated by a constant force. The well-known solution for velocity as a function of displacement is:

$$V^2 = V_c^2 + 2g\left(\frac{1}{6} - \frac{F_c}{W}\right)\left(X - X_c\right) \tag{18}$$

Where X is the coordinate defining the position of the payload

$X_c = x_c$ is the pad penetration at which honeycomb crushing is initiated, as determined previously

V = the velocity of the payload

$V_c = v_c$ is the velocity at the instant honeycomb crushing commences, as obtained from Equation (12) evaluated at $x = x_c$

and the other notation is as defined previously.

For $x > x_c$, the differential equation of motion for the mass of the pad can be written

$$\frac{w + w^*}{g} \cdot \left(\frac{dv}{dt} - \frac{g}{6}\right) = F_c - F_{stat} - F_{dyn} \tag{19}$$

in which all terms and notation are as defined previously. Note that after initiation of crushing of the honeycomb strut, the velocity V of the payload is no longer equal to the velocity v of the pad. Using Equations (5), (7), and (8), Equation (19) can be rewritten

$$\frac{dv^2}{dx} + f_1(x) \cdot v^2 = R_1(x) \tag{20}$$

where

$$f_1(x) \simeq \frac{2k_2\gamma(\pi rx)}{w + 2k_1\gamma\pi rx^2} \quad \text{for } x \leq \bar{x} \tag{21a}$$

$$\simeq \frac{2k_2\gamma(\pi r\bar{x})}{w + 2k_1\gamma\pi r\bar{x}x} \quad \text{for } x > \bar{x} \tag{21b}$$

and

$$R_1(x) = 2g\left(\frac{1}{6} + \frac{F_c - F_{stat}}{w + 2k_1\gamma\pi rx^2}\right) \quad \text{for } x \leq \bar{x} \tag{22a}$$

$$= 2g\left(\frac{1}{6} + \frac{F_c - F_{stat}}{w + 2k_1\gamma\pi r\bar{x}x}\right) \quad \text{for } x > \bar{x} \tag{22b}$$

The solution to Equation (20) is ($k_1 \neq 0$):

For $x \leq \bar{x}$,

$$v^2 = \left(1 + \frac{2k_1\gamma\pi rx^2}{w}\right)^{-\frac{k_2}{2k_1}} \left\{ V_c^2 \left(1 + \frac{2k_1\gamma\pi rx_c^2}{w}\right)^{\frac{k_2}{2k_1}} + \int_{x_c}^{x} R_1(u) \cdot \left(1 + \frac{2k_1\gamma\pi ru^2}{w}\right)^{\frac{k_2}{2k_1}} \cdot du \right\} \tag{23a}$$

For $x > \bar{x}$

$$v^2 = \left(1 + \frac{2k_1 \gamma \pi r \bar{x} x}{w}\right)^{-\frac{k_2}{k_1}} \left\{ \tilde{v}^2 \left(1 + \frac{2k_1 \gamma \pi r \tilde{x} \tilde{x}}{w}\right)^{\frac{k_2}{k_1}} + \int_{\tilde{x}}^{x} R_1(u) \cdot \left(1 + \frac{2k_1 \gamma \pi r \bar{x} u}{w}\right)^{\frac{k_2}{k_1}} \cdot du \right\} \quad (23b)$$

in which, if

$$x_c < \bar{x}, \ \tilde{x} = \bar{x} \quad (24a)$$

and

$$\tilde{v} = \bar{v} \quad (25a)$$

where $\bar{v}$ is obtained from Equation (23) evaluated at $x = \bar{x}$.

If

$$x_c \geq \bar{x}, \ \tilde{x} = x_c \quad (24b)$$

$$\tilde{v} = v_c \quad (25b)$$

As before, v_c is obtained from Equation (12) evaluated at $x - x_c$, and all other notation is as previously defined. Equations (23) can be evaluated numerically to determine velocity as a function of depth of penetration, the maximum penetration x_f of the pad being determined by the condition that $v = 0$ at $x = x_f$.

In many practical problems, it has been found that x_c is sufficiently large such that the expression for $R_1(x)$ can be simplified by taking advantage of the approximately linear character of the LEM pad static force-penetration curve for depths greater than about 2 inches (see Figure 4-80). Then if the average slope of the essentially linear part of the LEM pad static penetration curve for the particular target material is denoted by K,

$$F_{stat} - F_c \simeq K (x - x_c) \quad (26)$$

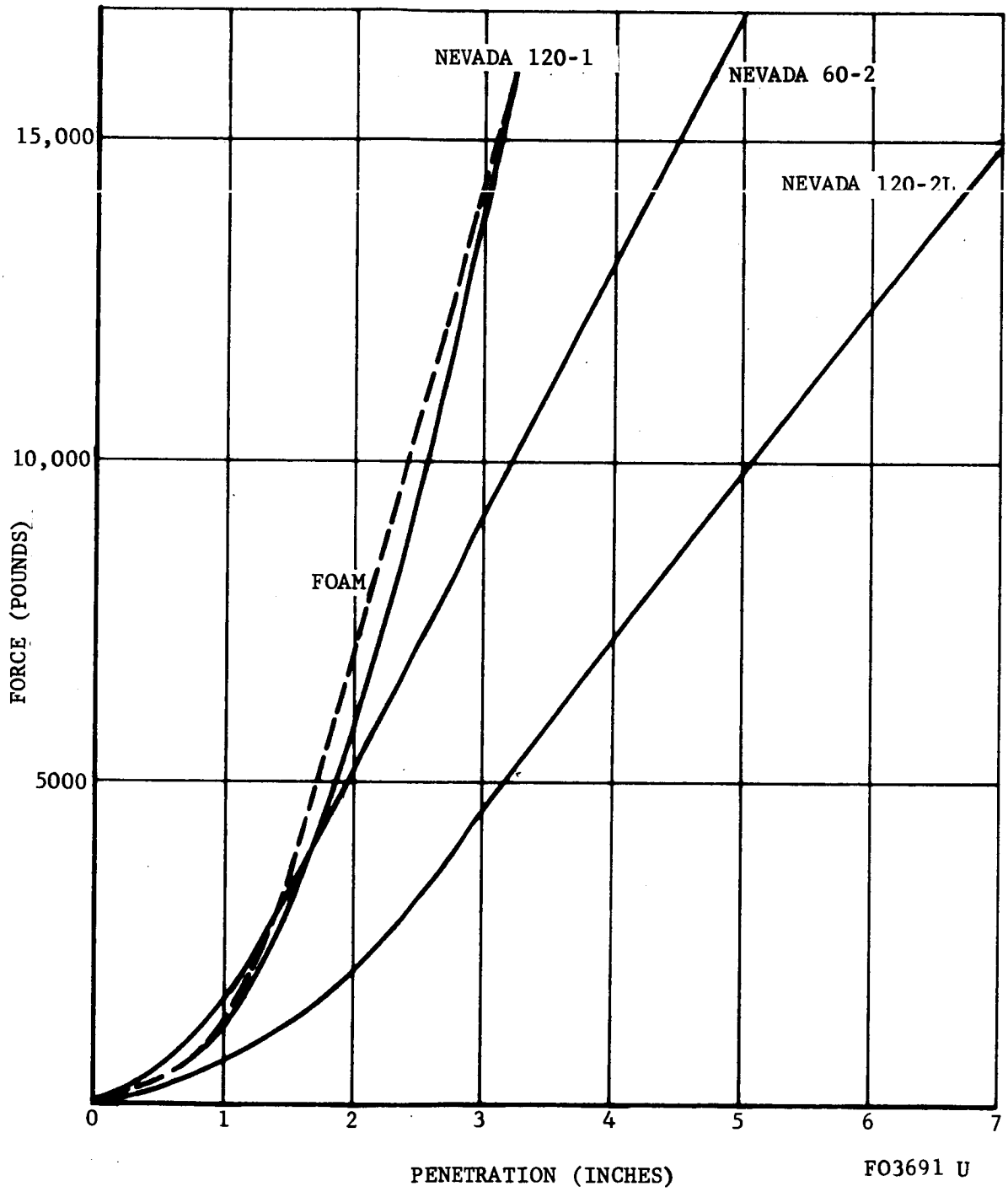

FIGURE 4-80. COMPARITIVE LEM PAD STATIC RESULTS

Closed form expressions constituting an upper bound to the mathematical solution represented by Equations (23) can be obtained by neglecting the target inertial resistance term (that is, setting $k_2 = 0$) in conjunction with the use of the approximate relation given by Equation (26). The resulting analytical expressions representing this upper bound to the solution are as follows:

For $x \leq \bar{x}$,

$$v^2 = v_c^2 - 2g\left\{\frac{K}{2k_1\gamma\pi r}\left\{\frac{1}{2}\ln\left(\frac{w + 2k_1\gamma\pi r x^2}{w + 2k_1\gamma\pi r x_c^2}\right) - \sqrt{\frac{2k_1\gamma\pi r x_c^2}{w}}\left[\tan^{-1}\left(\sqrt{\frac{2k_1\gamma\pi r x^2}{w}}\right) - \tan^{-1}\left(\sqrt{\frac{2k_1\gamma\pi r x_c^2}{w}}\right)\right]\right\} - \frac{x - x_c}{6}\right\} \quad (27a)$$

For $x > \bar{x}$,

$$v^2 = v_c^2 - 2g\left\{\frac{K}{2k_1\gamma\pi r\bar{x}}\left\{x - \tilde{x} - \left(\frac{w + 2k_1\gamma\pi r\bar{x}x_c}{2k_1\gamma\pi r\bar{x}}\right)\ln\left(\frac{w + 2k_1\gamma\pi r\bar{x}x}{w + 2k_1\gamma\pi r\bar{x}\tilde{x}}\right)\right\} - \frac{x - \tilde{x}}{6}\right\} \quad (27b)$$

where all notation is as previously defined. These upper bound expressions can be a useful aid in parametric investigations relating to studies of correlation between theoretical and experimental results.

The above theoretical development of a mathematical model for the dynamics of LEM pad penetration can be extended in a straightforward manner to the situation in which the honeycomb strut is constructed of two types of honeycomb material in a series arrangement, one type of material crushing at a higher load level than the other. It should be noted that it is possible for the LEM pad to be brought to rest before crushing of the higher strength honeycomb commences. If the higher strength honeycomb starts to crush, and if the corresponding load level is sufficiently high, pad penetration can be reinitiated. At the present time it is necessary to assume that the static force-penetration depth curve for this second phase of the pad motion is the same as that for the earlier phase of penetration.

b. Spring Model. In addition to revising the penetrometer model for studying LEM pad impact behavior, a considerably different approach was also investigated.

If the impacted material is assumed to be a semi-infinite region being compressed by a rigid body, i.e., the LEM pad, the target material beneath this body is subjected to a compressive stress field. This stress distribution is a function of both axial and radial coordinates, as has been established by the theory and experiment. The compressive stress field induces a penetration of the impacting body, static penetration tests of soil materials indicating a reasonably linear relationship in general.

This linearity suggests behavior analogous to a linear spring, the soil storing potential energy during the kinetic impact. The deformation is associated with the overcoming of friction between soil particles compressed against each other. Because of the apparent linear response, it is plausible to assume that beneath the penetrating body, the target material resists motion analogous to a multifold spring system. For the sake of analytical simplicity, this spring system will be reduced to a single spring with one degree of freedom. In the actual physical case, many different soil mechanics effects are involved. For example, lateral deformations and restraints influence motion as well as the amount of soil actually moving with the penetrating body.

In the present analysis, a linear relation between the assumed elastic resisting force and the penetration will be assumed, i.e., $P = Cx$, where x represents penetration depth, P the resisting force, and C is an "effective spring constant."

An expression for C is established as follows. From an actual static penetration curve, an equivalent modulus (E) can be determined as

$$E = \frac{\Delta P}{\Delta x} h \tag{28}$$

where Δp, an incremental change in resisting pressure, is equal to $\Delta P/A$, i.e., an incremental change in total resisting force divided by the projected area of contact. The term h is a characteristic depth of the soil material being considered. If the actual static penetration curve is slightly nonlinear, as is frequently the case, E can be assumed to define an average value. The term Δx represents an increment of penetration corresponding to Δp. Substituting $\Delta P/A$ for Δp in Equation (28) and solving for Δx gives

$$\Delta x = \frac{\Delta P}{EA} h \tag{29}$$

Therefore, C can be expressed as (using Equation (29),

$$C = \frac{\Delta P}{\Delta x} = \frac{EA}{h} \tag{30}$$

Because of the effect of the size of the penetrating body on static penetration behavior, the static test data used in determining the value of E in Equation (28) must be representative of the body used in the dynamic test. If both static and dynamic test data are not available for the same body, there are transformation formulas available which permit scaling from one size to another. These relations are based upon soil mechanics considierations and take the following form:

$$P_2 = P_1 \frac{N_1}{N_2} \tag{31}$$

where P_1 and P_2 are forces resisting penetration for two different size bodies and

$$N_1 = \left[\frac{h}{D_1^2 + 2D_1 h} + \frac{K}{D_1^3} \right]$$

$$N_2 = \left[\frac{h}{D_2^2 + 2D_2 h} + \frac{K}{D_2^3} \right] \tag{32}$$

The terms D_1 and D_2 represent the diameters of the two different bodies and $K = \alpha E$, where α represents the effect of lateral volume displacement of the soil and must be approximated.

Having obtained representative static penetration data either directly or by a scaling procedure, the value of C can be evaluated using Equations (28) and (30).

The dynamic behavior is then determined as follows: Using the linear spring concept, the law of conservation of momentum can be expressed as

$$M (v_i - v) = \int_o^t P \, dt \tag{33}$$

where M represents the mass of the penetrating body, v_i its initial velocity, v its velocity at some later time (t), and P - Cx, as previously defined.

Making this substitution for P, the solution of Equation (33) can be expressed as

$$x = \frac{v_i}{\omega} \sin \omega t \tag{34}$$

where

$$\omega = \sqrt{\frac{C}{M}} \tag{35}$$

Penetration (x) will be a maximum when $t = \frac{\pi}{2\omega}$

Therefore,

$$x_{max} = v_i \sqrt{\frac{M}{C}} \tag{36}$$

Since $P = Cx$, the resisting force at x_{max} will be

$$P_{x_{max}} = v_i \sqrt{MC} \tag{37}$$

In the present application, the frequency term (ω) of Equation (35) can also be modified to take into account the fact that two masses are involved, the main body and the foot pad itself. Also, the effect of the crushing honeycomb struts can be considered as it influences ω. In the numerical computations resulting in the curves of Figure 4-81, these influences are considered by using approximating assumptions. As can be seen, reasonable results have been obtained.

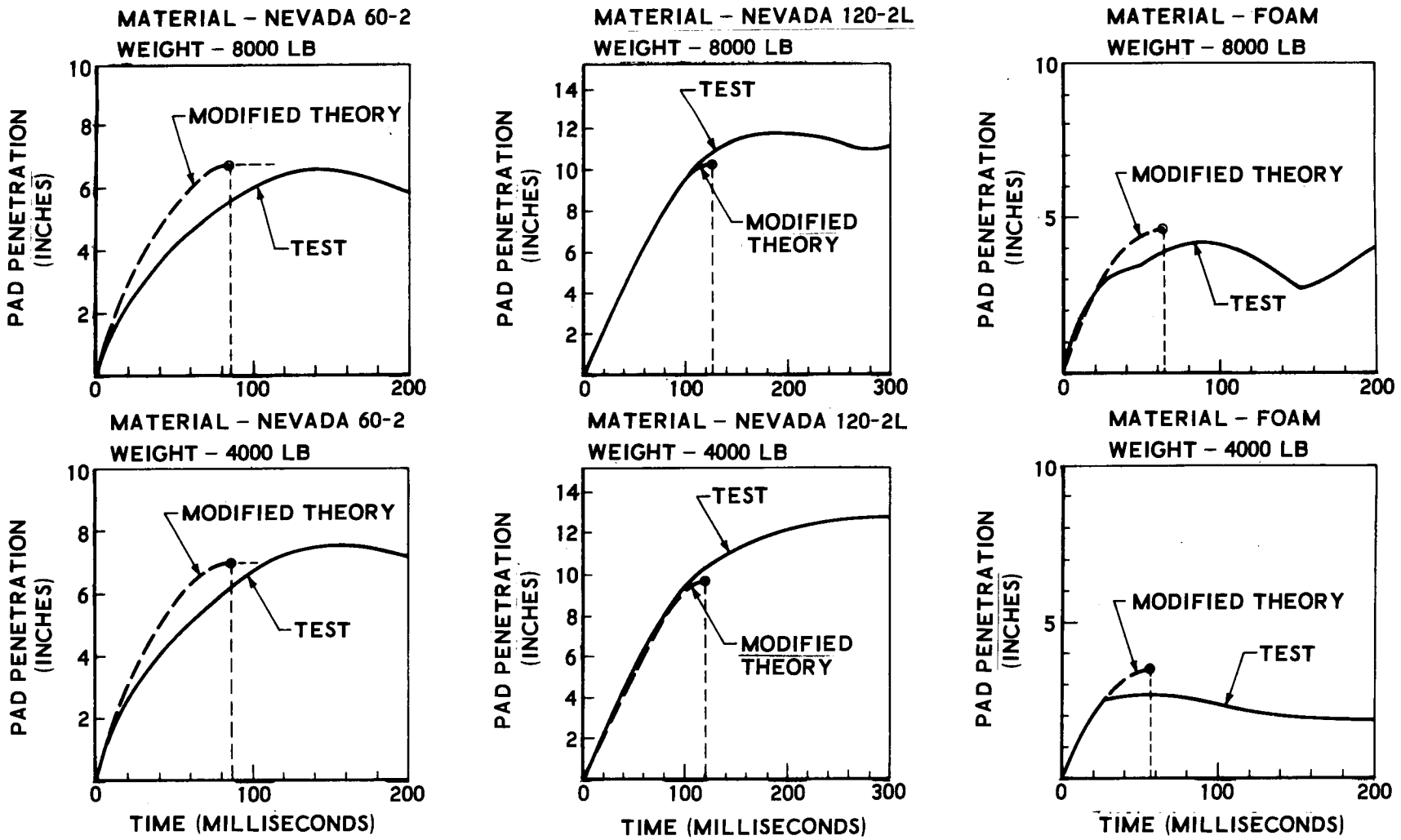

FIGURE 4-81. LEM PAD PENETRATION PREDICTIONS BY MODIFIED MODEL

F03692 U

4.5.4 LEM IMPACT

a. Analytical and Experimental Results for the LEM Mechanical Model. Table 4.11 presents a comparison of analytical and experimental LEM impact results.* The analytical effort concentrated on the 4000 pound load case. Both analytical and experimental results indicated that crushing of the higher strength honeycomb did not occur in this case. This simplifies the analytical considerations somewhat. Nevertheless, the results for two 8000 pound load cases are presented. In the 16,000 pound load LEM tests, complete crushing and bottoming out of the honeycomb material occurred. This situation was not investigated analytically during this study.

The analytical upper bound LEM penetration results which correspond to neglecting the target material inertial resistance (that is, setting $K_2 = 0$) in the analysis are presented for several values of the target material "virtual" or "stagnation" mass factor, K_1. Calculations have been made for $K_2 = 0$ with $K_1 = 0$ and $K_1 = 2$ and in one case $K_1 = 5$. The nominal values $K_1 = 2$ and $K_2 = 7$ were indicated by penetrometer impact research studies.** In those cases in which the analytical upper bound penetration depths calculated for $K_2 = 0$ and $K_1 = 2$ were significantly less than the experimental results, detailed calculations were not carried out with the target material inertial resistance effect included. Only the upper bound results are indicated in such cases. This situation resulted for the loose Nevada 120-2 and Nevada 60-2 sand materials. For the dense Nevada 120-1 and for the foam materials, penetration calculations were made including the target material inertial resistance for the parameter combination, $K_1 = 2$ and $K_2 = 7$. At the LEM impact speed of 10 fps the inertial effect in the foam material was negligible, but in the dense sand the target inertial resistance effect reduced the penetration by about 30 percent relative to the upper bound calculation ($K_2 = 0$, $K_1 = 2$).

* A value X = 3.6 was used in the analysis for the LEM pad geometrical parameter. The LEM test configuration has been discussed in a previous section. The LEM impact velocity was taken as 10 fps.

**See Paragraph 4.5.2.

TABLE 4.11

COMPARISON ANALYTICAL AND EXPERIMENTAL LEM PAD IMPACTS

Load (lb)	Target	K_2	Start Crush Theory Depth (6000 lb) (in.)	Start Crush Theory Depth (12,000 lb) (in.)	K_1	Pen. Depth (Theory) (in.)	Peak Pen (Exp) (in.)	Final Pen (Exp) (Meas) (in.)	Final Pen (Exp) (Data) (in.)	Honeycomb Crush (6000 lb) (Th) (ft)	Honeycomb Crush (6000 lb) (Exp) (ft)	Honeycomb Crush (12,000 lb) (Th) (ft)	Honeycomb Crush (12,000 lb) (Exp) (ft)
4000	N60-2	7	1.5	-	2	<4.6	7.5(7.9)	7.4	7.9	>0.7	0.6	-	-
		0	2.2	-	0	3.6							
					2	4.6							
					5	6.1							
	N120-2	7	2.0	-	2	<7.0	12.8	12.1	12.8	>0.6	0.15	-	-
		0	3.5	-	0	5.2							
					2	7.0							
	N120-1	7	1.5	-	2	2.5	3.1	2.5	2.3	0.9	1.0	-	-
		0	2.0	-	0	3.0							
					2	3.6							
	FOAM	7	1.9	-	2	2.9	2.7	2.0	1.9	0.9	0.8	-	-
			1.9		0	2.9							
					2	2.9							
8000	FOAM	7	1.9	2.7	2	2.9	4.2(4.9)	3.3	3.4	1.3	1.3	0.3	0.3
		0	1.9	2.7	2	2.9							
	N60-2	0	2.2	4.0	2	4.6	(6.6?)	8.4	(6.3?)	1.3	1.3	>0.2	0

For the 8000 pound load cases treated (foam and Nevada 60-2 materials), the analytical model indicated that the pad was brought to rest during crushing of the low strength honeycomb. The depth of penetration at this point was such that the force set up in the strut during high strength honeycomb crushing was insufficient to produce further pad penetration; that is, the available soil static resistance force at this depth exceeded the crushing load of the higher strength honeycomb material. The experimentally determined maximum penetration depths for the 8000 pound load cases exceeded the analytical predictions by 50 percent or more.

The experimental final penetration is shown as well as the peak penetration (values in parentheses indicate a second peak in excess of the first). Two values of final penetration are presented -- one is the yardstick measurement at the time of the test and the other is the result of data reduction (payload displacement minus honeycomb crush). The question marks indicate an apparent inconsistency between the yardstick measurement and the reduced data for the 8000 pound load case in Nevada 60-2 sand target material.

A comparison is also presented between analytical prediction and experimental results for the amount of honeycomb crushed. For the 4000 pound load case in foam and dense Nevada 120-1 target materials, the experimental and analytical honeycomb crush results are within about 10 percent of each other. The corresponding analytical LEM pad penetration depths are within about 10 and 20 percent respectively of the test results. For the loose Nevada 120-2 and 60-2 sand target materials, the experimental penetration depths are significantly greater than the analytical and, as would be expected under such circumstances, the analytically predicted lengths of honeycomb strut crushing exceed the experimentally determined values (that is, the lower analytically predicted depths of penetration imply less energy absorbed in soil deformation and more in honeycomb crushing). For the 8000 pound load cases, the experimentally determined peak penetration depths are significantly in excess of the analytical results, as indicated previously, but for the foam material the experimental and analytical results for the amount of honeycomb material crushed are in agreement.

b. Conclusions and Recommendations. For the 4000 pound load case, the analytical and experimental results are in reasonable agreement for the dense Nevada 120-1 sand and for the foam target materials.

For the loose Nevada 120-2 and Nevada 60-2 sand target materials, experimental penetration depths are significantly in excess of the analytical predictions. Even the analytical upper bound penetration depths obtained by neglecting the target material inertial resistance effects are significantly less than the test results for these loose materials. (It appears that in order for the penetration depth given by the upper bound solution to approach the experimental values, the target material "virtual" or "stagnation" mass factor must be increased by around 200 percent or more.)

For the 8000 pound load cases studied analytically, the experimental penetrations were considerably in excess of the analytical predictions.

The analytical model tends to predict that the target material resisting forces bring the LEM pad to rest considerably sooner than the honeycomb crushing loads can bring the much more massive payload* to rest.

The discrepancy between analytical and experimental results for the loose particulate materials could be explained by a degradation in material strength characteristics under dynamic conditions. A possible source of such strength degradation might be a vibration-like, "jack-hammering" action occasioned by the non-uniform honeycomb crushing action.**

Additional LEM testing appears desirable in order to study this apparent strength degradation effect and to develop empirical modifications to the analytical model which will result in a useful prediction tool. A possible approach might be to conduct static (low speed) tests under honeycomb crushing conditions to determine whether under such conditions there is any degradation in strength characteristics of loose granular target materials.

It also appears desirable to conduct additional penetrometer impact research with emphasis on the low speed, shallow penetration regime in order to study more thoroughly, under such conditions, the empirical coefficients K_1 and K_2.

---

* The LEM pad mass is less than 5 percent of the payload mass.

**Load cell traces indicate a random vibration-like, low-amplitude, relatively rapid load oscillation during honey-comb crushing.

SECTION 5

OMNIDIRECTIONAL PENETROMETER DESIGN AND DEVELOPMENT

The penetrometer subsystem consists of the following functional subassemblies:

(1) Omnidirectional accelerometer.

(2) Signal Electronics.

(3) Transmitter.

(4) Antenna.

(5) Battery.

(6) Timer-Regulator.

(7) Structure.

(8) Impact Limiter.

Considerable design, development, and testing at the subassembly level preceded the eventual successful construction and testing of two complete penetrometer subsystems, Prototype Nos. 2 and 3. Each of the subassemblies is described in detail in the succeeding paragraphs. The overall penetrometer design and functional description were presented in Section 3.

5.1 ACCELEROMETER

The decision was made early in the program to use the Endevco Model 204-M1 omnidirectional accelerometer. The accelerometer is required to produce unipolar signals proportional to the applied shock regardless of the direction of impact. It is also required to have an isotropic sensitivity within ± 5 percent over a range of from 50 to 10,000 g. The Endevco design is the only one presently available which meets these requirements.

The Model 2404-M1 accelerometer is shown in Figure 5-1. The sensing elements are two mated, hollow, hemispherical piezoelectric crystals filled with a fluid. The output of the crystal sensors are summed to provide a positive voltage (relative to the accelerometer case) proportional to the acceleration, regardless of the direction of the applied shock.

Originally, Endevco had promised delivery 10 weeks after receipt of order; however, this turned out to be an overly optimistic schedule. Finally, in August 1965, two Endevco 2404-M1 prototype accelerometers were delivered. These were conditionally accepted, since they did not meet the isotropic sensitivity specifications. At this point, Endevco indicated that a major redesign had been executed to improve these deficiencies. The redesign consisted of mounting the crystals in the base instead of in the cover to eliminate output sensitivity caused by connector movement.

A large number of the new design accelerometers were built with varying results. It was obvious from the wide scatter of results that some problems still existed. Therefore, Endevco initiated an experimental program designed to study the characteristics of size versus output of omnidirectional characteristics. The program originally planned involved three sizes of accelerometers to be designated 2404-M1 (existing size) 2404-M2, and 2404-M3. Also, various methods of mounting, namely keeper mounting, ring mounting, and encapsulation, were to be investigated for pressed crystal and machine crystal configuration.

5.1.1 2404-M1 DEVELOPMENT

The 2404-M1 development continued with an Aeronutronic engineer on-site at Endevco, Pasadena. His responsibility was to work with existing hardware to determine what caused the wide variation of results. The problem was divided as described in the following paragraphs.

a. Base Design. Experiments indicated that the slotted base provided a nonuniform support for the crystal, thus resulting in non-omnidirectional error signals. The new design eliminated the slots in the base.

b. Crystal Support - Keeper Design. Originally, the keeper was designed with a slot on one side. The slot resulted in non-uniform support similar to the base. The new design eliminated the slot. The slot was functional, however, in that it provided a space for the internal wiring. The new keeper design provides a hole for this purpose.

c. Crystal - Electrode Attachment. Experiments with conductive paint were not successful. The standard method of solder is now used and later data indicate that no adverse effects result because of a small amount of solder at the junction.

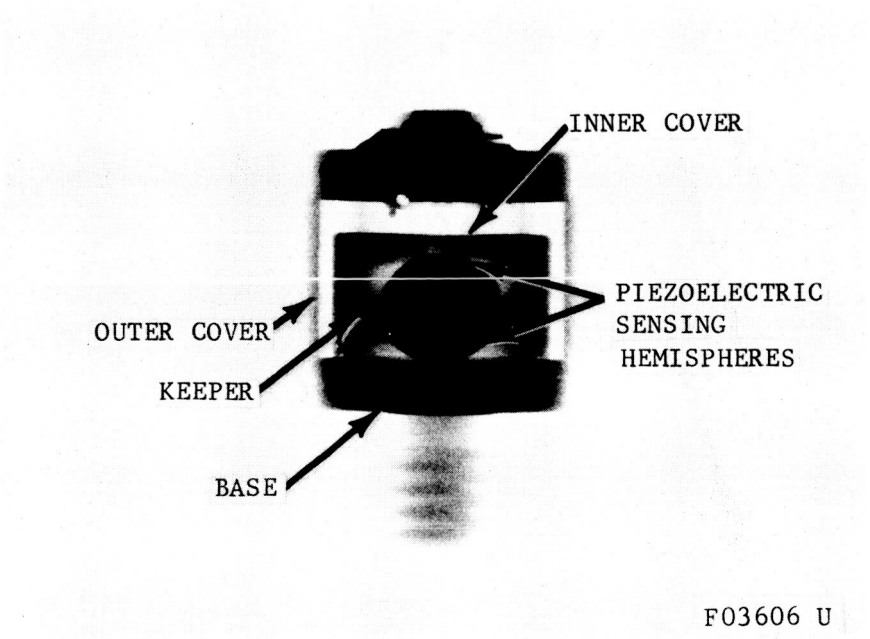

a. X-RAY VIEW SHOWING SPHERICAL SENSOR AND SUPPORTS

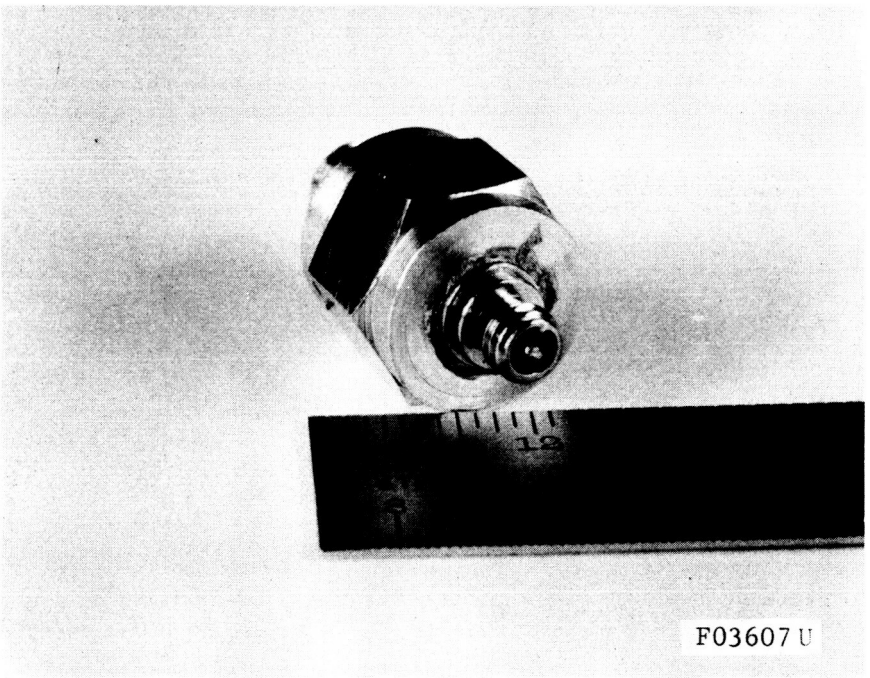

b. VIEW OF EXTERNAL MECHANICAL CONFIGURATION

FIGURE 5-1. PENETROMETER PROTOTYPE NUMBER 3
OMNI-DIRECTIONAL ACCELEROMETER

d. Crystal Selection. Early attempts to determine self-loading sensitivity as a criteria for matching the crystal hemispheres was unsuccessful. Recent techniques involve capacitance and size match in addition to the self-loading characteristics.

e. Cover Effect. Studies were conducted to determine if the cover contributed to the omnidirectional error. No design changes of the cover were made; however, attachment techniques, such as weld, solder or epoxy joints, were investigated.

f. Inner Cap. During the development program, it was determined that the addition of an inner cap improved the support of the sensing crystals.

In the span of 4 months, during which the Aeronutronic engineer was on-site at Endevco, many experiments were conducted from a component level up to the completed accelerometer. The results of these efforts produced accelerometer SN 50, shown in Figure 5-1. Sensitivity was 1.04 mv/g, omnidirectional error +6 percent at 1000 g and $\pm$7 percent at 6000 g shock levels. Internal resistance, capacitance, and linearity were within the required tolerances. The accelerometer was installed in the Penetrometer Prototype No. 3 and performed satisfactorily.

5.1.2 2404-M2, 2404-M3 DEVELOPMENT

These experiments have been continuing as a parallel effort along with the 2404-M1. The results have indicated, in general, that larger size accelerometers are easier to build and can meet the isotropic requirements. However, as the size increases, the fragility level decreases, and this was found to be unacceptable for the Penetrometer application. Further experiments are continuing with designs that should solve the fragility problem.

5.2 SIGNAL ELECTRONICS

5.2.1 FUNCTIONAL REQUIREMENTS

The function of the penetrometer signal electronics circuits is to provide required processing of the accelerometer output signal to a form suitable for modulating an RF transmitter. In the penetrometer, this function is three-fold:

(1) The signal electronics circuit must provide a high input impedance for the accelerometer to prevent offset errors associated with leakage and charging the transducer capacitance and to maintain a long-time constant to preserve low frequency response.

(2) The dynamic range of the acceleration data must be compressed in a stable circuit to prevent excessive communication link bandwidth requirements and preserve accuracy of low g-level signals.

(3) The data must be chopped to minimize the effect of rf carrier frequency shift on data accuracy.

5.2.2 SIGNAL ELECTRONICS PREAMPLIFIER INPUT STAGE

The Endevco piezoelectric omnidirectional accelerometer can be represented electrically as a charge source, a capacitance, and a large resistance all in parallel across the terminals of the device. Typical values are: 0.3 pico coulombs/g, 400 picofarads, and a resistance greater than 10^{10} ohms resulting in accelerometer time constant of 10 seconds. Since the minimum desired penetrometer time constant is 5 seconds, the accelerometer preamplifier must have a high input resistance on the order of 10^{11} ohms. Various amplifiers with high input impedance were thoroughly analyzed in the State-of-the-Art Review.[1] This study resulted in the selection of an extremely low leakage, low capacity, metal-oxide-semiconductor, field-effect transistor (MOS-FET) as a differential input stage. Conventional "charge-amplifier" techniques, commonly associated with accelerometer instrumentation, were discarded due to long settling times and instability requiring "re-zeroing."

The MOS-FET was selected primarily for low leakage and low gate-to-drain capacitance in order to prevent large turn-on errors associated with charging the transducer capacitance. The MOS-FET equivalent circuit is shown in Figure 5-2.

Turn-on transient errors for both MOS-FET's and junction FET's are covered in pages 70 through 76 of the State-of-the-Art Review.[1] An equivalent circuit is shown in Figure 5-3 for turn-on transient analysis. From this analysis it can be seen that both the low gate-to-drain capacitance and low leakage inherent in the MOS-FET reduce the turn-on error significantly as summarized in the following paragraphs.

a. MOS-FET Turn-on Transient

$$Eg_{t=o} = \frac{V R_{acc}}{R_{gd}} + \frac{V C_{gd}}{C_{acc}} \left(1 - \frac{\tau_1}{\tau_2}\right)$$

$$= \frac{V R_{acc}}{R_{gd}} + \frac{V C_{gd}}{C_{acc}} \quad \text{since } \frac{1}{2} \frac{\tau_1}{\tau_2} << 1 \qquad (1)$$

[1] State-of-The-Art Review, Aeronutronic Publication U-3132, June 1965.

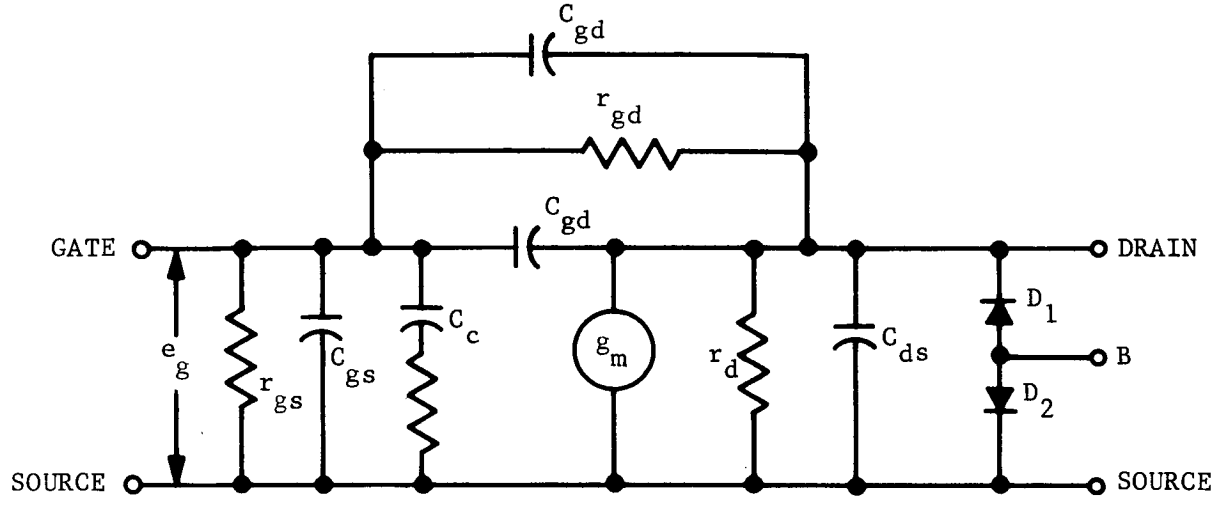

r_{gs} AND r_{gd}	REPRESENT LEAKAGE PATHS. r_{gs} IN PARALLEL WITH r_{gd} = 10^{15} OHMS TYPICAL LEAKAGE AT 85°C = 10^{-13} AMPS
C_c AND r_c	LUMPED APPROXIMATE AT DISTRIBUTED NETWORK FORMED BETWEEN ACTIVE CHANNEL RESISTANCE AND METAL GATE. FOR 2N98, C_c = 4 OF AND r_c = 100 OHM
g_m	TRANSCONDUCTANCE
r_d	OUTPUT RESISTANCE
r'_d	IN A FULL GATE MOS, r'_d APPROACHES ZERO. IN A PARTIAL OR OFFSET GATE MOS, r'_d IS A LOSSY ELEMENT IN SERIES WITH THE LOAD
C_{gd}, C_{gs}, C_{ds}	CASE AND INTER-LEAD CAPACITANCE
C_{gs}	CONSTANT FOR FULL GATE DEVICE. REDUCED IN PARTIAL DEVICE
D_1, D_2	JUNCTIONS OF THE n^+ DRAIN AND SOURCE TO SLIGHTLY P-TYPE SILICON SUBSTRATE

F03608 U

FIGURE 5-2. MOS-FET EQUIVALENT CIRCUIT

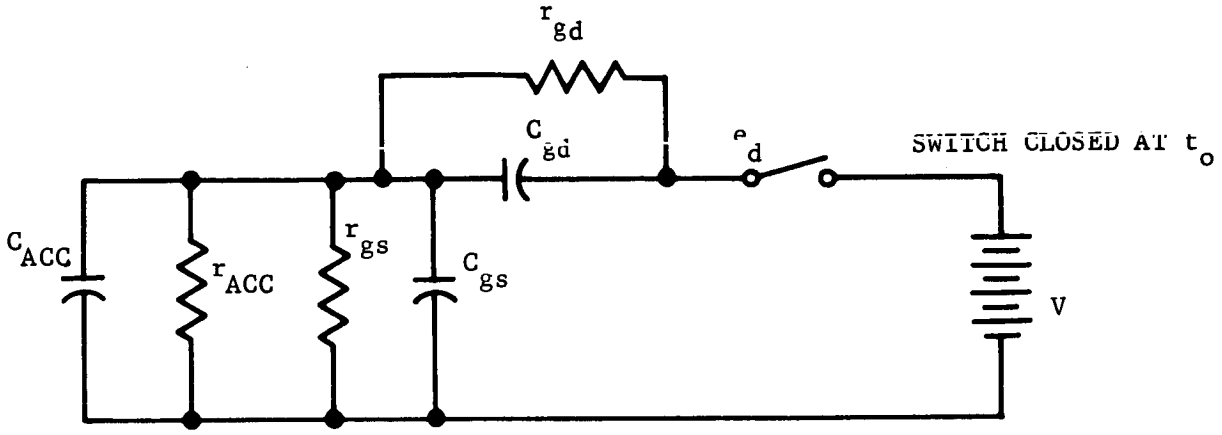

r_{ACC}	ACCELEROMETER TERMINAL SHORT RESISTANCE
C_{ACC}	ACCELEROMETER INTERNAL CAPACITANCE
r_{gs} & r_{gd}	LEAKAGE PATHS IN THE MOS-FET
C_{gs} & C_{gd}	CASE AND INTERELECTRODE CAPACITANCE IN THE MOS-FET

F03609 U

FIGURE 5-3. MOS-FET EQUIVALENT CIRCUIT FOR TURN-ON TRANSIENT ANALYSIS

which for a 3N99 MOS-FET with a 20-volt supply:

C_{gd} = 0.3 pf

R_{gd} = 2×10^{16} ohms

and:

R_{acc} = 2×10^{10} ohms

C_{acc} = 400×10^{-12} farad

= 15 millivolts or 20 g.

Following a given time, the turn-on transient settles to a dc value (20 microvolts) determined by the ratio of accelerometer internal resistance R_{acc} to gate-drain resistance (R_{dg}) and the supply voltage (V):

$$Eg_{t=\infty} = V \frac{R_{acc}}{R_{gd}} = \frac{20 \times 2 \times 10^{10}}{2 \times 10^{16}} = 20 \times 10^{-6} = 20\ \mu \text{ volts (0.03 g)} \quad (2)$$

b. Junction FET Turn-On Transient. A simplified circuit for evaluating junction FET turn-on transients is shown in Figure 5-4.

$$Eg = \frac{V\ C_{gd}}{C_{acc}} = 20 \times \frac{1.5 \times 10^{-12}}{400 \times 10^{-16}} = 75 \text{ mv (100 g)} \quad (3)$$

In addition, the gate to-drain leakage current I_c provides a constantly increasing error

$$eg = I_C R_{acc} \left(1 - e^{\frac{-t}{\tau_1}}\right) \quad (4)$$

where

τ_1 = R_{acc} C_{acc} (accelerometer parameters)

E_g = FET gate voltage

V = 20 volts

$$I_L = \frac{Eg}{R_{acc}} + C_{acc} \frac{de_g}{dt} \quad (5)$$

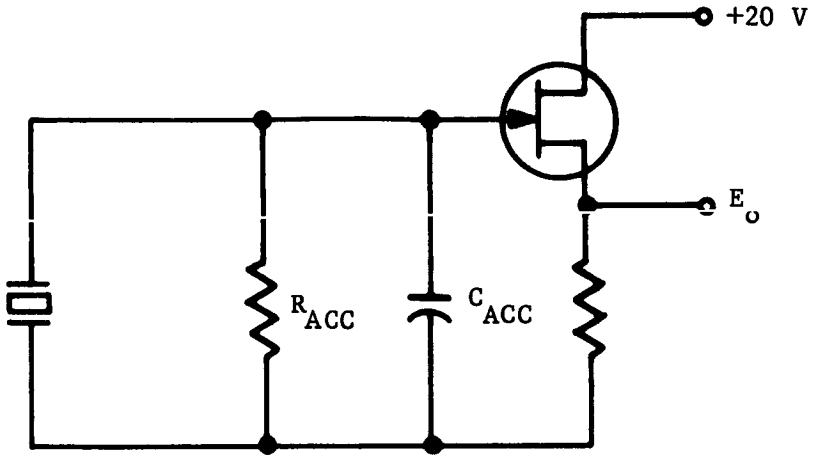

TYPICAL FET CIRCUIT

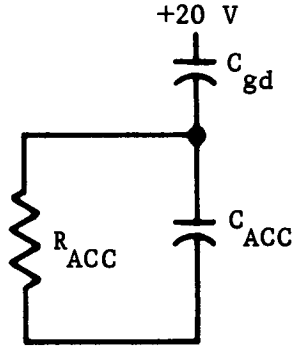

EQUIVALENT FET CIRCUIT AT TURN-ON

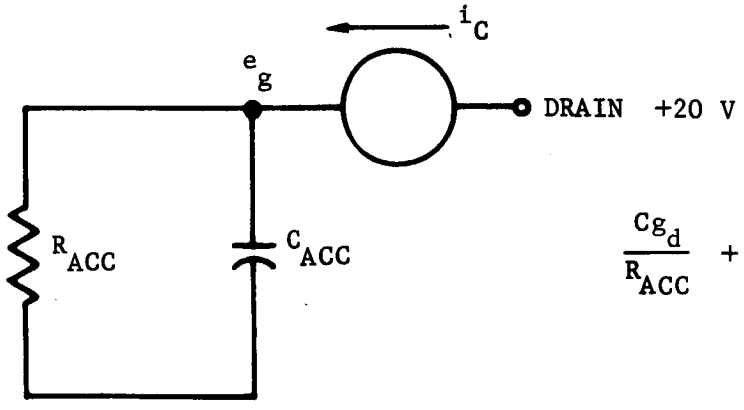

$$\frac{Cg_d}{R_{ACC}} + C_{ACC}\frac{deg}{dt} = i_C$$

F03610 U

FIGURE 5-4. FET EQUIVALENT CIRCUIT FOR TURN-ON TRANSIENT ANALYSIS

For a typical junction, FET leakage current of 10^{-10} amps, operating with a 20-volt supply, the gate voltage increases toward 2.0 volts with an 8-second time constant. The total error at any given time following turn-on is the sum of the transient error and leakage error. At turn-on, a transient of 75 millivolts exists, plus a constant increase given by

$$\frac{dE_g}{dt} = \frac{I_C}{C_{acc}} = 250 \text{ millivolts/sec} = 333 \text{ g/sec} \qquad (6)$$

Since the initial preamplifier design and MOS-FET selection, the input circuit has been modified by inclusion of 2000 megohm shunt resistor and a 3000 pf shunt capacitor. This was found necessary to prevent accelerometer thermal gradient induced dc offset voltage from displacing the quiescent point of the preamplifier beyond linear signal handling limits. Unfortunately, additional capacitance does not allow replacement of the MOS-FET by a conventional FET as the initial turn-on error is dependent only upon the FET leakage current and the g-error is unaffected by input capacitance.

5.2.3 MOS-FET RADIATION EFFECTS

Some hesitancy has been experienced in the industry to accept MOS-FET's on the basis of instability of the oxide layer between gate and drain. Devices fabricated by some manufacturers have definitely exhibited deterioration of this oxide layer and an indication of this is evident in the low gate-to-drain punch through ratings on some manufacturers' data sheets. However, the GME devices used in the penetrometer have the highest voltage ratings of this type device which reflects to some extent the stability of their oxide layer. Appendix J reviews the mechanism of degradation in MOS-FET devices. Recent work by Hughes[2] of NRL seems to indicate that N-channel devices in a differential amplifier configuration provide adequate immunity to 10^6 rads of gamma radiation. However, since the extent of radiation damage is determined by bias and circuit configuration, the actual GME MOS-FET's used in the penetrometer should be tested in the actual circuit configuration to reliably evaluate radiation effects in a penetrometer application.

5.2.4 METHODS OF DATA COMPRESSION

Because of the large dynamic range of accelerometer signals encountered in the lunar penetrometer, some method of signal compression must be utilized to preserve accuracy of low signal levels (50 g region) and minimize rf

---

[2]Hughes, H. L., and Girons, R. A., "Space Radiation versus MOS Devices and Circuits," presented at the 12th East Coast Conference on Aerospace and Navigational Electronics, 27-29 Oct, 1965, in Baltimore, Maryland.

link bandwidths. A number of methods have been investigated and reported in the State-of the Art Review (Reference 1, pages 88 and 89). These include:

(1) Compression by frequency shaping.

(2) Two-step linear compression.

(3) Switchable gain.

a. Amplitude Compression by Frequency Shaping (Integration). A comprehensive analysis of the use of a low-pass RC filter to provide frequency shaping is given in Reference 3. This method of amplitude compression utilized a priori information of anticipated accelerometer output signals. Fast rise times are associated with short pulses with relatively little frequency content.

This method of signal compression has the disadvantage of loss of data accuracy by system noise generated in the stages following the integrator. This includes the entire rf link and receiving system data processing circuits. Also, the noise output of an FM discriminator (typical penetrometer modulation method) contains a parabolic portion predominant at high signal-to-noise (SNR). Since the accelerometer signal has the opposite frequency characteristic, it is unavoidable that the SNR at the discriminator output will be poorer than that at the input.

b. Two-Step Linear Compression. Most of the methods of compression using nonlinear circuit elements (forward biased semiconductor junctions) share a common problem associated with a forward biased diode temperature characteristic and require elaborate temperature compensation. However, Zener diodes in the 6-volt range possess a nearly zero temperature coefficient, especially if operating current can be selected. Tests at Aeronutronic have shown that the temperature coefficient of randomly selected 7.5 volt Zeners was negligible in the region of the knee with only an 0.048 percent per degree C change above the knee. This insensitivity to temperature variations was the primary factor that led to the choice of this compression method for the prototype penetrometer. A Zener circuit, as shown in Figure 5-5, provides 14.5 db compression over a signal range of 1000 to 10,000 g, as shown in Figure 5-6. Figure 5-7 shows the relatively small temperature sensitivity of the compression characteristic.

c. Switchable Gain. Two-step linear compression utilizing the Zener diode has the disadvantage of providing poor resolution for high level data in the range beyond the knee of the transfer function characteristic. The

---

[3] Pitts, F. L , Amplitude Compression of Penetrometer Data, Langley Research Center, SIDS Technical Files, January 1965.

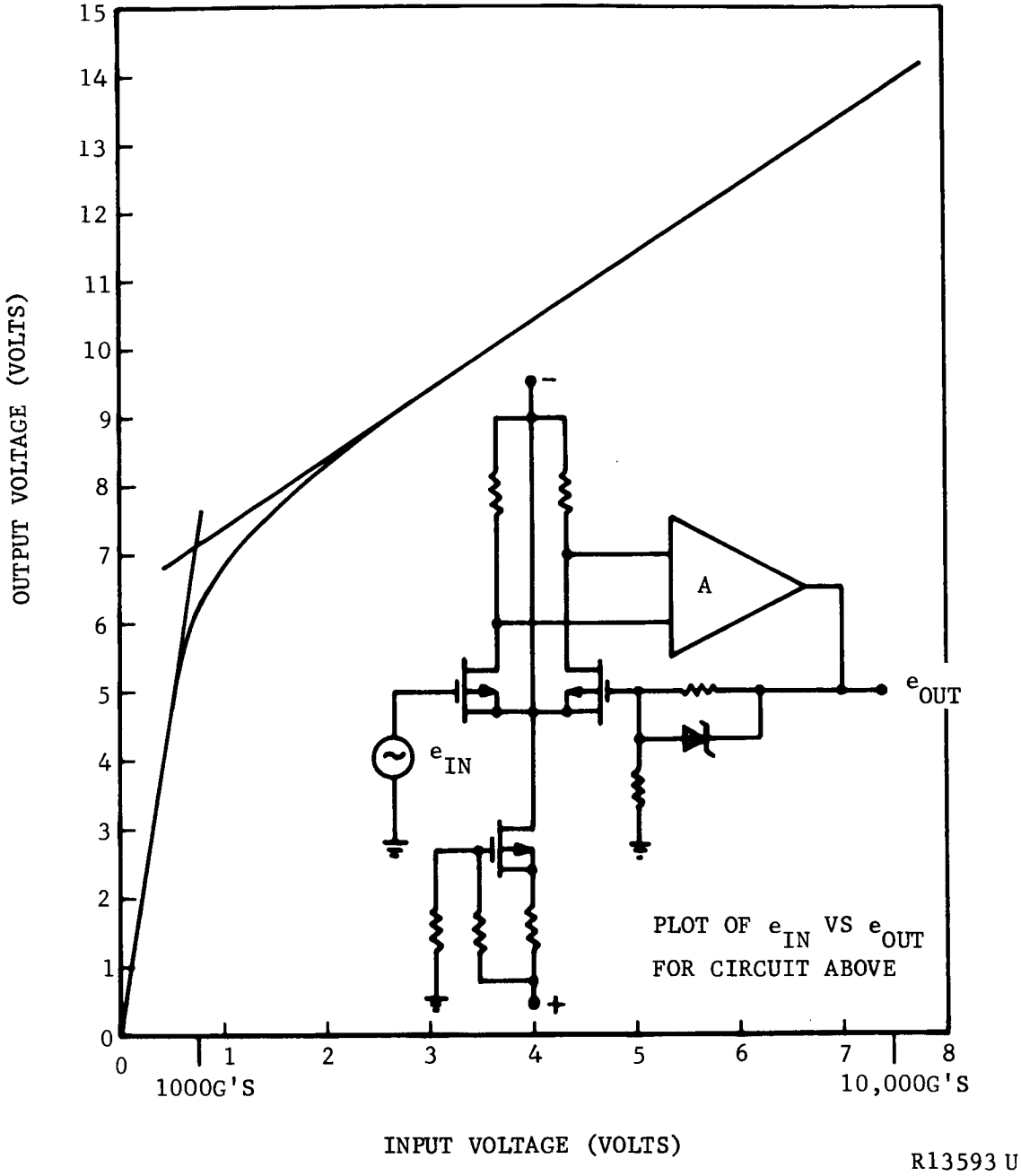

FIGURE 5-5. BASIC AMPLIFIER COMPRESSOR CHARACTERISTICS

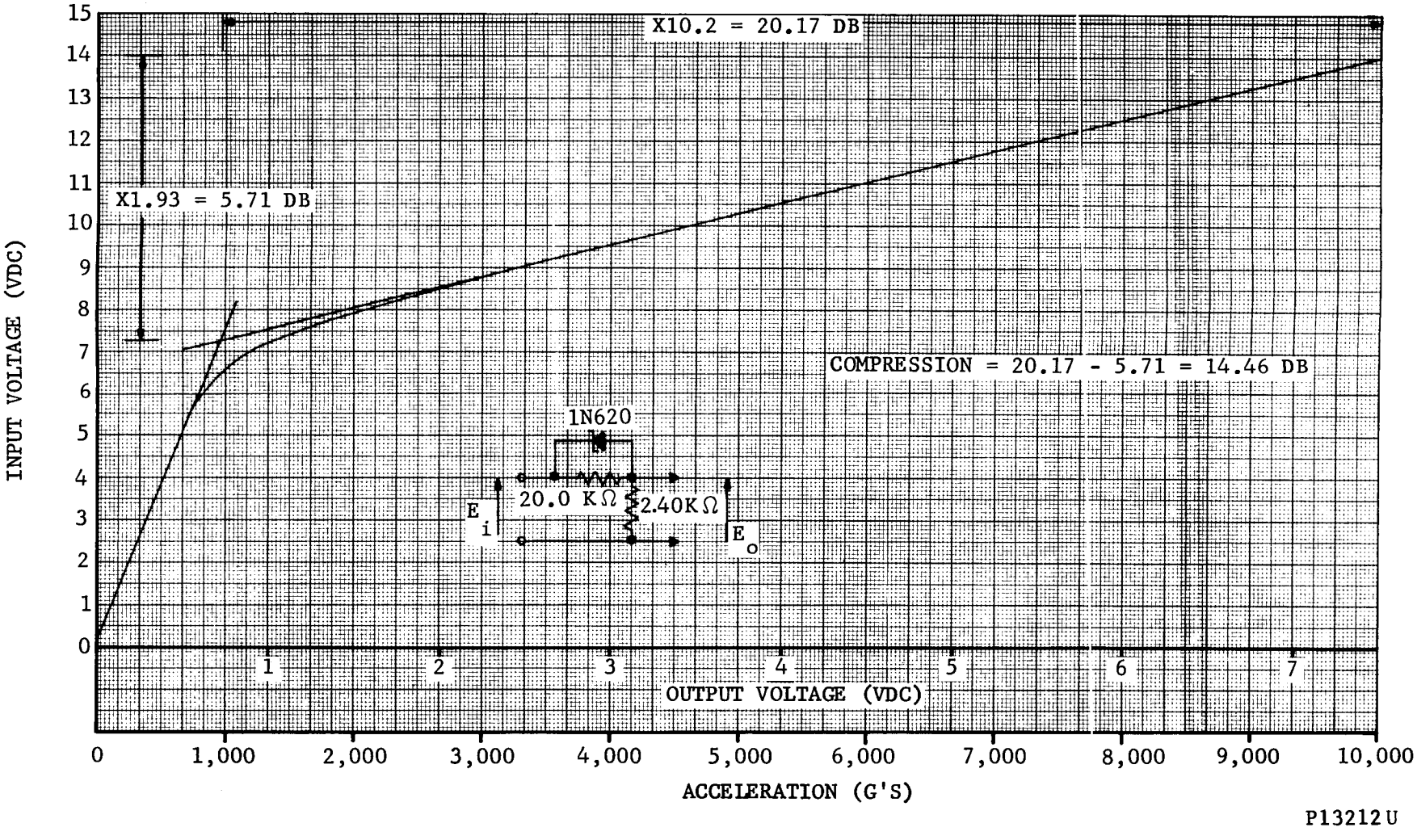

FIGURE 5-6. EVALUATION OF ZENER DIODE COMPRESSOR CHARACTERISTICS

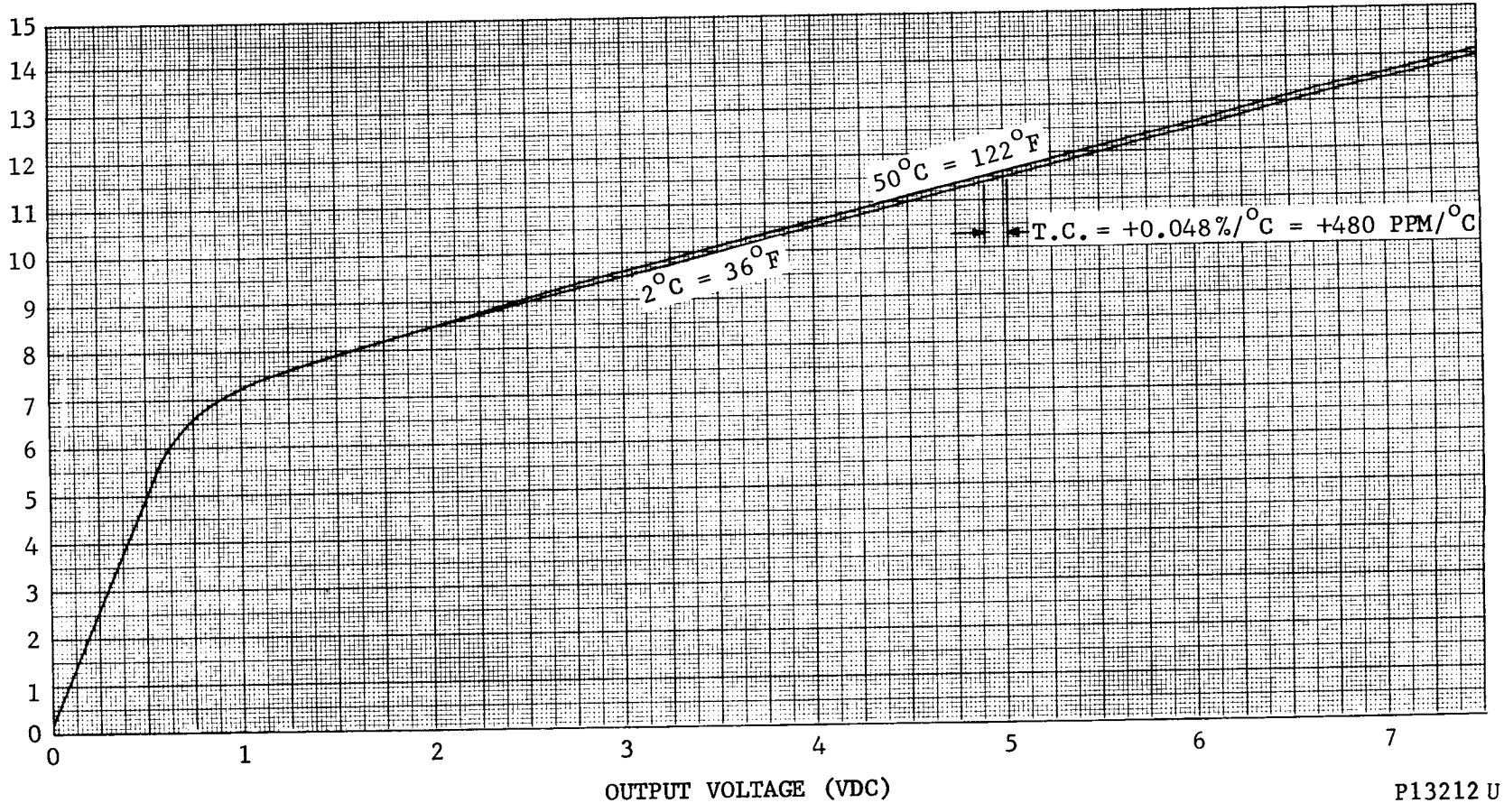

FIGURE 5-7. EVALUATION OF ZENER COMPRESSOR DIODE TEMPERATURE COEFFICIENT

circuit shown in Figure 5-8 provides much better resolution over the entire range of anticipated accelerometer signal levels by dividing the 0 to 10,000 g range into three ranges, 0 to 100, 0 to 1000, and 0 to 10,000 g's, with output scale factors of 0.150 volt/g, 0.0150 volt/g, and 0.00150 volt/g, respectively, based on 15-volt full-scale output, as shown in Figure 5-9. This provides better resolution than the presently used dual-slope compression circuit with 0.02 volt/g from 0 to 500 g, and 0.001 volt/g from 500 to 10,000 g. This circuit consists of three stable gain amplifiers with provisions to automatically select gain as a function of input level. For example, for signal levels up to 100 g, the accelerometer signal would be amplified by the X2, X10, and X10 stages giving a full-scale reading of 15 volts to a 100 g (0.075 volt input) signal. Should the signal exceed 100 g, the switch circuit in the output of the third amplifier (X10) would open, also removing a 1K load termination from the first X10 amplifier. The output would then be 1.5 volts and increase at 0.0150 volt/g. For pulses exceeding 1000 g, the first X10 amplifier output is disconnected, producing a 0.150 volt signal with a 0.0150 volt/g scale factor.

Disadvantages of this approach to dynamic range reduction are:

(1) Possibility of generation of switching transients.

(2) Additional data must be transmitted to define overall amplifier gain.

(3) Data are received in nonconventional form requiring processing to reconstruct actual accelerometer signal. (Also true of Zener diode compression techniques to a lesser degree.)

(4) Data interpretation may be difficult under conditions which produce an accelerometer signal which "rings" in the region of amplifier scale factor change.

5.2 5 DIFFERENTIAL INPUT STAGE

Two basic circuit configurations utilizing a MOS-FET can be used in the penetrometer input stage. These are the ac coupled source follower and the differential amplifier configurations.

a. AC Coupled Source Follower. A representative ac source follower amplifier configuration is shown in Figure 5-10. AC coupling is used in an attempt to minimize offset errors associated with bias and device instability. The basic problem with this circuit is the difficulty associated with holding

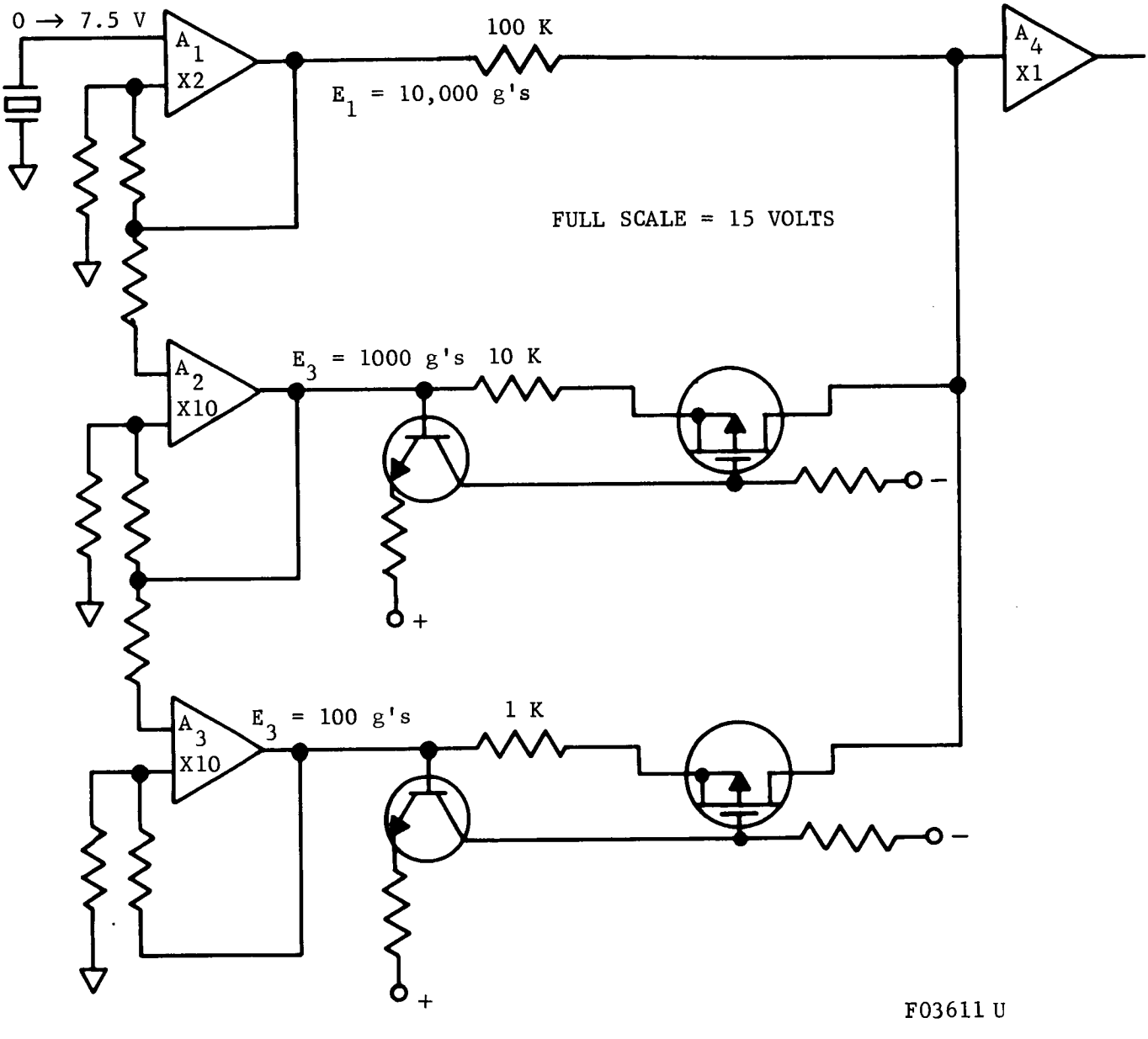

FIGURE 5-8. BASIC SWITCHABLE GAIN CIRCUIT

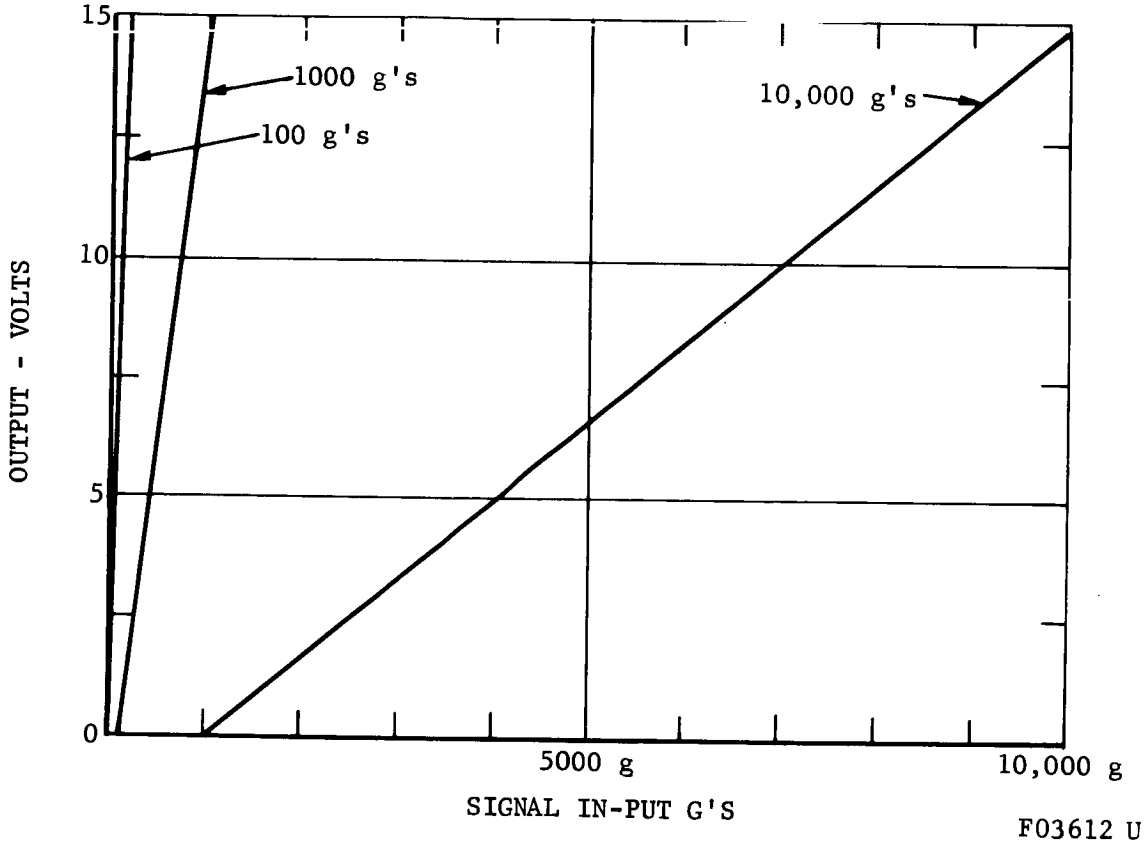

FIGURE 5-9. TRANSFER CHARACTERISTICS, RANGE SWITCHING

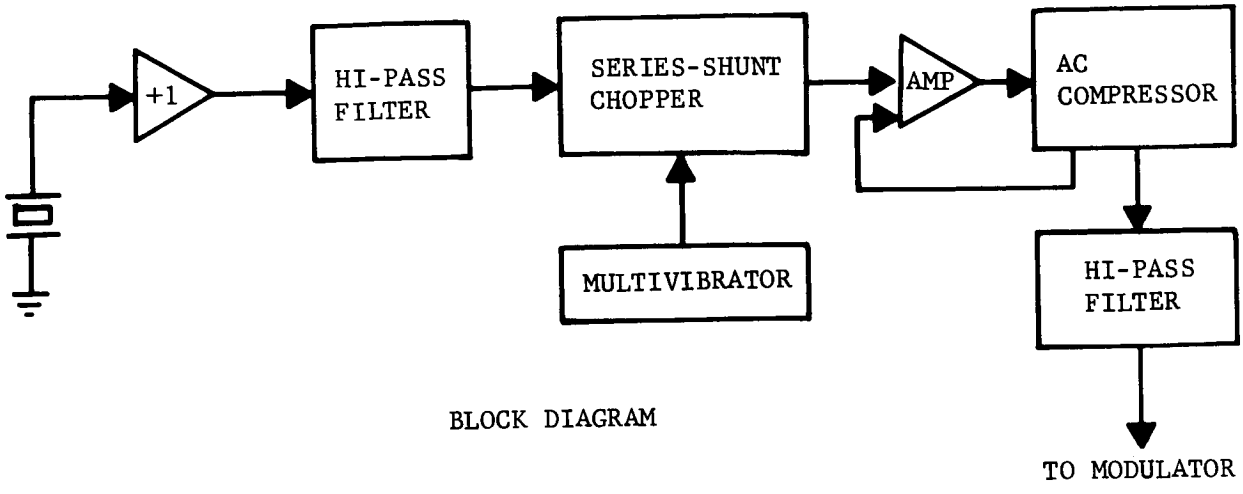

BLOCK DIAGRAM

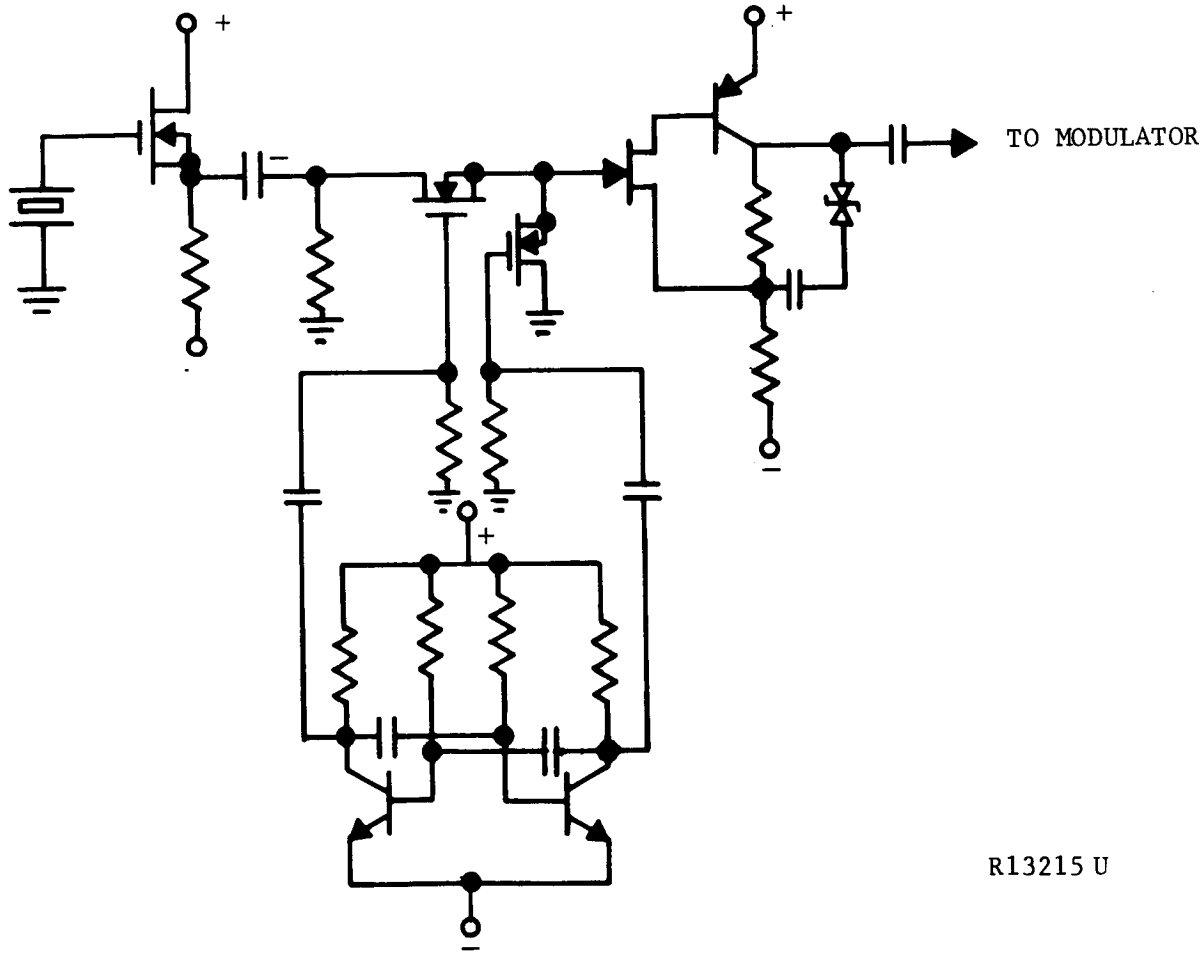

FIGURE 5-10. AC COUPLED MOS-FET SOURCE FOLLOWER SCHEMATIC DIAGRAM

a stable source voltage on the source follower. The tolerance on this voltage was estimated to be ±0.5 volt in the State-of-the-Art Review (Reference 1, page 84). Coupling capacitor valves must be large to maintain a 5- to 10-second time constant resulting in a large settling error necessitating turn-on prior to penetrometer launch on the order of several minutes. This is highly undesirable because of additional power supply capacity requirements.

b. Differential Amplifier, Direct Coupled. Figure 5-11 gives the signal electronics module schematic for the final prototype configuration. The direct coupled differential amplifier circuit configuration shown in the figure solves the time constant and offset problems associated with the ac coupled source follower circuit. With a matched pair of MOS-FETS (GME-1005) it is possible to establish the gate-source voltage of the input transistor to a level corresponding to the allowable data offset error. The GME-1005 consists of a matched pair of p-channel MOS field-effect transistors diffused into a common monolithic chip. As a result of the monolithic structure, this device has excellent thermal tracking characteristics between the two devices. The gate-source thermal tracking error over the anticipated operating range of 50°F to 90°F should not exceed 5 millivolts. A MOS-FET current source is used for the differential amplifier to ensure minimum common mode gain. The output of the MOS-FET differential amplifier drives a Fairchild μ702A integrated amplifier with an output voltage swing of from 0 to +15 volts. The output is fed back to a Zener diode "expander" to the differential input stage and back to the noninverting input of the μ702A. Selection of the values of the resistors in the feedback circuit permits control of amplifier gain and the knee of the overall compression characteristic.

5.2.6 2 KHz DATA BANDWIDTH FILTER

Initial performance specifications for the Endevco omnidirectional accelerometer included a 2 KHz frequency response. Selection of the 40 KHz chopping frequency was a compromise based upon minimum aliasing errors associated with a 2 KHz data response and maximum allowable receiver bandwidth related to a 40 KHz subcarrier. Penetrometer and receiver models were designed and fabricated using the 40 KHz chopping frequency and 2 KHz data bandwidth. However, frequency response tests on Endevco accelerometers received later indicated that the response extended beyond 5 KHz. To prevent extensive system design changes, a 2 KHz active filter was added in the signal electronics. This required additional active stages for impedance matching to properly drive the filter. Since the MOS-FET differential amplifier and μ702A operational amplifier had successfully been impact tested, an identical stage was chosen for the input stage of the signal electronics. This stage provided the high input impedance-low leakage required for accelerometer signal processing and operated at unity gain. The MOS-FET differential amplifier was retained for the compressor amplifier because of satisfactory operation during previous tests. The 2 KHz active filter is described in paragraph 5.2.9.

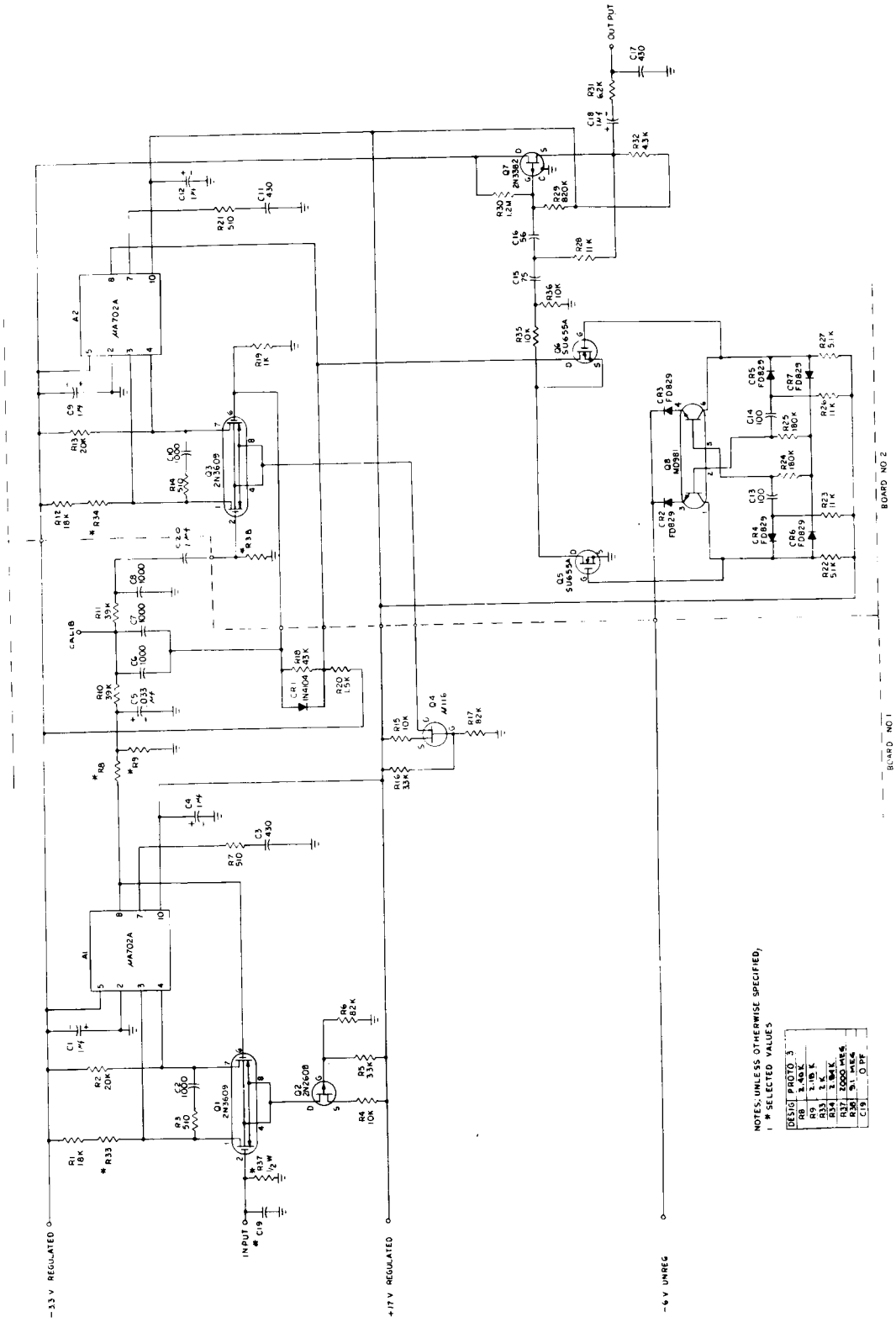

FIGURE 5-11. SIGNAL ELECTRONICS SCHEMATIC

F03805 U

5.2.7 AC COUPLING

During the development of the penetrometer, it was found that the Endevco omnidirectional accelerometer produced a dc output voltage related to the thermal gradient imposed upon the case. Since there was no convenient way of evaluating the accelerometer under actual internal penetrometer operating thermal environment, the signal electronics stages were ac coupled to prevent large, full-scale offset errors. To prevent long-time accelerometer charge buildup, which might possibly exceed the 21-volt gate-source voltage rating of the MOS-FET, a 2000 megohm resistor, R37, (see Figure 5-11) was added in parallel with the accelerometer. A 3000 pf capacitor (C19) was also added across the accelerometer to maintain a 6-second time constant. Voltage divider network R8 and R9 is adjusted to compensate for the added input signal attenuation.

5.2.8 SIGNAL ELECTRONICS CALIBRATION

Prototypes 2 and 3 penetrometers require ac calibration signals, since the calibration injection point is at the input of the 2 kc KHz active filter preceding the interstage coupling capacitor C-20 shown in the signal electronics schematic, Figure 5-11. An attempt was made in Prototype 2 to provide dc calibration by providing external access to the drain of Q_3 (Pin 1) but inadvertent shorting of this test point during calibration destroyed the MOS-FET. Also, full-scale signals could not be simulated because of the bias levels in the operational amplifier circuit.

5.2.9 SIGNAL ELECTRONICS, THEORY OF OPERATION

The accelerometer signal is applied to the gate of MOS-FET Q_1 connected as a differential amplifier. The MOS-FET provides the required high input impedance and low leakage to minimize turn-on transient errors. The differential circuit configuration permits direct coupling to following stages by minimizing the effect of operating point variations. R_3 and C_2 constitute an input frequency compensation network for the μ702A integrated amplifier and provide a 2 KHz frequency cutoff. R_7 and C_3 perform a similar function in the output and are selected for a 10 KHz cutoff. A two-stage RC response is provided in this manner which prevents oscillation in the 30 MHz region with inherent 180 degree phase shift.

The low impedance output of the μ702A is attenuated by R7 and R8 which provide scale factor adjustment. These values are also constrained to provide a 1.5 K ohm impedance for proper RC low-pass filter response in conjunction with C5.

The 2 KHz low-pass filter consists of the single section RC (R7, R8, and C5) combined with a second order active Butterworth consisting of C_6, C_7, R_{11}, and C_8. Unity gain feedback is provided from the second section of Q_3 to C_6 and C_7.

A single section RC high-pass is also incorporated and consists of C_{20} and R_{38}.

The second stage amplifiers in the signal electronics (Q_3 and associated μ702A) is identical to the first stage with the exception of the Zener diode compressor circuit.

The Zener diode located in the negative feedback path around A_2 (μ702A) Q_3 does not conduct until signal levels exceed the Zener point. During this time the overall amplifier gain is proportional to R18, R19, and R20. After the Zener conducts, the gain is reduced (feedback increased) by the ratio of the Zener impedance to R18.

The compressor amplifier also utilizes frequency compensator networks (C_{10} and R_{14} and R_{21} and C_{11}) for stability.

The output of A_2 is chopped by two MOS-FET switches driven by a 40 KHz multivibrator. MOS-FET choppers were selected because of the very low and stable offset voltage when turned on.

The 40 KHz multivibrator is of conventional design. Steering or speed-up diodes CR4 and CR5 provide more accurate timing by preventing collector current from flowing in the RC timing circuit (C14-R26 and C13-R23). Latch-up during initial turn-on is prevented by CR6 and CR7. CR_2 and CR_3 in the transistor emitter circuit prevent V_{BE} breakdown.

The amplitude modulated 40 KHz chopper output is attenuated by R_{35} and R_{36} which are selected to provide a voltage level compatible with transmitter modulator characteristics. C15, C16, R_{28} and R_{29} form a 40 db/decade active high-pass filter to minimize baseband data frequency aliasing errors. A low-pass filter section is provided by R_{31} and C_{17} in the source follower (Q_7) output.

5.3 TRANSMITTER

5.3.1 PRELIMINARY DESIGN CONCEPTS

The penetrometer system design was predicated upon performance at high shock levels. An initial estimate of carrier frequency stability (45 KHz) at 450 MHz with a 10,000 g impact proved quite representative of various transmitter configurations tested. This represents stability on the order of 0.001 percent more closely associated normally with crystal control than an L-C oscillator. However, from previous experience with impact survivable crystals (special CR-24 design) the problems associated with crystal control during impact were considered greater than those of an L-C oscillator. Later in the program special impact resistant crystals, developed by Valpey-Fisher and JPL, became available for evaluation. Preliminary tests indicated that the crystals were quite stable and perhaps could be used.

Initial oscillator frequency selection of 220 MHz was based upon the highest frequency at which realizable lumped-constant tank circuit components could be practically used. A parallel effort utilizing stripline oscillator techniques was followed. This effort was discontinued early in the program because of poor shock stability, poor form factor for penetrometer application, and difficulty of adjustment.

During development testing preceding fabrication of Prototype No. 2, the decision to lower the oscillator frequency to the 112 MHz range was made. This change was based upon the advantages inherent in the lower frequency operation, including:

(1) Use of higher capacity tank circuit which effectively swamps the effects of stray circuit and encapsulation capacity, thereby reducing thermal instability and the effects of structural displacements.

(2) Lower frequencies allow use of a slightly larger value of inductance (when capacity has also been increased as in (1) above) which is easier to trim to center frequency.

Lowering the oscillator frequency from the 220 MHz range to the 112 MHz range required the use of an additional frequency doubler stage. The addition of this stage was made possible by elimination of the original parallel (redundant) output stages and use of a single antenna feed loop.

5.3.2 TRANSMITTER PERFORMANCE REQUIREMENTS

The performance of the penetrometer transmitter is shown in Table 5.1

TABLE 5.1

ELECTRICAL PERFORMANCE REQUIREMENTS

Output Frequency, f_o	
Channel 1	432 MHz
Channel 2	435 MHz
Channel 3	438 MHz
Channel 4	441 MHz
Channel 5	444 MHz
Channel 6	447 MHz
Channel 7	450 MHz
Channel 8	453 MHz
Supply Voltage	
(a) Oscillator-Buffer	17 V $\pm$1% at 62 ma nominal
(b) Doublers	22 to 30 V at 114 ma nominal

TABLE 5.1 (Continued)

Data Modulation Deviation, $\Delta f_o(D)$	$\pm$160 KHz, max at 432 - 453 MHz
Modulation Sensitivity	$\pm$80 KHz/volt at 432 - 453 MHz
Modulation Linearity	1 percent
Impact Induced Deviation, Δf_o (i)	$\pm$80 KHz, max at 7000 g
Thermal Induced Deviation, Δf_o (t)	$\pm$66 KHz, max
RF Power Output, P_{out}	500 mw min (into 50 ohm resistive load) at 30 volts
DC to rf Efficiency, N	10 percent min
Spurious rf Power Output	30 db below carrier
Thermal Frequency Coefficient	6.6 KHz/^oF at 432 - 453 MHz
Thermal Range	$\Delta T \leq 20^o$ within the range of $+60^oF$ to $+100^oF$
Long Term Center Frequency Drift (1 year storage 0^oF to 100^oF)	$\pm$250 KHz
Output Impedance	50 ohms nominal
Modulation Input Impedance	5 K ohms resistive shunted by 300 mmf

5.3.3 PRELIMINARY TRANSMITTER DEVELOPMENT

a. Oscillator. During the preliminary design phase, two low-level 225 MHz oscillators, shown in Figures 5-12 and 5-13, were constructed, encapsulated, and impact tested to evaluate the lumped-element method of construction. The first oscillator used Rexolite coil forms and was mounted on fiberglass reinforced epoxy board prior to encapsulation. At an impact level of 5000 g, the peak deviation was approximately 5 KHz. Unfortunately, at higher impact levels, deformation of the mounting arrangement occurred, and the frequency deviation was very large. A second oscillator was constructed without coil forms or mounting board and encapsulated into a well, machined into an aluminum block, for assurance that mounting deformation was indeed responsible for the large frequency deviations previously observed. This oscillator exhibited a deviation of only 14 KHz at 12,500 g in the worst impact orientation, transverse to the coil. After impact, the encapsulated oscillator was removed from the aluminum block and cracks were observed in the epoxy.

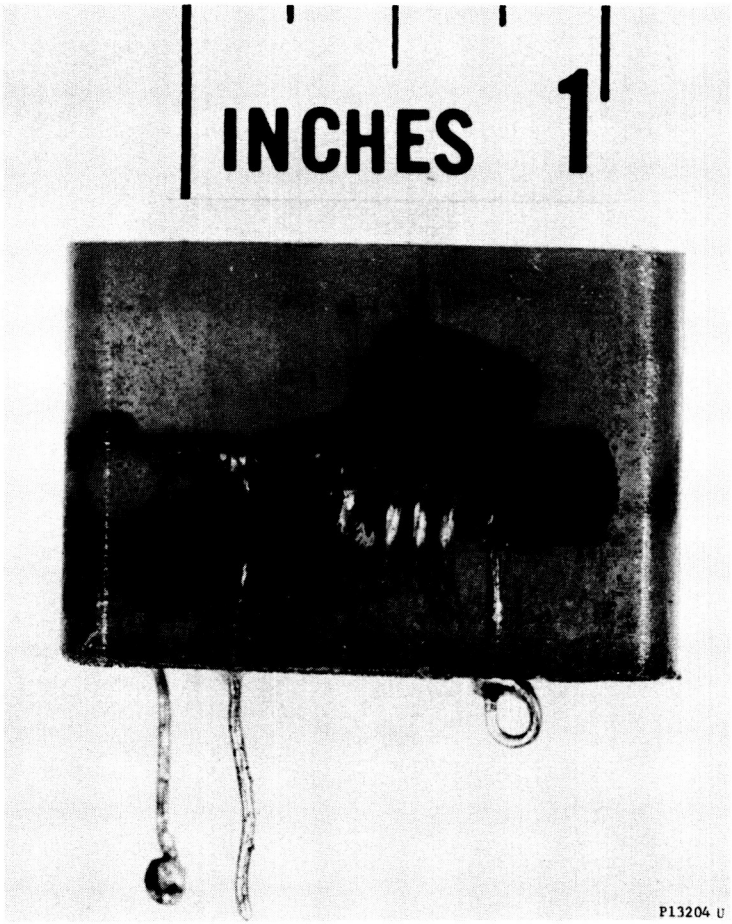

FIGURE 5-12. 225 MHz LUMPED CONSTANT OSCILLATOR WITHOUT COIL FORM

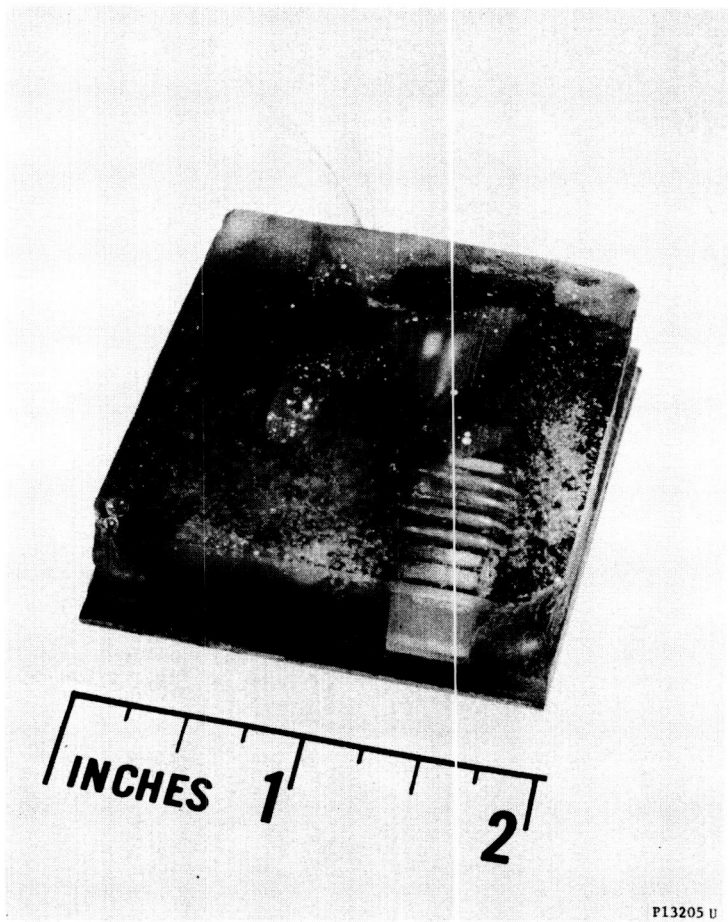

FIGURE 5-13. 225 MHz LUMPED CONSTANT COIL FORM WITH REXOLITE COIL FORM

Although no deterioration in performance caused by the cracks was observed, later encapsulations included fiberglass reinforcement. The impact test instrumentation is shown in Figure 5-14.

A push-pull oscillator with two outputs 180 degrees out of phase for driving push-push doublers was constructed using two 2N2369 transistors as shown in Figure 5-15. The oscillator provides two outputs of 90 milliwatts each with a circuit efficiency of approximately 25 percent. The amplitude balance is adjustable over a wide range. With suitable matching, the oscillator is capable of driving two push-push doublers.

A higher power single-ended oscillator was constructed to use in driving push-push doublers with resistive padding for load isolation. This oscillator used a TA2658 in a grounded collector Colpitts circuit and delivered 300 milliwatts with 33 percent efficiency. Adjustments in bias and tuning (without replacing components) provided an output of over 1/2 watt. The FM modulator consists of a varactor placed across part of the tank circuit. A deviation of $\pm$150 KHz with good linearity is achieved over a 7.5-volt input range. These three types of oscillators had one common problem, that of frequency stability at high shock levels. Also, in each case, frequency stability was very sensitive to load impedance. Two solutions to the loading problem were investigated. The obvious solution was the addition of a buffer amplifier. An amplifier was breadboarded which yielded an output of 220 milliwatts at an efficiency of greater than 50 percent and gain of 7 db. This output power allowed the use of a 3 db resistive pad for additional isolation. The 2N2369 transistor which had previously been qualified to the required g level by Aeronutronic was used in this circuit.

The second approach to the problem was the construction of a "load independent" oscillator as described in the State-of-the Art Review[1] and literature referenced therein. This is a grounded-collector Hartley circuit employing varactor modulation; the frequency changes 100 KHz with a 2:1 change in load resistance. The magnitude of the change in the input impedance of the push-push doubler with shorted output is not known because of the difficulty in making large signal impedance measurements on Class C circuits. Further testing indicated the advisability of utilizing a buffer amplifier in conjunction with a 112 MHz Colpitts oscillator.

b. Doubler Stages. A push-push doubler was constructed using two sample TA2658 RCA power transistors (Figure 5-16). This unit exceeded the 5 db power gain requirements, delivering a 500 milliwatt output with a drive power of only 125 milliwatts (6 db gain), with 37 percent collector efficiency using a coaxial output filter. The fundamental frequency component of the output was only 7 db down without the coaxial output filter, due probably to the use of unmatched transistors. A new socket was constructed for use with the General Radio Immitance Bridge, and measurements confirmed the fact that the input impedances of the sample transistors are significantly different.

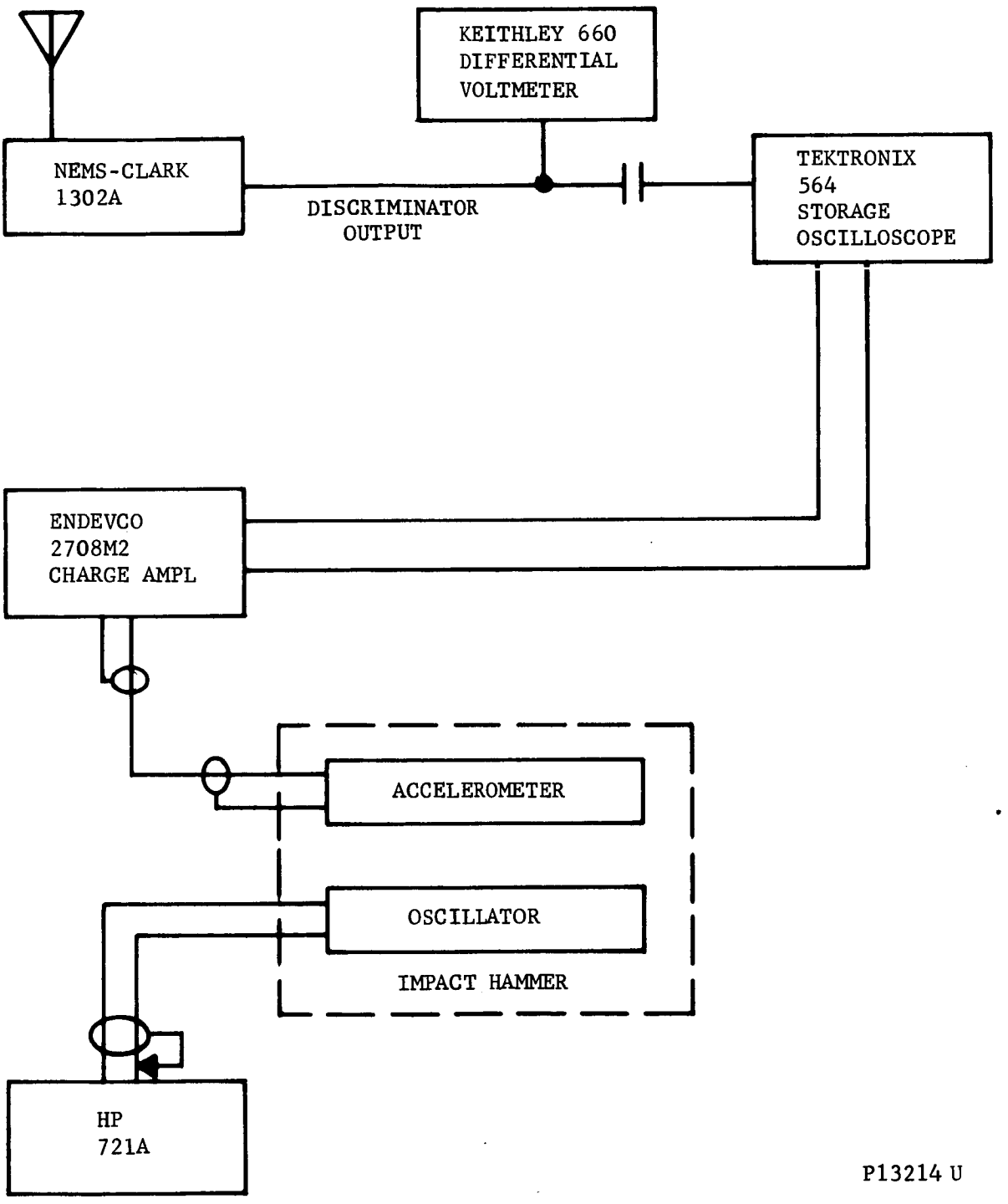

FIGURE 5-14. OSCILLATOR INPUT TEST SETUP

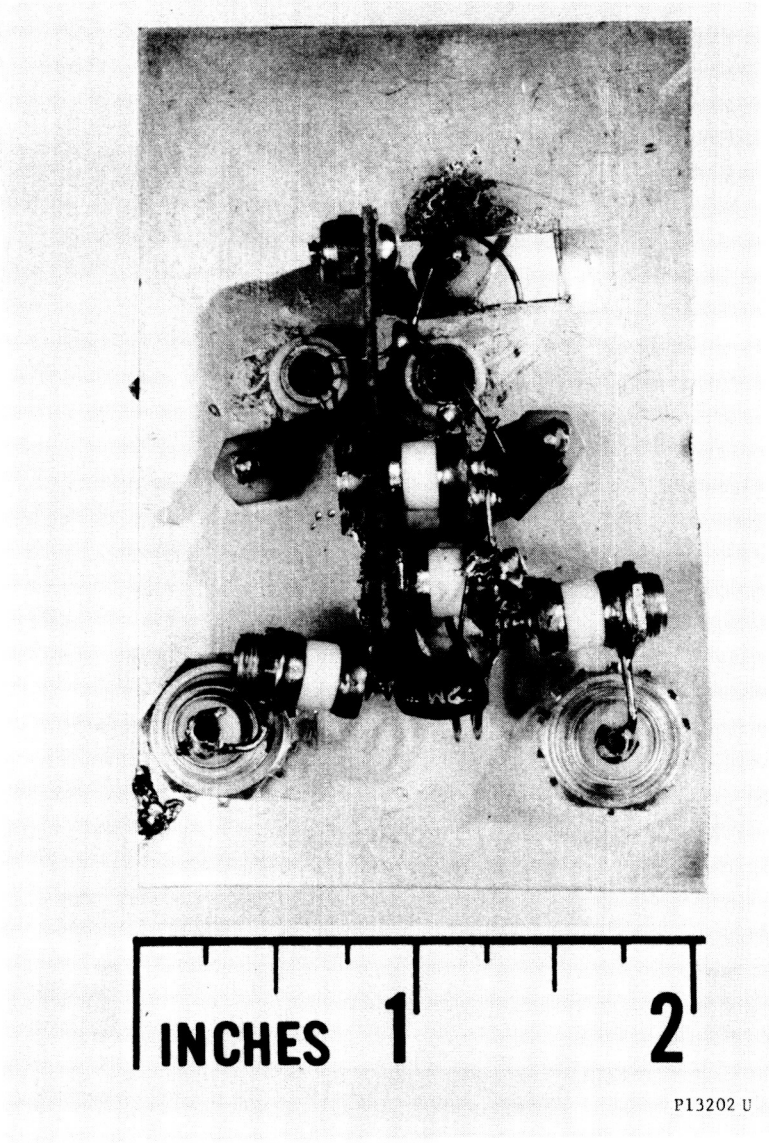

FIGURE 5-15. 250 MHz PUSH-PULL OSCILLATOR BREADBOARD

FIGURE 5-16. 225 MHz - 450 PUSH-PUSH BREADBOARD

A number of RCA 2N3866 (TA2658) transistors were checked for input and output impedance to allow selection of matched pairs for push-push doubler application. The sample TA2658 transistors were replaced with the 2N3866 and this resulted in a power gain of 10 db with over 40 percent efficiency compared to the 6 db, 37 percent efficiency previously obtained. The fundamental component in the output was still evident with matched transisters and was traced to a ground current problem in the base bypass arrangement. A new common base, grounded collector circuit, was constructed which achieved the same efficiency and gain of previous circuits and minimized fundamental feedthrough. Two of the RCA TA2658 transistors were opened and encapsulated with Shell 828 epoxy; no discernible difference in performance was noted after only slight retuning. This test proved that encapsulation of the device could be utilized to prevent lead bond problems at high g levels without sacrificing rf performance.

c. Transmitter Breadboard. An electrical breadboard of a complete transmitter consisting of a modulated power oscillator, resistive isolator-power driver, and two push-push doublers was constructed and tested. This unit delivered 0.5 watt to each of two 50-ohm loads with an overall efficiency of greater than 30 percent. The circuit configuration employed in the transmitter breadboard and in the engineering model is depicted in the block diagram shown in Figure 5-17. This circuit was chosen to allow the greatest possible isolation between the oscillator and the antennas. The forward gain of each buffer stage is +10 db while the reverse gain is -15 db. The doubler stages when tuned for broadband operation have a forward gain of +9 db and a reverse gain of -12 db. Thus, the isolation between the oscillator and a mismatch at either antenna terminal is 33 db, including the two 3 db interstage pads.

A test of frequency shift versus doubler output mismatch was performed which indicates the merit of this configuration. The output of one doubler was terminated by an rf power meter while the output of the other doubler was mismatched through all phase angles to a VSWR in excess of 20:1. Performance characteristics of the properly terminated doubler were monitored, including power output, frequency, and phase shift relative to the mismatched doubler. The change in output power was less than 0.3 db, the maximum total frequency shift was less than 20 KHz at the output frequency of 450 MHz, and the maximum total phase shift was 47 degrees. It should be noted that these shifts occur only at the complete limits of load mismatches resulting in the 20:1 VSWR noted above.

An antenna matching hybrid was designed to limit the maximum VSWR to less than 2.0:1, at which time frequency and phase shift caused by mismatch become extremely low. A model of one of these hybrid units was tested in conjunction with one of the output stages in the engineering prototype transmitter. The output of one hybrid leg was monitored for power output, phase change, and wave shape distortion; while the other leg was

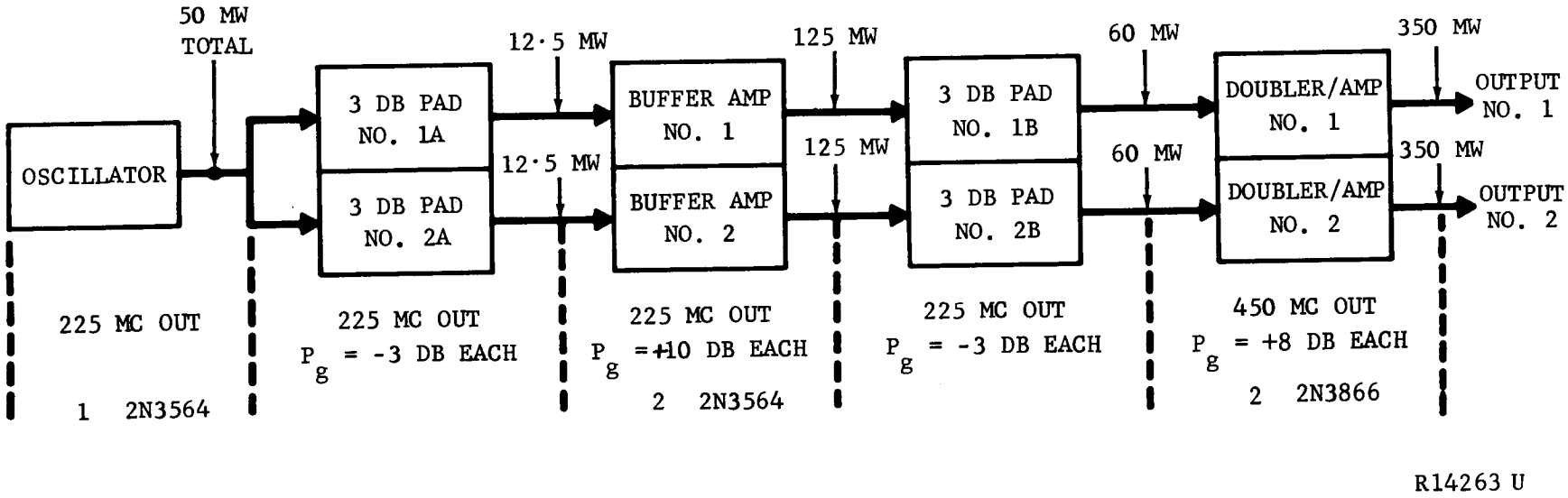

FIGURE 5-17. BREADBOARD TRANSMITTER BLOCK DIAGRAM

terminated in a short circuit, a matched load, and an open circuit. Negligible changes occurred in transmitter output characteristics as a result of these mismatches. Smith charts indicating the range of load mismatching are shown in Figures 5-18 and 5-19.

A major problem was uncovered during initial tune-up of the various transmitter stages. The materials selected for the component supporting boards proved to have too high a dielectric constant combined with a relatively high dissipation factor. As a result of these two characteristics, the potted rf circuits could not be properly tuned because of excessive lossy stray capacities. Another material has since been selected which has a dielectric constant of 2.9 and a loss tangent of only 0.0015. The new material is manufactured by General Electric Co., under specification number A19B22A1 Grade 11556.

Two stripline oscillators were constructed and impact tested. The first was a 450 MHz grounded base Colpitts circuit using Teflon-fiberglass dielectric board. The frequency shift was greater than 400 KHz at 8000 g because of a combination of dielectric resilience and proximity effects caused by the "hot" transistor case which is internally connected to the collector. A new oscillator using Rexolite dielectric board and a grounded collector Colpitts circuit exhibited a frequency shift of 25 KHz at 8000 g. The stripline construction technique has not proved superior to the lumped element construction and is inferior in the respect that design modifications are difficult and time consuming. Further stripline investigation was not done because of these test results.

During transmitter breadboard testing, emphasis was placed on evaluation of frequency dependency on supply voltage and temperature variations. A plot of frequency as a function of temperature for a 225 MHz Hartley breadboard (Figure 5-20) shows a slope of approximately 5.7 KHz/^{o}F. This represents a total frequency excursion of about 114 KHz at the oscillator frequency over a 20^{o}F temperature range, or 228 KHz at the output frequency. This is far in excess of the design limit of ±66 KHz and indicated temperature compensation was necessary. See Table 5.2 for revised transmitter performance requirements.

Frequency and output power as a function of supply voltage are plotted on Figure 5-21. This shows a frequency sensitivity of approximately 25 KHz/volt. Since the voltage regulator stabilizes the +17 volt supply within approximately 0.25 volt, the resulting transmitter output frequency could vary by 12.5 KHz. Further design effort was required to minimize the voltage sensitivity with an output frequency sensitivity of 10 KHz/volt as a design goal.

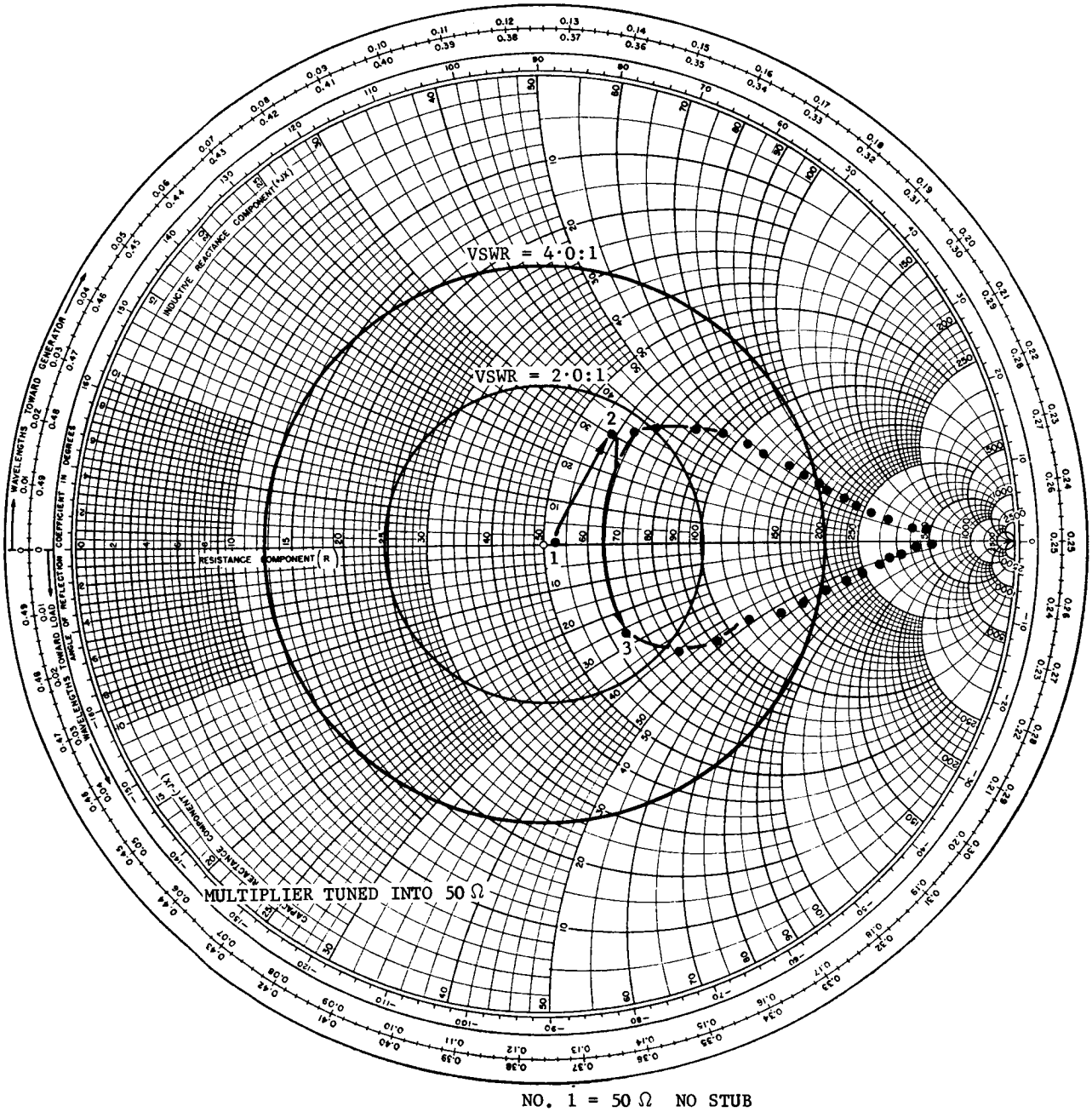

NO. 1 = 50 Ω NO STUB
NO. 2 = 50 Ω W/MATCHING STUB
NO. 3 = 50 Ω MISMATCHED

R14258 U

FIGURE 5-18. BREADBOARD TRANSMITTER MISMATCH TEST INTO 50-OHM LOAD

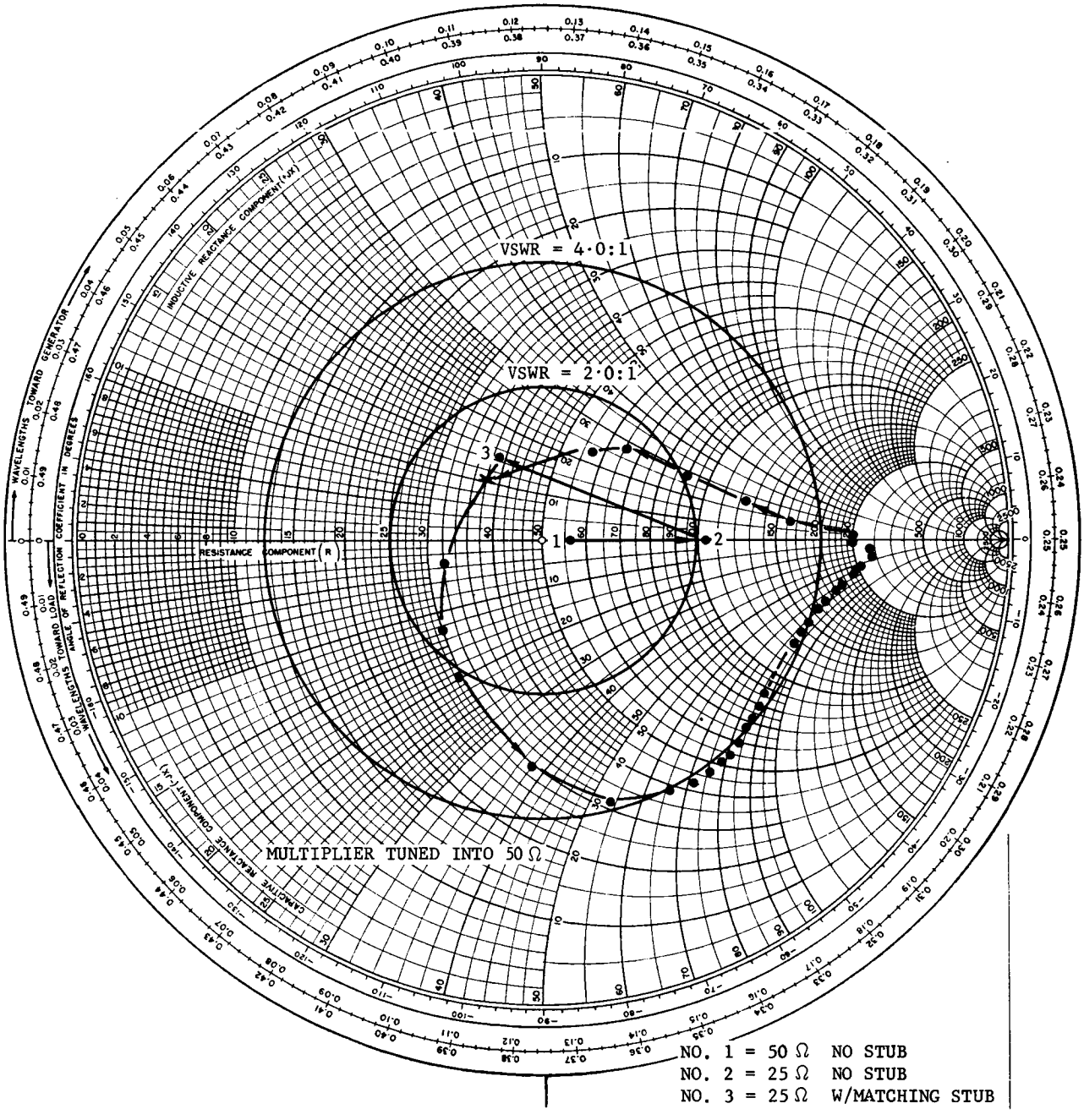

FIGURE 5-19. BREADBOARD TRANSMITTER MISMATCH TEST INTO 25-OHM LOAD

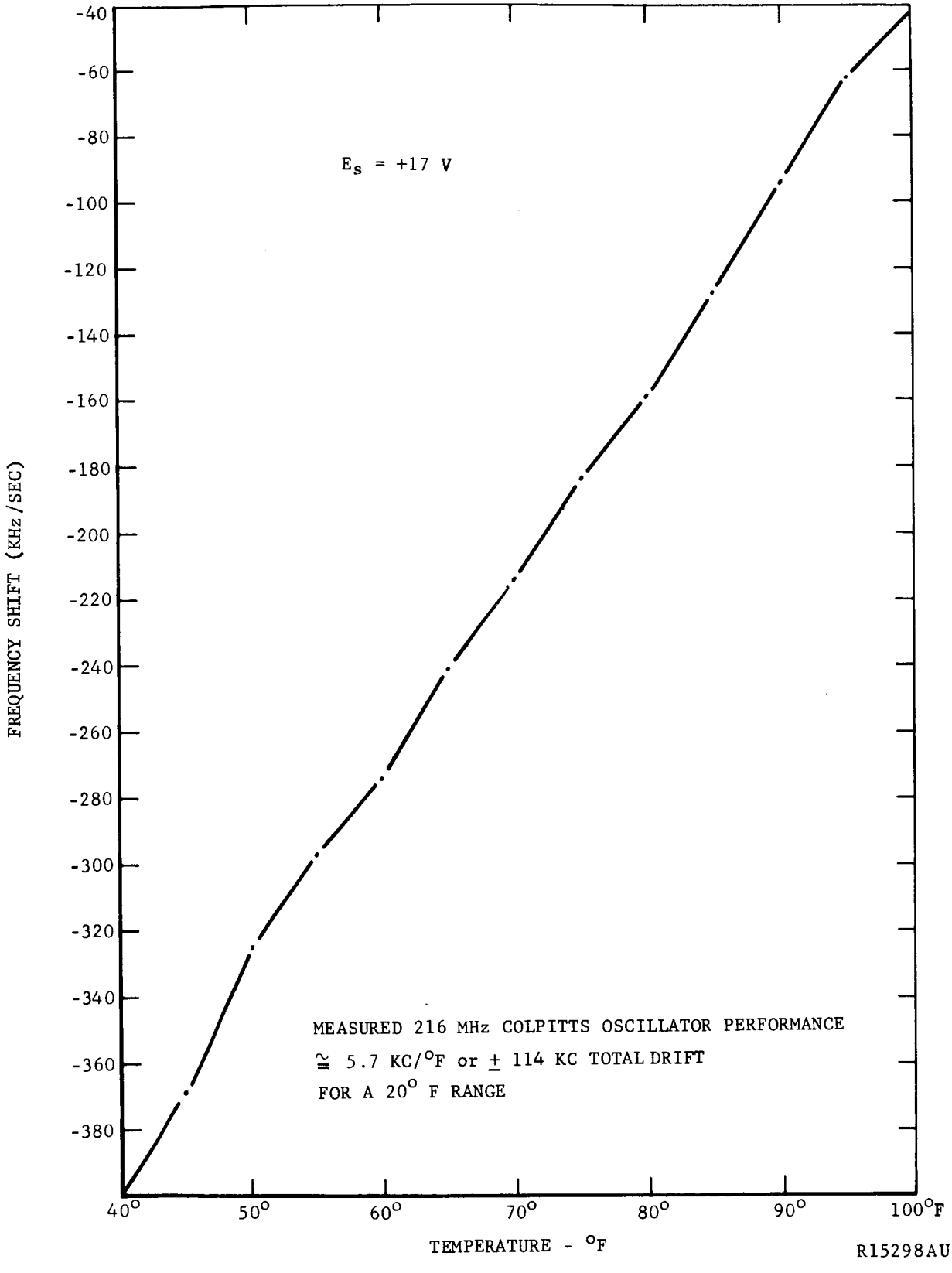

FIGURE 5-20. BREADBOARD TRANSMITTER FREQUENCY VERSUS TEMPERATURE

TABLE 5.2

REVISED TRANSMITTER PERFORMANCE REQUIREMENTS

	Old	New
Modulation Deviation	±160 KHz	±160 KHz
Thermal Range	+40°F to +100°F	$\Delta t \leq 20^{\circ}$ within the range +60°F to +100°F
Thermal Coefficient	833 cps/°F	6.6 KHz/°F
Total Thermal Drift	±25 KHz [±0.00055%]	±66 KHz [±0.015%]
Shock-Induced Δf	±45 KHz [±0.01%]	±80 KHz [±0.0175%]
Total Δf at 450 MHz	460 KHz p-p	612 KHz p-p
Receiver Drift	±10 KHz [±0.0022%]	±10 KHz
Receiver Disc BW	700 KHz	700 KHz

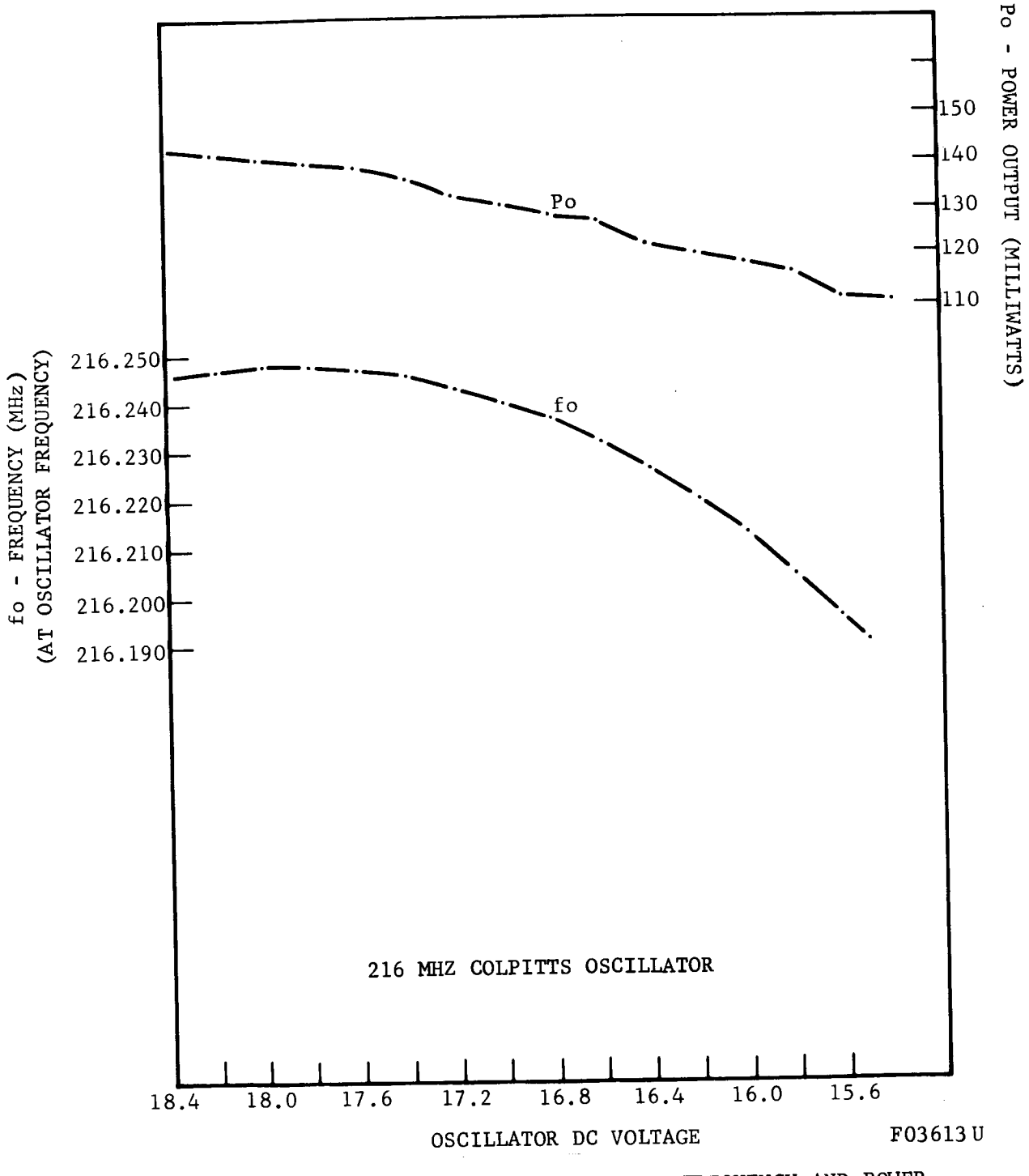

FIGURE 5-21. BREADBOARD TRANSMITTER FREQUENCY AND POWER OUTPUT VERSUS SUPPLY VOLTAGE

5.3.4 FIRST PROTOTYPE TRANSMITTER

After construction of modules to be used in the first prototype unit, a number of electrical and impact tests were conducted. The results of these tests indicated two major problem areas:

(1) Frequency instability at high g levels.

(2) Frequency instability as a function of temperature.

Measures taken to improve oscillator stability included use of a steel chassis with a stiff milled steel cover with multiple hold-down screws. Improved temperature performance was attained with negative temperature coefficient capacitors. The decision was made to utilize a fuzed-quartz coil form with a deposited platinum winding. This measure was taken to minimize the thermal and shock sensitivity problems.

a. Oscillator-Buffer. The frequency versus temperature characteristics of an uncompensated and compensated oscillator-buffer module are shown in Figure 5-22. The slope is approximately 29 KHz/^{o}F at the higher temperatures for the uncompensated oscillator. This is reduced to 1 KHz/^{o}F by the use of a -750 ppm temperature compensating capacitor across the oscillator tank circuit and by adjusting oscillator output level. Figure 5-23 shows the oscillator-buffer module power output as a function/of temperature. These data represent overall module performance including both oscillator and buffer power-temperature sensitivity. Figure 5-22 indicates that the frequency stability of a temperature compensated oscillator is well within transmitter performance requirements of 6.66 KHz/^{o}F, with 2 KHz/^{o}F measured over a temperature range of 40^{o}F to 100^{o}F. Figure 5-23 indicates that the transmitter power output varies only about 7 milliwatts over the same temperature range (1 db), which is within the allowable tolerance on output power.

b. Frequency Doubler-Amplifier. The frequency response of the frequency doubler-amplifier at various supply voltages is shown in Figure 5-24. These curves indicate acceptable tuned circuit stability for a push-push doubler output stage. The relative phase shift between output signals was monitored over the voltage range of +22 to +29 vdc. Variations did not exceed 5 degrees, which is well within an acceptable range.

c. Hyge Impact Tests. Hyge impact tests were conducted on the doubler-amplifier described above. Performance parameters monitored during impact included carrier power level and relative phase angle between the two outputs. The output power change was acceptable (less than 3 percent) and no phase shift was noted. (See Figures 5-25 and 5-26.)

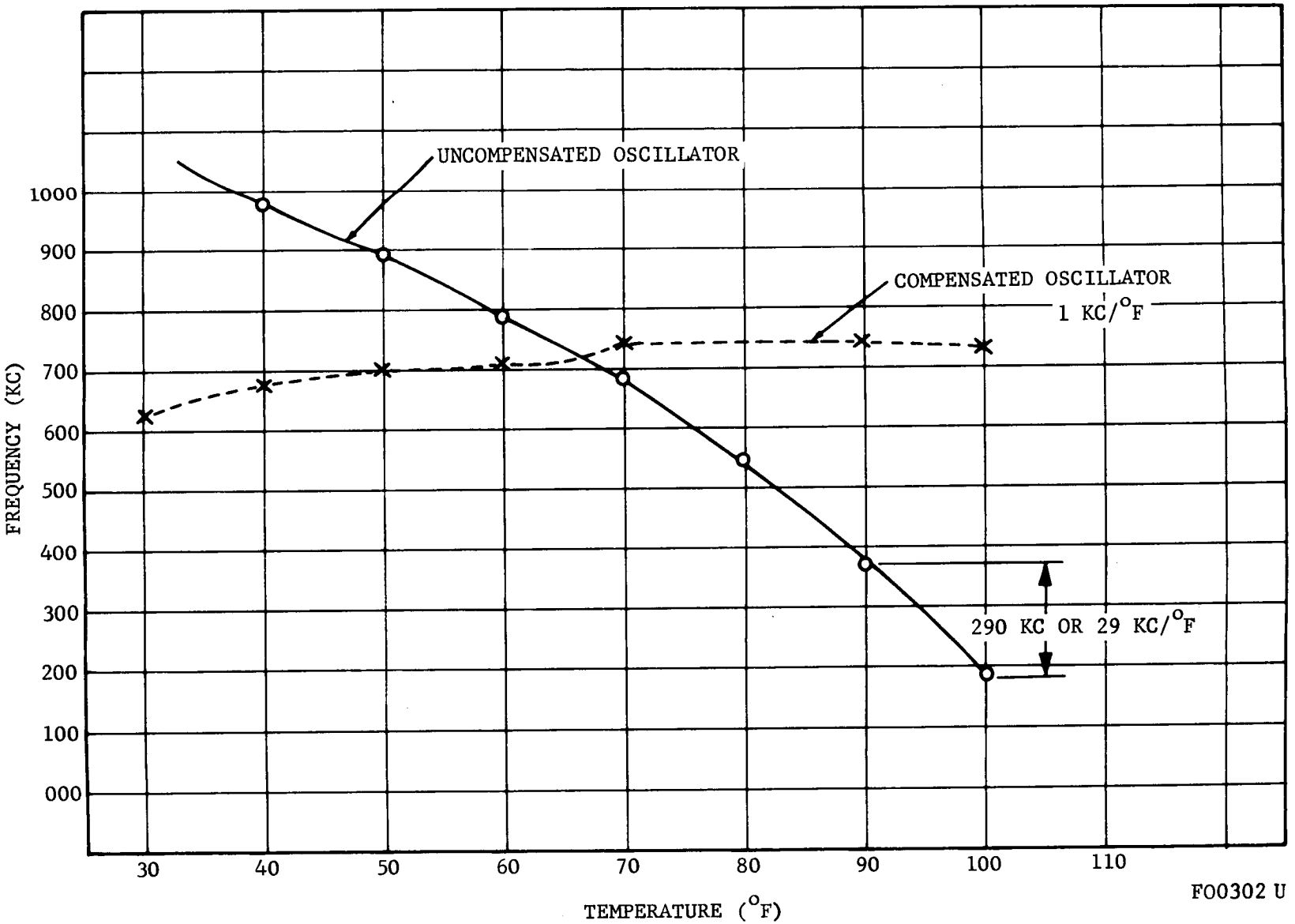

FIGURE 5-22. OSCILLATOR FREQUENCY VERSUS TEMPERATURE PROTOTYPE NO. 1

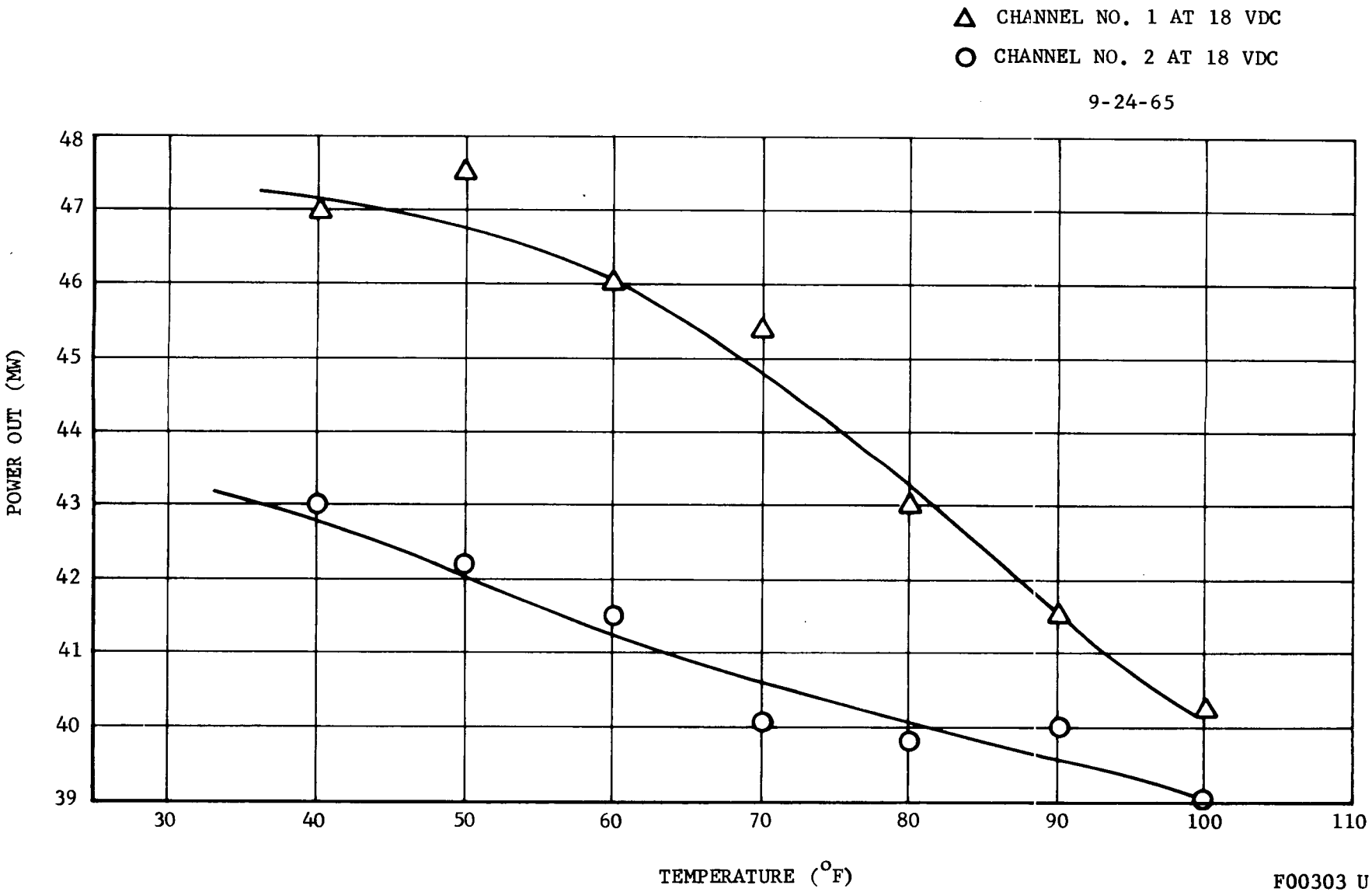

FIGURE 5-23. POWER OUTPUT OF OSCILLATOR-BUFFER PROTOTYPE NO. 1

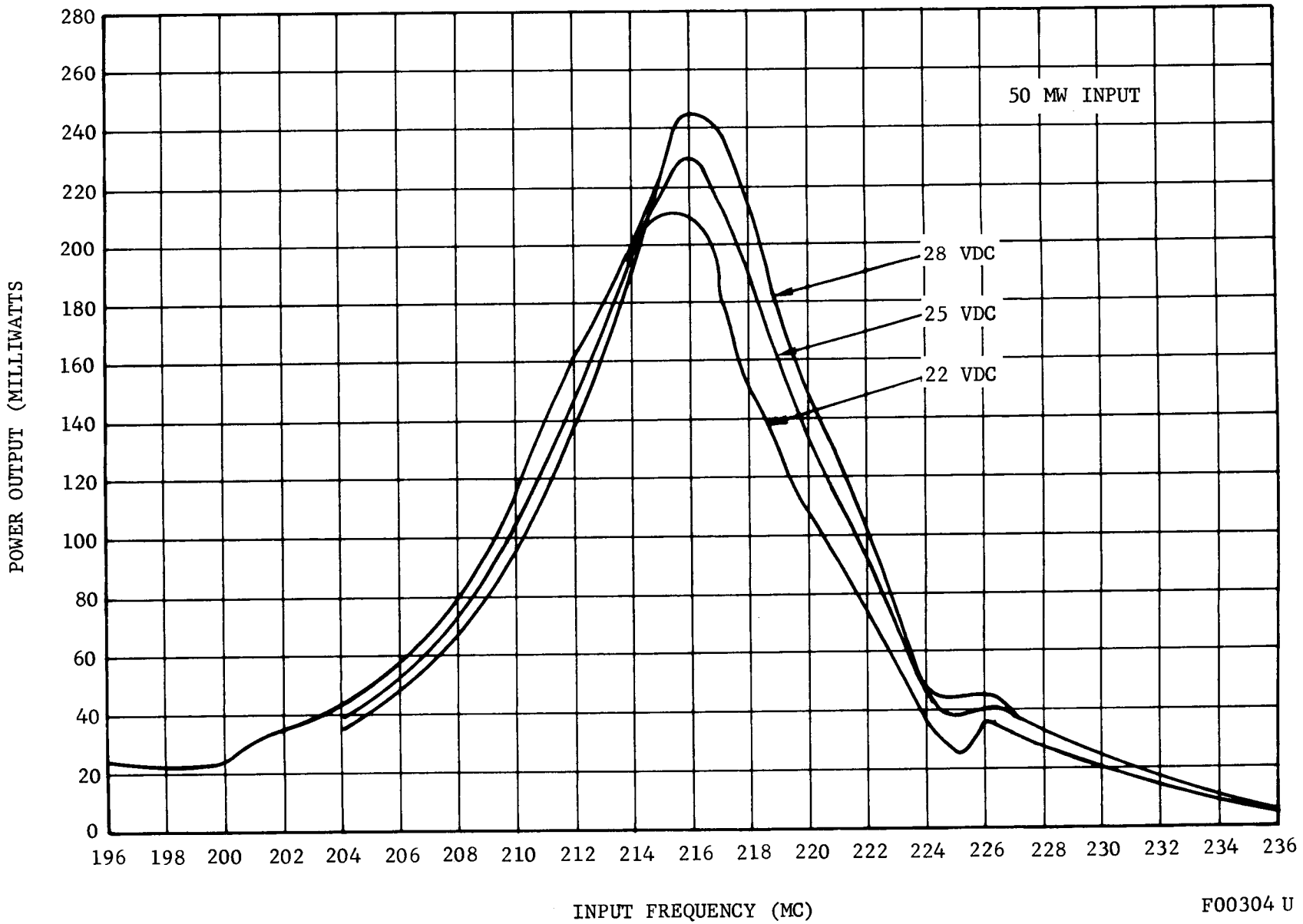

FIGURE 5-24. DOUBLE AMPLIFIER FREQUENCY RESPONSE

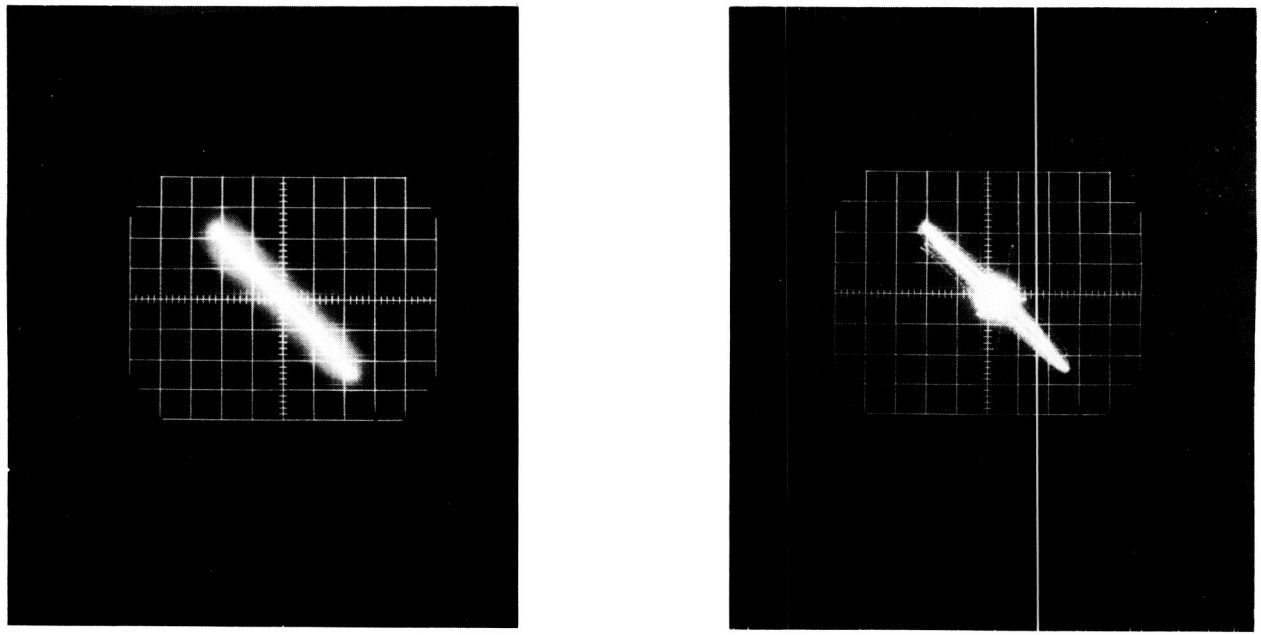

BEFORE IMPACT NUMBER 5

DURING IMPACT NUMBER 5

F00692 U

FIGURE 5-25. PHASE SHIFT DURING HYGE DOUBLER IMPACT

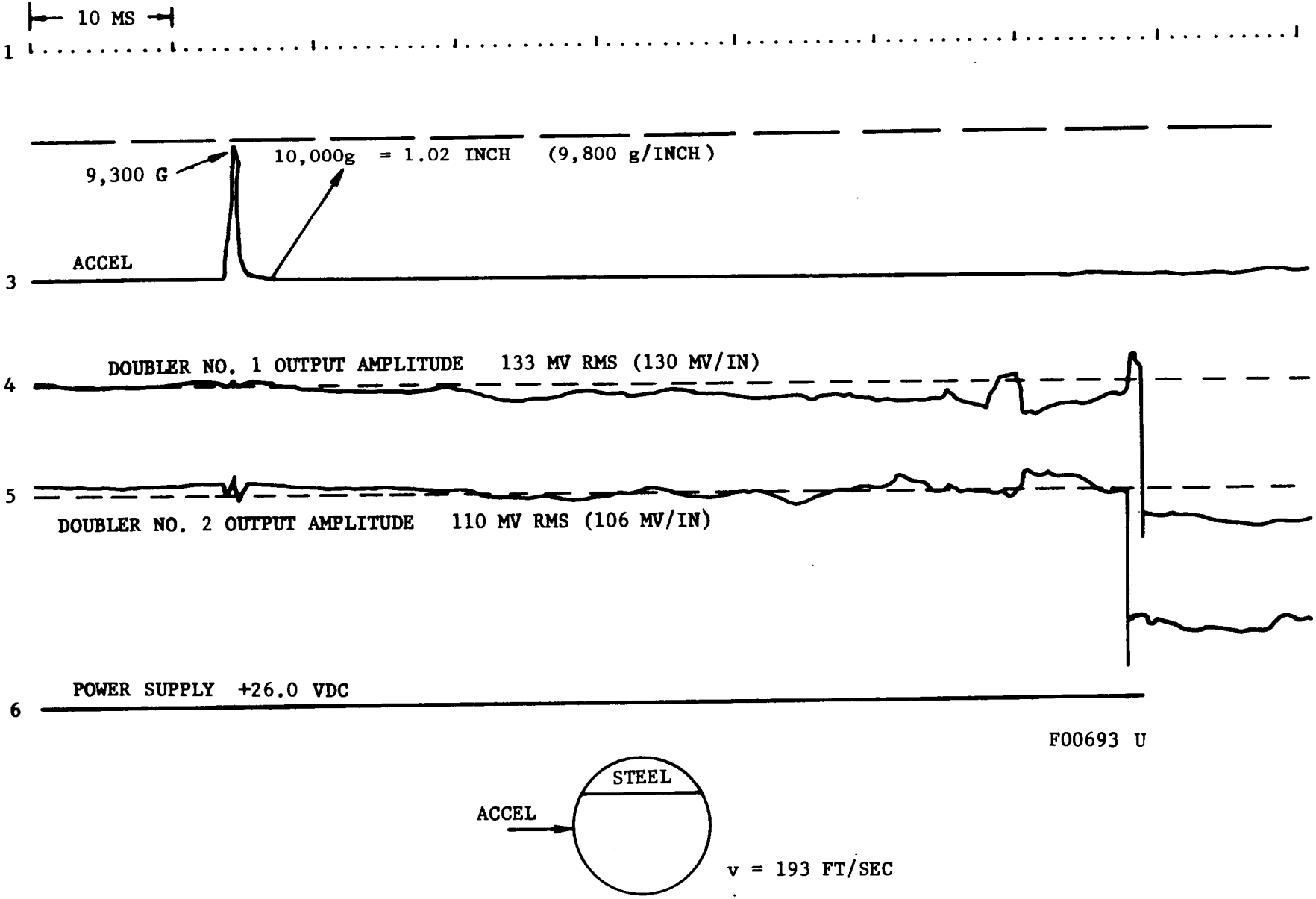

FIGURE 5-26. DOUBLER BALL NO. 1 (REWORKED), HYGE TEST SHOT NO. 5 (GOLF TEE)

Table 5.3 is a summary of doubler module Hyge tests. The first prototype oscillator-buffer module was also Hyge-tested. The results are summarized in Table 5.4. Figure 5-27 is a test record of one of the impact tests.

Following these tests, the test ball containing the prototype oscillator buffer module was disassembled. Large cracks in the unfilled 828-985 epoxy were noted which extended through the output coaxial jacks and to components in the modulation circuit. Because of the high carrier frequency shifts, a second module was fabricated incorporating a grooved fiberglass coil form and added structure to minimize deflections. In addition, JFD ceramic trimmers used for oscillator output matching were deleted as was a small 2-56 threaded brass slug used for oscillator fine tuning. The results for the second unit indicated excessive structural deflections accompanied by large frequency excursions when impacted on the polar axis. A new steel structure was incorporated into the third oscillator-buffer module. Initial test results were poor but, upon disassembly, a broken ceramic capacitor was found.

The mechanical configuration of the three oscillator-buffer modules shock-tested on the Hyge machine are:

Module	Potting	Chassis	Cover	Circuit
Oscillator Buffer No. 1	828-985	0.027 Brass	0.027 Brass (Not used for test)	Nonground fiberglass coil form. Ceramic JFD trimmers. Tuning slug.
No. 2	828-985 and Micro Balloons	0.027 Brass with added support structure	Brass Not used for test	Grooved fiberglass coil form. Removed trimmers and slug.
No. 3	828-985 and Micro Balloons	Steel Chassis	Steel with 31 0-80 screws	No trimmers. Grooved fiberglass coil form.

In all these tests, three significant parameters were monitored during shock. These were (1) oscillator frequency monitored at the output of a Nems-Clark 1302A receiver, (2) oscillator amplitude monitored with a Hewlett-Packard 432A detector in conjunction with a Boonton 230A power amplifier, and (3) 40 KHz AM signal amplitude monitored at the outputs were hard lined from the test ball to the instrumentation through about 75 feet of low noise instrumentation coaxial cable. This cable has a measured insertion loss of 20 db/37 feet and necessitated the use of the 230A power amplifier for amplitude detection.

TABLE 5.3

SUMMARY OF DOUBLER MODULE HYGE TESTS

Test	g-Level	Plane	Amplitude Change No. 1	Amplitude Change No. 2	Phase Change
1. Captive	1,600	Polar "A"	-1 db*	-1 db*	Less than 5°
2. Captive	1,450	Equator	-1 db*	-1 db*	Less than 5°
3. Captive	1,500	Polar "B"	-0.5 db*	-0.7 db*	Less than 5°
4. Golf-tee	9,200	Equator	None	-1 db	Less than 5°
5. Golf-tee	9,300	Equator	None	-0.5 db	Less than 5°
6. Golf-tee	10,500	Polar "A"	Lost cables		Less than 5°

Note: Polar "A" axis, acceleration toward hollow dome.

*These amplitude deviations are not believed to be attributable to shock as they are more representative of long-term drift. There is no time correlation with the accelerometer trace.

TABLE 5.4

IMPACT TEST SUMMARY FOR OSCILLATOR-BUFFER MODULE

Run No.	Type of Test	Axis of Force	Peak Accel (g)	Velocity (ft/sec)	Maximum Frequency Deviation (kc)	Remarks
1	Captive	Polar A	2,200	228	7.3	No perceptible change in 40 KHz level.
2	Captive	Polar B	1,180	228	11.9	No perceptible change in 40 KHz level.
3	Captive	45° off Polar A	1,430	230	10.0	No perceptible change in 40 KHz level.
4	Captive	Polar A	Cable broke	228	12.5	No perceptible change in 40 KHz level.
5	Ram Impact	Polar A	12,600	244	197.0	Shift in 40 KHz attributable to impact = 15.7 g = 0.13% data error. Carrier frequency shift assumed due to cracked epoxy evident during disassembly.
6	Ram Impact	Polar A	10,900	236	261.0	High carrier frequency shift due to cracked epoxy. Resultant data error less than 1%.
7	Ram Impact	Equator	9,620	225	23.5	Apparently favored axis for best carrier stability. Indicates structural deflections present in polar axis. Carrier shift near design goal specification of ±22.5 KHz at 7000 g.
8	Ram Impact	Polar A	10,700	225	225.0	Repeat of No. 7. Similar results indicating structural deficiencies and cracked epoxy. Reversal of polarity of disc output reflects reversal of impact direction. 40 KHz deflection may be caused by carrier excursion beyond FM discriminator range. Data error less than 1%.

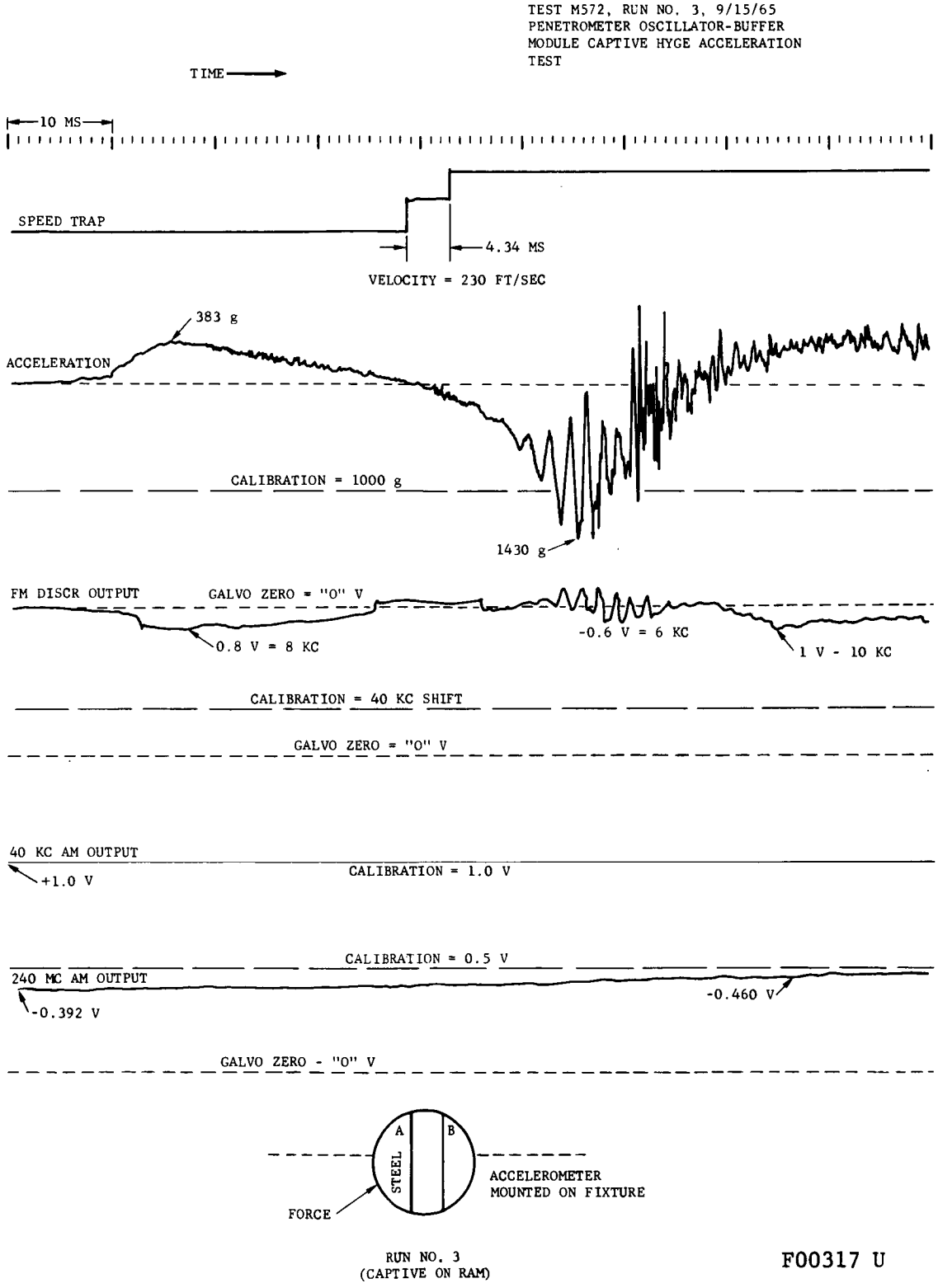

FIGURE 5-27. HYGE TEST RECORD FOR PROTOTYPE NO. 1 OSCILLATOR BUFFER MODULE

By modulating the oscillator with a 1-volt peak-to-peak square wave, simulating a 1000 g signal input, shock-induced variations in modulation sensitivity, corresponding to incidental signal error, could be evaluated. This did not exceed 1 percent in any test data reduced.

Prototype oscillator-buffer and doubler modules are shown in Figures 5-28 and 5-29. Because of lack of success in the area of oscillator shock stability, investigation continued in the areas of stable components, and ruggedized packaging techniques. Particular attention was directed towards methods of adjusting the oscillator frequency after potting. Possible solutions include varactor tuning, slug tuning the oscillator coil, or the employment of a very small piston trimmer capacitor (JMC 4702) made by the Johanson Manufacturing Company.

5.3.5 STABLE OSCILLATOR DEVELOPMENT

Because of the frequency instability noted in Prototype No. 1 transmitter, a rugged housing was designed to reduce structural deflections.

A series of hammer shock tests were performed on a Hartley oscillator in a steel housing. Three basic tuning methods were employed for comparison of frequency stability during impact. The tuning methods were: (1) fixed tuning capacitors, (2) variable Johanson 0.3 to 3.5 pf trimmer, and (3) PSI PC116 varicap. Short duration impact forces of 10,000 g were applied to the three configurations and at no time was a frequency shift of more than ± 5 KHz observed. After these preliminary hammer tests, this oscillator was further tested in the Hyge facility. Two such tests indicated a frequency deviation of approximately 20 KHz with 10,000 g impact of 3 milliseconds duration. This 20 KHz deviation is at oscillator frequency at 235 MHz corresponding to a deviation of 40 KHz at the output frequency. This deviation approaches an acceptable stability as per transmitter performance requirements (Table 5.1).

The oscilloscope photos in Figures 5-30 and 5-31 show frequency stability of this oscillator when tested with the hand-swung hammer.

Although frequency stability during impact was good, a wide frequency shift caused by temperature was noted, requiring excessively large values of temperature-compensating components. Repeatability of operating characteristics caused by the high oscillator frequency, as well as structural deflections was questioned.

5.3.6 FINAL TRANSMITTER CONFIGURATION

A major redesign effort was initiated following impact testing of Prototype No. 1 which yielded several important advantages over the original parallel redundant buffer amplifier/frequency doubler concept.

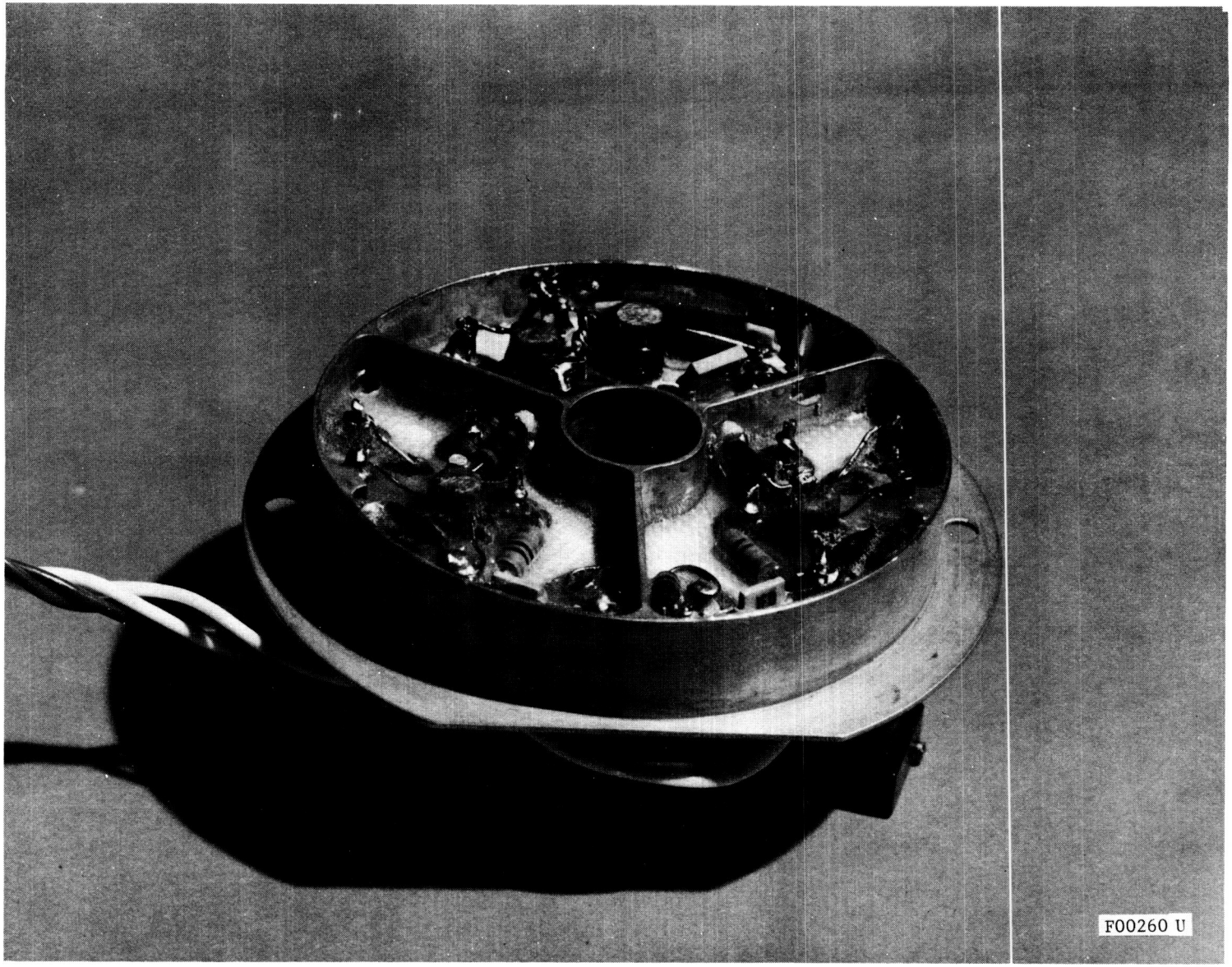

FIGURE 5-28. OSCILLATOR-BUFFER MODULE, PROTOTYPE NO. 1

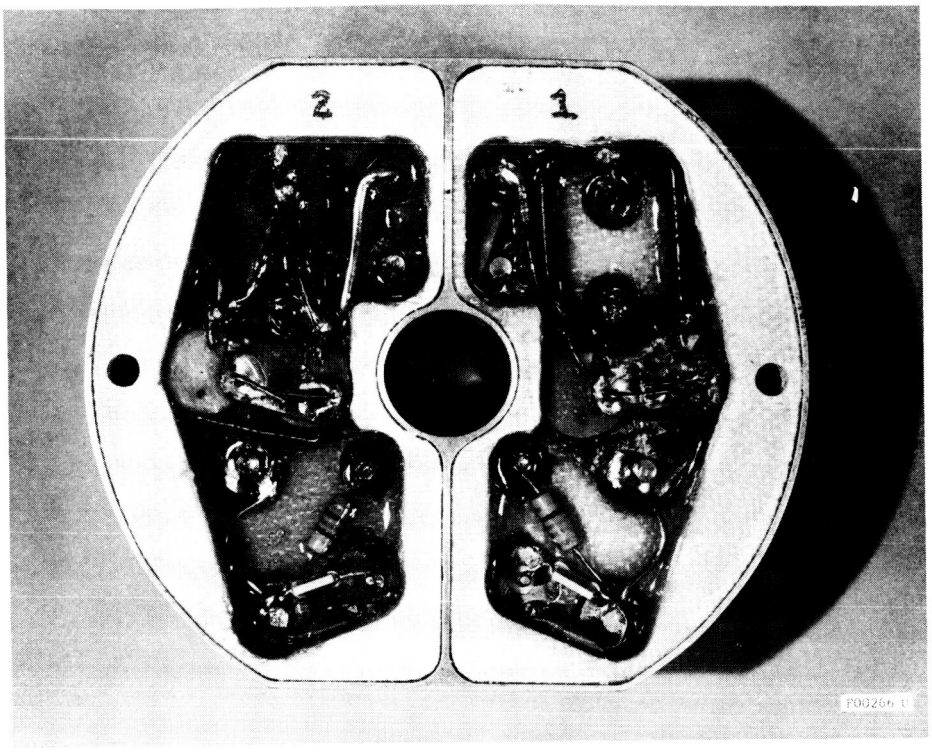

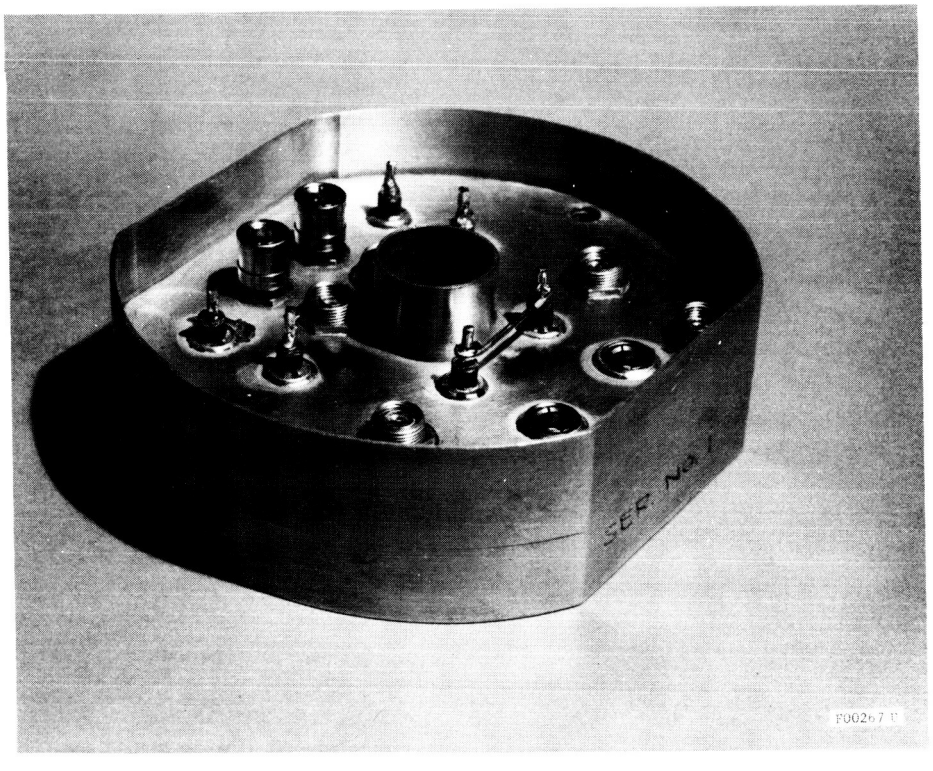

FIGURE 5-29. TWO VIEWS OF THE AMPLIFIER-DOUBLER MODULE, PROTOTYPE NO. 1

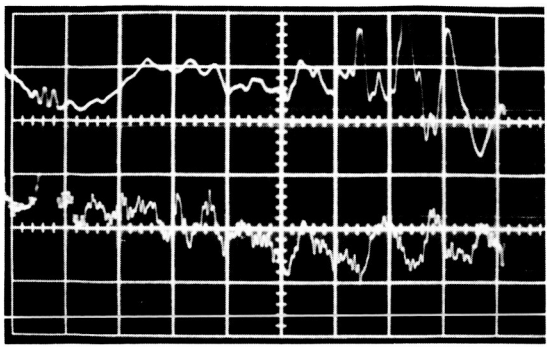

A 2E

TOP TRACE:	ACCELEROMETER OUTPUT 5000 g/cm
BOTTOM TRACE:	FM DISCRIMINATOR OUTPUT 5 KC/cm
G LEVEL:	> 10 KG
Δ F:	9 KC
TIME SCALE:	50 μs/cm

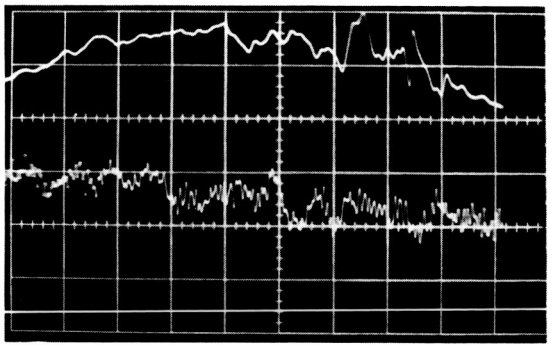

B 7E

TOP TRACE:	ACCELEROMETER OUTPUT 5000 g/cm
BOTTOM TRACE:	FM DISCRIMINATOR OUTPUT 5 KC/cm
G LEVEL:	10 KG
Δ F:	8 KC
TIME SCALE:	50 μs/cm

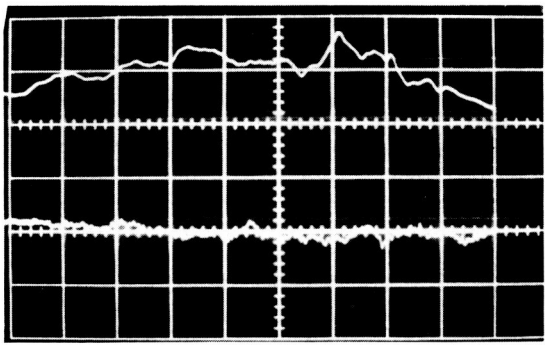

C 2D

TOP TRACE:	ACCELEROMETER OUTPUT 5000 g/cm
BOTTOM TRACE:	FM DISCRIMINATOR OUTPUT 10 KC/cm
G LEVEL:	8 KG
Δ F:	6 KC
TIME SCALE:	50 μs/cm

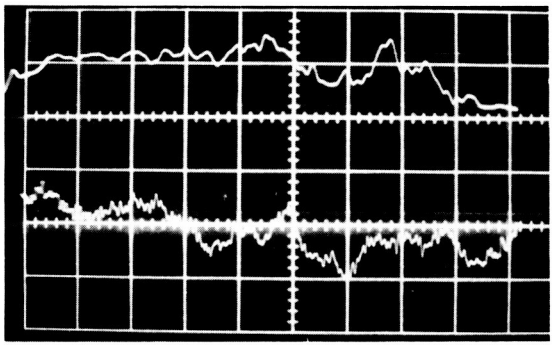

D 5D

TOP TRACE:	ACCELEROMETER OUTPUT 5000 g/cm
BOTTOM TRACE:	FM DISCRIMINATOR OUTPUT 5 KC/cm
G LEVEL:	8 KG
Δ F:	9 KC
TIME SCALE:	50 μs/cm

F00686 U

FIGURE 5-30. OSCILLATOR WITH PC +116 VARICAP TUNING ELEMENT

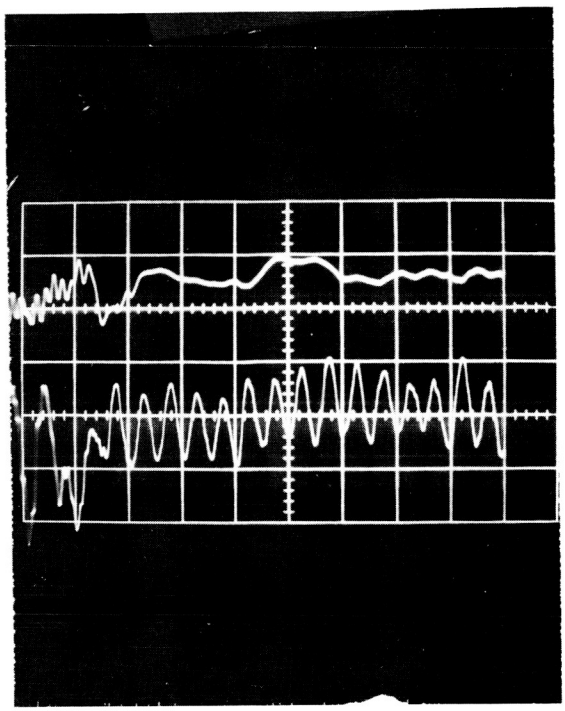

A 9

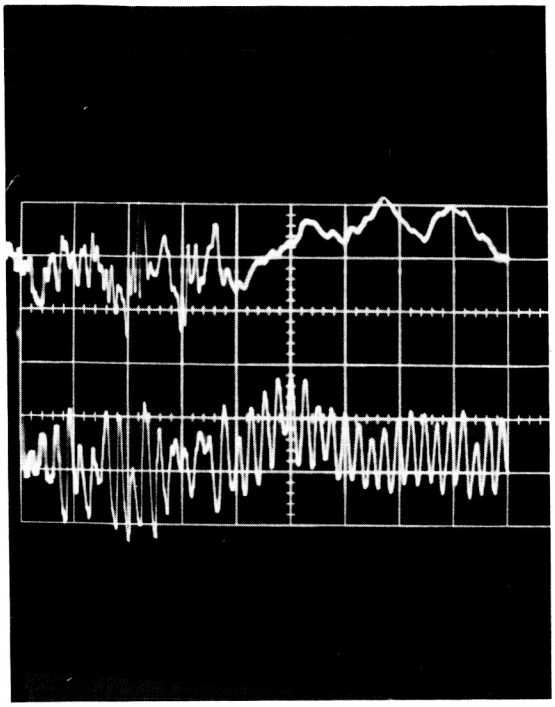

B 10

TOP TRACE:	ACCELEROMETER OUTPUT 5000 g/cm	TOP TRACE:	ACCELEROMETER OUTPUT 5000 g/cm
BOTTOM TRACE:	FM DISCRIMINATOR OUTPUT 10 KC/cm	BOTTOM TRACE:	FM DISCRIMINATOR OUTPUT 10 KC/cm
G LEVEL:	5 KG	G LEVEL:	11 KG
Δ F:	30 KC	Δ F:	30 KC
TIME SCALE:	50 μs/cm	TIME SCALE:	50 μs/cm

F00687 U

FIGURE 5-31. OSCILLATOR WITH FIXED TUNED TANK

These advantages include increased frequency stability and smaller size. A block diagram of the transmitter is shown in Figure 5-32. Utilization of this design approach permits packaging the complete transmitter into one common module as opposed to the two separate modules previously employed. The old package contained four mating pairs of coaxial connectors to interconnect the two separate "decks" to each other and to the antenna hybrids. The new package contains only one coaxial connector for the rf output.

a. Oscillator. A 112 MHz Colpitts oscillator was designed to replace the 225 MHz Hartley oscillator configuration. Consideration was given to this type oscillator operating on both the original frequency of 225 MHz and on half frequency of 112 MHz. The Colpitts offers several advantages, including (1) the elimination of the critical tap point on the tank coil by using a capacitive tap, and (2) increased value of the tank capacitors, reducing the frequency sensitivity caused by stray capacitance. The Colpitts oscillator is modulated by a varactor connected in parallel with the tank circuit. The varactor is also used to set the desired carrier frequency within $\pm$400 KHz after final potting. This method of modulation was selected because of its good modulation sensitivity stability as a function of temperature. To further improve the frequency stability at impact, this oscillator-buffer module is constructed in a steel housing with a wall thickness of 0.1 inch and employs multiple cover attachment screws.

Figure 5-33 shows a typical circuit of this type of Colpitts oscillator. A preliminary test on the Colpitts circuit indicated a greatly reduced frequency sensitivity with temperature variations, typically on the order of 2.5 KHz/^{o}F, as shown in Figure 5-34. This test was conducted on a breadboard oscillator using components proposed for prototype hardware. Further testing of this oscillator, encapsulated in a rugged steel housing properly packaged, indicated a frequency drift as a function of temperature to be on the order of 4 KHz/^{o}F.

b. Buffer. Early transmitter designs incorporated tuned buffer amplifiers between the oscillator and multiplier stages. Detuning of these buffers, resulting from shock-induced coil deformation, had a significant frequency pulling effect on the oscillator. To eliminate this problem, direct-coupled untuned amplifiers were evaluated as replacements for the tuned buffers.

During transmitter development it became evident that a buffer amplifier would be required. The three transistor connections (common collector, common base, and common emitter) were evaluated. Unlike the cathode follower, the emitter follower does not provide load isolation, as the input impedance is approximately β times the load impedance. For this reason, only the common base and common emitter connections were considered. The common emitter connection was chosen, based upon the analysis presented in Appendix K.

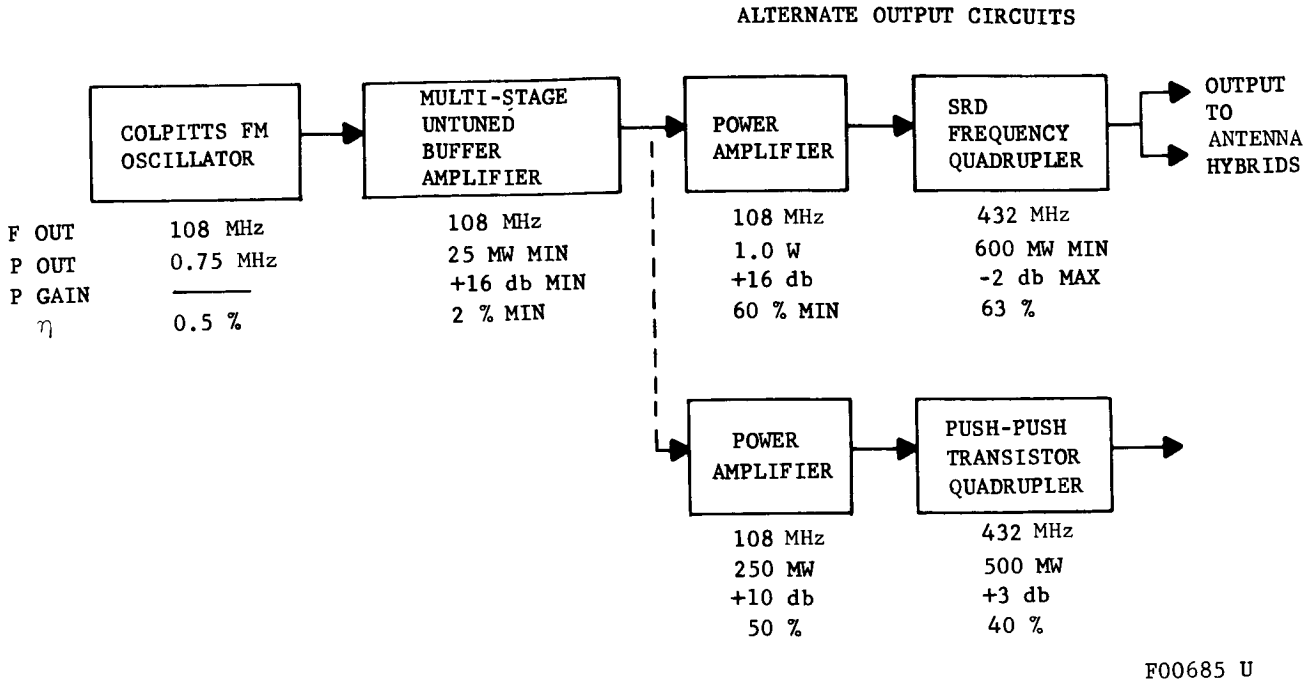

FIGURE 5-32. PROTOTYPE NO. 1 TRANSMITTER CONFIGURATION

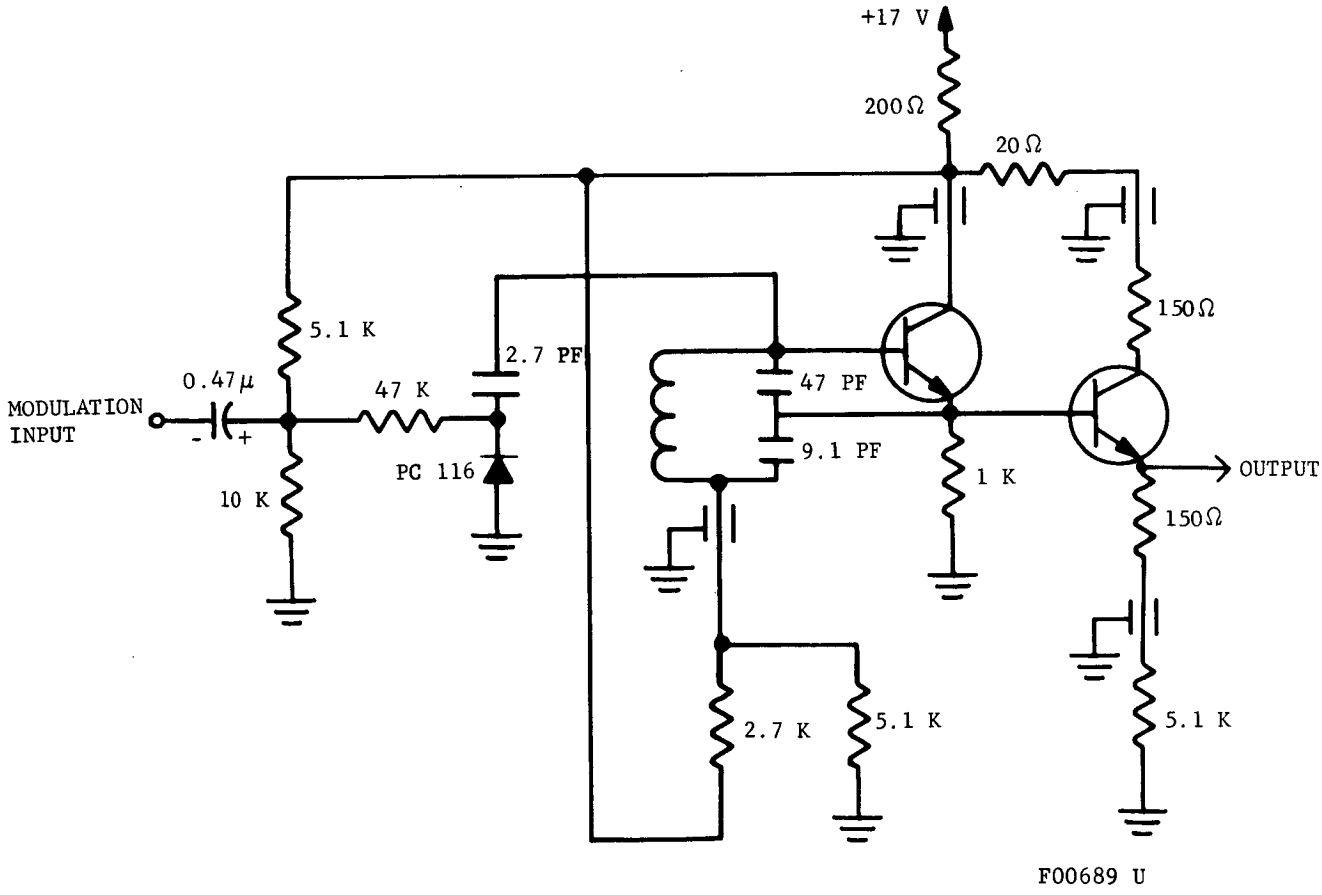

FIGURE 5-33. 112 MHz COLPITTS OSCILLATOR AND BUFFER

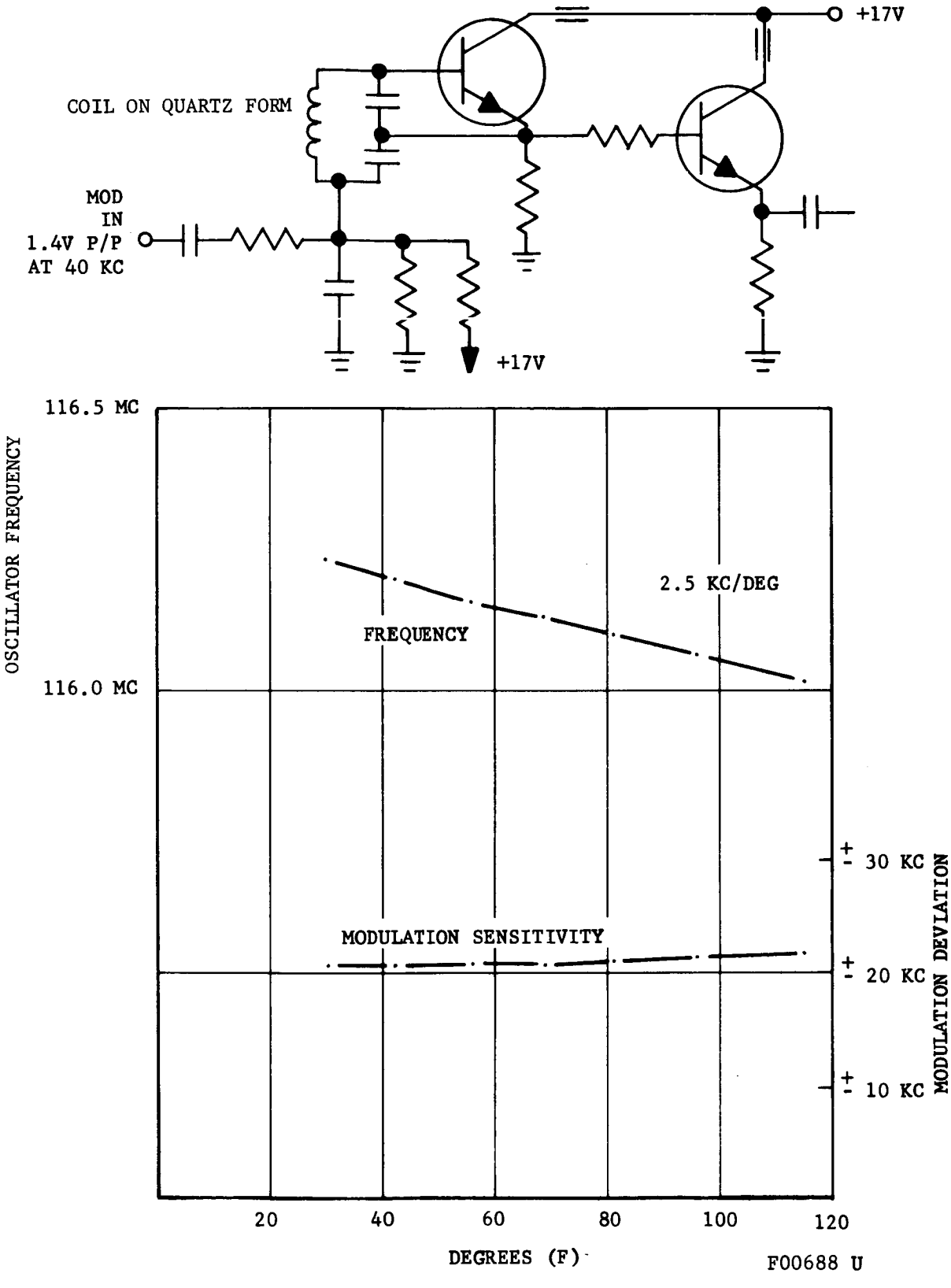

FIGURE 5-34. THERMAL STABILITY CHARACTERISTICS OF A COLPITTS OSCILLATOR AT 116 MHz

It is shown that the load isolation offered by the common emitter transistor connection is the same as that of the common base connection and greater than that of the common collector connection. In addition, cascaded common emitter amplifiers provide gain without the use of transformers or tuned circuits. The untuned buffer amplifier, therefore, uses common emitter stages throughout.

Both two-stage and three-stage buffer amplifiers have been tested. A schematic of a three-stage buffer is shown in Figure 5-35. These are direct-coupled amplifiers with a power output of 50 milliwatts and 17 db of gain at 112 megacycles. In both amplifiers, the voltage gain of the first stage was reduced using emitter degeneration to reduce the load-dependent Miller capacitance, while degeneration in the output transistor was small to obtain the required voltage gain and power output. Emitter degeneration, rather than collector loading, was used to lower the voltage gain to reduce the sensitivity of the circuit to changes in transistor parameters; the increase in load isolation may be achieved by either method.

The current drawn by the amplifiers is determined by the required output power and is approximately 75 milliamperes in both cases. The sensitivity of the two-stage amplifier to changes in load reactance is roughly double that of the three-stage amplifier. The three-stage amplifier requires an additional transistor, four resistors, and a bypass capacitor, but the increase in load isolation far outweighs the small increase in volume requirements.

c. Frequency Multipliers. The three methods of frequency multiplication which are in common usage utilize either transistor, varactor, or step-recovery diode circuits. The transistor circuits may be further divided into two classes: balanced push-push doubler circuits of the type employed in the original LPS system, and a single device configuration wherein the collector-base diode serves as a varactor. This latter version, like the standard varactor multiplier, is of a parametric nature and as a result is prone to problems, such as hard starting, parametric oscillation, and noise generation.

Parametric mode frequency multiplication, in general, requires complex circuitry to ensure proper operation at the desired harmonic while providing current flow at the harmonically related frequencies with idler circuits. This complex circuitry makes tune-up extremely difficult and requires many additional components which not only require considerable chassis volume but will, because of their number, also lower the overall system reliability.

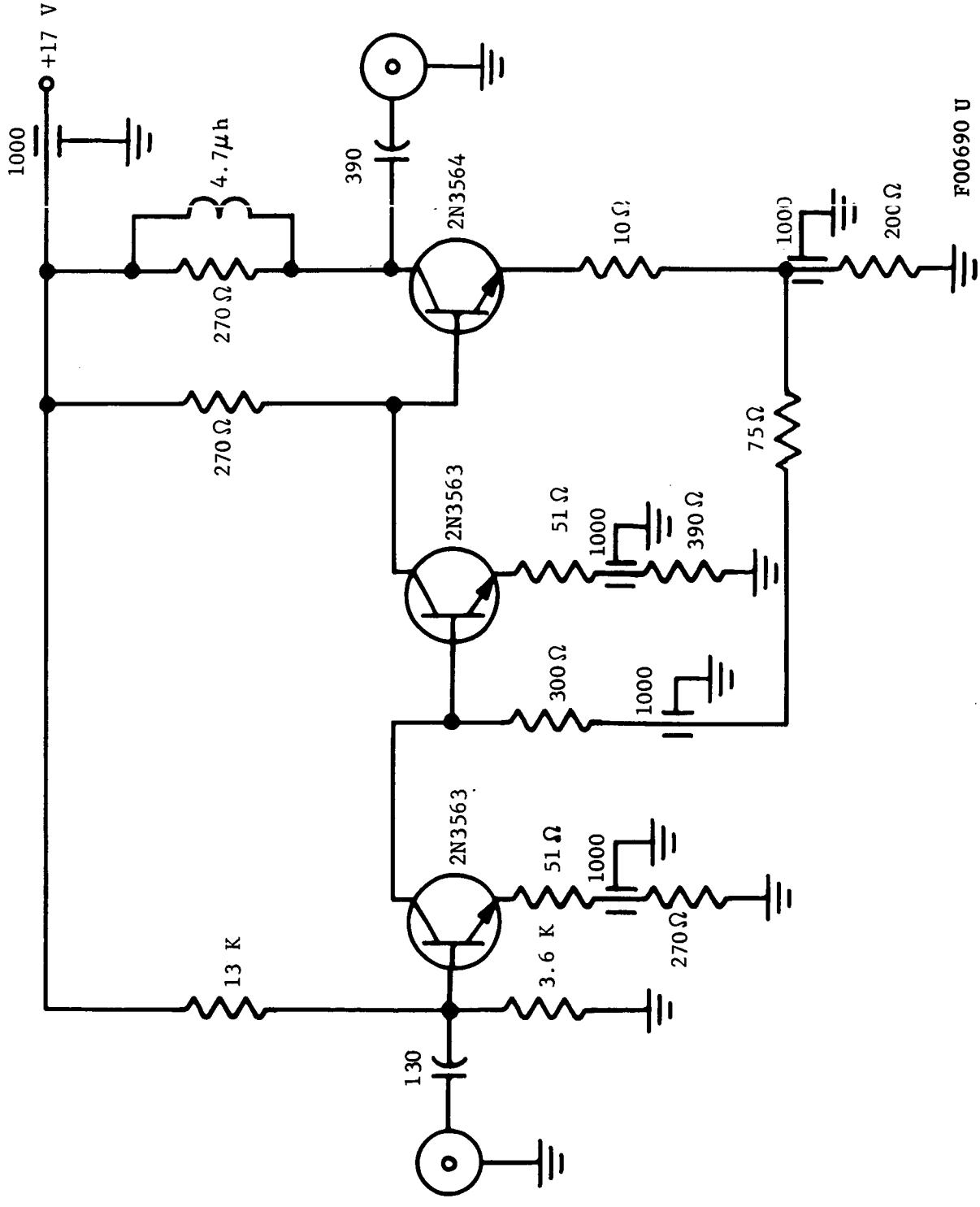

FIGURE 5-35. UNTUNED BUFFER AMPLIFIER

The step-recovery diode (SRD) multiplier, by comparison, requires very simple circuits. Idler or other harmonic traps are not required, since parametric mixing does not occur within the device. Figure 5-36 indicates the simplicity to be found in a typical SRD quadrupler. The input pi matching section, L_1, C_1, and C_2, is actually the output circuitry of the 1-watt, 108 Mc power amplifier. C_3 is a coupling capacitor. L_2 matches the 108 Mc, input to the diode, while C_4 matches the diode to the 432 Mc output filter formed by L_3, C_5, and C_6. The low order of frequency multiplication required in this application should permit use of this simple output filter. The HPA type 0241 SRD operating at this frequency, power level, and multiplication order will show a minimum efficiency of 60 percent with a typical conversion efficiency of 70 percent, resulting in appriximately 700 mw of power at 432 Mc.

The reduction in available multiplier packaging volume and the requirement for an X4 multiplication prompted the deletion of the original redundant output stages and initiated investigation of an X4 multiplier which could be packaged in the available volume. A step recovery diode X4 multiplier was designed and breadboarded. Performance was exceptional with 70 percent conversion efficiency (700 mw at 480 Mc with one watt drive at 120 Mc) and all spurious outputs 30 db below the output. However, difficulty was experienced in packaging the output filter consisting of nine reactive elements in the allocated volume. Some difficulty was also experienced in obtaining operation over a nominal frequency band without severe parasitic oscillation.

An alternate design, consisting of two cascaded push-push doublers, was also packaged in final configuration. The hairpin type of input coupling inductor used in earlier doubler designs was replaced with a conventional 3/16 inch diameter coil supported on a fiberglass form. The circuit is capable of providing 500 mw output at 480 Mc with 50 mw drive at 120 Mc at about 25 percent efficiency. Although this is lower than the 35 percent efficiency provided by the alternate output stage (1-watt amplifier - SRD quadrupler), the ease of construction and tune-up, spurious rejection, and stability justify its present use. Also, only previously shock-qualified parts are used in this approach.

Hyge impact tests were conducted on a transistor amplifier-doubler module. This unit is similar to the one shown in Figure 5-29 with the exception that this module was constructed in a reinforced steel chassis. The circuitry was totally potted with an unfilled Shell 828 epoxy and Furane 985 hardener. Each of the two doublers is tuned with three Johanson type 4335 piston trimmer capacitors. All six of the trimmers were oriented in the same plane which would have emphasized detuning effects during an equatorial impact. No serious amplitude deviations were noted during Hyge testing and, therefore, the Johanson trimmers can be used in this circuit application.

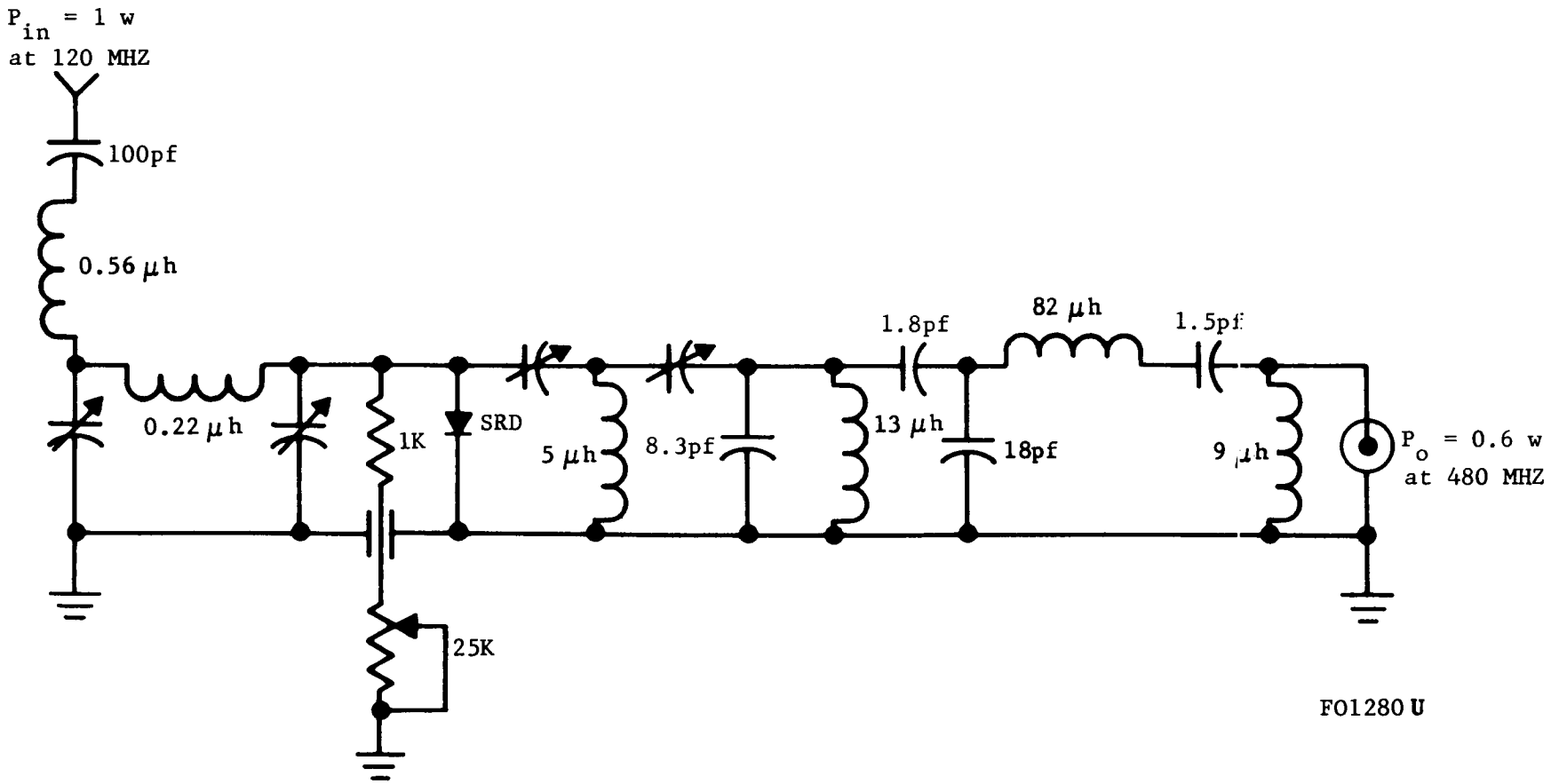

FIGURE 5-36. 120 MHz TO 480 MHz STEP RECOVERY DIODE MULTIPLIER

Performance parameters monitored during impact included dc supply voltage level, carrier power level out of each doubler, and the relative phase angle between the two doubler outputs. The relative carrier phase angle was displayed on a Tektronix type 661 sampling scope. No measurable change in phase angle between the two outputs was noted during impact. A change in output power of less than 3 percent was noted during impact. Laboratory measurements of power gain, power output, relative phase, bandwidth, and efficiency were made after the various Hyge tests, and in all cases doubler performance showed no measurable change. On the basis of these tests, the electrical and mechanical design of this type of doubler is considered to be shock qualified.

5.3.7 PROTOTYPE NO. 2 AND NO. 3 TRANSMITTER

Prior to building the oscillator module for the second prototype, a brass development model had been built and tested with good results (Figure 5-37). See Figure 5-38 for shock test results. The initial oscillator for the second prototype was similar in design except a steel chassis was used, some components were relocated, and air-gaps were left on three sides of the oscillator walls. However, this initial oscillator gave disappointing results when squeezed in a vise or when hammer shock-tested. The so-called "improved" steel module had worse shock characteristics than the prior brass module. A rather involved investigation, including perhaps 50 shock tests, was made to determine the reasons for the differences. The following conclusions were reached:

(1) The internal height of the oscillator cavity had been decreased which increased the capacitance effects by deflecting walls.

(2) The oscillator coil had been placed too close to the outer wall.

(3) In providing an air-gap under the oscillator cavity, the bottom wall had been left poorly supported at the edges.

(4) The components in the circuit had been coated heavily with epoxy rather than given a light freeze coat.

Therefore, another oscillator module was built to alleviate these shortcomings as much as possible with available hardware. The oscillator coil was located inward near stiffer walls. Less encapsulating epoxy was used. A metal shim was placed under the bottom wall of the cavity. This last oscillator module did give improved frequency stability when sequeezed or hammer shocked and was chosen for use in the second penetrometer prototype.

Further tests were conducted on this oscillator as well as the doubler fabricated to be used in Prototype No. 2. Figure 5-39 shows photograph of the complete transmitter module, ready for dry assembly into Prototype No. 2. Figure 5-40 is a schematic for oscillator, buffer, and output stabes as used in Prototype No. 2. This configuration was also used in Prototype No. 3. Hyge test results with this transmitter configuration are described in Section 7.

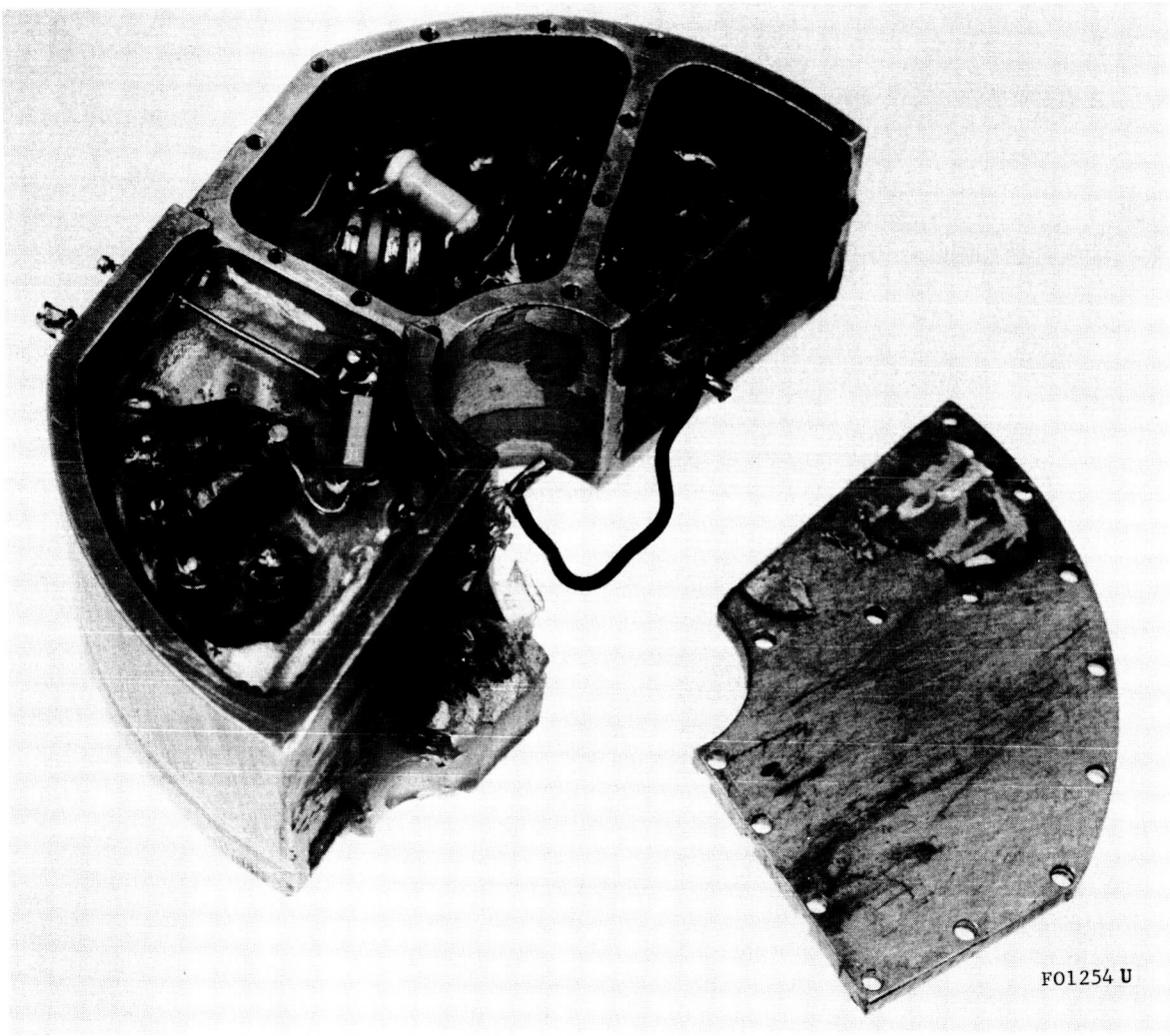

FIGURE 5-37. 112 MHz COLPITTS OSCILLATOR MODULE
AFTER REMOVAL FROM TESTING BALL

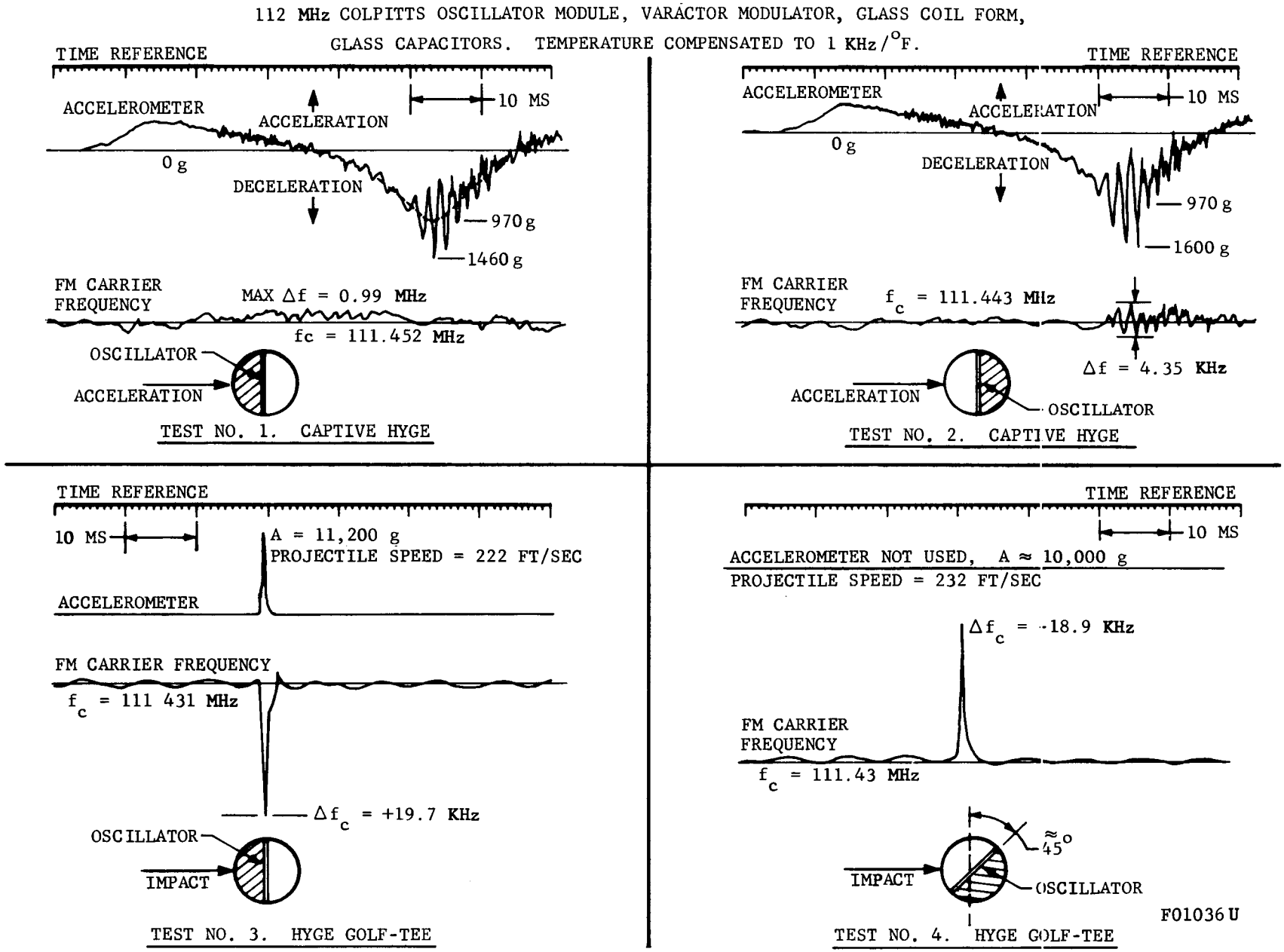

FIGURE 5-38. PROTOTYPE NO. 2 OSCILLATOR SHOCK TESTS

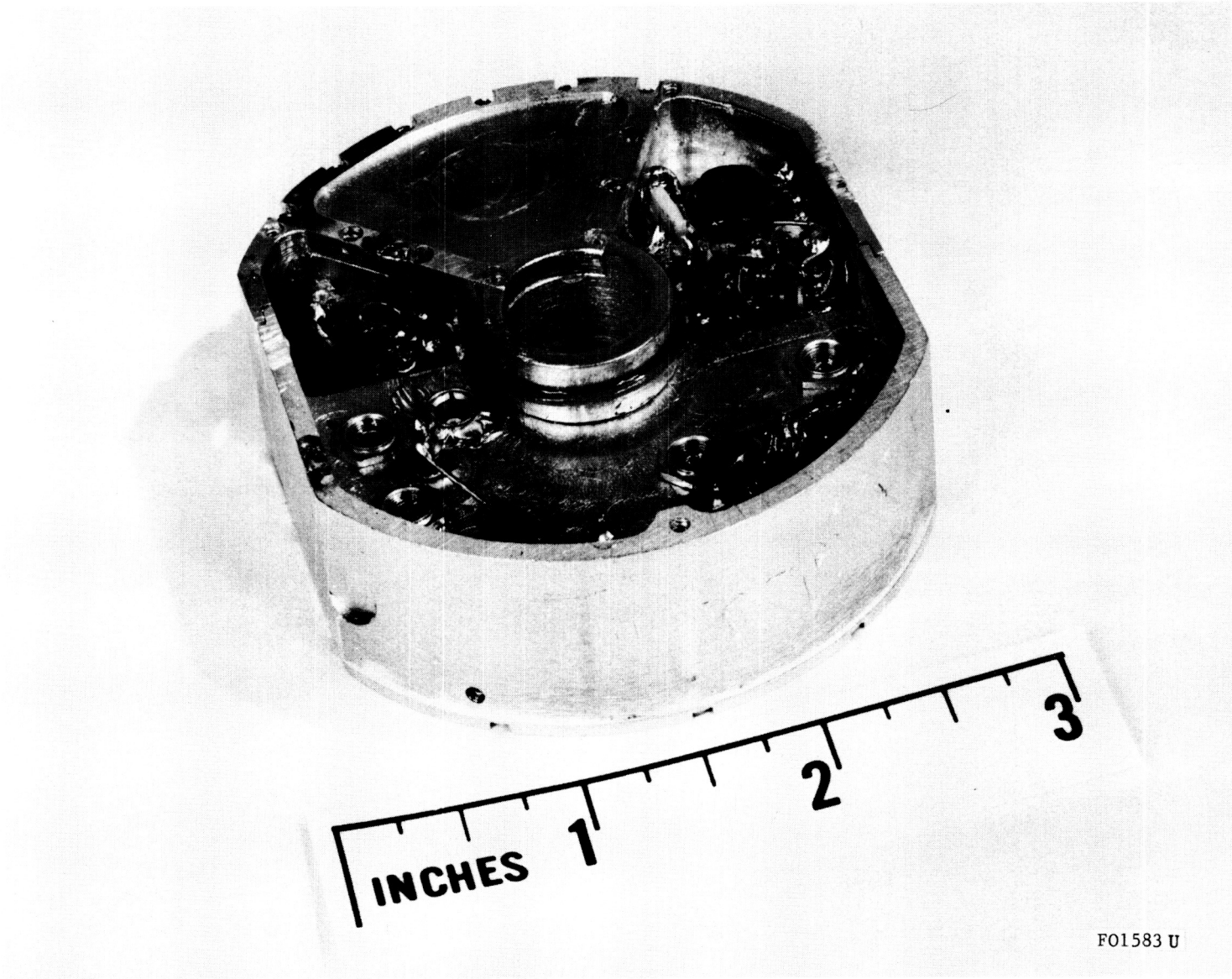

FIGURE 5-39. TRANSMITTER MODULE FOR NO. 2 PROTOTYPE PENETROMETER

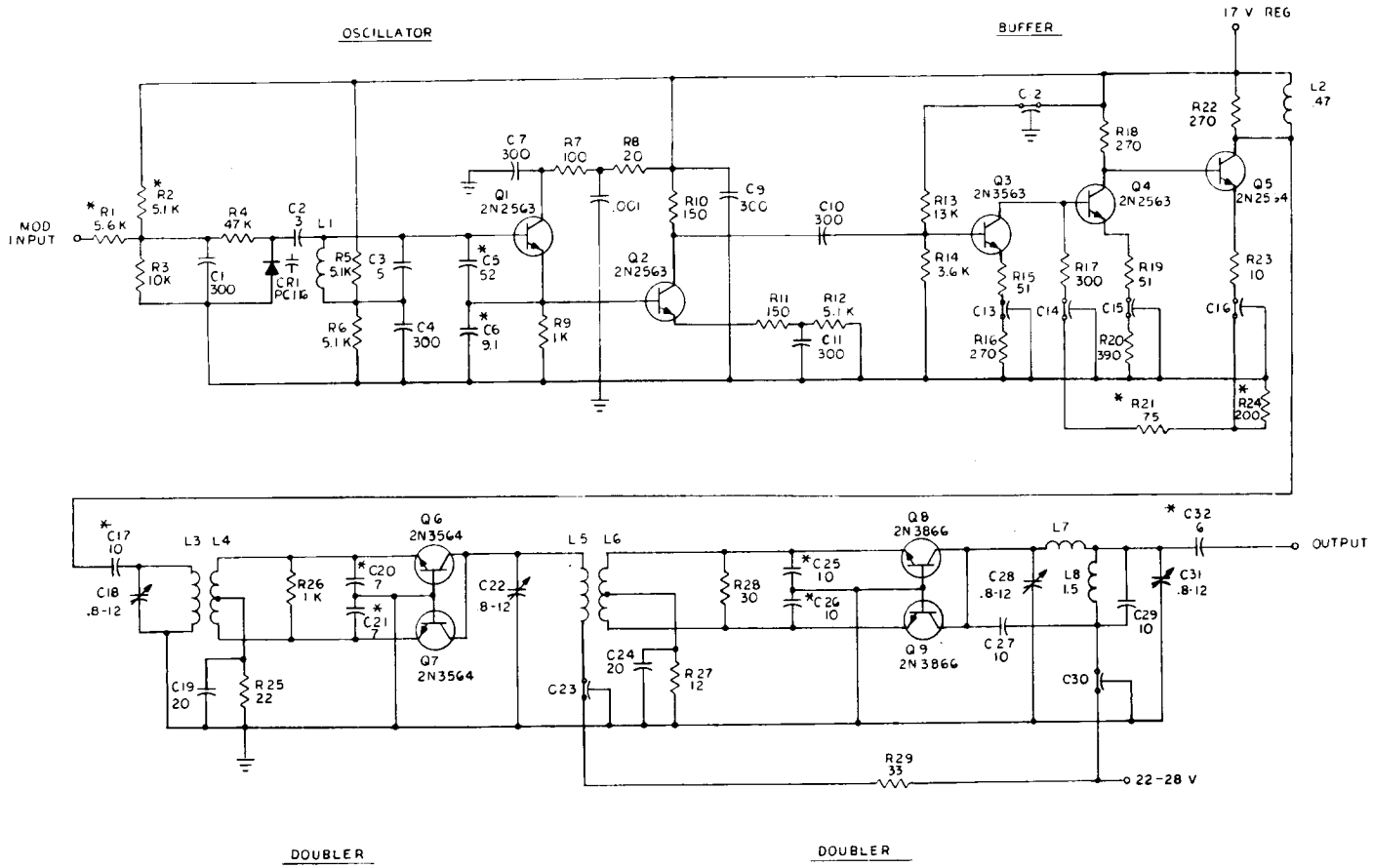

F01286 U

NOTES:
1. *SELECTED VALUES.

FIGURE 5-40. TRANSMITTER SCHEMATIC FOR PROTOTYPE NO. 2

5.4 ANTENNAS

5.4.1 INTRODUCTION

The antenna system consists of two orthogonal loops centered around the ball structure with approximately 0.5 inch spacing between the loop radiators and the ball. The two loops are fed in phase-quadrature to produce a quasi-isotropic field pattern. The loop radiators are self-resonant slow wave structures photo-etched on a flexible fiberglass base and supported by polypropylene rings.

The antenna feed consists of two orthogonal feed loops which inductively couple power into the radiating structures. Power is delivered to the feed loops by means of a transmission line hybrid network which divides the total transmitter power into two phase-quadrature components and also provides a large degree of load isolation. Tuning is controlled principally by the detail geometry of the slow wave radiating structure.

5.4.2 GENERAL DESIGN CONSIDERATIONS

In addition to the general problem of providing an efficient 450 Mc antenna on a 3.5 inch sphere, the difficulty of the antenna design was greatly increased by lack of published technical information in several problem areas.

(1) Although any antenna to be considered for use may be of a standard design type, such as an electrically small loop or dipole, its properties are considerably altered when in proximity to a metallic sphere.

(2) The antenna is to function when buried in a near-pure dielectric material and also in a material containing 5 percent magnetite.

(3) The balsa limiter is of a size such that the interface of the balsa and the burial material occurs in an intermediate region between the near field and the far field.

(4) The use of transistor output stages imposed a requirement for very low VSWR under both free-space and burial conditions to prevent reduction of incident power from the output stages as well as conventional reflection losses caused by antenna mismatch.

(5) The requirement for isotropic pattern coverage with redundant feed system imposed severe design restrictions.

In addition to these design problem areas, a number of difficult design constraints were imposed by the mechanical packaging.

(1) The limited space inside the structure prohibited the use of a conventional matching system of acceptable efficiency.

(2) All possible radiator, feed, and matching system designs were severely constrained by the high shock transients, as well as mechanical survivability.

5.4.3 INITIAL DEVELOPMENT

Initial tests were conducted on three antenna models representing three possible design types.

(1) Dual-feed loop.

(2) Circumferential dipole.

(3) Radial dipole.

A dipole pattern was desired from each of these configurations. It was intended that the final design would consist of two identical and orthogonally oriented elements of the chosen design type, fed in phase-quadrature to produce a total-field pattern which is quasi-isotropic.

The characteristics of special interest were:

(1) Minimum tuning sensitivity to presence of soil samples electrically representative of the lunar ground.

(2) Minimum tuning sensitivity to physical distortion of the antenna structure from impact.

a. Breadboard Models. The sketch, Figure 5-41, illustrates the three antenna types.

A photo of the dual-feed loop model is shown in Figure 5-42. The zigzag construction of the loop provides the necessary distributed capacity and inductance to resonate the structure at the design frequency. The feed and tuning system consists of two single-turn conductors diametrically located and coupled to the loop structure. A dipole-type pattern was

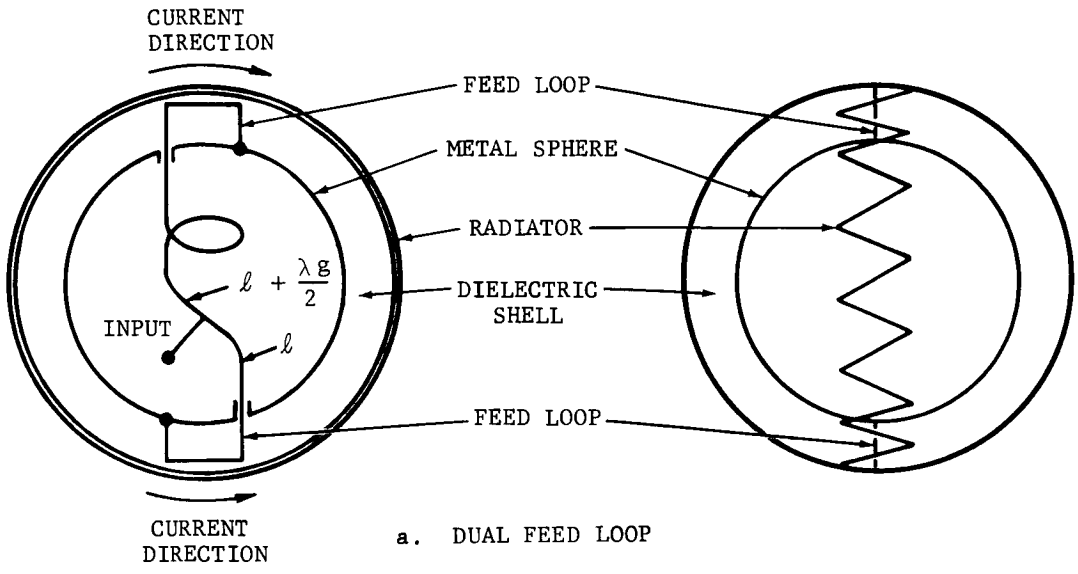

a. DUAL FEED LOOP

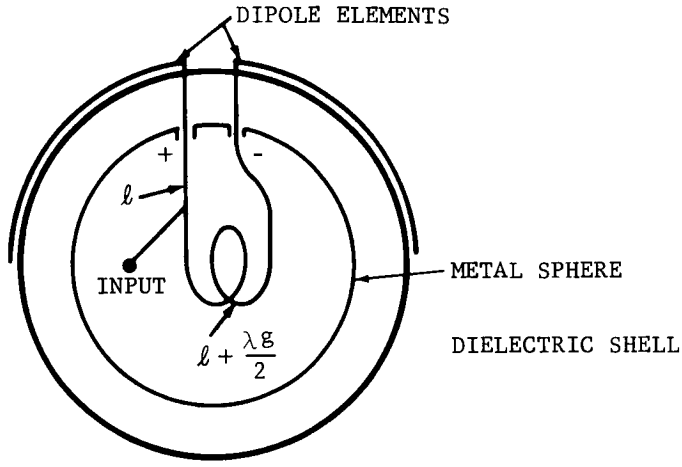

b. CIRCUMFERENTIAL DIPOLE

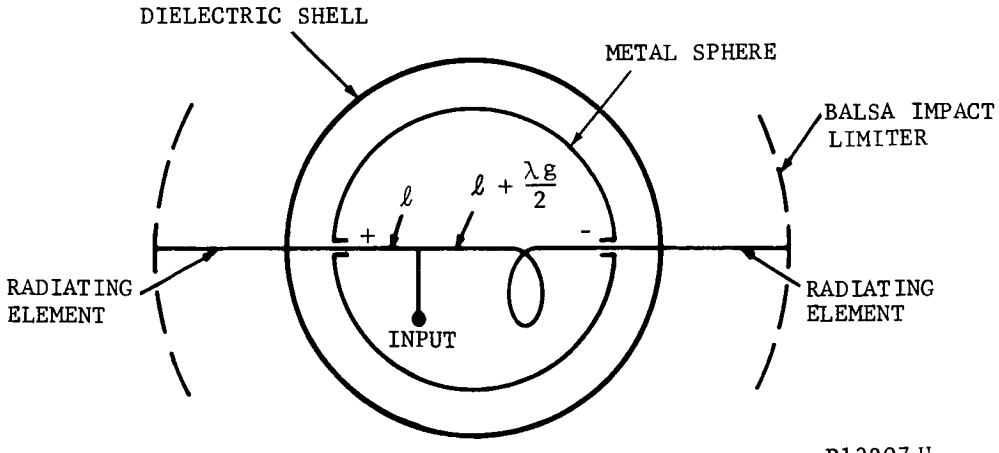

c. RADIAL DIPOLE

P13207 U

FIGURE 5-41. THREE POSSIBLE ANTENNA DESIGNS

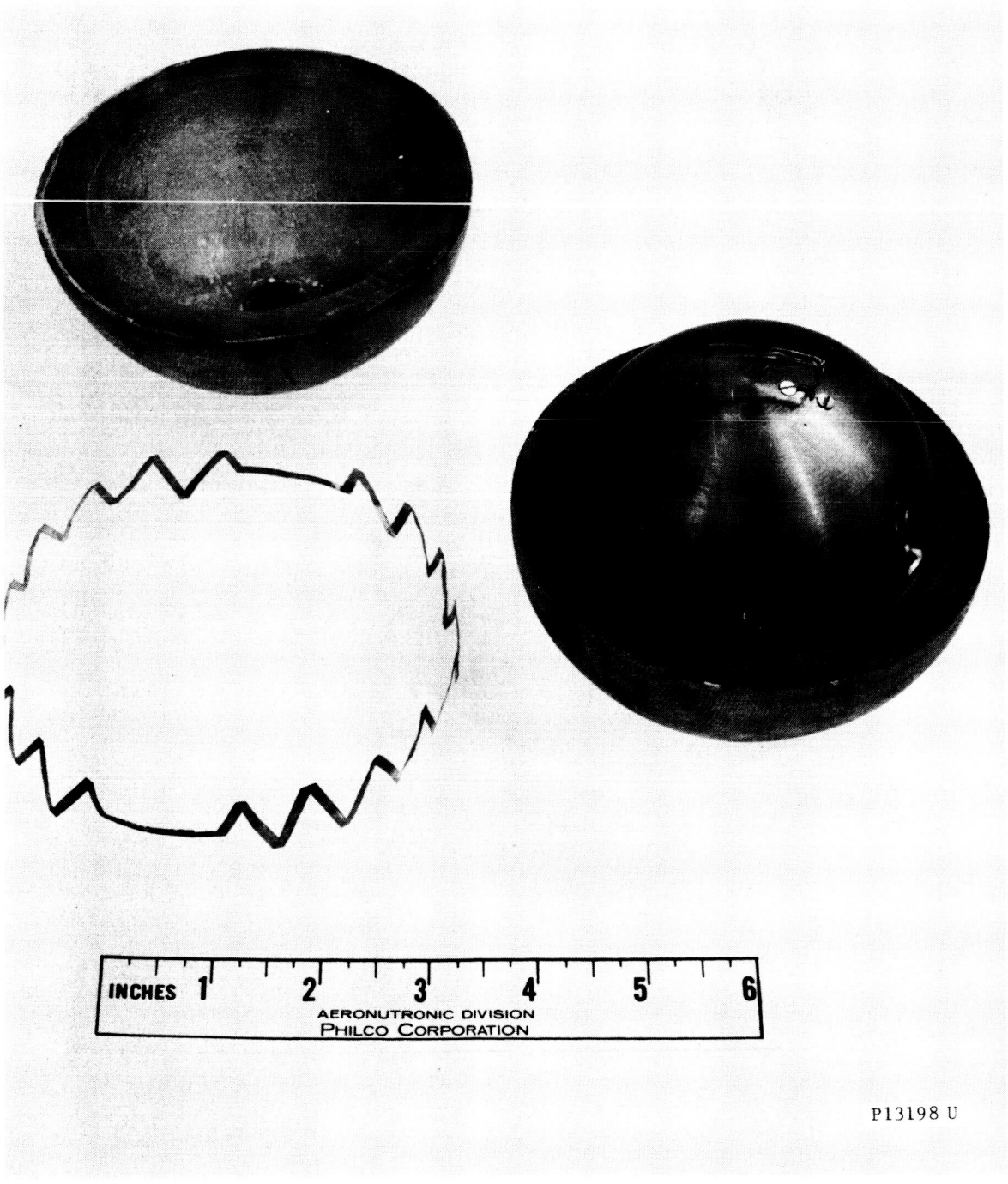

FIGURE 5-42. MODEL OF DUAL-FEED LOOP ANTENNA

achieved through use of the dual feed phased to provide currents as indicated in Figure 5-41. Patterns are shown in Figure 5-43. A bandwidth curve is shown in Figure 5-44 and an additional curve is included which shows the effect of proximity to a sample of medium grain quartz sand. For this test, 0.4 inch clearance was provided between the antenna structure and the sand. This separation corresponds to 80 percent crushing of the impact limiter and the antenna model was oriented for maximum effect. Appreciable detuning is noted, possibly because the loop, which is tuned by means of circuit elements on the radiating structure, does not have the sought-after low impedance properties of a nonresonant loop tuned at the base by means of a shielded network. Also, the loop is approximately 0.17 wavelength in diameter and generally not within the dimensional limits of electrically small loops.

The circumferential dipole model is shown in Figure 5-45. This system was impedance-matched by use of a commercial double-stub tuner. The VSWR of this combination is shown in Figure 5-46. The pattern is shown in Figure 5-47. Note that no pattern distortion results from the presence of the ball because of the electrically small diameter of the ball. Since the ball does not have the effect of a ground plane, it was predicted that impedance properties and efficiency would not be largely degraded by the presence of the ball. Results of a test of detuning caused by proximity to the sand sample are included in Figure 5-46. Again, 0.4 inch clearance and worst-case orientation was provided. No appreciable proximity effect is seen. It should be noted that these tests were of a preliminary nature, since the antenna models were mockups primarily intended for pattern investigation.

A photo of the radial dipole is shown in Figure 5-48. This system provided radiating elements 0.33 wavelength in length, tip to tip, since the elements extend to the outer surface of the impact limiter. In a final design the elements would be fabricated from a flexible steel braid and (in a complete system) phased for turnstile operation. Note that with a feed system, as shown in Figure 5-49, quasi-isotropic pattern coverage is provided even in the event of loss of one of the transmitter output stages or any one of the 4 elements. The bandwidth is indicated in Figure 5-50 along with results of the soil proximity test, as described for the other two models. To date, this model was impedance-matched only with a commercial double-stub tuner. The pattern is shown in Figure 5-51.

A series of burial tests were carried out on the three test models to indicate their relative impedance sensitivity to burial. Burial material was medium grain quartz sand (100 percent silicon dioxide) and results are shown in Figure 5-52. For these measurements the two dipole models were externally matched with a commercial double-stub tuner. The dual-feed loop has nearly matched input impedance and does not require external matching. For the dipole models, the amount of frequency shift under burial is reduced by loss in the matching system. The degree to which

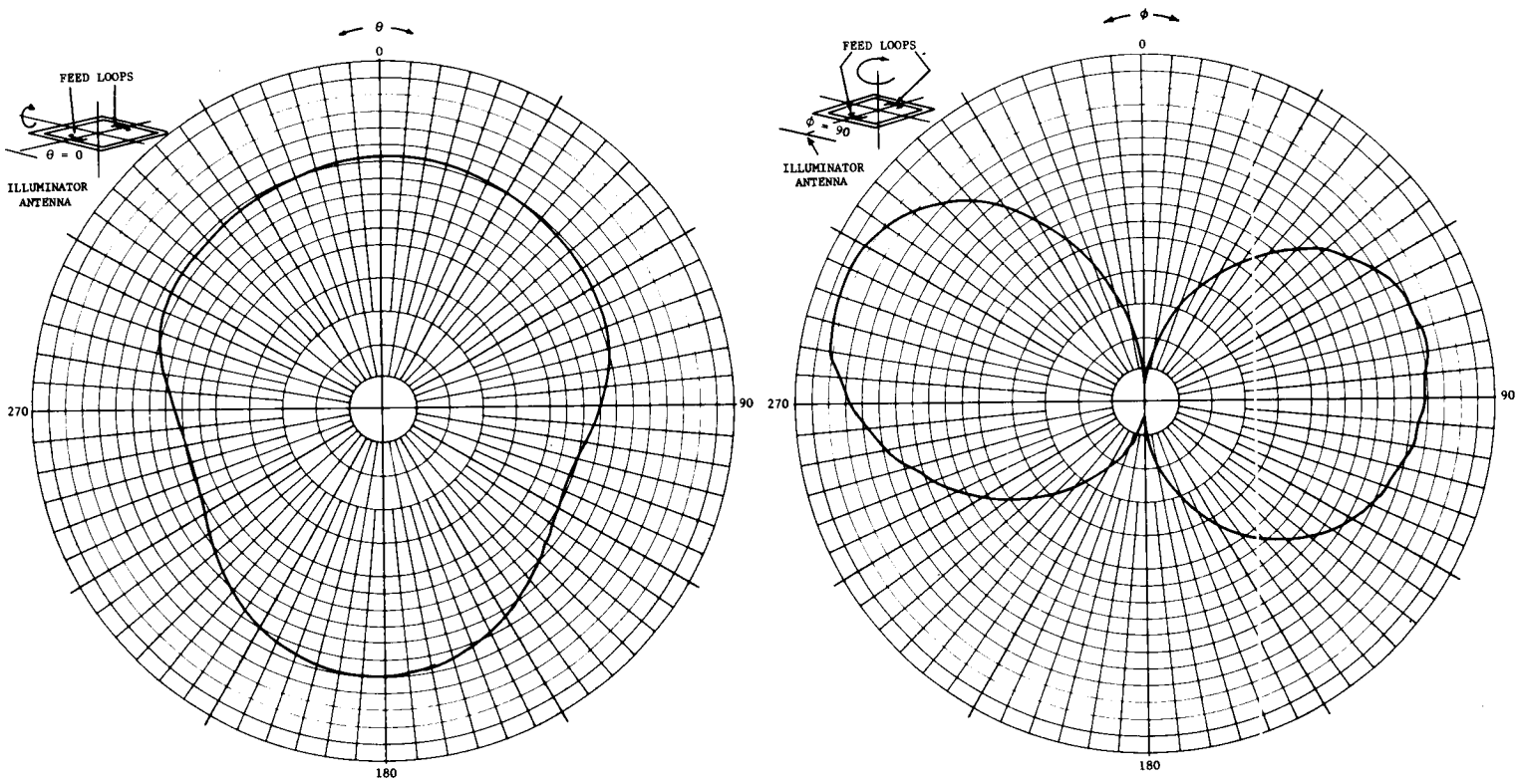

P13220U

FIGURE 5-43. DUAL-FEED LOOP ANTENNA PATTERNS

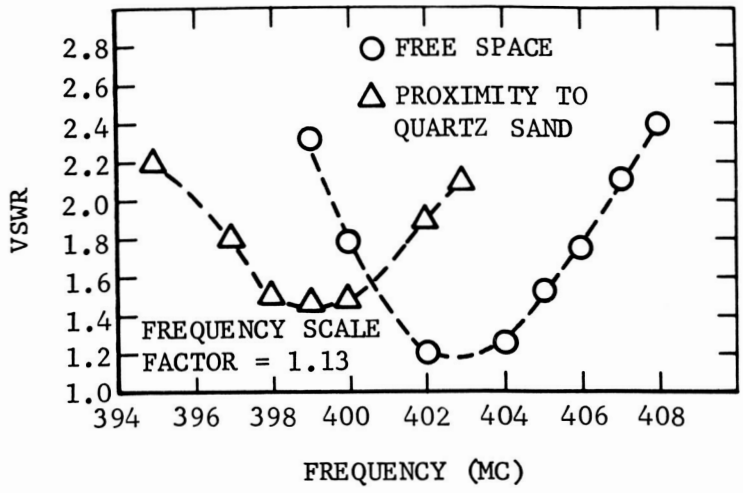

FIGURE 5-44. VSWR OF DUAL-FEED LOOP

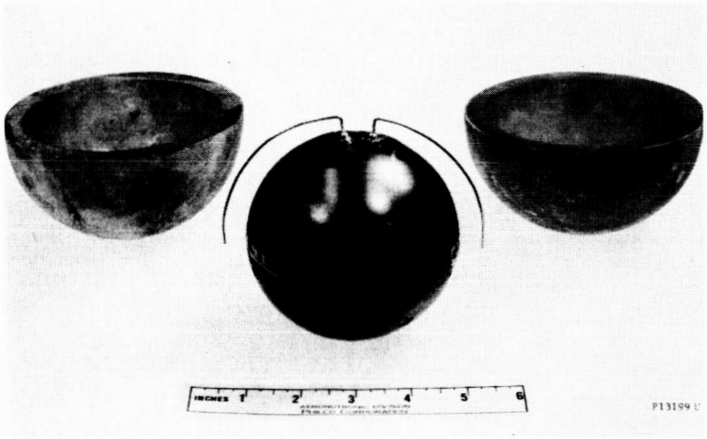

FIGURE 5-45. MODEL OF CIRCUMFERENTIAL DIPOLE ANTENNA

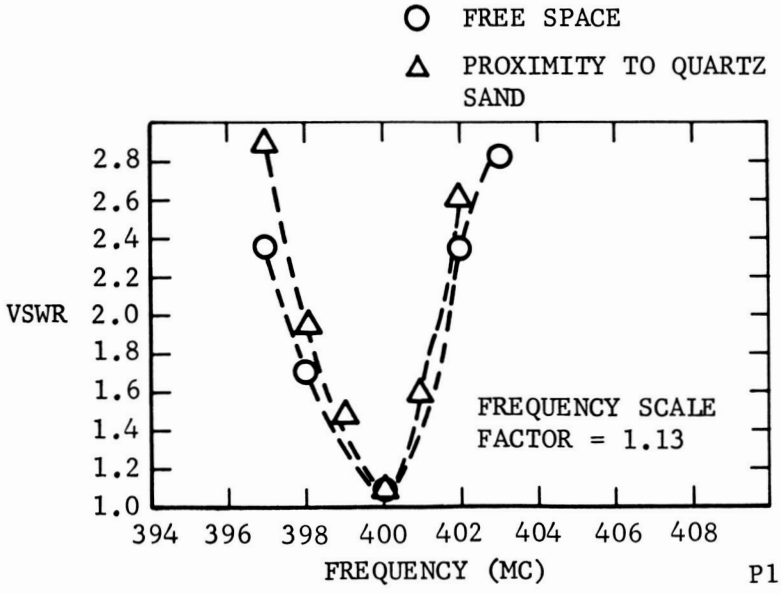

FIGURE 5-46. VSWR OF CIRCUMFERENTIAL DIPOLE

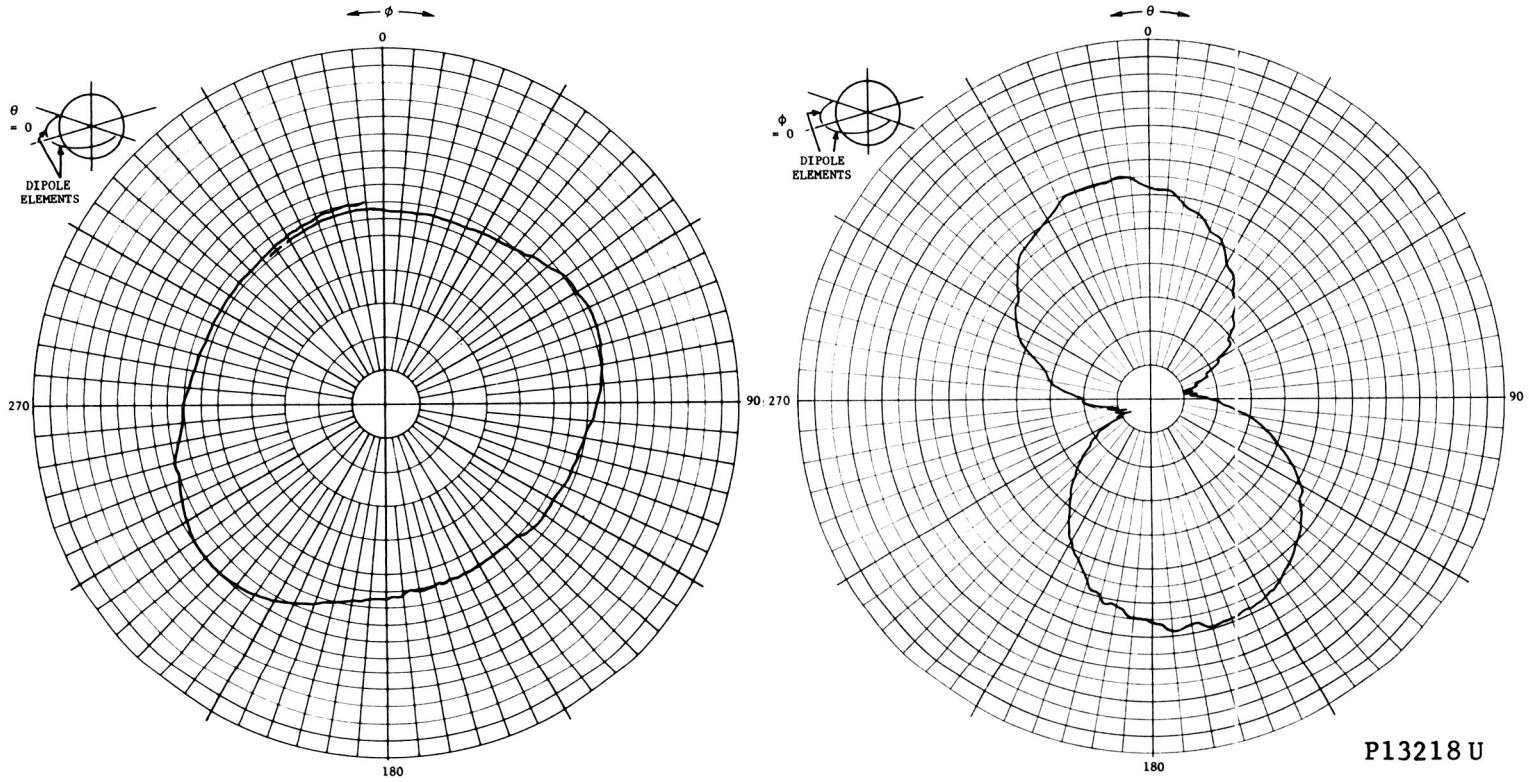

FIGURE 5-47. CIRCUMFERENTIAL DIPOLE ANTENNA PATTERNS

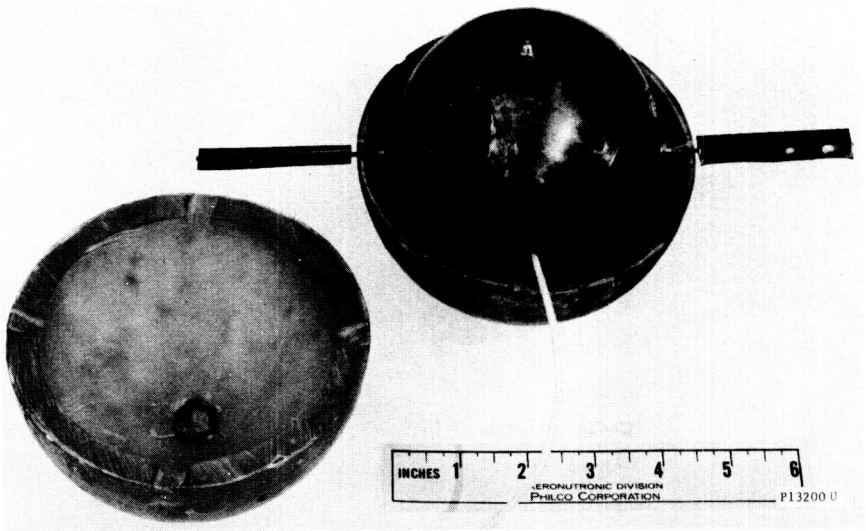

FIGURE 5-48. MODEL OF RADIAL DIPOLE ANTENNA

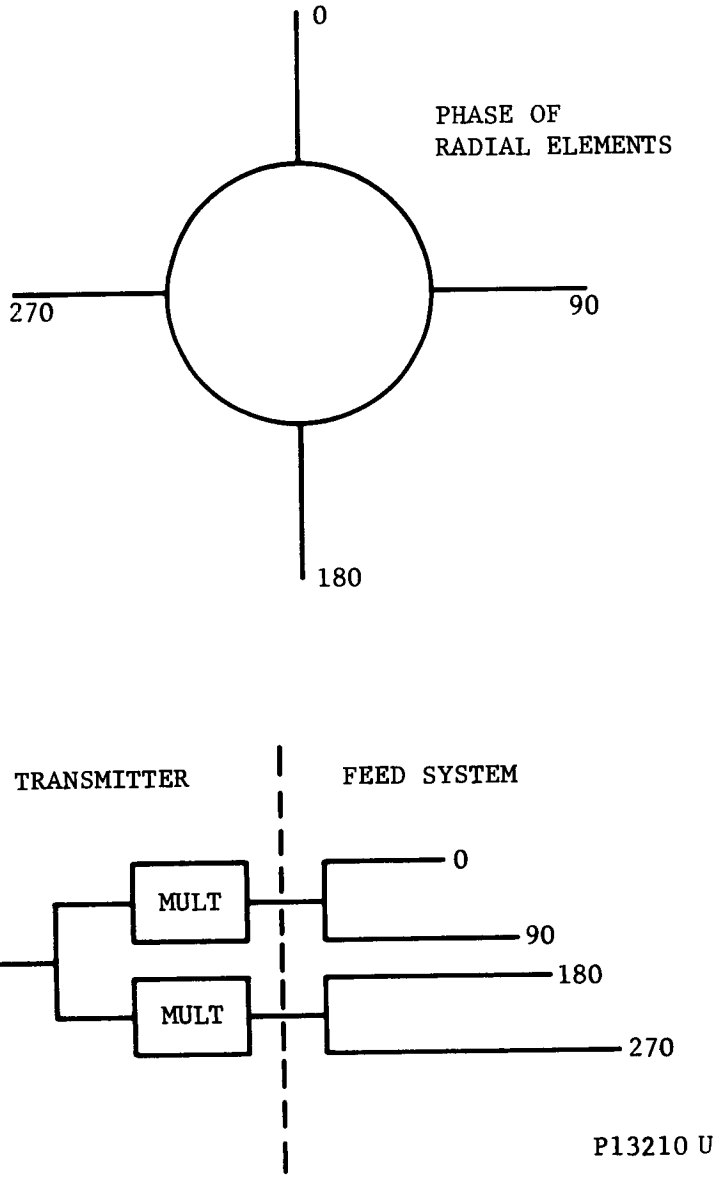

FIGURE 5-49. RADIAL TURNSTILE FEED SYSTEM

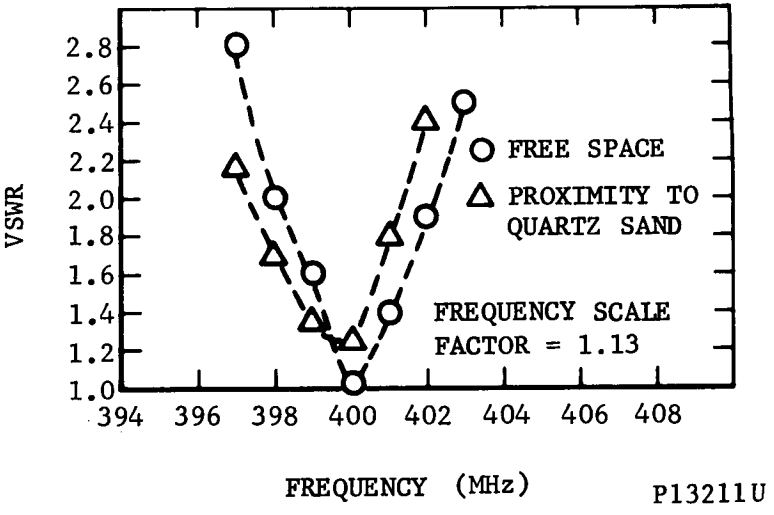

FIGURE 5-50. VSWR OF RADIAL DIPOLE

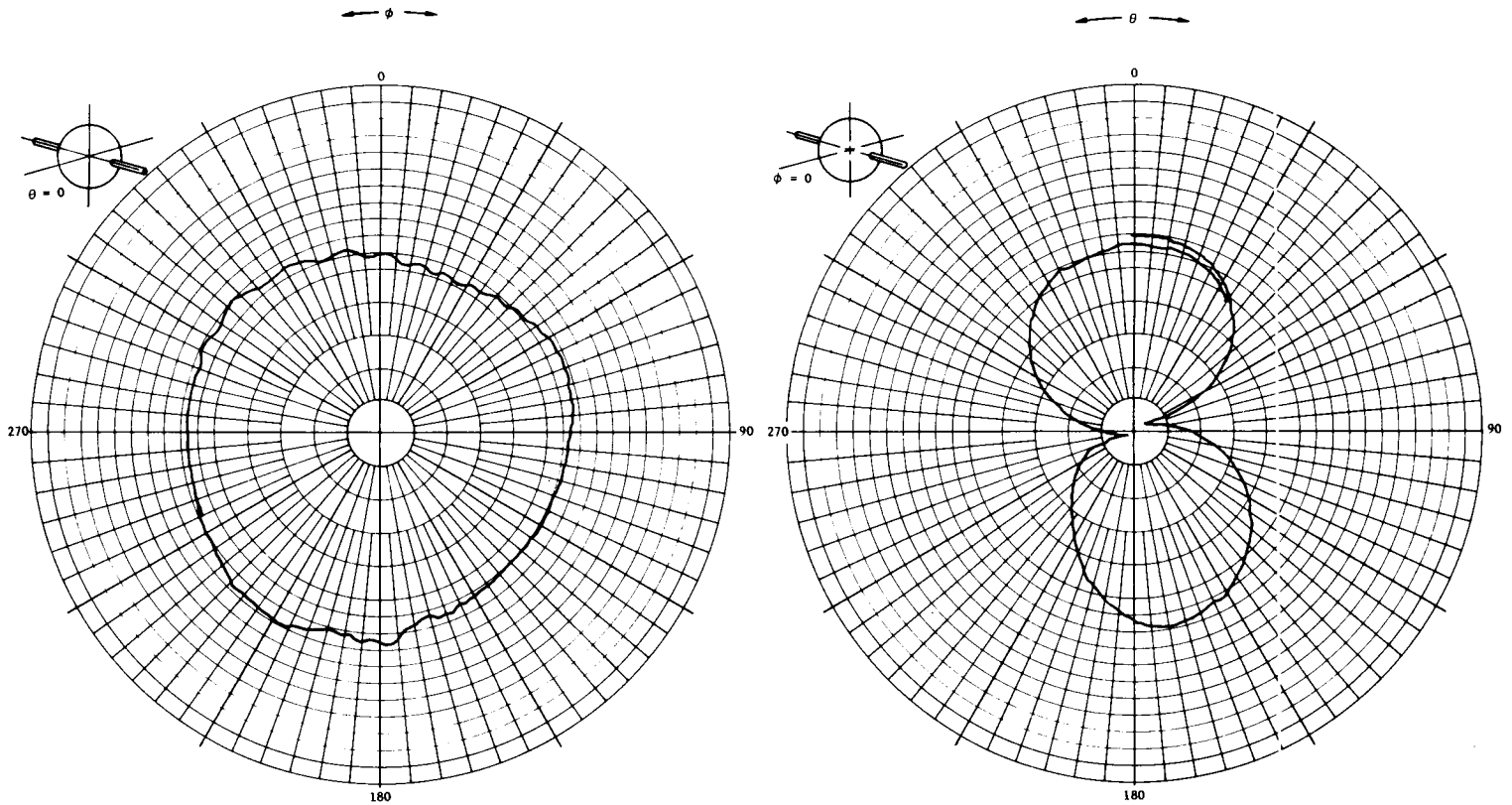

P13219 U

FIGURE 5-51. RADIAL DIPOLE ANTENNA PATTERNS

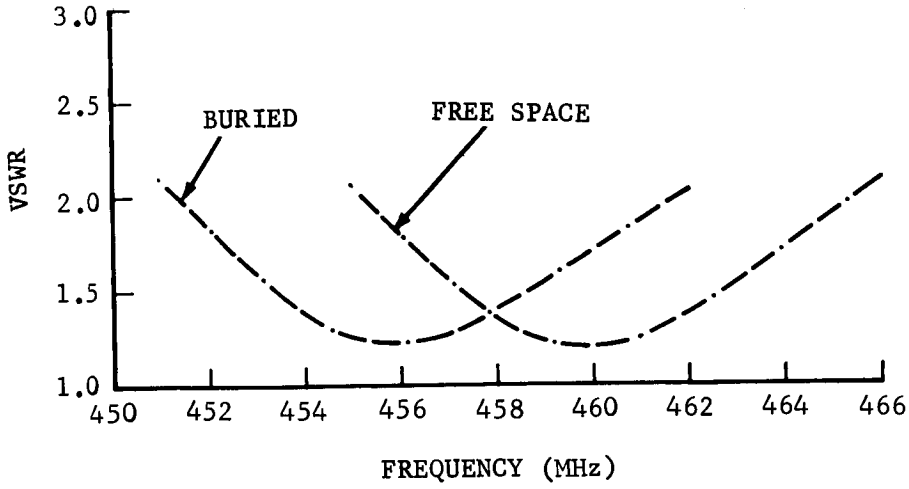

A. DUAL-FEED LOOP

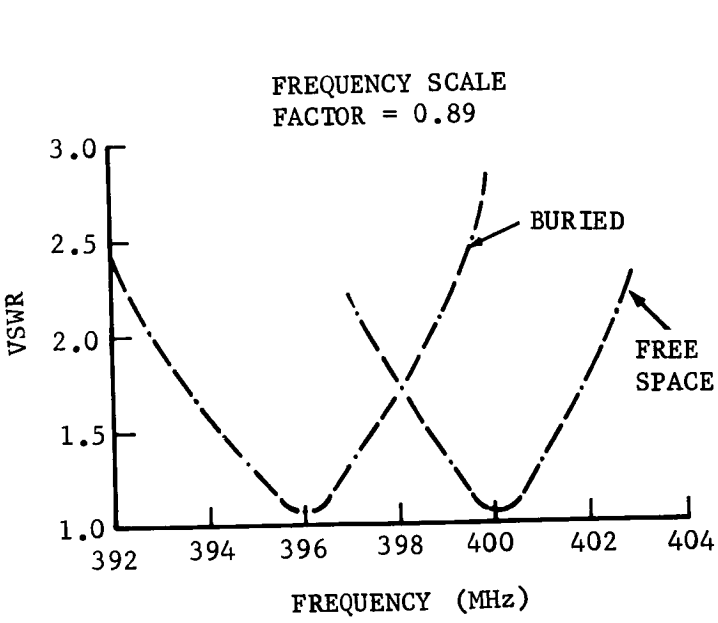

B. RADIAL DIPOLE

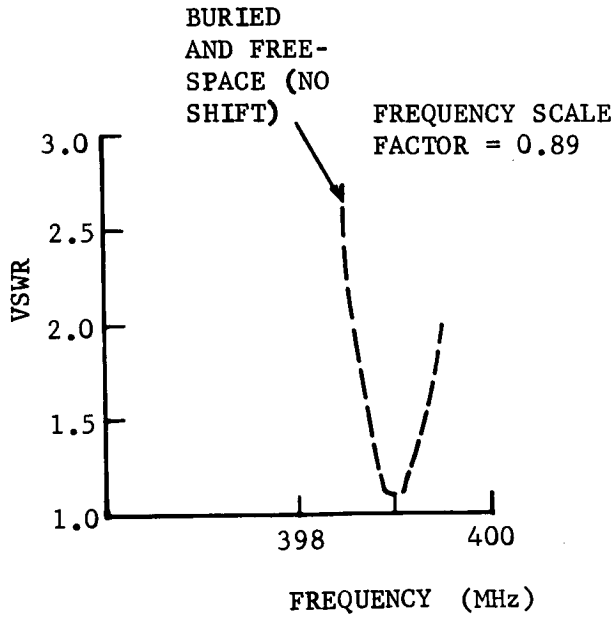

C. CIRCUMFERENTIAL DIPOLE

R13598 U

FIGURE 5-52. BURIAL TEST

the antenna detuning is masked by the matching network in a final system would depend on the efficiency of the matching network, which in turn is largely dependent on its physical size.

Since the three antenna types all exhibit essentially a dipole pattern, the relative efficiency of the three models is indicated by a relative gain measurement. In order to discriminate against reflections, the gain tests were made at a range distance of approximately 3 feet, which is well beyond the near field. The test set-up is shown in Figure 5-53. Again, for this measurement, the two dipole models were externally matched with a commercial double-stub tuner and the dual-feed loop which has a nearly matched input impedance did not require external matching. Results were as follows:

Antenna Model	Relative Gain
Dual-feed loop	0 db (reference)
Radial dipole	-4 db
Circumferential dipole	-12 db

b. Design Choice

(1) Antenna. Upon completion of these tests, it was decided to adopt the dual-feed loop design for the engineering model. The decision included the following considerations:

(a) Use of the circumferential dipole was considered to be prohibitive on the basis of its low efficiency. The efficiency of its radiating elements can be improved by means of increased conductivity and increased conducting area; however, this would tend to be offset by relatively large losses in the flight matching system which would necessarily be physically small and, thus, considerably less efficient than the laboratory double-stub tuner used in the gain measurement.

(b) The dual-feed loop is a self-resonant structure and is matched simply by adjusting the size and spacing of the coupling loop and thus requires no external matching network.

(c) From the standpoint of survivability under shock, the dual-feed loop has the advantage of requiring

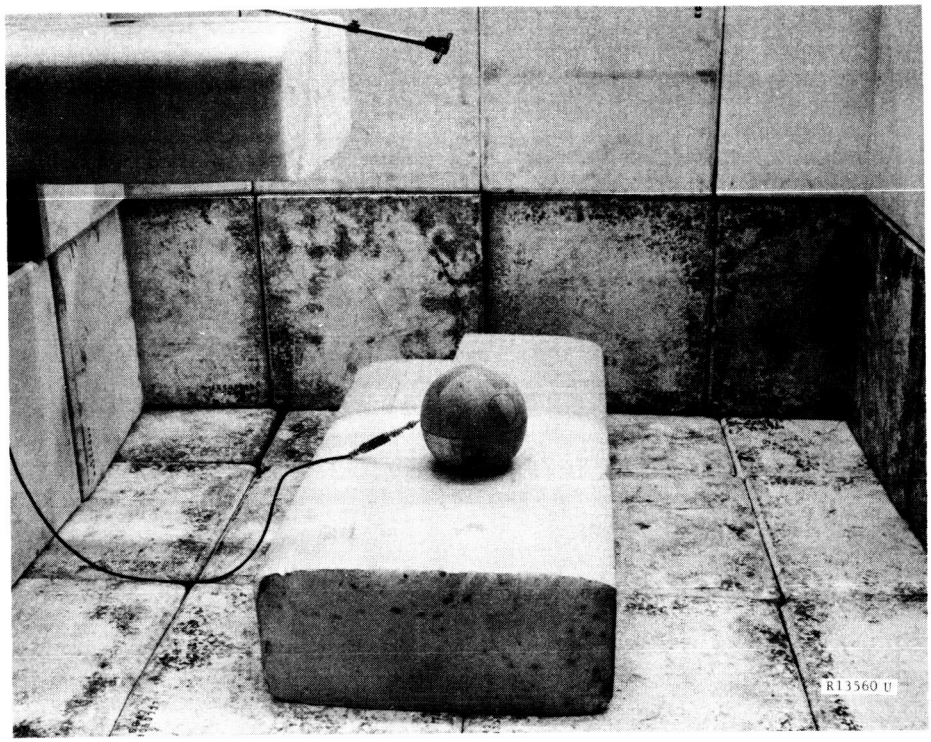

FIGURE 5-53. MEASUREMENT OF ANTENNA RELATIVE GAIN

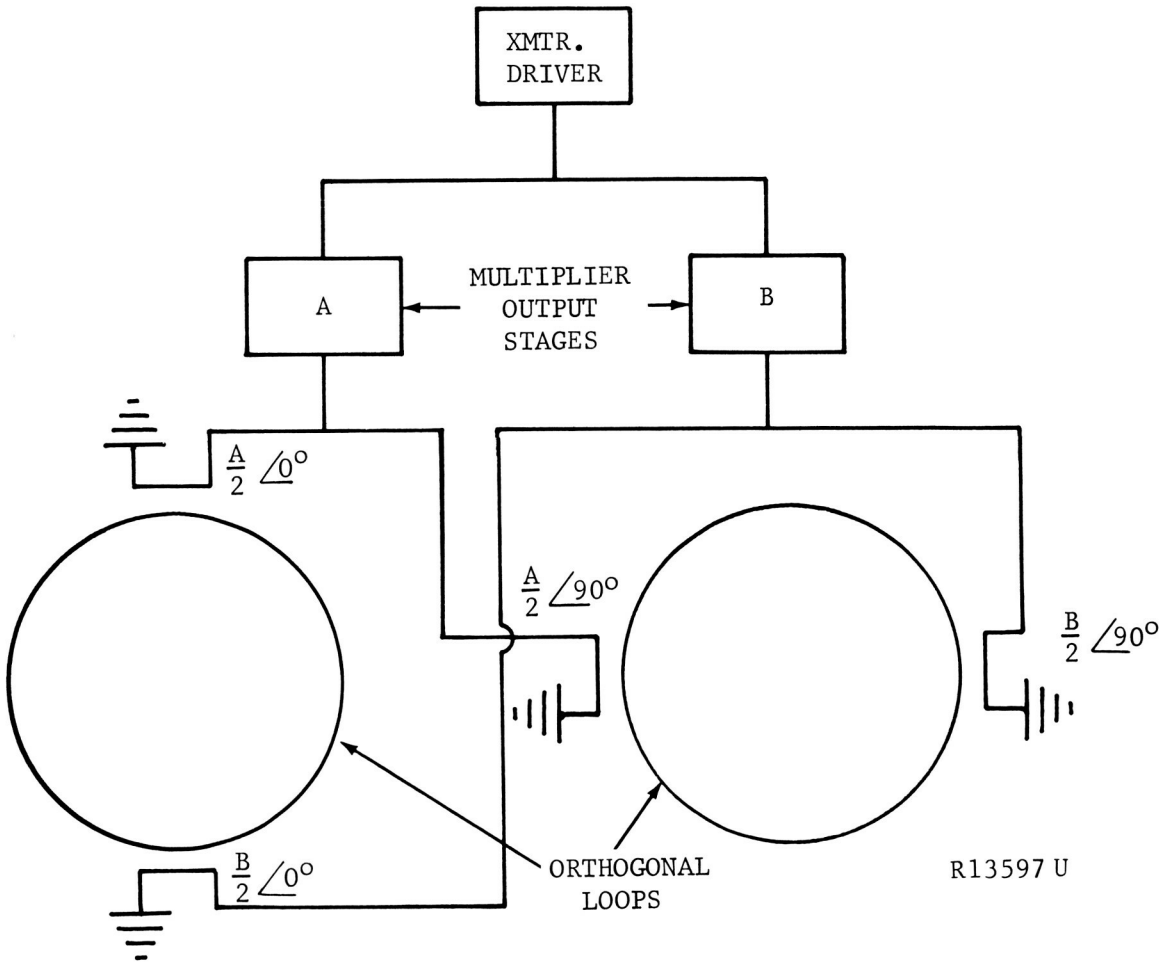

FIGURE 5-54. ENGINEERING MODEL ANTENNA FEED SYSTEM

no mechanical connection to its feed system, since coupling is provided by the magnetic field from the primary feed loops.

(d) It had been experimentally determined that, contrary to earlier indications, the dual-feed loop provides a satisfactory dipole type pattern with excitation to only one of the dual feeds. This allows the use of the feed system shown in Figure 5-54 in which a redundancy is provided which protects against loss of quasi-isotropic pattern coverage in the event of the failure of one of the two transmitter output stages.

(e) The radial dipole design has a possible advantage in the area of redundancy, in that redundant radiators are provided without excessive complexity. In the loop design antenna, redundancy is provided in the feed loops but not in the radiating structure. However, the loop structure is relatively simple, inherently rugged and has a wide latitude of mechanical design. Thus, it is in less need of redundancy, especially considering that the radial dipole elements would extend through the balsa limiter and be highly subject to partial damage.

(2) Feed System. An antenna feed system was devised which provides a large measure of isolation between transmitter and antenna, especially under conditions of burial where the impedance mismatch tends to be equal for the two crossed loops. The system is a result of a brief consulting effort by Dr. J. D. Dyson and was partially derived from a paper[4] by R. W. Masters.

The system is shown schematically in Figure 5-55 and its operation is explained as follows. The incident wave produces a like-polarity across R_1 with no resultant current flow. The reflected component in the lower branch of the circuit sketch is delayed 180 degrees relative to the reflected component in the upper branch, resulting in a plus-minus polarity across R_1. The resultant current flow in R_1 represents the dissipation of the reflected components.

Performance of the system is shown in Figure 5-56. It is seen that the input VSWR is nearly unity for equal mismatch of any value. For the case where one antenna is matched and the other open or short, (VSWR $= \infty$) the

[4] "A Power Equalizing Network for Antennas," R. W. Masters, Proceedings of the IRE, July 1949.

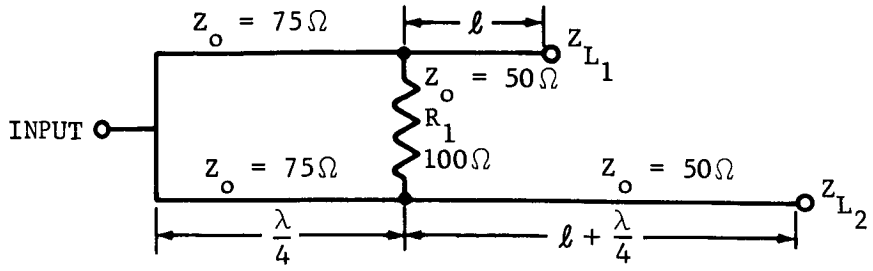

R14252 U

FIGURE 5-55. LOAD ISOLATION NETWORK

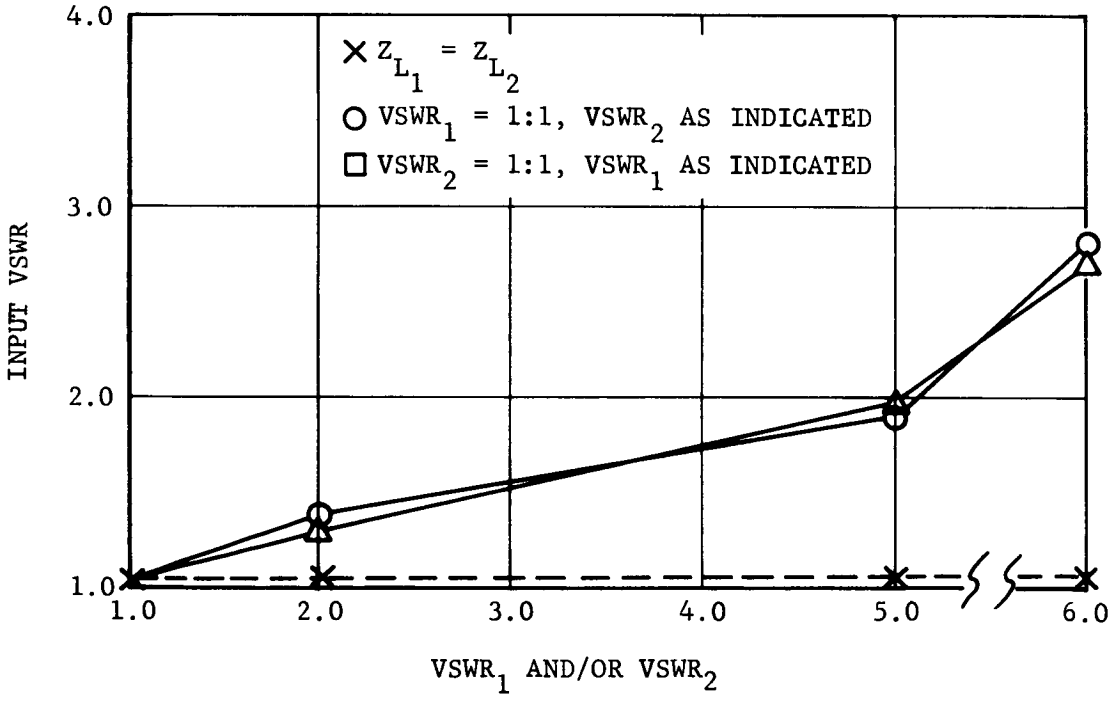

R14253 U

FIGURE 5-56. PERFORMANCE OF LOAD ISOLATION NETWORK

input VSWR is 2.8. A photo of the feed assembly is shown in Figure 5-57. Two such assemblies are required to provide excitation to four feed loops.

Experimental tests on the feed system indicated that the feed loops can provide a satisfactory input VSWR without coaxial connectors at the base, i.e., when fed by means of a coaxial cable and a simple dielectric supported feed-through. A VSWR of 1.2 was achieved for the engineering antenna model. VSWR measurements were made using the test setup shown in Figure 5-58 in which the input VSWR can be measured with or without coherent excitation to the opposite feed loop. In this way it was possible to measure the effect of failure of one output stage on the input impedance to the system. It was found that loss of excitation to one feed loop causes 0.2 db mismatch loss in the opposite feed loop.

5.4.4 ENGINEERING MODEL

The engineering model of the antenna system included both quadrature radiating loops, each with dual feeds. It is shown in Figures 5-59 and 5-60. Following initial impedance measurements, it was found necessary to position the feed loops to the configuration shown in Figures 5-61 and 5-62 to minimize coupling between the quadrature systems. Following this change, the measured isolation was 20 db. A plot of VSWR of one of the feed loops is shown in Figure 5-63. It was measured with excitation to its diametrically opposite redundant feed and with the quadrature system in place. It should be noted that the load isolation feed network (hybrid) was not in place for the VSWR measurements, since it largely reduces input VSWR because of load mismatch.

A field pattern is shown in Figure 5-64. The fine grain variations are generated by rotating the illuminating dipole to indicate polarization axial ratio. The pattern is seen to be essentially the sought-after turnstile which provides quasi-isotropic total field coverage with varying polarization, including all possible polarization states.

A gain measurement was made, yielding a gain value of -2.8 db along the axis which passes through the feed loops.

A test was performed to determine the sensitivity of the antenna zig zag structure to physical deformation from impact. A 1/2 inch portion of the zigzag conductor was depressed toward the ball in increments up to 3/16-inch with results as shown plotted in Figure 5-65. These results indicate a minimal sensitivity to deformation and this is attributable to the fact that the ball structure is small in terms of wavelengths and does not function as an electrical ground plane, as further evidenced by field pattern experiments earlier in the development program.

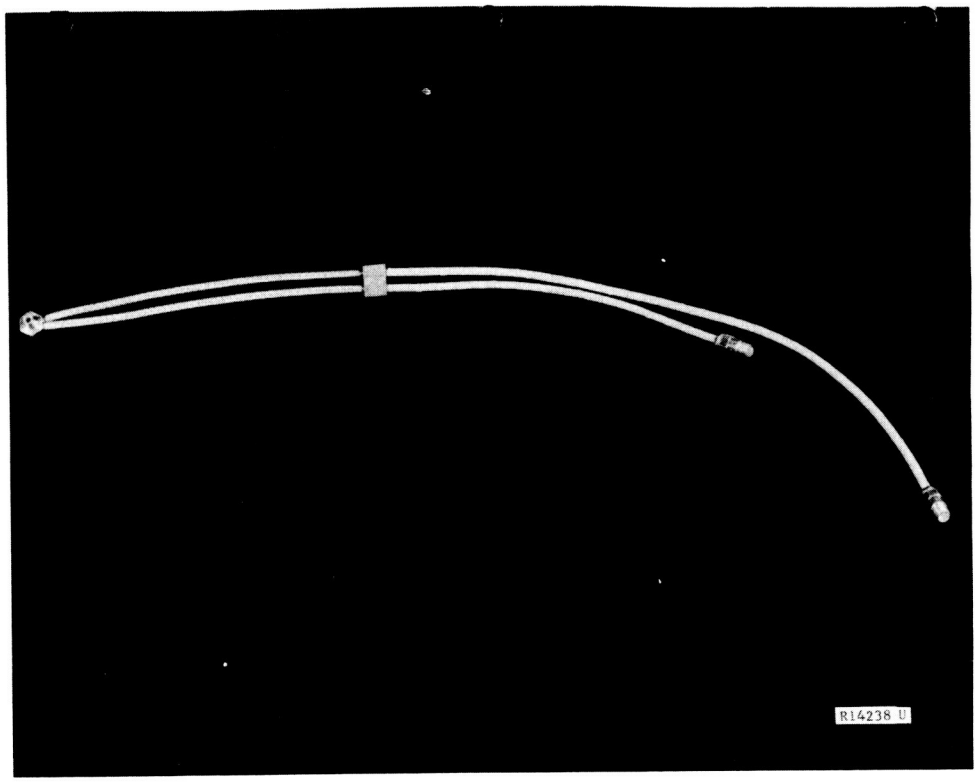

FIGURE 5-57. ANTENNA FEED ASSEMBLY

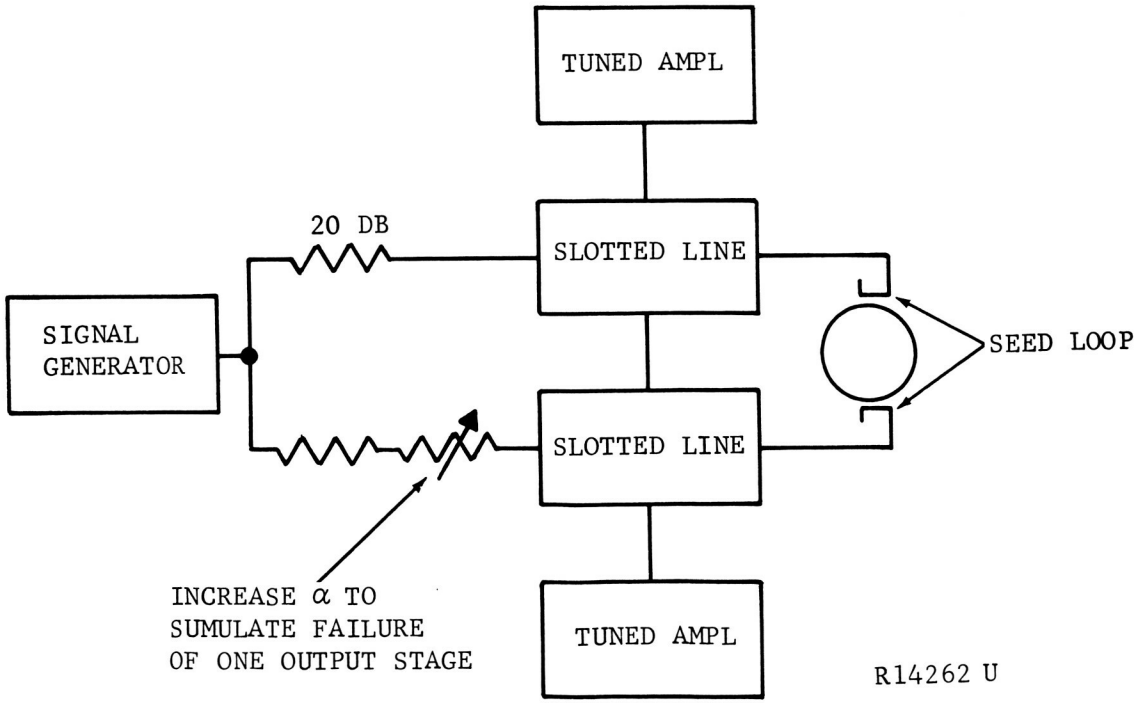

FIGURE 5-58. VSWR MEASUREMENT

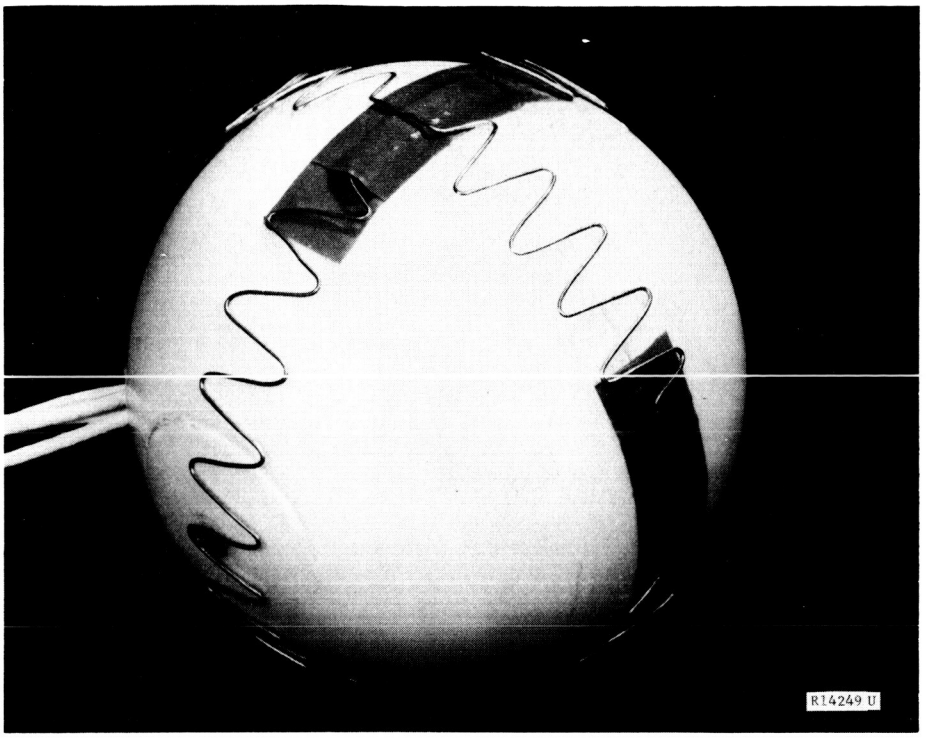

FIGURE 5-59. ENGINEERING MODEL OF THE ANTENNA

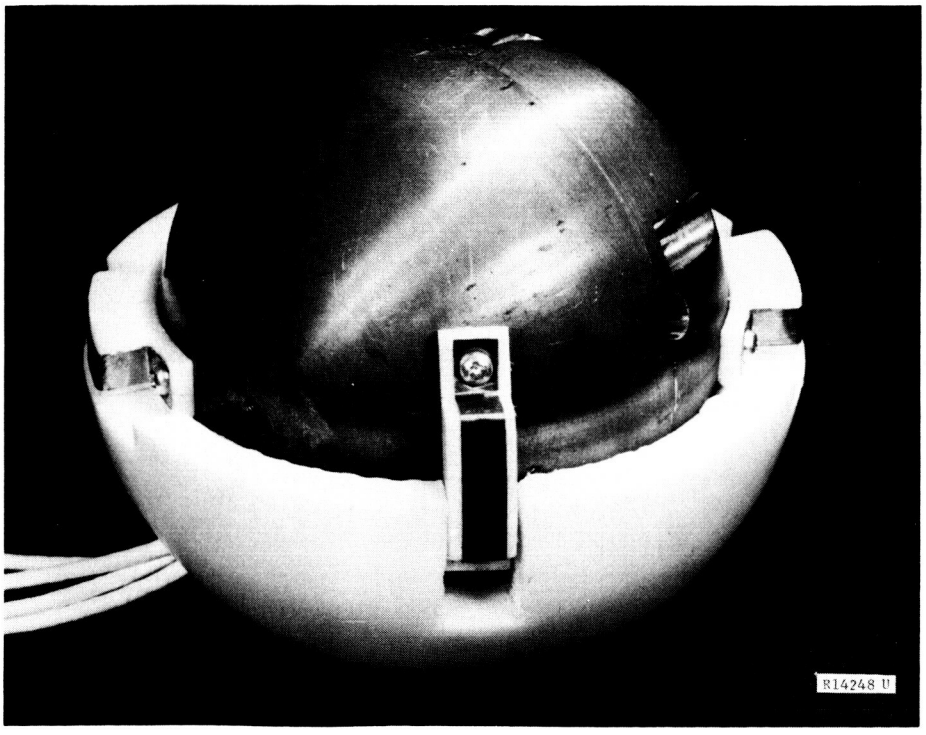

FIGURE 5-60. ANTENNA FEED LOOPS

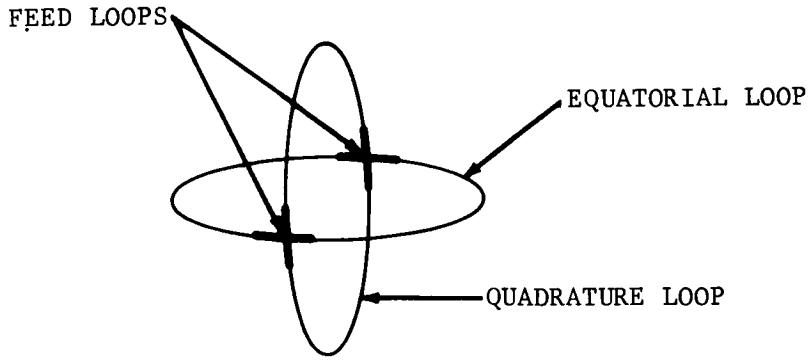

R15288 U

FIGURE 5-61. FEED LOOP POSITIONS

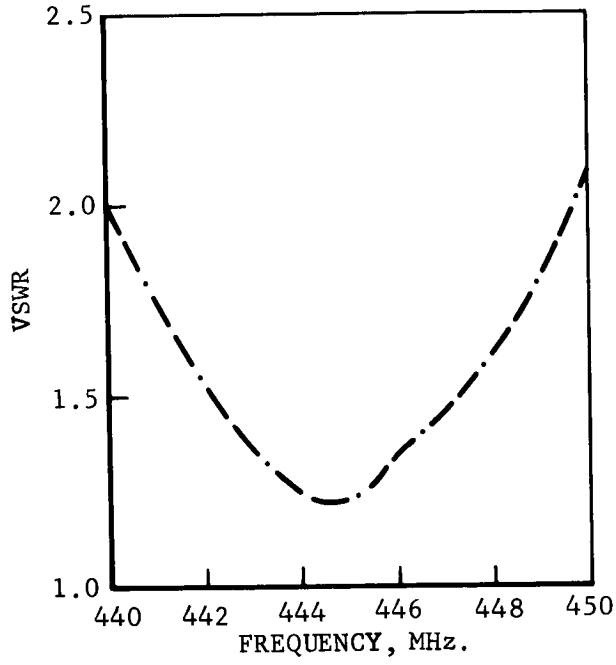

R15289 U

FIGURE 5-63. VSWR OF FEED LOOP

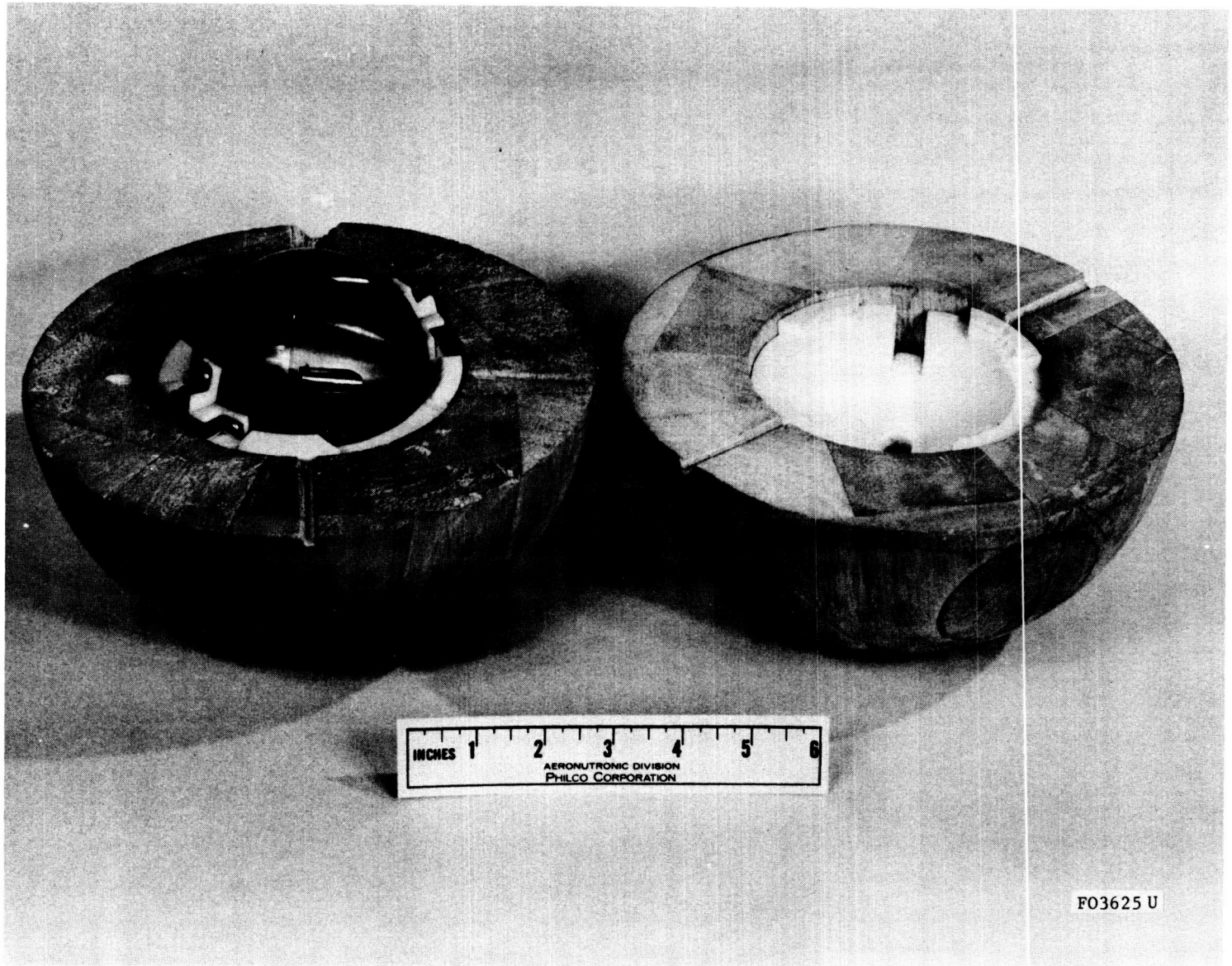

FIGURE 5-62. FINAL ENGINEERING MODEL WITH LIMITER

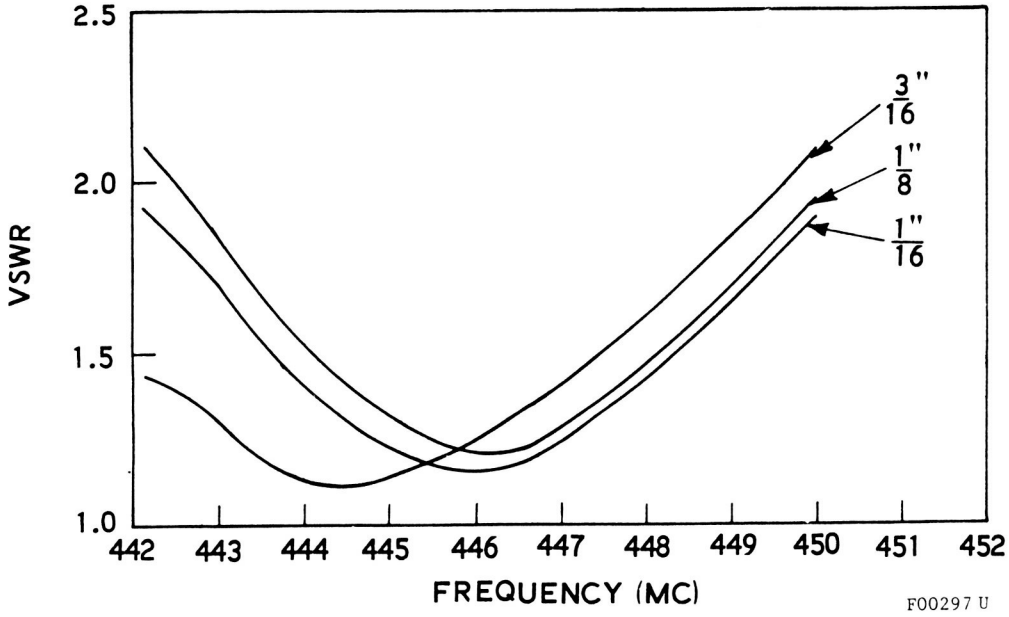

FIGURE 5-65. DEFORMATION TEST DATA

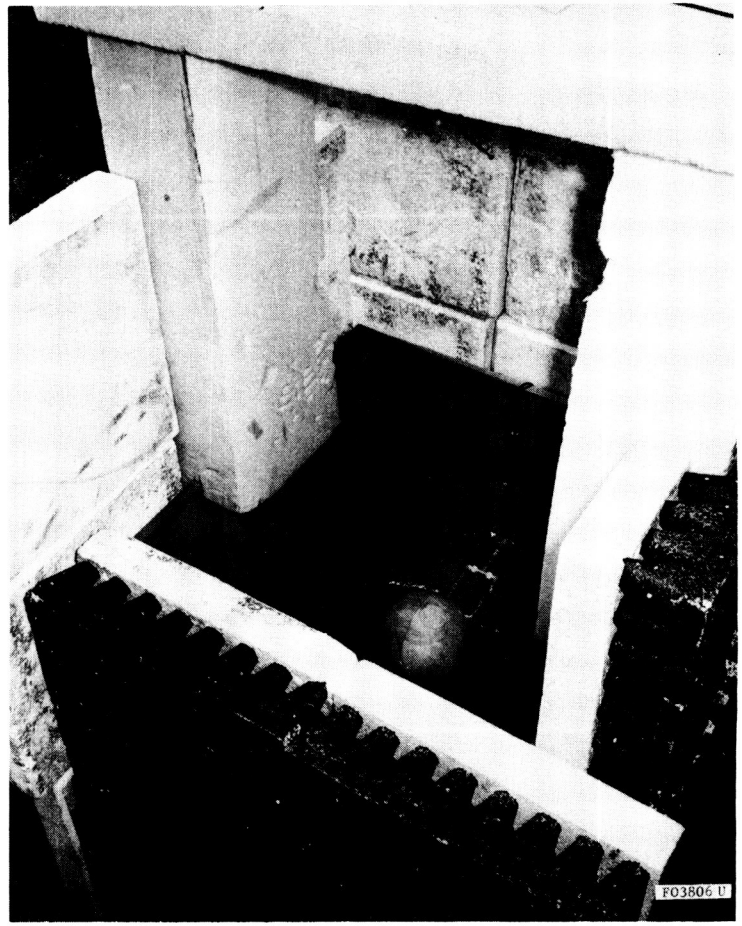

FIGURE 5-66. ANTENNA BURIAL TEST SETUP

A series of pattern tests were run to indicate the effect of a change of relative phase between the transmitter output stages. Phase shifts of 45 and 90 degrees were introduced by insertion of appropriate lengths of transmission line at the input to the hybrid feeds. Except for the expected overall amplitude decrease (3 db for 90 degrees) no pattern degradation was noted. The lack of sensitivity to phase change of the two output stages is an inherent property of the redundant feed system in which each feed loop is driven by half of the power from each of the two multipliers. Thus, any phase change in a multiplier stage has an equal effect on each of the two radiating loops and the desired phase quadrature is maintained.

a. Engineering Model Burial Tests. Signal loss caused by burial can be separated into three separate loss components.

(1) Loss caused by impedance mismatch.

(2) Dielectric loss in the burial material.

(3) Reflection at the surface interface.

Burial attenuation measurements were made in which an rf signal from the antenna model was measured at a remote distance, at normal incidence, before, and after introduction of soil sample material around the antenna model. These measurements constitute a direct measurement of the sum of the three loss components noted. Measurements were taken with two soil samples, Nevada 120, a medium grain quartz sand representing a nearly pure dielectrical soil material, and basalt silt containing 5 percent magnetite which represents a maximum loss soil.

The total signal loss when buried to the center of a cubic yard of Nevada 120 test material was 4.5 db. Earlier burial tests indicated approximately 0.25 db mismatch loss caused by detuning. This leaves 4.25 db caused by soil attenuation and reflection at the surface interface. The burial test setup is shown in Figures 5-66 and 5-67.

It should be noted that under conditions of burial the transmission line hybrid functions as a load isolator and prevents a decrease of incident power from the transmitter under conditions of mismatch. Thus, the mismatch losses are limited to the value given by

$$db = 10 \log \frac{(P + 1)}{4 P}$$

where P = load VSWR

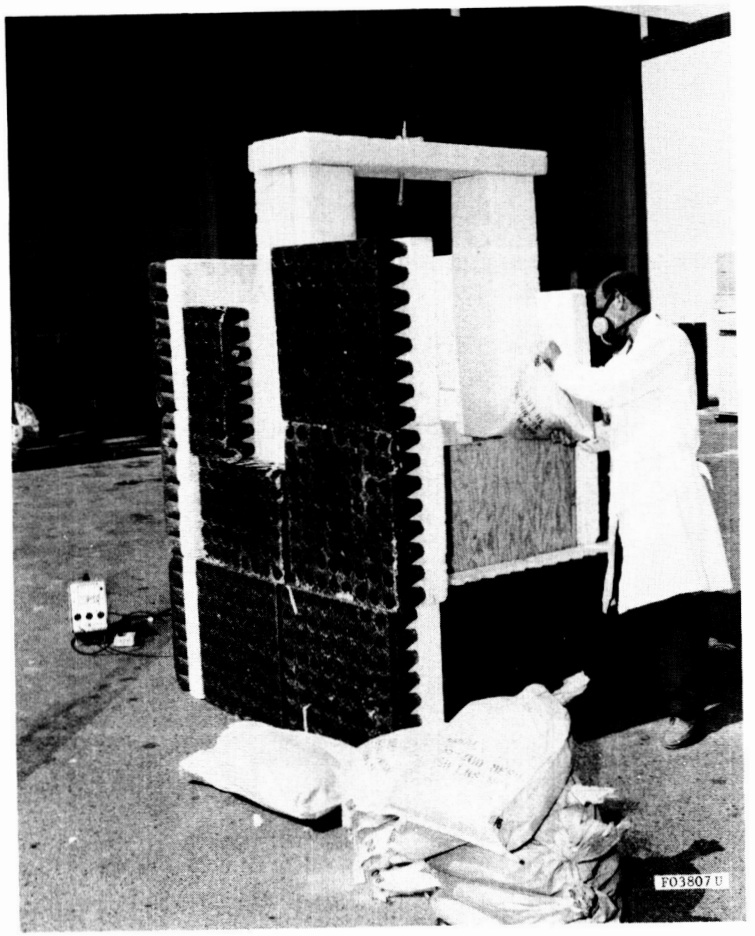

FIGURE 5-67. BURIAL TEST IN PROGRESS

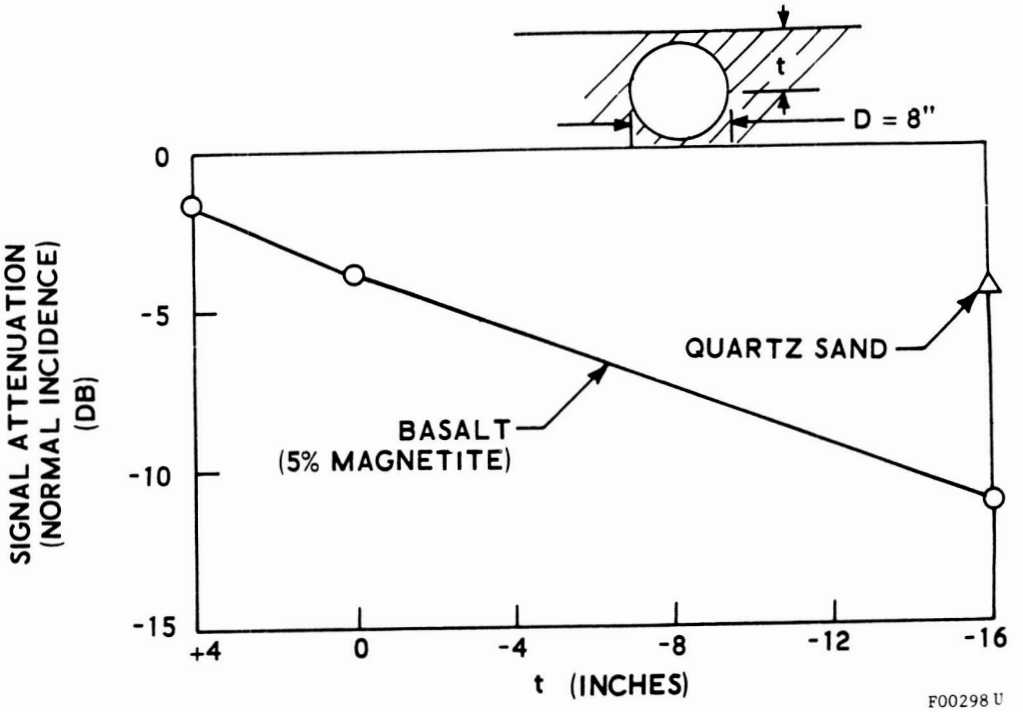

FIGURE 5-68. BURIAL SIGNAL ATTENUATION DATA

The curve shown in Figure 5-68 shows the total signal loss at normal incidence for burial in the basalt silt test material. On the basis of the estimated maximum penetration of 5 inches for this material, a total signal loss of 4 db is indicated. These tests were made with the feed isolation networks in place and an additional test series was run to determine the VSWR at the feed loop terminals (without the isolation networks). Results are shown in Figure 5-69 and it is seen that for all conditions of burial the antenna VSWR remained below 2:1, corresponding to 0.5 db mismatch loss. Thus, the sum of the dielectric loss and loss caused by reflection at the interface is indicated to be 3.5 db.

b. Power Reference Measurement. A measuring system was set up to establish a rf power output reference and a means to determine relative power output before and after system test intervals. It consists of an rf absorbing enclosure to house the penetrometer and a dipole receiving antenna, a bolometer mount to detect the rf signal and a tuned amplifier to indicate relative power output, plus the associated modulation equipment. It is shown schematically in Figure 5-70. The system also provided a means of determining the relative power outputs of the three prototype models.

5.4.5 PROTOTYPE ANTENNAS

Prototype No. 1 antenna is shown in the photographs, Figure 5-71 and 5-72. The slow wave loop radiators are photo-etched out of 0.015 inch copper on 0.005 inch fiberglass and supported by Teflon rings. The system includes two crossed feed assemblies diametrically located on the equatorial center section of the structure. The four feed loops are fed by two transmission line hybrids. Each hybrid is driven by one of the two redundant transmitter output stages.

The field pattern of Prototype No. 1 was measured after the 200 ft/sec test impact. No significant pattern change was noted (Figure 5-73). Also, no physical damage to the antenna system was found in the post-test inspection. The dashed lines in the pattern plot show the total field which is the vector sum of the orthogonal field components as measured by the rotating illuminator antenna. The pattern was also measured at various stages of the penetrometer assembly and at one intermediate point some degration of the pattern was noted. There is some evidence that the problem was due to extremely sharp bends in the miniature coaxial feed cables. The sharp bends were eliminated in the final configuration with good pattern results as shown.

In accordance with the change to a single transmitter output stage, Prototype No. 2 antenna system had a single feed system and, thus, only one hybrid feed assembly. With this circuit configuration, it was possible to feed both radiating loops with a single crossed-feed assembly

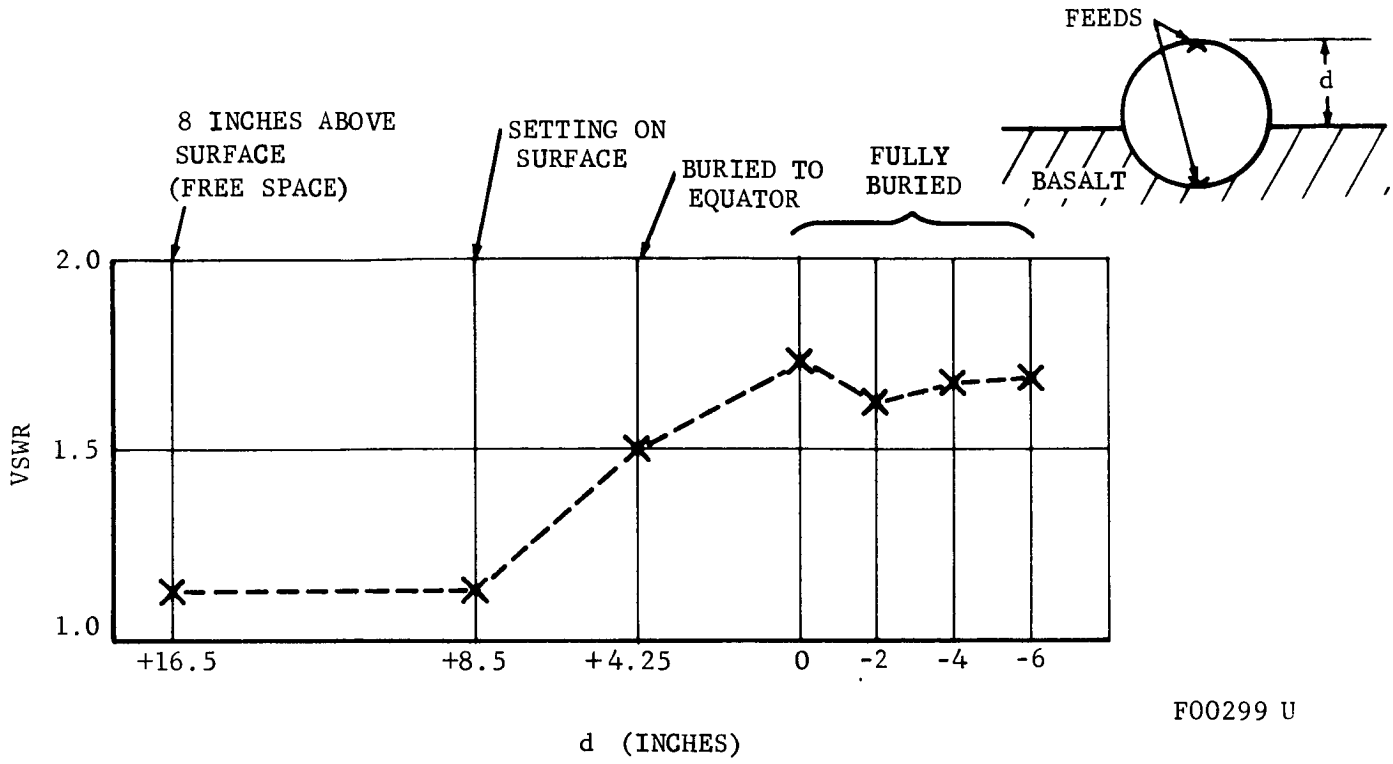

FIGURE 5-69. ANTENNA BURIAL TEST

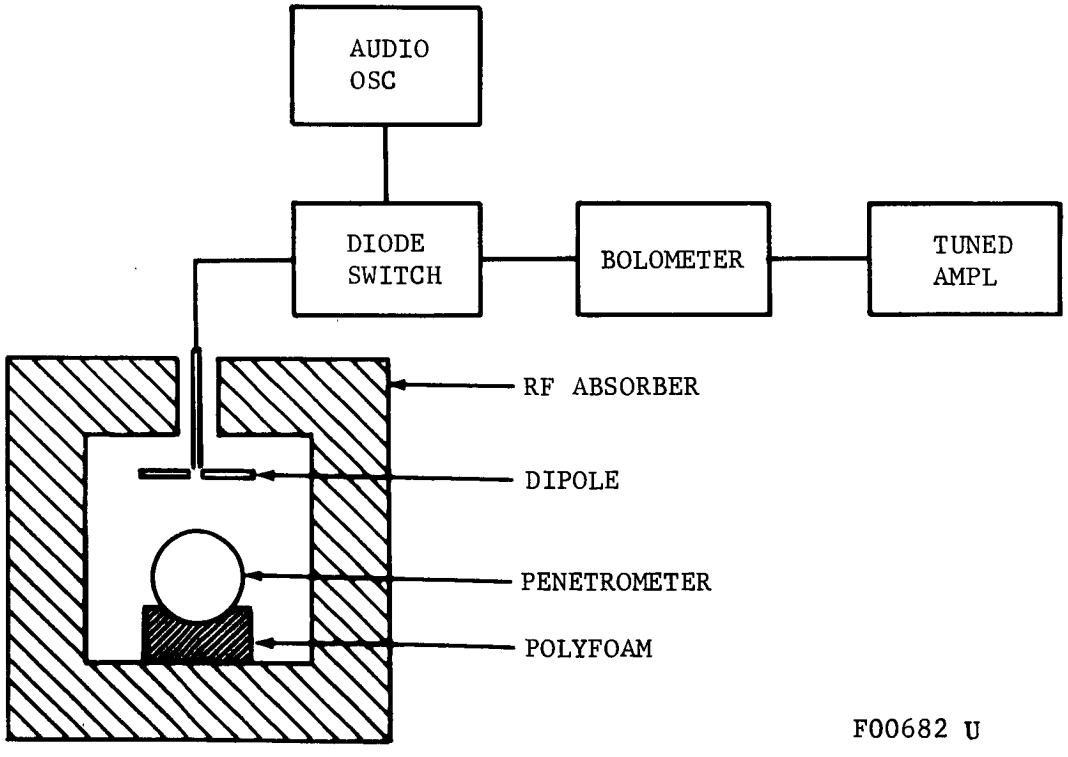

FIGURE 5-70. POWER OUTPUT REFERENCE TEST

FIGURE 5-71. ANTENNA RADIATING LOOPS

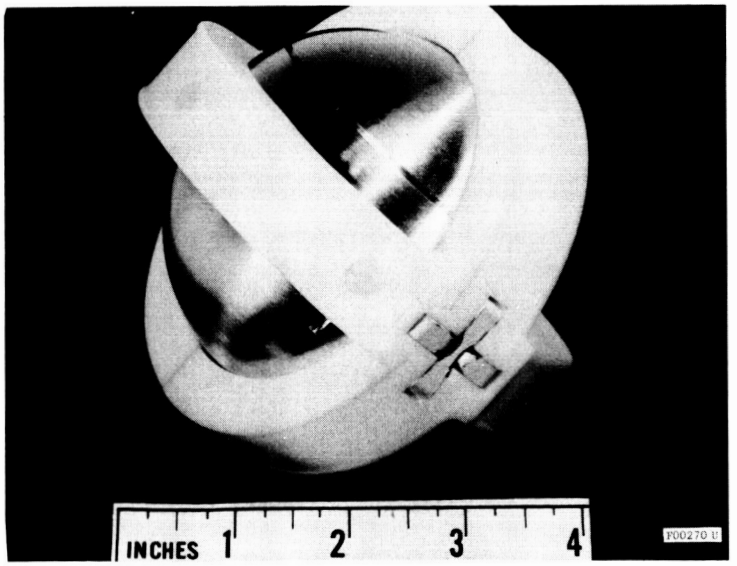

FIGURE 5-72. ANTENNA FEED AND RADIATING LOOPS

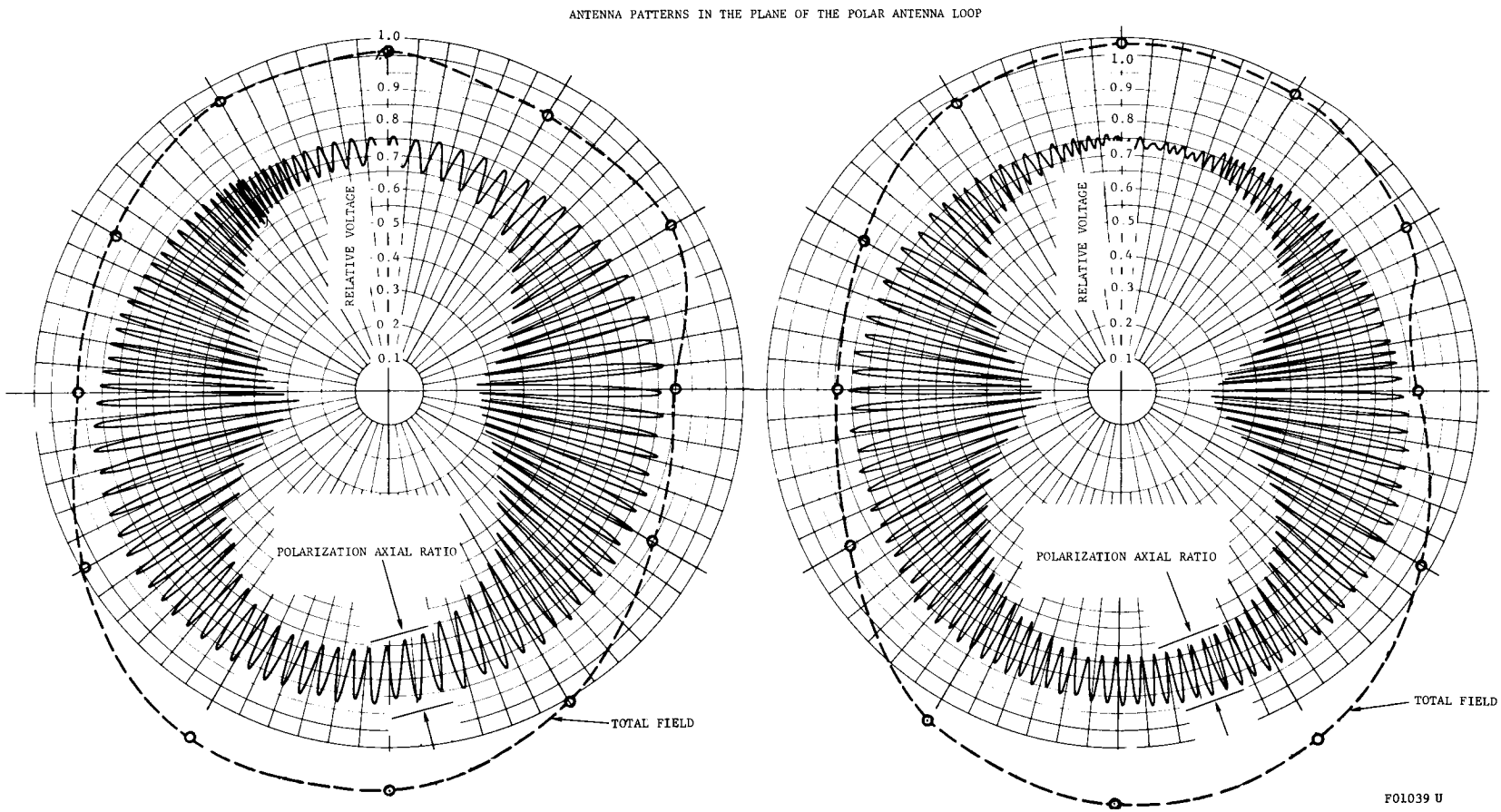

FIGURE 5-73. ANTENNA PATTERNS FOR PENETROMETER PROTOTYPE NO. 1

or alternately, to use to separate and orthogonal feeds at diametrically opposite ends of the ball. The latter arrangement, however, produces a considerably degraded pattern probably caused by a traveling wave effect which reduces current on the radiating loop with increased distance from the feed point. Under this condition, a phase error is introduced by the separation of the phase centers associated with the radiating loops with consequent degradation of the pattern and polarization axial ratio. Thus, it was elected to use the single cross-feed assembly on one side of the ball.

Two additional antenna changes were introduced in the Prototype No. 2. The feed loops were made slightly larger to improve the impedance match. This was required because of the increased density of the prototype balsa limiters relative to the engineering model limiter. Also, a new material was substituted for the Teflon used in the antenna spacers. It is a polypropylene having a dielectric constant of 2.2 and loss tangent of approximately 0.002. It is 43 percent lighter in weight and has superior structural properties relative to Teflon.

Following Hyge impact tests, the Prototype No. 2 was fitted with a replacement printed circuit radiator. Since it was not possible to gain access to the feed loop input terminals, the new antenna could not be tuned in the usual manner but rather was made physically as identical to the original antenna as possible. The resulting antenna pattern was somewhat degraded but provided adequate coverage for subsequent system tests.

The Prototype No. 3 antenna was installed, tuned, and tested in the normal manner with good results.

5.4.6 RECOMMENDATIONS

With the elimination of the redundant feeds in the Prototype No. 2, the total coupling to the radiating loops was reduced and the input VSWR at the feed loops could not be tuned to a value lower than 2.8. Although this effect is isolated from the transmitter by the transmission line hybrid, a mismatch loss of approximately 1 db is incurred. It is recommended that the feed loop be redesigned to eliminate this loss.

It has been previously noted that an appreciable variation in the field pattern has occurred between various assembly steps. These effects should be investigated and corrected to guard against possible serious tolerance problems in the future.

5.5 BATTERY

5.5.1 REQUIREMENTS

The penetrometer battery is required to supply a nominal current of 175 ma at +22 to 27 volts, and 130 ma at -4.4 to 6.0 volts. The operating time need not be over 2 minutes for the flight battery as deployed by the Lunar Survey Probe System, and operates for only 15 seconds per launch in the prototype test model penetrometers. The prototype test model battery must be capable of recharge or of supplying many operating periods to allow repeated testing. In the flight application, the operational life of the penetrometer is only a single 2-minute discharge but the battery should be capable of supplying several times this energy or preferably be capable of recharge to allow for test and checkout, and for recovery from inadvertent discharge. The requirements for the flight battery are detailed by Aeronutronic Specification 21526. A battery meeting this specification will serve the requirements for test model batteries, as well. The most unusual requirement upon the battery is that it must continue to supply its load without large transients ($\geq$1.5 volts) during a shock of 10,000 g peak and half-sine shape of 1.2 milliseconds duration. The battery is limited in weight to 200 grams. A prototype battery is seen in Figure 5-74 with the timer-regulator module installed on top.

A source for small, high-energy chemical batteries is the hearing aid battery industry which has developed an extensive line of sizes and types. Types which were examined as potentially suitable to the penetrometer are listed in Table 5.5. These batteries have been developed for low-drain rate, long-life application, and for the most part are not specified in terms directly related to the short operating life of the penetrometer. One exception is the Jupiter B-80 cell which the manufacturer states can be discharged at 200 ma for 1 to 2 minutes with no detrimental effects.

While the energy required for a single operating cycle of the penetrometer is approximately 6 milliampere-hours, it is necessary to use a battery rated by conventional standards at 50 milliampere-hours, or more, to provide the required power. This occurs because the power of a battery is a function of the ion diffusion rate and the plate area. The diffusion rate is essentially constant; therefore, the area has to be large enough to provide the required power.

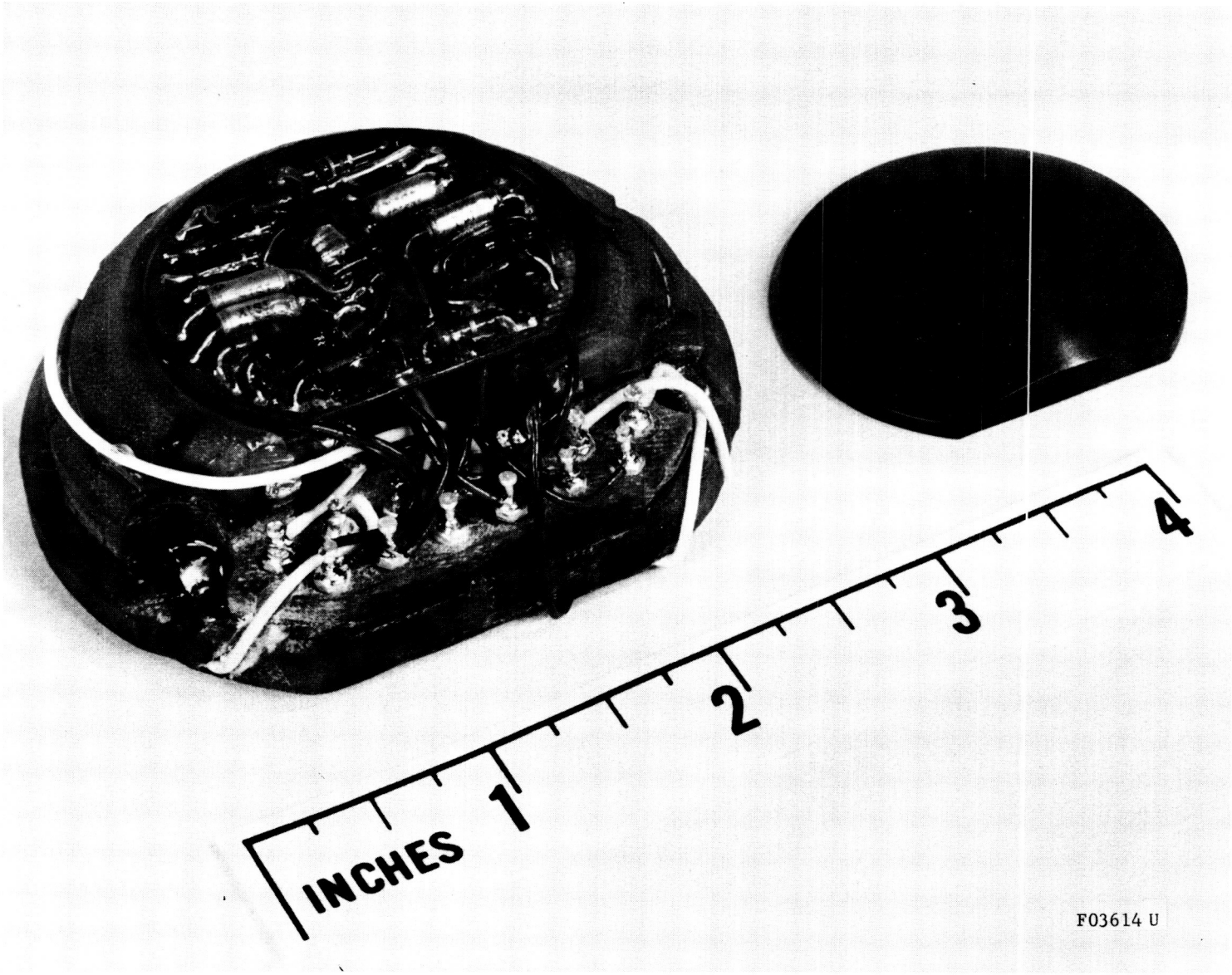

FIGURE 5-74. PROTOTYPE BATTERY WITH TIMER-REGULATOR INSTALLED

TABLE 5.5

PENETROMETER BATTERY CELL CANDIDATES

Cell Mfr	Type No.	Battery Type	Capacity (mah)	Cell Wt (ounces)	Charge Characteristics	Remarks
Union Carbide	N22T	Ni-Cd Button	20	0.04	Primary	Should not be recharged in stacks. Made in West Germany.
(Eveready)	N24T	Ni-Cd Button	50	0.12	Primary	
	E675E	Hg-Zn Button	165	0.07	Primary	
	S76E	Ag-Zn Button	165	0.08	Primary	
Jupiter	B50	Ag-Zn Button	50	0.07	Secondary	Lowest internal impedance.
Epic, Inc., Distributor	B80	Ag-Zn Button	80	0.14	Secondary	Made in Hungary.
General Electric	VB10	Ni-Cd Button	80	0.23	Secondary	Made in France.
Gould National	50B	Ni-Cd Button	50	0.09	Secondary	Contact springs broken in lot tested. Made in West Germany.
Sonotone	S-134	Ni-Cd Button	20	0.05	Secondary	Out of Production.
	S-132	Ni-Cd Button	150	0.34	Secondary	
Gulton	VO.180	Ni-Cd Button	80	0.23	Secondary	
	VO.180	Ni-Cd Button	180	0.40	Secondary	
Mallory	RM-400R	Hg-Zn Button	75	0.04	Primary	
	MS-13H	Ag-Zn Button	65	0.04	Primary	Higher voltage.
	6M576H	Ag-Zn Button	160	0.10	Primary	Formerly MS-675H
	RM640WA	Hg-Zn --	360	0.36	Primary	High-current cell examined for comparison.
Ray-O-Vac/ESB	625	Ag-Zn --	--	0.16	Primary	
	RS41G	Ag-Zn Button	115	0.06	Primary	
	RS76G	Ag-Zn Button	175	0.08	Primary	

These cells are similar in construction and utilize a button-shaped container with disc-shaped plates. They are available in the following cell types:

Materials	Type
Nickel-Cadmium	Secondary
Silver-Cadmium	Secondary
Silver-Zinc	Primary and Secondary
Mercury-Zinc	Primary

The construction of the cells consists of a shallow steel or nickel cylindrical container approximately 1/2 inch in diameter into which the disc-shaped plates and separators are assembled. A cover of the same material as the container is placed over the contents and a flange is formed on the container edge which retains the cover. A neoprene or plastic gasket is placed between the cover and container which seals and insulates the two electrically and permits them to serve as the battery terminals. A significant difference between the construction of the primary and secondary type is an air space provided in the secondary batteries to allow a small amount of gas emission without generating excessive pressure during charge. This air space is not necessary and not usually present in the primary cells; however, there is a means provided to relieve pressure. In the case of the ni-cad secondary cell, it is important to contain the gas in order to preserve the recharge capability of the battery and, thus, a void must be provided rather than a vent.

These cells inherently are rugged devices generally capable of withstanding large impacts. The plate materials are relatively strong, being formed of metallic ribbon, wire mesh, or sintered metals separated with fiberglass cloth. The primary difficulty encountered in operation during impact is maintenance of electrical contact between the plate materials and the external terminals.

The maintenance of the contact is complicated in the secondary types by the fact that an open space must also be provided which leaves some of the material of the battery nonuniformly supported and consequently subject to deformation or dislocation of contact surfaces during impact. A spring is used to maintain contact. Batteries made up of at least one type of nickel-cadmium cell and mercury-zinc primary cell have demonstrated an

ability to function during impacts approaching 200,000 g.[5,6] However, these were ballistic projectile applications, and the batteries may have been oriented in a preferred direction.

The requirement for repeated load application suggests a rechargeable secondary battery. However, it may be desirable to use primary cells because of their superior impact resistance. Two possibilities exist for doing this. One possibility stems from the fact that it is difficult to discharge even a small amount of a battery's total energy in one penetrometer operating cycle, the battery capacity having been established to supply a power requirement. Consequently, the battery will be capable of supplying as many as 10 cycles of operation provided that sufficient time is allowed for its recovery between cycles. A second possibility is to actually recharge the primary cell. Certain primary cells can be recharged if the charge-discharge cycle is limited to between 50 and 80 percent and the charge rate is carefully controlled.

Another type which has been used in high-impact applications is the thermal battery. Advantages of the thermal battery are its demonstrated high reliability, ruggedness, immunity to operating temperature extremes, and long storage life. Disadvantages of the thermal battery for this application are its size and weight and its one-shot nature. To obtain equivalent performance from a thermal battery, the same quantity of active battery materials must be provided as is used in conventional batteries, plus additional pyrotechnic material for activation.

Undoubtedly, batteries capable of meeting the penetrometer requirements could be developed. A large 1200 watt-hour battery was developed for the Ranger hard-landing lunar-capsule.[7] The development carried out by the Missile Battery Division of Electric Storage Battery Company yielded a 70 watt-hour per pound sealed, sterile, secondary Ag-Zn battery qualified to survive a 3000 g, 11-millisecond impact.

5.5.2 BUTTON CELL TESTS

a. Nickel-Cadmium Cells. It was originally planned to utilize the Gould-National (GN) model 50B nickel-cadmium (ni-cad) button cells because these cells had been used in several ballistic projectile applications. Also, preliminary high rate discharge tests, as seen in

5. Letarte, M., Moir, L. E., A High-G Telemetry System for Gun and Rocket Firing, Document No. AD 244 158, Defense Documentation Center, 1960.

6. Kingery, M. K., Choate, R. H., and Young, R. P., Progress Report on Development of Telemetry for a Hypervelocity Range, AEDC-TN-60-214, December 1960.

7. Lunar Rough Landing Capsule Development, Aeronutronic Publication No. U-2007, February 1963.

Figure 5-75, indicated that a dual string of these battery cells would readily supply the required current in a reasonably compact battery. The ni-cad cell is attractive from the standpoint of long shelf life and almost limitless charge-discharge cycle capability. Preliminary shock tests were performed on GN type 50B cells already on hand. Four cells were bonded to a hand-held hammer instrumented with an Endevco 2215C accelerometer. The hammer was impacted against a block of wood. Shock levels as high as 13,000 g were obtained with a total impact pulse width as long as 0.5 millisecond. No voltage dropouts occurred when the cells were impacted in a direction parallel to the diameter of the cell. The cells under test were supplying a load of current of approximately 100 ma. The cells were further tested under impact in a direction perpendicular to the diameter. A ripple of approximately 30 millivolts was detected when the cell was impacted with the negative terminal nearest the impact point. Voltage drop was also detected when the cell was impacted with positive terminal nearest the impact point. The first significant dropout occurred on the eighth impact. The dropout was thought to be caused by failure of the spring contact inside the cell, as the cells were opened and the springs were shattered. The electrodes and separator appeared to be undamaged. A sample test quantity of 100 type 50B (50 mah) nickel-cadmium button cells was obtained from Gould-National. Seven of the new cells were opened prior to any testing. All seven of the cells had broken spring contacts. A photograph of one of the opened cells is shown in Figure 5-76 which displays the individual internal parts. The spring which is normally a cruciform was found in five pieces in this cell. An attempt was made to examine other cells by X ray so they could subsequently be tested. However, the state of the springs could not be detected with X-ray photographs, since the materials inside the cells are approximately the same density as the spring. Representatives of Gould National were contacted. However, no definite explanation or promise of correction was obtained. These cells are manufactured in West Germany. As a result of this problem, quantities of small button cells of all types were placed on order for test. Also, inquiries were begun for the development of a special battery as described in Paragraph 5.5.4.

Nickel cadmium button cells from General Electric (VB10) and Gulton (VB080) were hammer tested. These cells are similar in construction. They contain spring contacts which caused voltage discontinuity during impacts of 10,000 g. The cell voltages dropped to zero during impact.

Eveready Type N24T cells were received and it was found that they were made in West Germany. They appear identical to the Gould National Type 50B. Six of these were opened and found to have broken springs. Of ten Eveready Type N22T cells, six were found to have holes punched in their cases by the tab welding action. They were nearly at 0 volts and would not accept a charge. The other four dropped to near 0 volts when loaded.

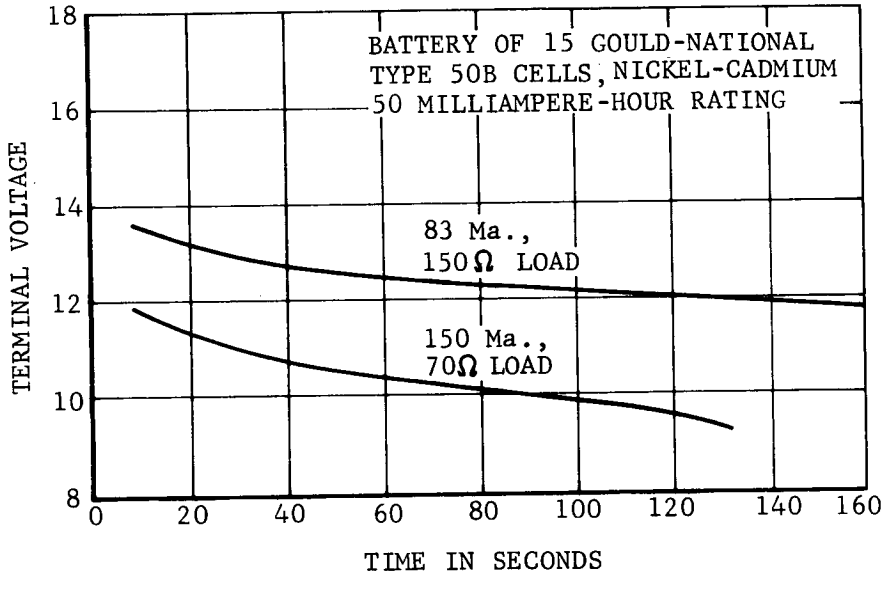

F03615 U

FIGURE 5-75. PERFORMANCE OF GOULD-NATIONAL TYPE 50B CELLS AT HIGH DRAIN RATES

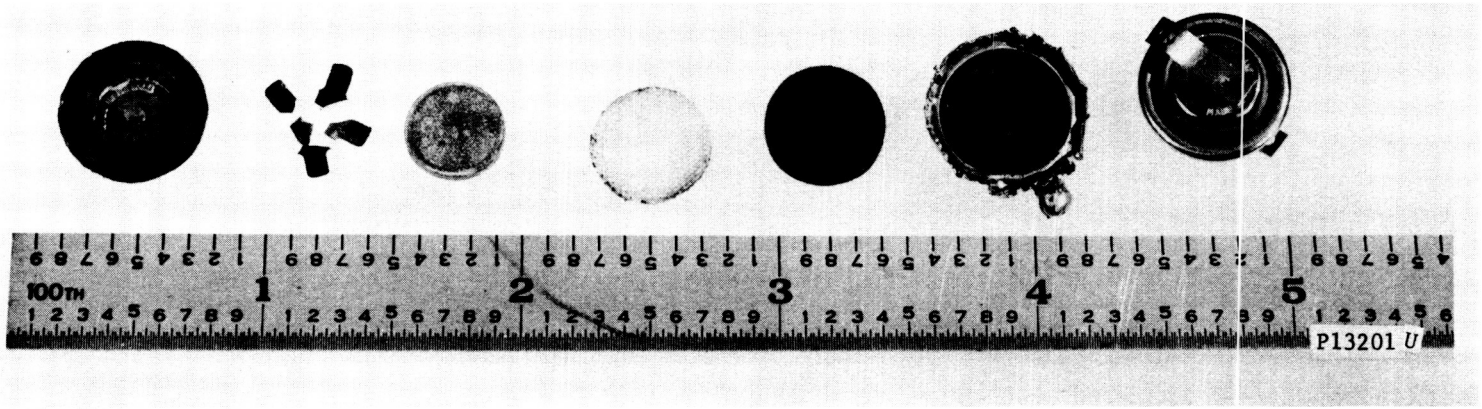

FIGURE 5-76. INTERNAL PARTS OF GOULD-NATIONAL TYPE 50B CELL

b. Jupiter Silver-Zinc Cells. The Jupiter silver-zinc button cells were of particular interest as the only small silver-zinc button cell rated as secondary (rechargeable) by the manufacturer who claims approximately 50 charge/discharge cycles. The manufacturer also rates these cells for high drain (to 200 ma) applications and claims that complete discharge by short circuiting the cell will not cause damage. These cells are manufactured in Hungary and available through Epic, Inc., a New York distributor. A quantity of the Jupiter B80 cell was ordered and preliminary testing established that these cells were unique in their electrical properties and shock resistance. Repeated impacts of 10,000 to 12,000 g in three orthogonal directions with the hammer typically resulted in voltage transients of 5 mv or less per cell loaded at 100 ma. Four cells were impacted 10 to 14 times each and displayed slowly increasing transients to 20 to 50 mv. There were no failures.

A discharge test at 150 ma was run on one cell with the results shown in Figure 5-77. The open circuit voltage was 1.6 volts. At turn-on, the voltage dropped to 1.29 volts. The voltage decreased slowly to 1.1 volts in 8 minutes. The voltage began to decrease rapidly after 8 minutes under the constant load to 0.9 volt in 9 minutes, 40 seconds. The load on the cell was removed at this time. The open circuit voltage returned to 1.45 volts and steadily increased to 1.56 volts after 10 minutes. The cell was again loaded at 150 ma. The cell voltage dropped to 0.9 volt after 3 minutes, 20 seconds.

Based on these encouraging results, a more complete evaluation was begun. Since loading of the power supply was to occur at approximate 1-minute intervals during penetrometer impact testing, a longer cell life between charges is expected than under the continuous load conditions of the first cell test. Therefore, discharge tests were conducted on a 20-cell battery with a discharge interval of one minute.

The test results are shown in Figure 5-78. This graph shows the open circuit voltage and load voltage for each discharge period. A discharge run consisted of alternate 1-minute cycles with and without load until the cells were discharged below 1.0 volt. The runs varied from 18 to 20 one-minute discharge periods. Between runs the battery was recharged at 20 ma for 4 hours. The results show that as many as 12 minutes of discharge time are available at 120 ma or more before the minimum penetrometer battery voltage of 24 volts (1.2 volt/cell) is reached. It is also seen that the battery is capable of repeated recharge at accelerated rates.

The discharge characteristics of a 20-cell battery with Jupiter B80 cells is shown in Figure 5-79 for a constant resistive load of 150 ohms at different temperatures. The performance at +50°F is satisfactory for the penetrometer as presently designed, which requires a minimum of 22 volts for proper operation of the +17 volt regulator. The loading on the

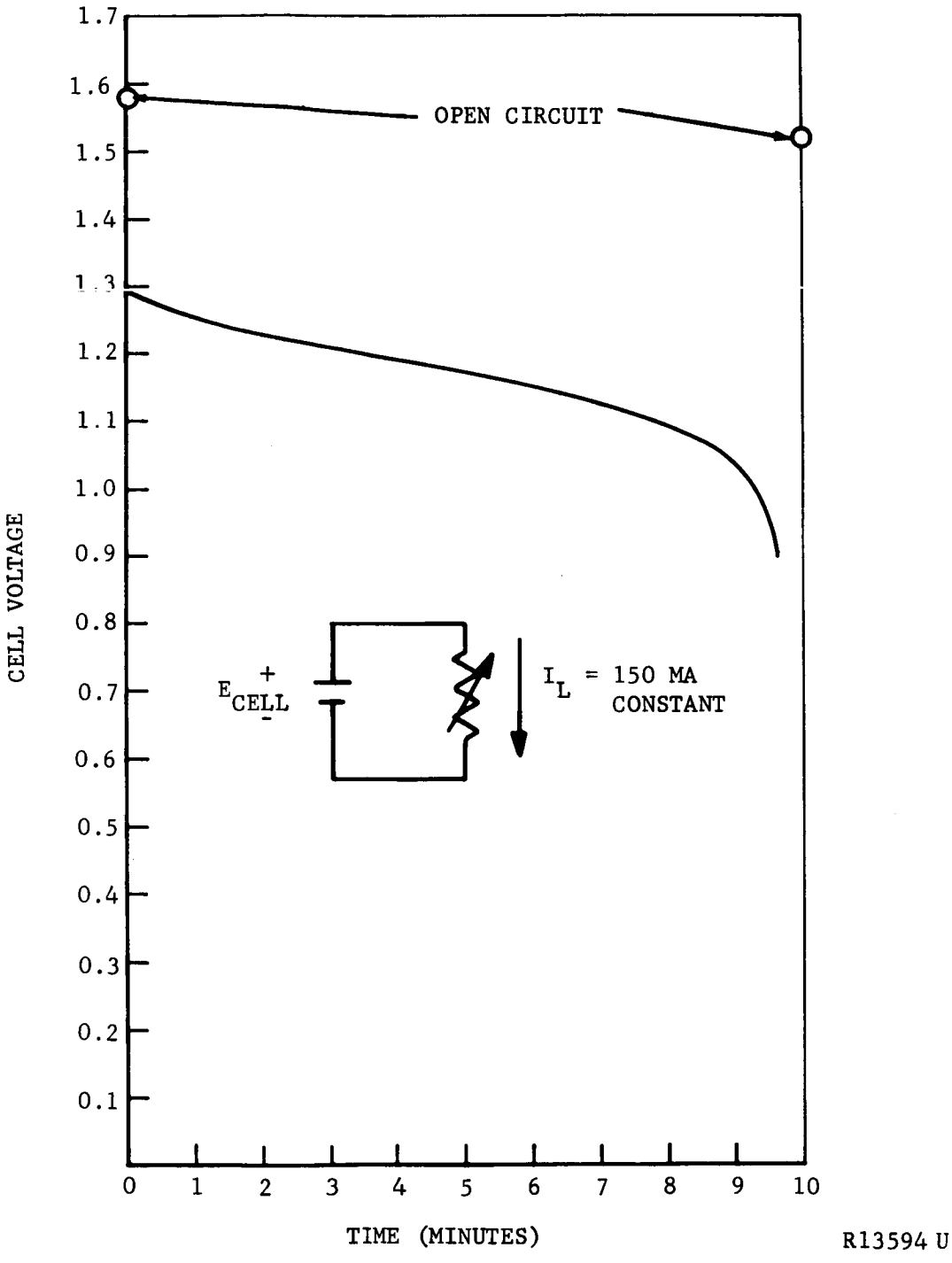

FIGURE 5-77. CELL VOLTAGE VS. TIME AT A CONSTANT LOAD (150MA) JUPITER B80 SILVER-ZINC CELL

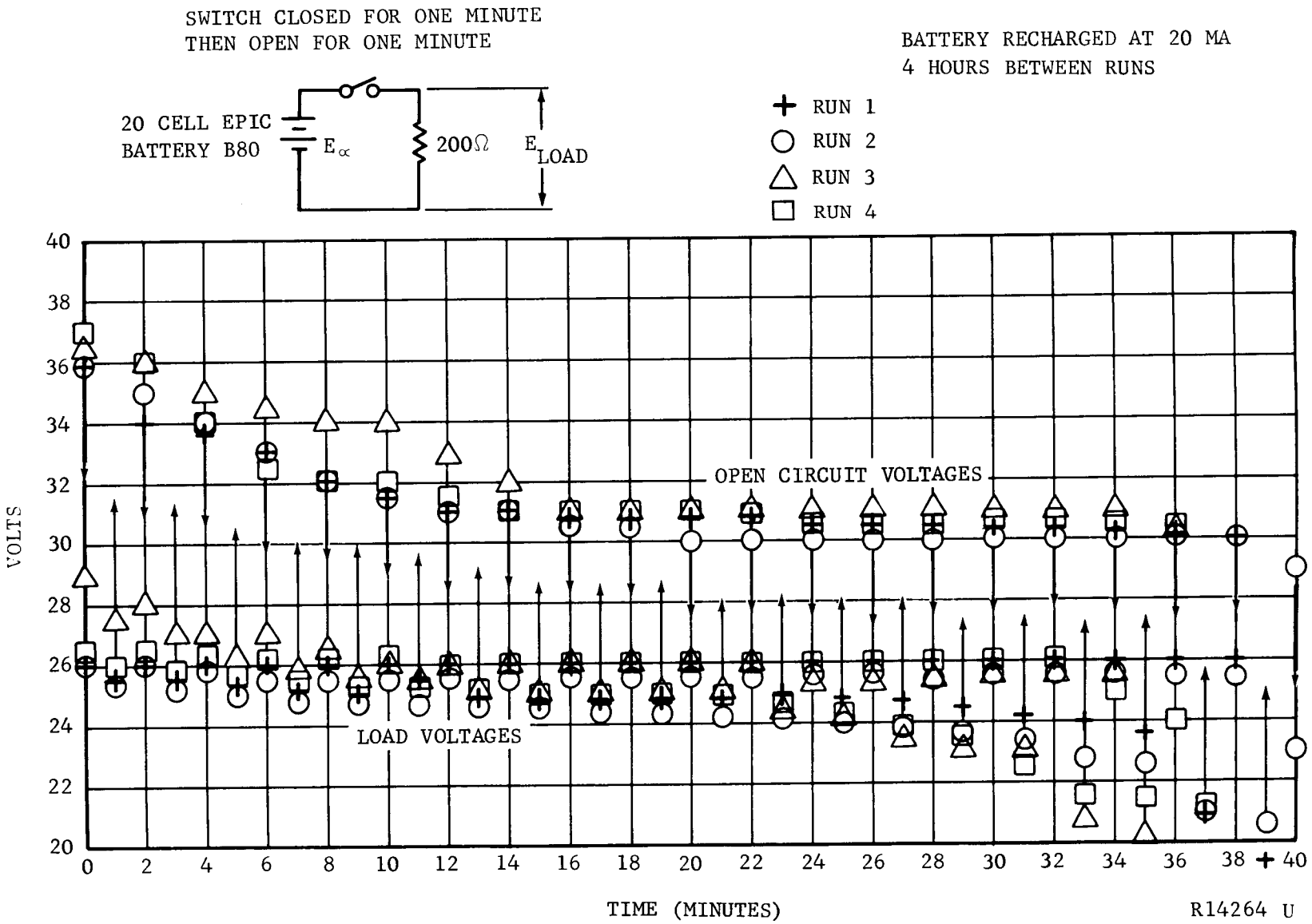

FIGURE 5-78. REPEATED TESTS OF 20 CELL JUPITER B80 BATTERY

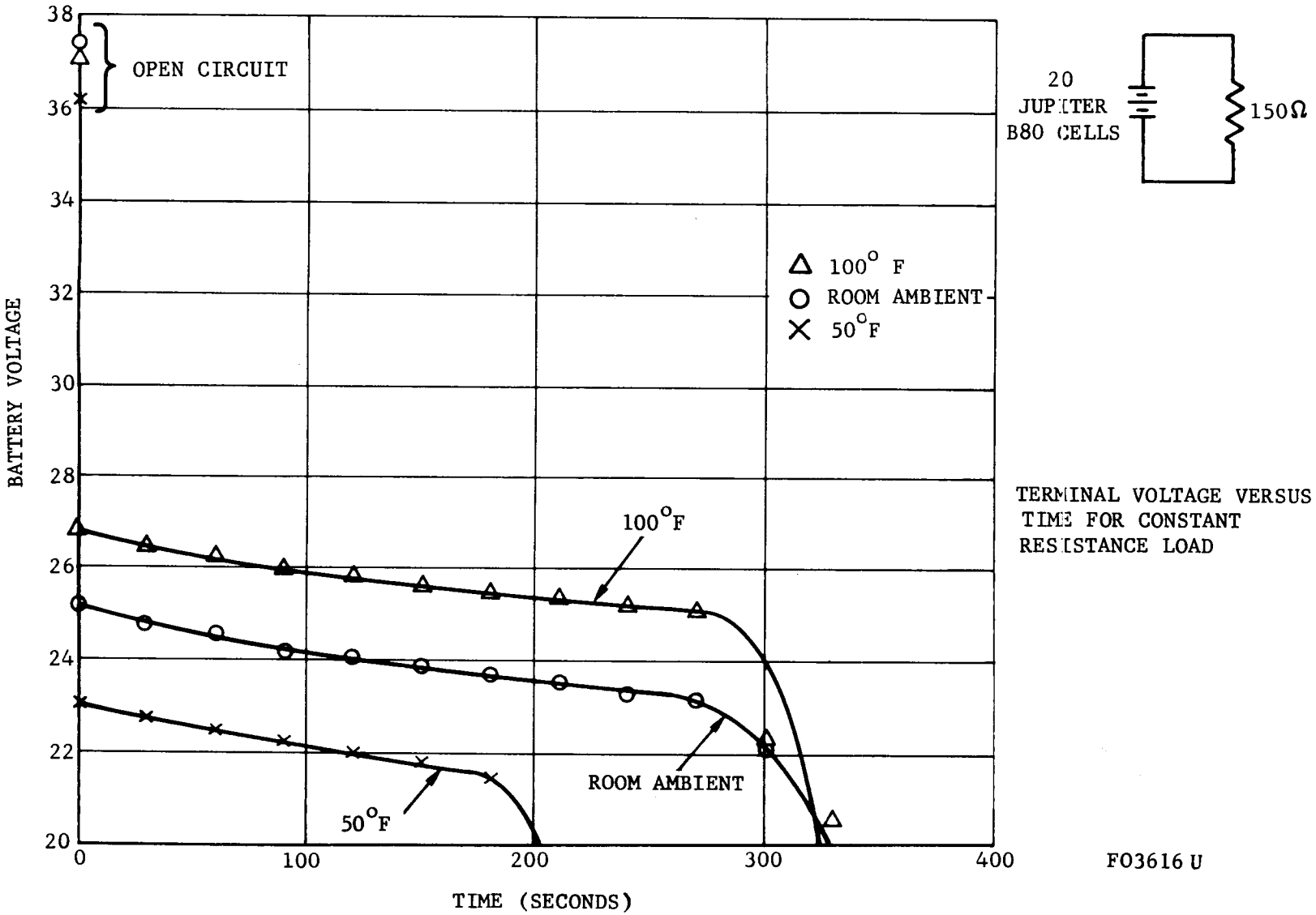

FIGURE 5-79. CONTINUOUS BATTERY LOAD TEST AT VARIOUS TEMPERATURES FOR 20 JUPITER B80 SILVER ZINC BUTTON CELLS

battery was increased from 200 ohms to 150 ohms as the expected penetrometer drain had increased during this time because of additional signal electronics circuits.

Two 5-cell batteries were made up of Jupiter B80 cells with welded nickel ribbon connections. The battery formed a cylindrical configuration which was totally encapsulated in a 4-inch diameter sphere made of Epon 828 and Shell 871. Load voltage (load = 36 ohms) was recorded on a recording oscillograph.

A sensitivity of 1-1/2 inches per volt was used. Additionally, the battery voltage was recorded on magnetic tape (FM) at 60 inches per second. A nominal 10,000 g shock, 250 feet per second velocity change, was applied along each of the two directions parallel to the battery's cylindrical axis and one in transverse axis.

The data are summarized in Table 5.6. No transient as large as 70 mv (the limiting resolution on two tests) was observed.

The Jupiter B80 cells have been used in all the penetrometers fabricated so far and much additional information has been gained in the fabrication and test of these batteries. This information is described in Paragraph 5.3.1d.

c. Domestic Silver-Zinc Cells. A potential domestic source for the Penetrometer battery may be derived from the small silver-zinc button cells currently produced in this country for the hearing aid industry. The largest of these cells are capable of supplying approximately half of the current required for the Penetrometer but they are small enough to permit a parallel series string to be packaged into the available space. The cells tested are not intended for rechargeable service but are designed to deliver 115 to 175 mah each, or roughly twice the rated energy of the Jupiter B80 cells (80 mah). With this amount of primary energy available from a parallel string, it may be possible to complete the mission without the recharge capability. Recharging is also a possibility as discussed later. A test series has been conducted which indicated the various characteristics of these cells at high drain rates. Cells from three manufacturers have been tested. The cell types and their characteristics are listed in Table 5.7.

TABLE 5.6

JUPITER B-80 SILVER-ZINC BATTERY HYGE IMPACT TESTS

LOAD EQUALS 36 OHMS

SAMPLE	1				2		
TEST	1	2	3*	4	1	2	3
$E_{OPEN\ CKT}$ (VOLTS)	9.22	9.22	9.29	9.07	——	——	——
E_{LOAD} (VOLTS)	5.50	5.5	5.85	5.45	5.38	5.35	5.28
Δ E	< 70 MV	< 70 MV	57 MV	33 MV	30 MV	< 6 MV	< 6 MV
RESOLUTION	70 MV	70 MV	5 MV	11 MV	6 MV	6 MV	6 MV
G-LEVEL	11,900	7240	10,300	11,000	11,700	11,000	10,000
VELOCITY (FT/SEC)	253	243	240	182	245	242	229
$E_{OPEN\ CKT}$ (VOLTS)	9.22	8.85	9.28	9.08	——	——	——
IMPACT DIRECTION	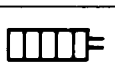		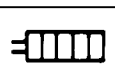	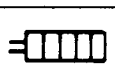	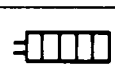		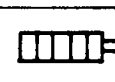
NO. OF CELLS	5 IN SERIES ⟶						

*THE MONITORING CABLE BROKE DURING THE IMPACT. THEREFORE THIS TEST WAS REPEATED.

TABLE 5.7

DOMESTIC SILVER-ZINC CELLS

Manufacturer	Part No.	Rated Capacity (mah)	Dia (in.)	Ht (in.)	Wt (oz)	Vol (in.^{3})
1. Ray-O-Vac	RS41G	115	0.455	0.160	0.06	0.025
2. Ray-O-Vac	RS76G	175	0.455	0.210	0.08	0.035
3. Mallory	6MS76H (Formerly MS-675H)	160	0.455	0.210	0.10	0.03
4. Mallory	RM640WA	360	0.625	0.380	0.36	
(This is a high-current Hg cell and was tested for comparison.)						
5. Eveready	S76E	165	0.455	0.208	0.08	0.03

These cells all have a nominal 90 percent rated yield after 1 year shelf life when stored at room temperature. This is accomplished by forming the cells from the more stable monovalent silver oxide instead of the peroxide silver which is used in the rechargeable types.

Three different types of tests were performed on these cells. First the cells were continuously discharged at various fixed loads to determine the usable power available during the required discharge times for the Penetrometer. The results are plotted in Figures 5-80 through 5-84 to show cell voltage as a function of the energy delivered per discharge in milliampere hours. This gives a convenient means of directly comparing the relative energy capacity, independent of time, which varies considerably with the load value. These data are representative of 20 cells. The results indicate that the Eveready S76E has the highest energy density of the cells tested.

A second test series was made to determine the recharge capability of these cells. Although the cell labels stated that these cells are not to be recharged, it was determined from conversations with the manufacturer's applications engineers that some success could be expected in recharging these cells if they were not deeply discharged and if they were recharged at one or two milliamperes. The results are shown in Figures 5-85 through 5-88. Figures 5-85, 5-86, and 5-87 show the results of the Ray-O-Vac cells when recharged, indicating that they are not capable of recharging without numerous failures. Figure 5-88 shows the results of a Mallory cell that was recharged four times successfully even though it was deeply discharged. Figure 5-89 shows a more realistic discharge of a similar Mallory cell because it was not subjected to deep discharge and was recharged more slowly. It is interesting to note that in Figure 5-88 the recharged performance was better than the initial performance because of the peroxide reaction induced by the recharge. Attempts at recharging deeply discharged Eveready cells were not successful. They may be rechargeable if the depth of discharge is controlled.

A third set of tests was made to give discharge data which were more directly relatable to the actual penetrometer load. This is important because the penetrometer loads are short duration discharge periods which are separated by no load periods during which the batteries can recover some of their power capability. The high discharge currents polarize the plates and increase the internal resistance of the cells. When disconnected, the cells recover from this condition in a few minutes. This is clearly indicated by the sawtoothed voltage plot of the test results shown in Figures 5-90, 5-91, and 5-92. Figure 5-90 shows room temperature performance of the Everready S76E type cell, and Figure 5-91 shows similar cell performance at 50°F. Tests on the Mallory 6MS76H cells

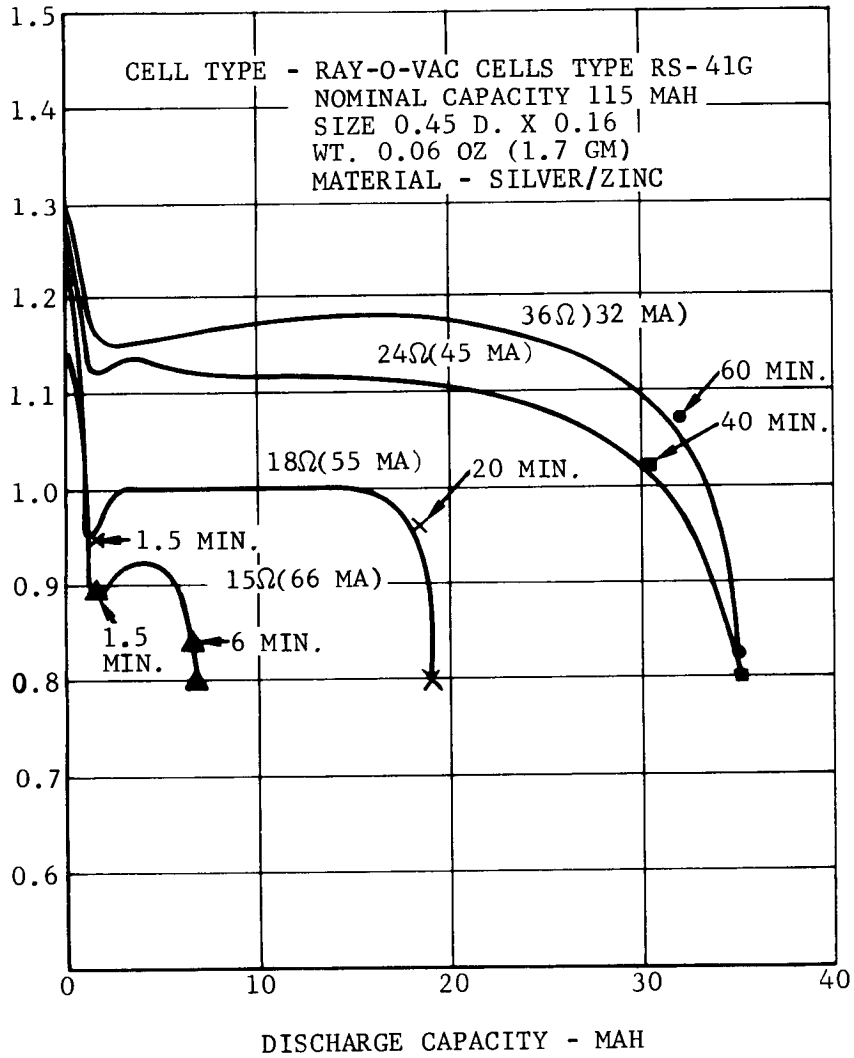

FIGURE 5-80. INITIAL DISCHARGE CHARACTERISTICS, RAY-O-VAC CELLS RS 41G

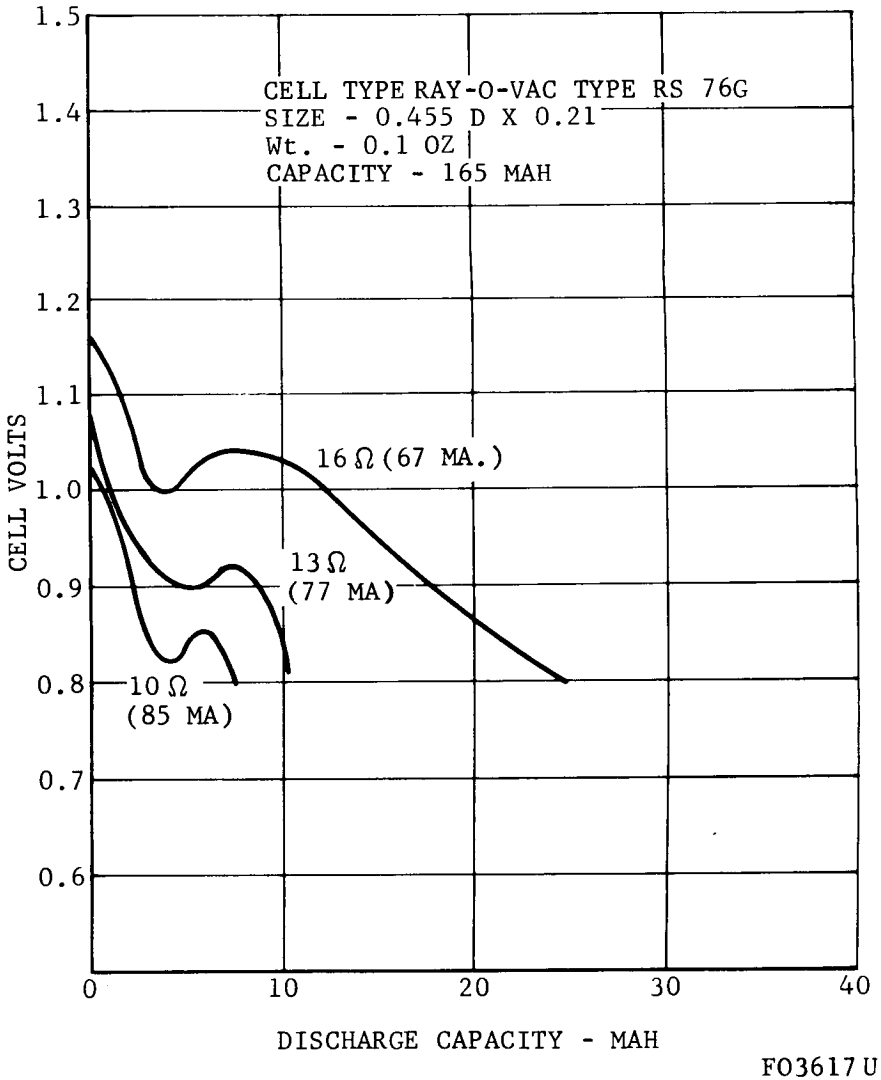

FIGURE 5-81. INITIAL DISCHARGE CHARACTERISTICS, RAY-O-VAC TYPE RS 76G

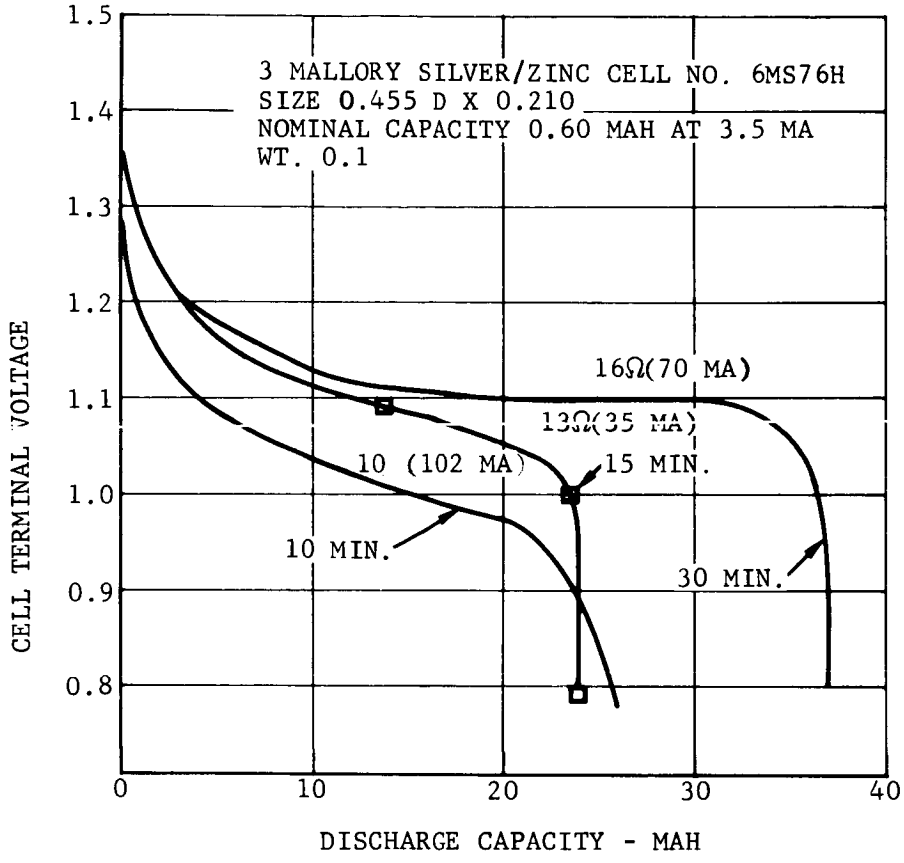

FIGURE 5-82. INITIAL DISCHARGE CHARACTERISTICS, MALLORY NO. 6MS 76H SILVER ZINC CELL

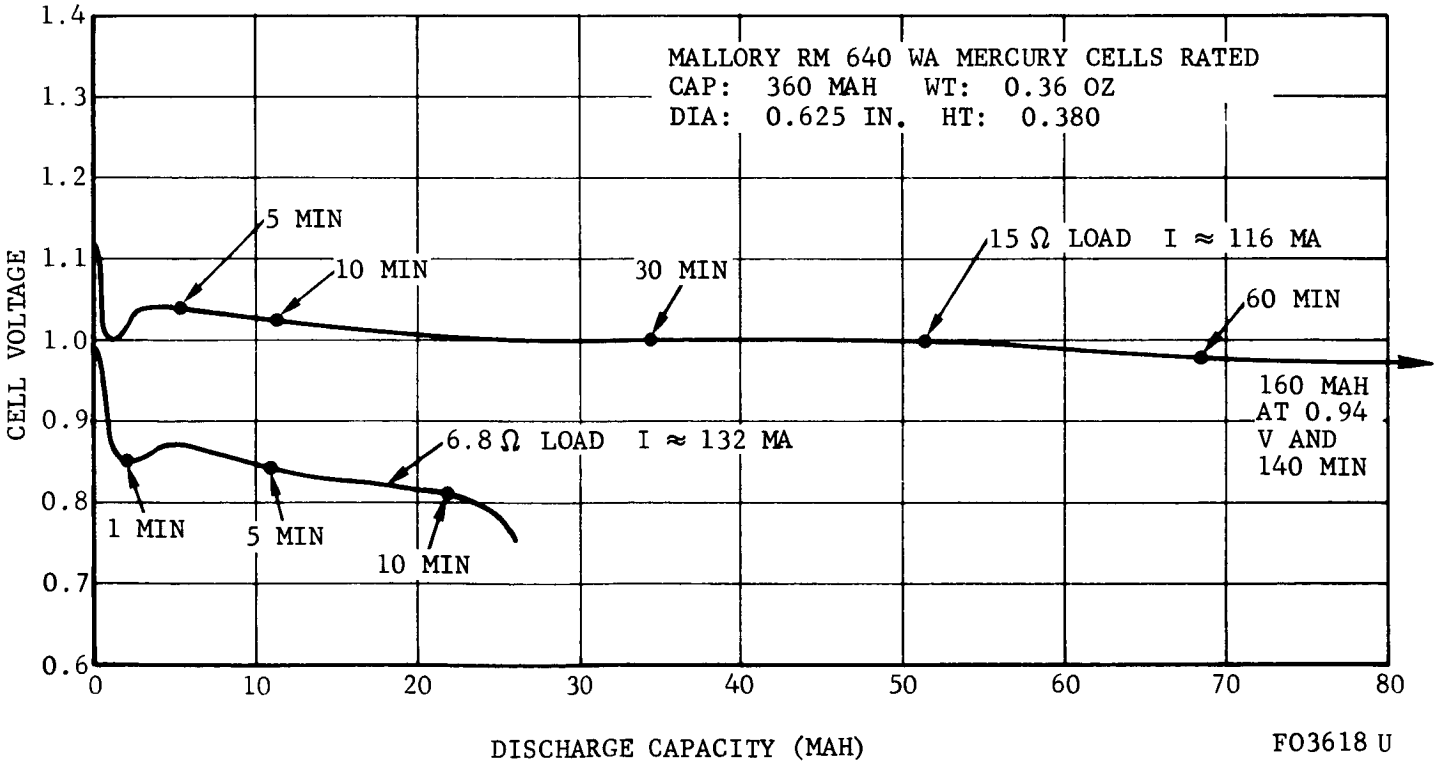

FO3618 U

FIGURE 5-83. INITIAL DISCHARGE CHARACTERISTICS, MALLORY RM 640 WA CELLS

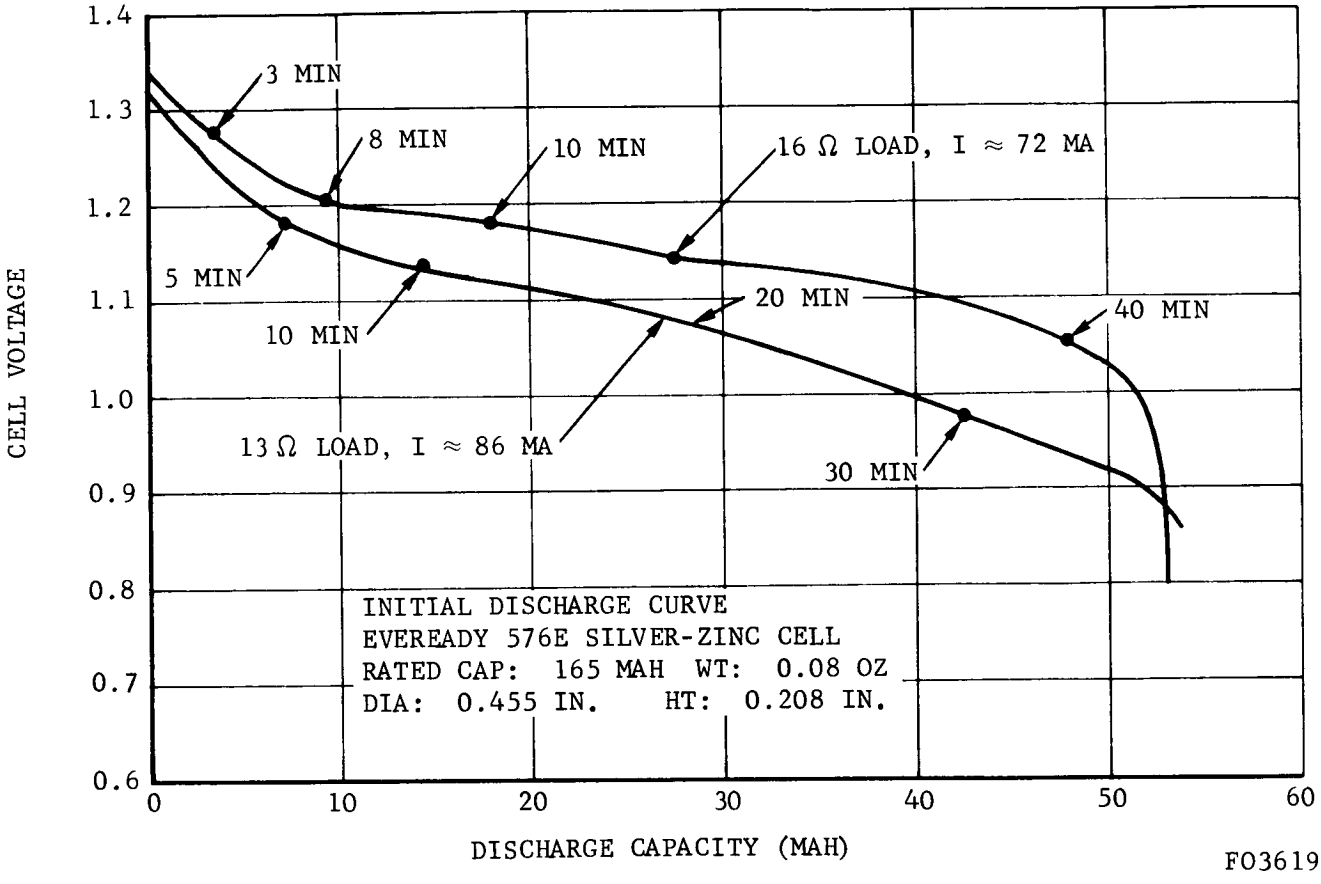

FIGURE 5-84. INITIAL DISCHARGE CHARACTERISTICS, EVEREADY 576E SILVER-ZINC CELL

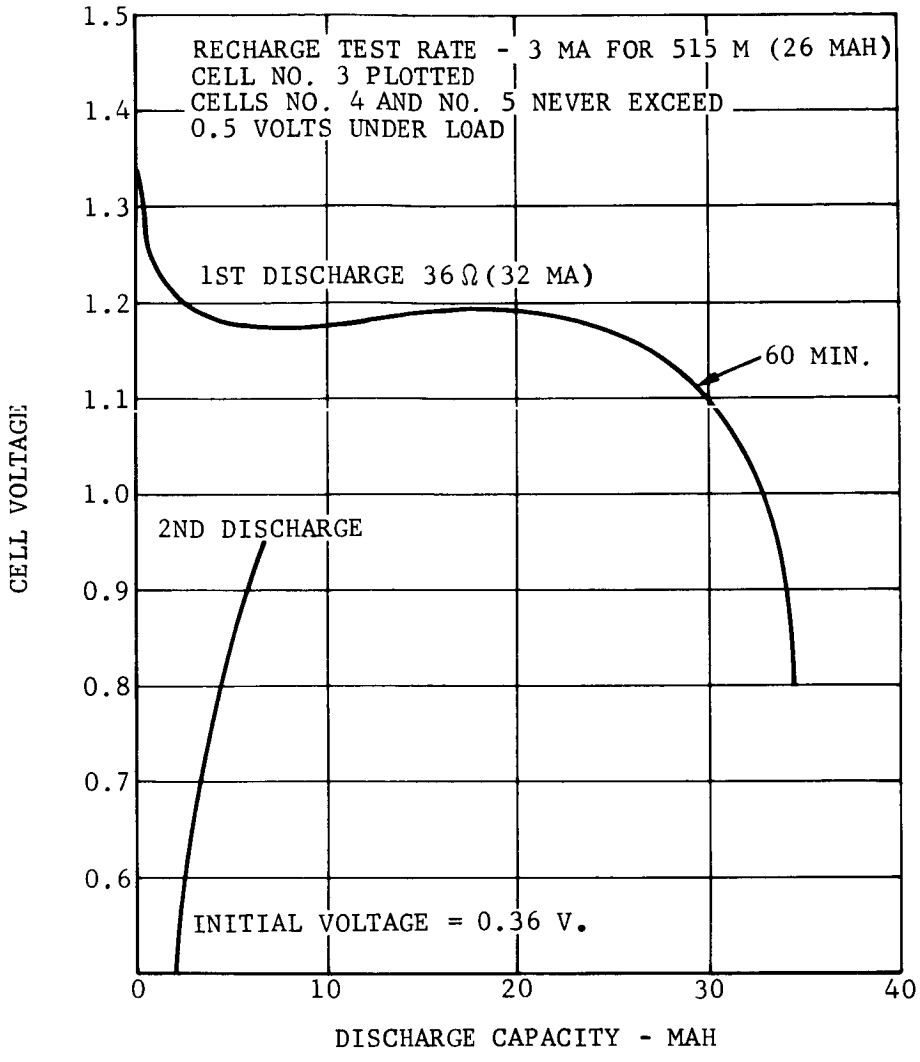

FIGURE 5-85. RECHARGE TEST, RAY-O-VAC RS 41-G CELL NO. 3

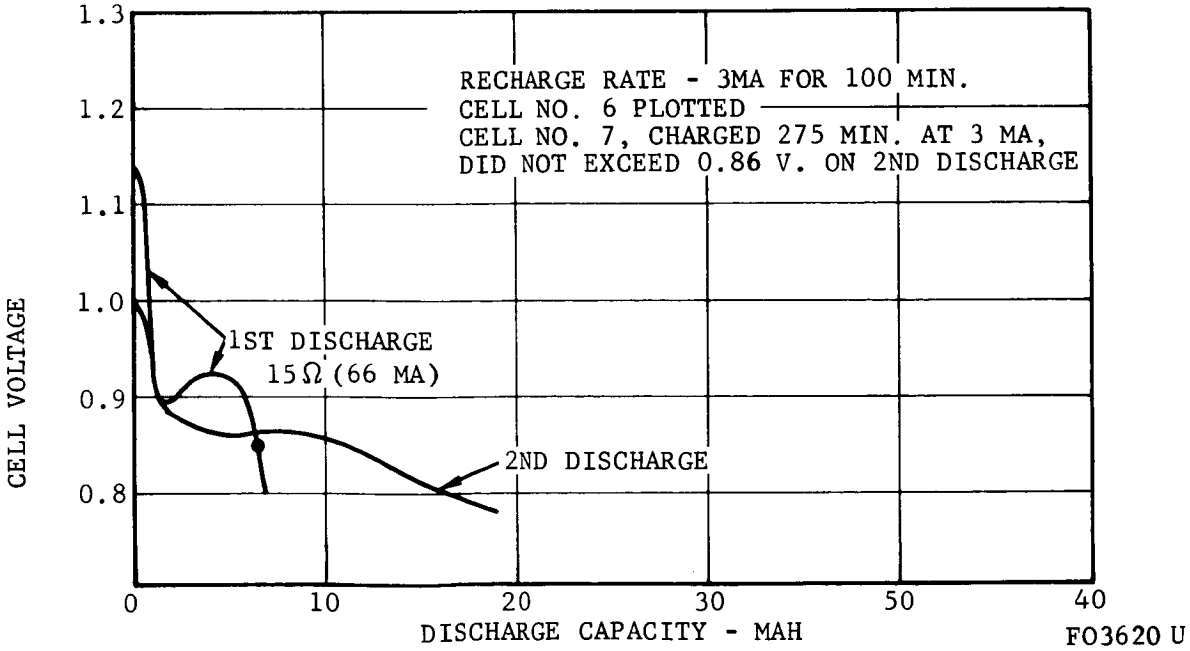

FO3620 U

FIGURE 5-86. RECHARGE TEST, RAY-O-VAC RS 41-G CELL NO. 6

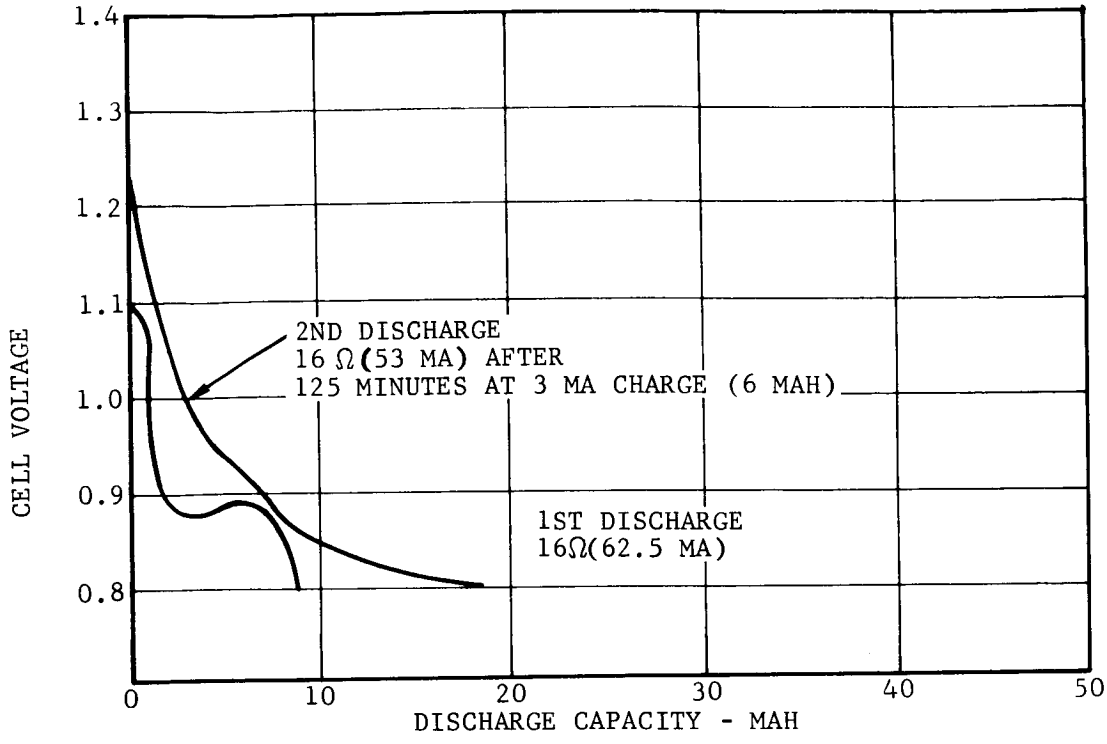

FIGURE 5-87. RECHARGE TEST, RAY-O-VAC TYPE RS 41-G CELL NO. 9

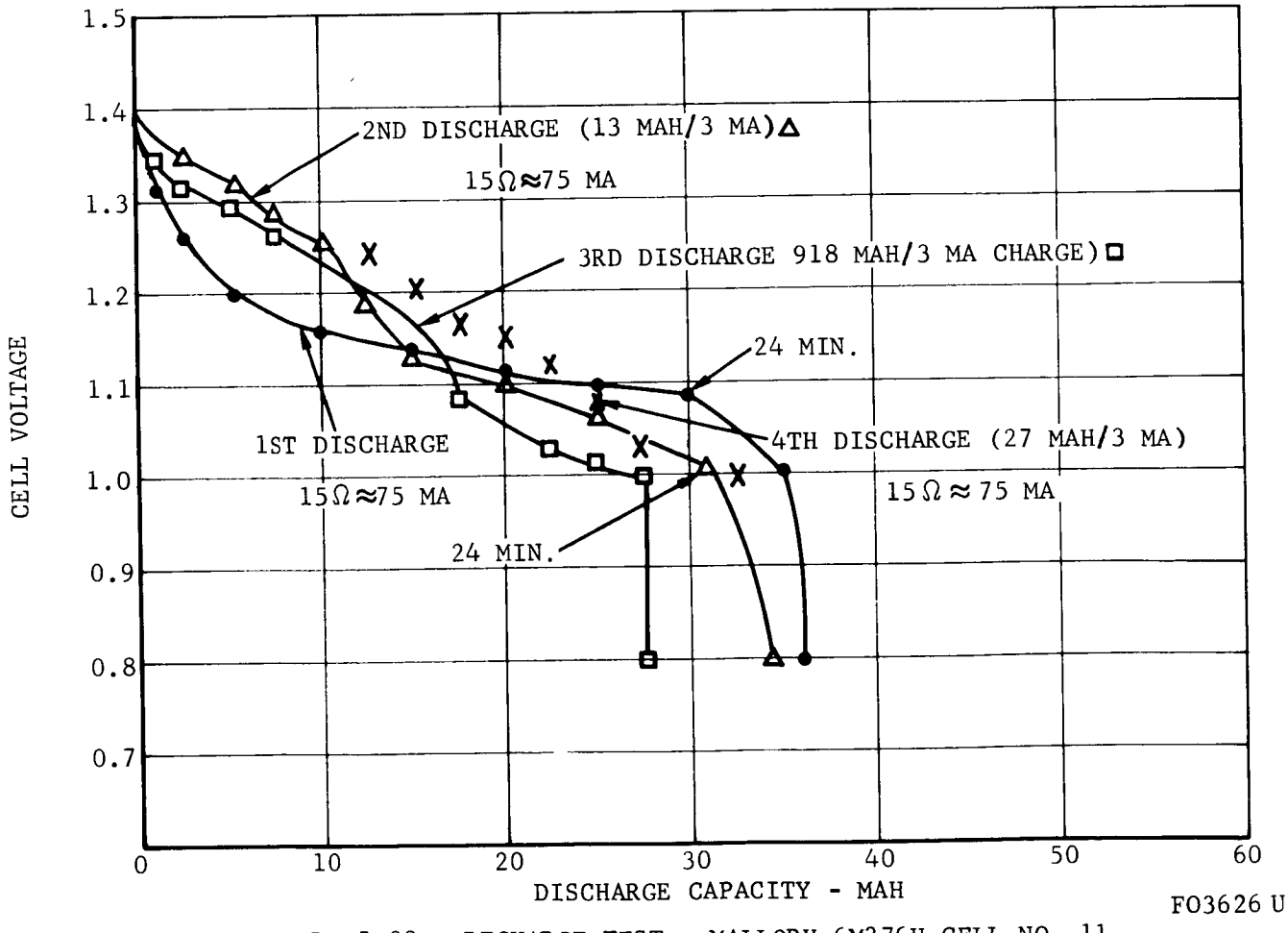

FIGURE 5-88. RECHARGE TEST - MALLORY 6M376H CELL NO. 11

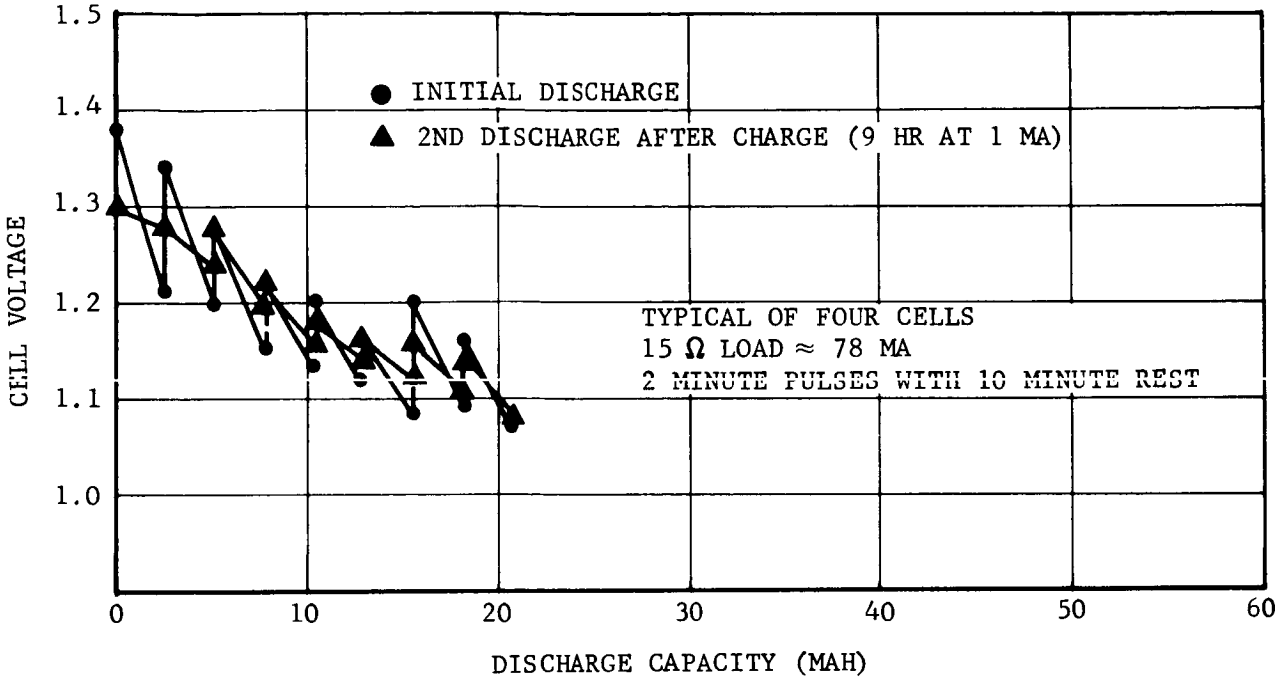

FIGURE 5-89. PULSE LOAD AND RECHARGE TEST - MALLORY MS675H CELL

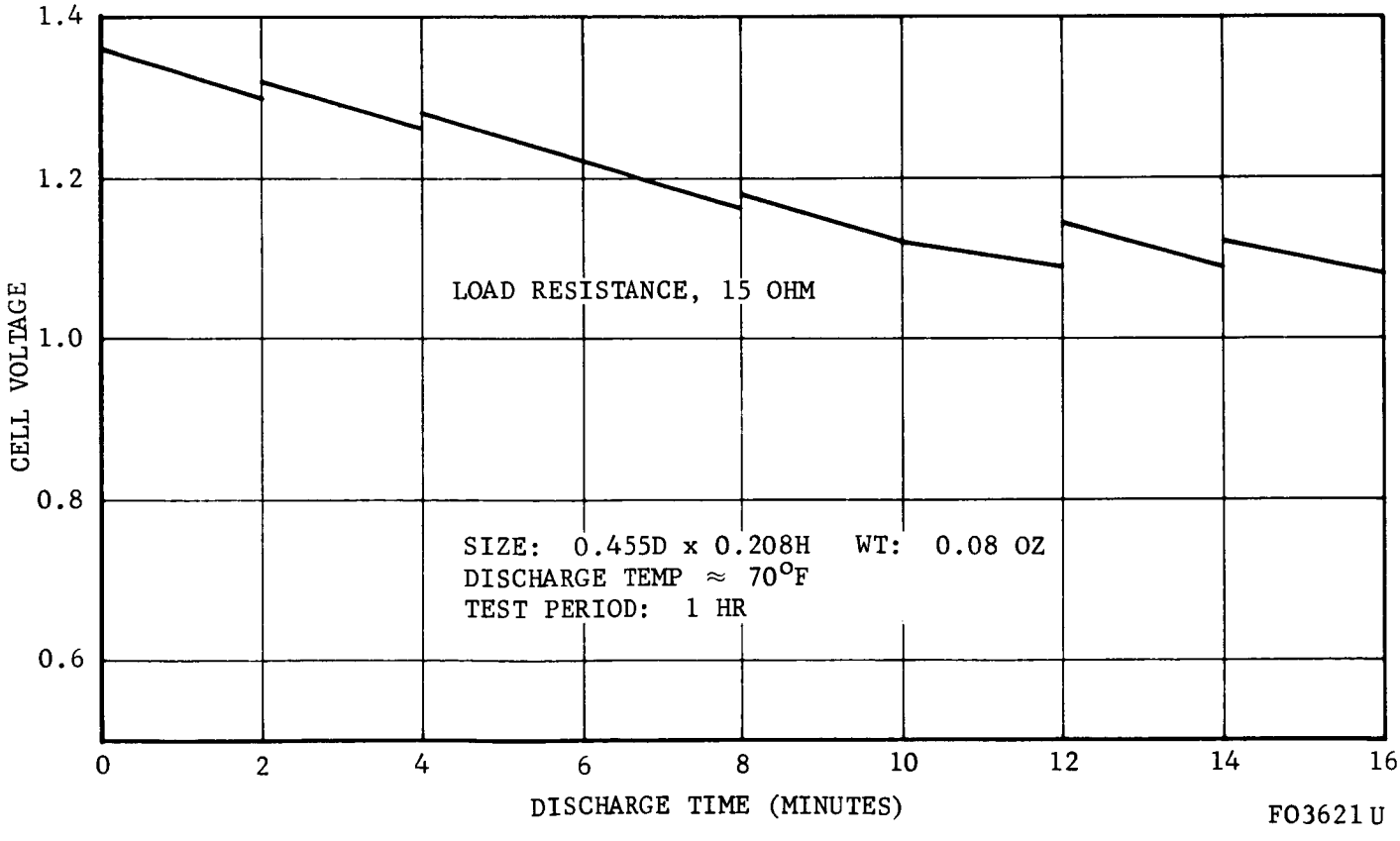

FIGURE 5-90. TWO-MINUTE PULSE LOAD TEST, EVEREADY 576E CELL AT ROOM TEMPERATURE

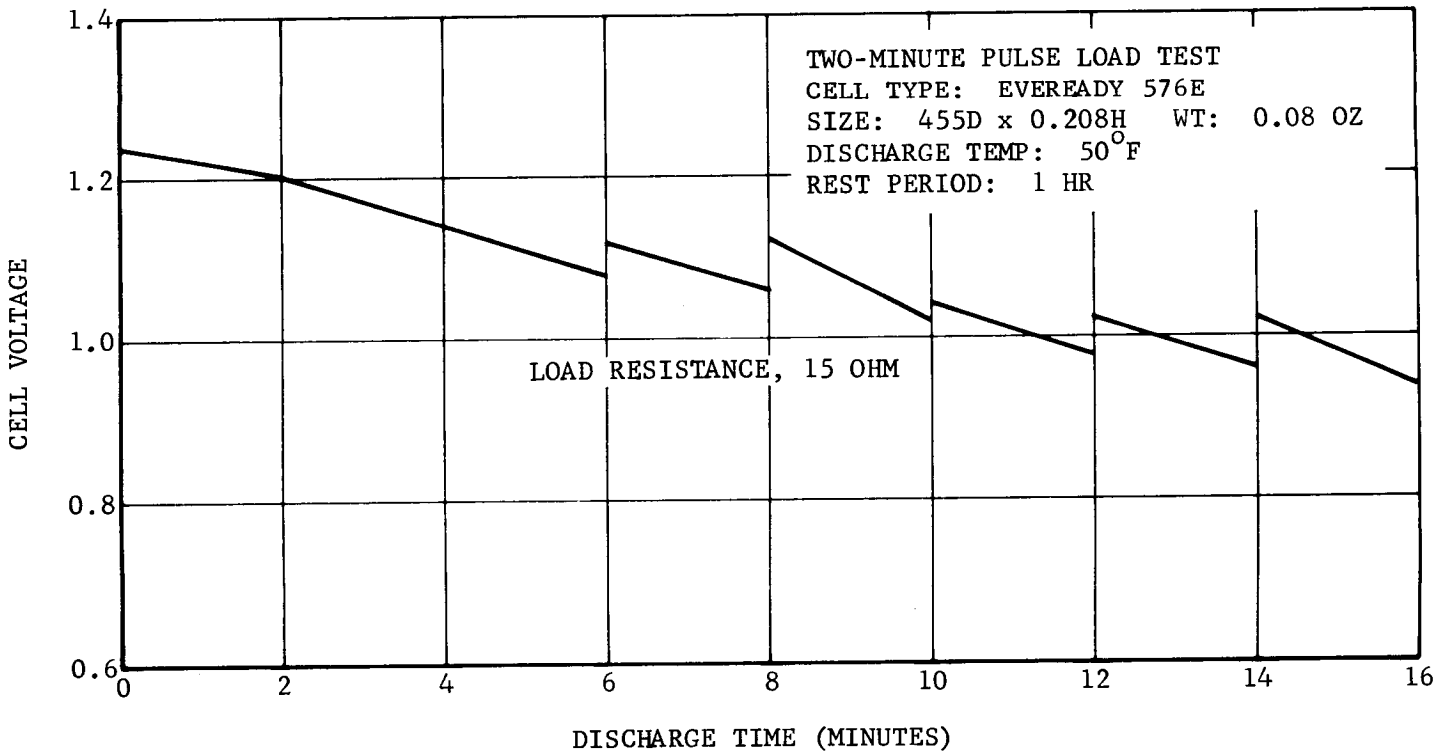

FIGURE 5-91. TWO-MINUTE PULSE LOAD TEST ON EVEREADY 576E CELL AT 50°F

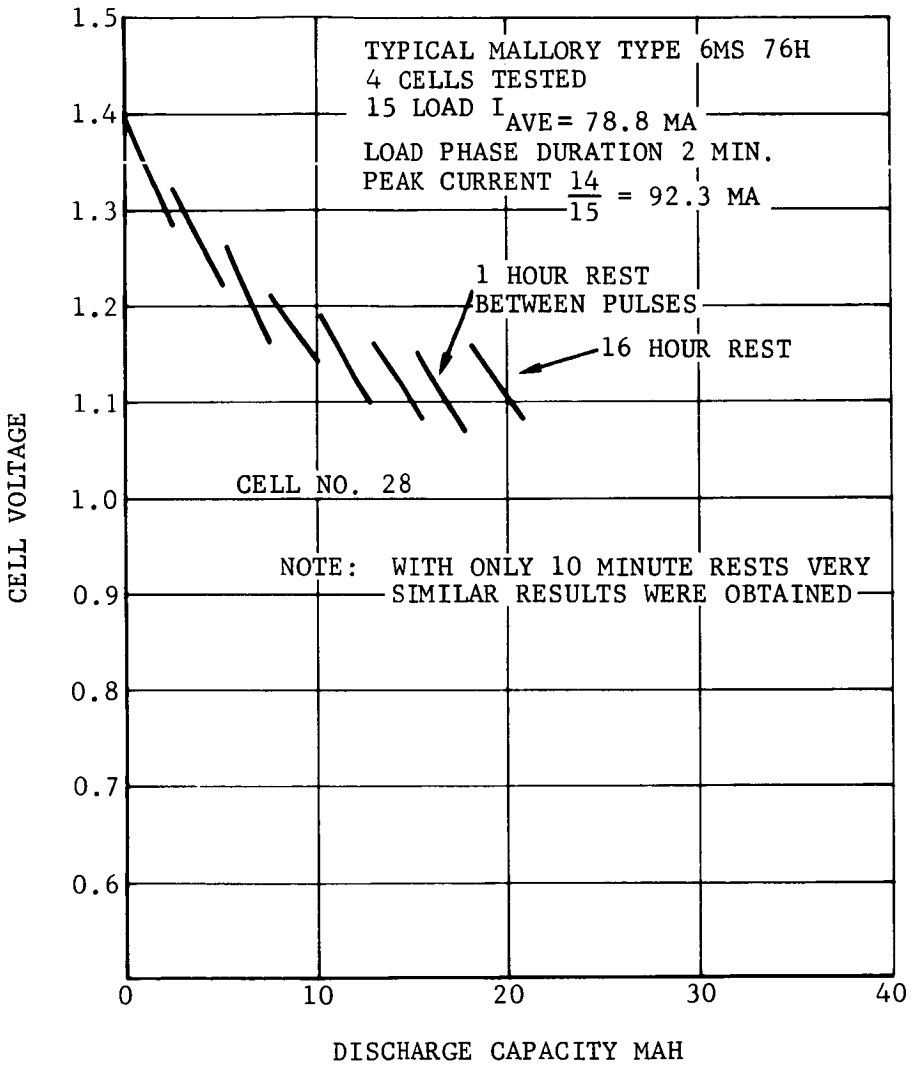

FO3623 U

FIGURE 5-92 PULSE LOAD DISCHARGE TEST, MALLORY 6MS 76H

yielded similar results as shown in Figure 5-92. These tests were not performed on the Ray-O-Vac cells as their performance was significantly below that of the other types, as seen in Figures 5-81 and 5-82. Shock tests were performed on Mallory 6MS76H and Eveready S76E cells as the electrical tests showed them to be the most suitable for the penetrometer application.

Shock tests on the Mallory and Eveready cells were performed using the instrumented hammer. The Mallory cells, which have an internal cup cathode structure, show a tendency to open up on the negative overshoots on the shock waveform. The cathode cup structure appears to be the cause of this, since it is conceivable that it may lose contact with the outer shell during the negative going waveforms. The Eveready cells have a cathode which is directly deposited in its outer shell and its shock test results showed no tendency to develop open circuits.

Four Union Carbide Eveready type S76E cells and four Mallory type MS76H cells were tested on the Hyge facility. Each group of four series-connected cells was impacted in three directions. During impact, a constant resistive load of 75 ohms was applied across the battery. The results of these tests are summarized in Table 5.8. The Eveready S76E cells appeared to be more shock resistant than the Mallory MS-76H cells, confirming the hammer test results. Approximately 1 volt deviation was noted on run No. 3 of the Mallory cells. This was the direction of weakness noted in the hammer tests.

d. Development of Prototype Test Model Battery. As discussed earlier, it was first planned to fabricate the penetrometer battery using Gould-National 50B button cells. The current requirements would have necessitated the use of a dual string of approximately 20 cells in each and two diodes to prevent self-discharge between the strings. The battery was to be designed so that one string of cells was oriented at 90 degrees to the other string for shock protection. Since the various cells typically exhibited one poor direction for shock, if one string failed in a hard impact, the other string would likely remain operative and would be able to supply the entire load current as the duration of a destructive impact would be only a few milliseconds at most. Use of the GN 50B cells was discouraged by the discovery of a broken internal spring in all cells examined in the two lots received. It was therefore decided to use the Jupiter B80 cell, although it is of Hungarian manufacture, until a reliable domestic source could be found.

The early model battery pack shown in Figure 5-93 used the Jupiter B80 cells and retained the orthogonally mounted dual string for shock reliability. However, the energy and power capabilities of the B80 cell

TABLE 5.8
BATTERY IMPACT TESTS

	EVEREADY CELLS S76E (4 CELLS IN SERIES 75 Ω LOAD)					MALLORY CELLS MS-76H (4 CELLS IN SERIES 75 Ω LOAD)			
RUN NO.	1	2	3	4	5	1	2	3	4
E_{oc} (OPEN CIRCUIT BEFORE TEST)	-6.371V	-6.338V	-6.637V	-6.36V	-6.373V	-6.394V	-6 389V	-6.300V	-6.325V
E_L (LOADED WITH 75 Ω)	-4.825V	-4.648V	-4.65V	-4.79V	-4.707V	-4.979V	-4 94V	-4.94V	-4.824V
Δ E (CHANGE IN E DURING IMPACT)	+0.2V (DECREASED)	+0.114V (DECREASED)	-0.107V (INCREASED)	NO * DATA	+27 MV (INCREASED)	-0.10V (DECREASED)	+0.202V (DECREASED)	+1.06V (DECREASED)	-95 MV (INCREASED)
RESOLUTION	0.5V/IN.	0.476V/IN.	0.485V/IN	0.485V/IN	0.447V/IN.	NONE	0.494V/IN.	NONE	0.473V/IN.
IMPACT LEVEL (G)	10,000 g's	13,000 g's	8,750 g	8,250 g	11,800 g	10,600 g	8,650 g	10,700 g	9300 g
VELOCITY FT/SEC	183 FT/SEC	183 FT/SEC	178 FT/SEC	228 FT/SEC	228 FT/SEC	185 FT/SEC	185 FT/SEC	191 FT/SEC	235 FT/SEC
E_{oc} (OPEN CIRCUIT AFTER IMPACT)	-6.351	-5.249V	-6.358V	NO * DATA	-6.31V	-6.389	CABLE BROKE	CABLE BROKE	-6.206V
DIRECTION OF FORCE	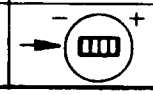	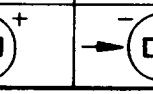	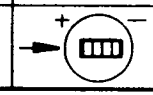	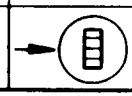	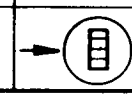	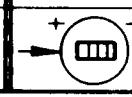	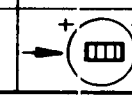	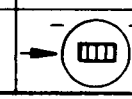	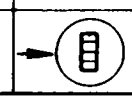

* FITTING DESTROYED DURING INITIAL ACCELERATION IMPACT.

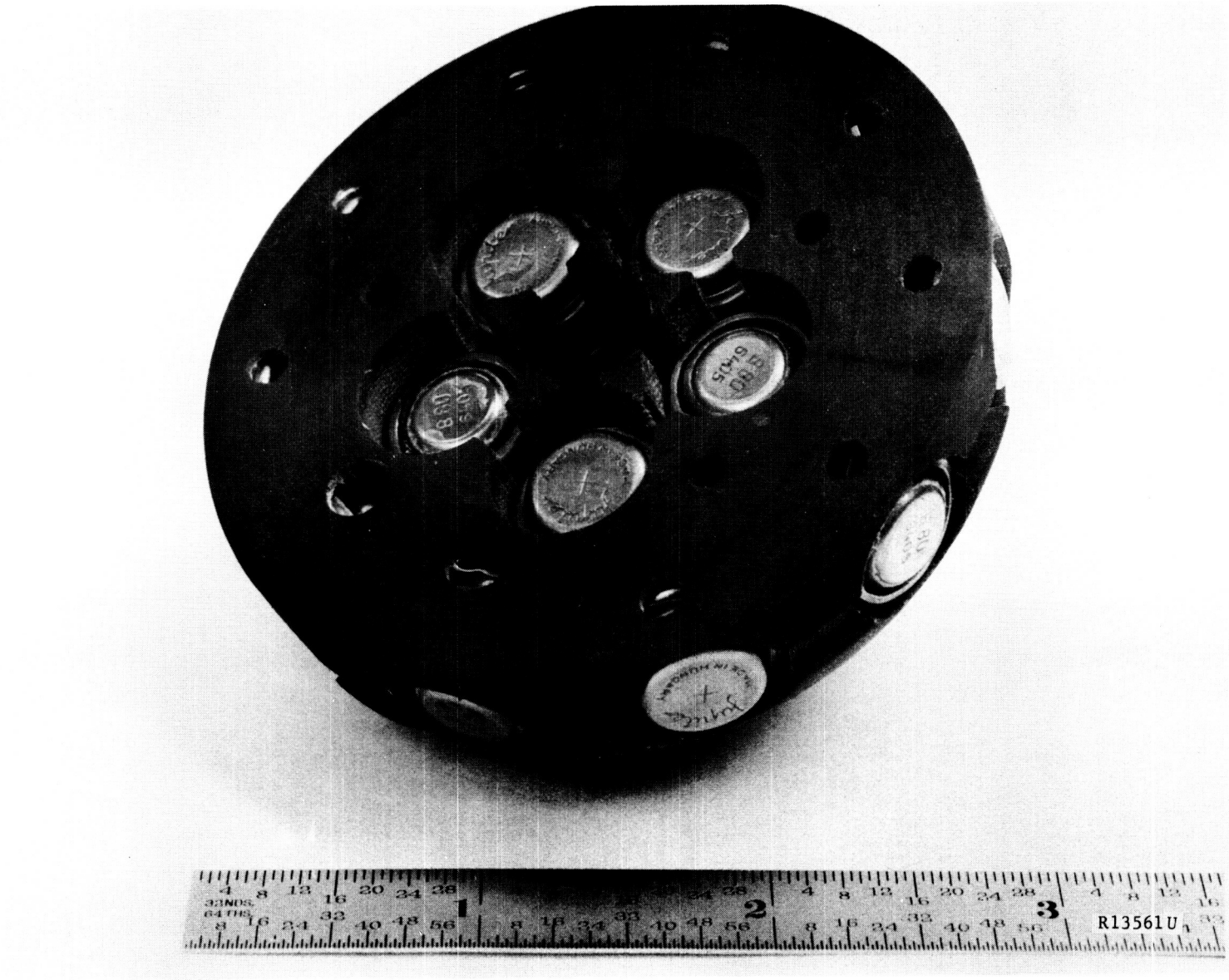

FIGURE 5-93. EARLY MODEL BATTERY PACK USING TWO REDUNDANT STRINGS OF JUPITER B-80 CELLS

are such that a dual string is not needed electrically. Therefore, as shock testing data demonstrated the reliability of the B80 cell and the volume requirements of the electronic modules grew, the redundant string was abandoned. The battery in the engineering model used 4 cells for the negative supply and 16 cells for the positive supply. The prototype batteries were increased to 20 cells in the positive supply and 5 in the negative supply for prototypes 2 and 3 to gain more operating time before recharging as sufficient space was available.

After Hyge of Prototype No. 1, the battery would not accept a full charge. The accelerometer or signal electronics had apparently also failed and the penetrometer was disassembled for autopsy. The findings are detailed on the Prototype No. 1 test report, Appendix A. It was found that one of the cells was leaking electrolyte, 3 had reversed polarity, one cell showed distinct swelling symptomatic of excessive outgasing, and it is likely that the battery was destructively overcharged. A commercial charger which had been used was found to have an excessive ripple in its output with voltage sensing of the average value. This would have caused overcharging of high-capacity cells. Cells of marginal capacity could have become reverse polarized during discharge. It appears discharge was complete because of leaking electrolyte entering the cabling and connector. To prevent recurrence of these problems in Prototype No. 2, an investigation into individual cell characteristics was conducted in order to determine representative values of charge capacity, retention, and discharge capacity. Results of these tests clearly indicate that there is a considerable spread in cell performance characteristics and a battery must be composed of selected cells with closely matched mah capacity.

The swelling of battery packs on Prototype No. 1 was probably caused by gasing caused by overcharge. Swelling has been evident on individual cells deliberately overcharged during cell evaluation tests. To minimize the possibility of overcharge henceforth, no cell was to be charged beyond the first voltage plateau which represents about 30 percent of rated mah capacity. In order to provide sufficient resolution in the charging voltage characteristic to determine the first plateau of a single cell, batteries are charged in short strings (5 four-cell strings, 1 five-cell string). This requires an additional seven-pin umpilical plug and additional wiring.

A sample lot of Jupiter B80 silver-zinc button cells was tested to evaluate the spread in mah capacity and the feasibility of matching cells of equivalent capacity. Cells in the condition received from the distributor were initially discharged at an 8 milliampere rate to a 1 volt end-of-life (EOL) level. This allowed monitoring the charge cycle voltage

and capacity to obtain comparison data on individual cells. Figures 5-94A and 5-95 show charging voltage versus time for six cells. From these data, it appears that limiting the charging time to that required to reach the first plateau limits mah capacity to about 30 mah instead of the rated 80 mah. The first plateau is easily recognizable even with series set of four cells and provides a definite control indication to prevent overcharge.

Discharge characteristics of the same group of cells are shown in Figures 5-96 and 5-97 Cell No. 7, which terminated charging shortly after reaching the first plateau (43 mah total charge), was able to deliver 30 mah at a 1-volt EOL. The recoverable mah capacity is expected to be somewhat less at the 180 ma penetrometer drain rate. Cell No. 8 reached the first plateau at a 27 mah capacity and supplied 25 mah at the 8 ma drain rate. Cell No. 9 accepted 42 mah charge and was able to deliver 34 mah at EOL. Other cells were charged for a longer time to obtain an 80 mah capacity. Discharge tests at an eight ma rate indicate that 80 mah can be recovered from typical cells. Discontinuities in Figures 5-96 and 5-97 result from termination of the discharge tests at night and show recovery capability of the cell when unloaded.

It is expected that a battery of cells, selected for at least a 30 mah capacity near the first plateau, can provide four to five 15-second operating cycles. This assumes a 30 mah charge capacity, and a 10 percent recovery at a 200 milliampere load which provides 54 seconds of continuous operation. Operation at well-spaced 15-second intervals should extend this operating time appreciably. Selection of cells and controlled limited charging should reduce problems associated with overcharging, gasing, and swelling to an absolute minimum.

Seventy-eight remaining cells were tested for charge-discharge characteristics following the procedure described above. The cells were matched in sets of four (and five) for use in Prototype Number 2 and 3 batteries. Selection was on the basis of charging time (mah capacity) required to achieve the first voltage plateau. This time ranged from 3 to 5 hours for the group tested at an eight milliampere rate with the large majority of cells falling within the range of 4.2 to 4.7 hours.

After completion of Penetrometer Prototype Numbers 2 and 3, both unaccountably developed a low voltage in one 4-cell string (not the same string) as though one cell had failed. Both penetrometers have since been through much testing with one 200 fps impact onto a steel plate for each and repeated battery recharging with no further evidence of battery deterioration. The batteries were also subjected to repeated hammer tests before being assembled into the prototype penetrometers.

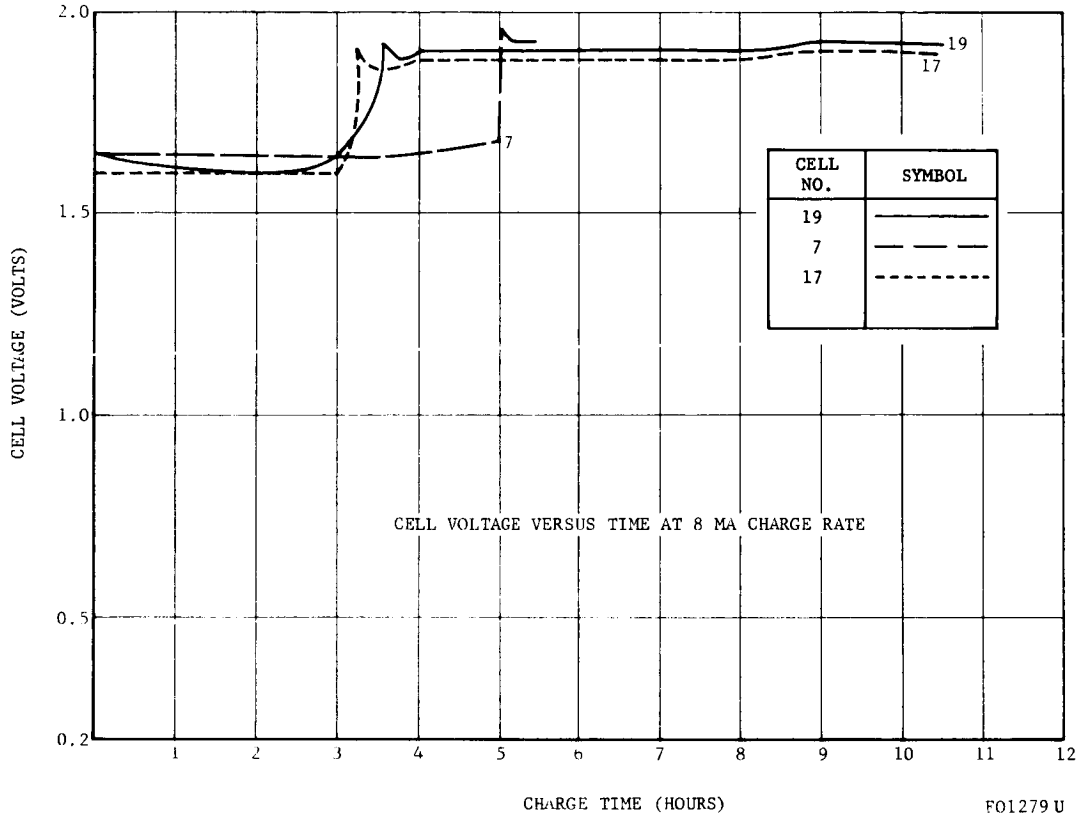

44

FIGURE 5-94. CHARGING CHARACTERISTICS OF JUPITER B-80 CELLS FOLLOWING INITIAL DISCHARGE

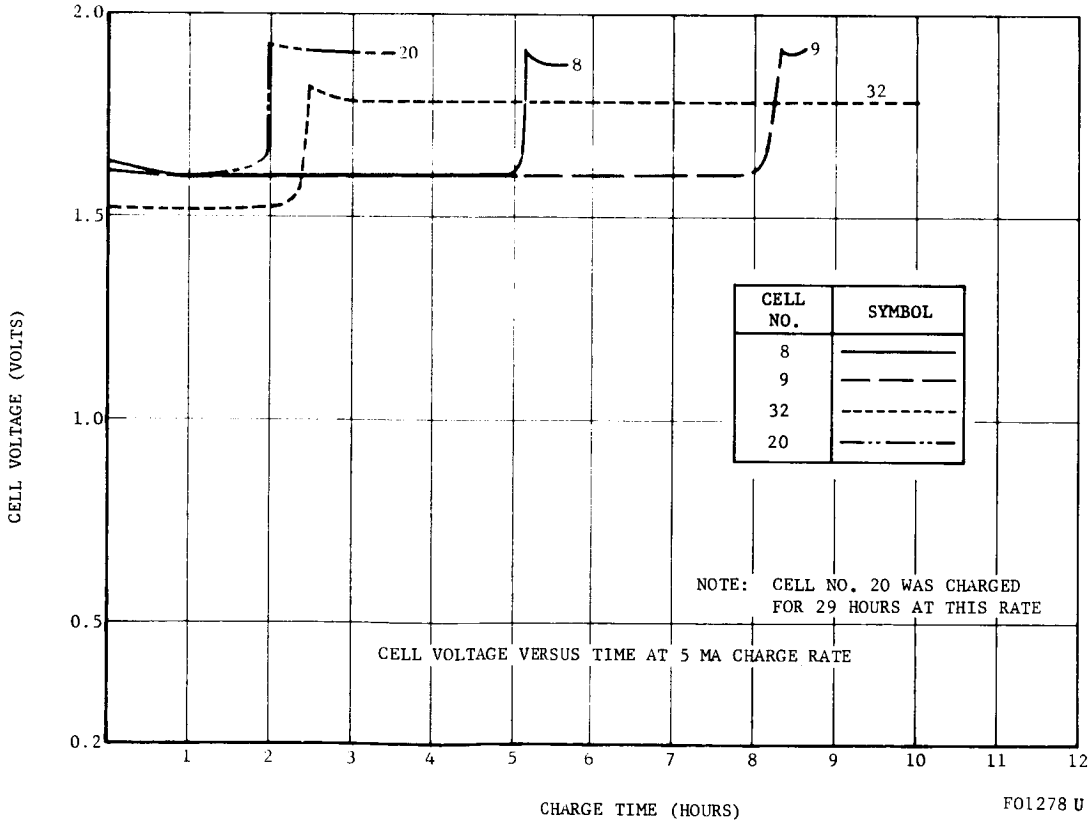

45

FIGURE 5-95. CHARGING CHARACTERISTICS OF JUPITER B-80 CELLS FOLLOWING INITIAL DISCHARGE

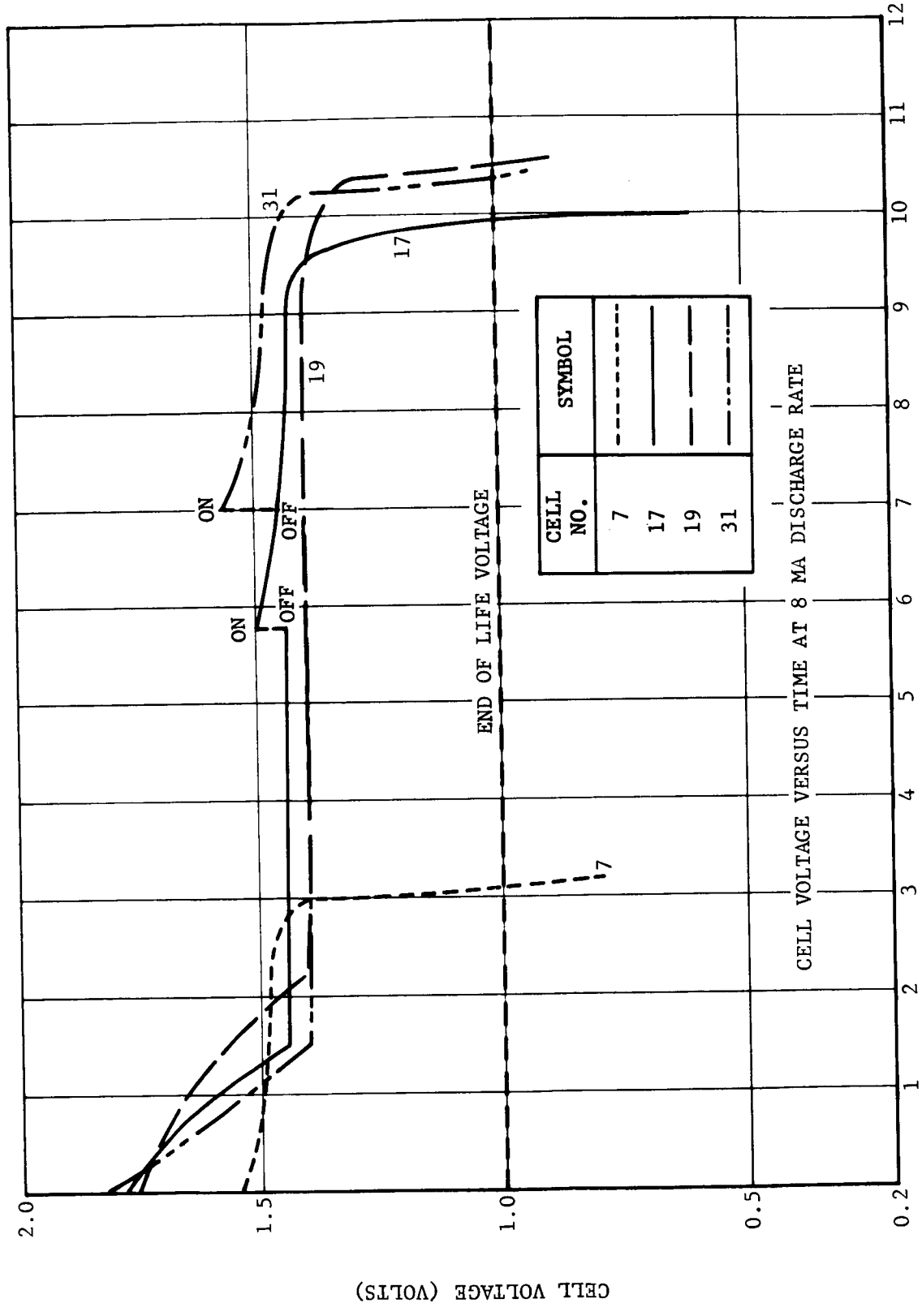

FIGURE 5-96. DISCHARGE CHARACTERISTICS OF JUPITER B-80 CELLS FOLLOWING CONTROLLED CHARGE CYCLE

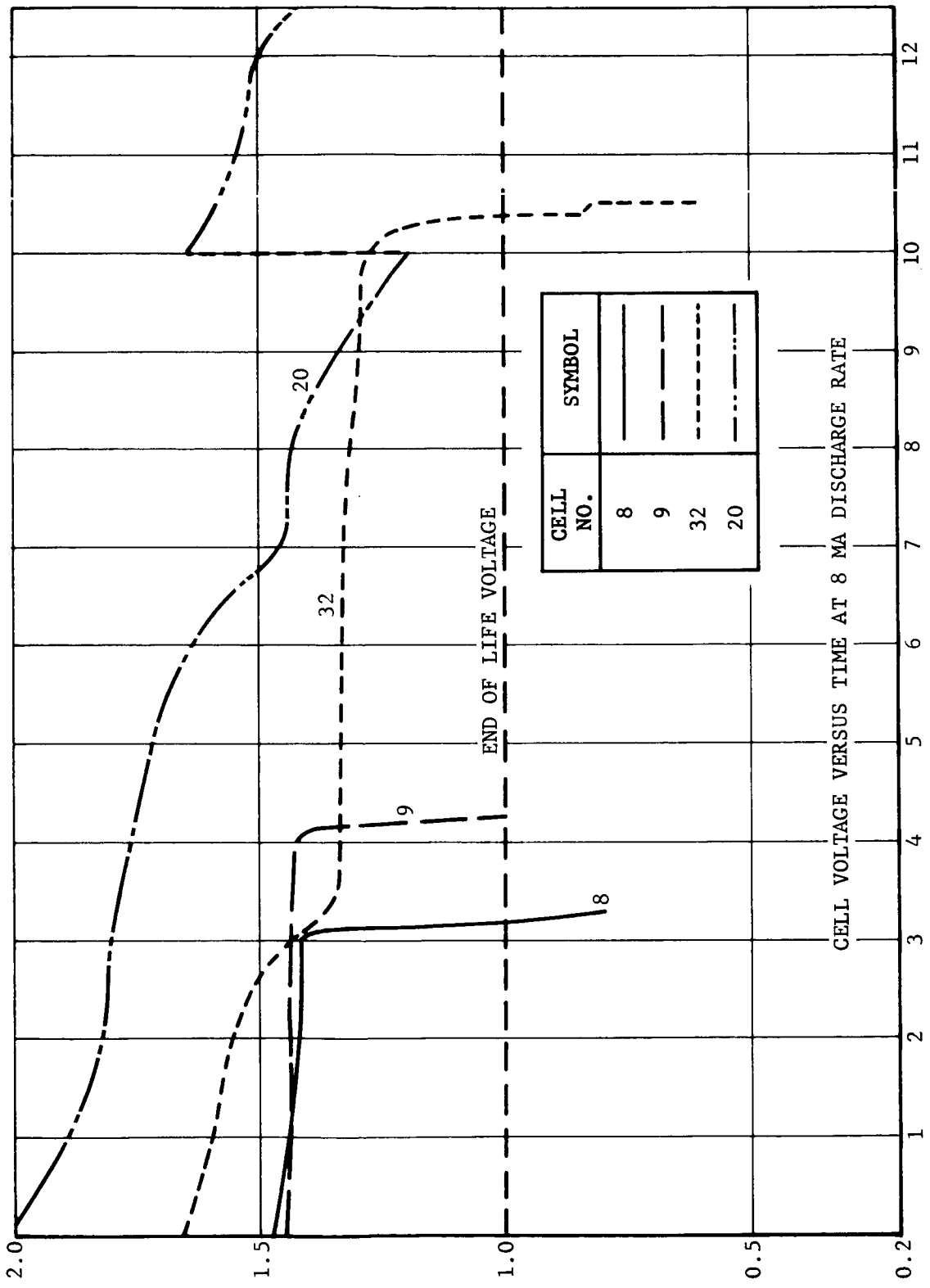

F01277 U

FIGURE 5-97. DISCHARGE CHARACTERISTICS OF JUPITER B-80 CELLS FOLLOWING CONTROLLED CHARGE CYCLE

The battery for Prototype No. 2, with timer installed, was shown in Figure 5-74. The battery is made up of three layers of cells. Each layer contains cells recessed in a machined fiberglass epoxy disc. Nickel ribbon leads are electric welded to both terminals of each cell and the leads are soldered together. Milar insulation is used between the battery layers.

e. Flight Model Battery Procurement. Two approaches have been explored to obtain a domestic source for the flight-type battery. These efforts were begun early in the program when use of the previously favored Gould-National 50B cells became questionable. It is clearly advantageous to have an American source for the battery and an early establishment would have allowed maximum development test experience. The first approach was to find a small cell with which batteries could be fabricated. These efforts were described in Paragraph 5.5.2c. A battery is feasible using a dual string of either the Eveready S76E or the Mallory 6MS76H cells. However, these batteries would not give the performance in the small size of the prototype battery which used the Jupiter (Hungarian) B80 cells.

In order to obtain a battery of equivalent performance to the prototype unit, a specification SK21526, was written describing its performance. A purchase information request (PIR), No. 208045 was submitted, with the specification, to various battery manufacturers soliciting fixed-price bids for the development of a battery and delivery of 10 units for evaluation. The vendors solicited were:

(1) Sonotone Corporation
(2) Yardney Electric Corporation
(3) Electric Storage Battery Company
(4) Ray-O-Vac
(5) Electrochemica Corporation
(6) Catalyst Research Corporation
(7) Mallory Battery Company
(8) Gulton Industries
(9) Union Carbide Consumer Products

The specification SK21526 required a minimum battery capacity to supply 10 minutes operation between charge cycles. This was to allow sufficient time to obtain antenna pattern measurements on the completed penetrometer.

Enough is now known about the antenna system that its pattern can be determined in much less time. Therefore, when no responsive bids were received, the specification was revised to require only 2 minutes operating time, a reduction in energy by a factor of 5. At the same time, the allowed volume was reduced by 40 percent in accord with the volume achieved in the final prototype battery design. This specification was included with PIR No. 208046 requesting new quotations.

There were still no bids offered to supply the battery, the consensus being that the revised specification was more difficult to meet than the previous one, although the energy requirement was reduced by a factor of 5 and the battery specification was based on requirements which have been adequately satisfied by the existing foreign-made Jupiter B80 cells. Table 5.9 is a summary of the bidding.

Discussion with several of the vendors revealed that there are several problems in obtaining bids to supply the penetrometer battery. Most sealed button cells are designed for low-current drain and use at room temperatures. The manufacturers themselves do not know the performance characteristics at high drain rates, from 50 to 100°F, and during a 10,000 g shock. Further, the battery vendors are reluctant to bid fixed-price on a development program which contains unknown problems and offers no large-quantity production possibilities.

While no satisfactory bids have yet been received, it is apparent that there would be responses if the risk of loss were reduced by some form of pricing other than straight fixed price. At least four companies are interested in developing an Ag-Zn cell equivalent to the Jupiter B80, and two or more others may bid on cells or batteries or both. The effort so far has identified the potential vendors and some of their individual capabilities and interests have been determined.

TABLE 5-9

SUMMARY OF PENETROMETER BATTERY BIDS

	Vendor	PIR No.	Phone	Visit	Response
1.	Sonotone	208045	No	No	No bid. No Ag-Zn cells.
2.	Yardney	208045	No	No	No bid. No button cells.
3.	Electric Storage Battery - Missile Battery Division	208045	Yes	No	No bid. However, they had previously stated that they might use Ray-O-Vac components.
4.	Electric Storage Battery - Missile Battery Division	208046	Yes	Yes	No bid. However, it was suggested that Electric Storage Battery research labs had facilities and experience in button cell development and that they may be interested.
5.	Ray-O-Vac	208045	Yes	No	No bid. No rechargeable cells. Could not meet temperature in volume available. They did once make a primary cell that could work at R.T. Not available now.
6.	Ray-O-Vac	208046	Yes	No	Verbal No Bid on cells or development. New PIR more difficult.

TABLE 5-9 (CONTINUED)

SUMMARY OF PENETROMETER BATTERY BIDS

Vendor	PIR No.	Phone	Visit	Response
7. Electrochemica	208045	Yes	No	Bid Ag-Cd but could not meet size requirement. Suggested Ag-Zn cell development.
8. Electrochemica	208046	Yes	Yes	No bid. Estimated that Ag-Zn cell development would require $30,000 and 6 months.
9. Catalyst Research	208045 208046	No No	No Yes	No bid. Do not make button cells.
10. Mallory Battery	208045	Yes	No	No bid. Second PIR was not submitted but battery tests and phone contacts indicate development possibilities. Their production hearing aid cell is very near meeting requirements.
11. Gulton	208045	No	No	No bid on cells. They are interested in cell development.
12. Union Carbide	208045	Yes	No	No bid on battery. However, their cells come close to meeting requirements and they may be interested in development.

TABLE 5-9 (CONTINUED)

SUMMARY OF PENETROMETER BATTERY BIDS

	Vendor	PIR No.	Phone	Visit	Response
13.	Burgess Battery	208046	Yes	No	No bid because they do not make Ag-Zn in production. They have developed a cell similar to the Jupiter B-80 and are interested in development of a cell for our requirement.
14.	Marathon Battery	208046	No	No	No bid.
15.	RCA	208046	No	No	No bid.
16.	General Electric	208046	No	No	No bid. They do not have facilities for making small cells.
17.	Eureka-Williams	208046	No	No	No bid. Not in their field.
18.	Eagle-Picher	208046	Yes	No	No bid. Volume is too small.

The following table summarizes this information:

Vendor	Potentialities
Electric Storage Battery Missile Battery Division Raleigh, North Carolina	A. M. Chrietzberg indicates interest and has experience in impact technology but has no button cell components. He could get them from Ray-O-Vac.
Electric Storage Battery Ray-O-Vac Division Madison, Wisconsin	They have declined to bid on previous requests for development but are still interested. They are heavily production oriented.
Electric Storage Battery Research Laboratory Yardley, Pennsylvania	They have developed Ray-O-Vac Ag-Zn hearing aid cells and have button cell facilities. No contact has been made.
Electrochemica Menlo Park, California	They have Ag-Cd cells which do not have high enough power density. Dr. Eisenberg estimates that Ag-Zn would require $30,000 and 6 months to develop. They are commercially oriented.
Mallory Battery Company Tarrytown, New York	They No Bid initial requests but have cells which have potential (limited recharge) and would be interested in development. Production oriented.
Union Carbide (Eveready) New York City	They No Bid original requests but subsequent communications have revealed that they have cells very nearly usable and are interested. Their research people have been identified but not contacted.
Burgess Battery Freeport, Illinois	H. J. Strauss, Research Director, has investigated and built cells similar to the Epic B-80 and definitely is interested in development.
Gulton Industries	They have declined to bid on a previous request but have mentioned an interest in development and do have Ag-Cd button cells available.

5.6 TIMER-REGULATOR

5.6.1 TIMER

A nominal 15-second timer was incorporated in the prototype penetrometer design to minimize battery discharge during qualification testing. The timer has the following performance characteristics:

(1) Capable of being triggered on by a momentary external connection.

(2) Provide less than 10 microamperes battery drain during "off" time.

(3) Switch up to 200 milliamperes of current in the +17 and -3 volt outputs.

Because of the low standby or off time battery drain requirements a MOS-FET was used in a one-shot circuit, shown in Figure 5-98. Q1A is normally biased "ON" and Q1B is "OFF." Capacitor C1 charges to approximately 20 volts. During the time Q1B is off, the source voltage at pin 7 is zero which holds the series switch Q2 "OFF" Series switch Q4 in the negative supply is also held "OFF" by maintaining a zero base to emitter voltage. When external short is applied to the battery activate contacts, C1 is discharged and Q1B is turned "ON," turning Q1A "OFF." This condition exists until the external short is removed. Following removal of the external short, C1 charges until the gate voltage of Q1B reaches out-off. Q1A then turns "ON" and the timing cycle is completed. During the time Q1B is "ON," the current through the device develops a positive voltage across R3 which turns "ON" the series switch Q2. This in turn drives the base of Q4 positive turning it "ON."

CR5 prevents damage to the gate of Q1B in the event a high positive voltage is inadvertently applied to the external activate terminal.

5.6.2 REGULATOR

A voltage regulator is required in the penetrometer because of the wide latitude (22 to 36 volts) of battery voltage. Both the LC oscillator and integrated circuit amplifiers (μ 702A) require well-regulated supplies for stable operation. A 17-volt supply level was selected for compatibility with both the oscillator and integrated amplifiers. Since the μ 702A's also required a negative bias, a -3 volt regulator was also included. The +17 volt supply current requirements approach 150 milliamperes necessitating the use of a series regulator transistor as the regulating element. A stable 17 volt reference voltage is furnished by a zener diode. Since the current requirements for the -3 volt supply are very small with corresponding small battery voltage excursion, a zener diode provides satisfactory regulation.

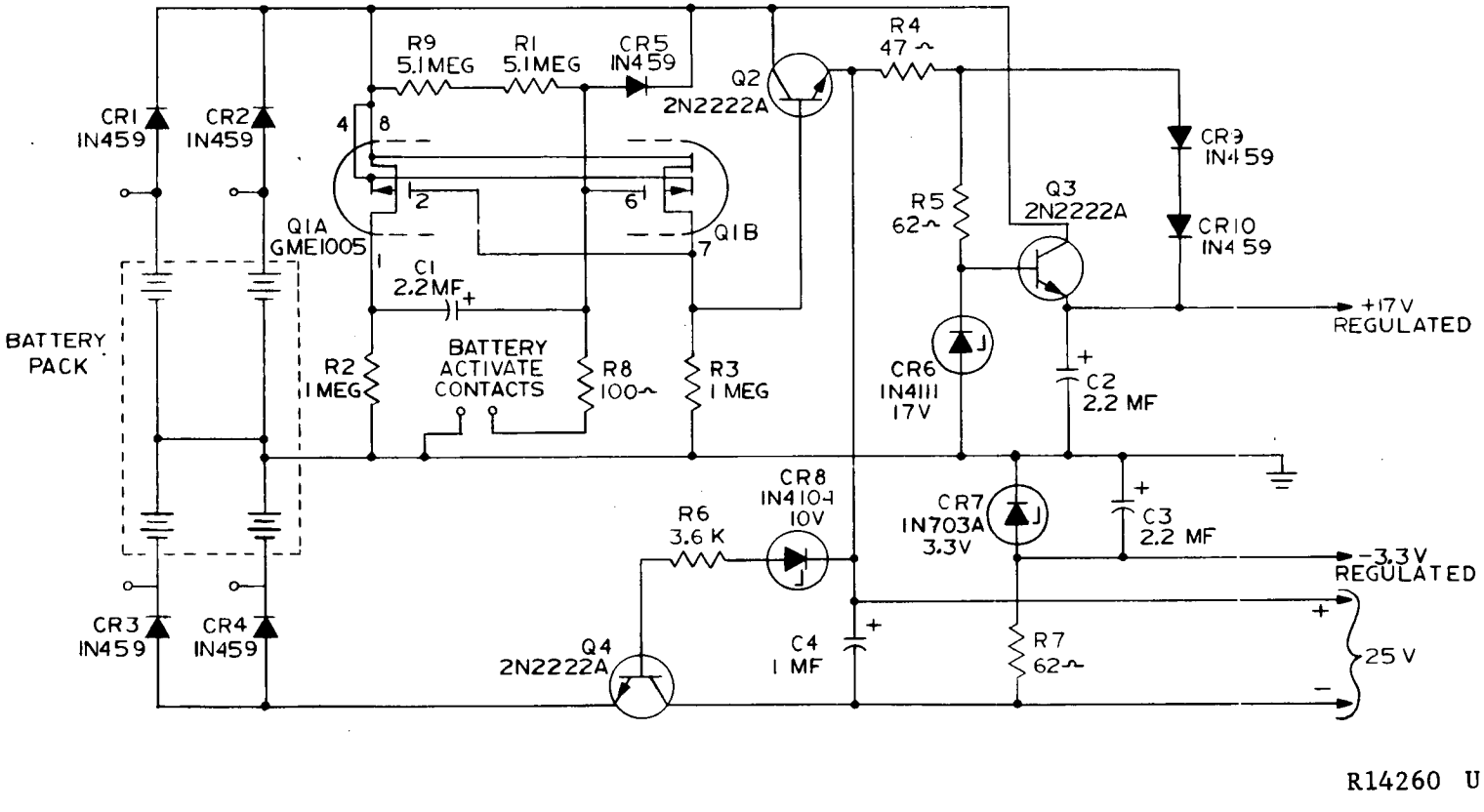

FIGURE 5-98. TIMER AND REGULATOR CIRCUIT

5.6.3 ENGINEERING MODEL

The regulator and timer circuit for the engineering model is shown in Figure 5-98. The breadboard layout is shown in Figure 5-99. Power is applied to the penetrometer circuits in 15-second intervals by the timer by momentarily shorting the turn-on terminals. An umbilical plug provides external access to activate the timer, to provide continuous operation for test purposes and to allow battery recharge. The regulator circuit provides +17 volts ± 3 percent and -3.3 volts ± 5 percent. Unregulated ±25 volts referenced to -4 volts is also supplied. The tolerances are based upon a minimum 26-cell battery and a minimum cell voltage of 1.2 volts.

The engineering model used 1/4 watt carbon composition resistors because of their availability instead of metal film resistors which exhibit superior shock sensitivity. Bourns metal film resistors have been incorporated in the prototype models. These resistors (Series 4200) proved very shock resistant in tests at Aeronutronic. The recommended IRC MMF resistors are no longer manufactured and the MCC type have a delivery of 8 weeks. The SCE type of American Component, Inc, evaluated by Carde, and Type 6928-FRP by P. R. Mallory are leadless cylindrical type. Such resistors require an additional process to attach leads for the penetrometer application. The Mallory units and type CE metal film resistors manufactured by American Component, Inc., are not presently available.

Evaluation of tests on the engineering model power supply indicate that 20 of the Jupiter battery cells should be used for the positive voltage supply. The 16 cells which were used in the engineering model did not provide sufficient voltage for the +17 volt regulator to operate within its regulation range. The additional cells, however, caused more power to be dissipated in the +17 volt regulator transistor (Q3) and therefore another transistor (Q4) was added in parallel for increased dissipation at high battery voltages. The regulator circuit is shown in Figure 5-100.

The regulated output voltages are shown in Figures 5-101 and 5-102 for the expected battery operating range of 22 to 28 volts for the positive supply and -4.4 to 6.0 volts for the negative supply. The +17 volt regulated output varies by 0.5 volt at a fixed temperature over a 22 to 28 volt input range. The -3.3 regulated output varies approximately 0.64 volt over the input range of -4.4 to -6.0 volts. The change in the -3.3 volt output is due to the poorly defined zener characteristics of the low voltage zener diode IN703A, which is typical for zeners in this voltage range. The change in the +17 volt output is due mainly to the zener diode characteristic and to a small extent the heating of the base-emitter junction of the output transistors Q3 and Q4. (V_{BE} decreases with temperature.)

Regulator characteristics with simulated battery transients were investigated after further discussions with Electrochimica. They could promise only a minimum of 1.38 volt drop for a 23 cell battery for 10 Kg impact.

FIGURE 5-99. TIMER AND POWER REGULATOR BOARD FOR THE ENGINEERING MODEL

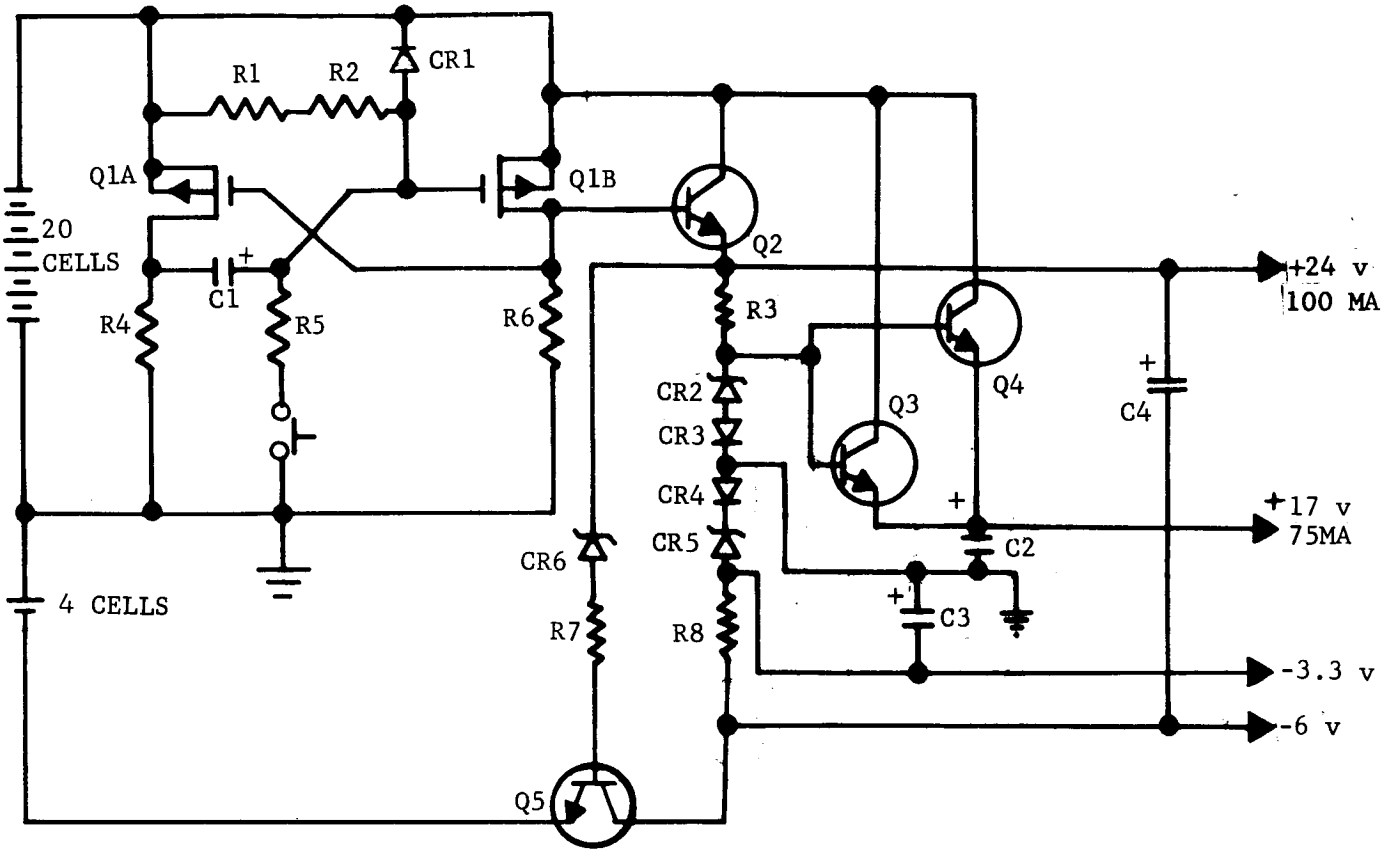

R1, R2 = (SELECTED FOR "ON" TIME)
R4, R6 = 1 MEG
R5 = 100Ω
R3 = 1K
R7 = 3.6K
R8 = 130Ω

C1, C2, C3 = 2.2μf (SEMCOR TS1-20-225) (20v)
C4 = 1μf, CS13AF010K (35v)

Q1 = GME1005
CR2 = UZ718
CR5 = IN703A
CR6 = 1N4104

NOTES: UNLESS SPECIFIED
1. ALL DIODES IN459
2. ALL TRANSISTORS 2N2222A
3. ALL RESISTORS ¼ WATT

R15282U

FIGURE 5-100. POWER SUPPLY AND TIMER SCHEMATIC, ENGINEERING MODEL

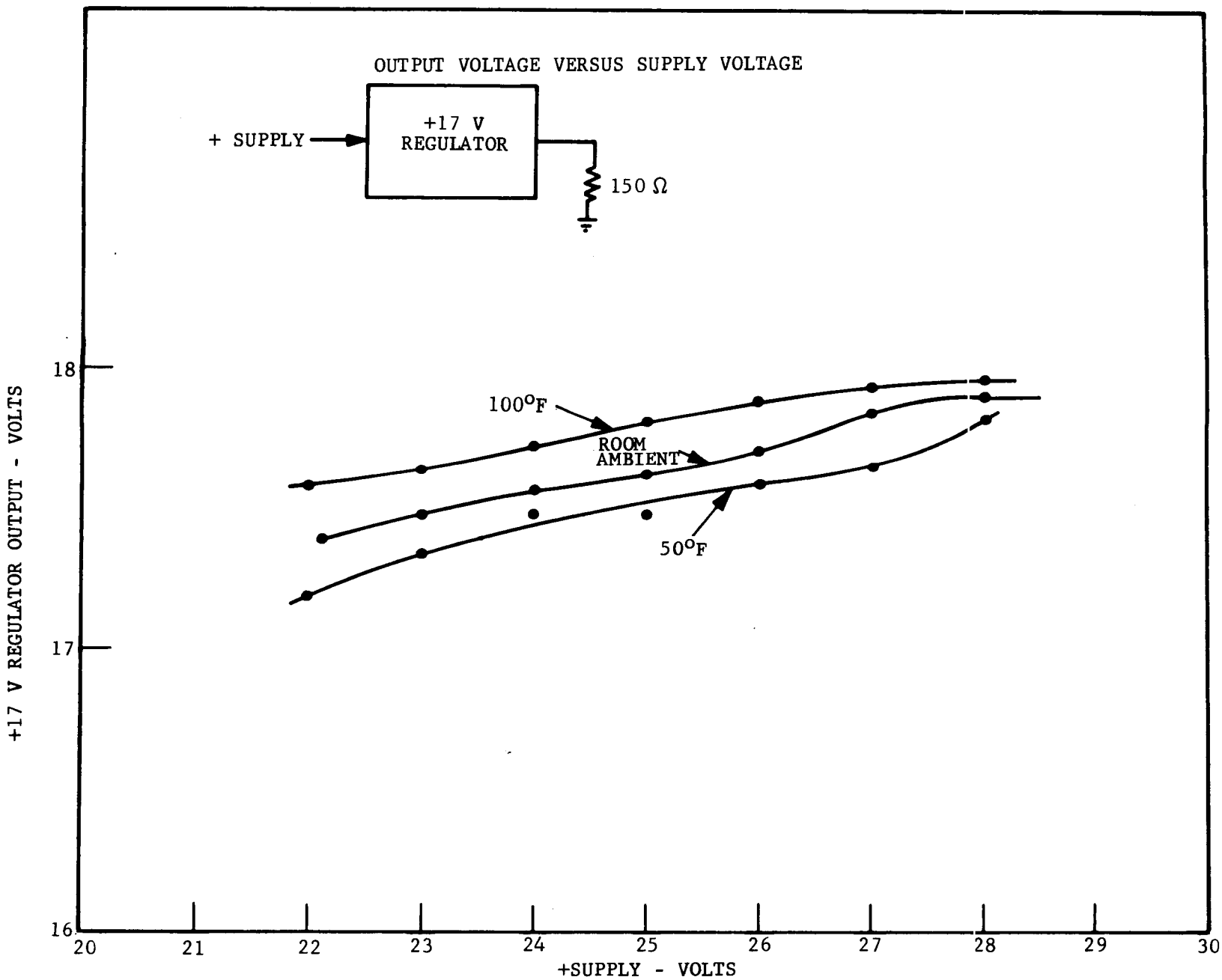

FIGURE 5-101. TYPICAL +17 VOLT REGULATOR CHARACTERISTICS AT VARIOUS TEMPERATURES

R15291 U

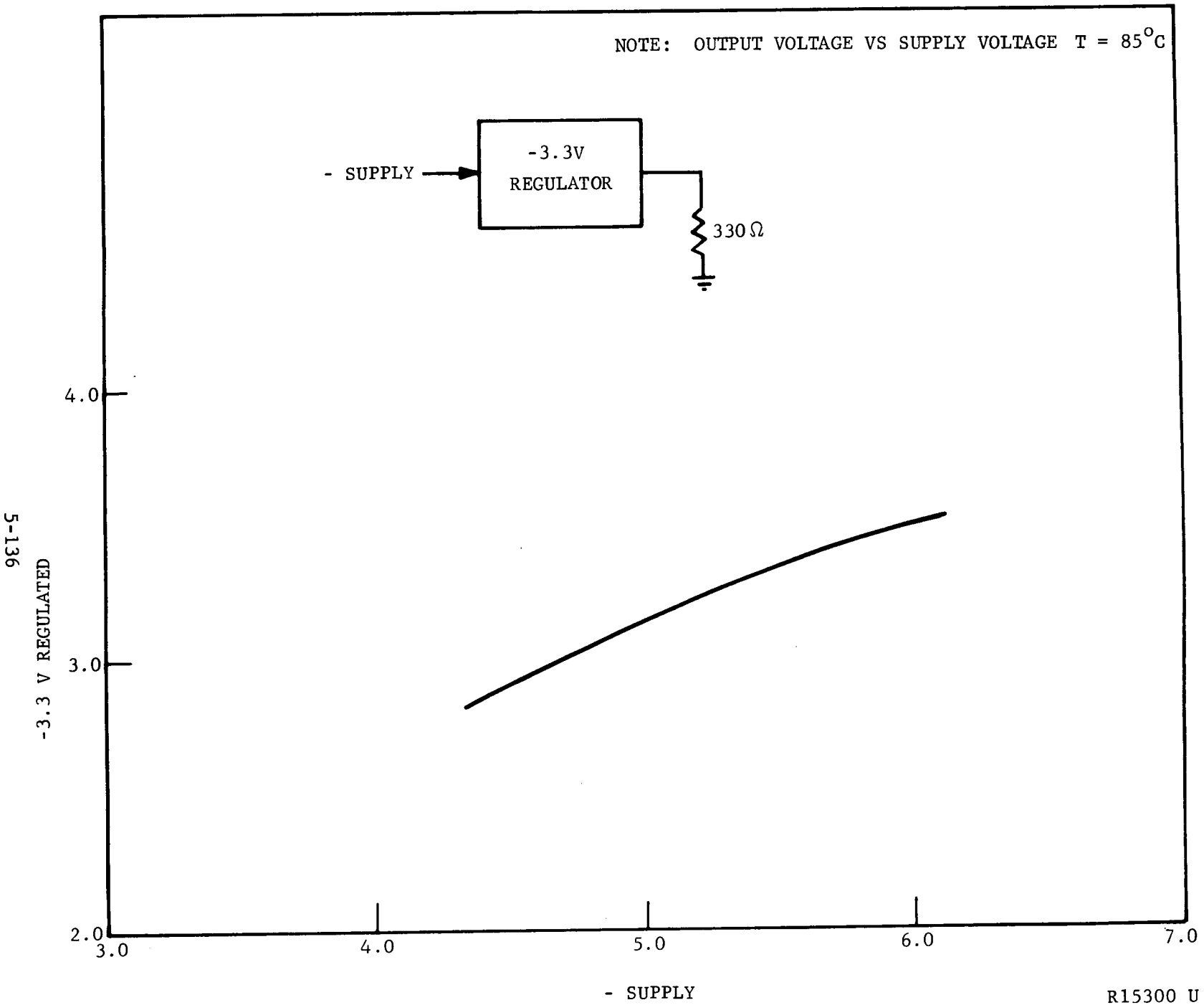

FIGURE 5-102. -3.3 VOLT REGULATOR CHARACTERISTIC

A 0.5 volt transient applied to the positive battery terminal causes a maximum transient of 30 millivolts at the +17 volt regulated output. The output recovers to normal within 0.4 second. A 0.5 volt transient applied to the negative battery terminal causes a transient at the -3.3 volt output of 0.25 volt. The output recovers within 0.4 second. These transients are shown in Figure 5-103. Additional testing with a 1.5 volt input transient characteristic of Electrochimica batteries produced a 70 mv output transient in the +17 volt regulated supply. This amplitude variation produces only 0.7 percent error at 50 g in the signal electronics. A 10 percent transient change in load current on the -3.3 volt causes a transient of 45 millivolts at the output which returns to normal after 0.3 second. These transients are shown in Figure 5-104.

5.6.4 PROTOTYPE NO. 1

The regulator and timer circuit shown in Figure 5-99 was used through Prototype No. 2 with no major changes.

Prototype No. 1 regulator timer operated erratically for a period of time. This was caused by leaking battery electrolyte resulting in low resistance shorts in the umbilical connector. When the unit was disassembled there was no evidence of power regulator/timer failure except for visible cracks in the glass diodes after the disassembly. These cracks could have been caused by the disassembly actions or by the epoxy shrinking. Recommended preventive action included coating all glass diodes with silicone rubber or covering diodes with shrink-fit sleeving.

The battery pack and timer-regulator module was assembled, inspected and potted. After completion, the unit was functionally tested to assure proper performance. A view of the completed unit and its protective dome was shown.

The battery-timer regulator module was mounted on the laboratory hammer and subjected to several blows of 4000 to 6000 g. The two critical regulated voltages (+17 and -3) were monitored for change during the shock interval along with the acceleration pulse. Figure 5-105 is the record of a typical impact test. The upper trace is the 4000 g shock pulse record and the lower that of the change in the +17 volt regulated supply. The sensitivity of supply voltage channel is 50 mv/cm. There was no detectable transient change in the supply voltage during the shock interval. Instrumentation problems resulted in the loss of data on this particular test for the -3.3 volt channel which was being monitored by a different oscilloscope and camera. Because the battery was almost completely discharged following eight impact tests, testing was discontinued and no additional -3 volt shock data was taken. Previous test data on the -3 volt channel were good.

+17 V LOAD TRANSIENTS
INPUT SET AT +25 V

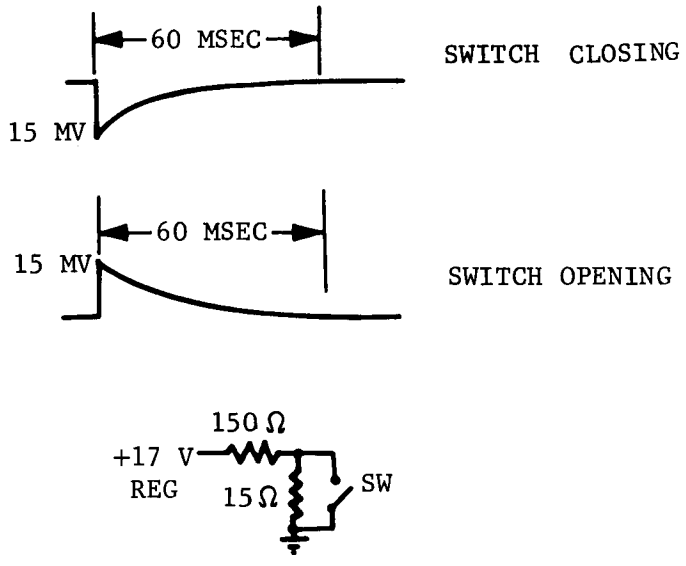

-3.3 LOAD TRANSIENT
INPUT SET AT -5 V

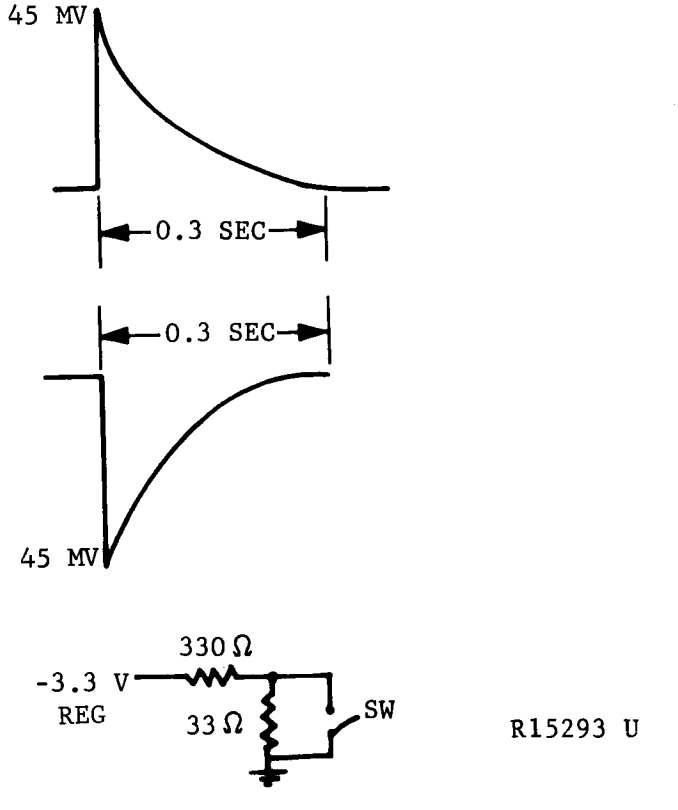

FIGURE 5-104. REGULATOR RESPONSE TO LOAD TRANSIENT

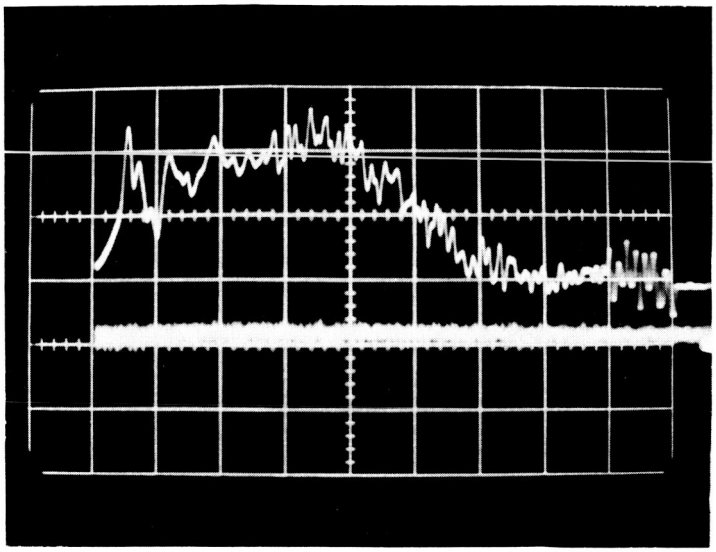

UPPER TRACE: SHOCK PULSE, 2000 g/DIV
LOWER TRACE: REGULATED +17 VOLTS, 50 MV/DIV
TIME SCALE: 100 μSEC/DIV

FIGURE 5-105. BATTERY-TIMER MODULE SHOCK TEST RECORD

After signal electronics in Prototype No. 2 became defective the battery-regulator timer module was removed to permit accelerometer removal and test. The regulator-timer board was damaged during disassembly and a modified regulator circuit was installed. No further problems in the regulator-timer were noted during extensive impact testing of Prototype No. 2 penetrometer.

5.6.6 PROTOTYPE NO. 3

Two minor problems were discovered during hammer testing of the power supply for Prototype No. 3.

(1) Solder points punctured the thin mylar insulator that separates the bottom of the battery from the center structural section. The mylar was replaced by a 0.015-inch thick sheet of fiber-glass board.

(2) The +17 volt supply did not turn off at the end of the 15-second period because of a shorted 2N2222 series regulator. The timer regulator board was replaced with a spare board. No permanent damage was done to the battery time-regulator circuit by these problems.

The +17 volt regulator circuit for Prototype No. 3 was changed to alleviate a major problem encountered in previous prototypes. In the initial design at high input voltages, the power dissipation in the series regulating transistors (Q_2 and Q_3) could exceed the maximum 500 mw rating. The two transistors must divide the load almost equally to stay within their power ratings. This problem is most dangerous when attempting to test the Penetrometer on external power because the external voltage is required to exceed the battery open circuit voltage.

This high voltage causes power dissipation beyond that normally encountered on battery power. The external power voltage must exceed the open circuit battery voltage which is in the range of 31 to 36 volts. The addition of a resistor in shunt across the series transistor shifts the power dissipation from the transistor to the resistor as the input voltages increase. In Prototype No. 3, this resistor consists of 3-1/4 watt resistors in parallel. Q_3 in the new circuit acts as a switch to keep power from being applied to the load through these resistors when the regulator is turned off. Required power dissipation is limited, since it is almost saturated during operation. This circuit change was evaluated on the breadboard regulator. The regulation observed was equal to or better than the engineering model circuit. Transient response tests were also conducted and the results were identical to those of engineering model circuit. Hammer tests of the

reworked battery-timer-regulator module are shown in Figure 5-106. The top trace (a) shows the +17 volt regulated output at 50 millivolts per cm. sensitivity. The lower trace is the accelerometer output at 2000 gs per cm. No transient is observable in the +17 volt regulated output. Similar results were observed on a 7000 g impact.

Figure 5-106c shows the battery open circuit voltage at impact. The Prototype No. 3 battery-regulator-timer module operated correctly through the entire series of drop and impact tests as well as many calibration runs.

The final prototype timer regulator circuit configuration is shown in Figure 5-107.

5.7 STRUCTURE

The primary structure for the Lunar Penetrometer is a 3-1/2 inch diameter hollow aluminum shell provided with a center web in the equatorial plane for mounting of the omnidirectional accelerometer. The structure is fabricated in three sections to allow easy access to the electronics during assembly and checkout. The center webbed structure provides the primary chassis upon which the omnidirectional accelerometer is centrally mounted; the telemetry assembly and power supply is built up; and the peripheral antenna feeds are installed. An upper hemispherical dome threaded to this center structure houses the telemetry electronics. A lower dome, which is retained to the center structure by a threaded equatorial coupling nut, houses the power supply and timer/regulator assembly. An exploded view of the structural components is given in Figure 5-108. Figure 5-109 shows the assembled penetrometer structure.

The deceleration force seen by the sphere during impact is equal to the reaction force imposed by the crushing balsa wood limiter. It is symmetric and is assumed to be of the form $P_o \cos \phi$ (where ϕ varies to $+ \pi/2$). For design purposes the total magnitude of the integrated vertical force was taken as 10,000 times a net inner payload weight of 2.7 pounds, resulting in a total imposed load of 27,000 pounds. The meridional membrane loads across a plane parallel to the plane of impact are pure compression and are not controlling. The critical design load occurs in a plane through the polar axis (direction of impact) where the circumferential membrane load varies from pure compression at the point of impact to tension at 16 degrees below the equator and back to compression at 38 degrees above the equator. Hence, for an impact in the plane of the equatorial threaded joint there is a tensile load of approximately 1300 pounds imposed over a 54 degree section of that joint. For loads of this magnitude any consideration of fastening by means other than the selected continuous threaded joint (e.g., individual fasteners) results in the consumption of an excessive amount of inner payload volume.

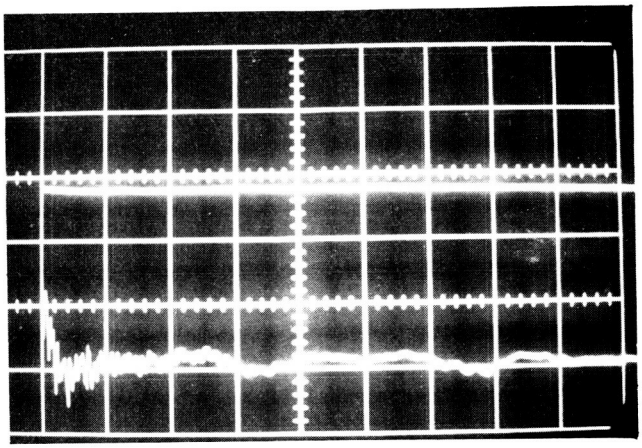

TEST A

UPPER TRACE: REGULATED +17 V OUTPUT
50 MV/DIV

LOWER TRACE: ACCELERATION, 2000 g/DIV

TIME SCALE: 500 μ SEC/DIV

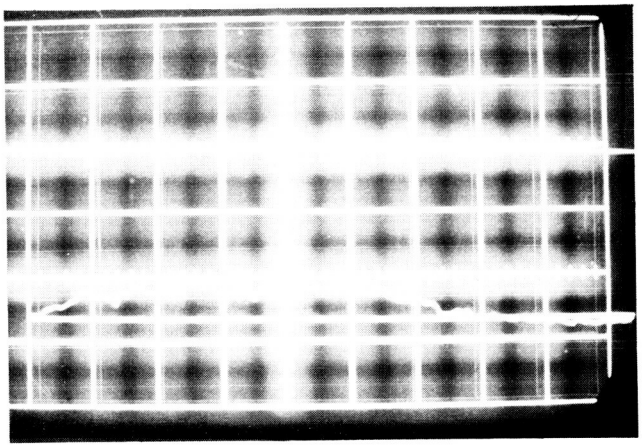

TEST B

UPPER TRACE: REGULATED -3.3 V OUTPUT,
50 MV/DIV

LOWER TRACE: ACCELERATION, 5000 g/DIV

TIME SCALE: 50 μ SEC/DIV

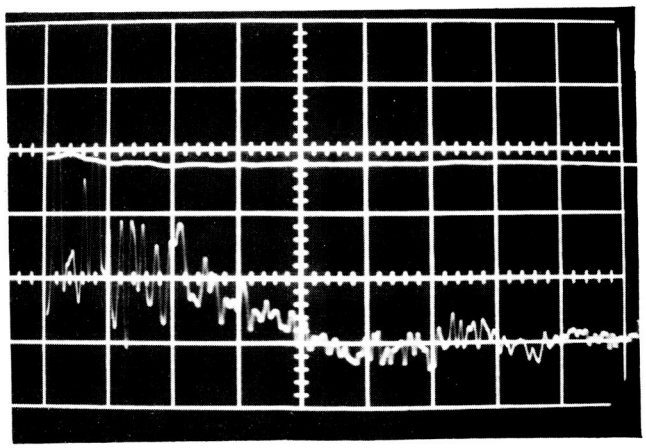

TEST C

UPPER TRACE: OPEN CIRCUIT BATTERY VOLTAGE,
50 MV/DIV

LOWER TRACE: ACCELERATION, 5000 g/DIV

TIME SCALE: 100 μ SEC/DIV

F02188 U

FIGURE 5-106. PROTOTYPE NO. 3 BATTERY AND REGULATOR HAMMER TEST RECORDS

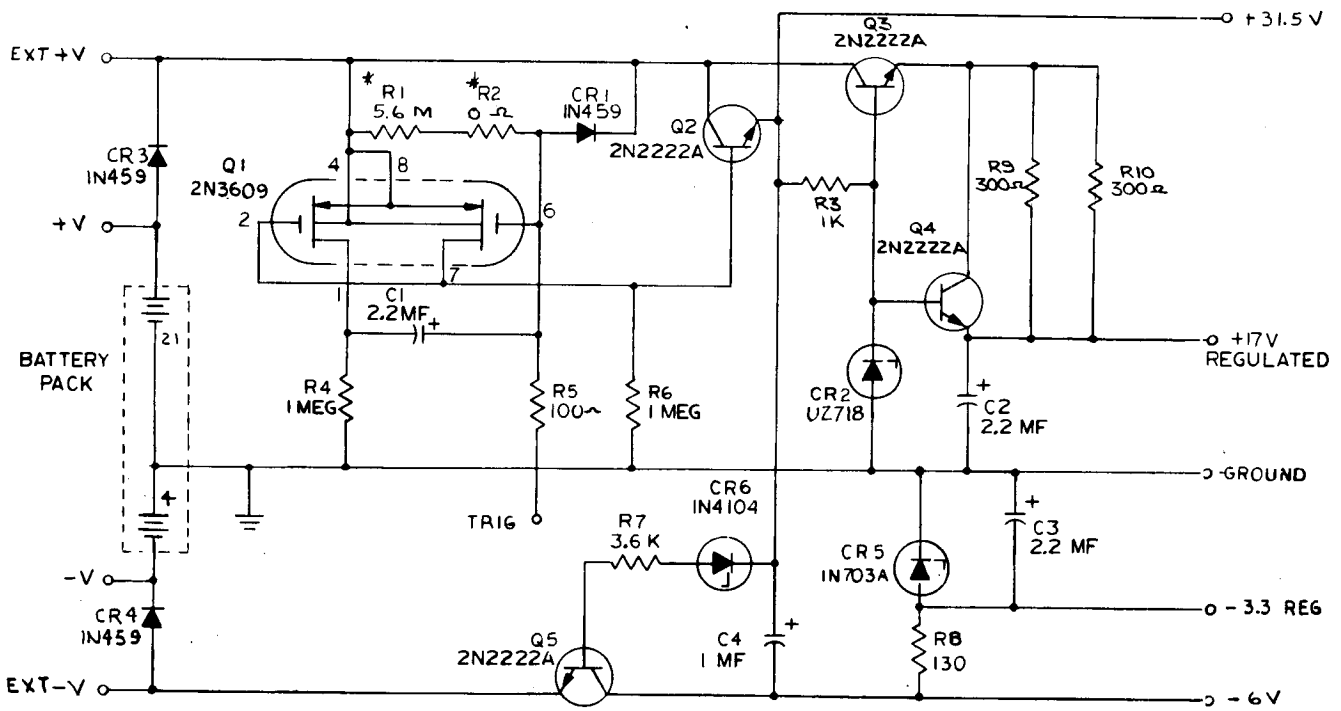

NOTES:

1. * SELECTED VALUES $(R_1+R_2)_{MEG} \cong \frac{\text{TIME (SEC)}}{2.2}$
2. FOR BOARD ASSY SEE DWG 24904

F'03808 U

FIGURE 5-107. TIMER/REGULATOR CIRCUIT - FINAL PROTOTYPE CONFIGURATION

FIGURE 5-108. PENETROMETER STRUCTURAL COMPONENTS

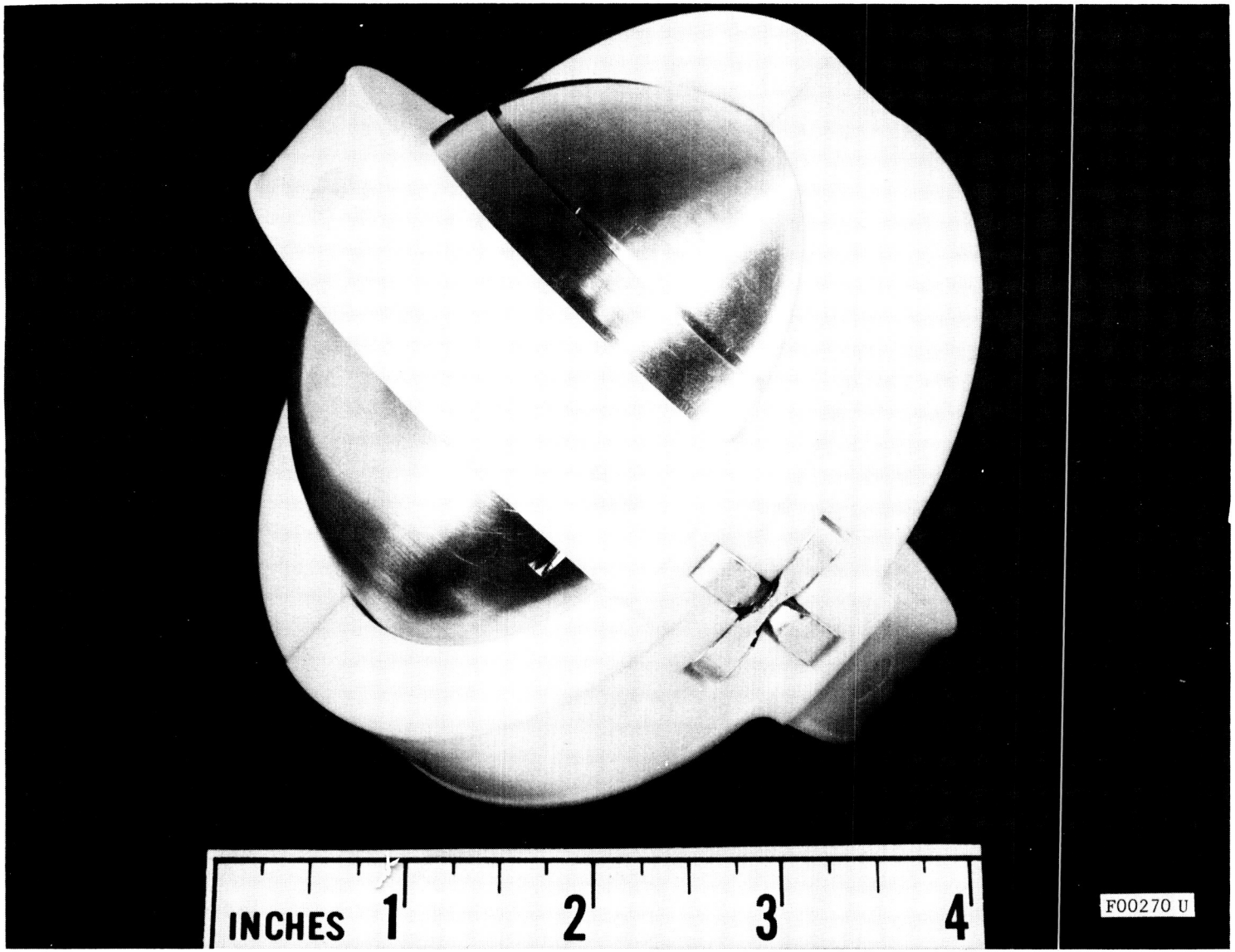

FIGURE 5-109. PENETROMETER STRUCTURAL ASSEMBLY

A secondary matter of interest is the natural resonant frequency of the structure and the effect of its noise upon measured impact deceleration data. In a configuration of this size, a natural frequency in the range of 1600 to 2000 cps is inevitable. If a 2.5 percent of critical damping is assumed, the time to damp that vibration to one-half its initial amplitude is 2.5 ms and the time to damp it to one-tenth its initial amplitude is 8.5 ms. For these reasons the encapsulation around the pressure sensitive accelerometer case has been eliminated to minimize coupling of the latter with its surrounding medium. In addition circuit modifications have been instigated to effect electronic filtering of the troublesome frequencies.

Tests conducted on the structural assembly at levels up to 7000 g have revealed no structural deficiencies in the design.

5.8 IMPACT LIMITER

It is the function of the impact limiter to impart a sufficient degree of protection to the penetrometer instrument to ensure that a meaningful signal is obtained and transmitted even under the severest impact conditions, i.e., a 200 ft/sec impact upon a hard unyielding surface. In the Lunar Penetrometer, this protection is provided by a 2-inch layer of balsawood which surrounds the 4-1/2 inch diameter inner payload to bring the total sphere diameter to 8-1/2 inches.

Balsawood was selected on the basis of its two outstanding physical characteristics; first, it yields at a substantially constant stress level through 80 percent of its initial thickness providing maximum energy absorption for a minimum imposed deceleration; second, it absorbs more energy per pound of material than any other known substance, thereby minimizing penetrometer weight.

5.8.1 ANALYTICAL MODEL

The analytical model used to predict the dynamic performance of the penetrometer impact limiter is presented in Figure 5-110. In this model, the balsa grain is assumed to be radially oriented and account is taken for its compression both parallel and perpendicular to the grain. The impacted surface is assumed to be hard and unyielding; that is, it is presumed to have infinite modulus of elasticity, yield stress and mass.

The three basic equations used to predict the performance of the spherical impact limiter are:

(1) A geometrical relationship which equates the total penetrometer weight to the sum of payload size and density and limiter size and density.

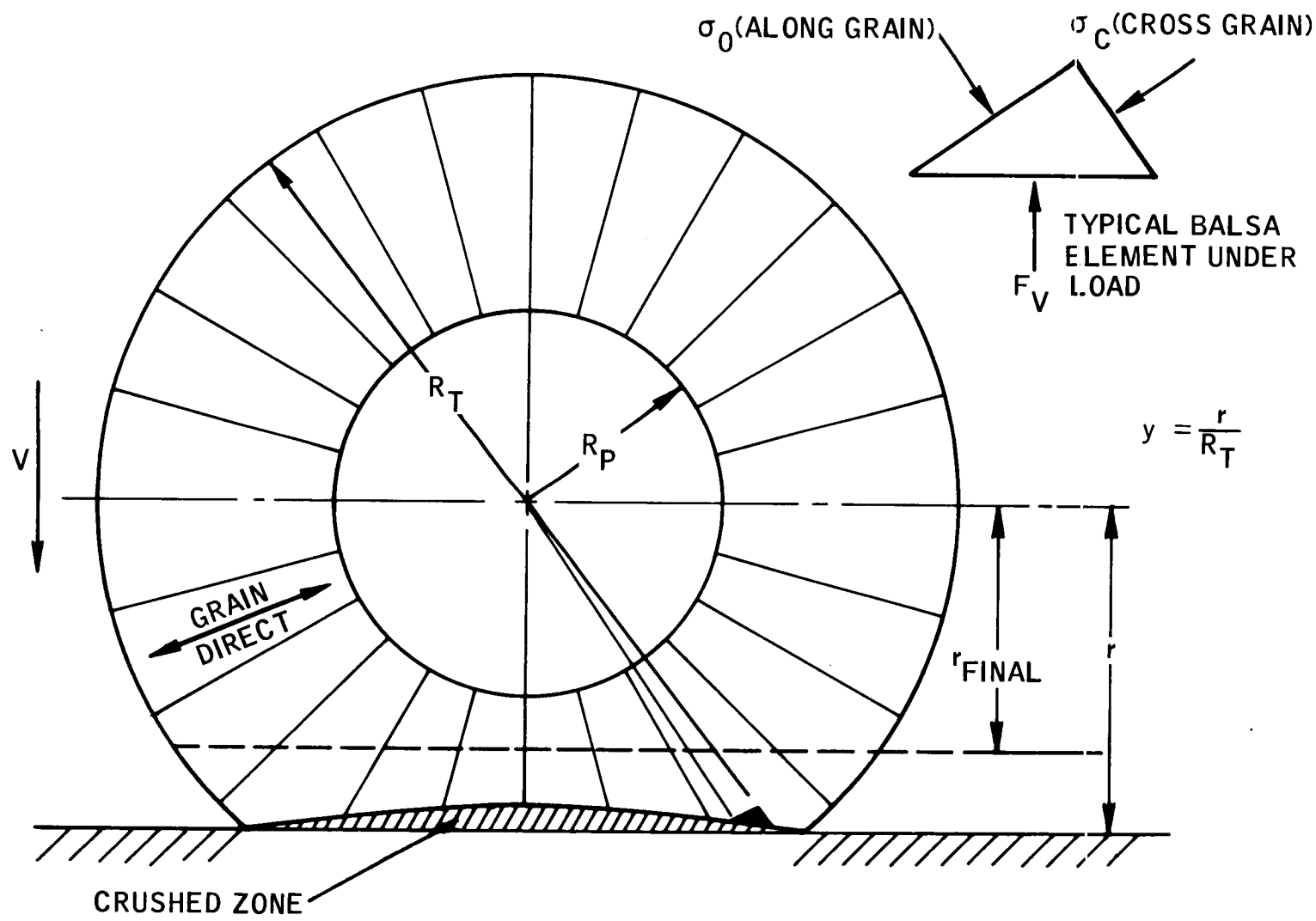

FIGURE 5-110. ANALYTICAL MODEL OF SPHERICAL BALSA WOOD IMPACT LIMITER

(2) A force equation which expresses the total vertical resisting force of the limiter as a function of its total radius, parallel and cross grain yield strengths, and stroke.

(3) An energy relationship which equates the integral of vertical force times stroke to the kinetic energy of the penetrometer at impact.

Based on these relationships and an equation expressing the axial and cross grain yield strengths of balsa as a function of its density, one can solve for the impact limiter density required to survive a 200 ft/sec impact. A value of 10.6 lb/ft^3 was found adequate to allow survival of a 3.2 pound penetrometer payload (including resin and outer cover) at a peak impact deceleration level of 7000 g.

5.8.2 MANUFACTURE

The spherical balsa wood limiter is fabricated in two hemispheres from 20 tetrahedral segments. Manufacture of these pieces is accomplished by installing the raw balsa block in a holding fixture which rotates the part about the axis of a right circular cone inscribed in the defined segment. The selection of this axis of rotation dictates that the dihedral angle of each side relative to the base is identical. Thus, the cutting of each segment is accomplished by tilting the blade of a radial arm saw at the dihedral angle and proceeding through three successive cuts and rotational indexing operations of the part; the latter is accomplished about an axis normal to the saw table. The completed parts are then assembled into 10 pairs of doublets and finally into 1 twenty-sided polyhedron. This icosahedron is next parted along an equatorial plane of symmetry and the two identical halves are machined into hemispheres. The inner contour of each is machined to accept the 3-1/2 inch diameter payload and provided with two, 3/4-inch grooves for protrusion of the antenna spacers. Note that the balsa material between the antenna spacers was not assumed to be present in the limiter design analysis and hence represents positive design margin. A view of the balsa limiter is given in Figure 5-111.

5.8.3 TEST

Three tests of the impact limiter on the prototype test spheres revealed no measurable damage to either the payload atructure or its peripheral antennas following impact at velocities up to 202 ft/sec against rigid

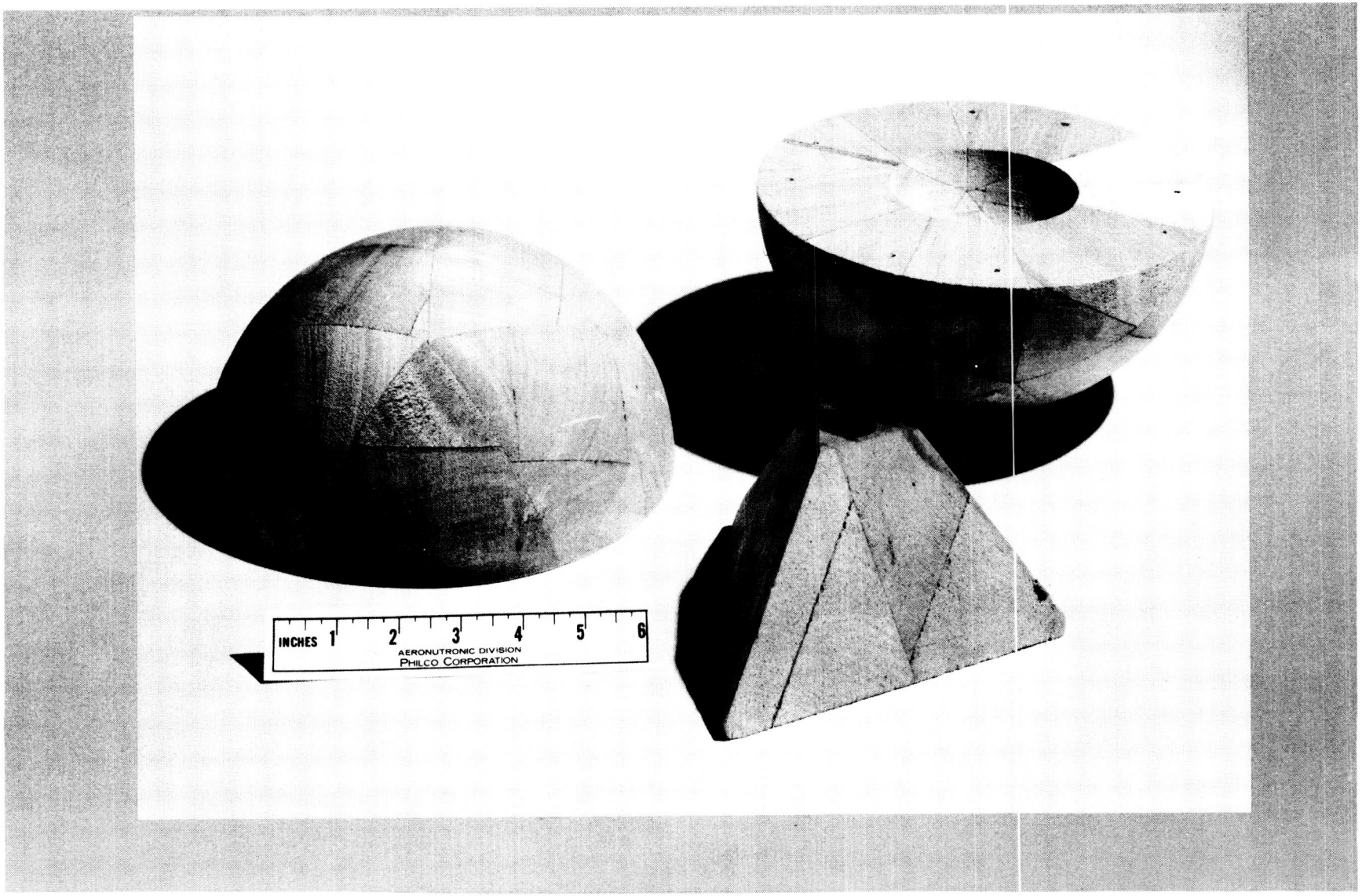

FIGURE 5-111. PENETROMETER IMPACT LIMITER

steel plates. Balsa wood crush occurred through a distance within 5 percent of its predicted value (1.7 inches). Unfortunately, however, no impact deceleration values were obtained due to malfunctions of the accelerometer and/or the telemetry electronics and power supply.

The results of additional tests conducted into various materials with 7 lb/ft^3 and 10.6 lb/ft^3 impact limiters in the course of the impact research program are presented in Table 4.8 of Paragraph 4.2.3. The materials are listed in terms of increasing compliancy.

SECTION 6

COMMUNICATION LINK PRELIMINARY DESIGN AND TEST

6.1 COMMUNICATION STUDIES AND ANALYSIS

6.1.1 MODULATION METHODS

a. General. Earlier penetrometer communications development have been carried out at Langley Research Center[1,2] and at Aeronutronic.[3,4] Mission requirements were found to dictate the use of multiple, small penetrometers deployed against the Lunar surface. In addition, real time data transmission via a relay communication system has been identified as a preferred mode of operation between the Lunar surface and Earth. This approach utilizes a hovering relay from which the penetrometers are

---

[1] McCarty, J. L., Beswick, A. G., and Brooks, G. W., Applications of Penetrometers to the Study of Physical Properties of Lunar and Planetary Surfaces, NASA TN D-2413, Langley Research Center.

[2] McCarty, J. L., Beswick, A. G. and Brooks, G. W., Penetrometer Techniques for Lunar Surface Evaluation, NASA TM X-890, 1963, pp 123-130.

[3] A Lunar Surface Measuring Capsule, Aeronutronic Publication No. U-5109, 8 January 1962.

[4] Lending Aids for the Lunar Excursion Module, Aeronutronic Publication No. U-2065, April 1963.

launched. Signals received from multiple impacting penetrometers are further combined and relayed to the assumed parent vehicle, the Apollo CSM, for subsequent transmission to Earth over the standard Unified S-Band Telecommunication Link. The communication studies and analysis reported in this section (and Appendices), therefore, pertain to the establishment of the following elements of a penetrometer communication system: Penetrometer-to-Data Relay Link, the Data Relay-to-CSM Link, and the basic CSM Interface Study.

b. Modulation Considerations. In the initial phase of the penetrometer program, a state-of-the-art review was conducted and varied aspects of applicable communication system designs were examined. An account of the salient features is presented in the following two paragraphs.

(1) Penetrometer. For Penetrometer data transmission, only frequency modulation (FM) of the carrier was considered. Phase modulation (PM) and amplitude modulation (AM) had been ruled out because of shock transients expected in these parameters. Figure 6-1 depicts four methods which received consideration. Method I, termed the simplest, has the analog data signal modulate the carrier directly. A high modulation index (wide deviation) would be employed to discriminate against the undesired shock modulation of the carrier. Being a wide-band system, penetrometer transmitter power requirements were typically more demanding than the other methods examined. Moreover, a dc signal handling capability through the FM modulator and in the relay receiver discriminator would be required.

Method II involves halfwave chopping of the signal, with narrower bandwidth requirements than in Method I, permitting a reduction in penetrometer transmitter power. A simple synchronous demodulator as noted would be required in the relay for data detection.

As an extension of Method II, Method III employs full wave chopping. Data is sampled with alternate phases of the chopping signal, resulting in the sampled data as sidebands on the AM (chopper) subcarrier. As denoted in Figure 6-1, translation of data to a subcarrier minimizes the shock modulation effects. In the relay, the data is recovered by means of a bandpass filter and full wave rectifier. This consititutes the selected approach and exhibits the best overall stability, since only ac signals are handled after the differential preamplifier, and (chopper) subcarrier frequency stability is not important.

Method IV employs the use of an FM subcarrier. Here (similar to Method I), dc signal handling capability through the subcarrier oscillator (SCO) and relay is required, thus calling for a shock stable SCO. This method was adjudged as requiring more complexity in the penetrometer and relay, particularly with regard to the SCO shock insensitivity constraint.

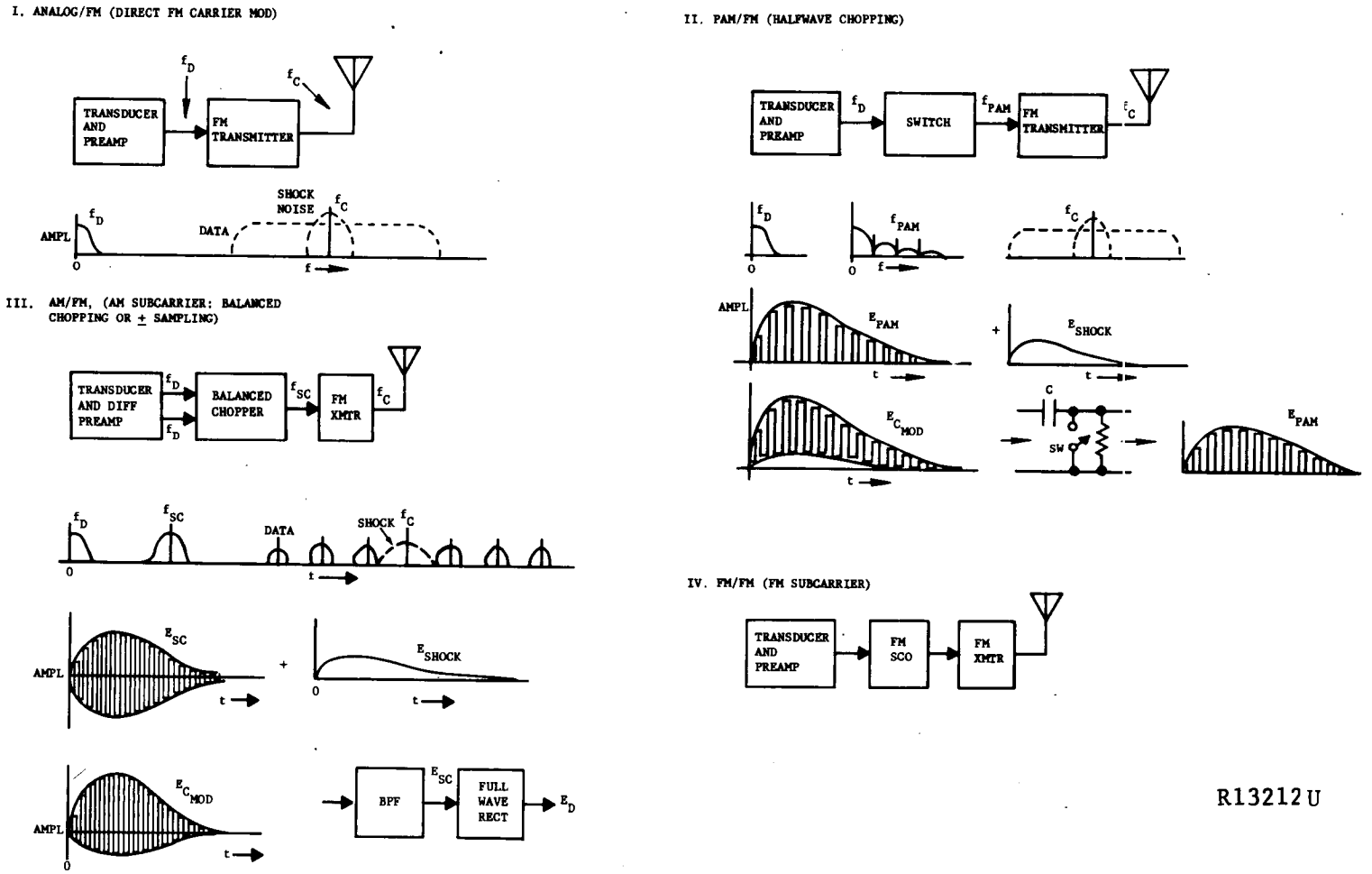

R13212U

FIGURE 6-1. PENETROMETER SIGNAL MODULATION METHODS

(2) Data Relay. Data acquisition and transmission methods for use in the data relay also received consideration in the state-of-the-art review. The principal techniques studied (involving UHF reception and VHF retransmission schemes) are shown in Figure 6-2. Relay reception criteria was based upon the premise that eight penetrometers with separately spaced carrier frequencies are salvoed at once. Polarization diversity reception was required in the relay system design to avoid possible reception nulls. Some form of recombination in the relay was desired because it halved the number of channels requiring retransmission. The FM/FM relay of Method I depicts an independent signal handling method which affords a partial system redundancy. Complete redundancy would be achieved using an alternating recombination scheme. Subcarrier demodulation is employed to recover data signals for subsequent remodulation onto the FM subcarrier channels which are applied as a composite modulation on the rf carrier. This method, modified to include an antenna switching polarization diversity capability, thus halving the basic receiver requirement, was selected to receive development and functional testing during this program. The selection was based upon the highly developed status and excellent availability of FM/FM hardware and performance characteristics that are well known. Use of the analog system is consistent with the overall data accuracy requirement and affords the desired simplicity with attendant improved reliability.

Method II represents an alternative to the demodulation of the subcarriers. This scheme employs frequency translation to facilitate retransmission of the received subcarrier data signals. Considerable complexity in the relay is required, however, to provide mixers, filters, and the generation of a set of stable mixer injection signals. Also required would be the attendant frequency stability constraints placed on the penetrometer data subcarrier frequency.

Method III, or the wideband rf relay, received consideration because it presents a minimum hardware demand. Acting as a single wideband transponder channel, it accommodates all eight incoming penetrometer signals in each polarization. The principal drawbacks are increased power requirements in both the penetrometer and relay transmitters. Diversity combination is not possible in this scheme. A variation of Method III is seen in Method IV, where operation is similar to Method III except that individual channel receivers are employed. This eliminates the two of the drawbacks cited for Method III, but the increased relay transmitter power (8 to 20 db) requirement would remain.

c. Comparison of Modulation Methods. The penetrometer-to-data relay communications link demanded the major attention in the communication studies and analysis performed during the penetrometer program. Environmental constraints, particularly the shock sensitivity characteristic, represented a significant weighting factor influencing the choice of a modulation method to employ in the Lunar Penetrometer prototype design.

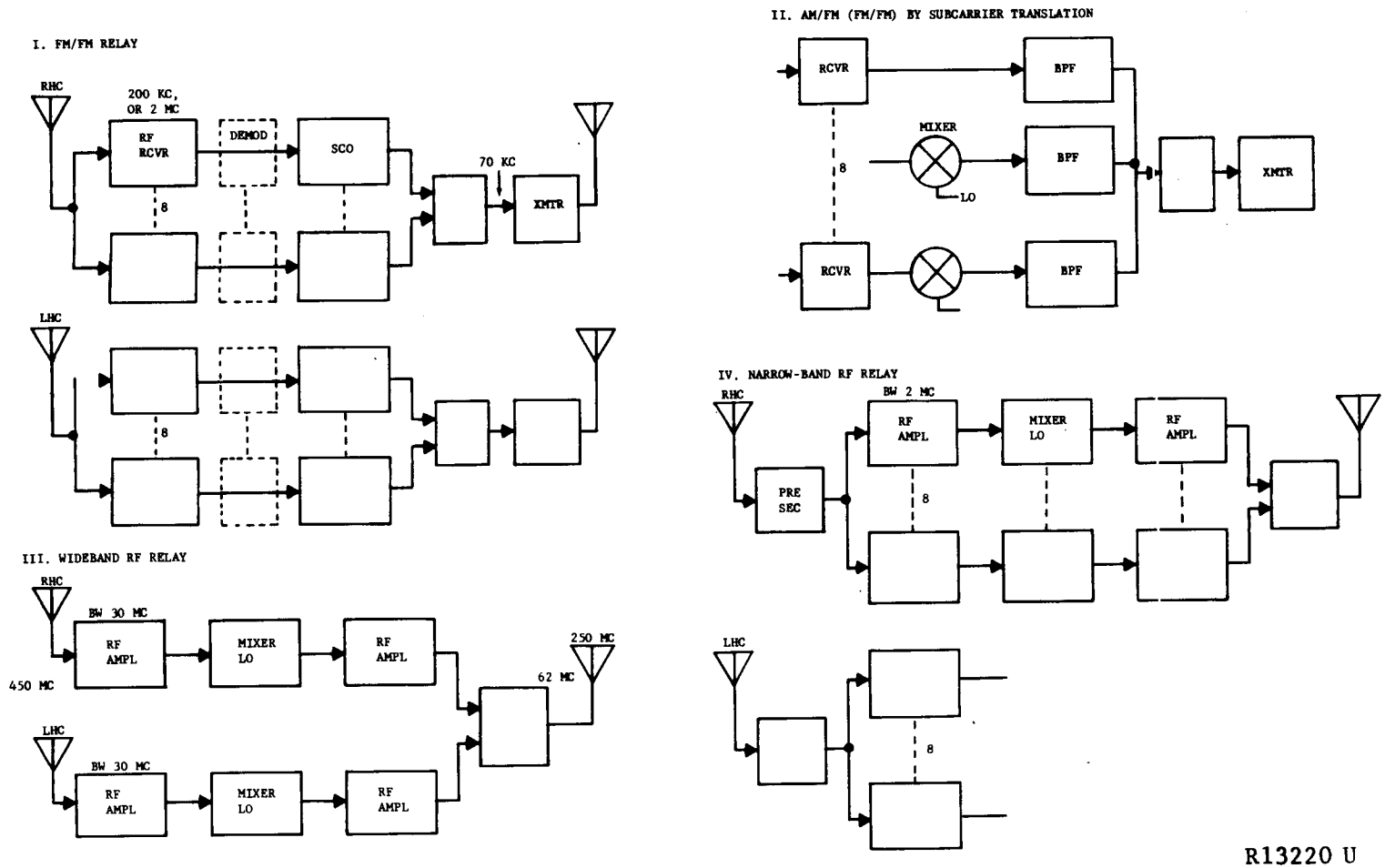

FIGURE 6-2. RELAY SIGNAL TO CSM MODULATION METHODS

The combination of considerations resulted in the selection of an AM/FM design approach early in the program. Effort was continued during the program, however, to extend the earlier modulation methods investigation and consider alternate modulation schemes. The results of these studies are reported in Appendices G and H of this report with a brief summary included herein.

A study of modulation methods was completed, based on sinusoidal modulation, resulting in expressions depicting penetrometer-to-data relay communication system performance above threshold. Mean output signal-to-noise power ratios (SNR) were obtained for AM, FM, AM/FM and FM/FM systems, based upon the following assumptions:

(1) Signal power much greater than noise power.

(2) Single frequency sinusoidal modulation of full scale signal amplitude.

(3) Signal power assessed with noise assumed absent and noise power in absence of signal (unmodulated carrier present).

(4) Identical input carrier power and noise spectral density applied to each system.

(5) All powers derived relative to unity loads.

The following table depicts the resulting expressions in normalized form.

Modulation Method	SNR_o		Explanation
AM	SNR_i	Δf_c	{carrier frequency deviation
FM	$3\left(\frac{\Delta f_c}{f_m}\right)^2 SNR_i$	f_m	{maximum data baseband frequency
AM/FM	$\frac{1}{2}\left(\frac{\Delta f_c}{f_{sc}}\right)^2 SNR_i$	Δf_{sc}	{subcarrier frequency deviation
FM/FM	$\frac{3}{2}\left(\frac{\Delta f_c}{f_{sc}}\right)^2\left(\frac{\Delta f_{sc}}{f_m}\right)^2 SNR_i$	f_{sc}	{subcarrier frequency

Numerical link calculations based upon further parametric studies are required before results may be applied to the penetrometer application.

6.1.2 CSM INTERFACE STUDY

A study was conducted to define the telecommunication equipment characteristics of the Apollo Block II Command and Service Module (CSM) and recommend the best CSM/LPS interface. The detailed study results are given in Appendix F.

The results of the study indicate that use of the operational CSM receiving and recording equipments, with the exception of the VHF antennas and multiplexer, is not feasible for the Lunar penetrometer system application. Neither the operational VHF/AM receivers or the Data Storage Equipment has the necessary frequency response to handle the eight channels of penetrometer data received via the Data Relay. The Service-Module mounted VHF antennas and the VHF 3-port multiplexer can be used, however. The Block II CSM VHF multiplexer has a spare port tuned to 228.2 MHz and reserved for scientific or R&D purposes. Hence, it is probably desirable to change the operating frequency of the Data Relay transmitter to this frequency from the present 260 MHz.

The study of the CSM Unified S-Band transmission system, used for CSM-to-MSFN (Manned Space Flight Network) communications, indicates that the received LPS data can easily be transmitted to Earth via the 2272.5 MHz FM transmitter. This transmitter is normally used for transmission of television, recorded operational data playback, or real-time transmission of three analog channels of scientific data. The transmitter has sufficient bandwidth to accommodate the eight constant-bandwidth subcarrier channels received from the data relay.

The appendix summarizes the functional performance requirements of the necessary additional equipment required for the lunar penetrometer system. This equipment encompasses a 228.2 MHz wide-band FM receiver and a wide-band analog tape recorder with playback capability.

6.1.3 PENETROMETER-TO-DATA RELAY LINK ANALYSIS

The communications analysis for the penetrometer-to-data relay link was originally completed and reported in the LPS Fourth Monthly Progress Report. Since then several of the parameters, notably the transmitter and receiver instabilities, have become better defined or established. An updating of the previous analysis is, therefore, presented herein.

The communications system utilizes AM/FM as the modulation method. To simplify the analysis, as before, a continuous sinusoidal modulation is assumed. A listing of the key parameters, including those revised, is presented as follows:

(1) Carrier frequency deviation, $\Delta f_c = \pm 160$ KHz

(2) AM subcarrier frequency f_{sc} = 40 KHz

(3) Maximum data frequency f_m = 2 KHz

(4) Transmitter frequency stability, ±66 KHz (±0.015%), [was ±25 KHz (±0.0055%)]

(5) Transmitter shock-induced Δf, ±80 KHz (±0.0175%) [was ±45 KHz (±0.01%)]

(6) Receiving system stability, ±10 KHz (±0.0022%) [was ±25 KHz (±0.0055%)]

(7) RMS value of stabilities, [items (4), (5), and (6)] = ±108 KHz (±0.024%) [was ±60 KHz (±0.013%)]

(8) Receiver bandwidth required for (Δf_c/fm of 4) = 480 KHz if criterion is that sidebands of amplitude less than 0.05 of the unmodulated carrier are neglected; [was 580 KHz based upon a criterion that sideband amplitudes less than 1 per cent of the unmodulated carrier are neglected].

(9) Total receiver bandwidth [items (7) + (8)], B_{if} ≈ 700 KHz

The left half of Table 6.1 shows the resulting penetrometer-to-data relay UHF link design control table which includes other important parameters not cited above. The threshold SNR is that required to overcome a fluctuation noise voltage error of ± 6.7 percent in the link while simultaneously providing the carrier improvement threshold requirement of 12 db.

The output SNR for full-scale input data signal (i.e., 7000 g) is obtained from:

$$\text{(Table 6.1)} \quad SNR_o = \frac{1}{2}\left(\frac{\Delta f_c}{f_{sc}}\right)^2 \frac{B_{if}}{2f_m} SNR_{if}. \qquad (1)$$

The SNR_o for the minimum value of input signal (i.e., 50 g) is taken as -26.0 db less, which is the smallest increment of the signal dynamic range following compression. The resulting performance data, including margins, are denoted in the referenced table. It should be noted that the results cited are derived from the preceding equation which represents an idealized expression based upon certain simplifying assumptions (e.g., rectangular

TABLE 6.1

LPS COMMUNICATION LINK DESIGN CONTROL TABLE

Parameter	Penetrometer-to-DRS UHF Link Nominal Value	Tolerance (db)		DRS-to-CSM VHF Link Nominal Value	Tolerance (db)	
Transmitter Power	-3.0 dbw (0.5 watt)	+1.0	-0.0	+16.0 dbw (40 watts)	+1.0	-1.0
Transmission Circuit Loss	-1.0 db	+0.5	-0.5	-1.0 db	+0.5	-0.5
Transmitting Antenna Gain	-3.0 db	+1.5	-1.5	0.0 db	+3.0	-3.0
Polarization Loss	-3.0 db	+3.0	-0.0	-3.0 db	+3.0	-1.0
Free Space Loss	-96.8 db (2 nm 450 MHz)			-126.1 db (100 nm 260 MHz)		
Receiving Antenna Gain	+4.5 db	+1.5	-1.5	0.0 db	+2.0	-9.0
Receiving Circuit Loss	-1.0 db	+0.5	-0.5	-1.0 db	+0.5	-1.0
Received Signal Power	-103.3 dbw	+8.0	-4.0	-115.1 dbw	+10.0	-15.5
Receiver Bandwidth	+58.5 db•Hz (700 KHz)	+0.5	-0.5	+54.8 db•Hz (300 KHz)	+0.5	-0.5
System Noise Figure	+6.0 db	+1.0	-0.0	+6.0 db	+1.0	-0.0
Noise Spectral Density	-204.0 dbw/Hz	—	—	-204.0 dbw/Hz	—	—
Received Noise Power	-139.5 dbw	+1.5	-0.5	-143.2 dbw	+1.5	-0.5
Threshold SNR	+23.5 db			+9.0 db		
Required Signal Power	-116.0 dbw	+1.5	-0.5	-134.2 dbw	+1.5	-0.5
SNR_{if}	+36.2 db			+28.1 db		
SNR_{out} (at 7000 g)	+67.7 db					
(at 50 g)	+41.7 db					
Margin (at 50 g)	+18.2 db	+8.5	-5.5			
Margin (carrier)	+12.7 db	+8.5	-5.5	+19.1 db	+10.5	-17.0

filter passbands, sinusoidal modulation, etc., also see Appendix G). Actual performance may be several db poorer. In any case, an excess margin of about 10 db is seen to result in the data channel after allowance has been made for the -5.5 db, worst case sum of the negative link tolerances. This quantity may also be referred to as a burial margin.

It must be further noted that final mission geometry and detailed operational constraints of a particular lunar penetrometer system measurement application will necessitate a re-evaluation and updating of the present analysis, which was based upon current penetrometer prototype hardware design and certain assumed data relay concepts.

6.1.4 DATA RELAY-TO-CSM LINK ANALYSIS

The communications analysis for the data relay-to-CSM link is presented to document the basic relay system concept employed for a lunar survey probe (LSP) mission. The data relay performs a real-time analog data acquisition and transmission function taking AM/FM UHF signals from the eight (salvoed) individual penetrometers and retransmitting them as an eight-channel FM/FM VHF link to the orbiting CSM. The choice of an analog system here is appropriate to the overall accuracy desired and represents a simple and reliable approach. The VHF link employed, therefore, is basically a standard FM/FM link operated in an eight (constant bandwidth) subcarrier channel configuration. The right half of Table 6.1 shows the various data link parameters involved and the resulting performance characteristics. The principal observation to be made is that there exists a large uncertainty in the CSM receiving antenna system gain which consequently dictates the need for relatively high power (40 watts) in the relay transmitter. Any further clarification or better definition of this and other receiving system characteristics will obviously have a significant effect on the relay transmitter power requirement. At present a basic 2.1 db excess margin is seen to exist in the link design. If CSM attitude constraints can be used, with an attendant significant increase in antenna gain, the relay transmitter power output can be reduced to approximately 10 watts and still retain a positive link margin.

6.2 DATA RELAY

6.2.1 PENETROMETER DATA RELAY RECEIVING SYSTEM

The purpose of the penetrometer data relay receiving system is to receive and demodulate the data from eight simultaneously-fired penetrometers operating on eight different carrier frequencies. The present functional model receiving system is shown in block diagram form in Figure 6-3. The design of the receiving system was well along when a decision was made to change the modulation method of the penetrometer carrier from very wide band direct FM to a narrower bandwidth AM-FM system. The receiver design was adapted to the changed requirements and its performance is not optimum for the flight model. The desirable changes are incorporated in the performance specification and described later in this section. Figure 6-3 also gives the typical gains and noise figures of the various blocks.

For a receiving system having a bandwidth of 700 KHz, a noise figure of 6 db, and operating at room temperature, the equivalent receiving system noise power (KTBF) is -109.5 dbm (see Paragraph 6.1.3). Using the gains of the preamplifier, power divider, and receiver, as shown on Figure 6-3, this noise power referred to the receiver IF output is of the order of 23 dbm. This is the level at which the limiter becomes operative, i.e., the limiter limits on noise which maximizes the useful receiver input amplitude range. From the communications system analysis of Paragraph 6.1.3, the nominal received power is -86 dbm. This, then, provides an SNR in the IF of nominally +23.5 db for good receiving system quieting.

a. RF Preamplifier. A low-noise preamplifier is required in the system to overcome the loss in the eight-way power divider. Since the eight input frequencies cover the range from 432 MHz to 453 MHz, this preamplifier should have a bandwidth greater than 21 MHz. The actual preamplifier used consists of two cascaded commercial units (C-COR Model 3584). This configuration provided 34 db of gain with a 3 db bandwidth of 45 MHz centered around 442.5 MHz and a noise figure of 5.5 db. These particular amplifier units were chosen mainly because they were readily available. The performance specifications define the requirements for a preamplifier contained in one sealed unit meeting or exceeding the specifications of the units now in use.

b. Power Divider (8-way). The rf preamplifier drives an 8-way power divider. This unit, available commercially (Adams-Russell Number 8U-50), exhibits an isolation between outputs of 30 db with only 1 db insertion loss over the straight power division (9 db) for a maximum overall insertion loss of 10 db. This unit is referred to as a distributive parameter device. It buys only about 1 db in overall system noise figure over that obtained with a conventional unit but, by virtue of its balanced configuration, provides considerably more isolation between output ports.

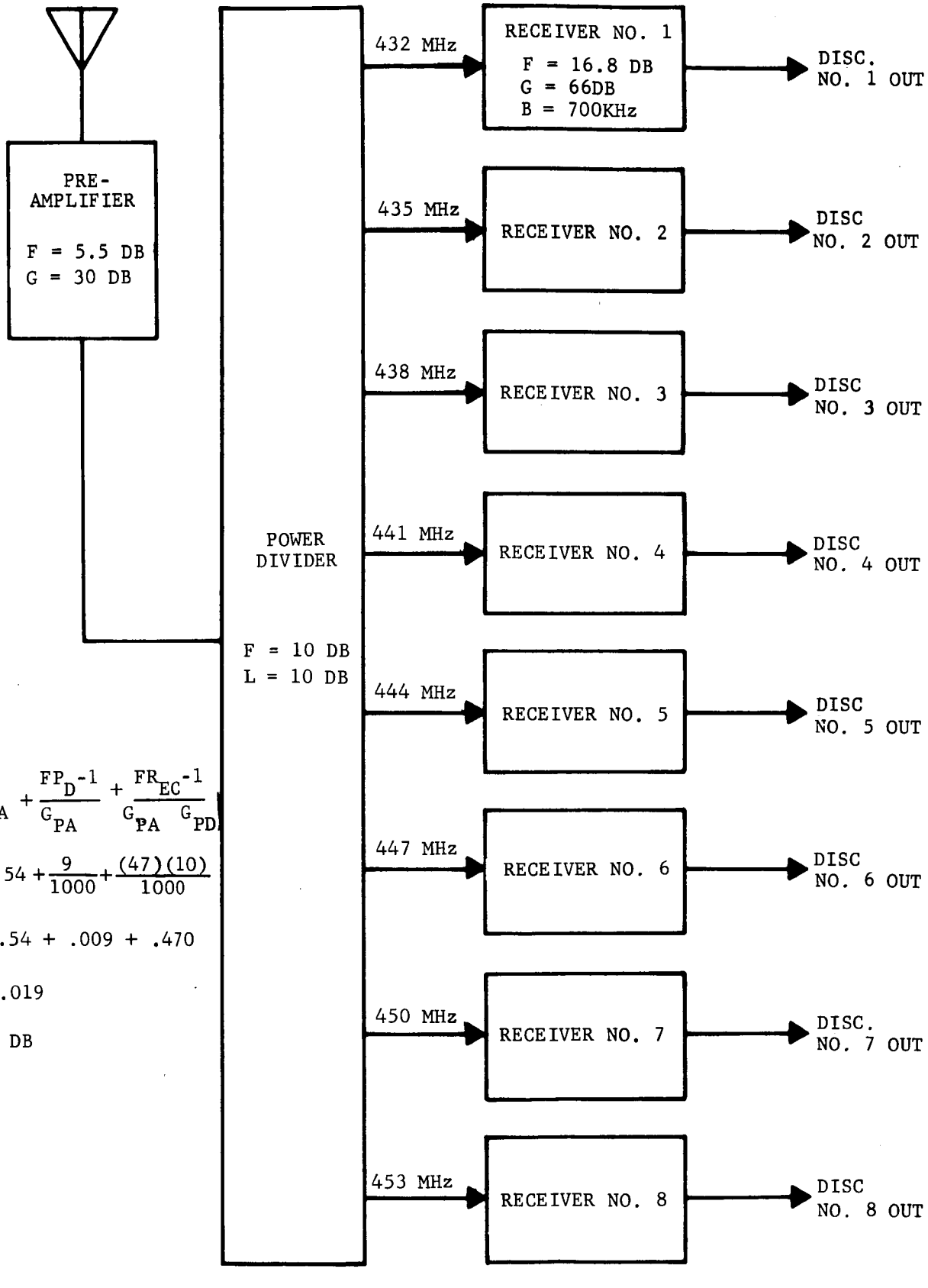

$$F_{Total} = F_{PA} + \frac{FP_D - 1}{G_{PA}} + \frac{FR_{EC} - 1}{G_{PA}\ G_{PD}}$$

$$F_{TOTAL} = 3.54 + \frac{9}{1000} + \frac{(47)(10)}{1000}$$

$$F_{TOTAL} = 3.54 + .009 + .470$$

$$F_{TOTAL} = 4.019$$

$$F_{TOTAL} \cong 6 \text{ DB}$$

FIGURE 6-3 RECEIVING SYSTEM BLOCK DIAGRAM

The power divider performance specification defines the requirements of a power divider similar to the one used. Another type of power divider, referred to as a frequency selective unit, is of interest. Its configuration would be more like a comb filter with considerably less insertion loss. This could lessen the effects of a "hung-up" ball overdriving the present preamplifier, rendering the entire receiving system useless. The approach, however, would require separate preamplifiers for each receiver (possibly incorporated in the preselector, making it an active rather than a passive preselector). Outside bids have been requested for a frequency selective power divider. The specification for this is found in Table 6.2. The low insertion loss requirements are necessary to keep the system noise figure down since in this case, with no amplification between the antenna and power divider, the loss of the power divider adds directly to the system noise figure. A few bids have been received to date (more are expected) with most bidders requesting more insertion loss allowance. Once all bids are received, they will be weighed for merit against the present power divider. Perhaps it would be more advisable to devise a positive scheme whereby a "hung-up" ball never gets turned on, which would remove the need for a frequency selective power divider.

c. Receiver. The block diagram of the receiver is shown in Figure 6-4, which shows gains, noise figures, and bandwidths of the individual blocks. A schematic of the receiver is shown in Figure 6-5. Figure 6-6 is a photograph of the rf and dc compartment of two of the functional model receiver units.

(1) Preselector. The function of the preselector is to provide a large amount of attenuation at the image and local oscillator frequencies with minimum attenuation to the incoming desired signal. In addition, large attenuation must be provided to adjacent receiver local oscillators, as shown in Appendix E. To accomplish this, a double-tuned circuit was employed as a completely passive preselector. Typical performance of this preselector shows attenuation of the receiver's local oscillator frequency of 40 db or more. The attenuation required of the local oscillator frequency at the relay antenna is 70 db minimum, which is based on a 2 milliwatt (+3 dbm) local oscillator drive at the first mixer, and on MIL-I-6181, which states that the local oscillator power at the input shall not exceed 200×10^{-12} watts (-67 dbm). Such attenuation is readily obtainable through the skirt selectivity of the preselector, plus the isolation of the power divider and the unilateral attenuation of the preamplifier.

(2) First Mixer. The first mixer uses both signal and local oscillator injection at the emitter with base at rf ground. Reasonable gain and stability requirements are easily met with this configuration. A crystal-controlled oscillator driving a frequency tripler is used as the first local oscillator. Provision is made for disabling the power to this local oscillator and applying an external local oscillator for variable frequency operation.

TABLE 6.2

SPECIFICATIONS FOR
8-WAY FREQUENCY SELECTIVE POWER DIVIDER

1.	Channel Center Frequencies	432 MHz (Channel 1) 435 MHz (Channel 2) 438 MHz (Channel 3) 441 MHz (Channel 4) 444 MHz (Channel 5) 447 MHz (Channel 6) 450 MHz (Channel 7) 453 MHz (Channel 8)
2.	Channel Bandwidths	(-3 db) 2 MHz (-15 db) 6 MHz maximum (-60 db) 60 MHz maximum
3.	Insertion Loss	2 db Maximum at Channel Center Frequency
4.	Input Impedance	50 ohms
5.	Output Impedance	50 ohms
6.	VSWR	1.5:1 maximum
7.	RF Output Power	1 watt maximum
8.	Size and Weight	Minimum (specify)
9.	Input/Output Connectors	BNC

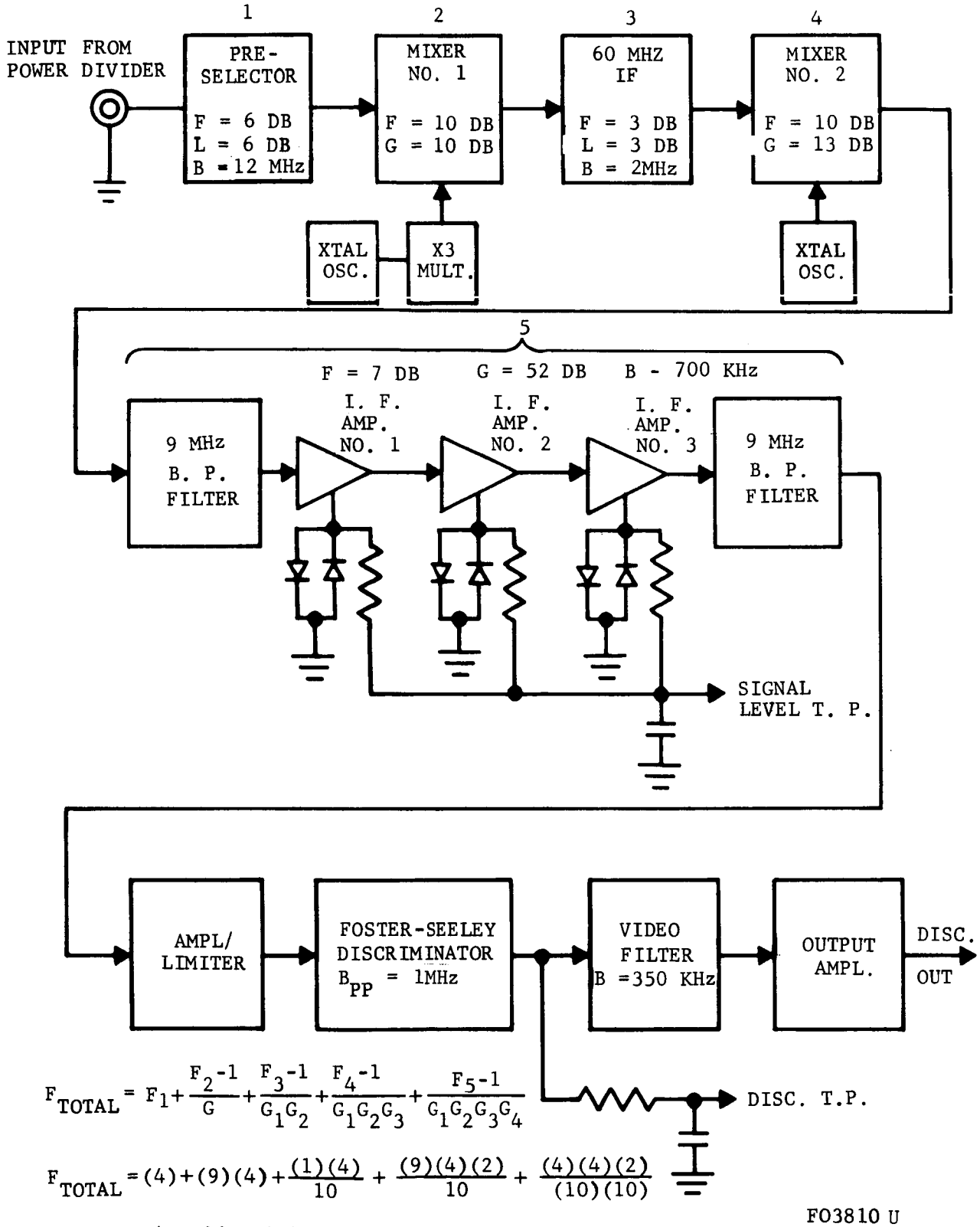

$$F_{TOTAL} = F_1 + \frac{F_2 - 1}{G} + \frac{F_3 - 1}{G_1 G_2} + \frac{F_4 - 1}{G_1 G_2 G_3} + \frac{F_5 - 1}{G_1 G_2 G_3 G_4}$$

$$F_{TOTAL} = (4) + (9)(4) + \frac{(1)(4)}{10} + \frac{(9)(4)(2)}{10} + \frac{(4)(4)(2)}{(10)(10)}$$

FO3810 U

$$F_{TOTAL} = 4 + 36 + 0.4 + 7.2 + 0.32$$

$$F_{TOTAL} \cong 48 \qquad F_{TOTAL} \cong 16.8 \text{ DB}$$

FIGURE 6-4. RECEIVER BLOCK DIAGRAM

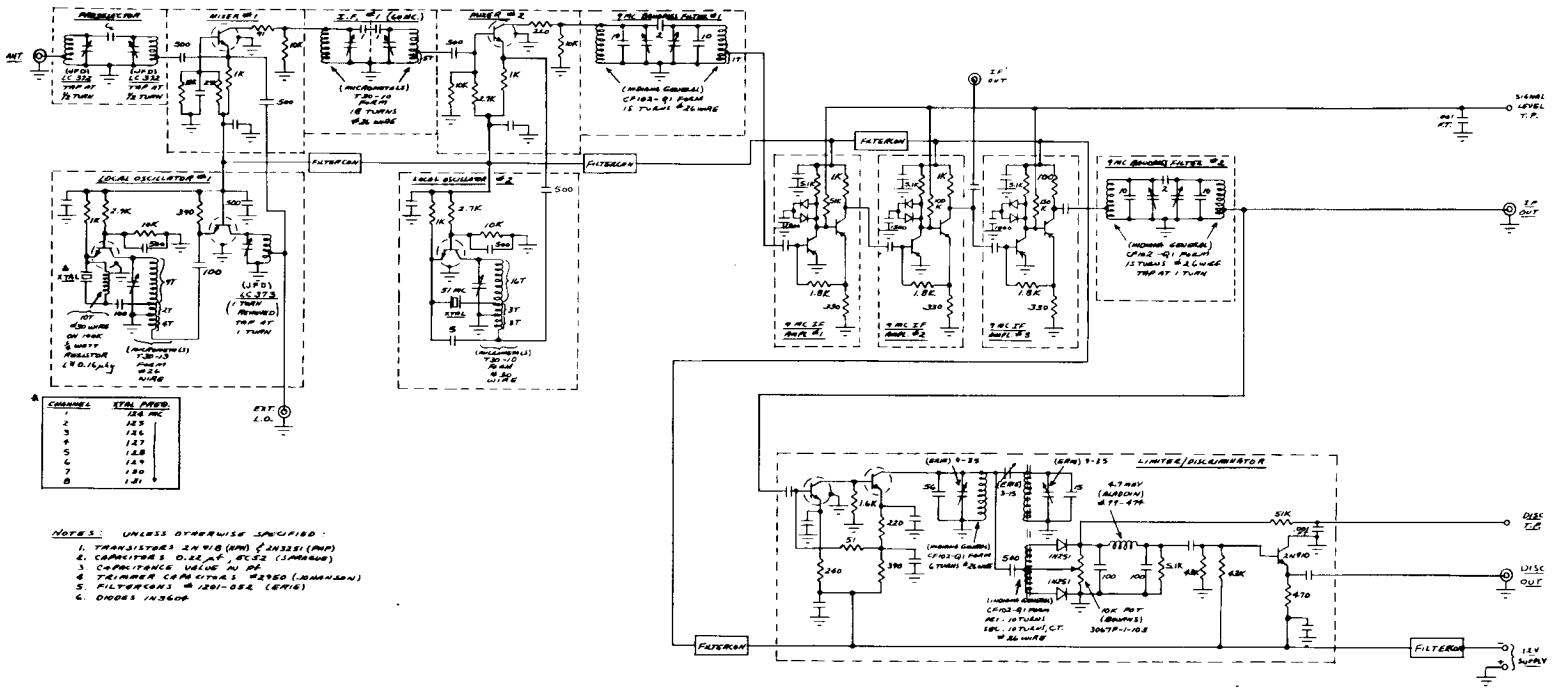

FIGURE 6-5. DATA RELAY RECEIVER SCHEMATIC

FO3811U

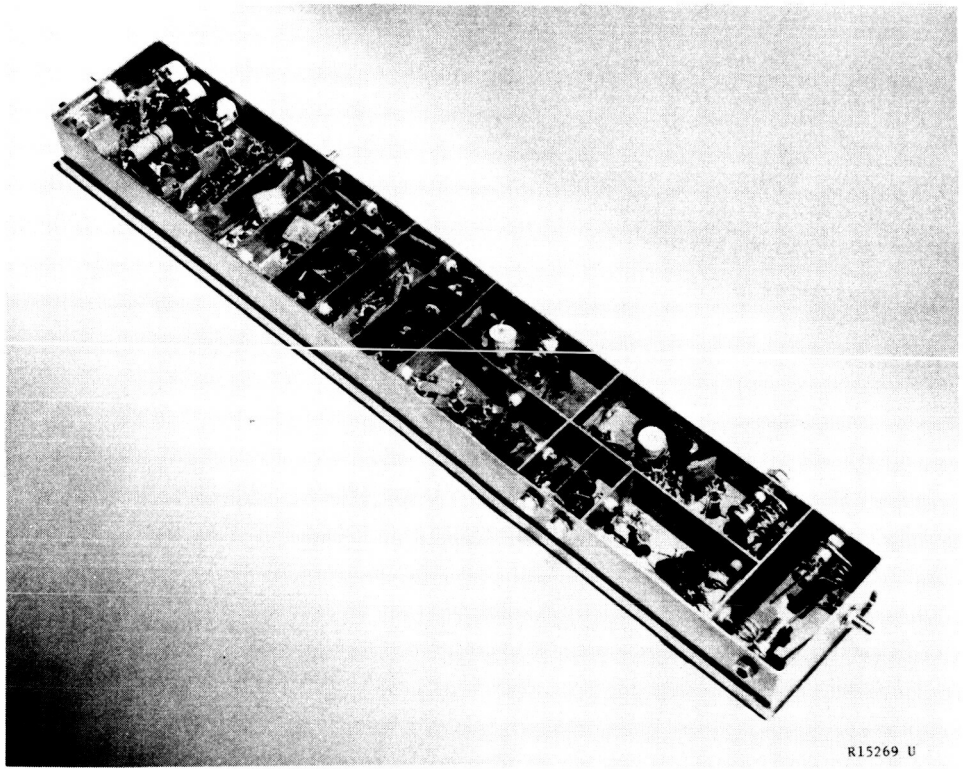

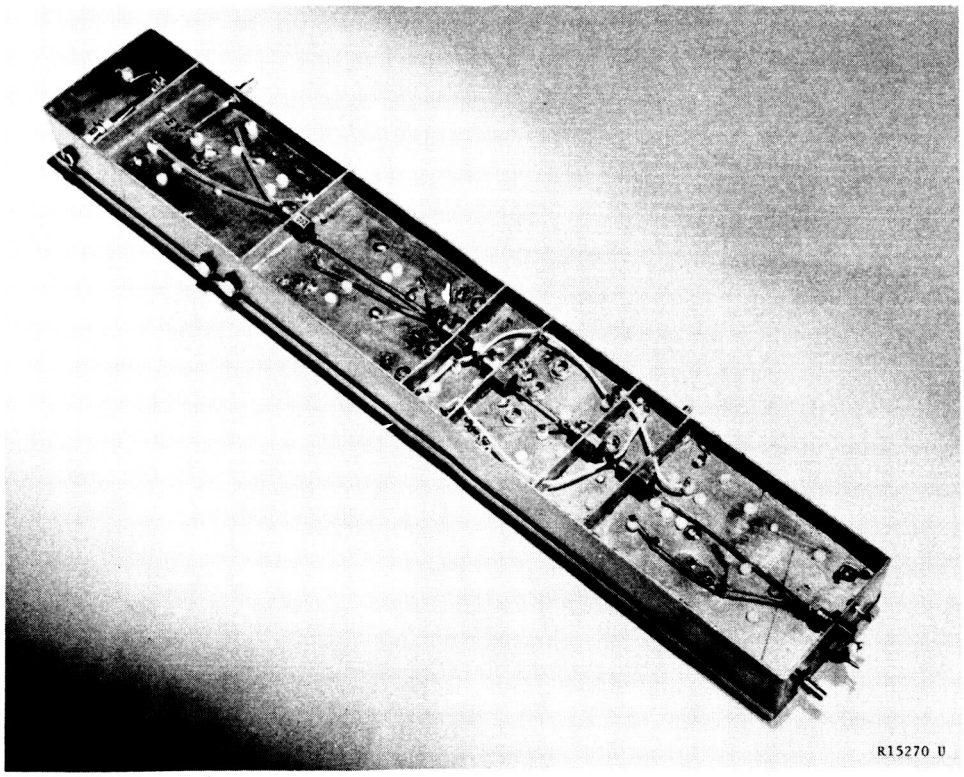

FIGURE 6-6. RELAY RECEIVER

(3) First IF. The first IF is similar to the preselector in that it is completely passive and made up of a critically coupled, double-tuned circuit. Its center frequency is 60 MHz with a 3 db bandwidth of 2 MHz. It has greater than 35 db attenuation at 72 MHz, which is the nearest spur, as described in Appendix E. This attenuation, coupled with the fact that the spur is eleventh order, provides more than adequate spur rejection.

(4) Second Mixer. The second mixer differs from the first in that the signal is fed at the base while local oscillator is fed in at the emitter. At these lower frequencies, this configuration proves to be most efficient. The second local oscillator is simply a crystal-controlled unit operating at 51 MHz to provide the second IF of 9 MHz.

(5) Second IF. The second IF consists of input and output double-tuned circuits (to establish the bandwidth) and three wide-band amplifier stages. The configuration used was chosen mainly due to the ease with which it could become integrated. The back-to-back diodes within each stage provide distributed limiting and also provide a means whereby the signal level may be monitored.

(6) Detector. Further limiting is provided by the amplifier/limiter unit following the second IF. Coupled with the distributed limiting in the IF, this provides sufficient limiting for good FM detection. The detector is a conventional Foster-Seeley FM discriminator. Its peak-to-peak bandwidth is set at approximately 1 MHz to provide essentially linear response over the 700 KHz + 50 KHz) range. This discriminator is then followed by a video filter, a low-pass cutting off at 350 KHz, to remove any carrier component remaining. An output emitter-follower completes the design.

A number of shortcomings in this functional model receiver design have been recognized and were taken into account in the performance specification for the flight model receiving system.

The specific items, their causes and remedies, are itemized as follows:

(1) Harmonics of the crystal oscillator in the first local oscillator (LO) can cause internal spurs. For example, the LO required in Channel 1 is 432 - 60 = 372 MHz. The crystal oscillator runs at one-third that frequency, or 124 MHz. The fourth harmonic of this is 496 MHz. An external spur could result if an input frequency of 496 - 60 = 436 MHz is present. This is close to

Channel 2 which operates on 435 MHz. This problem can be eliminated by increasing the first IF and by then using a doubler rather than a trippler in the first local oscillator. Such an approach is used in the performance specification with a first IF of 120 MHz.

(2) The present receiver design utilizes a second IF of 9 MHz. With a bandwidth requirement of 700 KHz, and taking bandwidth shrinkage due to cascaded tuned circuits into account, the loaded Q of the IF tuned circuits and discriminator becomes quite low and difficult to implement. The performance specification will allow more practical Q values to be maintained.

(3) The present receiver utilizes no AGC. Therefore, it is possible for a very strong signal to completely block the receiver front end and IF's. The performance specification defines a receiver using AGC which will provide AGC in the second IF and, if necessary, could be added into the pre-amplifier as well. This would eliminate the overload problem and make the receiver operational over a considerably wider dynamic input range.

d. Auxiliary Pulse Count Discriminator. A pulse-count type of discriminator was designed and four units were fabricated for use in the functional model relay. The pulse-count type of discriminator has a much wider linear bandwidth than the Foster-Seeley type described above. It was intended to be used if penetrometer ball frequencies would end up, after potting, outside the design frequency tolerances. The input to this discriminator comes from the receiver's IF test point. Each pulse-count discriminator contains its own limiter, followed by a divide-by-eight integrated circuit ripple-carry binary counter, a precise one-shot pulse generator, video filter, and amplification to the desired output level. This system bases its use on the fact that the average value of a pulse train with constant amplitude and pulse width, but with varying period, is proportional to the frequency. The one-shot, driven by the divide-by-eight circuit, provides the constant pulse amplitude and pulse width while the video filter provides the averaging function. Since the incremental changes in the output of this type of system are relatively small, considerable amplification is required to bring the output up to a reasonable level. Operating this discriminator, using the data relay power supply converter, resulted in intolerable noisy channel operation. The data relay power supply converter switching transient was apparently a major problem. Additional power supply decoupling was done but noisy performance was still evident. A schematic of this discriminator is found in Figure 6-7.

NOTE:
1. ALL CAPACITOR 0.22 UF UNLESS OTHERWISE NOTED
2. * SELECTED VALUE

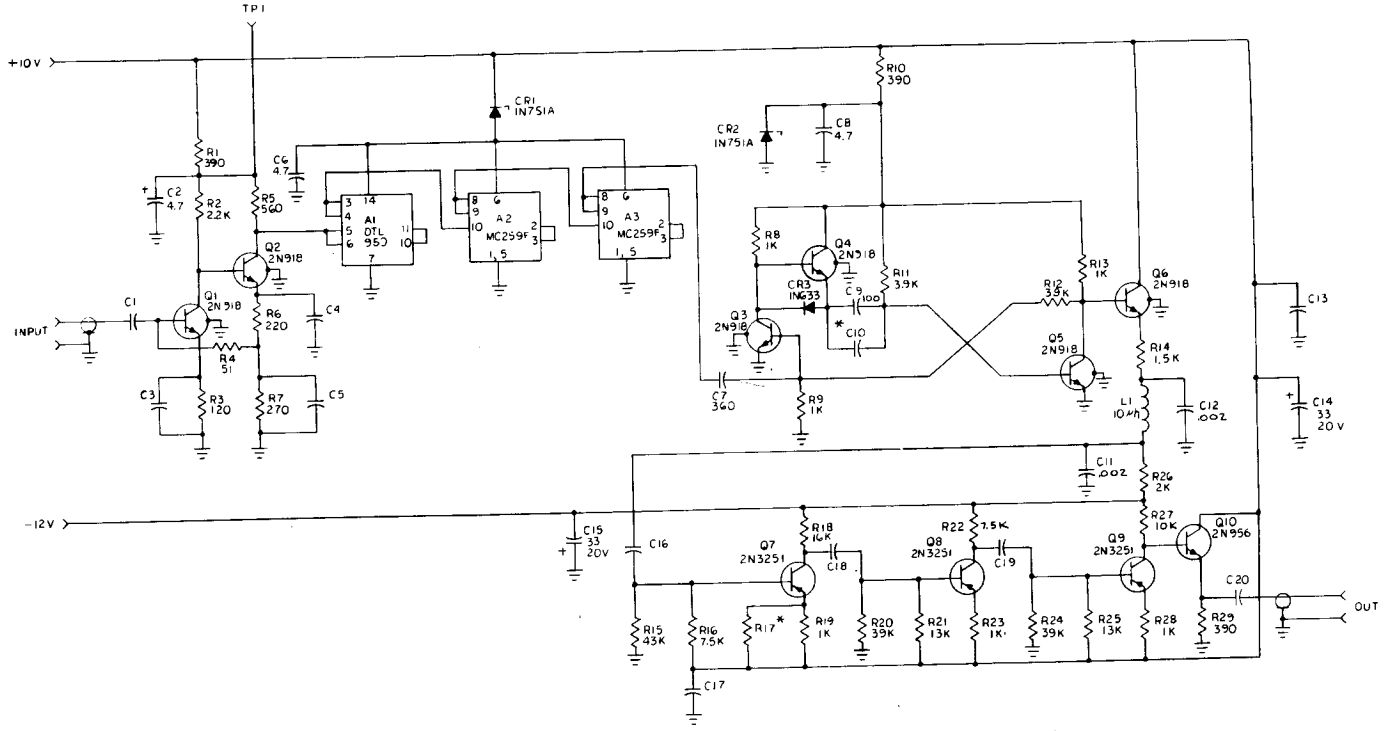

FO3812 U

FIGURE 6-7. PULSE COUNT DISCRIMINATOR

6.2.2 PENETROMETER DATA PROCESSING EQUIPMENT

The data processing equipment accepts the amplitude modulated output from the receiver discriminator and performs envelope detection. This envelope, being a function of received frequency deviation, represents the acceleration function and is used to control the frequency of an FM subcarrier oscillator. This oscillator, one of a set of eight, modulates the transmitter. A block diagram of the eight-channel unit is shown in Figure 6-8.

a. AM Subcarrier Demodulator. A precision full-wave receiver was developed which performs AM subcarrier demodulation. A block diagram is shown in Figure 6-9 and a schematic in Figure 6-10. The band-pass filter was designed to pass 40 $\pm$ 2.5 KHz with less than 0.1 db ripple over that band. The precision full wave rectifier was designed to have a threshold of less than 5 mv rms input. This was accomplished by utilizing an operational type amplifier with diodes in its feedback loop. The configuration is shown in Figure 6-11. Amplifier A1 acts as a half-wave rectifier. The conduction threshold of diodes D1 and D2 is reduced by the gain of the amplifier A1. The resulting half-wave rectified signal is inverted, amplified by two, and then added to the original signal at the input to A2. The result is full wave rectification at the output of A2. This rectified signal is then passed through an active RC filter with a cut-off frequency at 2 kc. This stage can also provide gain which can be adjusted to any desired output signal level. Components used include integrated operational amplifiers and a dual metal oxide field effect transistor as used in the penetrometer signal electronics.

The demodulator transfer characteristics indicate that the demodulator is essentially linear over the entire range of input levels from approximately 5 millivolts to 5 volts. The performance of the units developed is quite adequate for the flight model hardware.

b. Subcarrier Oscillator. Eight subcarrier oscillators were purchased with a dc/dc converter and mounting chassis as an integral unit. Condensed specifications for these oscillators are given in Table 6.3. The dc/dc converter was required due to the negative relay power supply not being compatible with the positive voltage requirement typical of available subcarrier oscillators. The dc/dc converter will not be required in the flight model as a positive power supply is planned and a power regulator/converter is specified which will supply the required voltages and regulation for all other units.

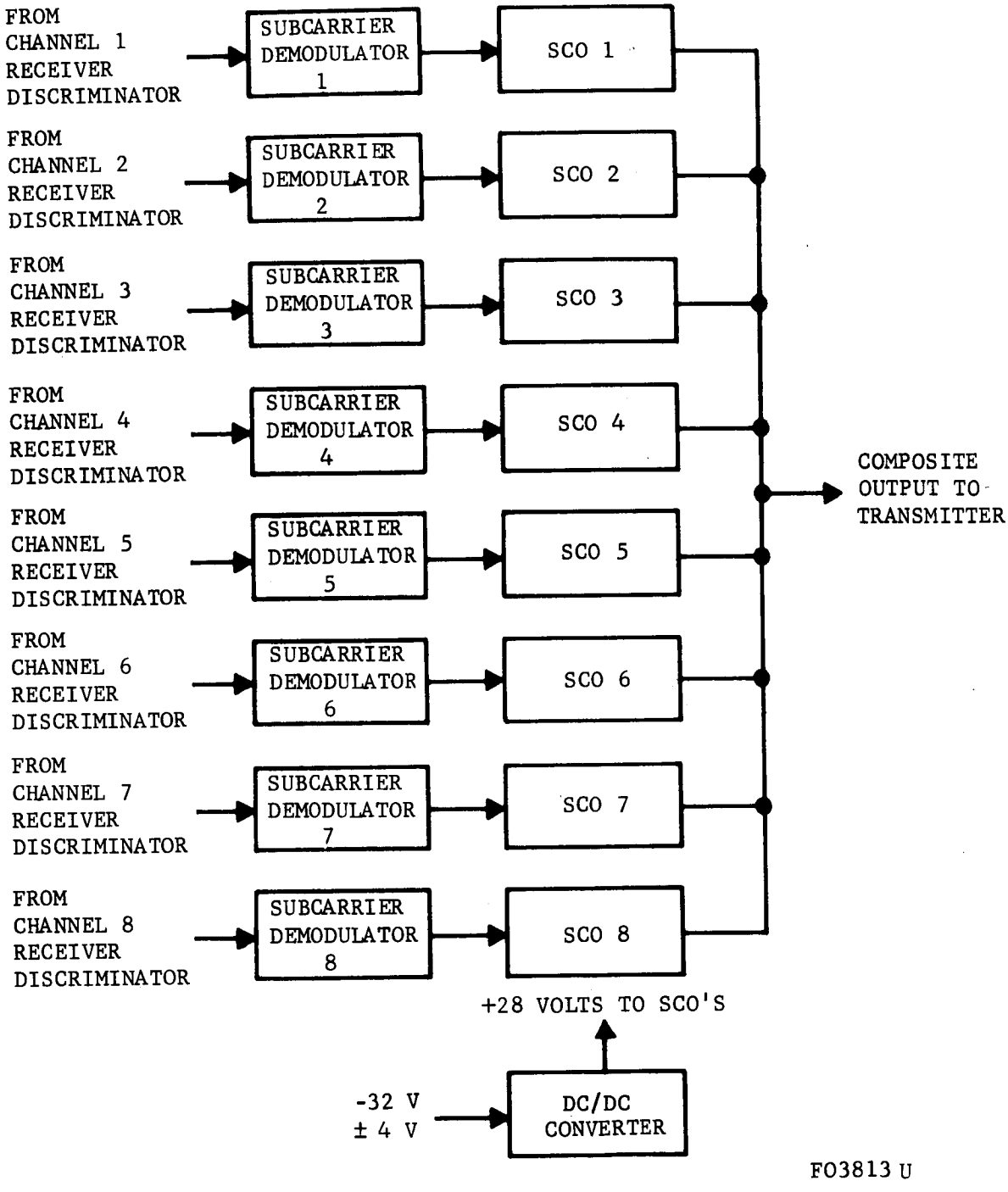

FIGURE 6-8. DATA PROCESSING EQUIPMENT BLOCK DIAGRAM

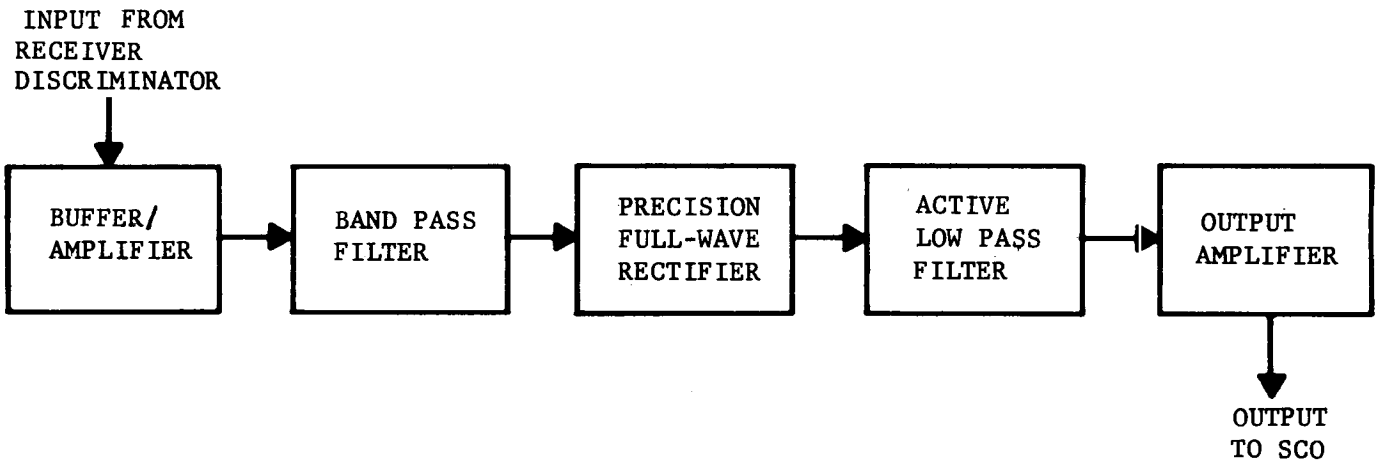

FIGURE 6-9. AM SUBCARRIER DEMODULATION BLOCK DIAGRAM

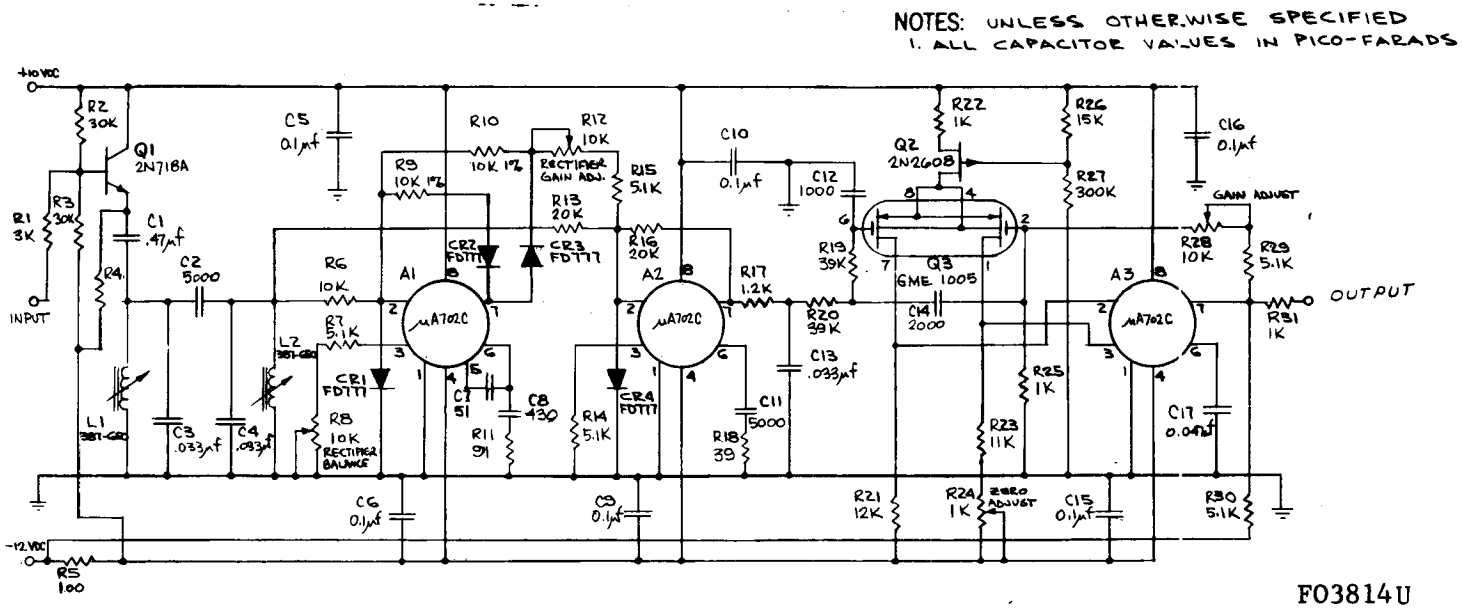

FIGURE 6-10. SUBCARRIER DEMODULATION SCHEMATIC

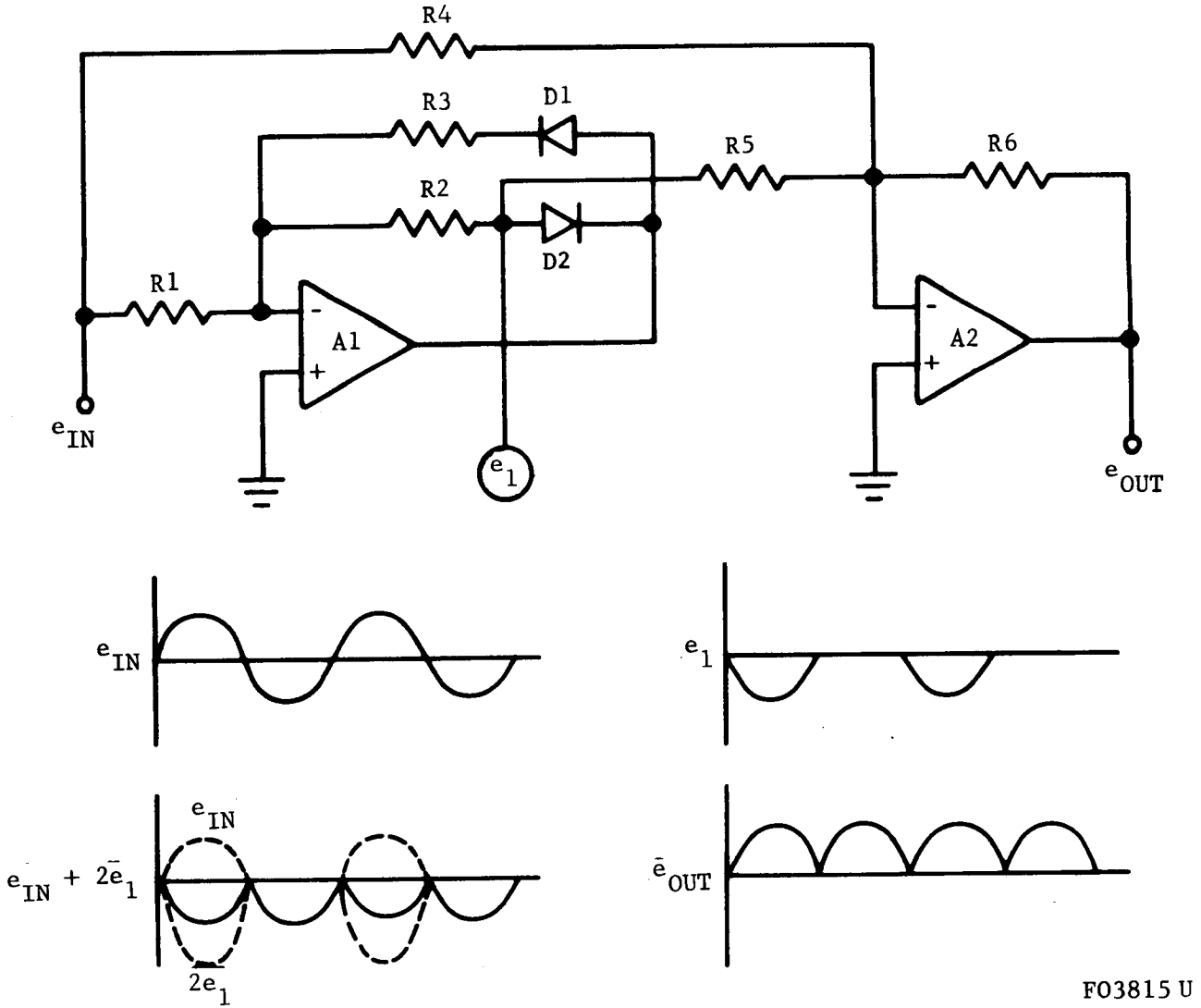

FIGURE 6-11. BASIC PRECISION FULLWAVE RECTIFIER AND WAVEFORMS.

TABLE 6.3

SUBCARRIER OSCILLATOR SPECIFICATIONS

Electrical Specifications

(1) Subcarrier Frequencies

Channel No.	Center Frequency (KHz)	Deviation (KHz)
1	12.5	±2
2	20.8	±2
3	29.2	±2
4	37.5	±2
5	45.8	±2
6	54.2	±2
7	62.5	±2
8	70.8	±2

(2) Input Voltage: 0 to +5 volts

(3) Input Impedance: 100 kilohms minimum

(4) Intelligence Response: Within ±0.5 db from dc to 2 KHz with ±2 KHz deviation.

(5) Linearity: ±0.25% or better with ±2 KHz deviation.

(6) Output Voltage: At each subcarrier frequency adjustable 0 to 0.4 volt rms or more across a common load of 500 kilohms resistance and 100 pf capacitance in parallel.

(7) Amplitude Modulation: ±0.5 db or less for ±2 kcps deviation.

(8) Subcarrier Distortion: Total rms harmonic distortion in the subcarrier output 1% or less.

(9) Frequency Stability: The subcarrier frequency shall remain stable within ±80 Hz anywhere within the input voltage range of 0 to -5 volts after a 5-minute warmup, including effects of power supply variation and temperature within the range +50°F to +150°F.

(10) Power Input: (a) Supply Voltage: +28 vdc ± 5%
(b) Current: 50 ma maximum

TABLE 6.3 (Continued)

Mechanical Specifications

(1) Size: 35 cubic inches maximum.

(2) Weight: 1.40 pounds maximum.

(3) Controls: Sensitivity, frequency, and output level of each subcarrier, all accessible at top of unit.

(4) Test Points: Individual subcarrier output signals all accessible at top of unit.

6.2.3 TRANSMITTER

The transmitter for the data relay was designed to meet the following performance criteria:

Output Frequency	260 MHz
Frequency Stability	$\pm$0.01 percent
Power Output	40 watts nominal
Spurious Output	66 db below output
Modulation	FM or PM, $\pm$125 KHz deviation
Modulation Response	1 KHz to 500 KHz
Modulation Linearity	$\pm$1 db from best straight line
Harmonic Distortion	2% maximum
DC Input Power, Max	-28 vdc at 6 amps maximum

Initial communications link design resulted in a 10-watt output power requirement. However, information on the CSM antenna resulting from contacting NAA personnel indicated that nulls of up to 6 db greater than initially expected might be encountered. Consequently, the power requirement was increased to 40 watts.

Since solid state transmitters suitable for battery operation were not commercially available in this power range, the decision was made to develop a 40-watt feasibility breadboard transmitter.

Initial design concepts included use of a VXCO (Voltage Controlled Crystal Oscillator) which is a frequency modulated oscillator with near-crystal control stability. However, commercially avilable units had long lead time delivery and did not have the deviation capability required. In addition, modulation response was typically limited to 20 KHz which was not suitable for the high frequency constant bandwidth subcarrier oscillators selected for use in the relay system. Therefore, a phase modulator was incorporated as a temporary expedient providing modulation characteristics compatible with FM receiving equipment in the simulated CSM data processing equipment and fulfilling the requirement for a functional test breadboard. A schematic of the 40-watt transmitter is shown in Figure 6-12. The transmitter consists of a 10-watt exciter module and a 40-watt 260 MHz power amplifier. The 10-watt exciter consists of a phase modulated crystal oscillator-buffer, four cascaded frequency doubler stages, and a 10-watt amplifier.

The series mode 16.278 MHz crystal oscillator Q_1 is followed by a phase modulated class A buffer Q_2. The 16.278 MHz frequency was selected for the following reasons:

(1) VXCO operation was contemplated requiring a fundamental mode crystal. Sixteen MHz is near the higher frequency limit of stability at cut fundamental crystals.

(2) A spurious analysis of the data relay receivers indicated that the exact oscillator frequency of 16.278 MHz would not produce harmonically related spurious signals in the data relay receivers.

A voltage variable capacitor, CR_2, is effectively in parallel with the collector tank circuit of Q_2. CR_3, a forward biased diode, provides temperature compensation for the voltage variable capacitor CR_2. The phase modulated buffer output is fed to a class C amplifier, Q_3, which provides approximately 100 milliwatts of drive at 16.278 MHz for the following multiplier stages.

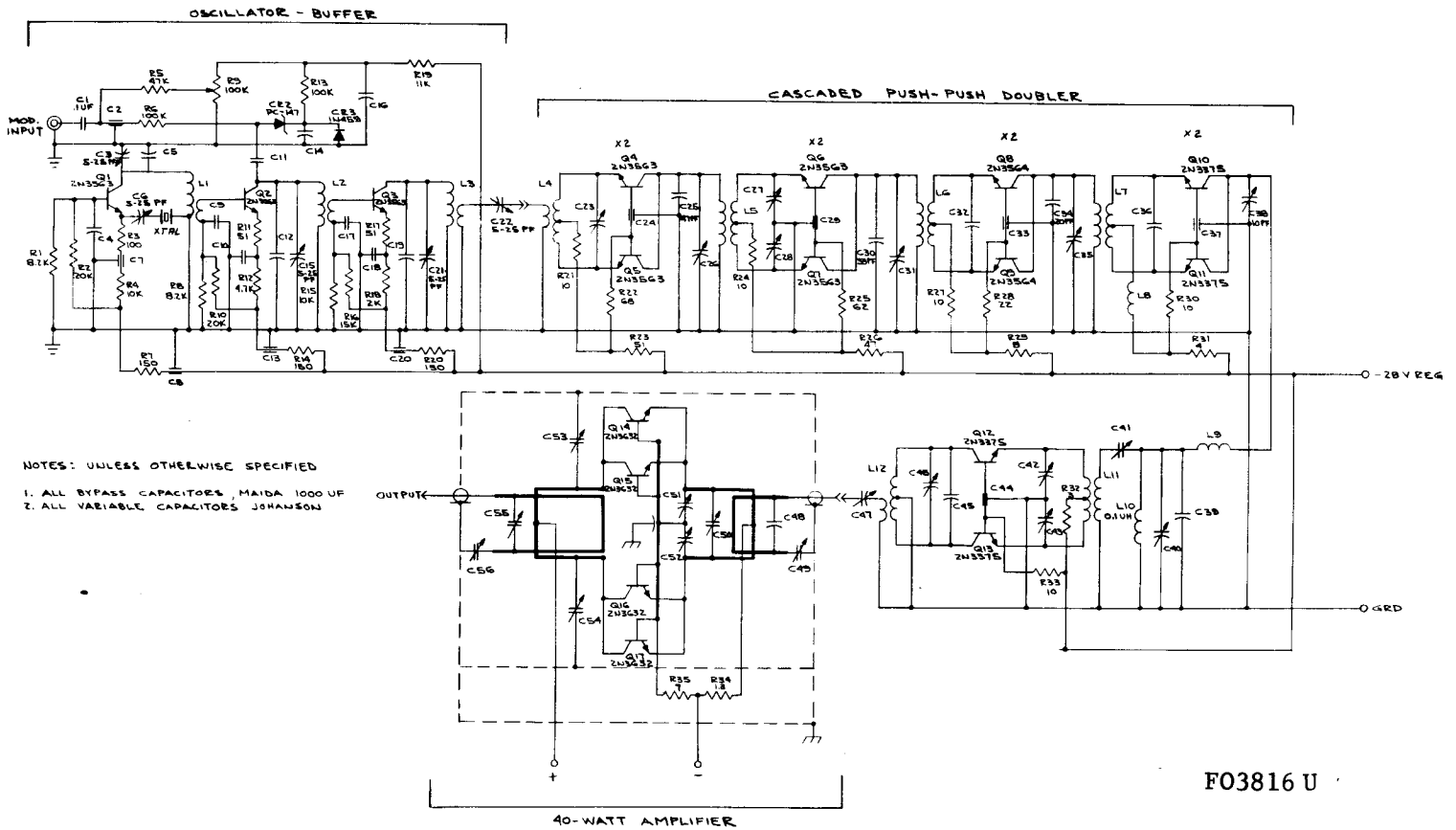

FIGURE 6-12. DATA RELAY TRANSMITTER SCHEMATIC

The data relay transmitter utilizes four cascaded push-push transistor doubler-multipliers to provide the times 16 multiplication factor to translate the 16 MHz oscillator frequency to 260 MHz. The push-push doubler configuration is ideal for this application in that fundamental and odd order frequency components are rejected by circuit symmetry and power gain is provided, eliminating intermediate gain stages.

The times 16 push-push doubler stages provide about 2 watts output at 260 MHz. The final doubler employs 2N3375 stud-mounted 10-watt power transistors because of the high power dissipation and high f_t.

The final stage in the 10-watt exciter module consists of a 10-watt push-pull Class C power amplifier with about 8 to 10 db power gain. Neutralization has not been found to be necessary but cross-coupled neutralization could easily be implemented.

The 40-watt amplifier presented the greatest design challenge because of the lack of commercially available rf power transistors which would provide the required power output. The amplifier was required to provide a 40-watt output at 260 MHz with a minimum 6 db power gain and a 40 percent minimum collector efficiency.

Many transistors were evaluated for use at 260 MHz. Since no 20-watt devices were available, four 10-watt devices were required. A push-pull parallel circuit configuration was selected for use rather than a more common parallel-device circuit because of the problems associated with the total output capacity of four paralleled devices. This would approach 80 pf with typical devices resulting in a tank circuit inductance of 5 nanohenries which is not easily implemented.

Preliminary common emitter and common base test circuits were constructed and used for device evaluation. These circuits are shown in Figures 6-13 and 6-14. Test data taken with the common base circuit are listed in Table 6.4. By adjusting the input and output stubs for optimum power gain, power output, and efficiency, devices could be selected with matching input and output impedances and power gains. Approximate Class C input and output device impedance can be found by removing the device from the test circuit and measuring the network impedance. The transistor input and output impedances are the conjugate of the measured network impedances.

Table 6.5 summarizes available device characteristics for 40-watt amplifier use. Of the ITT devices, only the 3TE440 could be used in a 2-device 40-watt amplifier. The 3TE440's were received late in the program. Power outputs from 10 to 15 watts were obtained at 260 MHz. Two devices were destroyed by parasitic oscillations during higher power testing. The device has a grounded emitter, making a positive supply a necessity. The devices are otherwise well packaged with a very wide ribbon leads for the base and collector terminals.

(a) TRANSISTOR TEST SHCEMATIC COMMON BASE

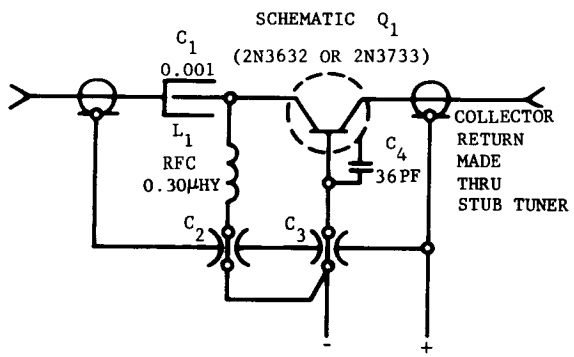

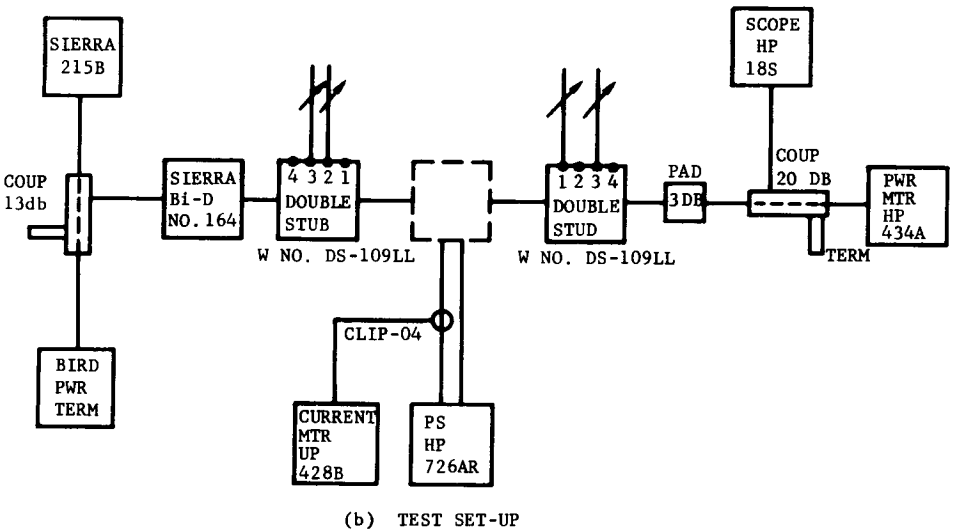

(b) TEST SET-UP

FIGURE 6-13. PRELIMINARY TEST AMPLIFIER SCHEMATIC AND TEST SETUP

(a) TEST CIRCUIT

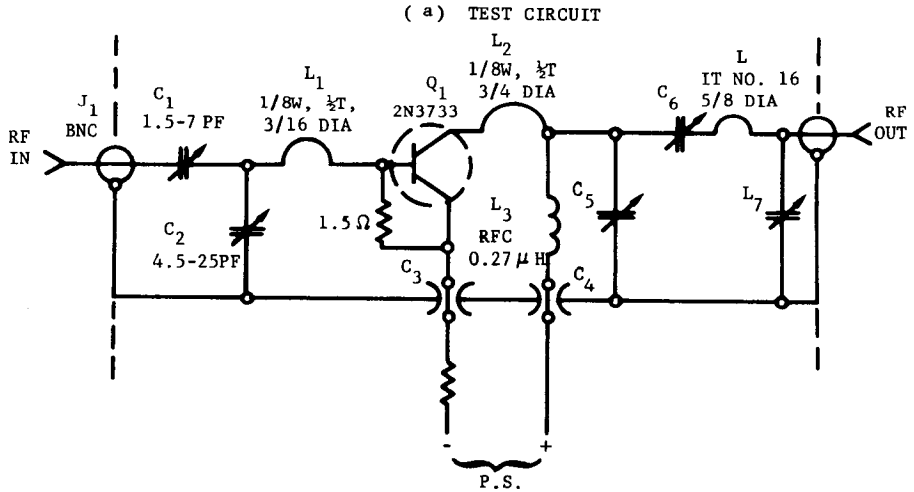

(b) TEST SET-UP

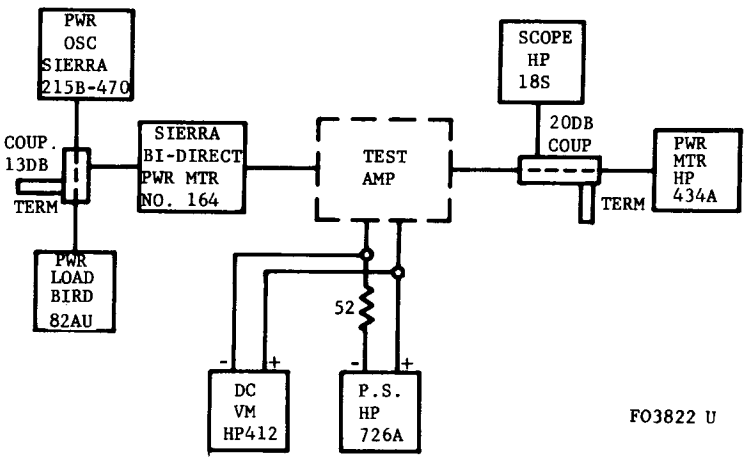

FIGURE 6-14. TRANSISTOR TEST CIRCUIT AND TEST SETUP

TABLE 6.4

MEASURED DEVICE PARAMETERS FOR 40-WATT POWER AMPLIFIER

Device Type and No.	Power Out/Current								Stub Length				P_{in} (Refl)	Notes
	26 volts		28 volts		30 volts		32 volts		Input		Output			
	watts	ma	watts	ma	watts	ma	watts	ma	3	2	1	3		
2N3632 RCA #1	6.4	480	7	495	7.4	510	7.6	520	57.1	44.3	43.7	33.8	0.04 w	
2N3632 RCA #2	7.4	510	7.8	495	8.4	500	8.8	510	0.75	40.4	43.5	23.1	0.040 w	Stubs fairly flat
2N3632 RCA #3	8.8	630	9.8	640	10.6	650	11.4	680	0.6	43.9	41.4	23.5	0.18 w	
2N3632 RCA #4	7.8	665	8.6	675	9.3	680	9.8	690	0	44.3	43.0	23.2	0.040 w	
2N3632 RCA #5	9.0	720	10	720	10.8	720	11.6	720	0.4	43.9	41.4	23.4	0.12 w	
2N3632 RCA #6	7.4	610	8.2	620	9.0	650	9.8	670	0.2	44.2	42.0	23.1	0.09 w	
2N3632 RCA #7	8.4	590	9.0	600	9.8	605	10.6	615	0.3	44.2	42.7	23.3	0.04 w	
2N3632 RCA #8	8.2	655	8.8	660	9.4	670	10.0	680	0.4	44.3	42.1	23.0	0.04 w	
2N3632 RCA #9	9.0	710	10	730	11	740	12	750	0	44.2	41.6	23.2	0.16 in #3	Distorted WF
2N3632 RCA #10	8.4	635	9.2	630	10	650	10.8	670	0	44.3	41.5	23.7	0.08 w	
2N3632 RCA #11	8.0	660	8.8	660	9.3	675	10.0	670	0.4	44.4	42.2	23.1	0.040	Abnormal tuning
2N3632 RCA #12	8.0	650	8.9	610	9.6	610	10.1	615	0.4	44.3	41.7	23.8	<0.04	
2N3733 #1 (P_{in} = 4 w)	9.8	728	10.8	730	12.0	750	13.2	765	0	44.4	40.9	23.5		

TABLE 6.4 (Continued)

Device Type and No.	Power Out/Current								Stub Length				P_{in} (Ref1)	Notes
	26 volts		28 volts		30 volts		32 volts		Input		Output			
	watts	ma	watts	ma	watts	ma	watts	ma	3	2	1	3		
2N3733 RCA #1	8.2	590	9.0	600	9.8	610	10.4	620	0	44.4	42.7	27.6	0.07	
2N3733 RCA #2														Shorted
2N3733 RCA #3														Shorted during test
2N3733 RCA #4	8.4	575	9.2	580	10.0	590	10.8	600	0.2	44.4	42.6	23.1		Shorted
2N3733 RCA #5														Destroyed during test

TABLE 6.5

40-WATT AMPLIFIER TRANSISTOR CHARACTERISTICS

Manufacturer	Type	Applicable Ratings	Comments
ITT	3TE240	P_o = 5 w, P_g = 7 db at 28 v and 250 MHz	Emitter connected to case Max P_{diss} = 25 w at 25°C TO-3 case C_{ob} = 25 pf, F_T = 270 MHz
ITT	3TE245	P_o = 10 w, P_g = 7 db max at 28 v and 250 MHz I_c max = 1 amp	Similar to 2N3632 (RCA) Max P_{diss} = 23 w at 25°C TO-60 case C_{ob} = 25 pf, F_T = 450 MHz
ITT	3TE440	P_o = 20 w, P_g = 4 db at 28 v and 400 MHz Est 8 db P_g at 250 MHz at 28 v	Emitter connected to stud Max P_{diss} = 25 w
RCA	2N3632	P_o = 10 w, P_g = 5.2 db at 28 v and 260 MHz	Two 2N3375 in parallel TO-60 C_{ob} = 20 pf Gnd Emitter required Max P_{diss} = 23 w at 25°C
RCA	2N3733	P_o = 10 w, P_g = 10 db at 28 v and 260 MHz	Emitter tuning used TO-60 C_{ob} = 30 pf P_{diss} = 23 w at 25°C
RCA	TA2675	P_o = 20 w, P_g = 7 db at 28 v and 430 MHz	TO-60 Two samples received late in program No test data
TRW	PT4690	P_o = 10 w, P_g = 10 db at 28 v and 260 MHz	4-Lead case P_{diss} = 17 w at 25°C I_c = 1.5 amp max C_{ob} = 15 pf 10 w P_o max
TRW	PT5690	P_o = 40 w, P_g = 7 db at 24 v and 179 MHz	Very low input impedance High C_{ob} = 80 pf
TRW	PT5692	P_o = 16 w, P_g = 6 db at 25 v and 250 MHz	Max P_d = 35 w C_{ob} = 50 pf (high)
TRW	PT5694	P_o = 10 w, P_g = 7 db at 250 MHz and 25 v	P_{diss} = 20 w max C_{ob} = 25 pf I_c max = 1.5 amps

The RCA 2N3733 did not meet manufacturer's ratings and better performance was obtained with the 2N3632 with about half the rated 2N3773 power gain. This apparent discrepancy in rated performance was confirmed by the RCA sales engineer and was evidentally characteristic of the prototype lot available at the time.

Two TA2675 samples were received too late in the program for evaluation but seem to be ideal for a two-transistor 40-watt amplifier.

TRW recommended use of four TR4690 devices with some reservation about an overall 40-watt output from 4 devices. The PT5690 was not recommended because of low power gain and high C_{ob}. A 40-watt amplifier was constructed utilizing four 2N3632 devices in a push-pull parallel configuration. A power output of 32 watts was obtained at 28 volts collector supply. Increasing the collector supply to 34 volts brought the output power up to 40 watts with 10 watts drive, and 43 percent efficiency. The transistor stud temperature was a measured 115°F at a 32 watt level with a large heat sink partially simulating the data relay structure. No difference in stud temperature was noted between the four devices. Further performance improvement can be made by optimizing bias and tank coil configuration. The present tank capacitors cannot handle the high rf currents and heat excessively. Input and output matching is very good with VSWR's measured around 1.2:1. A more optimum circuit configuration would provide individual adjustable bias to each device. This would minimize the extent of parameter match now required and ensure more stable and equal power distribution between the four devices.

6.2.4 TRANSMITTING AND RECEIVING ANTENNAS

The design and configuration of the relay antennas are dependent upon knowledge of the vehicle on which they mount, the required geometric coverage and the polarization of the external antennas with which they are to operate. Much of this information was lacking in the early part of the program and firm definition of the delivery system and the CSM receiving antenna system is not yet available. Therefore, antenna parameters were specified which would serve the needs of the functional test model with coverage and placement which appeared reasonable for the flight requirements also. The coverage and placement factors were deemed important to assessment of potential rf interference in the relay between its transmitter and receiving complex.

a. Transmitting Antenna. The requirements for the functional model relay transmitting antenna were defined as follows:

Frequency:	260 $\pm$ 10 MHz
Power:	40 watts
Polarization:	vertical linear
Gain:	+2 db
Pattern:	Nominal omnidirectional, upward, null overhead acceptable
VSWR:	1.2:1 at midband
	2.0:1 at band edges
Usage:	for ground tests only

The functional model transmitting antenna consists of a quarter-wavelength monopole over a ground plane (Figure 6-15.) This configuration satisfied all of the electrical requirements and is of a suitable geometry to be situated at the upper end of the relay vehicle. The radiating monopole is 10.8 inches in length and the ground plane is 21.6 inches in diameter. The ground plane shown was used for antenna test purposes only. In the functional test model data relay the housing top plate, 26 inches in diameter, forms the ground plane for the centered vertical stub. The polarization was chosen to suit the receiving antenna, also a vertical stub, at the Aeronutronic ground station which was used to simulate the CSM receivers and recording capability.

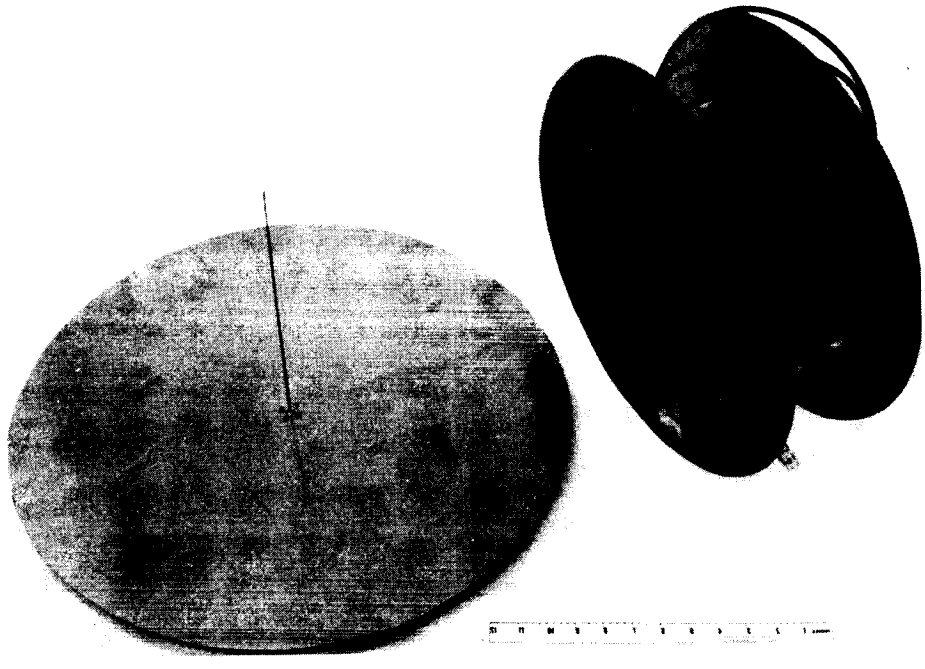

FIGURE 6-15. RELAY ANTENNAS

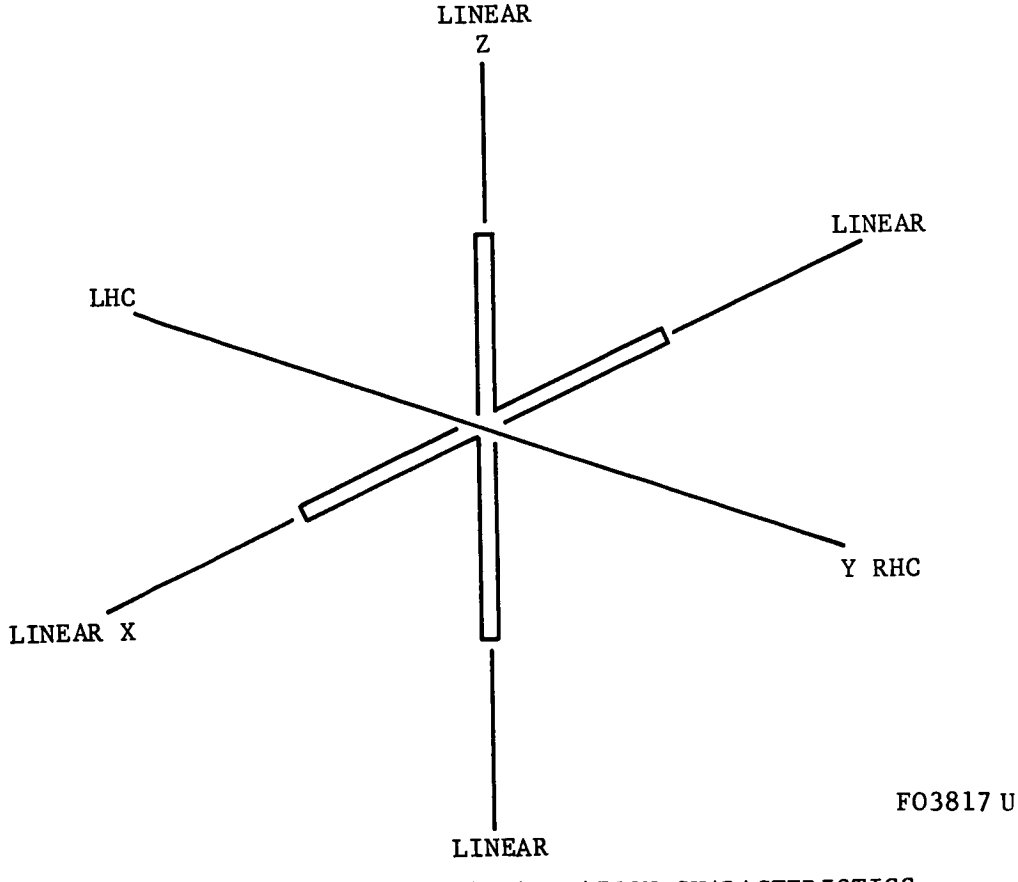

FIGURE 6-16 TURNSTILE POLARIZATION CHARACTERISTICS

b. Receiving Antenna. The polarization of the radiated field from the penetrometer varies around the sphere and includes all possible states and varying orientation of the polarization ellipse. Therefore, a polarization diversity receiving antenna is required to avoid nulls in reception. It can be shown that any field of any given state of polarization can be resolved into two components having mutually conjugate polarization states. Thus, the receiving antenna system could consist of, for example, two orthogonal linear elements or, alternately, a right-circular and a left-circular antenna. The choice was made partly on the basis of minimum switching in the receiver system (assuming antenna switching diversity combination) and included the following considerations.

The penetrometer antenna yields a pattern nearly identical to that of a standard turnstile and it is convenient to examine the polarization of the penetrometer signal in terms of the signal from a turnstile. Referring to the diagram, Figure 6-16, note that the polarization received by a receiving system located on the forward Y axis would initially be RHC. If the turnstile were then rotated about the Z axis, the polarization would change from RHC to vertical linear, to LHC, again to vertical linear and return to RHC. Between the states of circular and linear, polarization would be elliptical. If the diversity receiving system employed RHC and LHC antennas, switching would need to occur twice per spin revolution. If, however, the receiving system employed a vertical and a horizontal linear antenna, the system would remain switched to the vertical linear antenna during this mode of spin rotation. If we consider all of the possible combinations of major axis receiving station locations and choice of major spin axis, the following table results.

Location Axis of Receiving Station	Axis of Rotation	Diversity Antenna Type for Minimum Switching
Y	Z	Linear
X	Z	Linear
Z	Z	Circular
Y	Y	Circular* or Linear
X	Y	Linear* or Circular
Z	Y	Linear* or Circular
Y	X	Linear
X	X	Circular
Z	X	Linear

* 3 db advantage relative to alternate choice.

Note that the diversity system employing linear antennas results in a disadvantage in only two out of nine cases and the disadvantage is incurred only if the spin axis lies within an approximate 45 degree cone centered about the X or Z axis. Additionally, considering the mode of deployment, it is relatively unlikely that the angle between the spin axis and the axis on which the receiving station is located will be small, i.e., less than 45 degrees. Thus the choice of dual crossed-linear elements is indicated. This is also a simple configuration with half the hardware required for dual turnstiles, for instance, which could be used to obtain left and right-hand circular polarization.

The exact requirements for the functional model receiving antenna are defined as follows:

Frequency:	432 MHz to 453 MHz
Polarization:	Dual linear
Gain:	+4 db on axis
Pattern:	Unidirectional, 3 db down approximately $\pm 60^{o}$ downward.
VSWR:	Not to exceed 2.0:1
Usage:	For field tests only

The actual antenna consists of two crossed dipoles, each 12.5 inches long and spaced 5.25 inches above 15.7-inch diameter circular ground plane.

A photo of the antenna is included in Figure 6-15. The dipole elements are flat copper strips bonded onto a fiberglass disk. The aluminum ground plane is separated from the dipole elements by four dielectric rod spacers. A half wave coax balum was used to feed each dipole.

c. Flight Model Antennas. Although the final requirements for the flight model antennas have not been defined in detail, the current design concept is defined in Specifications LPS-201 and LPS-209, included in the Program Plan. Because of restrictions in the flight model system, as now configured, the antennas will have different locations on the vehicle, relative to the functional model antennas and, consequently, will be of a different design type. The transmitter antenna will consist primarily of two orthogonal quarter-wavelength monopoles mounted parallel to the vehicle roll plane. The elements will be interconnected through a hybrid junction to provide circular polarization. Additional driven or parasitic elements will be included to provide pattern directivity as reqired by systems considerations. The receiving antenna will be of the same design type except that the orthogonal elements will provide separate inputs to the diversity combiner.

6.2.5 DATA RELAY POWER SUPPLY

a. Functional Test Model. The present functional test model power supply is shown in the block diagram of Figure 6-17. Sealed lead acid batteries were used to obtain reasonable operating times for testing. The operative time between charges is approximately 1.5 hours with 40 watts rf output, or 3 hours with 10 watts rf output. The negative side of the battery is off ground as this was convenient for the functional model receiver and transmitter. A positive voltage is required and is provided by a dc/dc converter. Three regulators are required to provide -28V, -12V, and +10 volts. Schematics of these units are shown in Figures 6-18 and 6-19. The regulators are of conventional design utilizing a transistor series regulating element. They provide ±1 percent regulation worst case against line and load variations at room ambient.

The dc/dc converter utilizes a 20 KHz transistor power oscillator and diode bridge rectifier to obtain a positive dc voltage. The +10 volt converter-regulator is packaged in an aluminum housing with output line filtering to remove the switching transients generated by the converter. The -12 and -28V regulators are packaged in a separate housing. All the circuits are at essentially the breadboard level of construction.

b. Flight Model. The power supply for the data relay will consist of a sealed silver-zinc battery and a converter/regulator unit to supply the various requirements. The turn-on action for operation will be provided by the Payload Delivery System (PDS). An interface discussion concerning the Penetrometer Data Relay System (DRS) and the PDS was held at MSC Houston on 11/5/65. The desirability of a common power supply for the DRS and the PDS was discussed but no conclusions could be reached. For maximum flexibility, a separate battery is assumed for the DRS. It will be of +28 volts potential with respect to ground, the same as presently conceived for the PDS.

(1) Relay Power Requirements. A dc-dc converter/pre-regulator is shown in Figure 6-20 which is suitable for the LPS relay application. This type unit with a switching input regulator can efficiently supply multiple outputs to constant loads from a widely varying source. The principle of operation is to vary the duty factor of an input current switch which avoids the losses inherent in resistive series regulating elements. The +12 volt and -6 volt outputs require the highest regulation of ±1 percent, and also +12 volts is a convenient potential to feed back for reference comparison as shown. A regulation of ±1 percent of the referenced output is readily obtained. The same regulation is obtained for the other outputs when low internal impedance is maintained and the load is constant as in this application. The regulation of the outputs which supply the transmitter, +28V and especially +36V, is least critical.

NOTES:
1. ALL RESISTORS 1/2 WATT
2. * SELECTED VALUE

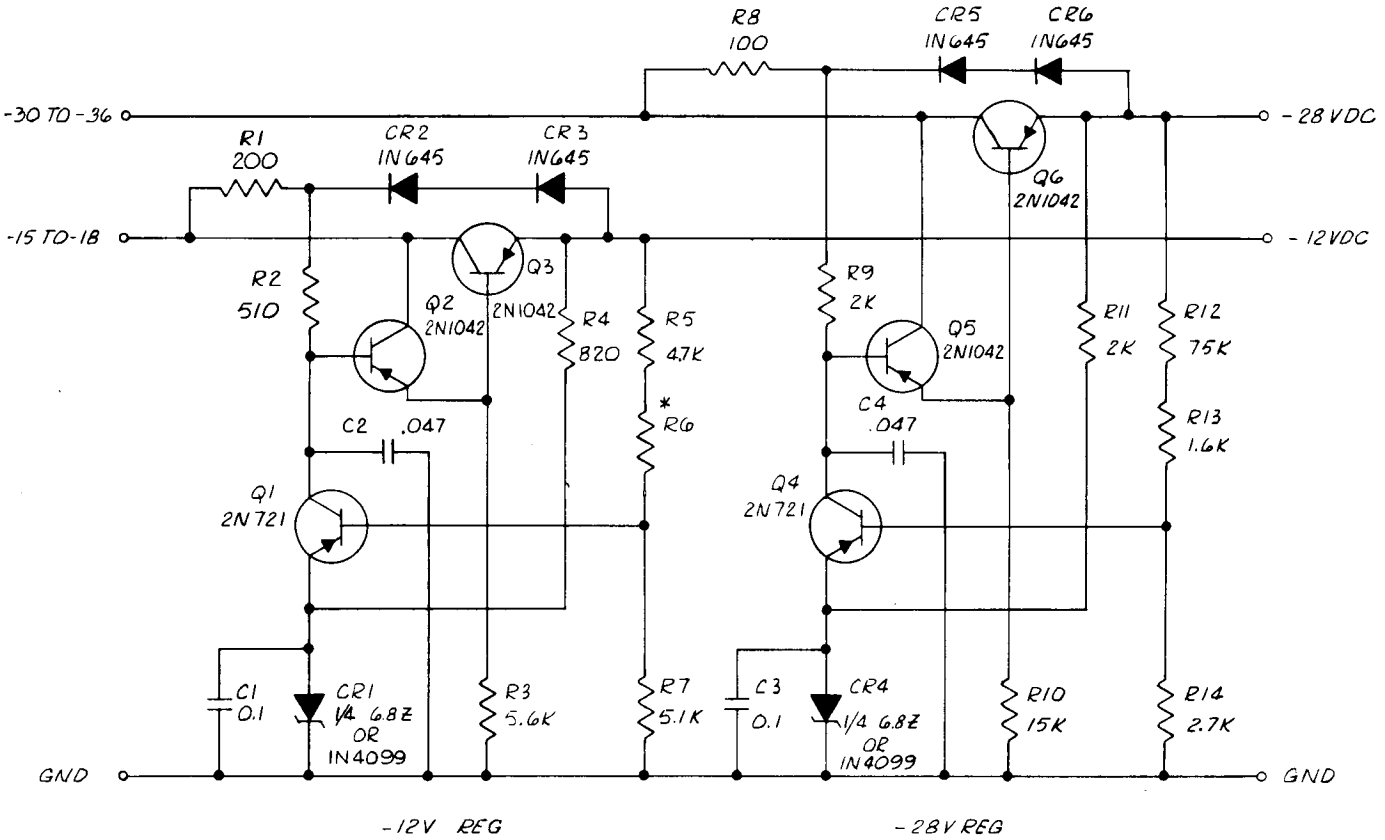

FIGURE 6-18. CONVERTER/REGULATOR +10 VOLTS, LPS RELAY

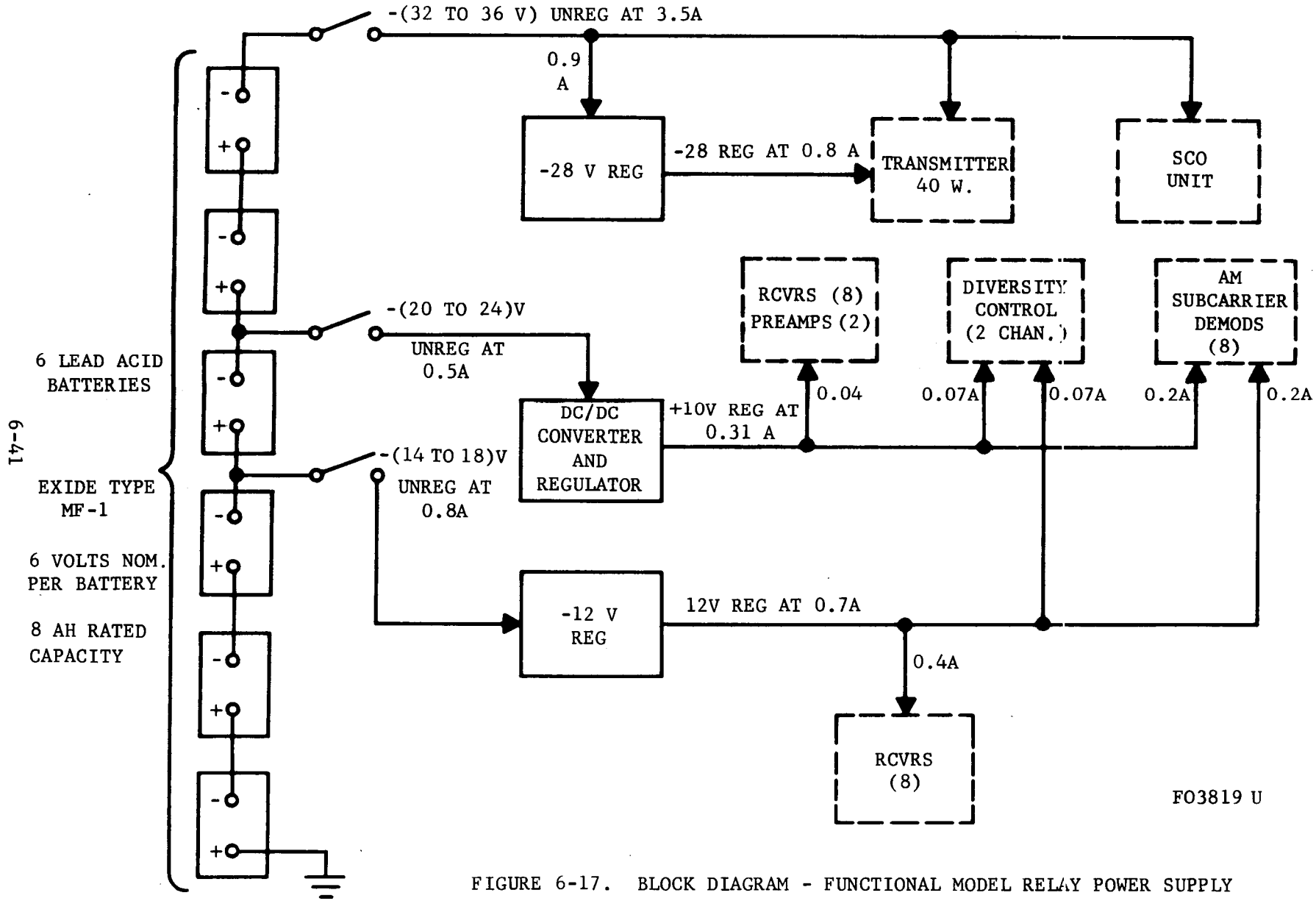

FIGURE 6-17. BLOCK DIAGRAM - FUNCTIONAL MODEL RELAY POWER SUPPLY

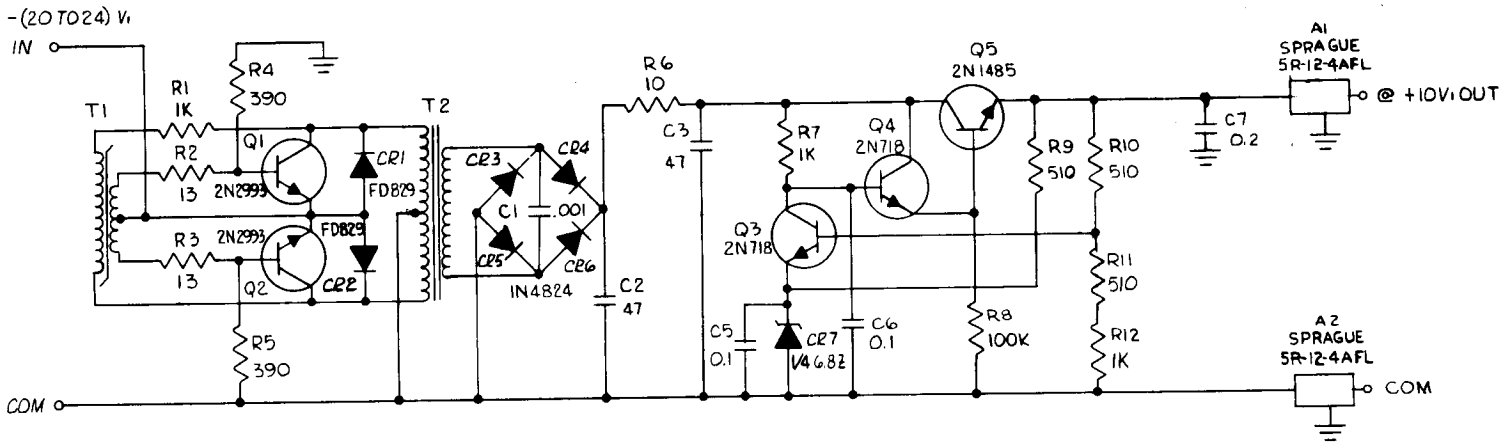

FIGURE 6-19. VOLTAGE REGULATOR - 12 AND 28 VOLTS, LPS RELAY

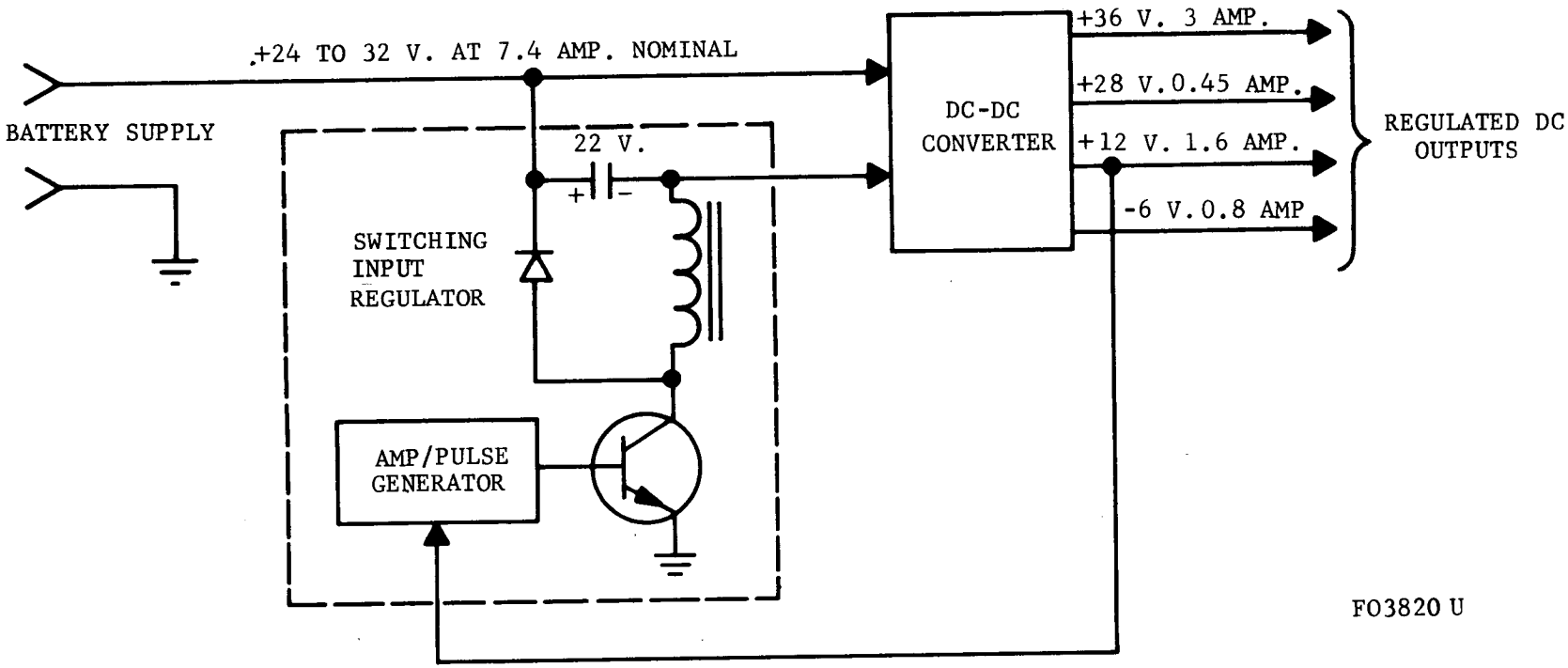

FIGURE 6-20. DC-DC CONVERTER/PRE-REGULATOR DIAGRAM

The transmitter takes over 80 percent of the total power. The 40-watt figure used for rf output power is intended to be conservative (based upon a CSM receiving antenna gain of -9 db) and should be re-examined when the CSM receiving antenna gain is more accurately defined.

Although the operation period of 10 minutes shown in Table 6.6 is intended to include brief status checks, additional battery capacity must be available, depending upon various considerations. If the battery is charged prior to launch, stand-time loss of about 1 percent per day storage at room temperature must be allowed for. This loss is accelerated at elevated temperature as might arise during pad storage and lunar transit. Added reserve will be required if the penetrometer batteries are to be charged by the relay power supply, or if the penetrometers are to be operated prior to launch for warm-up (stabilization). Also, battery capacity for the types of interest is typically quoted as the basis of a 1-hour discharge. A 10-minute discharge will be less efficient because of loss in the internal cell resistance. If a 100 percent capacity loss is allowed for the various factors above, a nominal battery capacity of twice that shown in Table 6.1, or 69.2 watt-hours results. If fully redundant transmission is utilized, the required capacity may (conservatively) be doubled.

(2) Power Source Selection. The energy requirements for the flight model data relay are best supplied by an electrochemical secondary (rechargeable) battery. Sealed chemical batteries are highly developed for space applications and have the features of ruggedness, compactness, efficiency, availability, and reliability. Two types are in general use in space and missile applications. These are the nickel-cadmium and silver-zinc types, referring to the electrode materials; both use KOH electrolyte. Silver-cadmium batteries are under development and have seen limited use, but this type is not yet readily available. These three types are inherently rugged, efficient, sealable, rechargeable (secondary design), and can supply high peak loads.

For the penetrometer relay, the silver-zinc battery is preferred because it has the highest energy density and drain rate for chemical batteries; typical figures are 60-watt-hours per pound, a drain rate of 100 watts per pound. Based on these figures, it is seen that the relay battery is sized by the required drain rate rather than the nominal capacity. The silver-zinc battery is typically capable of the order of 10 charge-discharge cycles. The other battery types are capable of more cycles but the energy density for silver-cadmium is about one-half that for silver-zinc, and, for nickel-cadmium, about one-fourth that of silver-zinc. If necessary, the silver-zinc battery can be designed for longer cycle life at a sacrifice in energy density.

TABLE 6.6

FLIGHT MODEL DATA RELAY POWER REQUIREMENTS

Item	Voltage	Current	Power (watts)	Watt-Hours (for 10-minute Oper)
Preamplifier (2)	+12 v reg -6 v reg	32 ma 32 ma	0.4 0.2	0.06 0.03
Receiver Complex (16 channels)	+12 v reg	800 ma	9.6	1.6
Transmitter (40 watts)	+36 v reg +28 v reg	3.0 amp 400 ma	108.0 11.2	18.0 1.9
Data Processing Diversity Control Circuit (8)	+12 v reg -6 v reg	400 ma 400 ma	4.8 2.4	0.8 0.4
AM Subcarrier Demodulators (8)	+12 v reg -6 v reg	400 ma 400 ma	4.8 2.4	0.8 0.4
FM Subcarrier Oscillators (8) and Mixer	+28 v reg	50 ma	1.4	0.2
Subtotal Power and Energy			145.2	24.2
Power Converter/ Regulator (70% Efficiency)	+28 v $\pm$4 v	7.4 amp	62.2	10.4
Total Power and Energy			207.4	34.6

(3) Vendor Survey. A survey of battery vendors shows that two types of battery construction have applicability to this requirement. The more conventional approach is to use the readily available prismatic cells in a sealed metal case. Such a battery could be made from the cells from various manufacturers as typified by those listed in Table 6.7. The resulting battery constructed from 20 such cells would weigh approximately 5 pounds if an allowance of 30 percent of the basic cell weight is made for the case, cover, connector, and pressure relief valve.

The second approach is to use the pile-type batteries which are manufactured in an encapsulated block. Typically, less choice of sizes is available. However, two standard sizes near our requirement are shown in Table 6.8. The Eagle-Picher 1045 battery utilizes the pile construction to obtain high-power density, but is currently unsealed and limited to primary applications because of the method of fabrication and filling. The ESB/MBD 181 battery has been designed for rechargeable applications and is completely sealed. It has a rated life of 30 deep discharge cycles. The type 181 battery has a mean voltage of 9 volts and three of these, totaling 3.3 pounds plus added wiring, connectors, and housing, would be required for the relay application.

Thus, it is seen that battery cells and pile batteries are presently available which would appear to meet all requirements imposed by the LPS relay application in a unit of 4 to 5 pounds weight. Alternately, it should be possible to effect some saving in weight if a battery is developed specifically for the relay application..

The dc-dc converter/pre-regulator would likely be designed to the specific relay requirements. This is of conventional design and any of several specialty manufacturers can carry out such a design in a short period. A unit recently developed has very nearly the required performance for the relay application and can be used for preliminary design information. This unit supplies 160 watts at 5 different voltages from a 30 to 40 volt input and an average efficiency of 74 percent. It weighs 16 ounces and occupies a volume 3 by 5.5 inches by 1 inch.

TABLE 6.7

TYPICAL PRISMATIC BATTERY CELLS

Manufacturer	Rated Capacity A-H	Part No.	W (in.)	H* (in.)	Th (in.)	Vol ($in.^3$)	Wet Wt (oz)
Eagle-Picher	3	1515	1.58	2.63	0.64	2.7	3.2
Power Sources	3	SC-3	1.76	2.94	0.71	3.7	3.4
Yardney	3	HR-3	1.72	2.86	0.59	2.9	3.2
ESB/MBD**	4	S-4	1.58	2.84	0.64	2.9	2.9

TABLE 6.8

PILE-CONSTRUCTION BATTERIES

Manufacturer	Part No.	Capacity A-H	Voltage	W (in.)	L (in.)	H (in.)	Vol ($in.^3$)	Wt
Eagle-Picher	1045	4	30	4.05	2.87	4.18	55	62 oz
ESB/MBD**	181	4	9	3.0	3.0	1.5	13.5	1.1 lb

*Includes terminals

**The Electric Storage Battery Company, Missile Battery Division.

6.2.6 DIVERSITY

Diversity reception of the signal from an impacting penetrometer may be necessary for any or all of the following reasons:

(1) A variety of signal polarizations are present

(2) There can be signal nulls due to reflections from the lunar surface.

(3) There can be a combination of amplitude and phase modulation of the received signals due to spinning of the penetrometer as it impacts.

There are four main types of diversity systems in practical use which could be used to combine two received penetrometer signals. These four can be defined as follows:

a. Scanning Diversity. In this method, either signal is chosen and kept as long as the S/N ratio remains above some arbitrary threshold. Should the chosen signal drop below the threshold, the output is then switched to the alternate signal. Antenna switching falls into this diversity category.

b. Selection Diversity. The two signals are continuously compared to see which has the better characteristics and this one is selected to furnish the output signal. IF switching falls into this diversity category.

c. Maximal-Ratio Diversity. The two signals are added together in proportion to the square of their S/N ratios.

d. Equal Gain Diversity. The two signals which have passed through exactly-equal-gain receivers are added coherently.

The first two types listed are of the switching types, while the last two types actually combine the two signals. All but the first type (antenna switching) require two receivers. A more complete discussion and analysis of these four types of diversity systems are found in the State-of-the-Art Review.[1]

On the present penetrometer program two channels of antenna switching diversity were implemented. This system was chosen due to its relative simplicity and to the fact that only one receiver was required.

In order to determine the transient effects of antenna switching, an experiment was performed as shown in Figure 6-21. The input to an FM receiver was alternately switched over different cable lengths ℓ_1 and ℓ_2 from an FM signal generator. The different cable lengths result in different phases of

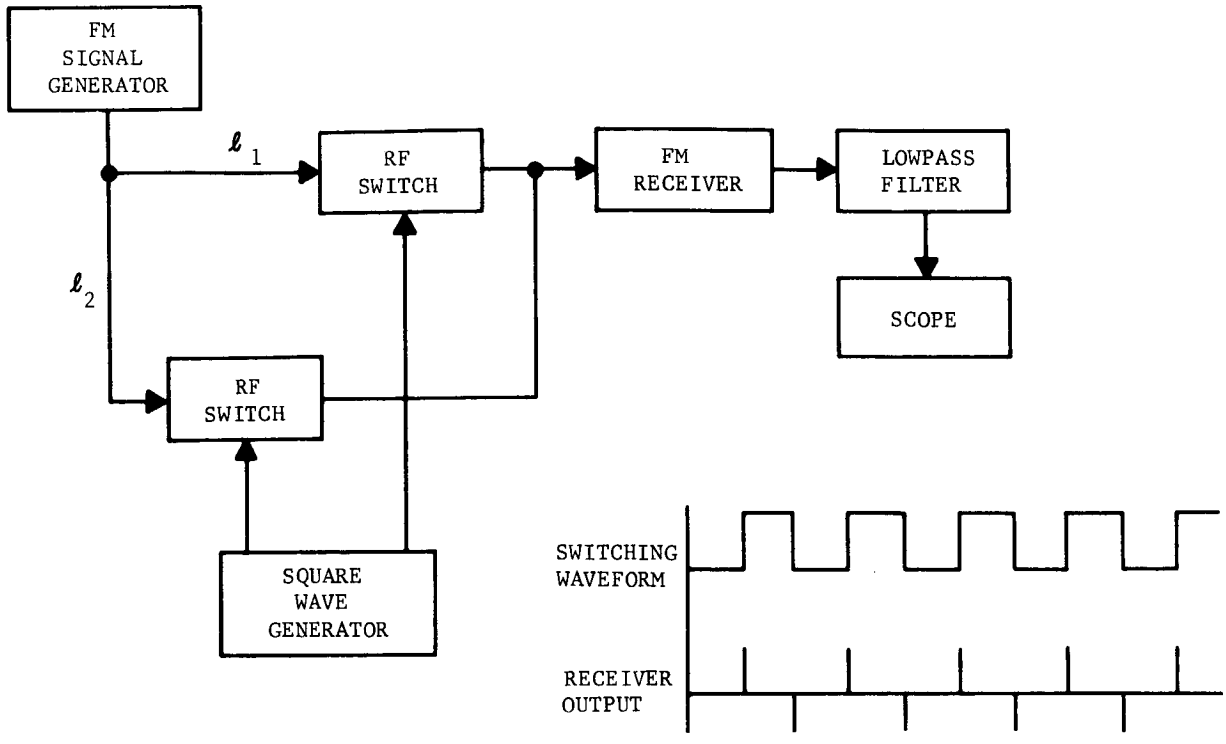

FIGURE 6-21. ANTENNA SWITCHING TRANSIENT TEST BLOCK DIAGRAM

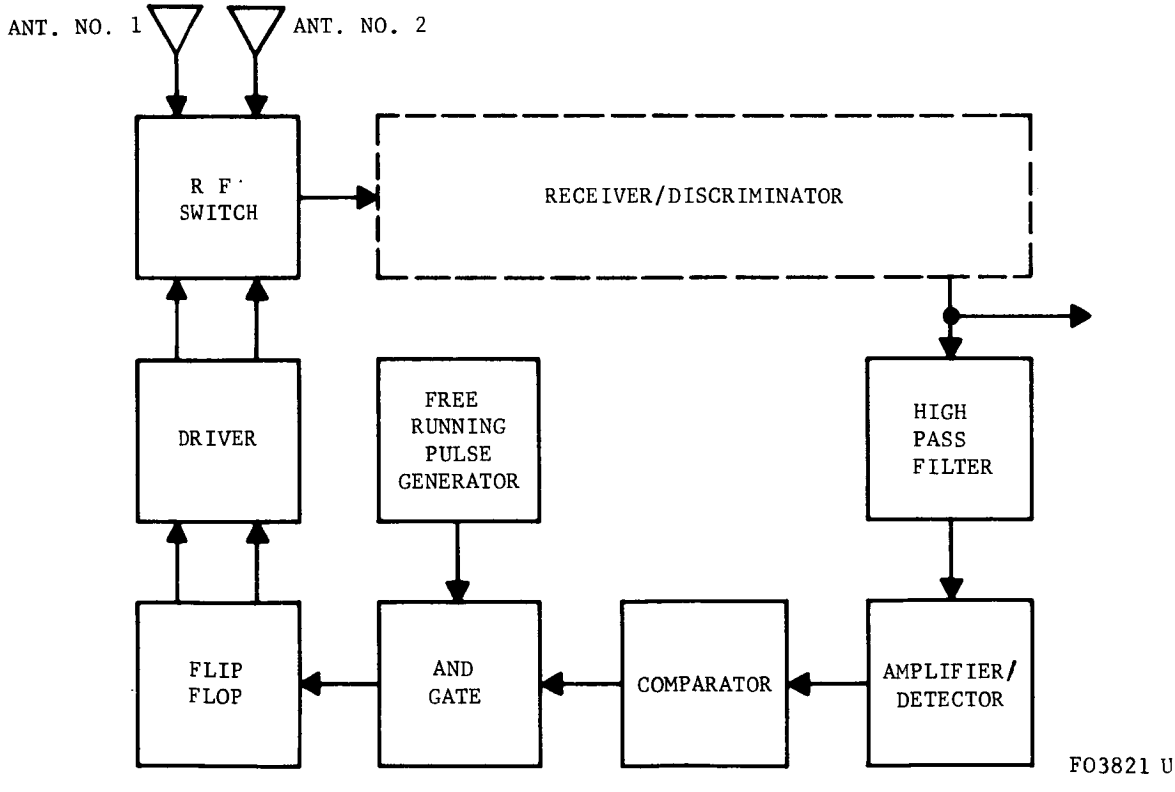

FIGURE 6-22. ANTENNA SWITCHING DIVERSITY SYSTEM BLOCK DIAGRAM

signals to the receiver. Also shown on the figure are waveforms corresponding to the transient at the receiver output, which were eliminated by the low-pass filter. The duration of the transients is a function of the rf switching time and receiver bandwidth, and in this case is quite narrow with little energy at the switching frequency. This test suggested pursuit of antenna switching as a possible solution to diversity reception with hardware simplicity. Later tests were performed using the subcarrier demodulator at the receiver output with a 40 KHz modulating frequency at the FM signal generator, and a 200 Hz square wave frequency. For approximately equal large signals at the rf switch, the transient amplitude was about $\pm$25 millivolts at the demodulator output, with a duration of about 400 microseconds. This transient was about $\pm$10 percent relative to a 50 g signal value. At 7000 g, the transient was about $\pm$0.5 percent relative to signal value.

A block diagram of the functional model antenna switching diversity system is shown in Figure 6-22. The schematic of the diversity switch driver circuitry is shown on Figure 6-23, while the schematic for the rf switch is shown in Figure 6-24.

The output of the receiver discriminator is fed to the high-pass filter which eliminates the signal frequency (40 KHz), but passes broadband noise. This noise level is rectified, filtered and amplified to provide a dc level which is a function of the noise level of the discriminator output. Thus a "quiet" receiver with a strong received signal would provide a very low dc level, while a receiver channel with weak signal would be noisy and provide a higher dc level out. This dc level is compared to a reference level. If this predetermined reference level is reached the AND gate is enabled, thus allowing the free running pulse generator pulse to toggle the flipflop, which in turn selects the other rf switch. This causes a new noise level to occur at the discriminator output. If this level is sufficient, switching again occurs. In this way, if no signal is present from either antenna, the system will switch from one to the other continuously, and once a signal above threshold is found the system will allow it to remain. The individual circuits in this diversity scheme were checked out but time did not allow for complete system checks.

The need for diversity reception should be re-examined, especially if the operating range drops appreciably under the 2 nautical mile figure now designed for. In the various tests carried out so far with actual penetrometers, there have been no signal dropouts nor antenna switchings. These have all been short-range tests with high average received signal strength. However, multipath interference has been a potential problem with highly reflective surroundings, and the penetrometers have been deliberately launched in many different aspects and turned slowly.

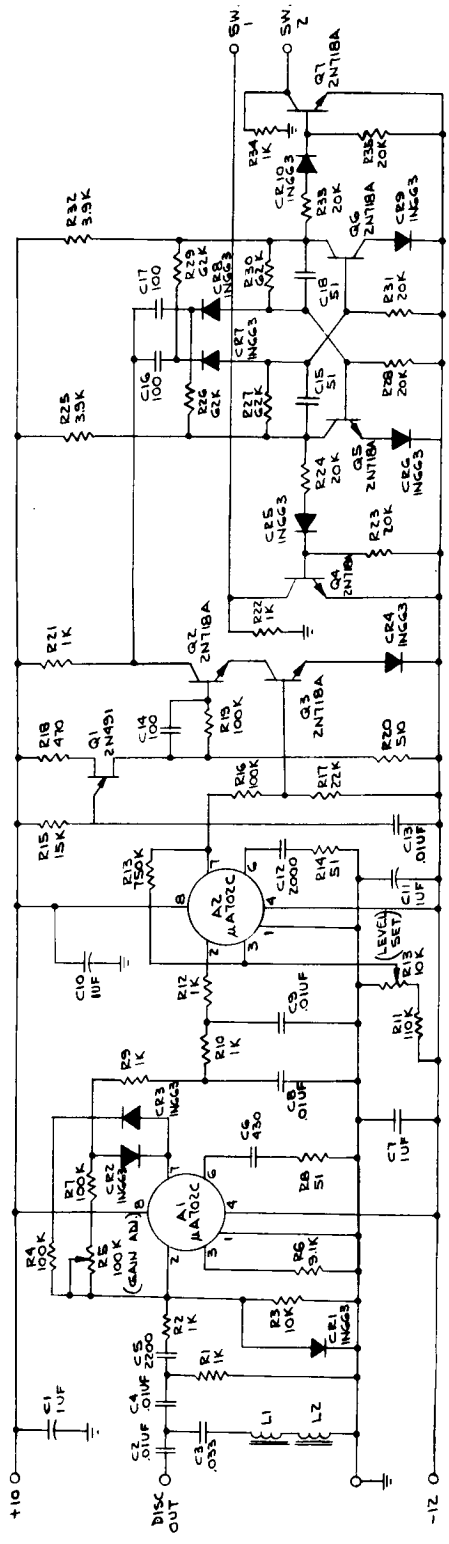

FO3823 U

FIGURE 6-23. DIVERSITY SWITCH DRIVER SCHEMATIC

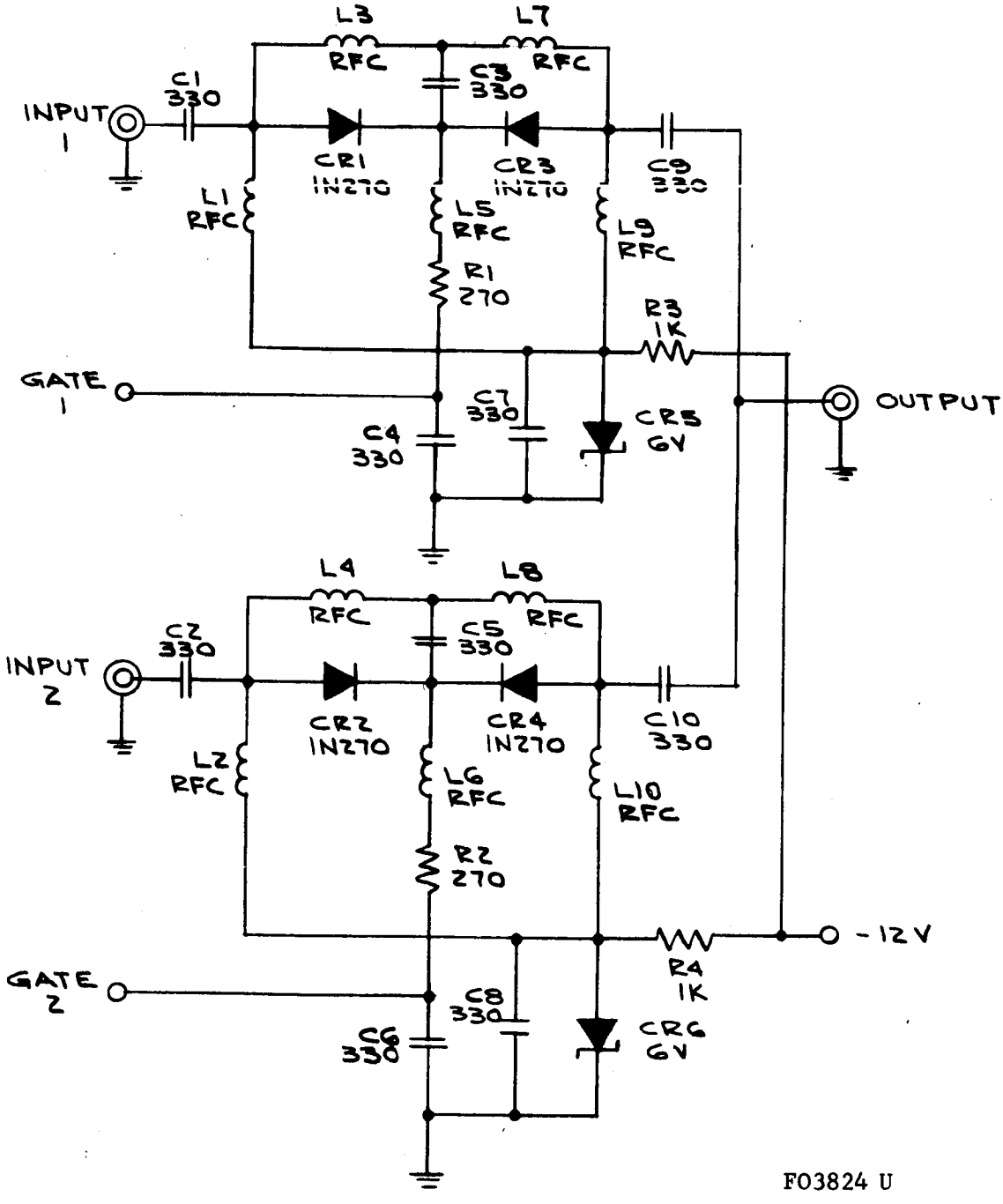
L3
RFC
L7
RFC
C1
330
C3
330
INPUT
1
CR1
IN270
CR3
IN270
C9
330
L1
RFC
L5
RFC
L9
RFC
R1
270
R3
1K
GATE
1
C7
330
CR5
6V
C4
330
OUTPUT
L4
RFC
L8
RFC
C2
330
C5
330
INPUT
2
CR2
IN270
CR4
IN270
C10
330
L2
RFC
L6
RFC
L10
RFC
R2
270
-12V
R4
1K
GATE
2
C8
330
CR6
6V
C6
330

F03824 U

6.3 DATA RELAY FUNCTIONAL MODEL TESTS

6 3.1 FUNCTIONAL MODEL DESCRIPTION

A functional block diagram of the data relay in its typical flight configuration is shown in Figure 6-25. The actual test model utilized all the principal elements identified with one exception, only one rf switch and diversity scanning circuit was employed. The photo of Figure 6-26 illustrates the basic test configuration. The bottom shelf accommodates the data acquisition section housing rf preamplifiers (2), rf power divider (1), FM receivers (8), and FM pulse count discriminators (4) with the polarization diversity antennas hidden from view just below the shelf.

The middle shelf houses the battery power supply and regulator assembly. The top shelf accommodates the data transmission section comprising AM demodulators (8), FM subcarrier oscillators (8), FM transmitter (1), and power amplifier (1). The transmitting monopole antenna is located topside and centered in the 26-inch diameter top plate. Coaxial and power feedthrough connections are employed to route signal and power between shelves. Bulkhead connectors (3) provide signal and external power interface connections to external monitoring and power supply test equipment.

The overall basic relay configuration may be further represented as laboratory and field test (multiple drop) configurations. The laboratory hook-up utilized a more flexible and variable interconnection of elements, while the multiple drop test setup employed a fixed four-channel hook-up (see Paragraph 7.3 for the multiple drop detailed test setup)

6.3.2 FUNCTIONAL MODEL TESTS

a. General. The data relay functional tests were aimed at determining basic relay performance and pointing up overall system integration problems. Multichannel operation, polarization diversity UHF reception and relative high power VHF transmission were modes of operation to be examined for potential system problems. Each of these modes of operation was achieved to varying degrees with satisfactory test results ranging from the qualitative to quantitative.

It should be noted that testing was originally scheduled to coincide with prototype penetrometer development test schedules. Relay receiver channel operation would, therefore, provide required test support to facilitate test operations at the several prototype test site locations. Relay functional testing, however, did not proceed according to plan and ultimately certain of the testing had to give way to test support functions and final multiple drop system testing. Similarly, penetrometer assembly and test problems demanded additional test support which aggravated an already tight schedule.

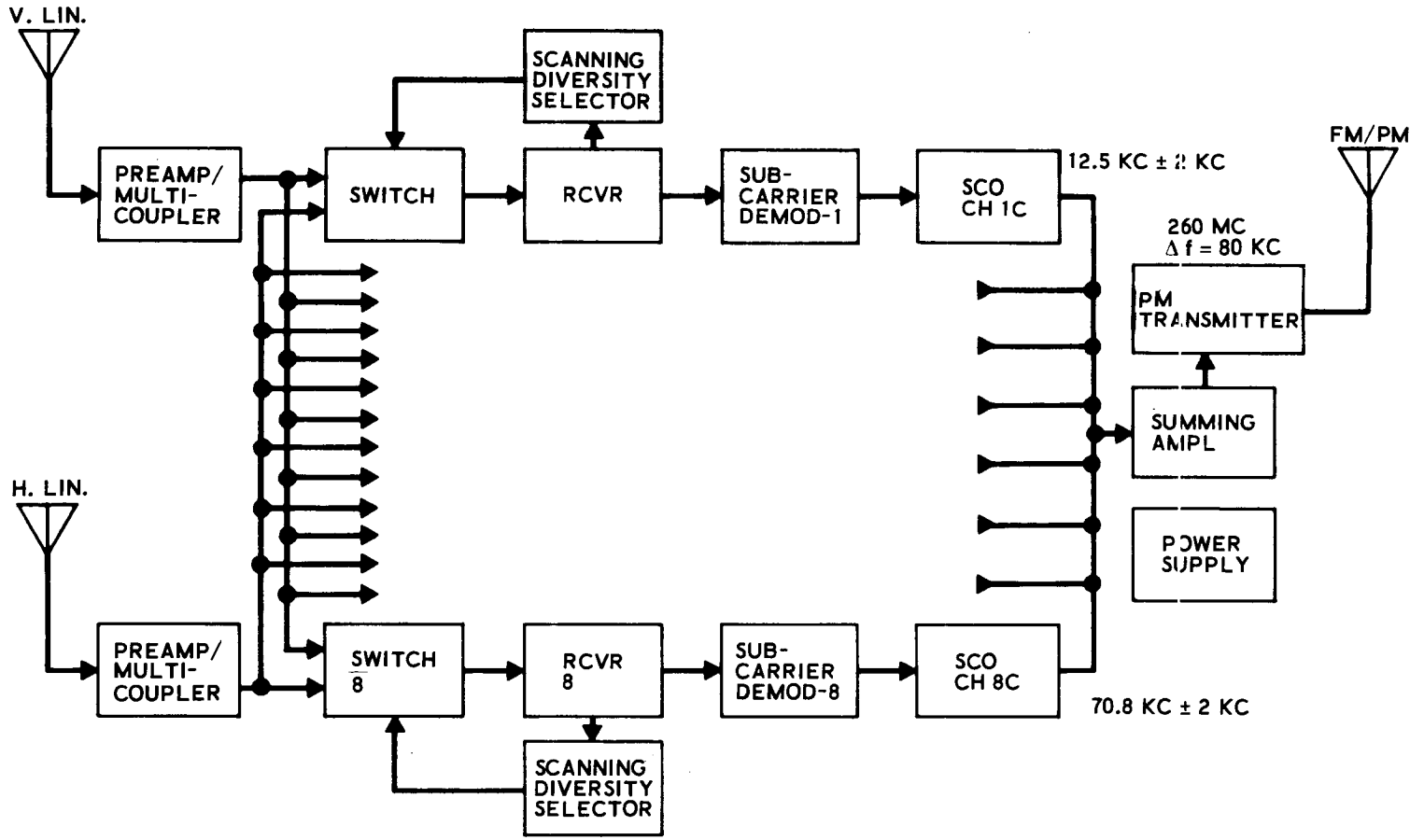

FIGURE 6-25. PENETROMETER DATA RELAY - BLOCK DIAGRAM

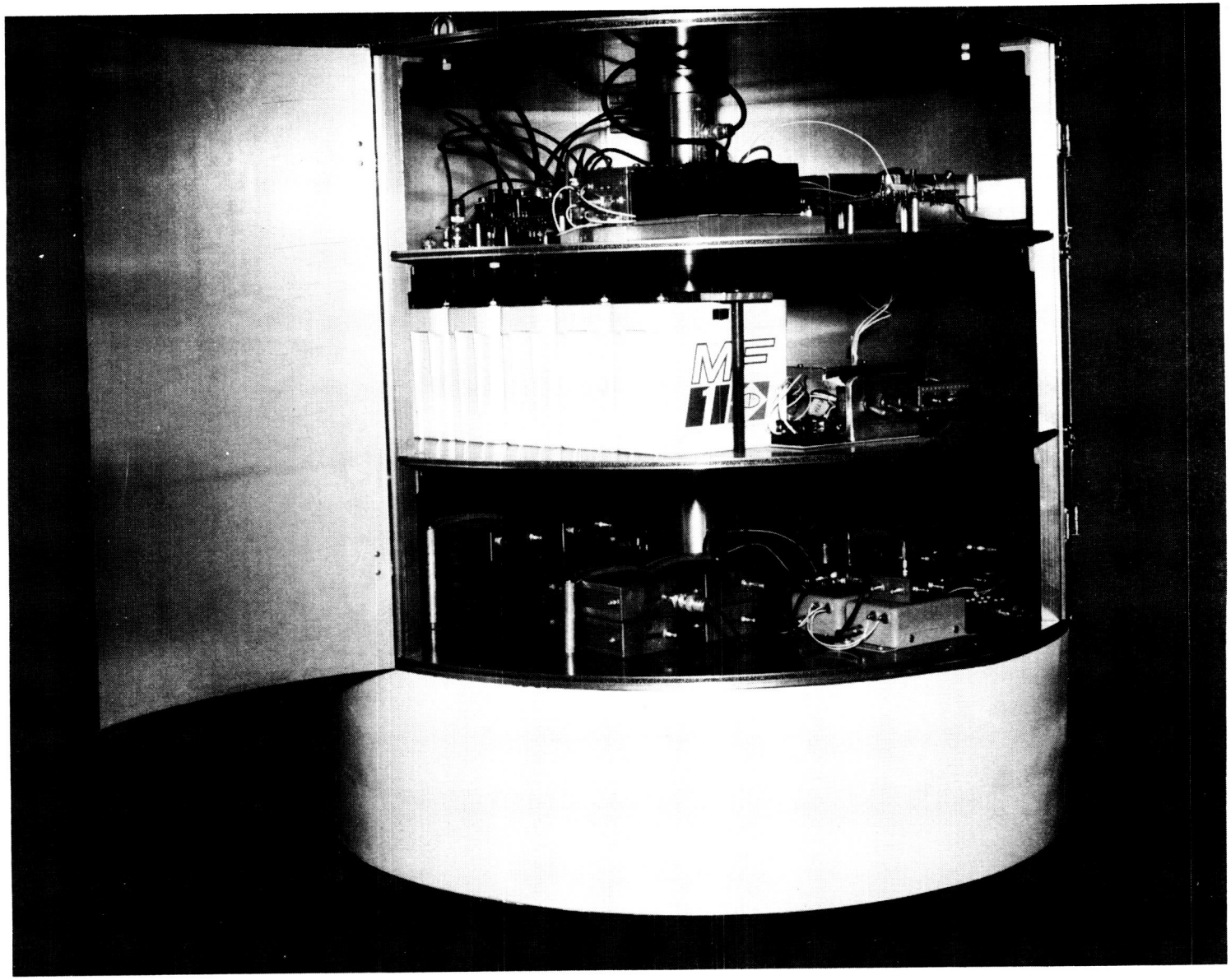

FIGURE 6-26. DATA RELAY FUNCTIONAL TEST MODEL

b. Principal Observations. Before detailing the number of quantitative tests performed on the functional model, it is possible to summarize the more salient observations that were derived from penetrometer system and test support operations. Relay receiving system operation exhibited a susceptibility to overload and internal spur generation. The need for AGC control was identified during early system test support operations when receiver overload occurred in the presence of strong signals. The existence of internal spurs caused by harmonics of the first crystal local oscillator were observed in laboratory tests. Each of these problems were rectified in the establishment of the flight model receiver performance specification.

By virtue of the multiple drop tests, straight-through polarization diversity reception did not point up any obvious rf signal degradation problems. Observations are, however, basically one-shot in nature and further evaluation is required. Operation of the antenna switching diversity circuitry was not optimized prior to discovering the receiver overload problem and no attempt was able to be made thereafter to achieve a measure of system performance.

UHF data acquisition in the presence of relatively high VHF transmitter output power yielded no evidence of degradation. True multichannel relay operation could not be evaluated without placing more emphasis on the build up or availability of multi-signal sources. The multiple drop test yielded some measure of multichannel operation, but even its use constituted a modification of the basic relay configuration. The multiple drop test did, however, successfully demonstrate the functional operation of the overall Lunar penetrometer system.

c. Test Results.

(1) System Integration. Basic system integration tests were performed with major elements of the data acquisition section of the data relay operating together for the first time. Initial qualitative checks of power supply operation were made which demonstrated proper basic operation.

Four data relay rf channels were exercised next. Basic individual receiver channel performance, which included Foster-Seeley discriminator operation was noted to agree with previously established receiver component data. Similar checks of pulse count discriminator operation resulted in intolerable noisy channel operation. The data relay power supply converter switching transient was found to be the major problem. Operation with laboratory regulated power supplies resulted in an improvement, but noisy performance was still evident. Considerable improvement was obtained by adding decoupling capacitors in the pulse count discriminator +10 volt (and -12 volt) supply lines. Still some channel interaction remained which additional decoupling in the power supply was expected to alleviate. It should be noted that the Foster-Seeley discriminator output did not

exhibit this degree of interaction; circuit operation of the pulse count type is apparently more susceptible to power supply variation. Subsequent tests were made with the addition of the data transmission section and no anomalies were noted. Efforts to minimize the switching transient with better packaging and layout of regulator components were made, but went unfinished as schedule limitations prevailed. To facilitate test operations all subsequent performance testing of the relay was conducted with external power.

(2) Single Channel. Single channel operation was established with unmodulated carrier testing, yielding basic sensitivity, dynamic range and spurious response data. Receiver sensitivity for an unmodulated carrier was noted for an output (S + N)/N = 3 db, measured at the IF test point (BW = 700 kc) across a 50 ohm load. A -106 dbm value was noted, giving an apparent noise figure of 7 db. A dynamic range calibration was also obtained, as noted in accompanying system test data Table 6.9. Also shown are the selectivity/spurious response data based upon the above sensitivity criteria with relative sensitivity denoted with respect to the carrier reference level. The internal spur previously reported is evident in the data.

Testing proceeded with use of an FM carrier modulated with a 40 KHz sine wave resulting in the pulse count discriminator and AM detector overall channel characteristic shown in Table 6.10. Figure 6-27 is a plot of the AM detector output versus input peak deviation. The same basic data were taken for channel 6 following its modification for use at 432.4 MHz (spurious data not noted). The data are shown in Tables 6.11 and 6.12, and in Figure 6-28.

AM/FM carrier testing was accomplished in conjunction with prototype penetrometer calibration tests and is shown (with compression) in the electrical calibration plots of the individual prototypes.

(3) Multichannel. The principal multichannel tests involved dual channel single frequency reception in support of individual penetrometer prototype tests; and dual polarization diversity four channel, two frequency reception in support of the multiple drop system test. There was no degradation observed in data channel outputs in the former case for signal reception which included receiver overload protection. The same was true in the latter case. Qualitative two-frequency, cross-talk checks were made in both cases cited with no observed outputs observed in the data channel outputs. As part of the multiple drop pre-run system checkouts, dual channel calibration data were obtained using an FM signal deviated by a 40 KHz subcarrier frequency The data are shown in Figure 6-29. The data in channels AM 1 and AM 2 exhibit more dispersion than the other two which was attributed to increased waveform distortion.

TABLE 6.9

TEST DATA FOR DATA RELAY CHANNEL

1. Individual Carrier Channel 432 MHz LPS CH1

(a) Unmodulated Carrier

(1) Sensitivity. $\frac{S+N}{N}$ = 3 db BW = 700 KHz

	W/rf Preamp
Ref Output Noise Level	-24.0 dbm
Above, +3 db	-21.0
Channel Sensitivity	-106.0 dbm

Remarks: kTB = -116 dbm $\frac{S+N}{N}$ = 3 db Apparent NF = 7 db

(2) Dynamic Range

Input Level (dbm)	Noise	-90	-80	-70	-60	-50	-40	-30
Output Volts SS T.P. (dc)	-1.32	-1.21	-1.11	-1.03	-0.98	-0.92	-0.85	-0.82

Remarks: W/Preamp

(3) Selectivity/Spurious Response

Freq	Sens (dbm)	$\frac{S+N}{N}$ = 3db	Rel Sens (db)
432		-106	0
436		-75	-31
416		-48	-58
426		-35	-71
Others*		-	<-71

*Data Relay Xmt
260.448 MHz

*CSM VHF Freq
Recov Beac 243 MHz

AM Rcvr 259.7 MHz
AM Xmtr 296.8 MHz
NASA R&D 247.3 MHz

TEST SETUP

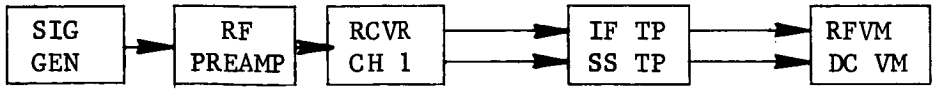

TABLE 6.10

TEST DATA FOR DATA RELAY CHANNEL

1. Individual Carrier Channel, Cont. 432 MHz LPS CHI

(b) FM Carrier - Static AM Subcarrier (40 KHz)

w/o rf Preamp

Input Modulation				(1) Discr Charac		(2) Det Charac
Ref Rcvr (16 KHz/V)		40 KHz AM Subcar		#1 F.S. Discr V_{RMS} Output	#1 P/C Discr V_{RMS} Output	#1 AM Det VDC Output
Vpk	Vrms	% F.S	P-P Dev (KHz)			
10	7.07	100	±160	0.97	1.04	-5.0
9	6.37	90	±144	0.884	0.925	4.41
8	5.65	80	±128	0.79	0.82	3.94
7	4.95	70	±112	0.70	0.72	3.30
6	4.24	60	±96	0.60	0.615	2.93
5	3.53	50	±80	0.505	0.515	2.38
4	2.83	40	±64	0.412	0.416	1.90
3	2.12	30	±48	0.318	0.318	1.43
2	1.41	20	±32	0.216	0.217	0.995
1	0.707	10	±16	0.118	0.122	0.505
0	0	0	0	0.058	0.066	-0.014
15	10.5	150	±240	1.32	1.52	7.2
20	14.1	200	±320	1.58 Distorting	2.06	8.0
0.5	0.35	5	±8	0.076	0.0825	0.270
10.0	7.07	100	±160	0 97	1.04	5.00

(3) Frequency Response

	Ref Level 40 KHz	LOf_{CO} (-3 db)	$Hi f_{CO}$ (-3 db)
F.S. Discr Out	0 db	50 HZ	50-90 KHz
F.S. Discr TP	0 db	0	2400 Hz
P/C Discr Out	0 db	1200 Hz	50 KHz

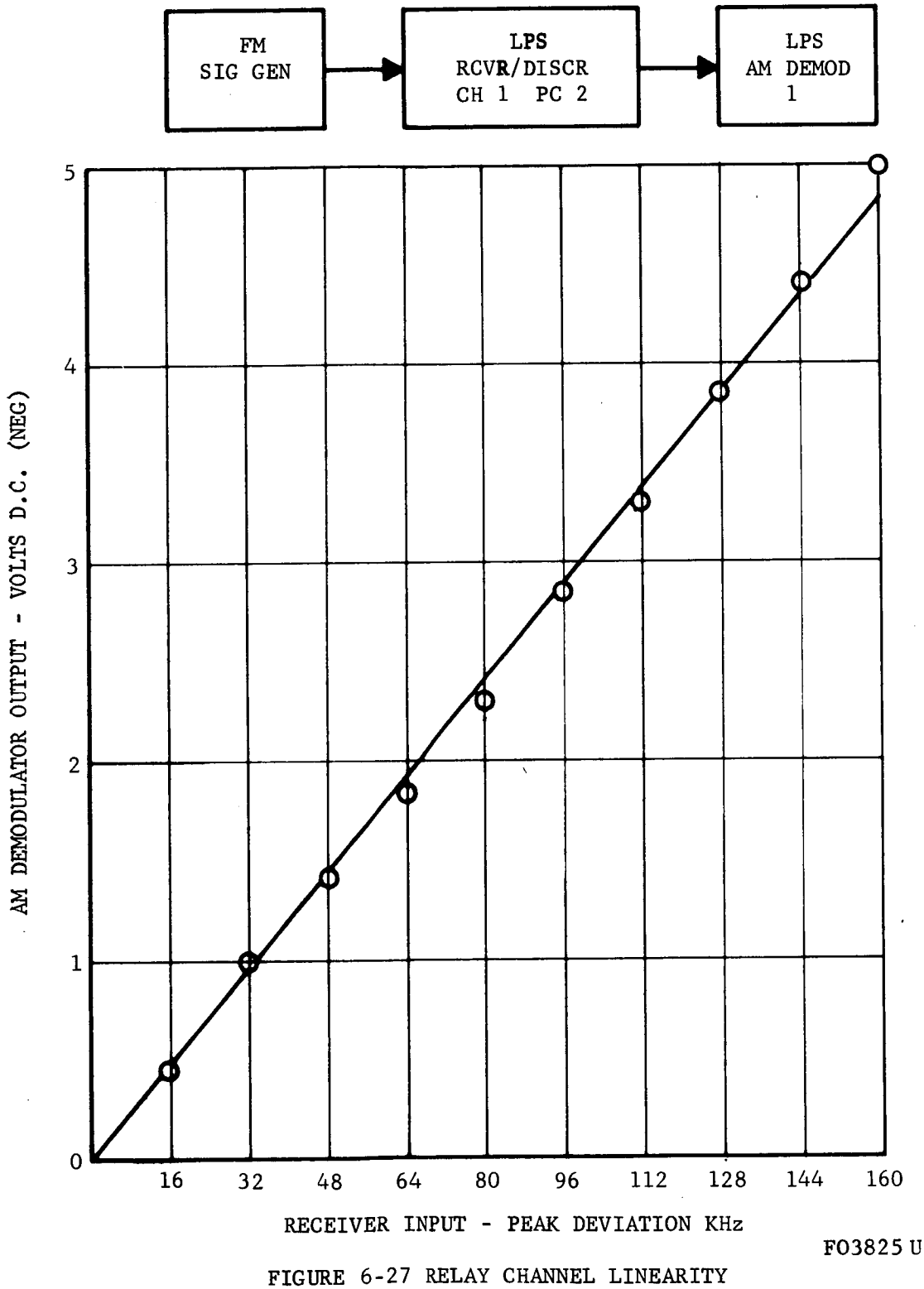

FO3825 U

FIGURE 6-27 RELAY CHANNEL LINEARITY

TABLE 6.11

TEST DATA FOR DATA RELAY CHANNEL

1. Individual Carrier Channel CH 6M 432.4 MHz
LO 372.4 MHz

(a) Unmodulated Carrier

(1) Sensitivity $\frac{S+N}{N}$ = 3 db BW = 700 KHz

	W/Preamp
Ref Output Noise Level	-26.2 dbm
Above +3 db	-23.2
Channel Sensitivity	-103.0 dbm

Remarks: kTB = -116 dbm $\frac{S+N}{N}$ = 3 db Apparent NF = 10 db

(2) Dynamic Range

W/Preamp								
Input Level (dbm)	Noise	-90	-80	-70	-60	-50	-40	-30
Output Volts SS T.P (dc)	-1.31	-1.28	-1.20	-1.08	-1.02	-0.98	-0.94	-0.91
W/O Preamp								
Output Volts SS T.P. (dc)	-1.31	-1.31	-1.31	-1.25	-1.18	-1.07	-1.02	-0.98

TABLE 6.12

TEST DATA FOR DATA RELAY CHANNEL

1. Individual Carrier Channel, Cont. 432.4 MHz CH 6M
LO 372.4 MHz

(b) FM Carrier - Static AM Subcarrier (40 KHz)

W/O Preamp

Input Modulation				(1) Discr Charac		(3) Det Charac
Ref Rcvr (16 KHz/V)		40 KHz AM Subcar		#6 F.S. Discr V_{RMS} Output	#4 P/C Discr V_{RMS} Output	#1 AM Det VDC Output
Vpk	Vrms	% F.S.	P-P Dev (KHz)			
10	7.07	100	±160	1.00	1.05	-5.00
9	6.37	90	±144	0.90	0.94	4.42
8	5.65	80	±128	0.815	0.827	3.85
7	4.95	70	±112	0.718	0.722	3.30
6	4.24	60	±96	0.624	0.624	2.85
5	3.53	50	±80	0.520	0.520	2.30
4	2.83	40	±64	0.420	0.425	1.84
3	2.12	30	±48	0.323	0.325	1.41
2	1.41	20	±32	0.214	0.229	0.955
1	0.707	10	±16	0.109	0.143	0.478
0	0	0	0	0.0158	0.098	-0.0175
15	10.5	150	±240	1.34	1.54	7.4
20	14.1	200	±320	1.64	2.04	7.86
0.5	0.35	5%	±8 kc	0.0538	0.109	0.220

(3) Frequency Response

	Ref Level (40 KHz)	Lo f_{CO} (-3 db)	Hi f_{CO} (-3 db)
6M F.S. Discr Out	0 db	50 Hz	➧ 70 KHz
6M F.S. Discr TP	0 db	0	2.4 KHz
4 P/C Discr Out	-1.4 db	10 Hz	50 KHz

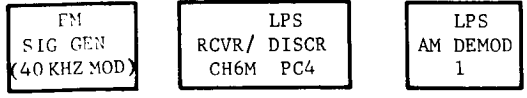

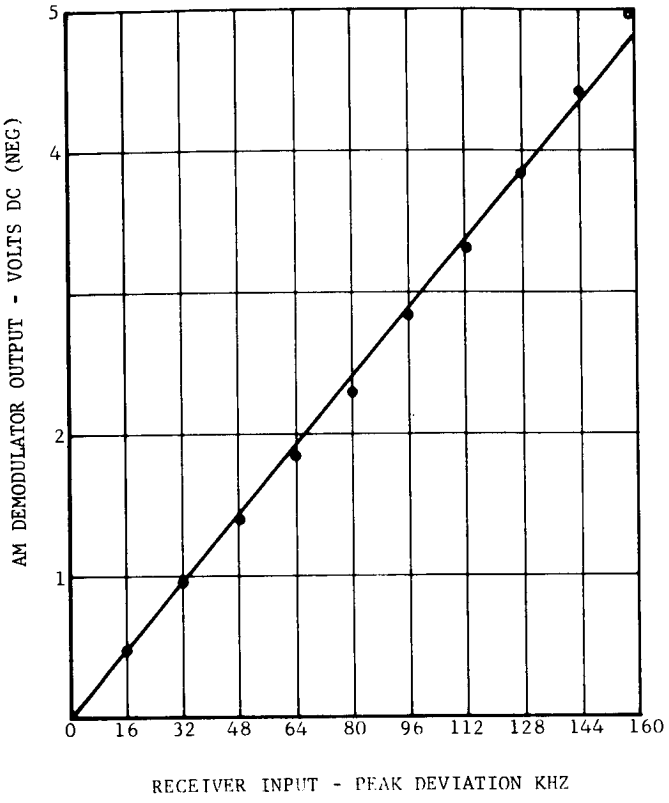

FIGURE 6-28. RELAY CHANNEL LINEARITY, CHANNEL 6

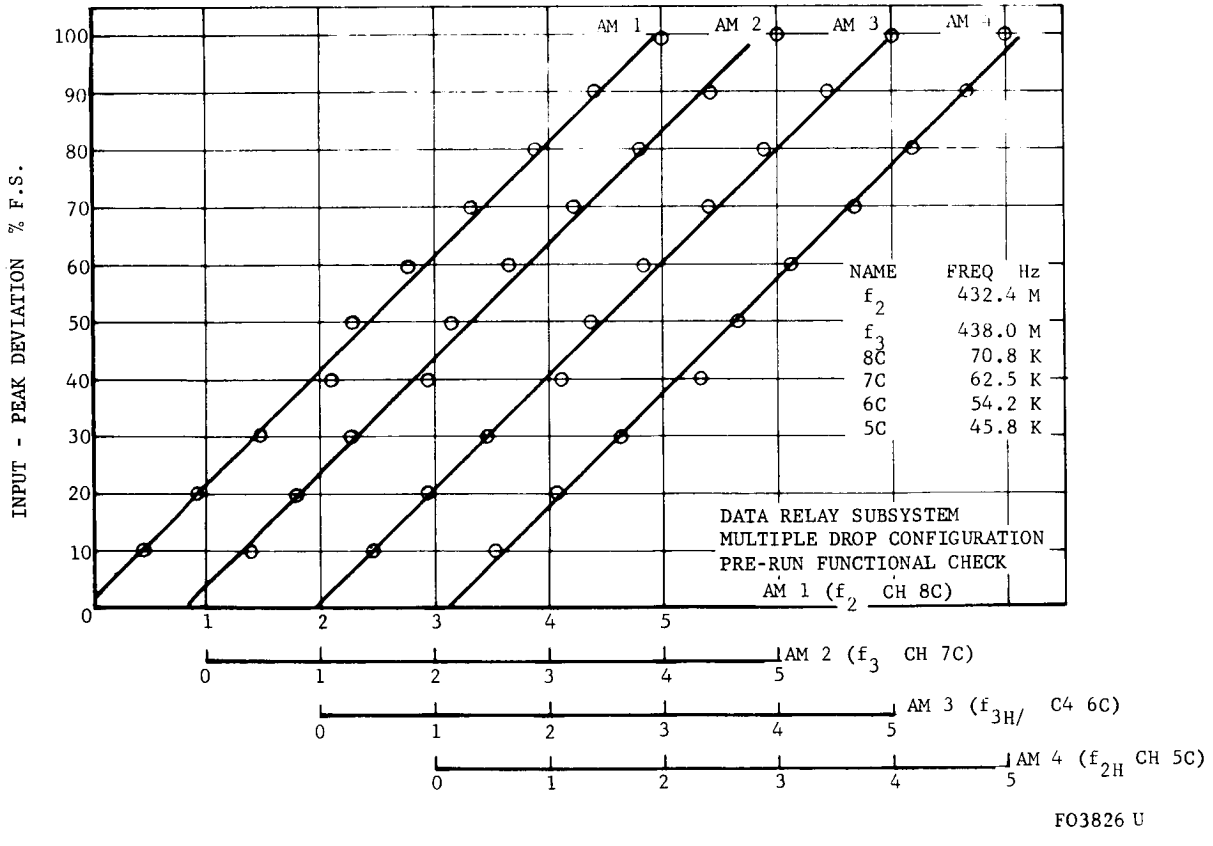

FIGURE 6.29. DATA RELAY CHANNEL FUNCTIONAL TEST

(4) Special Frequency Transient Test. A special test was made with the data relay equipment to investigate the effects of frequency shift transients on resulting output data signals. The purpose was to explore system accuracy when subjected to simulated frequency transients. The test setup is shown below.

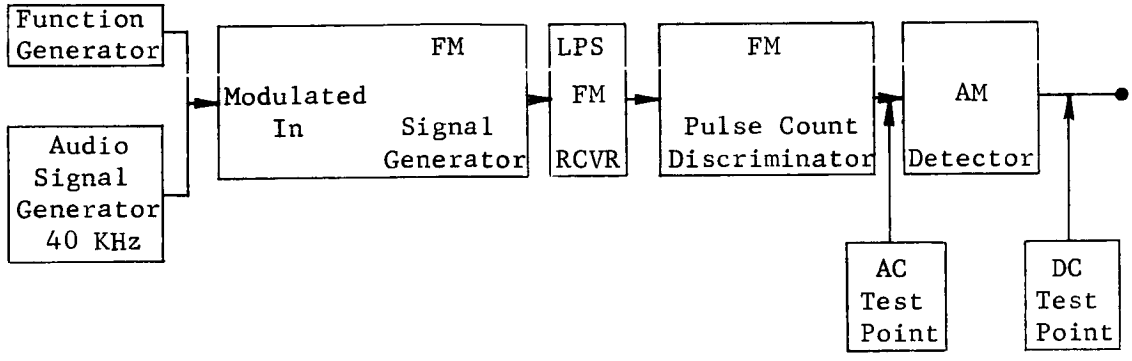

SPECIAL FREQUENCY SHIFT TEST

A basic full-scale signal was applied initially to the LPS receiver/discriminator/detector channel. That is, a nominal ±160 KHz frequency deviation modulated at a 40 kc rate was the applied full scale input. Superimposed on this waveform was an additional frequency ramp. Two magnitudes of added frequency shift transients were employed, i.e., ±160 KHz and ±80 KHz nominal values. Triangular waveforms were used for the simulated frequency transient.

Figure 6-30 illustrates the case where the frequency transient employed was produced by a triangular waveform with a 0.4 millisecond rise time. Photos 1 and 2 of Figure 6-30 correspond to a nominal ±67KHz and ±160 KHz added frequency shift, respectively. A 1200 Hz triangular wave was added to the 40 KHz modulating waveform. One-sided deflections observed in the dc output trace are 2.0 percent and 6.0 percent for the smaller and larger ramps, respectively. Sweep speed is 0.2 ms/cm. The principal observation to be made from the special test results is that the LPS data subcarrier scheme provides an added degree of shock insensitivity which enhances overall system performance.

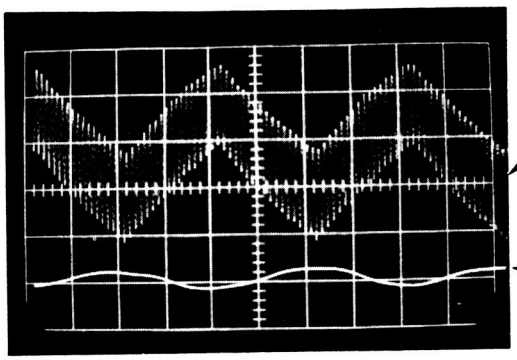

DATA RELATIONSHIP TO CARRIER SHIFT
UPPER TRACE:
±160 KHz DEVIATION WITH
±67 KHz CARRIER SHIFT

LOWER TRACE:
AM DETECTOR OUTPUT,
EQUIV 6% ERROR

1 0.2MS/DIV

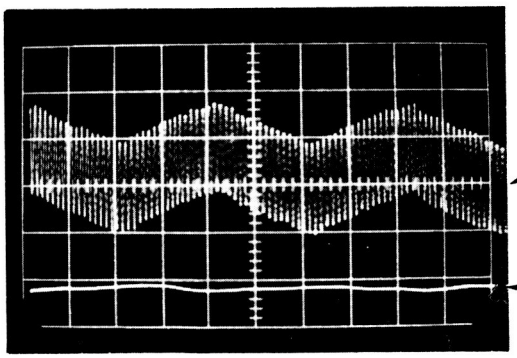

UPPER TRACE:
±160 KHz DEVIATION WITH
±160 KHz CARRIER SHIFT

LOWER TRACE:
AM DETECTOR OUTPUT,
EQUIV 2% ERROR

2 0.2 MS/DIV

FO3756 U

FIGURE 6-30. DATA DEGRADATION VERSUS CARRIER SHIFT

SECTION 7

PENETROMETER PROTOTYPE FUNCTIONAL TESTING

7.1 COMPONENT AND SUBASSEMBLY TESTS

7.1.1 OMNIDIRECTIONAL ACCELEROMETER

a. Acceptance Tests. Accelerometers delivered to Aeronutronic were subjected to a series of tests to verify compliance to the performance specification shown in Table 7.1. The summary of test results appears in Table 7.2. Tests were conducted as described in the following paragraphs.

(1) Open Circuit Sensitivity and Sensitivity Pattern. Tests to determine sensitivity and isotropicity were conducted on a drop tester for levels up to 1500 g and using the golf tee method for levels to 6000 g. A block (see Figure 7-1), capable of positioning the accelerometer in three mutually perpendicular planes, either direction, provided the basic holding fixture for both the drop tester shown in Figure 7-2 and the ball (Figure 7-3) used in the golf tee shot. The output of the omni-accelerometer was compared with the output of a Standard Endevco Model 2225 accelerometer. Instrumentation used during all tests was the standard setup described in Paragraph 4.3.1.

(2) Amplitude Linearity. This information was obtained by comparing the sensitivity values obtained in Paragraph (1) above at the various shock levels. However, due to the lack of hardware that met the isotropic sensitivity criteria, very little work was accomplished in this area. One accelerometer that was tested, SN 50, met the requirements of the linearity specification. However, since this accelerometer was to be installed in Prototype No. 3, the amount of tests were limited to isotropic sensitivity determination and the total range for linearity was not determined.

TABLE 7.1

OMNIDIRECTIONAL ACCELEROMETER PERFORMANCE SPECIFICATIONS

(a) Open Circuit Voltage Sensitivity - 0.60 mv/g min. As a design goal, the sensitivity shall be 0.8 mv/g minimum.

(b) Amplitude Linearity - ±10 percent maximum deviation from sensitivity at 100 g, 1/2 sine, 3 millisecond shock over the range of 20 to 2000 g. As a design goal, the deviation in sensitivity shall be less than ±10 percent to 5000 g and less than ±15 percent to 11,000 g under the same conditions.

(c) Sensitivity Pattern - Deviation from true isotropic sensitivity shall not exceed ±5 percent of the value observed along the axial centerline of the instrument case.

(d) Frequency Response - Sensitivity as a function of 1/2 sine shock period shall not deviate more than ±10 percent from the 100 g, 3 millisecond value over the range of 1 millisecond to 100 milliseconds when used with a load resistance of 10^{12} ohms.

(e) Temperature Coefficient of Sensitivity - Sensitivity shall be within +5/0/-10 percent at $0^{o}/20^{o}/60^{o}C$, respectively.

(f) Case Pressure Sensitivity (Hydrostatic) - 0.01 g/psi maximum as a design goal.

(g) Capacitance - 300 pf min. As a design goal, the capacitance shall be as large as possible without degrading the open circuit voltage sensitivity.

(h) Internal Leakage Resistance - Greater than 2×10^{10} ohms.

TABLE 7.2

SUMMARY OF TEST RESULTS

		Range
1.	Open Circuit Voltage	1.04 - 1.54 mv/g
2.	Amplitude Linearity	5% to 25% (SN 50 was 5%)
3.	Sensitivity Pattern	$\pm$ 7% to $\pm$50% (SN 50 was $\pm$7%)
4.	Frequency Response	Not conducted (see discussion)
5.	Temperature Coefficient of Sens	Not conducted (see discussion)
6.	Case Pressure Sensitivity	Deleted
7.	Capacitance	494 to 789 pf
8.	Inerternal Leakage Resistance	3×10^{10} to 20×10^{10}

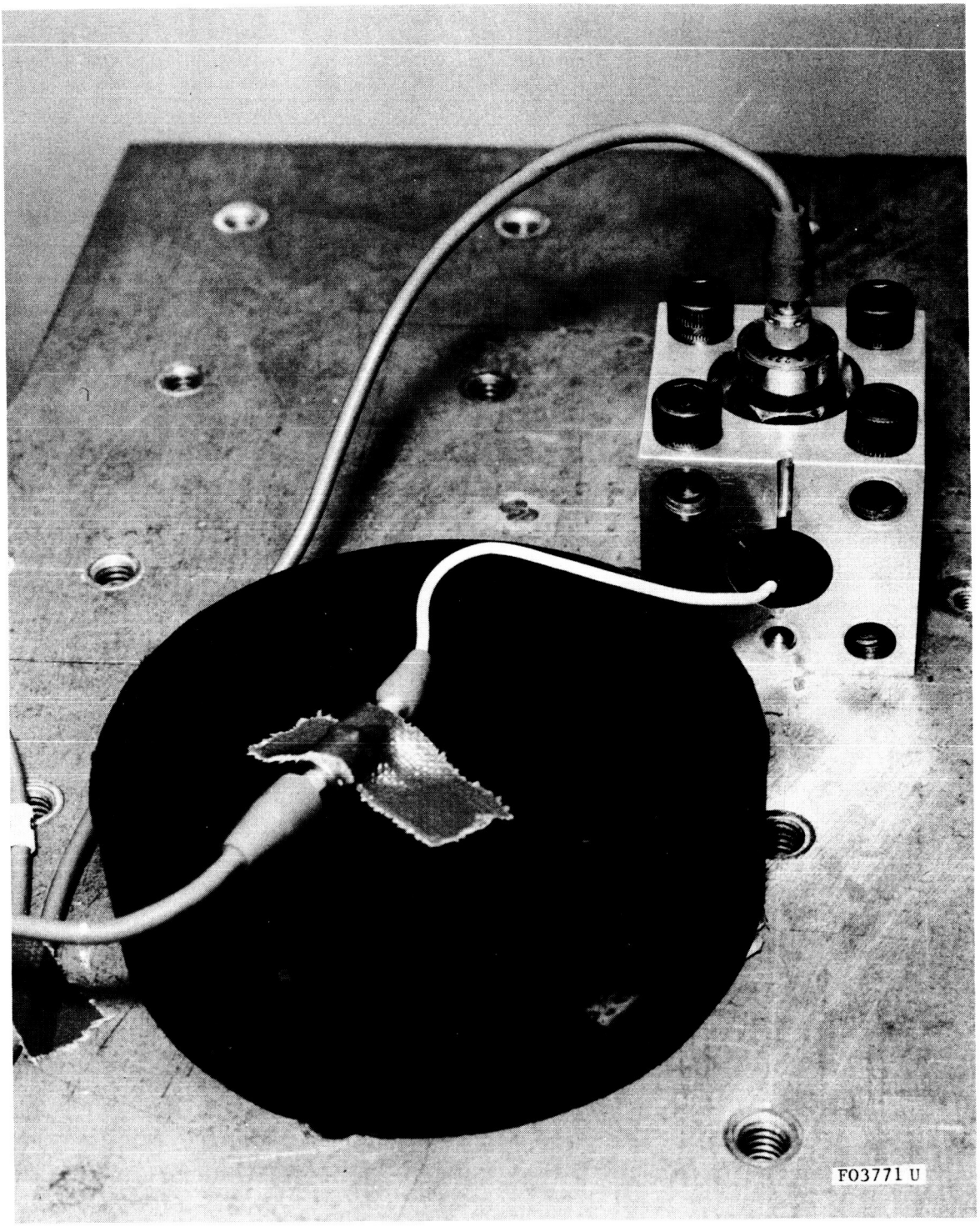

FIGURE 7-1. ACCELEROMETER TEST MOUNTING BLOCK

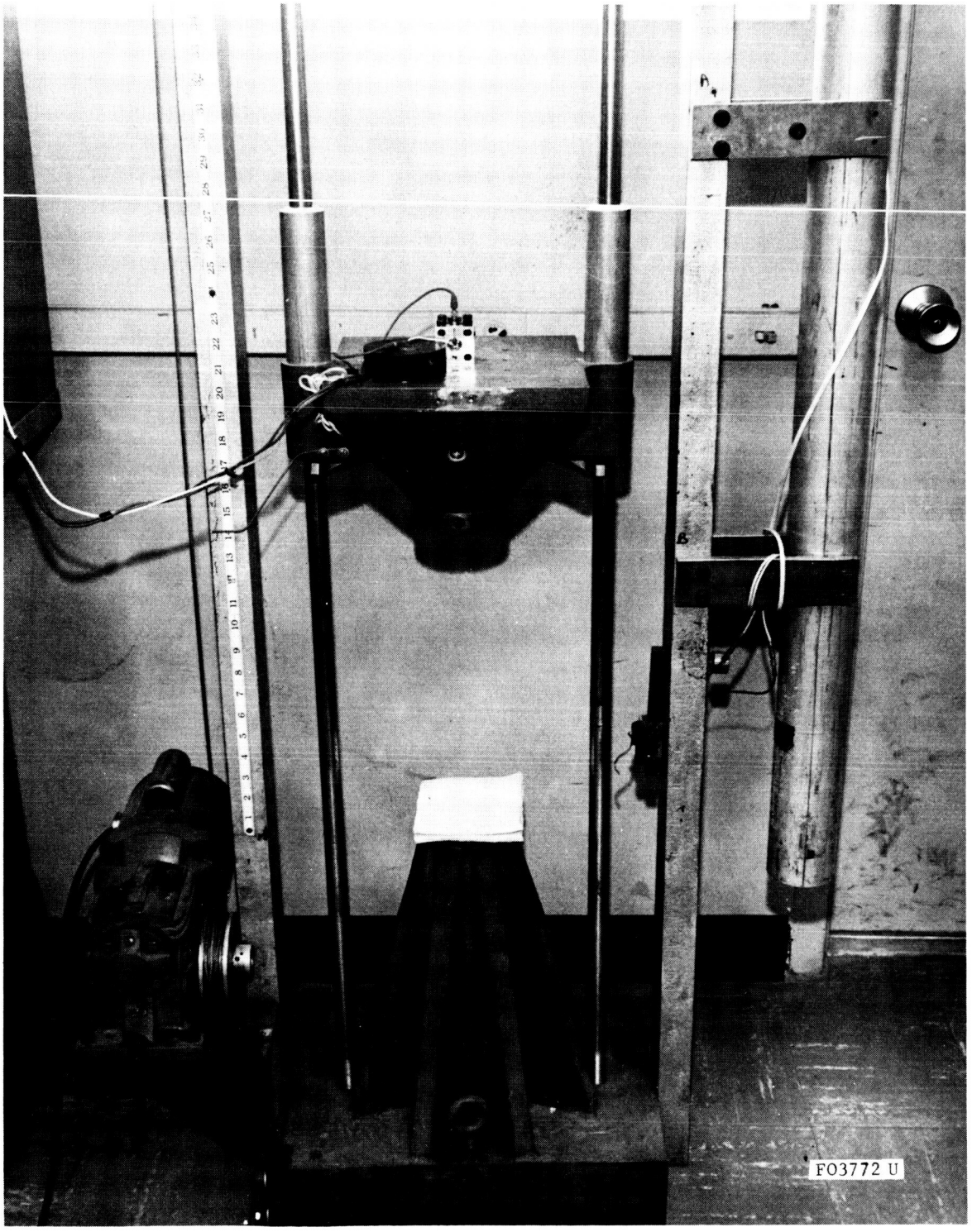

FIGURE 7-2. ACCELEROMETER DROP TESTER

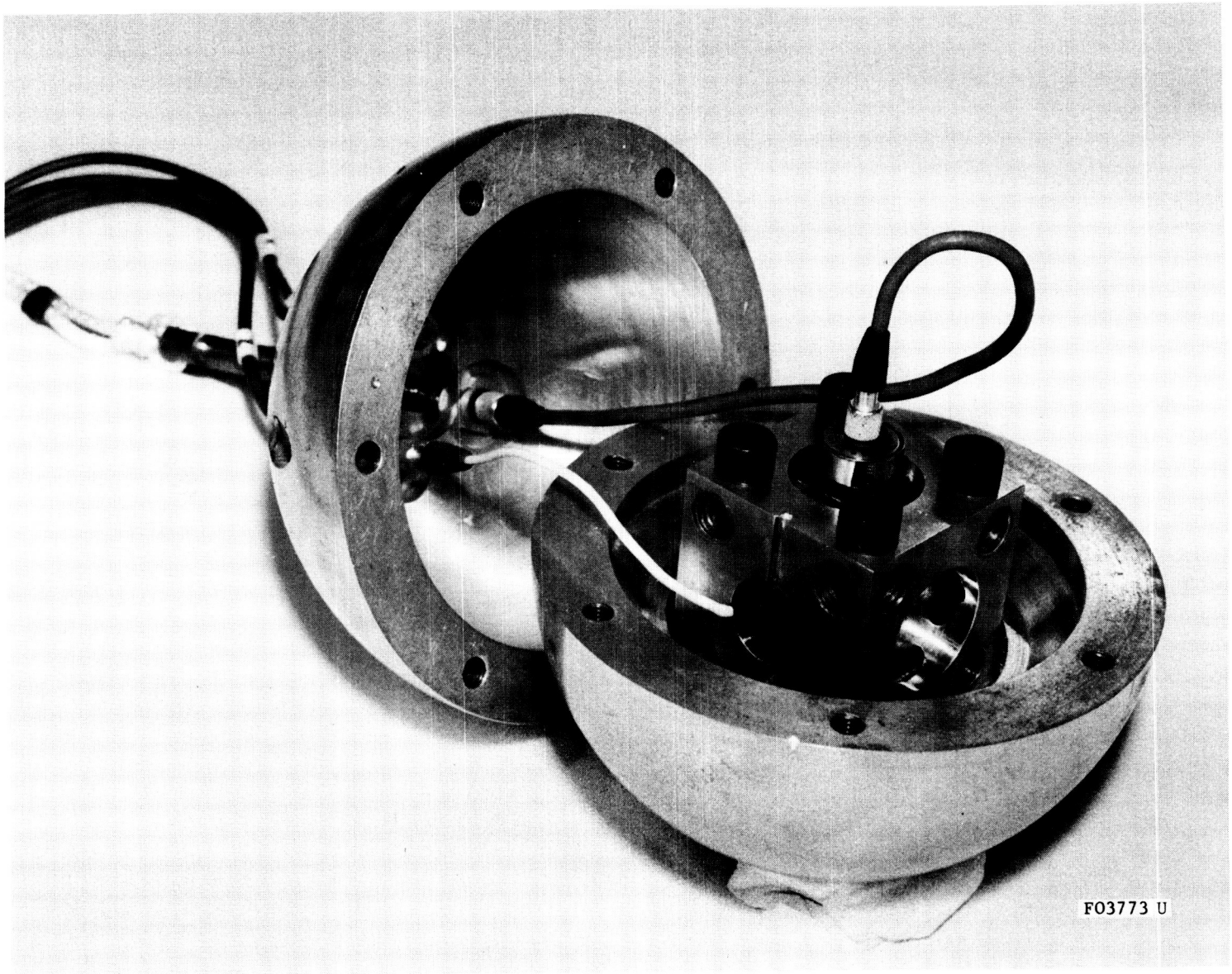

FIGURE 7-3. BALL ENCLOSING ACCELEROMETER AND MOUNTING BLOCK FOR GOLF TEE TEST

(3) Sensitivity Pattern. Deviation from the true isotropic sensitivity was determined from Paragraph (1) above.

(4) Frequency Response. The accelerometer was to be subjected by the vendor to a 1/2 sine, 100 g, 3 millisecond shock pulse. The output would then be compared to 100 g shocks with varying time durations such as 1, 2, 3, 5, 10 milliseconds.

(5) Temperature Coefficient of Sensitivity. Accelerometer output was compared at various temperatures.

(6) Case Pressure Sensitivity. This was deleted when it was decided not to encapsulate the accelerometer in the ball.

(7) Capacitance. Measurement of capacitance was with a Ballantine Capacitance Meter, Model 520.

(8) Internal Leakage Resistance. Measurement of resistance was with a General Radio Megohmeter, Model 1862-B, using 50 volts test voltage.

b. Discussion. The portions denoted "not conducted" are so shown because of lack of both late model hardware and time to conduct those tests. During the development program, some testing occurred to determine the frequency response and temperature characteristics; however, they were on old hardware. The results which were obtained appeared satisfactory and the indications were that no problem exists in these areas. It is obvious from the summary of test results that open circuit sensitivity, capacitance, and internal resistance are well within the requirements. Linearity and the sensitivity pattern criteria remain the problem area. The last accelerometer delivered, SN 50, passed the linearity criteria and was only $\pm$2 percent from meeting the $\pm$5 percent criteria.

7.1.2 SIGNAL ELECTRONICS

The signal electronics modules for both Prototypes No. 2 and 3 were evaluated for performance during impact utilizing the hand-swung hammer. These tests provided a method by which the modules could be tested for intermittent connections or shock-sensitive components prior to assembly and encapsulation within complete penetrometers.

a. Prototype No. 2 Signal Electronics Hammer Tests. The signal electronics module for Prototype No. 2 penetrometer was calibrated for use with SN18 omnidirectional accelerometer and encapsulated within the signal electronics structure. The module had undergone microscopic inspection to detect damaged components, poor solder joints, and printed circuit wiring defects.

The module consisted of two circular interconnected printed circuit boards expoxied into a semihemispherical housing. The space between the two printed circuit boards is devoid of encapsulant to prevent external shock loading from being transmitted through the components. A photograph of this module is shown in Figure 7-4. The encapsulated module was hammer-tested at from 5000 to 7000 g at up to 0.250 millisecond duration. An equivalent 50 g signal was supplied to the calibration input and the 40 KHz output was connected to a 40 KHz AM demodulator. A typical test record is shown in Figure 7-5. Transient variations in the output level did not exceed 1 percent of the applied shock level and the unit was acceptable for prototype use.

b. Prototype No. 3 Signal Electronics. The circuit configuration of Prototype No. 3 signal electronics was essentially the same as that in Prototype No. 2 with the exception of the location of the external calibration test point and various selected components required for accelerometer matching. The calibration test point on Prototype No. 3 signal electronics has been changed back to the original location. This is at the input of the 2 KHz filter following the resistive attenuator. This provides ac calibration only but should eliminate difficulties encountered in Prototype No. 2 with calibration points at the gate and drain of the second MOS-FET differential amplifier. The problems associated with previous attempts at dc calibration include:

(1) External dc calibration at the gate of the second MOS-FET differential amplifier at a 9-megohm impedance level caused very large extraneous shock-induced transients probably due to cable noise.

(2) Locating the external dc calibration at the drain of the same MOS-FET restricted dynamic range calibration to about 75 percent of full scale and made the circuit vulnerable to damage by improper external connection.

Hammer test results of the Prototype No. 3 signal electronics module are shown in Figure 7-6. In all tests, the 40 KHz chopped output was monitored directly instead of monitoring the AM demodulator output as was done in Prototype No. 2 testing. This was done to better evaluate short-time duration transient effects which would be filtered by the 40 KHz AM demodulator.

Figure 7-6a shows the 40 KHz transient output with the accelerometer terminals shorted. The transient is about 60 millivolts peak-to-peak for a 1000 g impact and represents a circuit-induced error of less than 0.1 percent.

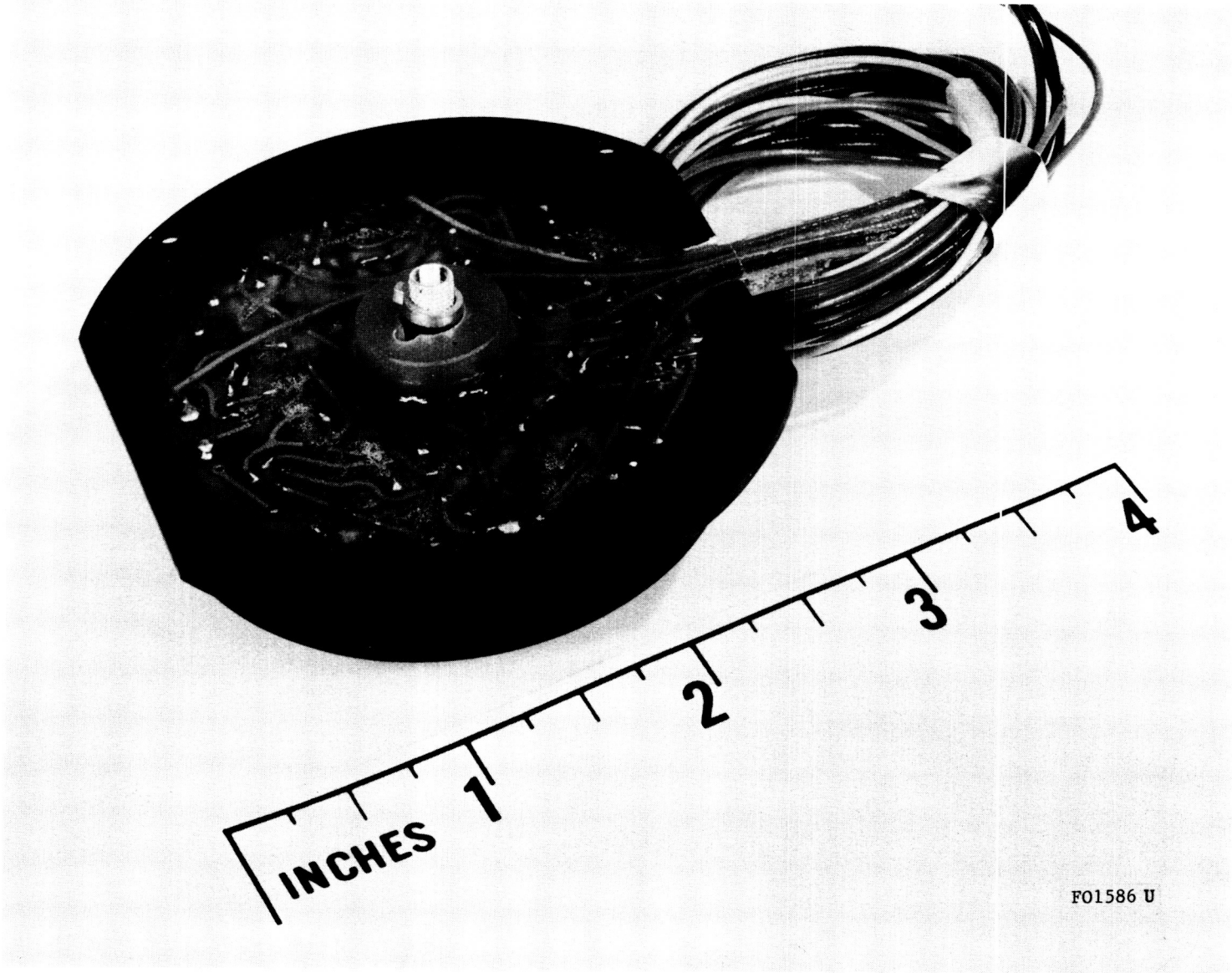

FIGURE 7-4. SIGNAL ELECTRONICS MODULE FOR NO. 2 PROTOTYPE PENETROMETER

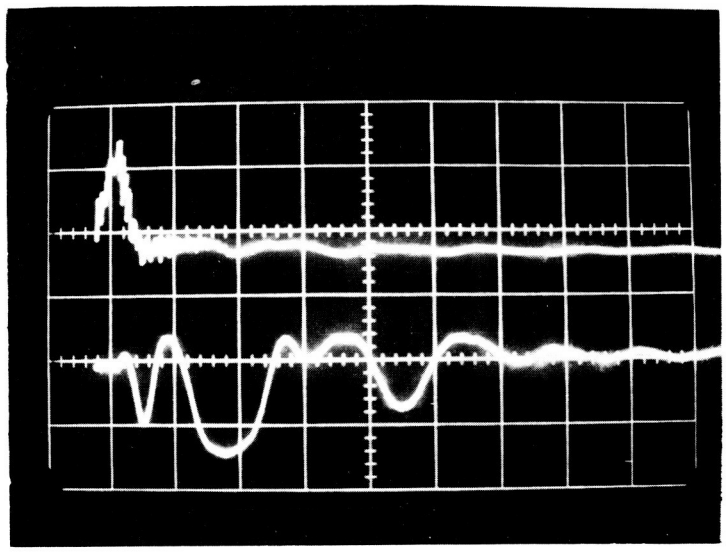

UPPER TRACE: SHOCK PULSE, 2000 g/DIV

LOWER TRACE: DEMODULATED OUTPUT SIGNAL, EQUIVALENT TO 12 g/DIV

TIME SCALE: 200 μSEC/ DIV

FIGURE 7-5. FREQUENCY TRANSIENT TEST RESULTS FOR SQUARE WAVEFORM, PROTOTYPE NO. 2

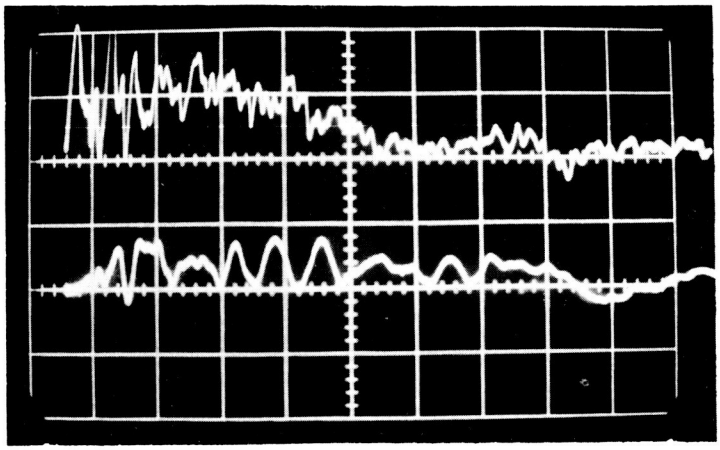

a. POLAR AXIS

SHOCK PULSE: 5000 g/DIV

FREQUENCY DEVIATION: 8 KHZ/DIV
AT 110 MHZ
TIME SCALE: 100 μ SEC/DIV

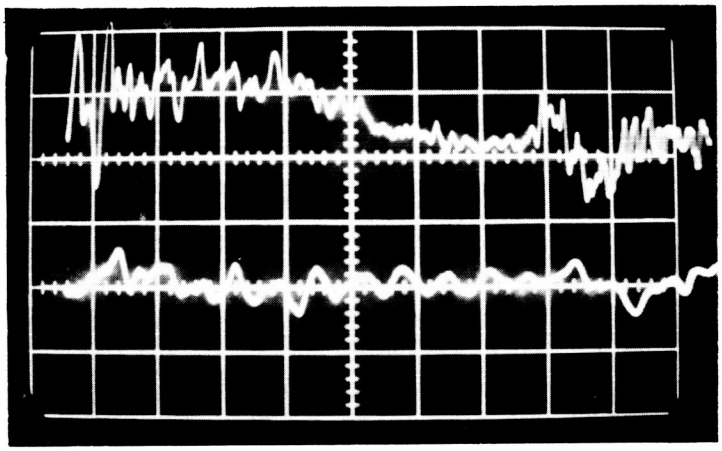

b. POLAR AXIS

SHOCK PULSE: 5000 g/DIV

FREQUENCY DEVIATION: 8 KHZ/DIV
AT 110 MHZ
TIME SCALE: 100 μ SEC/DIV

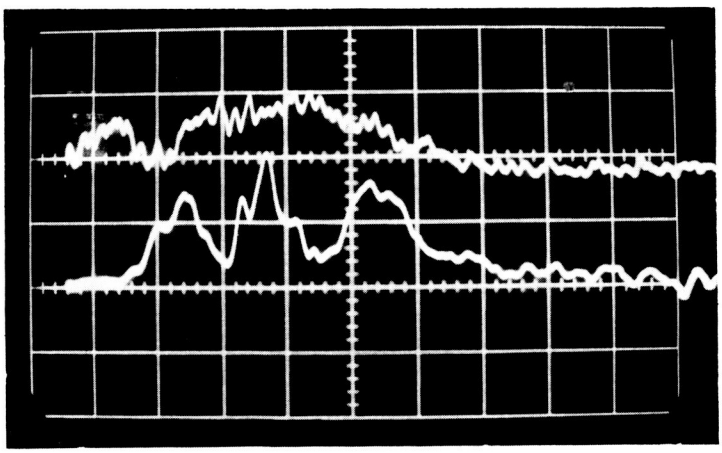

c. EQUATORIAL PLANE

SHOCK PULSE: 5000 g/DIV

FREQUENCY DEVIATION: 8 KHZ/DIV
AT 110 MHZ
TIME SCALE: 100 μ SEC/DIV

FIGURE 7-8. OSCILLATOR SHOCK TEST RECORDS

Figure 7-6b shows the 40 KHz transient with the signal electronics input open-circuited with no shunt capacitance. The transient contributes about 1 percent error for a 900 g shock. Figure 7-6c shows the effect of added capacity on the input as provided by the accelerometer (560 pf). The signal electronics transient output is negligible during a 4000 g impact with some transient effect noted following the acceleration pulse. This represents only 300 millivolts peak-to-peak at 4000 g which is less than 2 percent error.

Following hammer test acceptance of this signal electronics module, the module was diverted to Prototype No. 2 refurbishment to replace a signal electronics module damaged by improper connection to the external dc calibration point during umbilical plug rework.

A third signal electronics module was fabricated and hammer-tested for Prototype No. 3 penetrometer. Hammer-test results are shown in Figure 7-7. These test results were very similar to those obtained from previous module testing. Error due to component sensitivity during an 8000 g shock was about 130 millivolt peak-to-peak, corresponding to about 150 g or 1.9 percent.

7.1.3 TRANSMITTER PROTOTYPE TESTS

The final transmitter used in Prototype No. 2 was hammer-tested as a complete unit. Test results are shown in Figure 7-8.

Figure 7-8a and b show the frequency transients as the oscillator module was impacted in the polar axis at approximately 10,000 g. Maximum frequency excursion is about 6 KHz at 110 MHz or 24 KHz at the 440 MHz output frequency. Similar data for an impact in the equatorial plane are shown in Figure 7-8c. Maximum frequency shift during impact is about 16 KHz at 110 MHz or 64 KHz at the 440 MHz output frequency. During preliminary hammer tests of the oscillator alone, it was noted that both the shape and magnitude of the frequency excursion trace was dependent upon the method of attachment to the hammer head. It was noted during removal of the complete transmitter module from the hammer fixture that the module could move slightly in the equatorial plane.

Figure 7-9 shows the hammer shock test results for the output stages of the transmitter. The amplitude of the 432 MHz output was monitored during an equatorial impact. The record shows less than a 1 db change in output during the 10,000 g shock.

Oscillator-buffer and doubler modules were constructed for Prototype No. 3. This transmitter is similar in design to Prototype No. 2 except for small bosses provided in the oscillator compartment to allow drive pin cover attachment. Hammer tests were conducted on the complete transmitter module consisting of the oscillator-buffer and doubler modules.

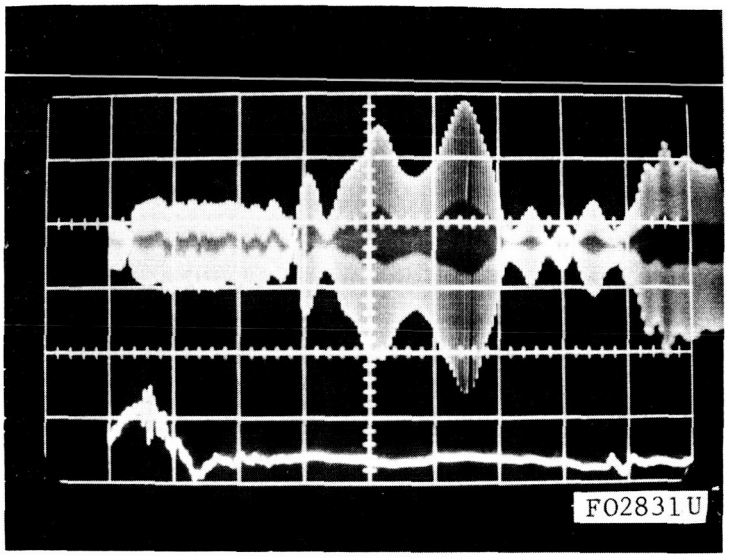

UPPER TRACE:
SIGNAL ELECTRONICS OUTPUT
AT 100 MC/CM
LOWER TRACE:
ACCELEROMETER OUTPUT
AT 5000 G/CM
TIME SCALE: 500 μS/CM

FIGURE 7-7. PROTOTYPE NO. 3 SIGNAL ELECTRONICS HAMMER TEST RESULTS

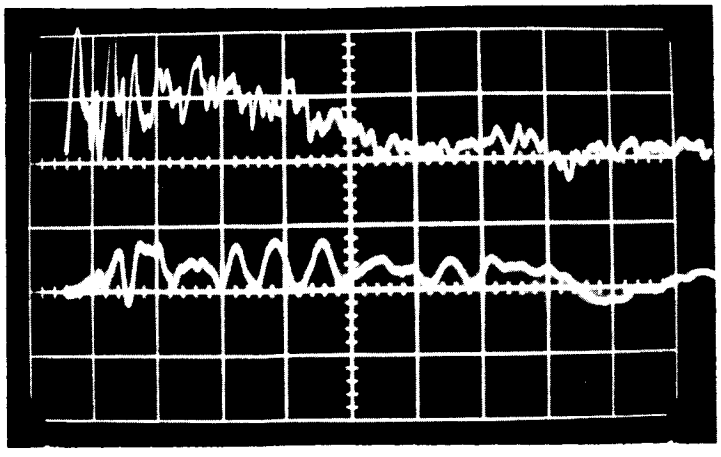

a. POLAR AXIS

SHOCK PULSE: 5000 g/DIV

FREQUENCY DEVIATION: 8 KHZ/DIV AT 110 MHZ

TIME SCALE: 100 μ SEC/DIV

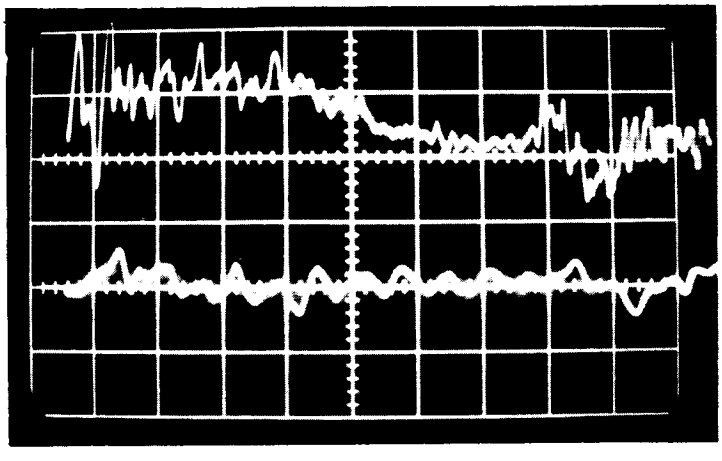

b. POLAR AXIS

SHOCK PULSE: 5000 g/DIV

FREQUENCY DEVIATION: 8 KHZ/DIV AT 110 MHZ

TIME SCALE: 100 μ SEC/DIV

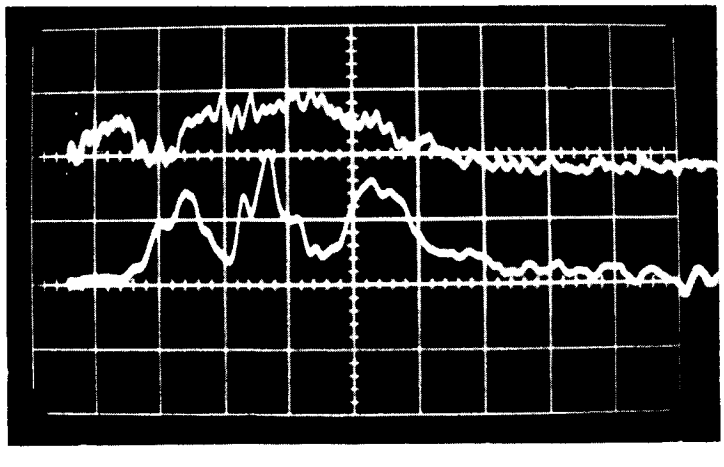

c. EQUATORIAL PLANE

SHOCK PULSE: 5000 g/DIV

FREQUENCY DEVIATION: 8 KHZ/DIV AT 110 MHZ

TIME SCALE: 100 μ SEC/DIV

FIGURE 7-8. OSCILLATOR SHOCK TEST RECORDS

Initial hammer tests indicated a 12 KHz (at 112 MHz) frequency excursion due to a 10,000 g impact in the polar plane. The excursion was greater in the equatorial plane, approaching 30 KHz. During subsequent tapping with a ballpeen hammer, two glass capacitors were broken. These were replaced and the module was again impacted. One of the capacitors, a collector supply bypass, used only during hammer testing to minimize cable noise, had been mounted across the oscillator-doubler module interface which had flexed during impact. A more stable mounting location was found for the replacement.

The other capacitor which had cracked was a base bypass and was mounted directly to the oscillator cavity side wall. Figure 7-10 shows the results of final hammer tests on the transmitter module. The frequency stability is much better in the polar plane than in the equatorial plane, as was the case in Prototype No. 2 transmitter. Polar plane transient frequency shifts are on the order of 8 KHz compared to 25 KHz in the equatorial plane. This may be the result of less rigid coil mounting provisions equatorially since static squeeze tests do not indicate greater sensitivity to structural deflection. The doubler amplitude stability was monitored during an impact and exhibited less than 1 db amplitude variation.

To determine long-term and short-term frequency stability as a function of temperature, a temperature run was made allowing the chassis to stabilize at approximately every $10^{o}F$ through a range from 30 to $120^{o}F$. At each selected temperature, the oscillator was turned on for 40 seconds and frequency was measured at 2 second intervals. Figure 7-11 shows results at three typical temperatures. Figure 7-12 shows frequency stability as a function of temperature as well as short term drift at various temperatures. Figure 7-13 is a plot of modulation sensitivity and power output as a function of temperature. During various temperature tests, the output frequency spectrum was monitored (Figure 7-14). The results of this test indicate very excellent spectral stability over anticipated penetrometer thermal range.

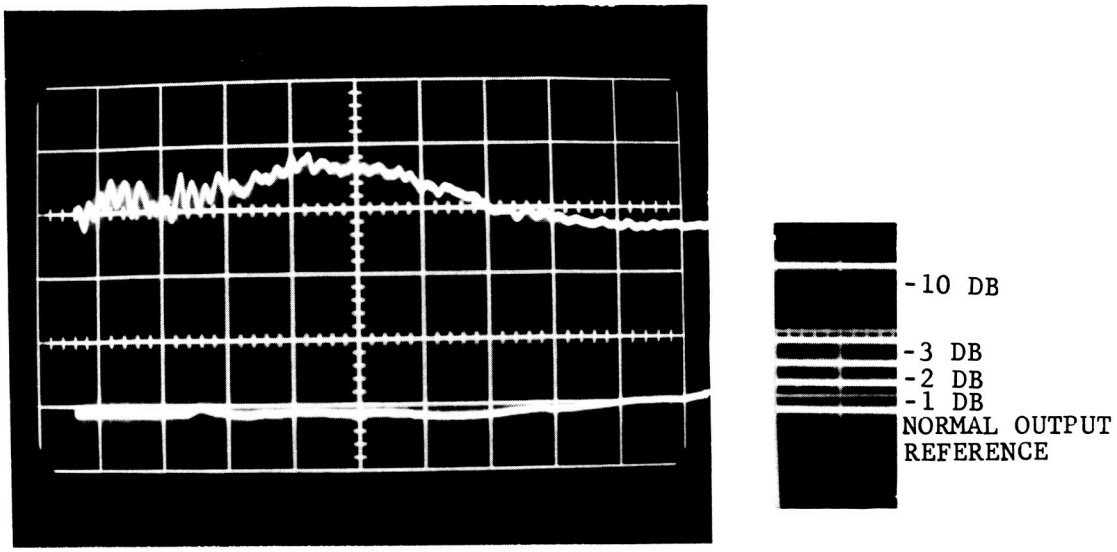

UPPER TRACE: SHOCK PULSE, 10,000 g/DIV

LOWER TRACE: TRANSMITTER OUTPUT AMPLITUDE,
432 MHZ INTO 50 OHMS,
CALIBRATION AS SHOWN

TIME SCALE: 100 μSEC/DIV

FIGURE 7-9. SHOCK TEST RECORD FOR TRANSMITTER OUTPUT

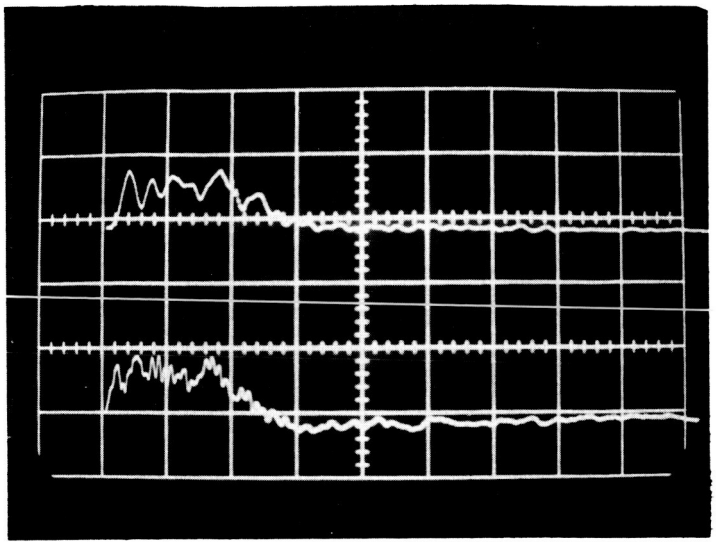

A. POLAR AXIS TEST

UPPER TRACE: FREQUENCY SHIFT, 8 KHz/DIV

LOWER TRACE: ACCELERATION, 5000 g/DIV

TIME SCALE: 200 μ SEC/DIV

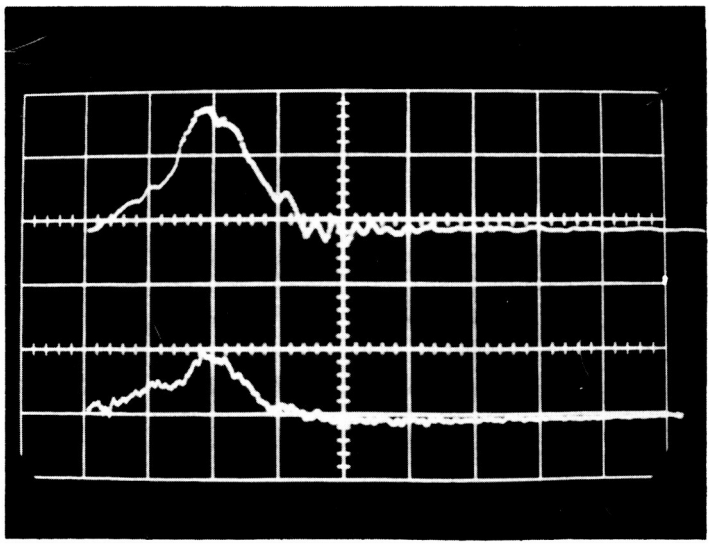

B. EQUATORIAL PLANE TEST

UPPER TRACE: FREQUENCY SHIFT, 16 KHz/DIV

LOWER TRACE: ACCELERATION, 5000 g/DIV

TIME SCALE: 200 μ SEC/DIV

F02190 U

FIGURE 7-10. PROTOTYPE NO. 3 TRANSMITTER HAMMER TEST RECORDS

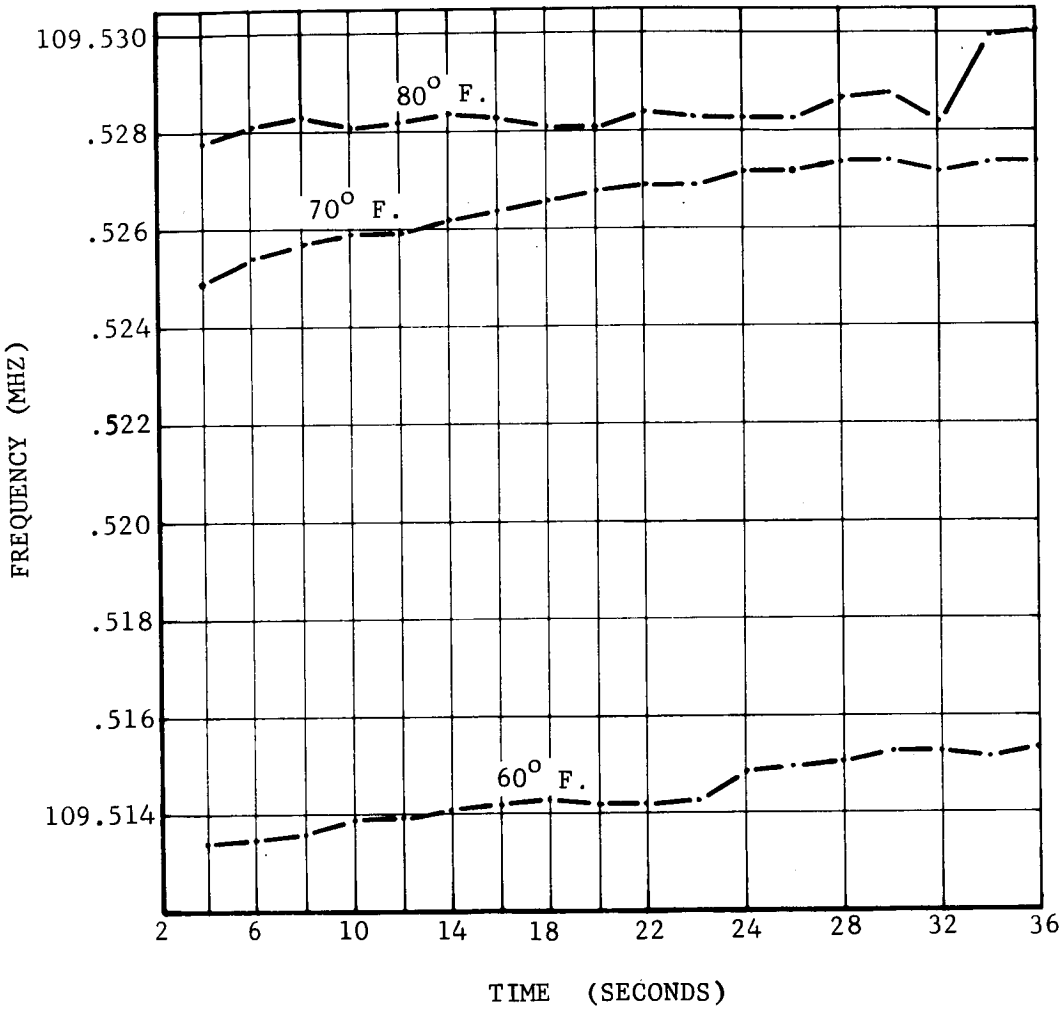

FO3774 U

FIGURE 7-11 SHORT TERM FREQ. SHIFT VS TIME AT VARIOUS TEMPERATURE

NOTE: TRANSMITTER FREQUENCY FOR 40-SECOND INTERVALS FOLLOWING TURN-ON AND THERMAL STABILIZATION AT VARIOUS TEMPERATURES

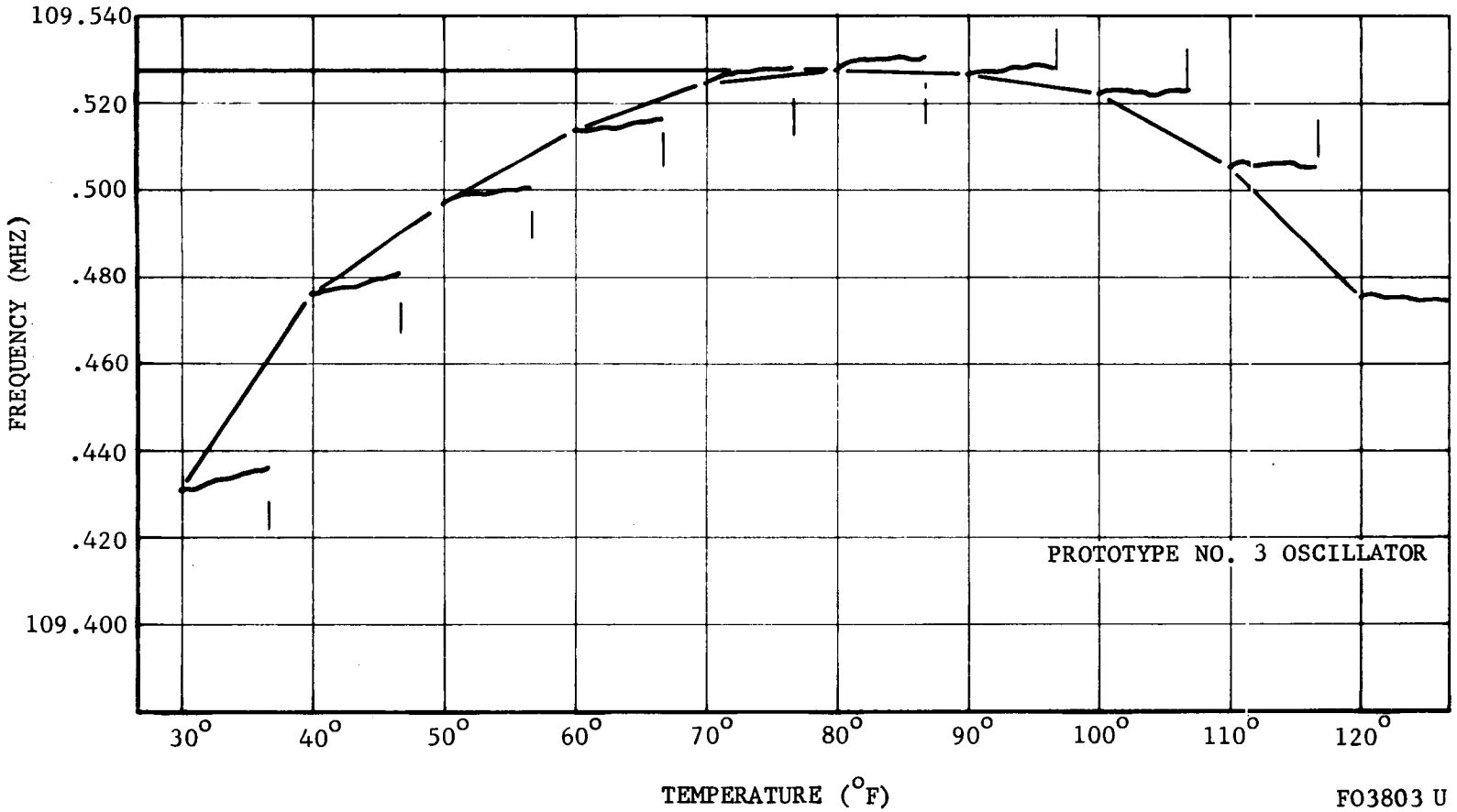

FIGURE 7-12. TRANSMITTER TURN-ON CHARACTERISTIC

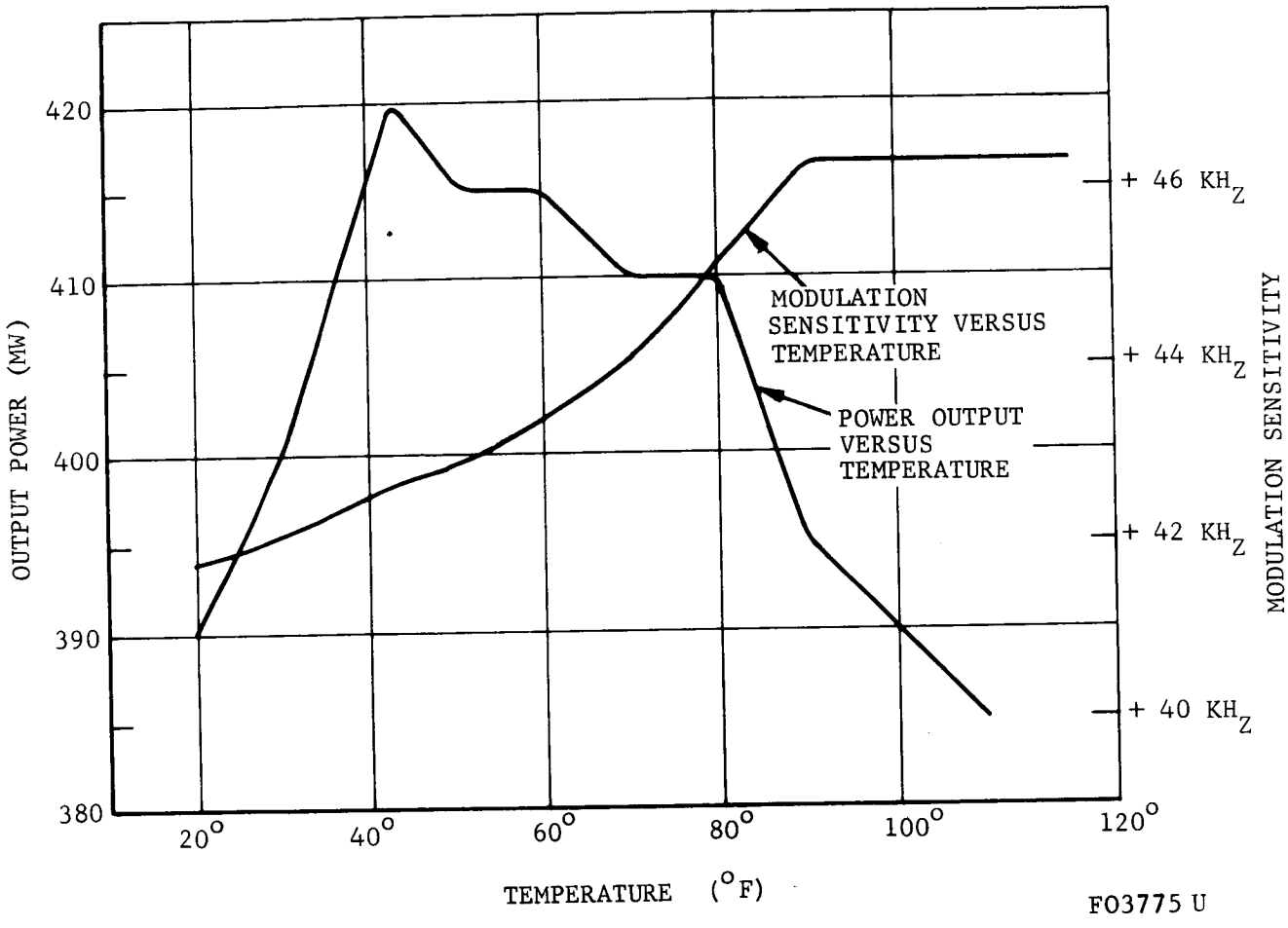

FIGURE 7-13. MODULATION SENSITIVITY AND POWER OUTPUT VERSUS TEMPERATURE

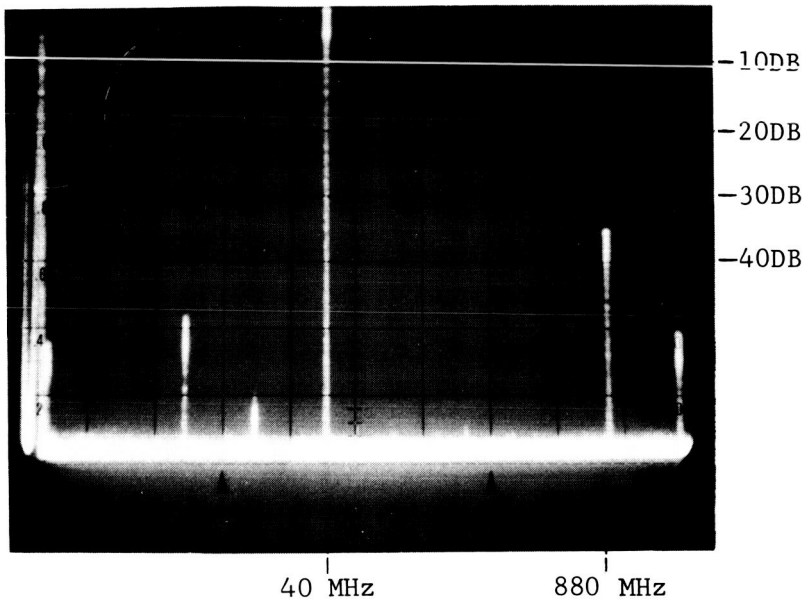

VERTICAL DISPLAY ON LOG SCALE
SWEEP TIME 3MS/CM
SPECTRUM WIDTH 100 MHz
CARRIER OUTPUT 500 MW.

FO3788 U

FIGURE 7-14. TRANSMITTER OUPUT FREQUENCY SPECTRUM

7.1.4 CRYSTAL OSCILLATOR INVESTIGATION

Three crystal oscillators were constructed using two crystals from Harry Diamond Laboratories (HDL) and one from JPL. Oscillators No. 1 and No. 2, with HDL crystals, operate at a frequency of 50 Mc, and Oscillator No. 3, with the JPL crystal, at 40 Mc. These units were built in a steel housing suitable for both hammer testing and Hyge testing. A photograph of two of the units is shown in Figure 7-15. The schematic is shown in Figure 7-16.

a. Oscillator No. 1. This oscillator was first constructed without using either varicap modulation or a variable tuning element. This made the selection of the tank capacity extremely critical and difficult due to the sharp series resonance of the crystal in the feedback loop. The capacitance of the crystal holder was resonated by a small inductance across the crystal. This oscillator was extremely sensitive to supply voltage change; the tendency was for the oscillator to free-run out of crystal control. This was due in part to the fact that this crystal has a comparatively high series impedance at resonance on the order of 60 ohms. A series of hammer tests were performed on this oscillator (see Figure 7-17). The basic frequency of the oscillator remained stable with changes of less than 2 KHz after impact. However, four times during the series of seven impacts, the oscillator shifted out of crystal control, requiring a slight adjustment of the supply voltage to again lock in. During impact, a series of short-duration (20 μsec), high-magnitude pulses were noted in the discriminator output. These pulses represent a shift in carrier frequency on the order of 40 KHz.

From this series of tests, a decision was made to modify this oscillator so it would have modulation capabilities and also a variable tuning element in the form of a varicap. After modification, the unit was again hammer-tested. During impact, the crystal shifted frequency beyond oscillator control and the oscillator would not function properly. It was necessary to discontinue further testing on this unit as the crystal apparently fractured. No photo is available for this second test due to poor selection of oscilloscope scale factor.

b. Oscillator No. 2. During assembly of Unit 2, one lead pulled out of the crystal. The crystal housing was opened and a new lead soldered to the proper contact point on the crystal mount. During this operation, it was noted that during assembly of this crystal, the original lead had not been properly soldered. Assembly of Oscillator No. 2 was continued and, upon completion, the unit appeared to perform properly in a manner similar to Oscillator No. 1.

An attempt to hammer-test Unit No. 2 was made. On the first impact, the oscillator shifted more than 80 KHz out of crystal control and, like Unit No. 1, would no longer lock on to the crystal. No photos are available on

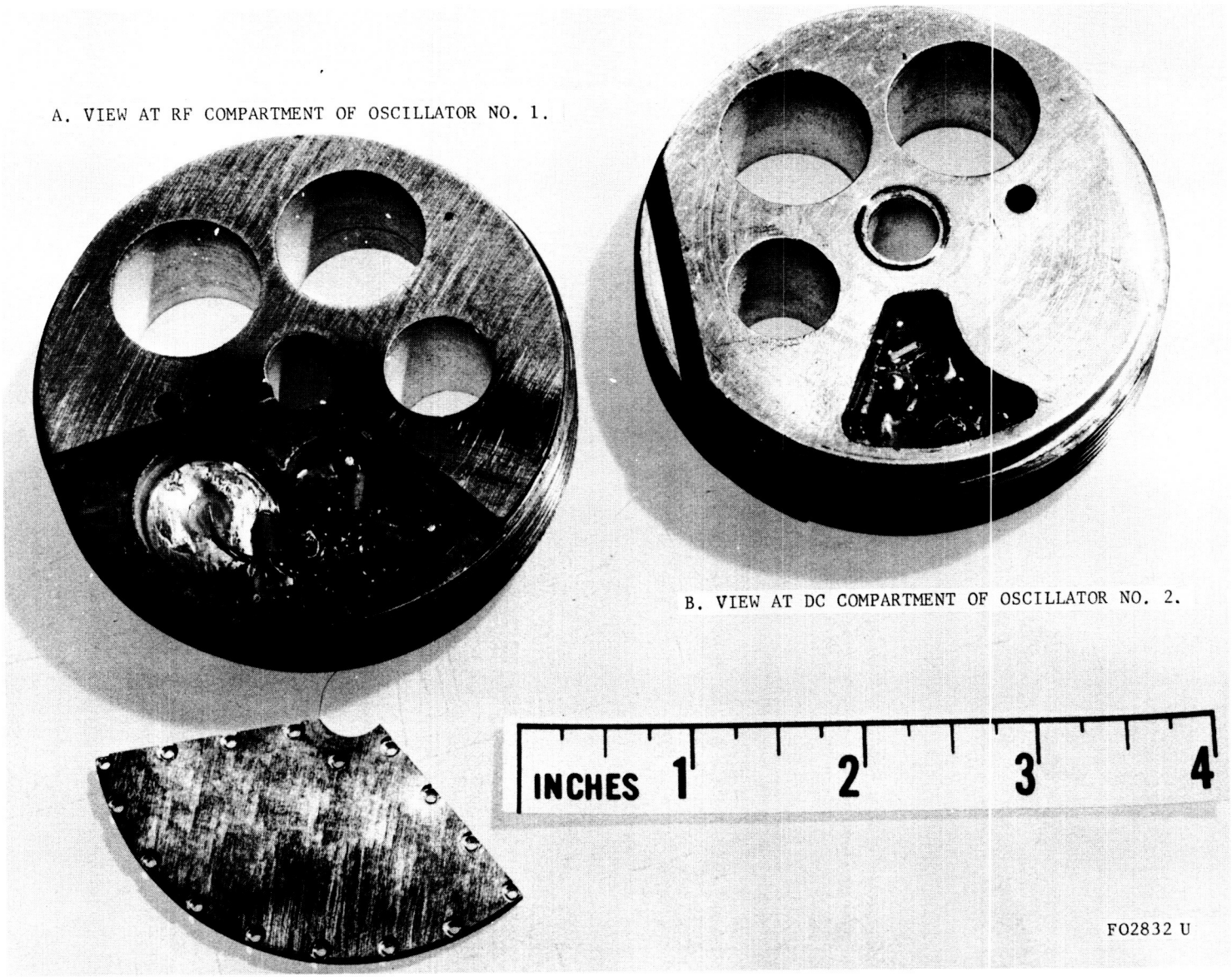

FIGURE 7-15. TWO CRYSTAL OSCILLATORS MOUNTED IN HIGH-G TEST UNITS

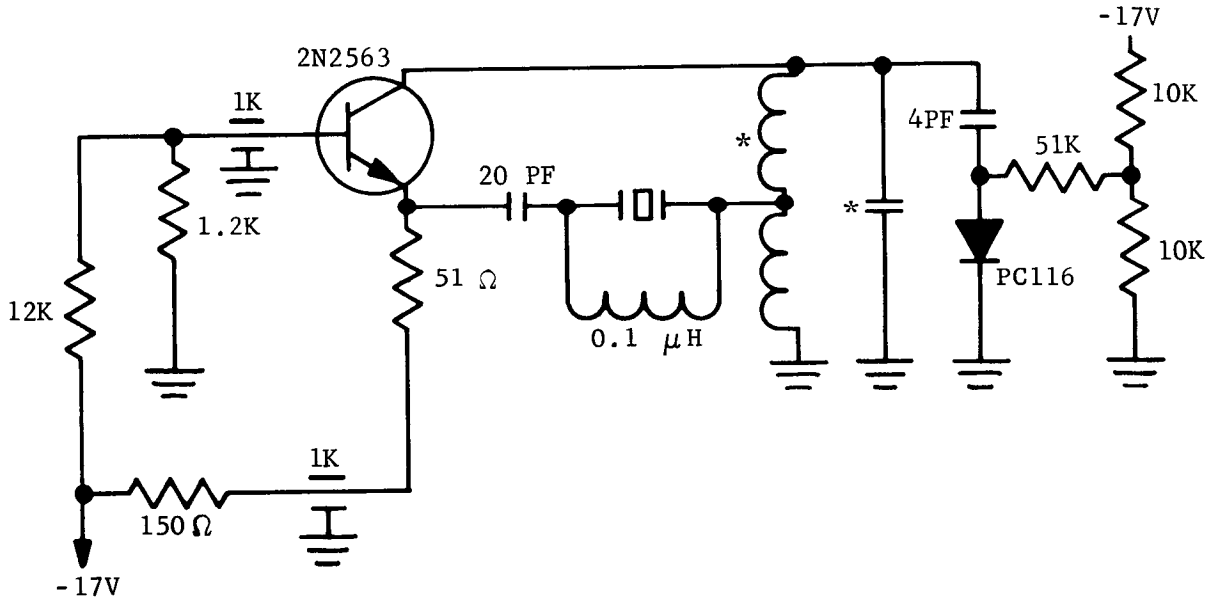

* SELECTED VALUES

FO2833 U

FIGURE 7-16. CRYSTAL OSCILLATOR TEST CIRCUIT SCHEMATIC

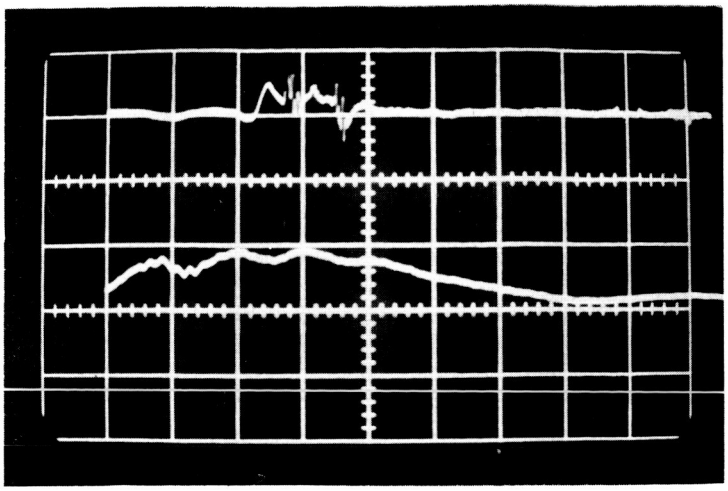

(a) IMPACT IN POLAR DIRECTION

UPPER TRACE: 4 KHZ/CM

LOWER TRACE: 5000 G/CM

TIME SCALE: 100 μS/CM

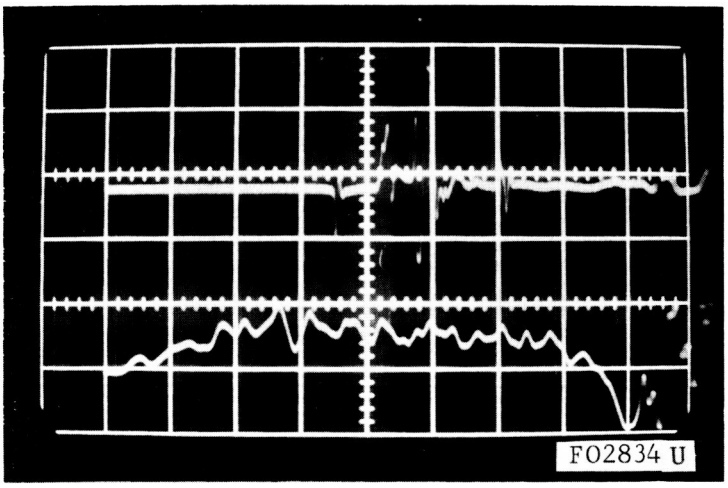

(b) IMPACT IN EQUATORIAL DIRECTION

UPPER TRACE: 8 KHZ/CM

LOWER TRACE: 5000 G/CM

TIME SCALE: 100 μS/CM

FIGURE 7-17. IMPACT TEST RESULTS FOR OSCILLATOR #1 (H.D.L. CRYSTAL) BEFORE MODIFICATION

this hammer test due to a failure of the Polaroid camera used to monitor the scope display during impact. Like Unit No. 1, it was decided to conduct no further tests on this unit.

c. Oscillator No. 3. Unit No. 3 was assembled using the JPL crystal operating at 40 MHz, using the same test circuit as Units 1 and 2. This oscillator is not sensitive to changes in supply voltage. With a supply voltage change of ± 50 percent, the carrier frequency did not vary more than 100 Hz and could not be pulled out of crystal control. This is due in part to a much lower series impedance at resonance, on the order of 20 ohms.

A series of hammer tests was performed on the oscillator (see Figure 7-18). No measurable shift in carrier frequency was noted during or after impact. The same type short-duration, high-magnitude pulses as found in Unit No. 1 were noted on this oscillator during impact.

d. Hyge Shock Test of Crystal Oscillator No. 3. Upon completion of hammer testing of the three crystal oscillators, it was decided to Hyge golf tee only the oscillator employing the JPL crystal (Oscillator No. 3). The oscillator was secured into a standard 3-inch test ball: a solid aluminum hemisphere with a steel dome. The crystal oscillator rf carrier was received in the same manner as during hammer testing by coupling the antenna of a Nems-Clark receiver to the oscillator power supply line. Three high-impact golf tee tests were conducted in different axes. In impact test No. 1, the Hyge ram impacted the ball in the polar direction with the ram impacting directly on the steel dome. In Test No. 2, the ram impacted the ball on the equator. Test 3 was also on the equator with the ball rotated 90 degrees from Test 2.

On impacts one and two, a reference accelerometer was used (Endevco Model 808A) to give an accurate level reading on ram impact. Use of the reference accelerometer was impossible on Test No. 3 because of limitations in accelerometer mounting positions on the test ball. However, on each test, the Hyge ram speed shortly prior to impact was measured and from this a fairly good approximation can be made as to the actual g level on impact at Test 3.

On each shot, three oscillograph channels were used to record the frequency deviation during impact. Each channel utilized 5 kc galvonometers set with different scale factors. Channel No. 1 was set for 0.5 v/inch deflection, corresponding to 2 KHz/inch (20 KHz/inch at the penetrometer output frequency). Since the crystal oscillator frequency is 40 MHz, a times ten multiplier must be used in actual penetrometer application. This multiplies crystal frequency shift as recorded by a factor of ten. Channel No. 2 was set for 2 v/inch corresponding to 8 KHz/inch (200 KHz/inch at penetrometer output frequency). These three channels were used because the actual amount of frequency shift during impact could not be predicted. Hyge test traces of the crystal oscillator impact evaluation are shown in Figures 7-19, 7-20 and 7-21. Table 7.3 summarizes the test results.

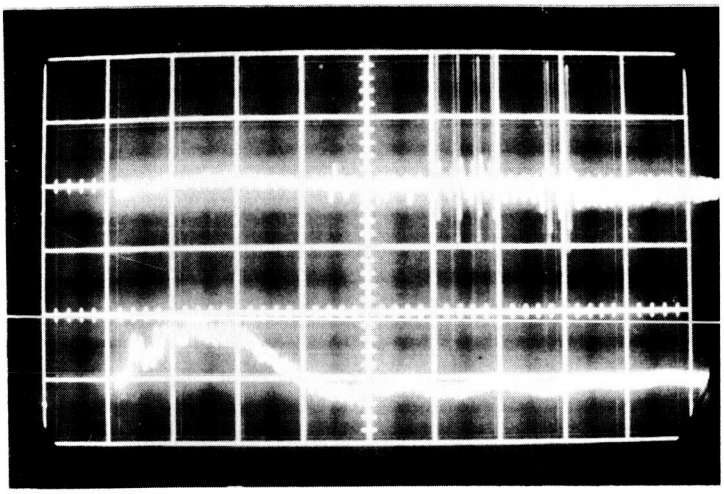

(a) IMPACT IN POLAR DIRECTION

UPPER TRACE: 4 KHZ/CM

LOWER TRACE: 5000 G/CM

TIME SCALE: 200 μS/CM

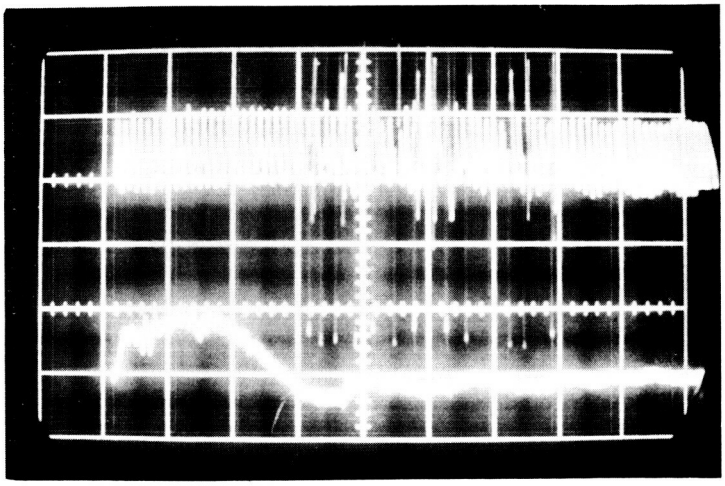

(b) IMPACT IN POLAR DIRECTION WITH 40 KHZ MODULATION FREQUENCY

UPPER TRACE: 4 KHZ/CM

LOWER TRACE: 5000 G/CM

TIME SCALE: 200 μS/CM

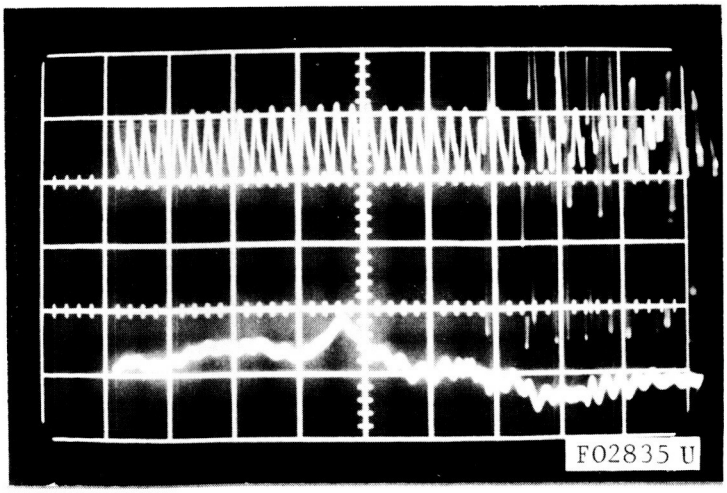

(c) EQUATORIAL IMPACK WITH 40 KHZ MODULATION FREQUENCY

UPPER TRACE: 4 KHZ/CM

LOWER TRACE: 5000 G/LM

TIME SCALE: 100 μS/CM

FIGURE 7-18. OSCILLATOR NO. 3 (JPL CRYSTAL) IMPACT TEST RESULTS

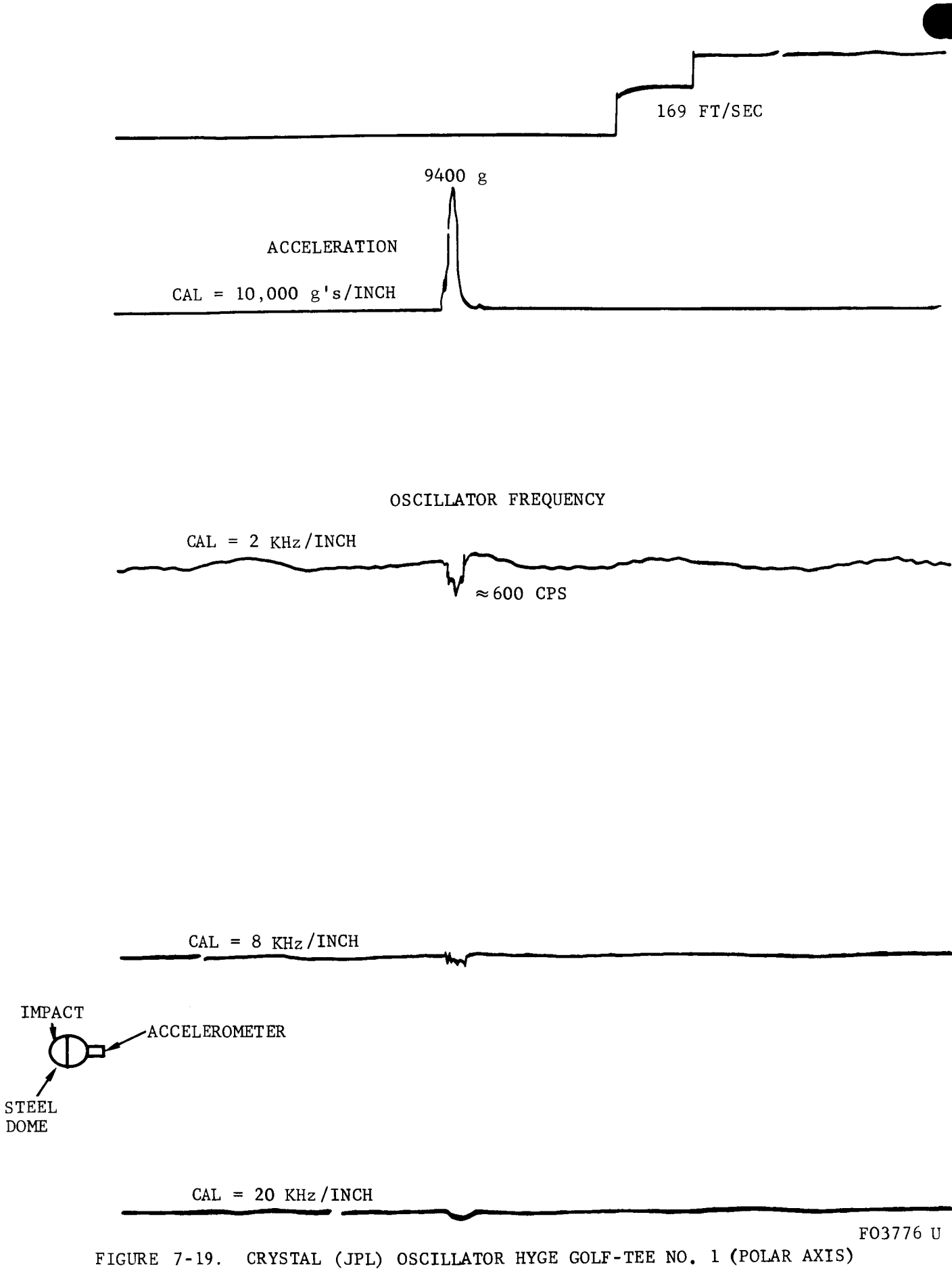

FO3776 U

FIGURE 7-19. CRYSTAL (JPL) OSCILLATOR HYGE GOLF-TEE NO. 1 (POLAR AXIS)

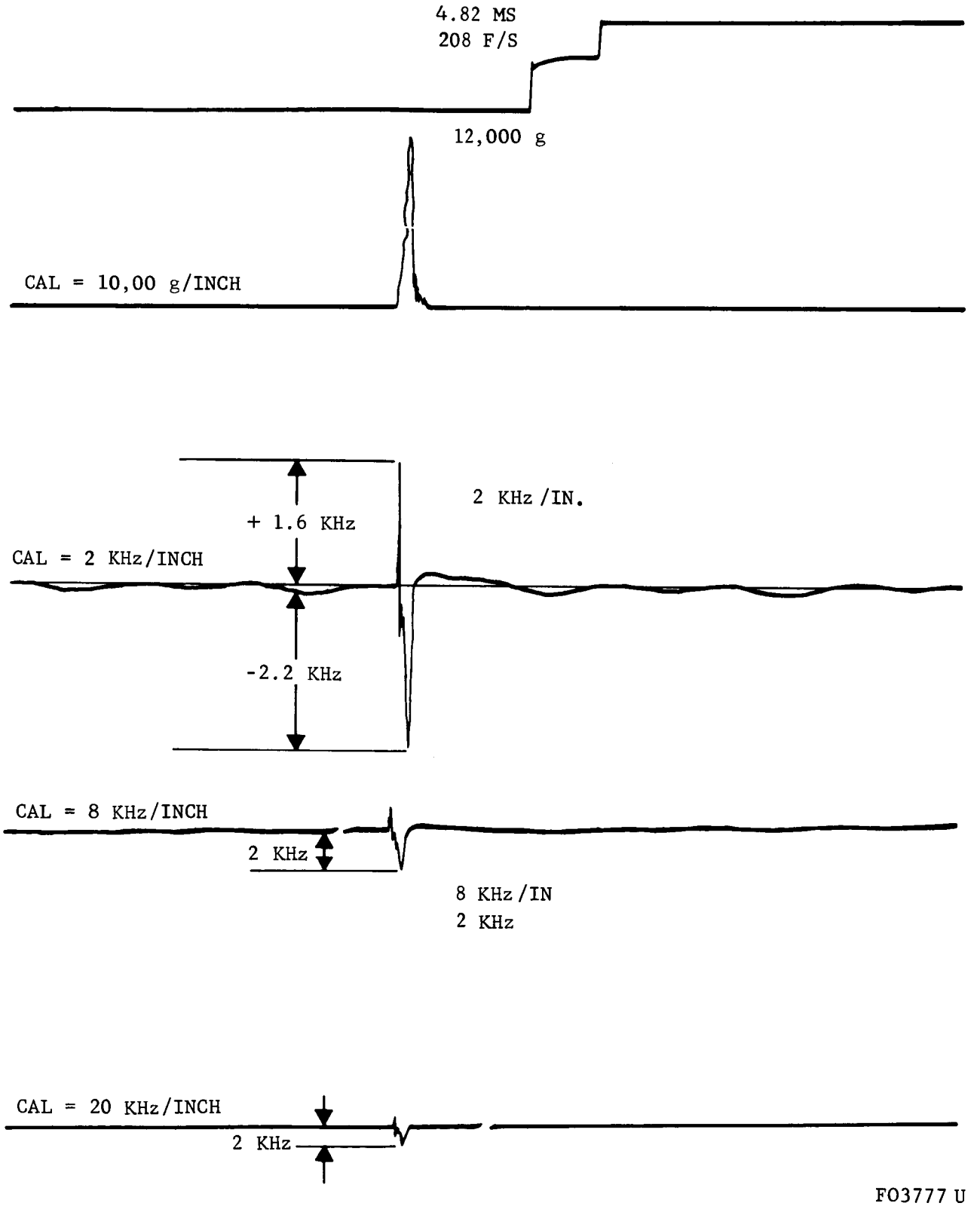

FIGURE 7-20. CRYSTAL (JPL) OSCILLATOR HYGE GOLF-TEE SHOT NO. 2 (EQUATORIAL AXIS)

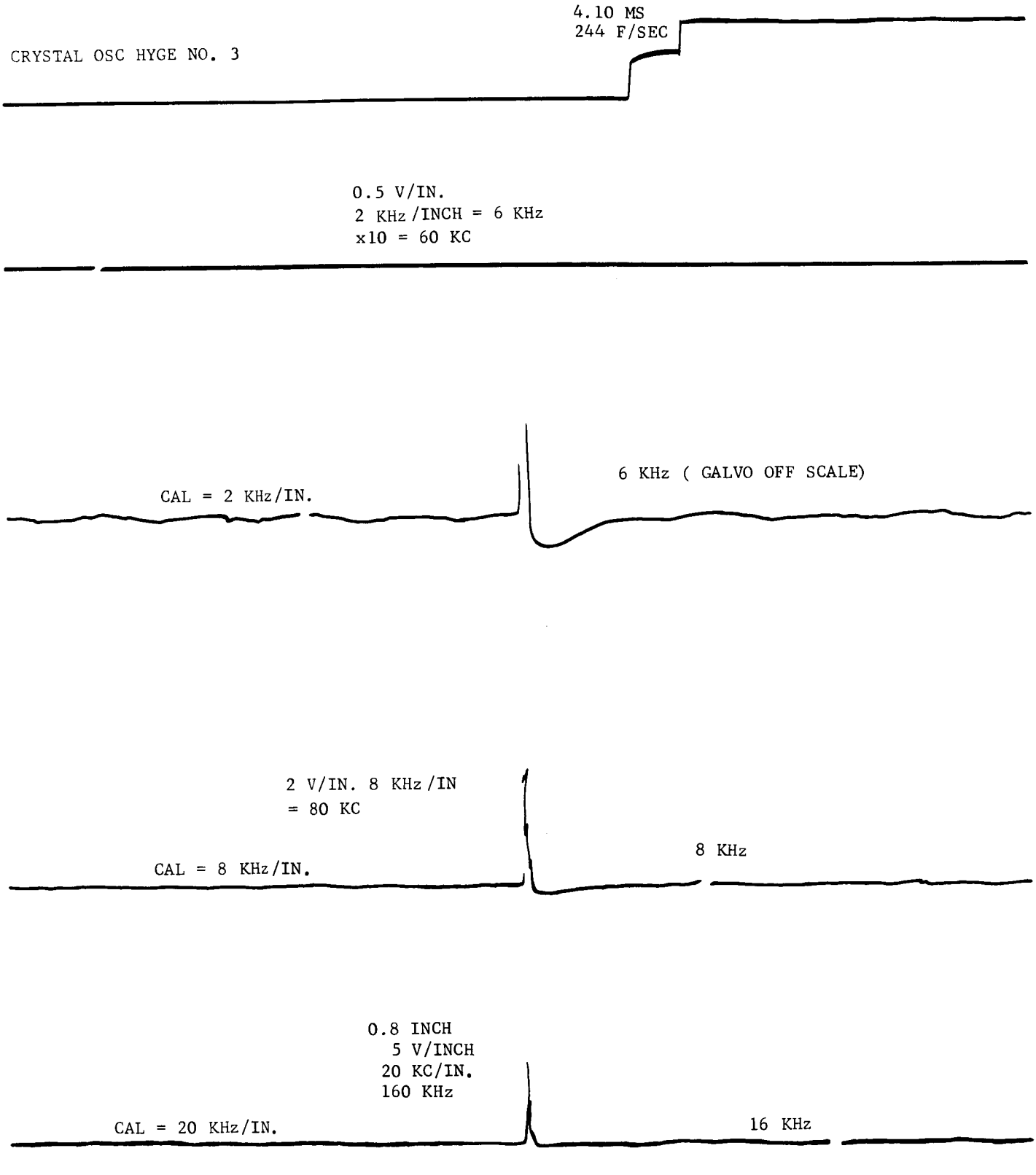

FIGURE 7-21. CRYSTAL (JPL) OSCILLATOR HYGE GOLF-TEE SHOT NO. 3
EQUATORIAL AXIS

TABLE 7.3

SUMMARY OF HYGE GOLF TEE JPL CRYSTAL OSCILLATOR TESTS

Impact One	
Crystal frequency before impact	40.155545 MHz
Crystal frequency after impact	40.155529 MHz
Projectile speed at impact	169 ft/sec
Nominal peak acceleration	9400 g
Crystal frequency shift at impact	0.600 KHz
Equivalent penetrometer frequency shift	6.000 KHz
Impact Two	
Crystal frequency before impact	40.155500 MHz
Crystal frequency after impact	40.155508 MHz
Projectile speed at impact	208 ft/sec
Nominal peak acceleration	12,000 g
Crystal frequency shift at impact	+1.6 KHz -2.2 KHz
Translated penetrometer frequency shift	+16 KHz -22 KHz
Impact Three	
Frequency before impact	40.155476 MHz
Frequency after impact	No record due to failure of power cable after impact. Later lab tests indicate: 40.155282 MHz
Projectile speed at impact	244 ft/sec
Nominal peak acceleration - approximation	14,000 g
Frequency shift at impact	Due to the high frequency characteristic of the crystal transient and the limited 5 KHz response of the galvonometers. the frequency transient was recorded with three different scale factors to better evaluate total excursion. Channel Frequency Shift 1 6 KHz 2 8 KHz 3 16 KHz

7.1.5 PENETROMETER PROTOTYPE FUNCTIONAL TESTING

Since the antenna system is functionally inseparable from the ball structure and balsa impact limiter, prototype functional tests were not performed on the antenna system separately but rather as part of the prototype system tests. There is also a major problem in monitoring performance of the antenna system during environmental tests. Electrical interference would result from the coax feed cable which would need to be fed through the antenna structure.

7.1.6 COMPONENT HIGH ENERGY SHOCK TESTING

a. General. Battery cells, resistors, capacitors, and squib switches were subjected to nominal 10,000 g shocks resulting from velocity changes of 250 feet per second. Continuous monitoring of each component during the shock tests was employed so that its shock stability could be observed.

For those tests, the components were totally encapsulated in 4-inch diameter epoxy spheres made of Epon 838 resin, Shell 871 diluent, and accelerator D in the ratios of 100:60:15.6, respectively. Threaded holes and flat mounting surfaces were provided on the test spheres for attaching accelerometers.

Figure 7-22 illustrates the typical physical setup. This setup has been referred to as the golf tee setup because of the obvious circumstance of the specimen. Here the test sphere containing samples of test components is placed 27 inches in front of the Hyge accelerator piston (lower left). That is the location of maximum piston velocity when the accelerator is fired. The leading edge of the piston is fitted with two 1-inch thick pieces of 55/65 durometer neoprene rubber. The neoprene pulse shaper gives a nominal 10,000 g shock resulting in a final projectile speed of 250 feet per second when a 4-inch diameter, 1.5 pound projectile is used.

The importance of using the golf tee shock method is in the fact that the entire shock has been completed and the projectile is up to speed before it has moved a distance of two inches. Hence, instrumentation cable motion has been nil and all of the shock data have been obtained before cable noises become large. Generally, the best cable service has been obtained when it was supported overhead (see Figure 7-22) from alligator clips. That method prevents the projectile from running into its own cable and also keeps the cable off the floor and out of the way of foreign objects in the test pit.

Speed measurement is accomplished with a 12.0-inch long photoelectric speed trap. Prior to each firing, a shadow template is held in the projectile path through the speed trap, and the effective light beam separation is adjusted to 12.0 ± 0.05 inch. Time for the projectile to pass through both light beams is indicated on an electronic counter to three significant

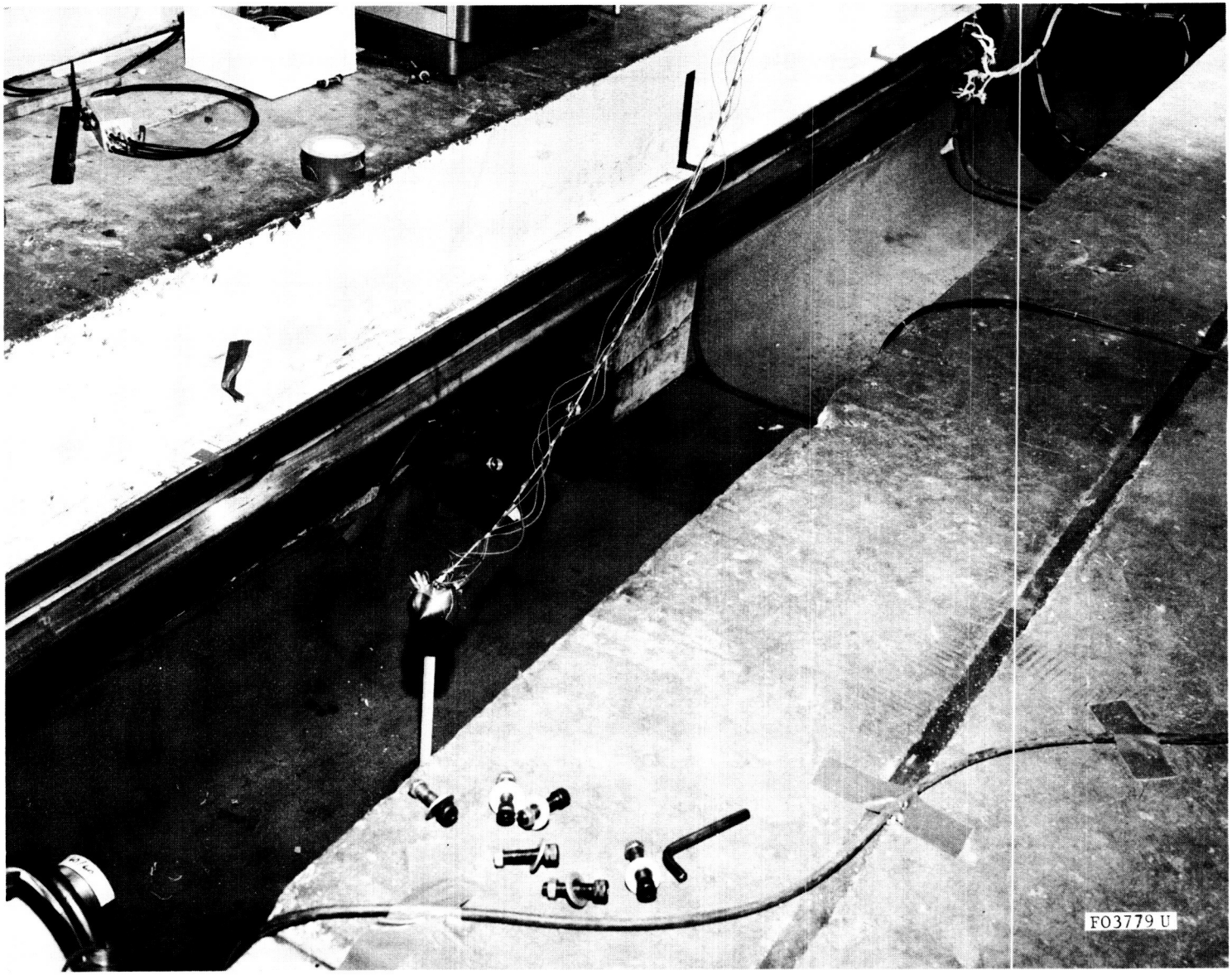

FIGURE 7-22. COMPONENT SHOCK TEST SETUP

figures ± one count, or at least ± 1 part in 400. Rise time of the photo diode driven switches under full load has been measured as less than 1 microsecond. Figure 7-23 is a schematic of the electronic portion of the speed trap. The photo diodes were selected as a matched pair with respect to dc resistance when fully illuminated and when fully darkened.

A fish net beyond the speed trap is rigged on 3/8-inch bungee cord and arrests the flying projectile by a trapping action. Layers of foam rubber padding on the walls and floor of the Hyge pit protect the projectile from undue damage during the arresting action.

b. Battery Cell Shock Tests. Battery cells from three vendors were subjected to high energy shock tests. Battery packs of five cells in series constituted each test specimen. Load voltage while under a normal penetrometer load was recorded during each test. Shocks were applied along at least the three major axes of each specimen. From Table 7.4 it is seen that the most stable performance was obtained from the Jupiter B-80 cells. In all cases, the tabulated change in load voltage (ΔE_L) was of a transient nature occurring coincidentally with the shock pulse.

c. Capacitor Shock Tests. Vitramon type VY and Corning type CYFM (glass) fixed capacitors of values from 51 pf to 1000 pf were subjected to high energy shock tests. The instrumentation scheme was based on the classical definition of capacitance: $C = Q/V$. Figure 7-24 illustrates the method. Unfortunately, large amounts of spurious charge were generated during the test impacts which masked the desired information. The spurious charge mechanism is not well understood at this time, but it is believed to be associated with friction of the neoprene pulse shaper against the epoxy specimen sphere. Later tests of signal electronics subsystems indicated the Vitramon VY capacitors to be the better choice in an operating circuit.

d. Resistor Shock Tests. Fifteen Bournes 4200A-1-(resistance code)J resistors ranging in value from 1.4 kilohms to 170 kilohms were taken five at a time and subjected to high energy shock tests while monitoring each with a wheatstone bridge circuit. The specimens were 1/10 watt devices having a resistance tolerance of ±5 percent. The largest change in resistance due to the applied shock was 4.8 percent for a 170 kilohms resistor. Table 7.4 summarizes the data.

e. Squib Switch Shock Test. Five prefired Atlas MS 2.1-0-WRT1 squib switches were shocked along the direction of their piston shafts while monitoring the open and closed contacts of each switch. There was no evidence of contact bounce, chatter, etc. Table 7.4 lists the data.

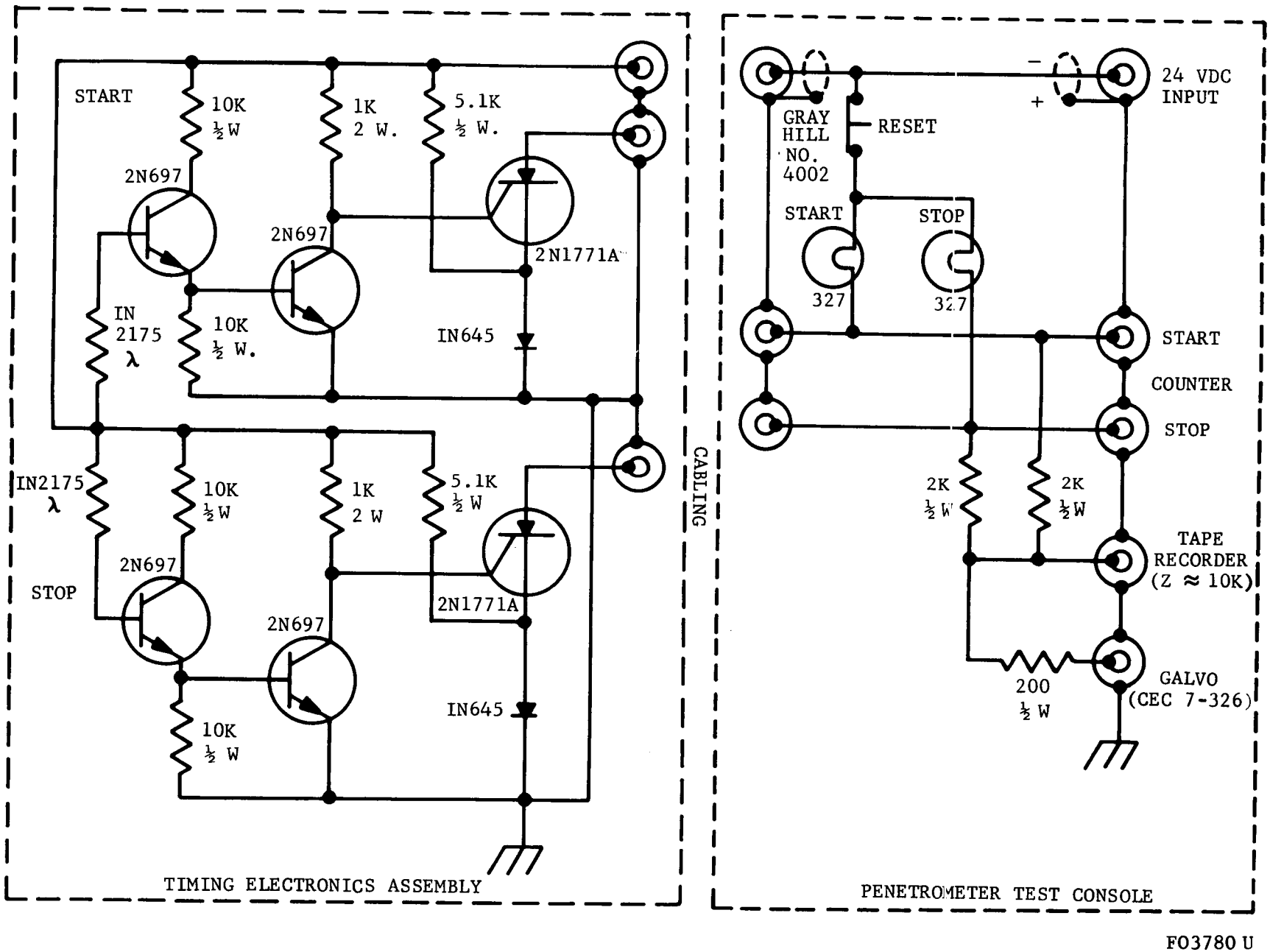

FIGURE 7-23. SPEED TRAP SWITCH

TABLE 7.4

HYGE SHOCK TEST SUMMARY, COMPONENTS

Test Date	Specimen	Test Parameter	Effect of Shock	Peak Shock (g)	Final Velocity (ft/sec)
7/7/65	Battery Cells (5), Epic	Load Voltage	ΔE_L < 50 mv	11,900	252
7/7/65	B-80, Ag-Zn		ΔE_L < 50 mv	7,240	250
7/14/65	Sample #1		(Broken cable)	8,500	?
9/9/65	$E_L \cong$ 4.7v		ΔE_L < 35 mv	11,000	182
7/29/65	Battery Cells (5), Epic	Load Voltage	ΔE_L = 30 mv	11,700	245
7/29/65	B-80, Ag-Zn		ΔE_L < 25 mv	11,000	242
7/29/65	Sample #2		ΔE_L < 25 mv	10,000	229
	$E_L \cong$ 4.7v				
10/15/65	Battery Cells (5),	Load Voltage	ΔE_L = 200 mv	10,000	183
10/15/65	Eveready S76E Ag-Zn		ΔE_L = 110 mv	13,000	183
10/15/65	$E_L \cong$ 4.7v		ΔE_L = 110 mv	8,750	178
10/15/65			?	8,250	228
10/18/65			ΔE_L = 27 mv	11,800	228
10/22/65	Battery Cells (5),	Load Voltage	ΔE_L = 100 mv	10,600	185
10/22/65	Mallory M# 76H Ag-Zn		ΔE_L = 200 mv	8,650	185
10/22/65	$E_L \cong$ 4.7v		ΔE_L = 1060 mv	10,700	191
10/22/65			ΔE_L = 100 mv	9,300	235
9/7/65	Bournes 4200A Resistors (5)	DC Resistance	Max ΔR = 1.2%	12,000	239
9/7/65	Bournes 4200A Resistors (5)	DC Resistance	Max ΔR = 4.8%	11,000	187
9/8/65	Bournes 4200A Resistors (5)	DC Resistance	Max ΔR = 0.2%	7,000	187
9/8/65	Atlas MS2.1-0-WRT1 Switch (5)	Contact Bounce	None discernible	12,000	182

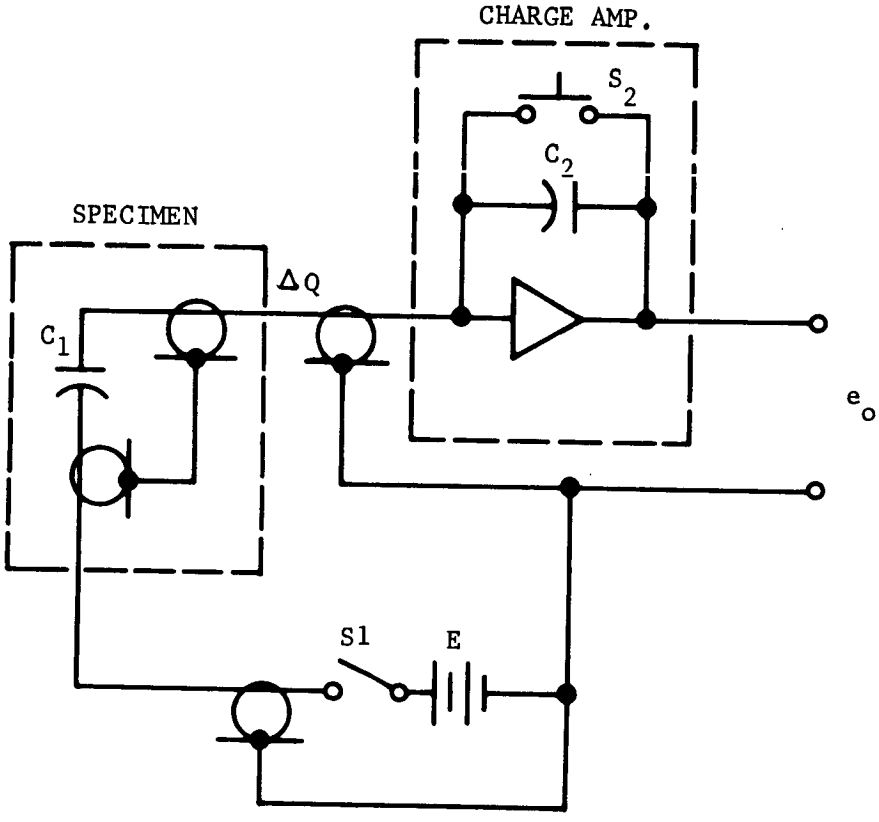

1. CLOSE S_1 THEN DISCHARGE C_2 THROUGH S_2

2. $e_o = -\frac{\Delta Q}{C_2}$

$\Delta Q = E \Delta C_1$

$e_o = -\frac{\Delta C_1}{C_2} E$

$\Delta C_1 = -\frac{e_o}{E} C_2$

FO3781 U

FIGURE 7-24. CAPACITOR SHOCK TEST INSTRUMENTATION

f. Subassembly High Energy Shock Tests. Signal electronics, oscillators, and frequency multipliers of various configurations were subjected to nominal 10,000 g shocks resulting in specimen velocities of 250 feet per second. The physical setups were identical to those used in component shock tests. Figure 7-25 is a photograph of a typical test setup showing how the instrumentation cables are rigged overhead. Test results have been discussed in preceding paragraphs. Table 7.5 summarizes the environmental conditions.

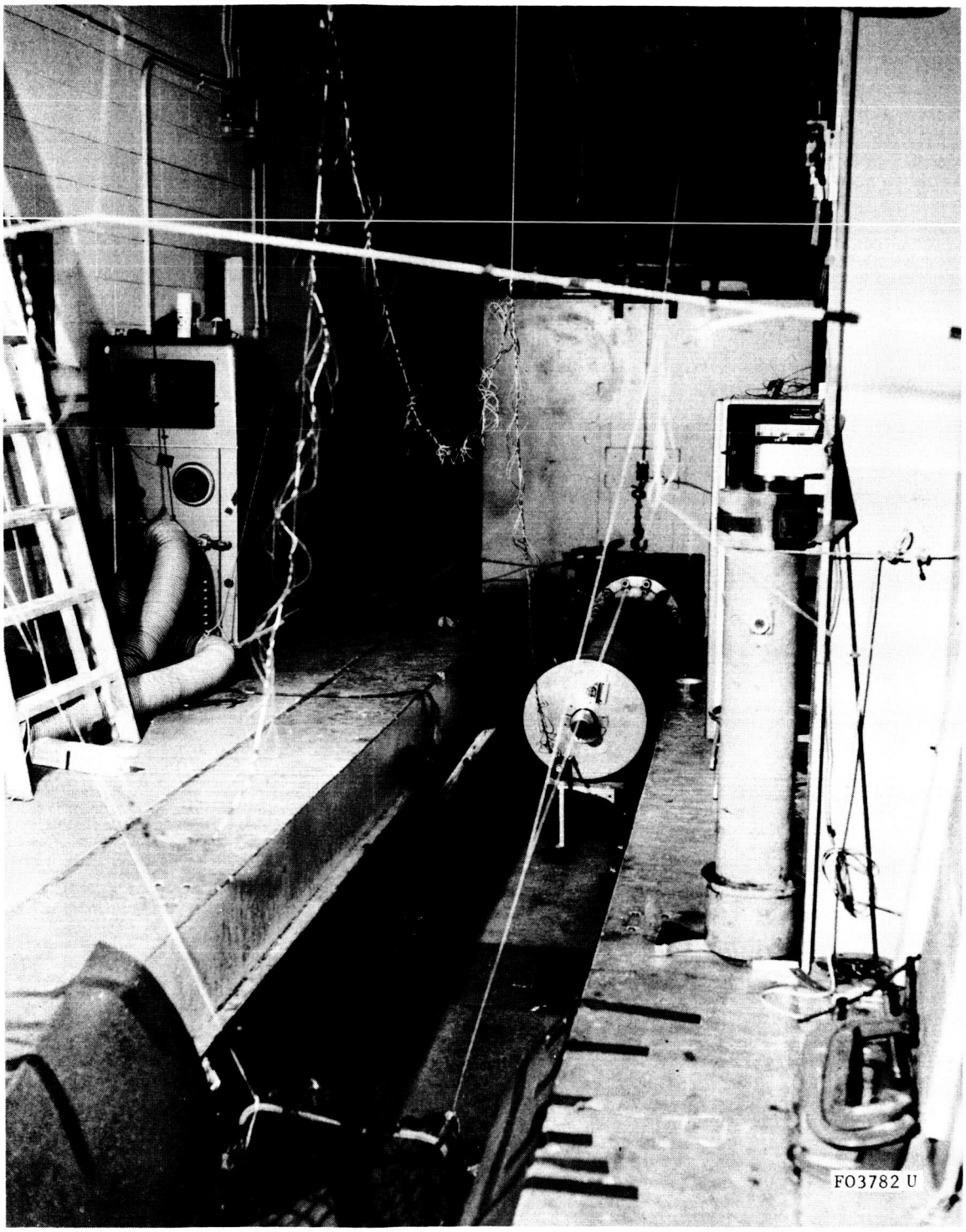

FIGURE 7-25 SUBASSEMBLY SHOCK TEST SETUP

TABLE 7.5

HYGE SHOCK TEST SUMMARY, SUBASSEMBLIES

Test Date	Specimen	Peak Acceleration (g)	Final Velocity (ft/sec)
9/15/65	Oscillator No. 1 (216 MHz)	12,600	244
9/15/65	Oscillator No. 1 (216 MHz)	10,900	236
9/15/65	Oscillator No. 1 (216 MHz)	9,620	225
9/15/65	Oscillator No. 1 (216 MHz)	10,700	225
9/15/65	Oscillator No. 1 (216 MHz)	?	242
9/22/65	Oscillator No. 2 (216 MHz)	?	220
9/22/65	Oscillator No. 2 (216 MHz)	11,000	222
9/22/65	Oscillator No. 2 (216 MHz)	12,000	254
9/22/65	Oscillator No. 2 (216 MHz)	?	237
10/25/65	Oscillator No. 4 (200 MHz)	?	248
10/27/65	Oscillator No. 4 (200 MHz)	9,800	236
10/27/65	Oscillator No. 4 (200 MHz)	?	238
11/17/65	Oscillator No. 5 (111 MHz)	11,200	222
11/17/65	Oscillator No. 5 (111 MHz)	?	232
3/5/66	Oscillator No. 6 (40 MHz Xtal)	9,400	169
3/5/66	Oscillator No. 6 (40 MHz Xtal)	12,000	208
3/5/66	Oscillator No. 6 (40 MHz Xtal)	?	244
9/24/65	Signal Electronics (pair)	?	242
9/24/65	Signal Electronics (pair)	12,140	281
10/14/65	Frequency Doubler and P.A. No. 1	9,200	212
10/16/65	Frequency Doubler and P.A. No. 1	9,300	193
10/18/65	Frequency Doubler and P.A. No. 1	10,500	?
10/22/65	Frequency Doubler and P.A. No. 2	11,800	237
12/6/65	Frequency Quadrupler	10,700	230
12/6/65	Frequency Quadrupler	?	231

7.2 SUBSYSTEM TESTS

The penetrometer prototypes were each submitted to a series of environmental and functional tests to assist in the evaluation of the basic omnidirectional system performance characteristics. Each represented a complete subsystem comprised of an omnidirectional accelerometer, quasi-isotropic antenna, transmitter, signal electronics, battery, and power regulator-timer assemblies. The primary emphasis of this test series is placed on the investigation of subsystem characteristics and the determination of interface problems in sufficient time to benefit succeeding prototype models. The tests principally involved bench static and transient testing, field test low and high velocity impact testing, and captive Hyge calibration testing. The following paragraphs describe the test results in general while referencing the detailed test reports which are included as appendices.

7.2.1 PROTOTYPE NO. 1 TESTS

The test results obtained for Prototype No. 1 are reported in detail in Appendix A. This paragraph presents only a summary of the test results and conclusions. Prototype No. 1 was the first complete penetrometer subjected to environmental and functional tests. The testing was completed in accordance with a written general test plan which underwent minor modification as test details warranted.

The tests reported in Appendix A qualified the design of many subsystems within the penetrometer. Unformtunately, the failure of the internal battery, which was attributed to probable misuse because of initial equipment uncertainties, prevented certain needed tests. Some of the penetrometer assemblies and subassemblies performed as anticipated because of their particular development status. Other problems occurred which had not been anticipated but design changes were effected to eliminate similar deficiencies in the subsequent prototypes. The following paragraphs present an account of the individual assembly test results.

a. Antenna. The test results showed no substantial changes in the antenna pattern due to the high velocity impact. Further, no mechanical damage to the antenna loops or their supports was noted. The crushing impact was in a quadrant of the sphere between loops such that the antenna supports were subjected to compression and shear. Therefore, the mechanical design of the antenna was judged satisfactory.

b. Accelerometer. The test results indicated that the accelerometer failed sometime during the test sequence by leakage of the "fluid" from the piezoelectric sphere. It was believed that this happened during assembly of the penetrometer. The failure was believed due to improper sealing of the fill hole with epoxy. The recommended cure was better assembly and inspection techniques by the vendor.

c. Battery. The battery failed during the tests by leaking of electrolyte and failure to retain a charge. This occurred before any real environmental extremes were experienced. There was evidence that the battery was overcharged during the penetrometer assembly procedure. The battery was charged with a charger which was found to have excessive ac in its output. The charge limiting voltage was set by a meter which read average voltage but the battery charged to the peak voltage. Additionally, the two sections of the battery were charged in series despite their prior discharge at different rates. The individual cells did not have equal charge capacities. It appeared that similar battery failures in the future would be prevented by:

(1) Selecting cells for similar capacities.

(2) Charging cells individually or in small groups.

(3) Carefully monitoring cell voltages during charging to avoid overcharging.

The final discharged condition of the positive battery was probably due to conduction in the test connector caused by leaking electrolyte.

d. Power Regulator/Timer. There was no evidence of power regulator/timer failure in the prototype except for visible cracks in the glass diodes after disassembly operations. These cracks could have been caused during disassembly or by epoxy shrinkage. Revisions in the assembly process (i.e., sleeving the glass diodes prior to encapsulation) were effected to prevent a possible recurrence. The fact that the predictable timer shutdown did not occur was attributed to conditions brought about by battery electrolyte leakage.

e. Signal Electronics. Failure of the accelerometer prevented test observation of the signal electronics characteristics during most of the tests. The post disassembly findings, and the actions during two of the captive Hyge shocks, indicated some sort of intermittent, erratic condition existed in the signal electronics. Unformtunately, there were not enough external test points to fully diagnose this behavior. Therefore, it was assumed that this trouble, which had not occurred on previous modules, was caused by a faulty component or an improper connection.

It was recommended that future prototypes have additional external test points for the signal electronics. It was recognized that connector limitations and impedance considerations placed restrictions on such test points.

f. Transmitter. The oscillator module within the transmitter was known to have poor shock and temperature characteristics when the penetrometer was assembled. The module used thin brass walls and all components were completely encapsulated. Improved oscillator modules were not available at the time of assembly.

The oscillator did not meet either shock or temperature stability requirements. In captive Hyge tests, an acceleration of 1000 g produced at least a 40 KHz frequency transient at the output frequency of 435 MHz. The transmitter output frequency varied considerably with temperature and always drifted about 170 KHz in the first two minutes of operation. These were not unknown problems, and consequently were being separately analyzed and solved. The transmitter did not exhibit any permanent changes due to shock and no unsuspected troubles were encountered.

g. Structure. The metal structure passed the severe impact test satisfactorily. No permanent deformation of the structure was observed. The fact that the balsa impact limiter was not well bonded to the outside of the metal sphere in no way caused trouble. However, it was recommended that the metal surface be treated differently in future models to enhance the adhesion of the epoxy.

h. Impact Limiter and Cover. This particular penetrometer model had the fiberglass cover but not the thin mylar covering. The mylar covering is mainly for a moisture seal in vacuum and was not needed in these tests. The depth of balsa crushing in the impact test agreed closely with the predicted value. There was no direct acceleration measurement obtained within the sphere during the impact, but it is presumed by analogy that the deceleration was limited to 7000 g. There was no evidence of payload movement, or cannon-balling, within the limiter. Small voids were noted in the glue joint between limiter halves but these were not considered serious. In general, the impact limiter design proved successful.

7.2.2 PROTOTYPE NO.2 TESTS

Two basic testing sequences were performed for Prototype No. 2. The initial series of tests are reported in detai in Appendix B. The second series of tests was required following a refurbishment of Prototype No. 2, and is reported in detail in Appendix C. The refurbishing operation was performed to eliminate damage to signal electronics which had occurred in the original limiter assembly operation. With the rework of Prototype No. 2, a milestone was reached by achieving complete functional operation of an omnidirectional penetrometer. To facilitate the summary description of the test results and conclusions, separate accounts of the two test series are presented in the following paragraphs.

a. Prototype No. 2 Tests (Original). Prototype No. 2 final assembly problems resulting in the signal electronics failure prevented a complete functional test and evaluation of the omnidirectional penetrometer. However, significant test data were obtained on all other operating assemblies. The design improvements arising from Prototype No. 1 testing resulted in basic model improvements which minimized previous deficiencies. A summary description of the test results and conclusions is presented as follows.

(1) Antenna. The electrical and mechanical integrity of the antenna subassembly was again demonstrated by the results of Prototype No. 2 testing. The effect of a high velocity impact in the vicinity of the antenna feed loop was satisfactorily evaluated. No degradation in omnidirectional characteristics was noted.

(2) Accelerometer and Signal Electronics. Failure of signal electronics operation prevented the evaluation of the accelerometer and signal electronics subassemblies. However, the signal electronics did not fail due to shock or faulty construction. It was concluded that the signal amplifier was accidentally shorted to a battery voltage while attempting to remove the umbilical connector which had been inadvertently epoxied in the impact limiter.

(3) Battery and Power Regulator/Timer. Battery operation was satisfactory except for the degradation in performance of the 18 to 24 volt cell grouping. This did not hamper the testing of Prototype No. 2. It contributed to the low capacity performance noted at the conclusion of the final Hyge test. The power supply regulator and timer were found to operate satisfactorily throughout Prototype No. 2 testing. More than ten cycles of timer controlled operating periods were obtained successfully during testing. Active monitoring of the +17 volt power regulator during Captive Tests 2 and 3 showed no adverse effects from low level shocks.

Degradation in battery performance actually was observed prior to Prototype No. 2 system tests; i.e., during hammer testing operations. Probably 1 cell in the 18 to 24 volt cell grouping was under voltage. Charging operations resulted in bringing the cell group up to acceptable performance levels for the few cycles required in the test sequence.

(4) Transmitter. The important observation made in Prototype No. 2 tests regarding transmitter performance was the fact that only a 48 KHz frequency transient occured at Hyge impact. The transmitter, as in Prototype No. 1 tests, did not exhibit any permanent changes due to shock and no basic problems were encountered.

Data taken in the initial turn-on transient test depicted good temperature and frequency stability characteristics for a completely assembled penetrometer for the specified set of conditions (see Figure C-1 of Appendix C). Additional testing of complete penetrometer assemblies is required before any final conclusions are reached regarding overall temperature and frequency stability characteristics. For example, repeated test runs for varied (soak temperatures) initial conditions would yield a more complete performance picture over the anticipated operational temperature regime.

b. Prototype No. 2 Tests (Refurbished). A milestone was reached by achieving complete functional operation of an omnidirectional penetrometer in this series of tests. Extensive testing was accomplished in accordance

with a written general test procedure. Numerous low velocity impact testing was performed as part of controlled field tests and multiple drop system tests. The results of the tests completed were generally very satisfactory with few anomalies observed. The principal anomalies observed were in the area of system calibration; i.e., resolving electrical calibrations with actual physical g (acceleration) inputs and of Hyge rigid impact performance. The calibration problem is believed to be one of refinement or improvement of the entire calibration approach. The rigid impact test, which indicated g levels much lower than anticipated, constituted information not previously encountered. Further investigation and testing of improved calibration techniques will be conducted as part of a work extension authorized under the present contract. Results are expected to provide answers to the stated anomalies. An account of other conclusions and/or observations derived from the variety of tests reported herein are presented according to assemblies in the following paragraphs. The detailed test report is given in Appendix C.

(1) Antenna. The electrical and mechanical integrity of the antenna assembly was maintained as a result of the extensive testing performed on the refurbished model of Prototype No. 2. The pattern of Figure C-13 depicts the basic antenna performance characteristics and exhibits only a minor degradation from that which is typical. This was primarily because usual antenna final tuning procedures were unable to be performed on the reworked prototype.

(2) Accelerometer and Signal Electronics. Satisfactory functional operation of the accelerometer and signal electronics was demonstrated in the numerous tests and under a variety of operating shock environments. As stated previously and in the detailed test results, both a calibration and rigid impact performance anomaly existed. Further investigation of these anomalies was recommended and is scheduled to be carried out in the subsequent work extension. The turn-on transient characteristic of the signal electronics appeared allowable over the interval observed although improvement would be sought in subsequent development.

The multiple plot of individual uniaxis sensitivity of Figure C-11 depicts the omnidirectional sensitivity observed during Hyge captive test calibrations. The variation is illustrated by examining the high sensitivity portion below the knee. A variation of about ± 10 percent about a mean value of 0.133 KHz/g is seen to exist. This is presumably due to the accelerometer since electrical scaling checks of the associated electronics did not appear to exhibit this same characteristic.

(3) Battery and Power Regulator/Timer. The battery and power regulator/timer performed satisfactorily, and no additional significant degradation developed over that previously reported for the original Prototype No. 2 configuration. It should be noted that the battery and

power regulator/timer are, of course, the same assemblies employed in the original Prototype No. 2. Some degradation in charge retention was observed but frequent recharge cycles brought the battery up to acceptable performance levels for the test sequences employed herein.

(4) Transmitter. Transmitter shock sensitivity under Hyge rigid impact was commensurate with that observed in the previous tests on the "original" prototype. This constituted an indication of repeatability. No permanent changes because of shock were observed in this repeat test. Data taken in the turn-on transient tests depicting temperature and frequency stability characteristic agreed essentially with that previously observed. Frequency stability was within the revised transmitter performance drift characteristic.

7.2.3 PROTOTYPE NO. 3 TESTS

Prototype No. 3 testing was abbreviated somewhat over that employed for the preceding prototypes. Additional testing, however, is scheduled to take place during a work extension period currently in progress. A detailed account of those tests completed and resulting conclusions are contained in Appendix D. The salient results and observations are presented here in summary form.

Complete functional operation of an omnidirectional penetrometer prototype design was demonstrated by Prototype No. 3 test results. Prototype No. 3 was the second completely functional omnidirectional penetrometer successfully developed. On the basis of the test results, certain conclusions and observations may be made. They are presented in the following paragraphs according to major assemblies.

a. Antenna. The electrical and mechanical integrity of the antenna assembly was maintained throughout the Prototype No. 3 series of tests.

b. Accelerometer and Signal Electronics. Satisfactory functional operation of the accelerometer and signal electronics was demonstrated by virtue of the tests performed. Numerous low velocity impact tests, performed as part of an interim work extension but not reported herein, also demonstrated very satisfactory operation and repeatability. Turn-on transient data depicted satisfactory initial decay times of several seconds and exhibited a slower perturbation with excursions similar to that observed in Prototype No. 2 data.

Electrical calibration data (Figure D-3) taken during bench tests was found to differ from the Hyge captive calibration data (Figure D-10) by a factor of better than 1.5. The discrepancy between electrical and physical transfer functions occurred in a manner similar to that observed for Prototype No. 2. Excellent omnidirectional sensitivity was observed in Prototype No. 3 as evidenced in the composite plot of Figure D-10.

c. Battery and Power Regulator/Timer. The battery and power regulator/timer performed satisfactorily during all Prototype No. 3 testing. No degradation in characteristics was observed during or following the numerous low velocity impact tests conducted in the follow-on period.

d. Transmitter. Transmitter performance was very satisfactory during all prototype testing. Operation at the design frequency of 438.0 MHz was achieved and maintained with temperature and frequency stability characteristics remaining within latest performance requirements.

7.3 MULTIPLE DROP SYSTEM TESTS

The multiple drop system tests were performed at the close of the program to demonstrate the basic overall system functional operation of the Lunar Penetrometer System. For this test, two penetrometers, Prototype Nos. 2 and 3 (i.e., refurbished 2), were dropped "simultaneously" onto test soil samples with the resulting impact data radiated as VHF transmissions to the data relay. The data relay was operated in a modified configuration to facilitate the acquisition and transmission of the penetrometer data to the CSM equivalent Aeronutronic ground station for final data acquisition, recording, and real time display. It should be noted that the multiple drop test was primarily a functional demonstration and consequently only qualitative results were expected to be gathered.

Satisfactory impact velocities were obtained by performing the drop tests at the Aeronutronic antenna range tower where heights of approximately 30 feet were available. The basic test configuration employed is shown in Figure 7-26. With 25-foot heights actually obtained, velocities of 40 ft/sec were achieved. Target materials of foam and sand (Nevada 120-2) were selected to yield resulting deceleration magnitudes to 400 g to yield corresponding good data SNR performance.

Other general objectives and operating constraints achieved and/or observed are noted as follows. Polarization diversity reception was provided in the reception of both Prototype Nos. 2 and 3 rf transmissions. Good rf SNR performances above threshold was preset with the aid of supplementary attenuators to limit signal power into relay receiver input terminals. This was necessary to eliminate the subceptibility to receiver blocking which occurred when operating in close proximity to penetrometers radiating their 0.5 watt output power. External local oscillator signals to two (Prototype No. 2) receiver channels were required while fixed tuned reception of the Prototype No. 3 rf signals occurred as per design. Basic functional operation of the data relay in a multichannel mode was achieved although test implementation requirements necessitated the omission or variation in certain of the operating subsystems.

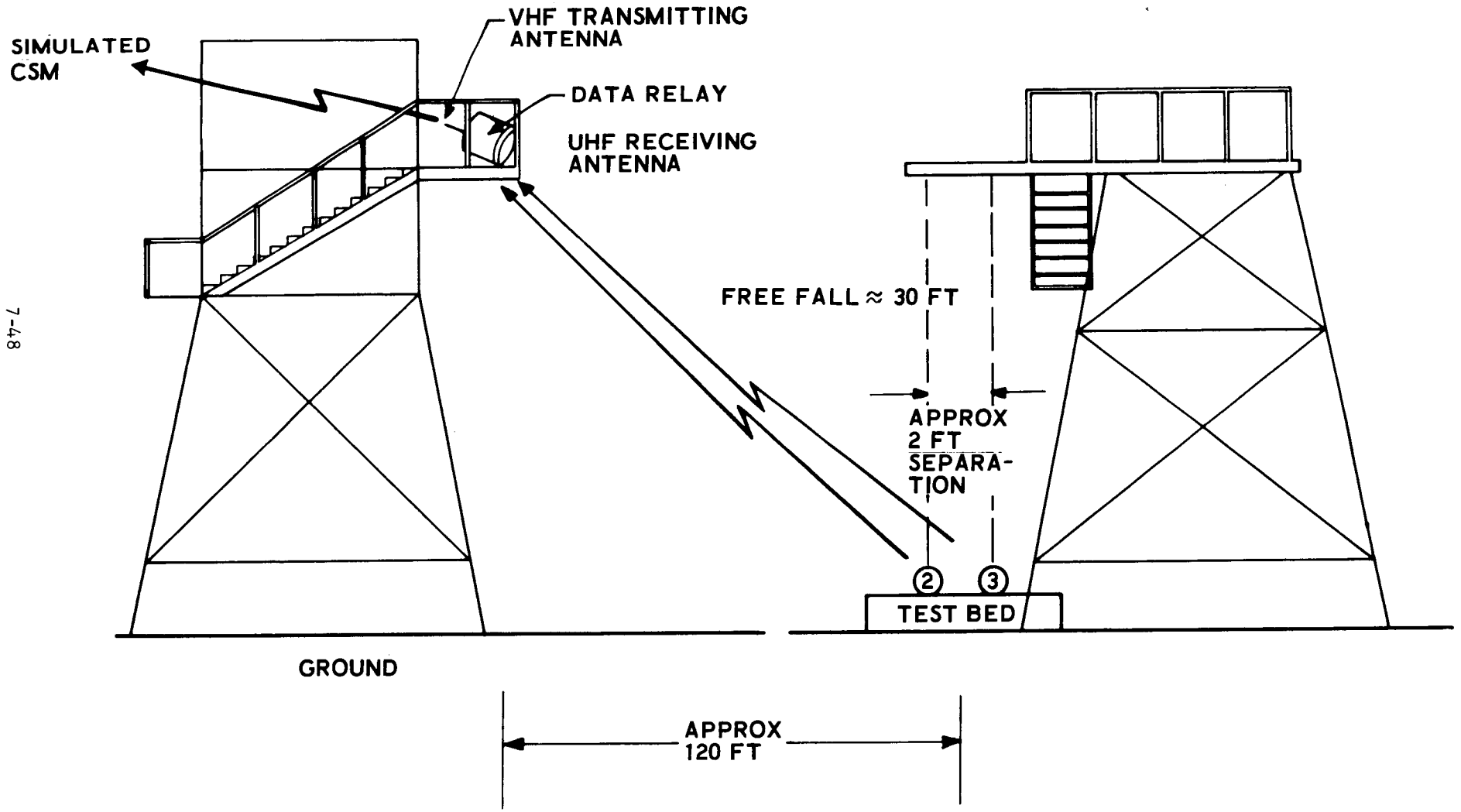

FIGURE 7-26. MULTIPLE DROP TEST SETUP

7.3.1 PENETROMETER AND DATA RELAY OPERATION

The block diagram of Figure 7-27 identifies the major elements and subsystems employed in the multiple drop test. Prototype Nos. 2 and 3 simultaneously radiated UHF signals to the data relay. These signals were received and detected with the data signals recorded onsite with an FM tape recorder. The primary signals monitored were carrier shifts (2), impact data signals (4), diversity switch position, and a reference timing signal. With operation of the data transmission section of the relay, the data signals were relayed for reception, recording, and real time display at the Aeronutronic ground station (CSM equivalent). Carrier and subcarrier channel frequencies employed are also shown in Figure 7-27.

Prior to the multiple drop system tests, basic operation of the data relay was verified. The functional testing performed included receiver channel tuning and sensitivity checks, discriminator sensitivity, AM detector performance, and VCO and transmitter performance checks. All active relay channels were adjusted for standard full scale input-output signal levels.

System integration checks with the Aeronutronic ground station (simulating the CSM receiving function) were accomplished utilizing existing roof-mounted auxiliary transmitting and receiving antennas. Reception at the Aeronutronic ground station was verified and data channels were exercised. Initial operation was not completely satisfactory because of an apparent low rf SNR at the ground station receiver. The lack of adequate SNR was attributed to lossy transmission lines running between the equipment and the roof-mounted auxiliary antennas. Another contributing factor was a lower than desired transmitter modulation sensitivity as evidenced by the earlier transmitter performance checks. Basic operation, however, was functionally correct despite the noisy performance. Improved operation was anticipated from the actual test site.

Penetrometers utilized external power for all bench tests and preliminary testing. Penetrometer internal temperature was noted periodically during tests. A basic three point functional calibration check (i.e., 0, 100 mv and 200 mv, 500 Hz full sine wave input) was utilized to check the penetrometer sensitivity characteristic. Basic penetrometer operation of Prototype Nos. 2 and 3 checked satisfactorily.

7.3.2 AERONUTRONIC GROUND STATION CSM EQUIVALENT

The Aeronutronic ground station was employed to simulate the reception function performed by the CSM. The Aeronutronic facility is a standard IRIG FM/FM telemetry ground station equipped with constant bandwidth subcarrier discriminator reception capabilities. The standard channels 1C through 8C (as identified in Figure 7-27) were set up and adjusted in accordance with channel limits.

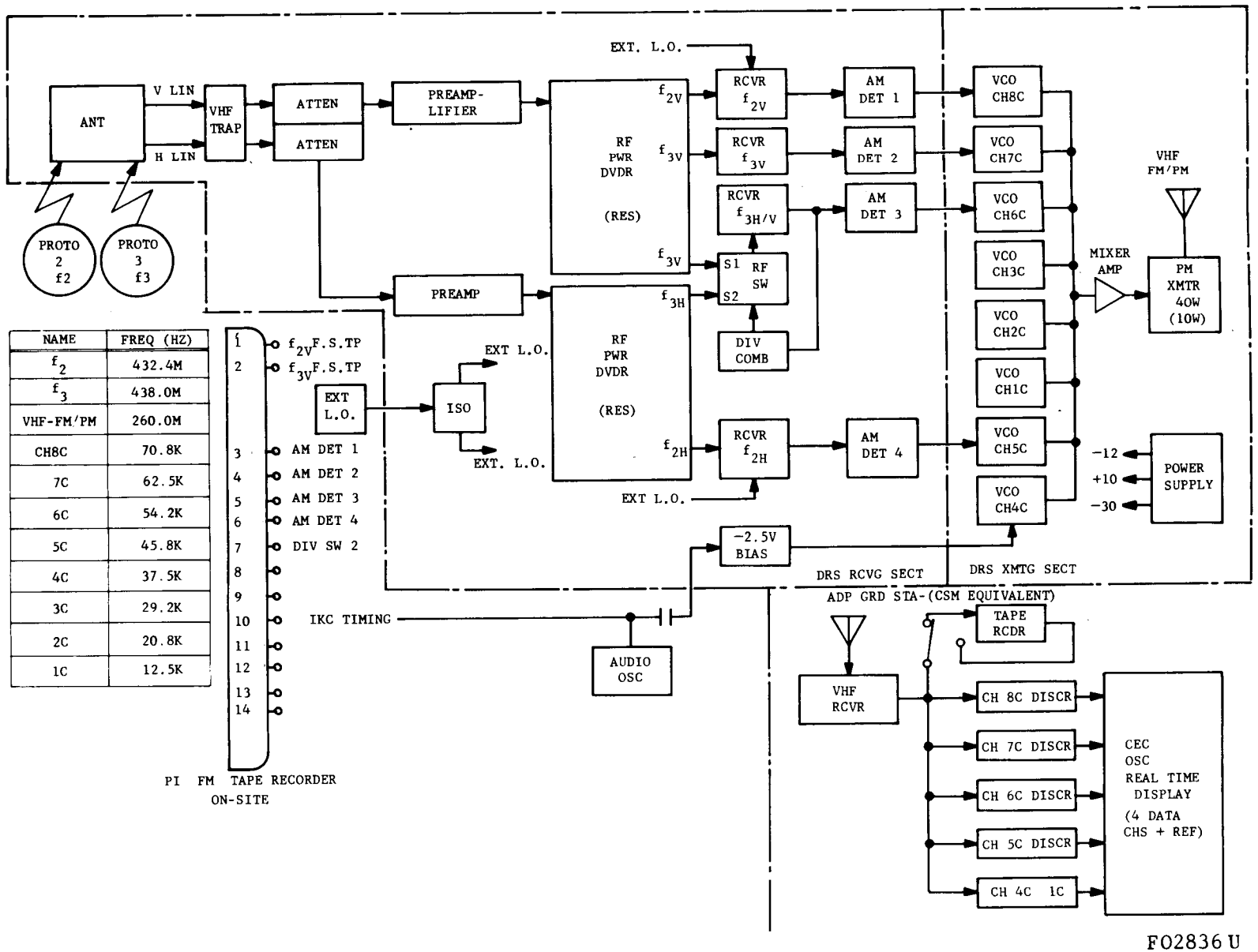

NAME	FREQ (HZ)
f_2	432.4M
f_3	438.0M
VHF-FM/PM	260.0M
CH8C	70.8K
7C	62.5K
6C	54.2K
5C	45.8K
4C	37.5K
3C	29.2K
2C	20.8K
1C	12.5K

F02836 U

FIGURE 7-27. LPS MULTIPLE DROP SYSTEM TEST CONFIGURATION

Reception of data relay transmissions consisting of simulated electrical input signals to the relay or of actual penetrometer derived input signals was verified. Data recording and realtime oscillograph operation was verified.

7.3.3 MULTIPLE DROP TESTING

Prior to actual test runs, equipment was set up as denoted by Figures 7-26 and 7-27 and overall system functional tests were performed. On-site and Aeronutronic ground station data acquisition and recording functions were checked. Initial penetrometer drop tests were performed to exercise the overall system and determine rf and data channel performance levels. The initial tests exhibited poor rf signal-to-noise performance at the Aeronutronic ground station receiving system. A relay transmitter-antenna mismatch problem in conjunction with reduced modulation sensitivity of the transmitter, coupled with possible Aeronutronic ground station receiving antenna anomalies, was believed to be the cause of the poor SNR performance. To expedite the tests, an FM signal generator and power amplifier combination, modulated with the composite constant bandwidth subcarrier data, was employed as the data relay transmitter. Satisfactory SNR performance was achieved at the receiving station and multiple drop testing resumed.

The initial drop tests resulted in progressively poorer impact data signatures. Further troubleshooting and testing was conducted and the problem was traced to inadequate penetrometer battery charge capacity. Penetrometer batteries were recharged and subsequent tests were run to verify the test findings.

Multiple drop tests were again resumed and the basic overall system functional performance of the Lunar Penetrometer System was successfully demonstrated. A series of four tests were completed. Prototype Nos. 2 and 3 were "simultaneously" dropped from a height of 25 feet. Impact velocities of 40 ft/sec were achieved. Excerpts of the real time data recorded at the Aeronutronic ground station are shown on Figure 7-28. The g values obtained were derived from Hyge captive calibration data for each penetrometer. The f_{2v} and f_{3v} designations refer to "vertical" polarization reception channels for Prototype Nos. 2 and 3, respectively. The "horizontal" polarization reception channels were similarly received with good fidelity, although they were not excerpted for presentation. Because the testing was conducted at the very close of the program, only limited time remained to qualitatively evaluate the test results.

The multiple drop test was considered an adequate functional demonstration of the system operation; however, any real quantitative evaluation of system performance would demand a more extensive detailed test and evaluation program. Certain elements of the system, such as transmitter and antenna switching operation, were not adequately demonstrated because of last minute substitutions or earlier development delays. Morever, the one-shot nature of the multiple drop test would constitute only a qualitative demonstration of these elements at best.

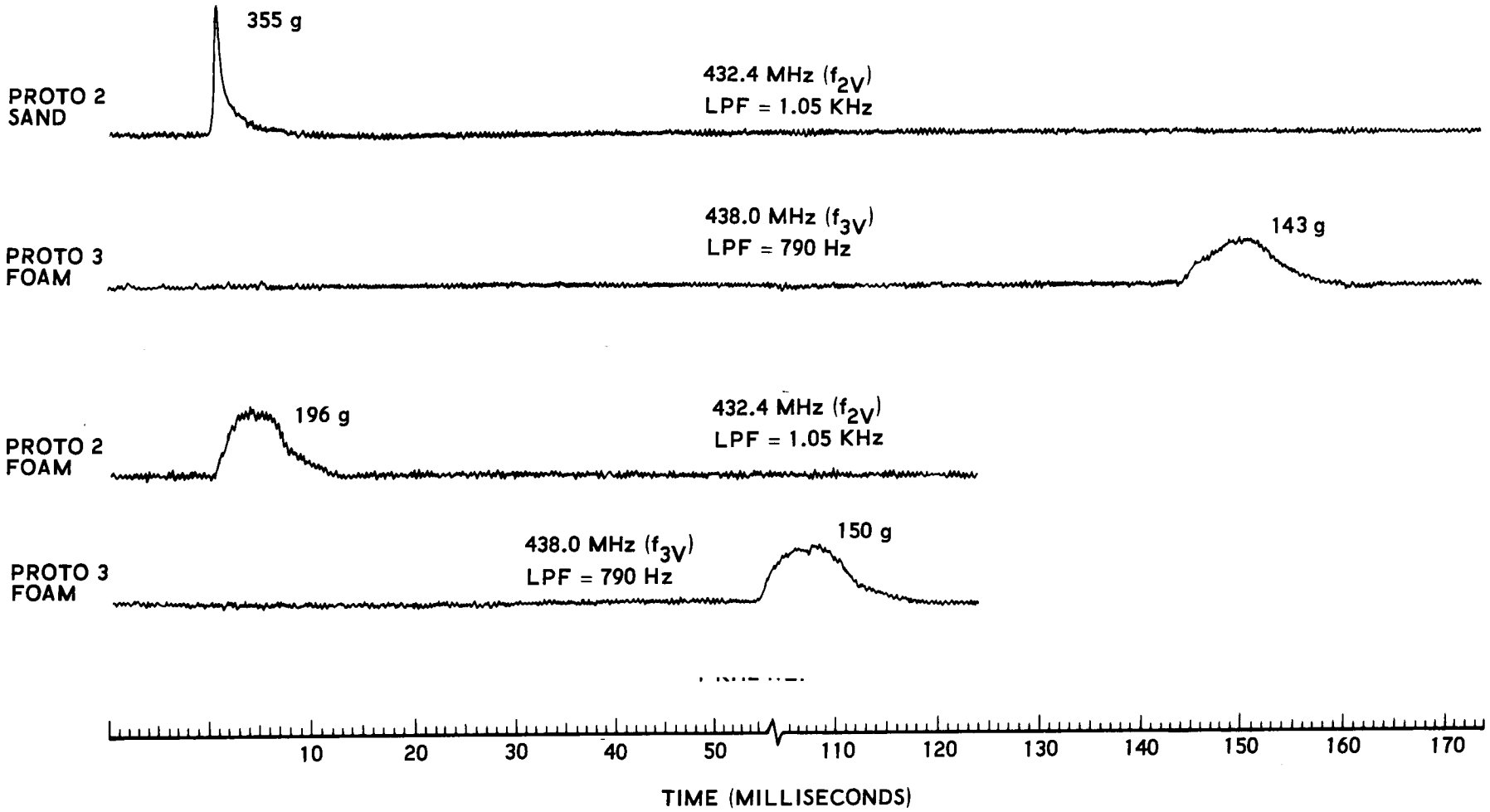

FIGURE 7-28. MULTIPLE DROP TESTS

SECTION 8

RELIABILITY

8.1 SUMMARY OF RELIABILITY ACTIVITIES

has been active in Phase I of the Lunar Penetrometer Program in the following areas:

(1) Performing reliability tradeoff studies and analyses

(2) Performing and updating reliability predictions

(3) Establishing and updating a parts status list

(4) Supporting design review activities.

8.1.1 TRADEOFF STUDIES AND REDUNDANCY ANALYSES

Early in the program, a reliability tradeoff study was performed to determine the optimum of the following two data relay configurations:

(1) A relay system for the salvo of eight penetrometers, consisting of two receiving antennas and rf preselectors, a power divider, eight diversity switches, eight receivers, eight SCO's, and one transmitter and antenna;

(2) A relay system for the salvo of two sets of four penetrometers This system is similar to (1) except that there are only four each of

the diversity switches, receivers, and SCO's. In addition, a frequency switch is required for each receiver.

The results of the study indicated that the probability of the system functioning properly for all eight penetrometers is greater for (2) than it is for (1). This was expected since there is less equipment which must operate. However, (1) has a higher probability of successfully providing the desired functions if any number less than eight of eight is considered. That is, there is a higher probability of receiving and transmitting data from at least seven of eight penetrometers with (1) than with (2). Then, from an overall mission success standpoint of returning some useful data from each flight, of the two systems considered, (1) was recommended.

A redundancy analysis was performed to determine the reliability advantage gained by having redundant transmitters in the data relay system. It was predicted that a system with a single transmitter would have a reliability of 0.975. Redundant transmitters increase the system reliability to 0.979. These results indicated that there was not enough gain in system reliability to warrant recommendation of redundant transmitters.

A comparative reliability evaluation of the data relay systems utilizing scanning diversity and maximal-ratio diversity was performed. The scanning diversity system analyzed utilized 8 receivers with diode switching between antennas. The maximal ratio system utilized 16 receivers and signal combining. This analysis indicated that the reliabilities of the two systems were comparable: 0.975 for the scanning diversity, and 0.977 for the maximal ratio. From a component parts count, the maximal ratio method is more complex than the scanning diversity method. A lower reliability with the maximal ratio method might be expected; however, an assumption was made that if any single receiver fails, there is a 60 percent chance that the other receiver can satisfactorily receive and process the penetrometer signal.

An investigation was performed on the relative merits of solder joints and resistance welded joints for high impact applications. Each of these methods of making an electrical connection has merit for particular applications. Based on the results of a test program conducted by the Bell System at their Columbus laboratory, it was determined that the solder connection was best for the penetrometer application since it performed best under shock environments. The basic assumption was made that the solder connection was made properly. The 100 percent microscopic inspection by a qualified Q.C. inspector provides assurance that the soldering is being done properly on the penetrometer.

8.1.2 RELIABILITY PREDICTIONS

Early in the program, a rough-cut reliability prediction for the penetrometer ball of 0.990 was made. This value was based on the very limited information available on the system at the time.

At a later date the prediction was revised to a value of 0.983 and was based on more updated information. The predominant factor in this prediction was the estimate of the probability of solder joints surviving a 10,000 g impact.

The prediction of 0.9945, which is included in Paragraph 8.2 of this report, is a further updated value based on the most recent information available. The increase in reliability over the previous prediction was due mainly to a higher probability of impact survival of solder joints which was based on the additional shock testing performed without a solder connection failure.

8.1.3 PARTS STATUS

A parts qualification status list for those parts used in the Prototype 1 penetrometer was prepared and submitted as a part of the Preliminary [illegible] 25 November 1969.

An updated parts status list is included in Section 5 of this report.

8.1.4 DESIGN REVIEW ACTIVITIES

Reliability participated in the five design reviews held during Phase I of the lunar penetrometer program. This participation included the critical review and comment on the design, the taking and publishing of minutes and action items, and the follow-up required to assure successful completion of all action items.

8.2 RELIABILITY PREDICTIONS

8.2.1 SYSTEM RELIABILITY

The predicted reliability of the lunar penetrometer system is 0.954. This is defined as the probability that all eight acceleration versus time profiles will be successfully transmitted to the CSM.

Since the successful functioning of all equipment is required for complete mission success, the reliability model is merely a series system as shown in Figure 8-1. The reliability of series systems is given by:

$$R_{system} = \prod_{i=1}^{n} R_i$$

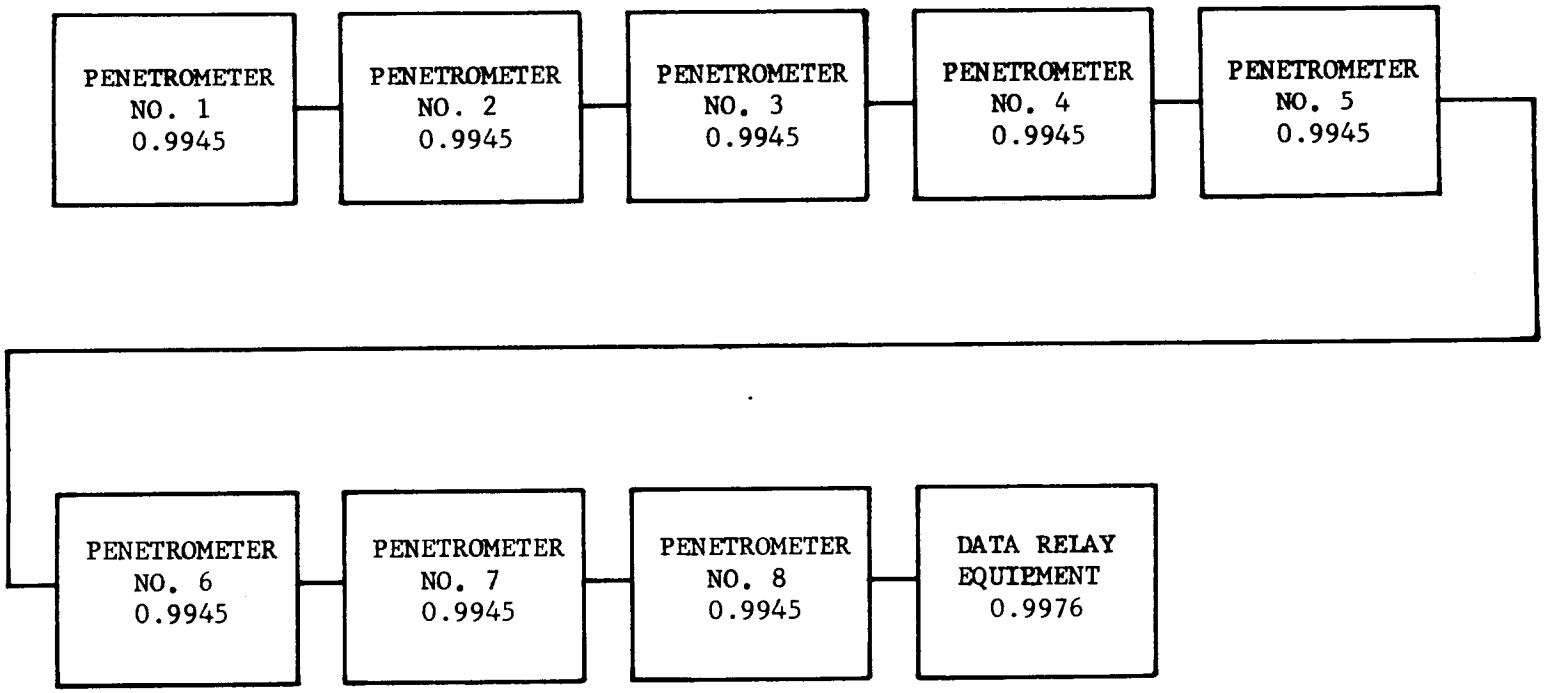

FO3753 U

$$\text{SYSTEM RELIABILITY} = \prod_{i=1}^{n} R_i = 0.954$$

FIGURE 8-1. RELIABILITY LOGIC DIAGRAM - LUNAR PENETROMETER SYSTEM

Where

R_i = reliability of the i^{th} series element

n = total number of elements in the system

π = an operational symbol denoting a repetitive product containing n factors.

8.2.2 PENETROMETER

The predicted reliability of one penetrometer is 0.9945. The reliability logic diagram for the penetrometer is shown in Figure 8-2. The subassembly predictions summarized in Table 8.1 were calculated utilizing the failure rates contained in MIL-HDBK-217 and the methods described in MIL-STD-756A. The following is a list of the assumptions made:

(1) All parts are electrically stressed at 60 percent of maximum ratings. Since all of the actual stress levels are not yet available, a realistic average will be used.

(2) [illegible] is the maximum design limit.

(3) An environmental stress factor of 100 will be used for the operational reliability predictions. MIL-STD-756A lists an environmental stress factor of 80 for missile equipment under launch and/or boost environments and the penetrometer high impact shock is considered more severe than the missile launch and boost environments.

(4) The failure rate of the accelerometer is the worst case value as listed in the FARADA failure rate data. Sufficient information is not available to justify a lower failure rate even though it is suspected that the value used is somewhat high.

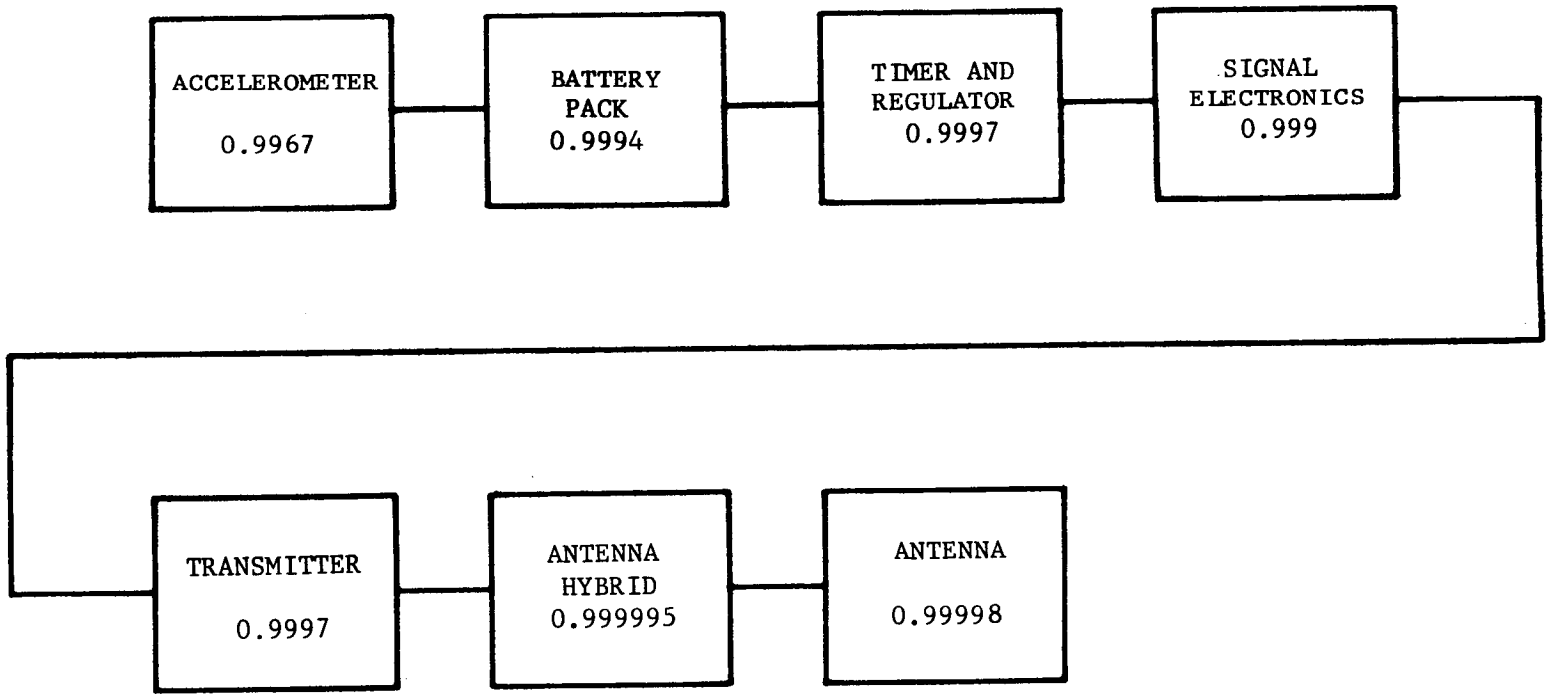

$$\text{PENETROMETER RELIABILITY} = \prod_{i=1}^{n} R_i = 0.9945$$

FIGURE 8-2. RELIABILITY LOGIC DIAGRAM - LUNAR PENETROMETER

(5) The battery cell failure rate is the upper limit value listed in the AVCO Corporation "Reliability Engineering Series - Failure Rates," dated April 1962. Sufficient information is not available to justify the use of a lower failure rate even though it is suspected that the value used is somewhat high.

(6) The probability of impact survival of a solder connection is 0.999995. This estimate has been updated since the Preliminary Report due to the numerous shock tests performed on the module and ball level without a solder connection failure.

(7) The failure of any one component or the opening of any solder connection will fail the mission.

TABLE 8.1

PENETROMETER SUBASSEMBLY RELIABILITY PREDICTION SUMMARY

Subassembly	Operational Reliability	X	Probability of Impact Survival	=	Subassembly Reliability
Accelerometer	0.9967		0.999995		0.9967
Battery Pack	0.9994		0.99998		0.9994
Timer & Regulator	0.999988		0.99972		0.9997
Signal Electronics	0.99994		0.999		0.999
Transmitter	0.999981		0.9997		0.9997
Antenna Hybrid	0.99999998		0.999995		0.999995
Antennas	0.99999997		0.99998		0.99998
Penetrometer Reliability					0.9945

The predicted reliability of the penetrometer has improved from 0.983 predicted in the Preliminary Reliability Report to the 0.9945 predicted in this report on the basis of an improvement in the probability of impact survival of a solder joint. Further improvement is possible in this area as well as in the area of accelerometer and battery cell failure rates resulting in an expected overall penetrometer reliability improvement.

The math models and calculations of the subassembly reliability predictions are shown in Tables 8.2 through 8.8.

TABLE 8.2

ACCELEROMETER RELIABILITY PREDICTION

Operational Reliability = $e^{-k\lambda t}$ = 0.9967

where

k = environmental factor = 100

λ = operational failure rate = 200%/1000 hr, and

t = operating time = 1/60 hour.

Probability of Impact survival = $(P_s)^n$ = 0.999995

where

P_s = probability of impact survival of one solder joint = 0.999995, and

n = number of solder joints = 1.

Subassembly Reliability = $(e^{-k\ t})\ \ (P_s)^n$ = 0.9967

TABLE 8.3

BATTERY PACK RELIABILITY PREDICTION

Part Type	Quantity	Failure Rate (%/1000hr)	Total F.R. (%/1000hr)
Battery cell	25	1.43	35.75

Operational Reliability = $e^{-k\ t}$ = 0.9994

where

k = environmental factor = 100,

= operational failure rate = 35.75%/1000 hr, and

t = operating time = 1/60 hour.

Probability of Impact Survival = $(P_s)^n$ = 0.99998

where

P_s = probability of impact survival of one solder joint = 0.999995, and

n = number of solder joints = 30.

Subassembly Reliability = $(e^{-k\lambda t})\ (P_s)^n$ = 0.9994

TABLE 8.4

TIMER AND REGULATOR RELIABILITY PREDICTION

Part type	Quantity	Failure Rate (%/1000 hr)	Total F.R. (%/1000 hr)
Resistor, Fixed Carbon Comp	11	0.002	0.022
Capacitor, Fixed, Ceramic	4	0.001	0.004
Diode, IN459	5	0.036	0.180
Diode, zener, VZ 7.18	1	0.036	0.036
Diode, zener, IN4104	1	0.036	0.036
Diode, zener, IN703A	1	0.036	0.036
Transistor, 2N2222A	4	0.072	0.288
Transistor, dual, 2N3609	1	0.144	0.144
TOTAL			0.746

Operational Reliability = $e^{-K\lambda t}$ = 0.999988

where

k = environmental factor = 100,

λ = operational failure rate = 0.746%/1000 hr, and

t = operating time = 1/60 hr.

Probability of Impact survival = $(P_s)^n$ = 0.99972

where

P_s = probability of impact survival of one solder joint = 0.999995, and

n = number of solder joints = 57.

Subassembly Reliability = $(e^{-K\lambda t})\ (P_s)^n$ = 0.9997

TABLE 8.5

SIGNAL ELECTRONICS RELIABILITY PREDICTION

Part Type	Quantity	Failure Rate (%/1000 hr)	Total F. R. (%/1000 hr)
Resistor, Fixed, Metal film	27	0.024	0.648
Resistor, Fixed, Carbon Comp.	9	0.002	0.018
Capacitor, Fixed, Glass	2	0.0004	0.0008
Capacitor, Fixed, Tantalum	6	0.016	0.076
Capacitor, Ceramic	9	0.001	0.009
Capacitor, Mica	1	0.007	0.007
Diode, FD829	6	0.036	0.216
Diode, 1N4104	1	0.036	0.036
Transistor, 2N2608 FET	1	0.072	0.072
Transistor, μ116	1	0.072	0.072
Transistor, 2N3382 FET	1	0.072	0.072
Transistor, 5U655A	2	0.072	0.144
Transistor, dual, 2N3609 FET	2	0.144	0.288
Transistor, dual, Md981	1	0.144	0.144
Integrated CKT, A702A	2	0.885	1.770
TOTAL			3.575

Operational Reliability = $3^{-K\lambda t}$ = 0.99994
where
k = environmental factor = 100,
t = operating time = 1/60 hr,
= operational failure rate = 3.575%/1000 hr

Probability of impact survival = $(P_s)^n$ = 0.999
where
P_s = probability of impact survival of one solder joint = 0.999995, and
n^s = number of solder joints = 210.
Subassembly Reliability = $(e^{-k\lambda t})$ $(P_s)^n$ = 0.999

TABLE 8.6

TRANSMITTER RELIABILITY PREDICTION

Part Type	Quantity	Failure Rate (%/1000 hr)	Total F. R. (%/1000 hr)
Resistor, Fixed, Carbon Comp.	17	0.002	0.034
Resistor, Fixed, Metal	12	0.024	0.288
Capacitor, Fixed, ceramic	21	0.001	0.021
Capacitor, variable, air	4	0.010	0.040
Capacitor, Feed-thru, Mica	7	0.007	0.049
Diode, PC116 (varicap)	1	0.036	0.036
Transistor, 2N2563	3	0.072	0.216
Transistor, 2N3563	1	0.072	0.072
Transistor, 2N2564	1	0.072	0.072
Transistor, 2N3564	2	0.072	0.144
Transistor, 2N3866	2	0.072	0.144
Inductors	8	0.050	0.050
TOTAL			1.166

Operational Reliability = $e^{-K\lambda t}$ = 0.999981

where

K = environmental factor = 100

λ = operational failure rate = 1.166 %/1000 hr, and

t = operating time = 1/60 hour.

Probability of Impact survival = $(P_s)^n$ = 0.99973

where

P_s = probability of impact survival of one solder joint

n = number of solder joints = 54.

Subassembly Reliability = $(e^{-K\lambda t})\ (P_s)^n$ = 0.9997

TABLE 8.7

ANTENNA HYBRID RELIABILITY PREDICTION

Operational Reliability = $e^{-k\lambda t}$ = 0.99999998

where

K = environmental factor = 100

λ = operational failure rate = 0.001%/1000 hr., and

t = operating time = 1/60 hour.

Probability of impact survival = $(P_s)^n$ = 0.999995

where

P_s = probability of impact survival of one solder joint = 0.999995, and

n = number of solder joints = 1.

Subassembly Reliability = $(e^{-k\lambda t})$ $(P_s)^n$ = 0.999995

TABLE 8.8

ANTENNA RELIABILITY PREDICTION

Part Type	Quantity	Failure Rate (%/1000 hr)	Total F. R. (%/1000 hr)
Antenna	2	0.001	0.002

Operational Reliability = $e^{-k\lambda t}$ = 0.99999997

where

k = environmental factor = 100

λ = operational failure rate = 0.002%/1000 hr, and

T = operating time = 1/60 hour.

Probability of impact survival = $(P_s)^n$ = 0.999980

where

P_s = probability of impact survival of one solder joint = 0.999995

n = number of solder joints = 4.

Subassembly Reliability = $(e^{-k\lambda t})$ $(P_s)^n$ = 0.99998

8.2.3 DATA RELAY EQUIPMENT

The predicted reliability of the data relay equipment is 0.9976. This figure is an extremely rough estimate since little or no design information is available on the data relay at the present time.

The subassembly predictions are summarized in Table 8.9 and were based on estimated parts count. The operating time of the data relay equipment was assumed to be 1/5 hour.

TABLE 8.9

DATA RELAY EQUIPMENT
SUBASSEMBLY RELIABILITY PREDICTION SUMMARY

Subassembly	Reliability
UHF Antennas (2)	0.9999996
Pre-amplifiers (2)	0.9998
Power Dividers (2)	0.9999
Diversity Switch Subsystem	0.9997
Receiver, sub-carrier demod, and FM SCO (8)	0.9988
Transmitter	0.9998
Power Amplifier	0.9998
VHF Antenna	0.9999998
Battery	0.9999
Converter-Regulator	0.9999
Data Relay Equipment Reliability =	0.9976

The realiability logic diagram is shown in Figure 8-3.

The data relay equipment reliability predictions will be updated to more accurate values during Phase II of the lunar penetrometer program.

8.3 PARTS STATUS LIST

An updated list of the parts used on the lunar penetrometer containing part number identification, next assembly identification, manufacturer, MIL specification number, Aeronutronic test history, other qualification

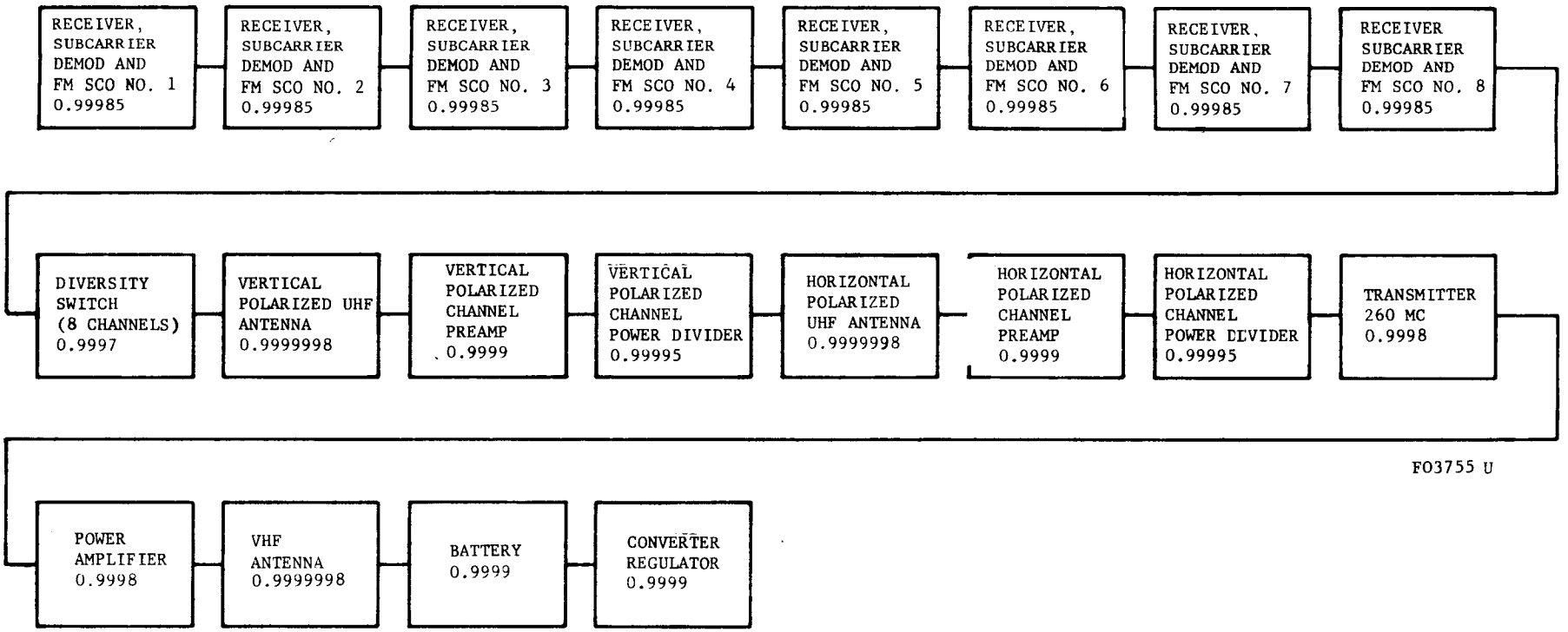

$$\text{DATA RELAY EQUIPMENT RELIABILITY} = \prod_{i=1}^{n} R_i = 0.9976$$

FIGURE 8-3. RELIABILITY LOGIC DIAGRAM - DATA RELAY EQUIPMENT

history, and a statement on whether its qualified for the program or not is included as Table 8.10.

TABLE 8.10

PARTS STATUS LIST

TRANSISTORS

Part No.	Next Assembly	Manufacturer	Mil Part	Aeronutronic Test History	Other Qualification Information	Qual. for Program
2N2222A	Timer Reg. Q2,3,4,5	Raytheon	No	Note 1. Assemblies of parts successfully passed four 10,000 g shocks and three 1000 g shocks on Hyge machine without catastrophic failure.	2N2222A is same basic part as USA 2N2222 which has a good reliability history. 2N2222A is faster switching and higher breakdown.	Yes
2N3609	Timer Req. Q1	General-Micro Electronic	No	See Note 1.	Note 3. No additional reliability history on this part. This is due primarily to comparative newness of part. Note 4. Primary construction is planar epitaxial which has good reliability history.	Yes
SU655	Signal Electronics No. 2 Q5, Q6	Siliconix	No	See Note 1.	See Notes 3 and 4.	Yes
MD981	Signal Electronics No. 2 Q8	Motorola	No	See Note 1.	See Notes 3 and 4.	Yes
2N3609 (Field Effect)	Signal Electronics No. 2 Q3	General-Micro Electronics	No	See Note 1.	See Notes 3 and 4.	Yes
2N3382	Signal Electronics No. 2 Q7	Siliconix	No	See Note 1.	See Notes 3 and 4.	Yes
2N2608	Signal Electronics No. 1 Q2	Siliconix	MIL-S-19500 -295	See Note 1.	See Note 4.	Yes
MA720A (Integrated Circuit)	Signal Electronics No. 1 & 2, A1, A2	Fairchild	No	See Note 1.	See Notes 3 and 4. There are no integrated circuits qualified to MIL SPEC, however, the Fairchild MA702A has been used quite extensively in the industry.	Yes
2N3564	OSC-Buffer Q2, 5	Fairchild	No	See Note 1. Note 2. One assembly of parts passed 50 hammer shocks of 10,000 g or greater, without catastrophic part failure. Part transient parameter shift is unknown.	See Notes 3 and 4.	Yes
2N3563	OSC-Buffer Q1,3,4	Fairchild	No	See Notes 1 and 2.	See Notes 3 and 4.	Yes
2N3866	Frequency Doubler Model 1 Q1,2,3,4	RCA	No	See Notes 1 and 2.	See Notes 3 and 4.	Yes

TABLE 8.10 (Continued)

Part No.	Next Assembly	Manufacturer	Mil Part	Aeronutronic Test History	Other Qualification Information	Qual. for Program
U116	Signal Electronics No. 1 Q4	Siliconix	2N2608 is a MIL part	Has passed system shock and vibration	Same unit as 2N2608 except in TO-46 Package.	Yes
FD829	Signal Electronics No. 2 CR2 to CR7	Fairchild	No	See Note 1.	See Note 4. This part has faster recovery than MIL parts. Fairchild is a leader in this type device.	Yes
1N4104 Zener	Signal Electronics No. 1 and Timer Req CR1, CR6	Motorola	No	See Note 1.	This is a special low level part with noise spec. Basic zener part has good reliability history. Part is of "Whisker" type construction.	Yes
PSI116 Varicap	OSC-Buffer Assy. CR1	PSI(TRW)	No	Limited hammer tests and Hyge shock.	History on PSI varicaps is good. They have been in this field for many years.	Yes
				Resistors		
RCO	Signal Electronics Timer-Regulator	Probably Ohmite or Allen Bradley	MIL-R-11	See Notes 1 and 2.	Parts of this type have had many years of successful application, although carbon composition resistors are not too stable under some environments, such as humidity.	Yes. If transient parameter shift is satisfactory for application.
4200A	Signal Electronics 34 parts	Bourns	No	See Notes 1 and 2 and Aeronutronic document "Penetrometer Component Tests" by H. B. Schellhase dated 15 September 1965.	Not much data available. Vendor reports NASA has used some of these parts; vendor is to supply additional information.	Yes. If ckt requirements permit, the larger transient resistance shifts for higher value units.
CBT-1/2	Signal Electronics R-37, 2000 MEG	IRC	No, although lower resistance value meets MIL-R-11.	See Note 1. Temperature coefficient determined to be satisfactory for this unit. Possible shock instability.	None obtained to date.	Additional shock tests should be performed.
				Additional Diodes		
1N703A	Timer Req. CR5	Motorola	No	See Note 1.	Very old type, selected USN1N746A or 1N747A per MIL-S-19500/127 might be better.	Yes
UZ718	Timer Req. CR2	Unitrode	No	See Note 1.	Unitrode has very good record on Minuteman.	Yes

TABLE 8.10 (Continued)

Part No.	Next Assembly	Manufacturer	Mil Part	Aeronutronic Test History	Other Qualification Information	Qual. for Program
1N459	Timer Req. CR1,3,4	Motorola	MIL-S-19500/193	See Note 1.	Older type with many component hours of experience.	Yes
			Capacitors			
Type RLA	OSC-Buffer, Quadrupler	Mucon	MIL-C-11015 except ribbon leads.	See Notes 1 and 2.	Similar to CK05, CK06 on MIL-C-11015. Mucon on QPL. See IDEP 152.20.50.40-08-02 and IDEP 152.20.50.40-D5-01	Yes
Style 2404	OSC-Buffer, Quadrupler	Erie	MIL-C-11015 Types CK70, CK80, CK81 except for solder mtg.	See Notes 1 and 2.	Erie on QPL for CK70, CK80, and CK81.	Yes
CYFM	Signal Electronics BD No. 2, C13, C14	Corning	CY10, CY15 CY20	Showed approximately 15X greater transient C during shock than VY type capacitor.		Further investigation of this unit required.
VY	Signal Electronics BD No. 1 and No. 2	Vitramon	Similar to CY12, 16 except thinner.	See Notes 1 and 2, Aeronutronic report "LPS Component Shock Test" by BGM dated 10/14/65.	No IDEP reports. Vitramon on QPL for CY12, 16.	Yes
4335	Quadrupler	Johanson	Similar to PC types MIL-C-14409	Have satisfactorily passed a number of hammer tests.	Extensively used for military equipments having high shock and vibration. Used on Ranger at 3000 g. Used by JPL on 60000GT program.	Yes
DM19	Signal Electronics BD No. 1 C19	Elmenco	CM06	See Note 1.	Standard MIL part with excellent history.	Yes
150D	Signal Electronics Timer	Sprague	CS 12, 13 CS 14, 15	See Note 1.	Standard MIL part with good history.	Yes
TS-1K	Timer Req. C1,C2,C3	Semcor	CS 12, 13 CS 14, 15	See Note 1.	IDEP reports very favorable.	Yes
			Connectors			
52-052-000 OSC.	Buffer, Quadrupler	Selectro	No	See Note 1.	No information except meets environmental requirements of MIL-C-22557.	Yes

APPENDIX A

LUNAR PENETROMETER SYSTEM
TEST REPORT FOR PENETROMETER PROTOTYPE NO. 1

A.1 INTRODUCTION

This appendix describes the test results for the Penetrometer Prototype No. 1, the first complete penetrometer to be subjected to environmental and functional tests. The test work was started in accordance with a written general test plan, but the procedures had to be modified during the test sequence because of the condition of the test item. The following sections of this report describe the test sequence in chronological order, present the test results, and draw conclusions from the results.

A.2 TEST SEQUENCE

A.2.1 ANTENNA PATTERN

The first test after complete assembly of the prototype was measurement of the antenna pattern. The pattern was measured at the Aeronutronic antenna range site with a spinning dipole in the standard method used previously for development tests. Figure A-1 is the measured pattern in the plane of the polar loop. The small peaks in the pattern are due to the spinning dipole used for measuring and indicate the polarization axial ratio. The pattern shows the desired omnidirectional characteristics. The bonding of the balsa impact limiter did not degrade the pattern.

A.2.2 POWER OUTPUT REFERENCE

A measurement of relative radiated field strength was made to use as a later comparison for power output. The penetrometer was placed in an

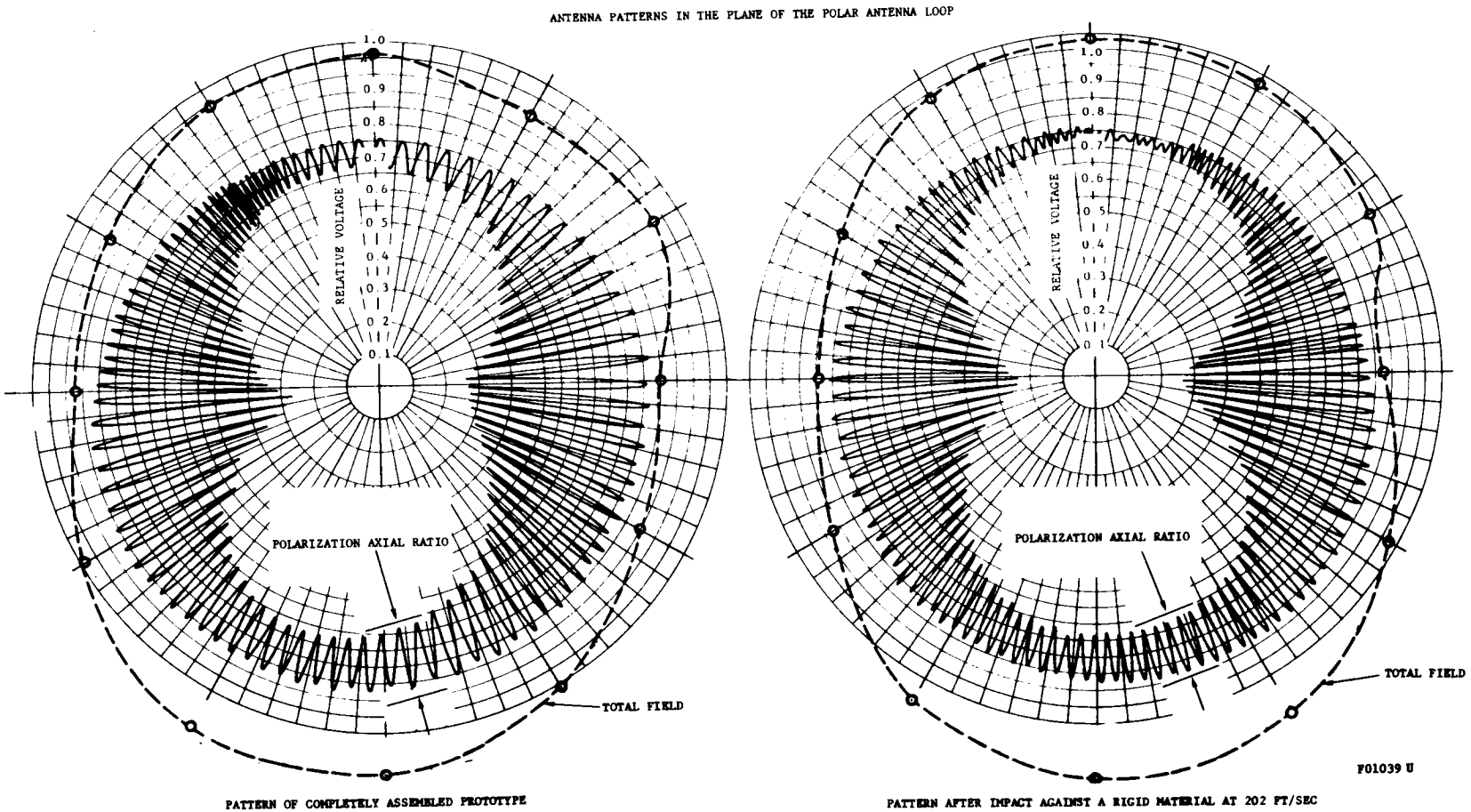

FIGURE A-1. ANTENNA PATTERNS FOR PENETROMETER PROTOTYPE NO. 1

enclosure of rf absorbing material, while the field strength was measured at one known location. The receiving dipole was rotated about its axis to obtain both minimum and maximum values of field strength. The test setup and results are shown in Figure A-2. This measurement was made using the internal battery power of the penetrometer.

A.2.3 BENCH TESTS

Bench tests were made with the assembled penetrometer to measure the linearity and frequency response characteristics. Signals from standard laboratory generators were fed into the signal electronics test point via the umbilical connector. The signal went to the "CALIB" point shown in the schematic on Page 36 of the Seventh Monthly Progress Report, MPR-65-136. The radiated signal from the penetrometer was received by an FM receiver at 435 Mc. The 40 kc output signal was detected by a breadboard AM demodulator. Thus, the measurements involved not only the penetrometer but also a receiver and demodulator. Some difficulty was experienced in making these measurements because of continual transmitter frequency drift.

Figure A-3 shows the measured frequency response characteristics. This measurement included the characteristics of the demodulator filter and part of the low-pass signal electronics filter. The voltage response was found to be down 50 percent or 6 db at 2000 cycles/second.

Figure A-4 is a curve of the measured voltage linearity of the overall penetrometer and receiving equipment. The curve shows the expected compression effect for large signals. The knee in the curve is not as sharp as desired but this may be due to instrument errors and excessive noise pickup.

A.2.4 TEMPERATURE TESTS

Figure A-5 is a graph showing the transmitter frequency drift which occurred during the first two minutes after the penetrometer was turned on. During these tests, there was a pronounced tendency for the penetrometer to stay on several minutes longer than the normal 15-second period after releasing the momentary switch.

At this time, the test probe was withdrawn from the test connector and found to be wet and corroded. The test connector within the penetrometer was also wet and corroded. A piece of litmus paper poked into the probe hole gave a strong base reaction. The open-circuit positive battery

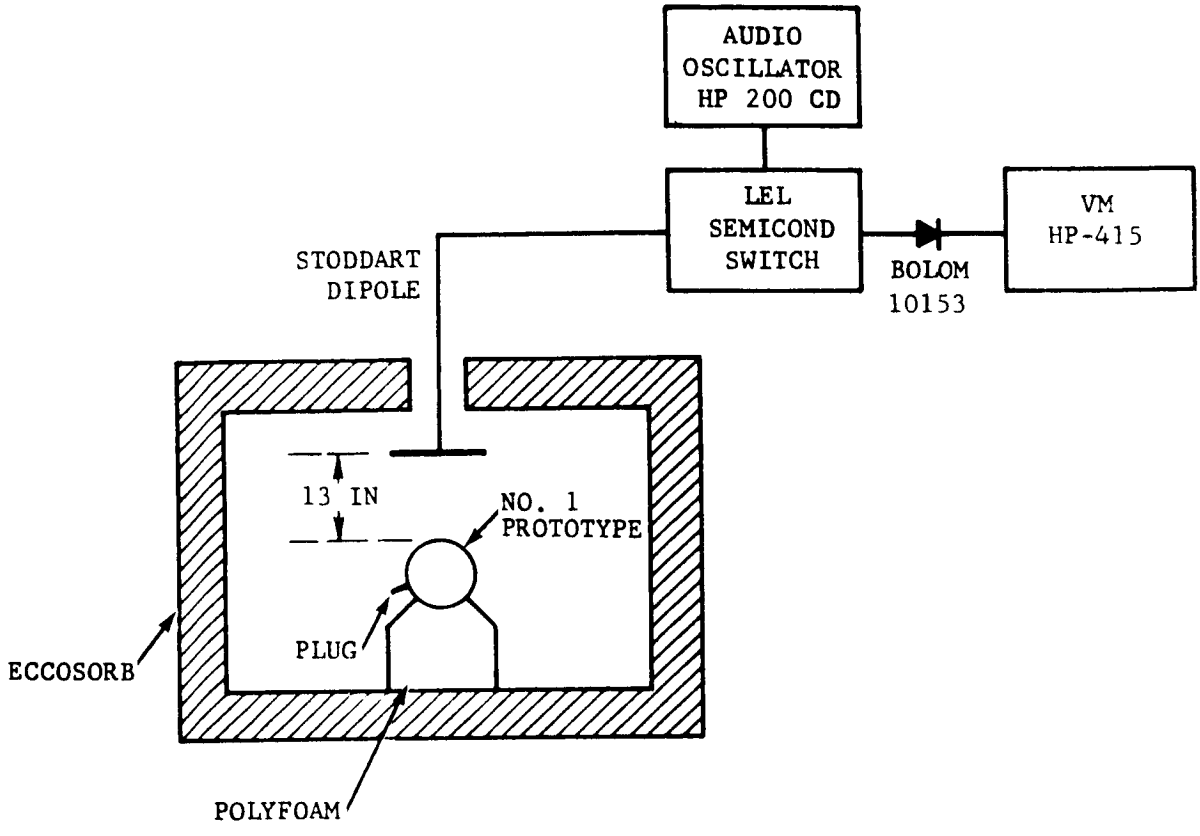

CONDITION		MAXIMUM READING	MINIMUM READING	RELATIVE FIELD STRENGTH
BEFORE IMPACT	10/28/65	-1.5 DB	-3.5 DB	1.34
AFTER IMPACT	11/2/65	-0.3 DB	-3.5 DB	1.76

FO1108 U

FIGURE A-2. POWER OUTPUT REFERENCE MEASUREMENT

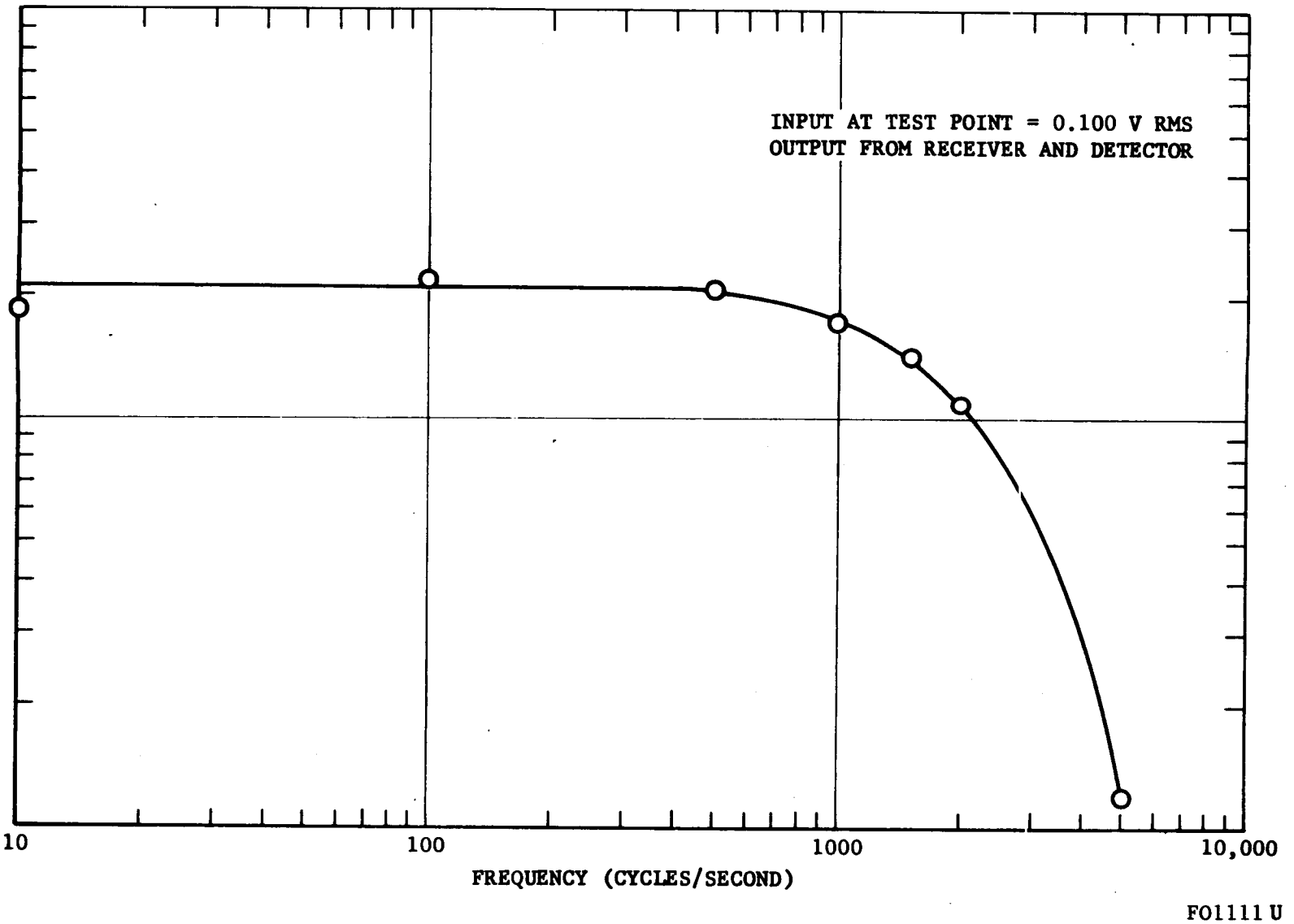

FIGURE A-3. FREQUENCY RESPONSE OF NO. 1 PROTOTYPE

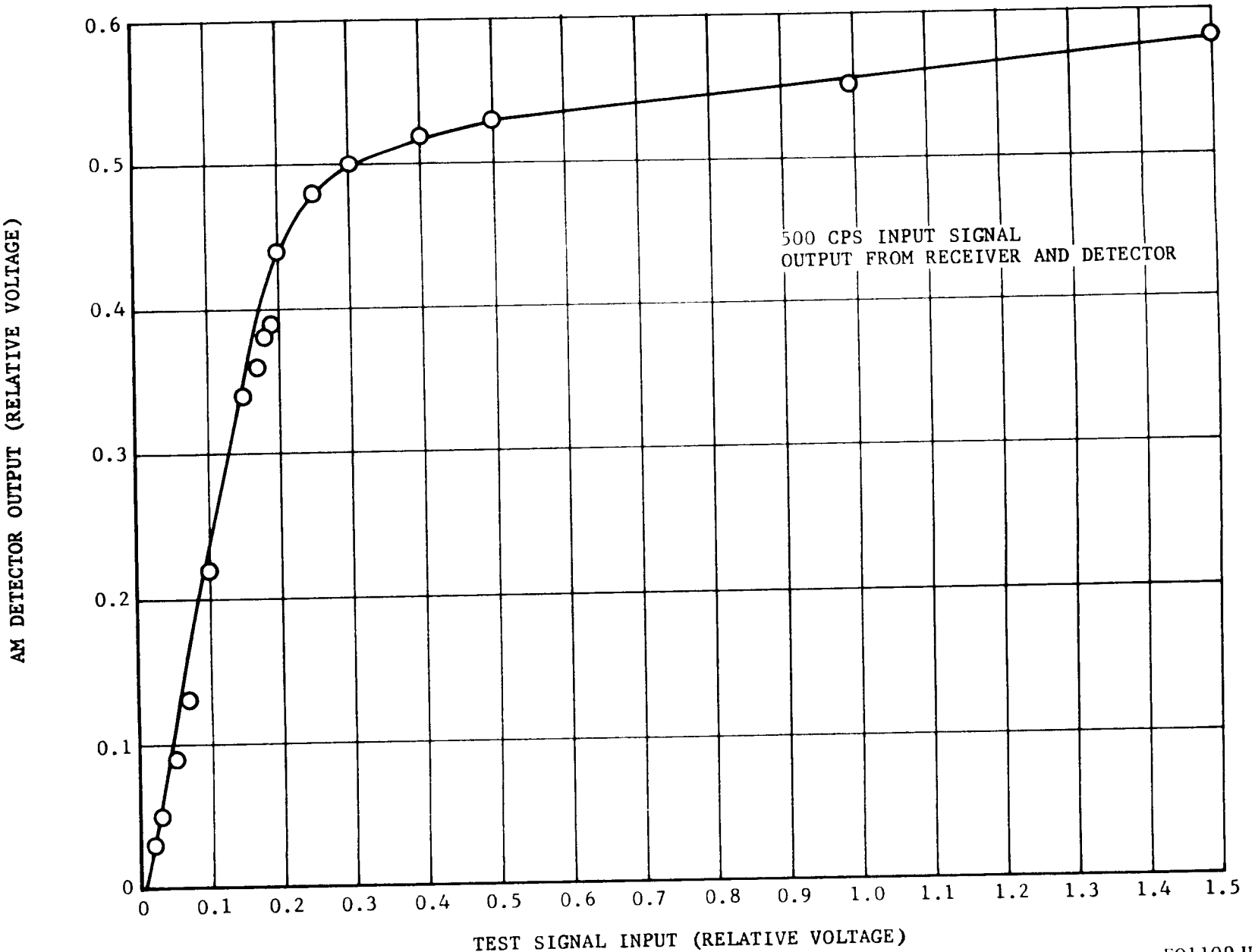

F01109 U

FIGURE A-4. VOLTAGE LINEARITY OF NO. 1 PROTOTYPE

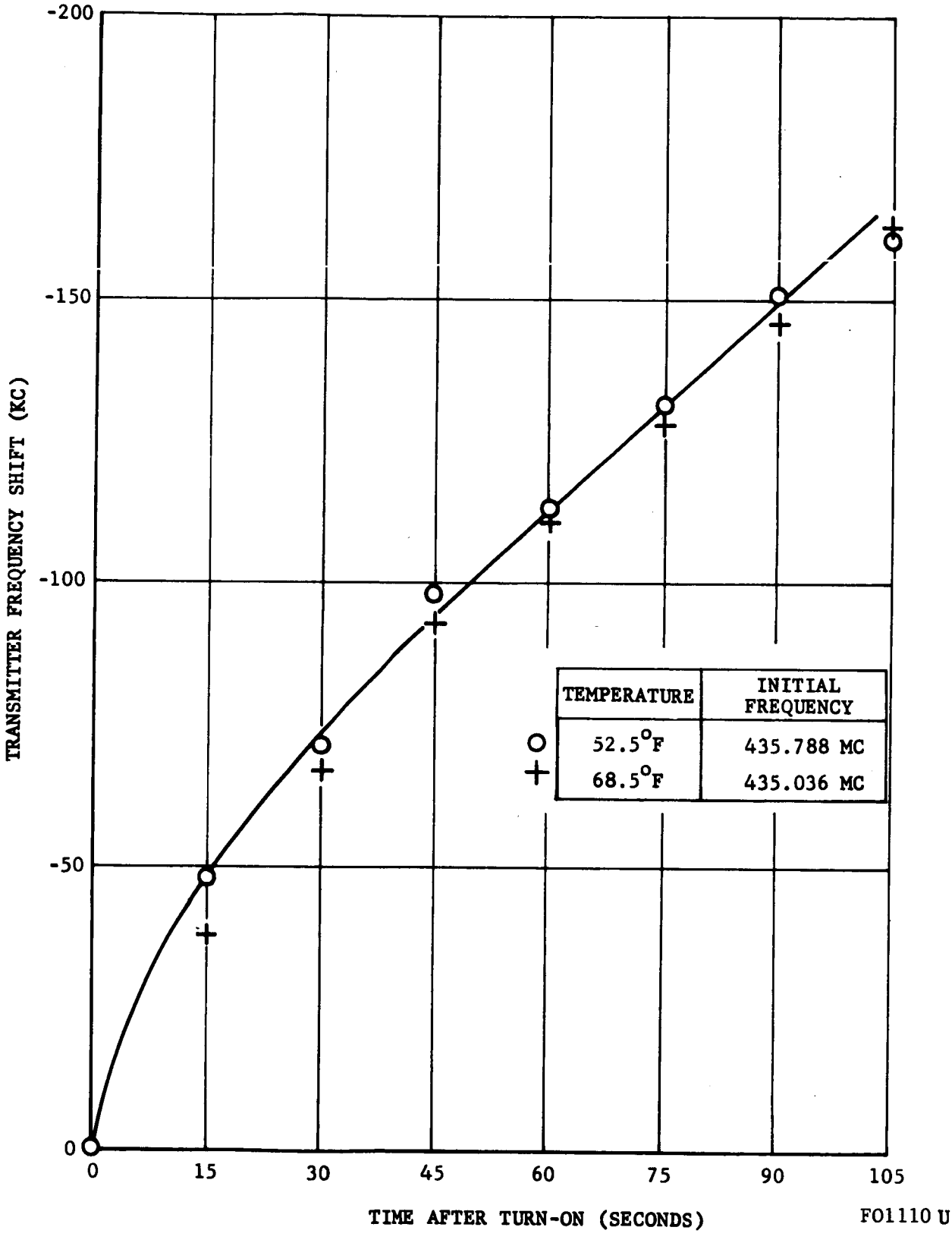

FIGURE A-5. NO. 1 PROTOTYPE TRANSMITTER FREQUENCY TURN-ON TRANSIENT TEST

voltage at this time measured approximately 10 volts instead of the normal 36 volts. It was concluded that the battery was leaking KOH electrolyte and that the test plan would have to be modified. All subsequent testing would have to be done with external power. The testing would have to be accelerated and abbreviated because of the internal damage being done by the leaking electrolyte.

A.2.5 HYGE CAPTIVE ACCELERATION TESTS

The next test was an acceleration calibration in the Hyge captive fixture as shown in Figure A-6. Power was supplied by cables from external regulated supplies. The radiated signal from the penetrometer was received to furnish both AM and FM signals for the oscillograph recorder. The output from a reference accelerometer on the Hyge fixture was also recorded.

The record for the first test is shown in Figure A-7. The acceleration along the polar axis consisted of a peak 433 g pulse followed by a peak 1100 g deceleration. The maximum carrier frequency transient was about 40 kc. There was hardly any discernible AM output, indicating that the accelerometer and signal electornics were not functioning. After the test, strong tapping of the penetrometer failed to produce any acceleration output in the AM channel.

The second test was a repeat of the first except that a constant amplitude 1,000 cps calibration signal was connected to the test point in the signal electronics via the umbilical connector. This signal corresponded roughly to a 200 g half-sine, 1,000 cps acceleration waveform. The oscillograph test record is shown in Figure A-8. The acceleration experienced in this test and the induced transmitter frequency transient were nearly identical with the first test. During the movement of the penetrometer, the AM signal from the constant calibration signal varied in amplitude from 56 to 137 percent of its prior value, in a rather random manner not related to the acceleration.

For the third test, the penetrometer was rotated in the fixture so the acceleration axis was in the plane of the penetrometer equator. A constant simulated acceleration signal was again fed into the signal electronics. The test record is shown in Figure A-9. A transmitter frequency jump of over 100 kc occurred at four places in the test record. These jumps appear to be due to some component movement within the transmitter. The AM output, corresponding to the constant calibration signal, had the same random amplitude variations recorded in the previous test.

A.2.6 HYGE IMPACT TEST

The captive acceleration tests were followed by a hyge impact test in which the penetrometer was thrown at 202 feet/second against a solid concrete block.

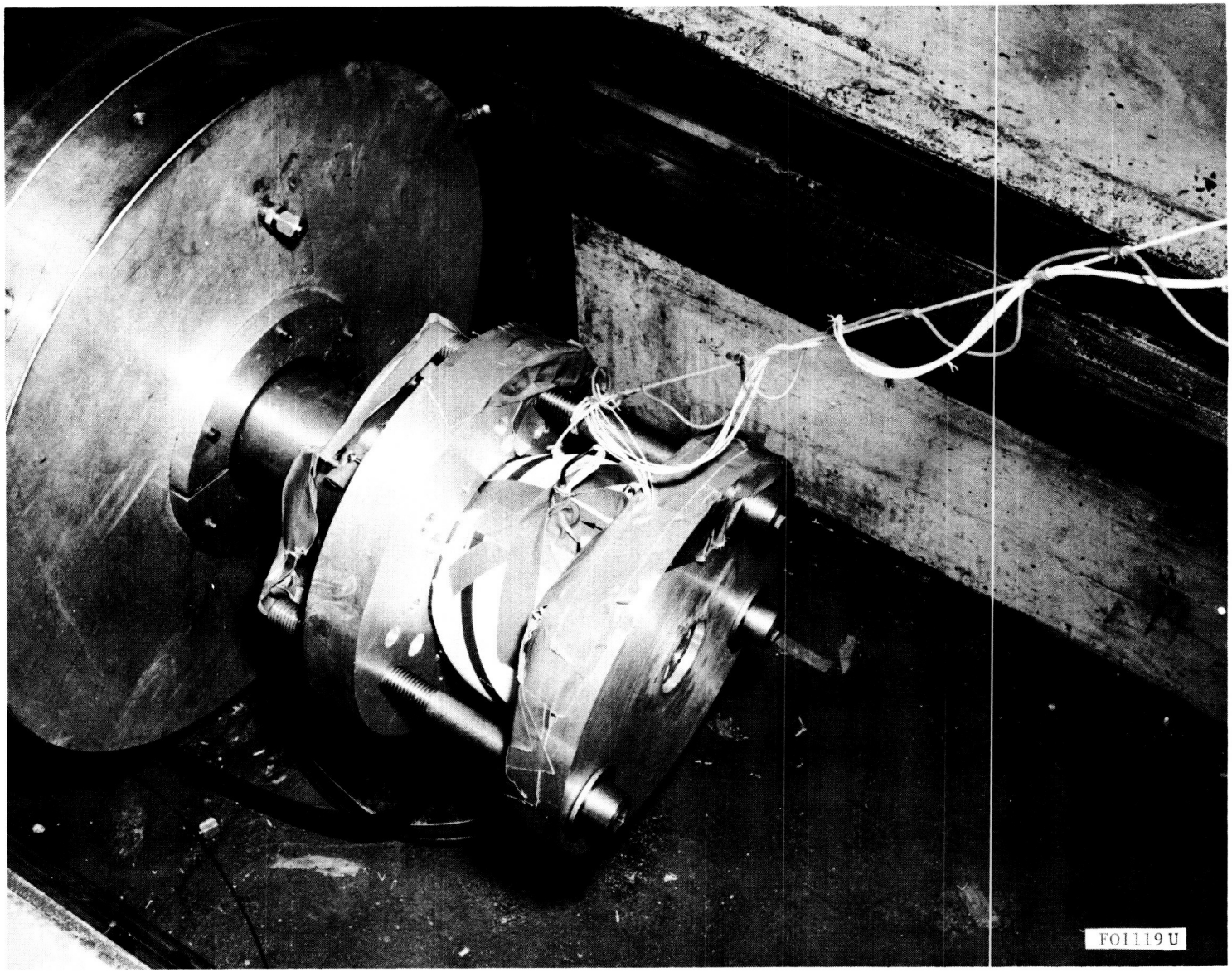

FIGURE A-6. PROTOTYPE PENETROMETER IN HYGE CAPTIVE FIXTURE

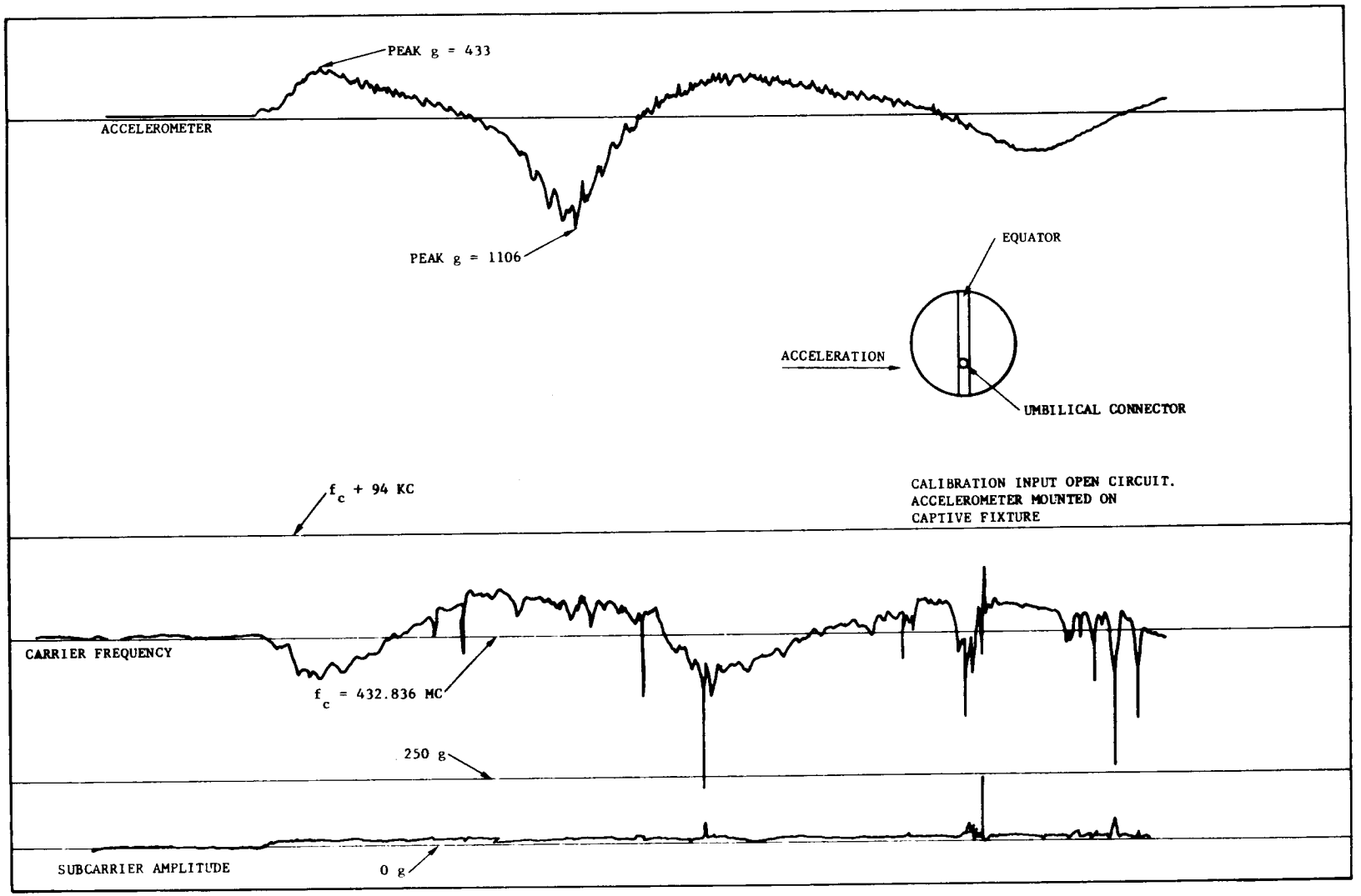

FIGURE A-7. HYGE CAPTIVE TEST RECORD, RUN NO. 1

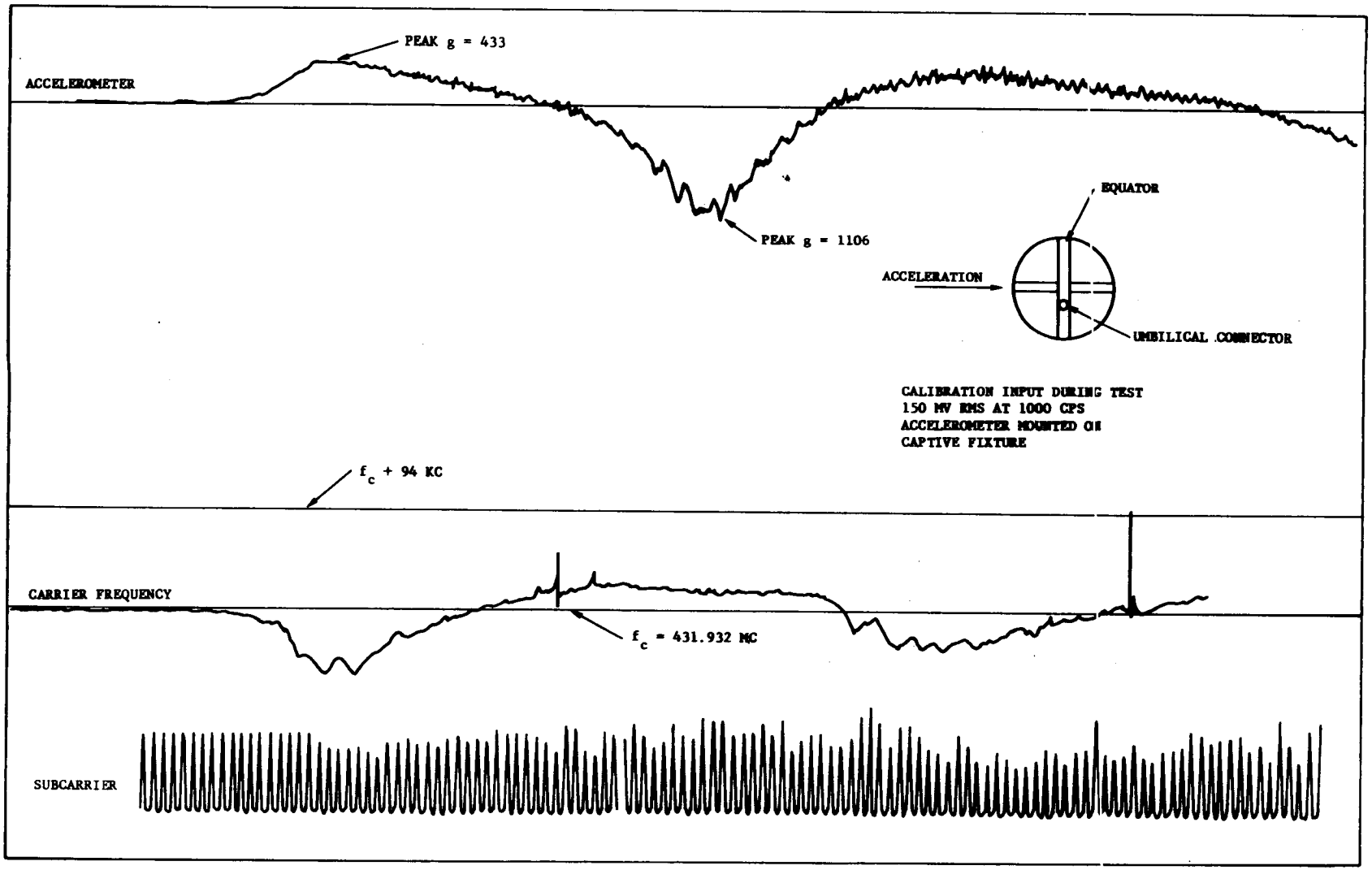

FO1121 U

FIGURE A-8. HYGE CAPTIVE TEST RECORD, RUN NO. 2

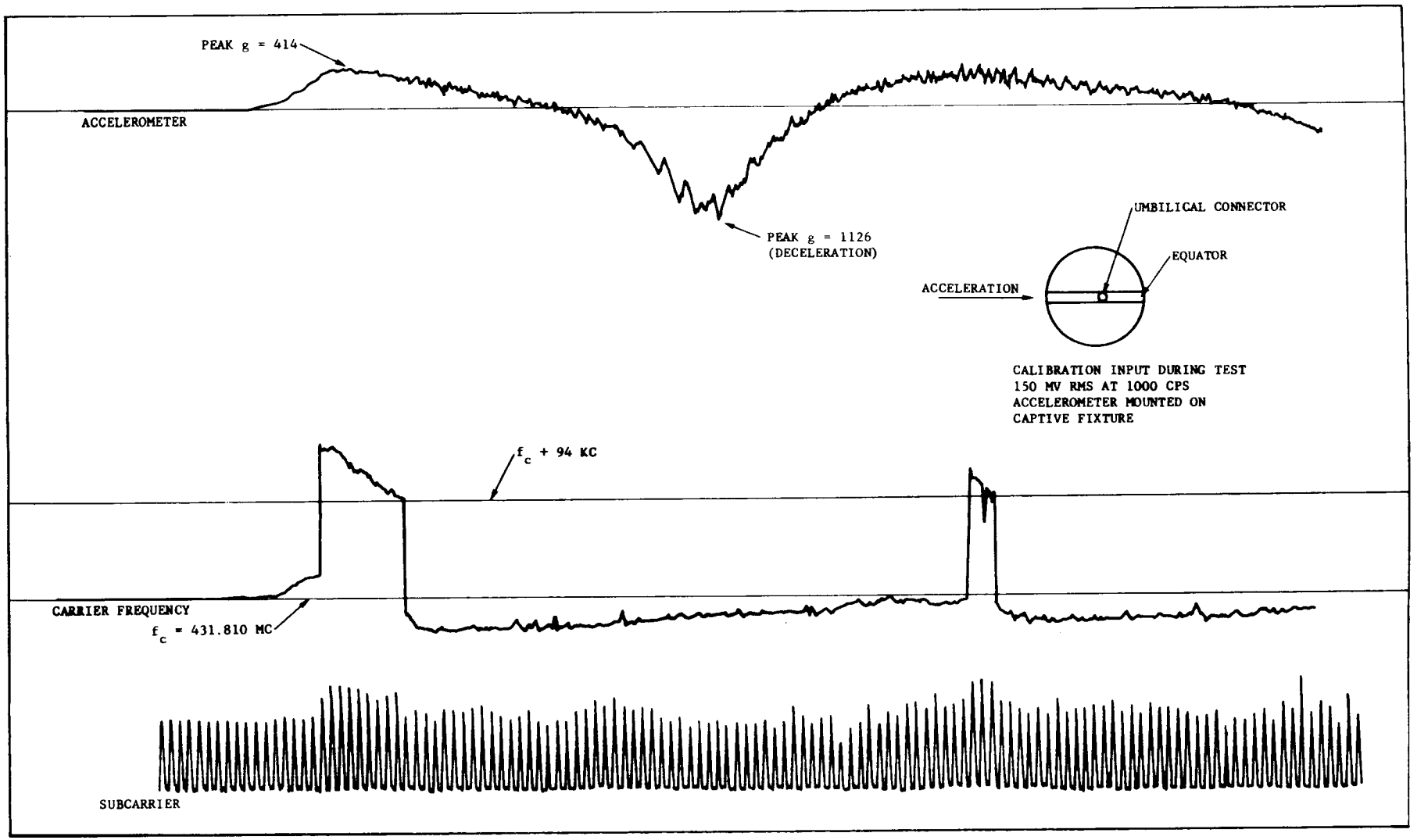

FIGURE A-9. HYGE CAPTIVE TEST RECORD, RUN NO. 3

For the test, the penetrometer was taped into a hemispherical cup on the end of the Hyge ram. External power was supplied by an umbilical cable which was anchored to a metal pin epoxied into the balsa limiter. Velocity of the penetrometer was measured by a photo-cell trap near the impact block.

Figure A-10 is the oscillograph record for this test. A carrier frequency shift of about 90 kc occurred during the launch acceleration of about 500 g. As in the first captive hyge test, there was no AM output signal corresponding to the acceleration sensed by the penetrometer. The external power leads sheared off at the outside of the test probe at the instant of impact. Therefore, there was no measurement of transmitter frequency transient during the impact acceleration of probably 7000 g.

Figure A-11 shows the condition of the penetrometer after impact and also shows the footprint area left on the steel plate covering the concrete block. The diameter of the footprint measured on either the balsa limiter or the impact plate was 6-3/4 inches. This amount of limiter crushing is diagrammed in Figure A-12. The maximum crushed depth is shown to be 1.68 inches. The total available crushing distance over the antennas is 2.00 inches, and elsewhere is 2.50 inches.

The two painted stripes on the penetrometer cover, in Figure A-11, indicate the interior locations of the two antenna loops. The wider red stripe indicates the loop in the equatorial plane.

A.2.7 POWER REFERENCE MEASUREMENT

A post-impact measurement was made to compare the radiated power to that obtained after initial assembly. The procedure was the same as described in Paragraph A.2.2. The results are shown in Figure A-2. The post-impact measurement was slightly higher--probably indicating a change in field pattern rather than a change in output power. Some of the change could also be attributed to the use of external power, the presence of the umbilical cable, and the general inaccuracy of the measurement method.

A.2.8 ANTENNA PATTERN

The antenna pattern measurement, described in Paragraph A.2.1, was repeated except that external power was furnished to the penetrometer. The pattern obtained is shown also in Figure A-1. When this pattern is compared with the pre-impact pattern, it can be seen that no major change occurred in the omnidirectional pattern of the antenna due to the severe impact test.

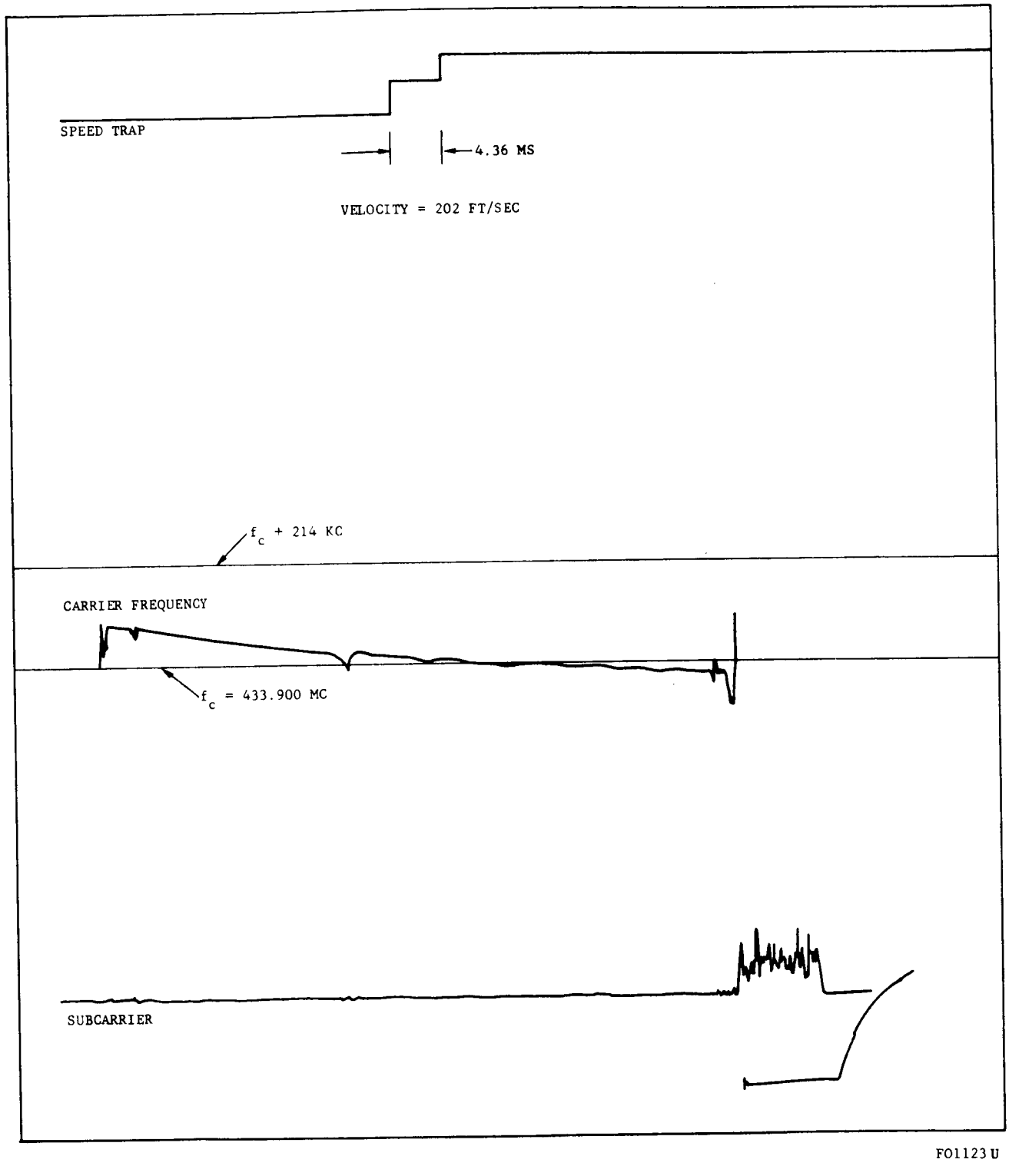

FIGURE A-10. IMPACT TEST RECORD FOR PENETROMETER PROTOTYPE NO. 1

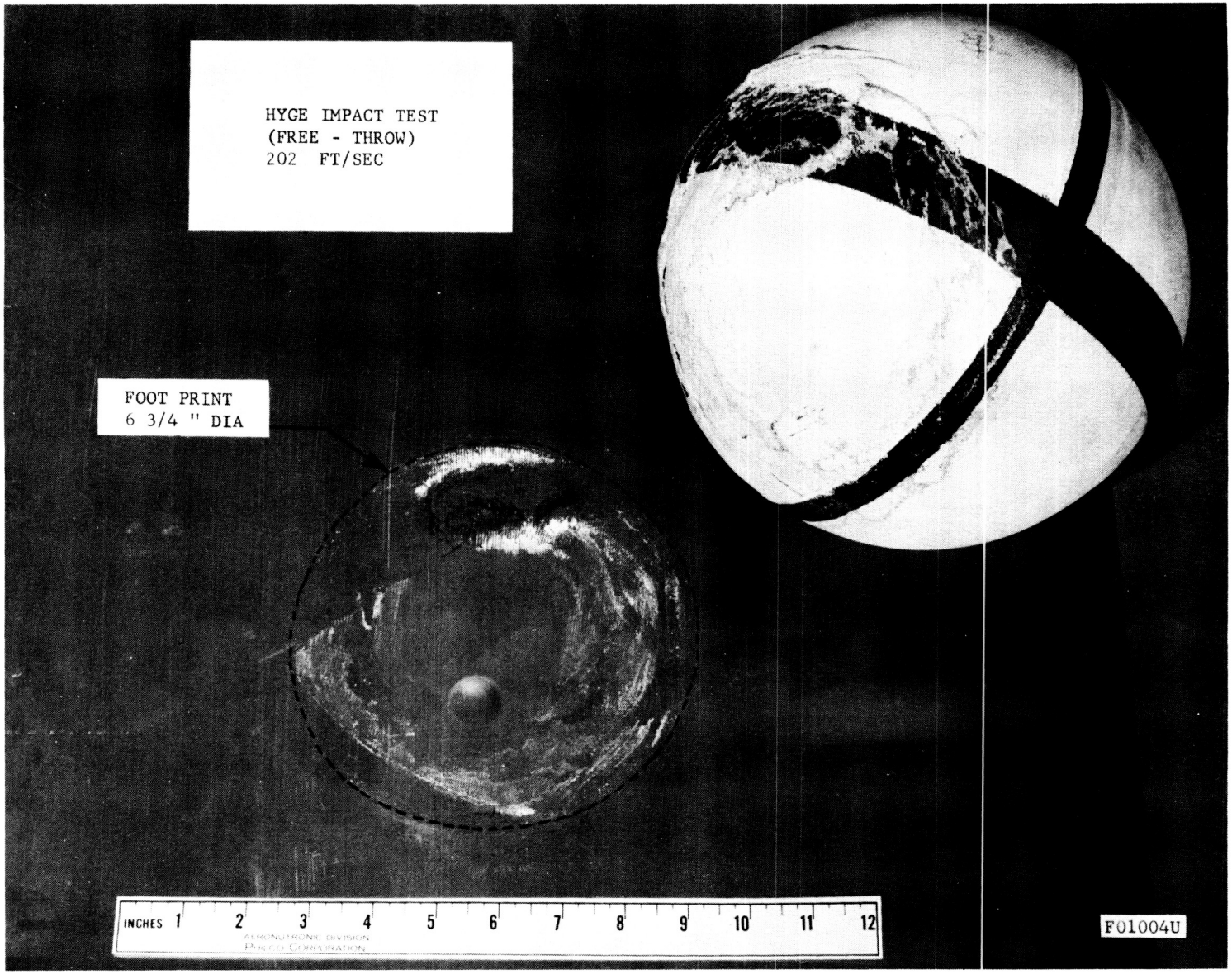

FIGURE A-11. PROTOTYPE PENETROMETER

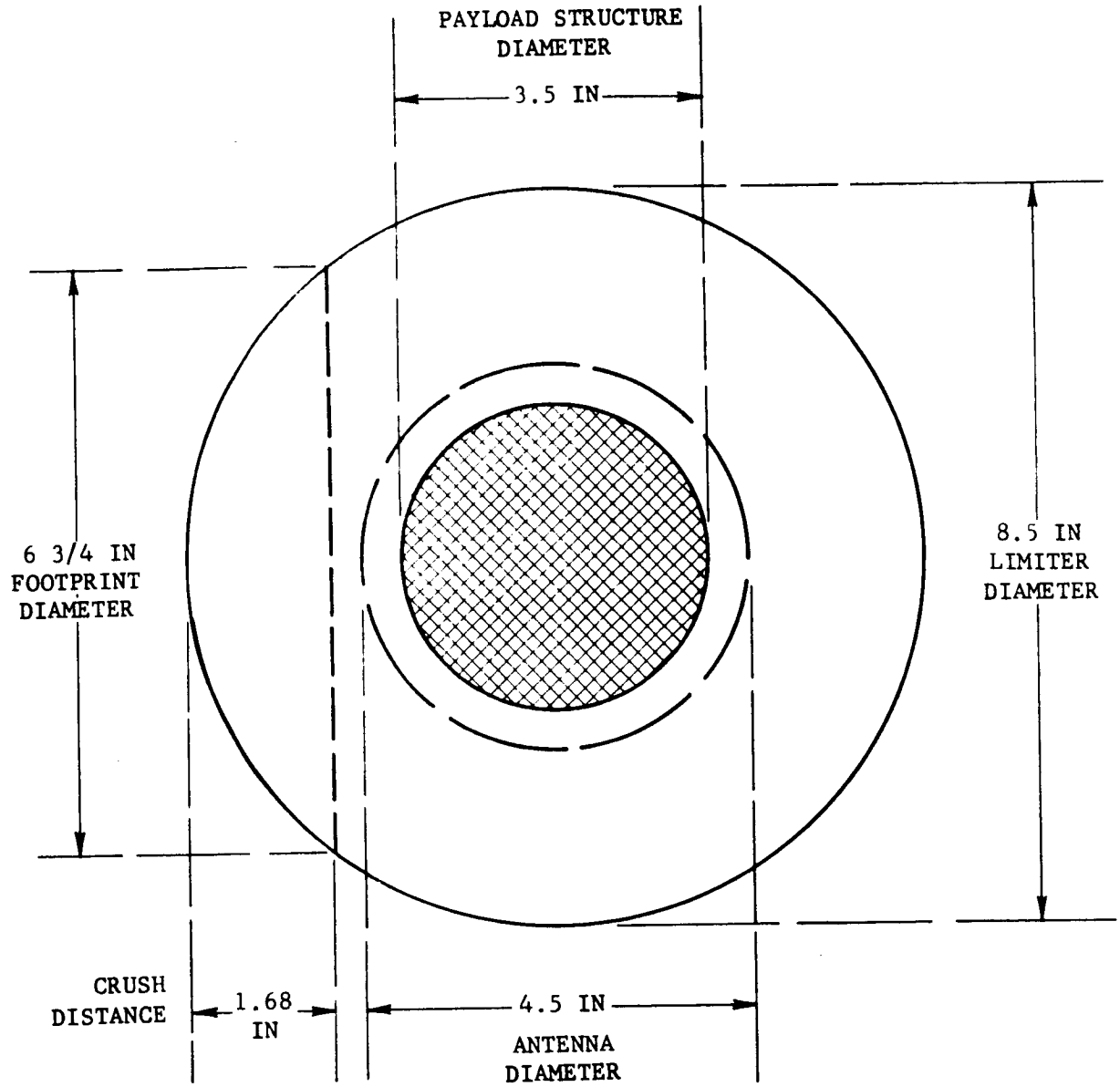

FIGURE A-12. PENETROMETER AFTER IMPACT

A.3 DISASSEMBLY PROCEDURE

A.3.1 STRUCTURAL INVESTIGATION

The crushed penetrometer was X-rayed in two orthogonal directions to look for antenna damage before beginning the disassembly process. These views, shown in Figures A-13 and A-14, indicate no distortion of the antenna support was caused by the combined compression and shearing loads during impact. The impact limiter was then removed from the penetrometer with saw and chisel. Figures A-15, A-16, and A-17 illustrate the several stages of removal and show where good bonding of the balsa occurred. The epoxy did not adhere well to the metal structure of the inner payload. Bonding to the teflon antenna support was excellent. No damage to the antenna loops or their supports was noted. These elements had to be hammered off the spherical structure.

A.3.2 LOWER HEMISPHERE INVESTIGATION

There was evidence that the lock ring nut about the equator had bottomed during assembly before the lower hemisphere. This allowed epoxy to flow into the threads and prevented intact removal of the lock ring nut. Therefore, the lower hemisphere cap was removed in segments by machining grooves through it and prying sections off. The encapsulated interior which was revealed was well potted. No cracks were apparent and there were only small voids (probably produced by epoxy contraction during hardening). The encapsulating epoxy was filled with silica and therefore opaque and too hard to cut. To examine the battery cells and circuit board in the lower hemisphere, this section was subjected to an epoxy dissolving solution. This attempt was successful and the cells and circuit board were recovered for further inspection. However, the solvent was very destructive to the epoxy-glass-laminate circuit board and some electronic components.

Examination of the regulator/timer circuit board showed three diodes with cracked glass cases. These diodes are identified as CR1, CR3, and CR5 on Page 35 of the Fifth Monthly Report, MPR 65-108. The diodes eventually became open-circuited due to handling, but it is thought they were electrically functional when first disassembled.

The open-circuit voltages of the 24 individual battery cells were measured and are reported in Figure A-18. As shown, only one cell was visibly leaking electrolyte. One other cell was appreciably expanded and three cells had reversed polarities. The four cells in the negative battery appeared normal--all of the faulty cells were in the positive 20 cell battery.

It appeared that the electrolyte had followed the thermocouple wire from the battery area to the outside connector area. The pins in the connector were badly corroded and conductive paths probably existed between them. Electrolyte had not spread to other areas within the penetrometer.

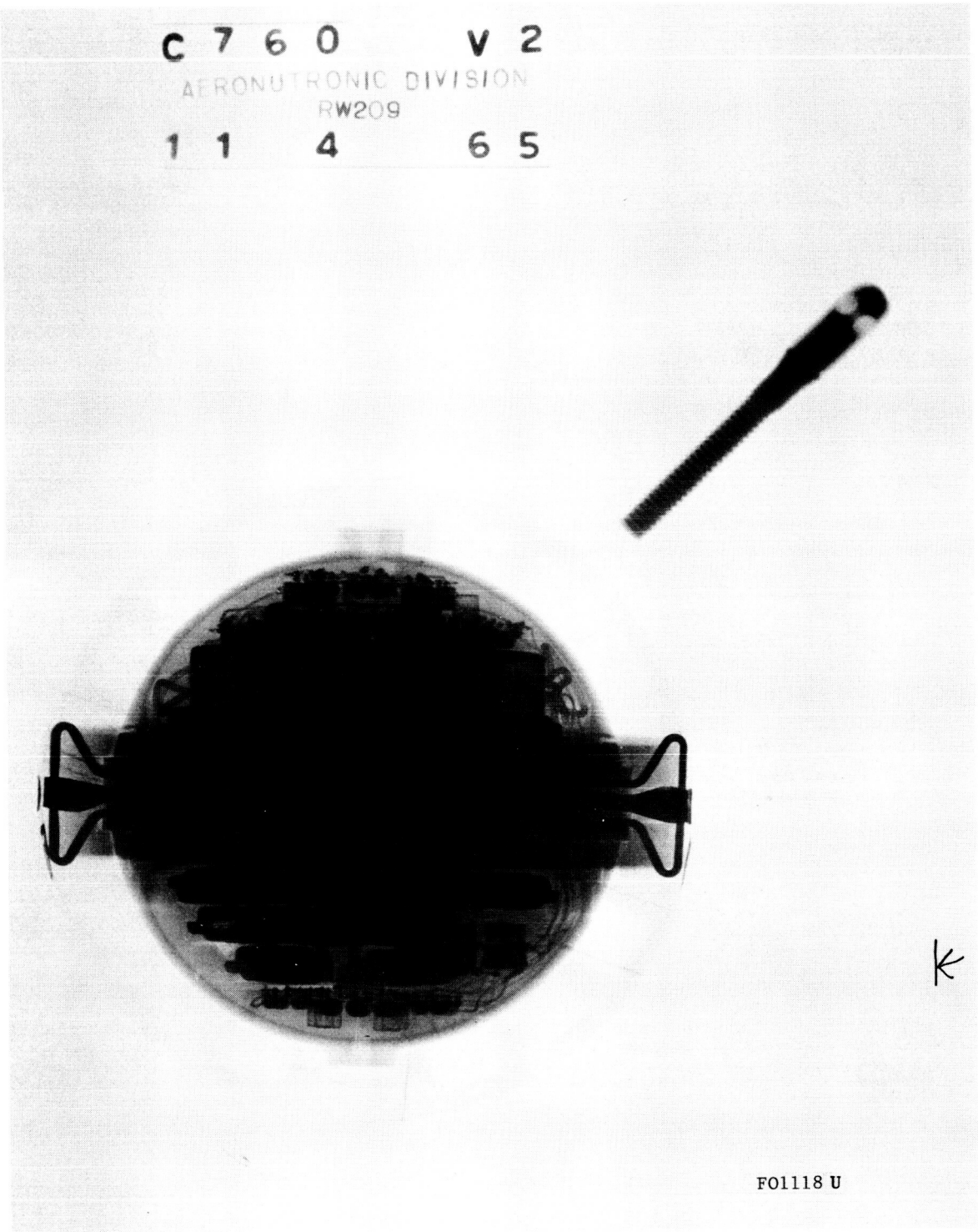

FIGURE A-13. X RAY OF PENETROMETER AFTER IMPACT

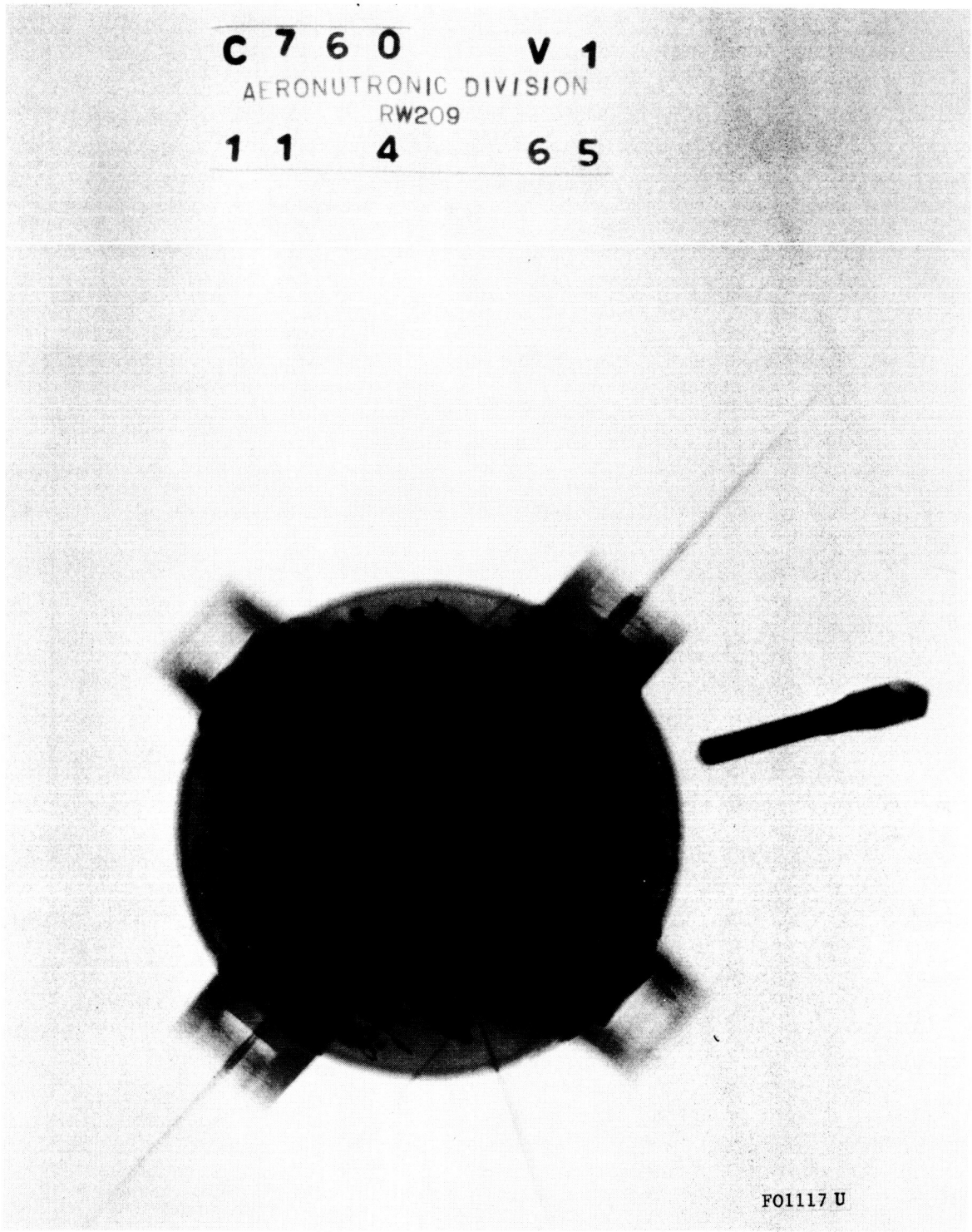

FIGURE A-14. X RAY OF PENETROMETER AFTER IMPACT

FIGURE A-15. PROTOTYPE PENETROMETER WITH BALSA SLICE REMOVED

FIGURE A-16. PENETROMETER AFTER IMPACT WITH BALSA LIMITER REMOVED

F01116 U

FIGURE A-17. PENETROMETER AFTER IMPACT WITH BALSA LIMITER REMOVED

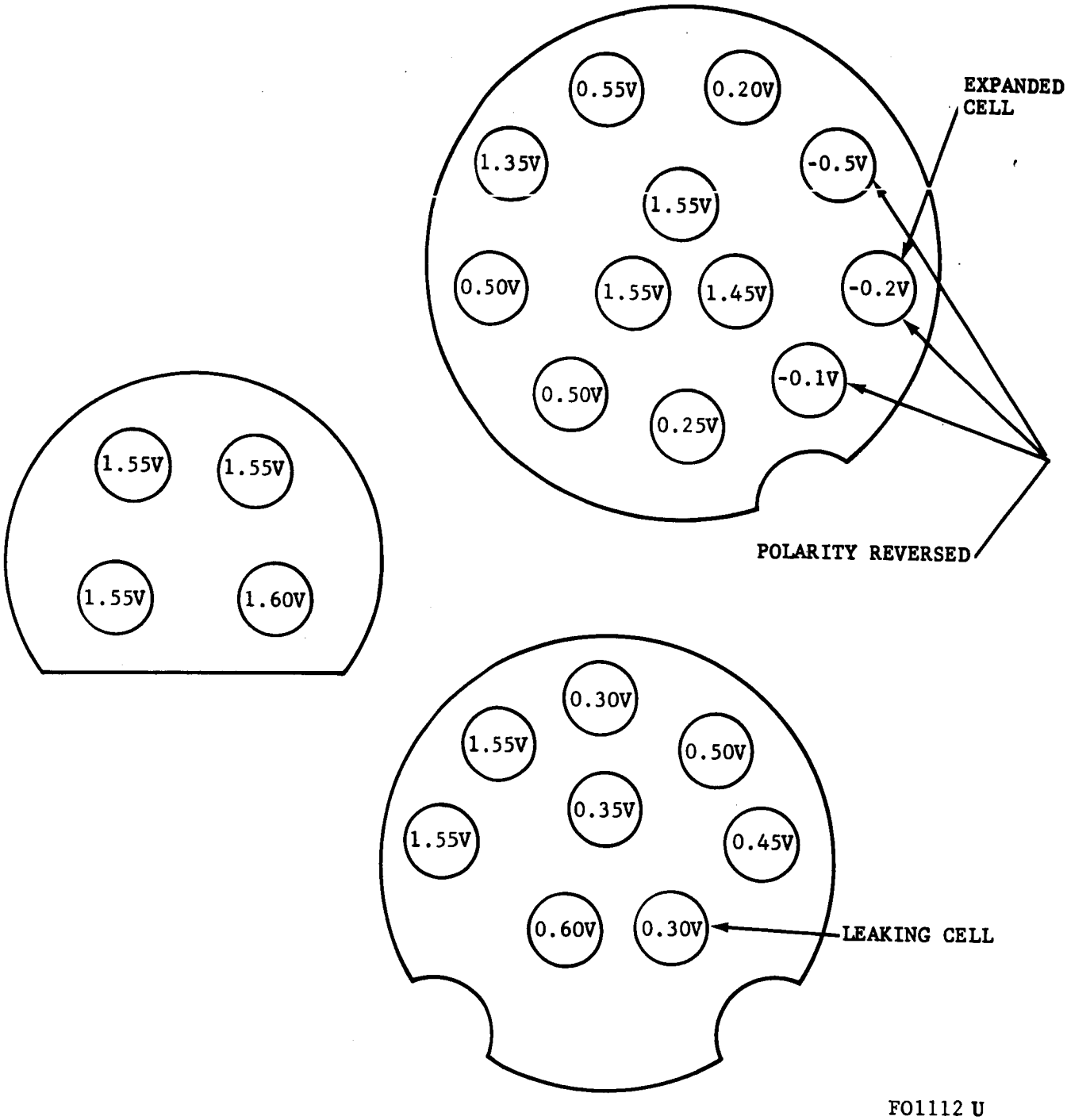

FIGURE A-18. OPEN-CIRCUIT CELL VOLTAGES AFTER DISASSEMBLY

A.3.3 UPPER HEMISPHERE INVESTIGATION

The accelerometer was removed from the upper hemisphere by machining through the center support structure from the bottom side. It was noted that the accelerometer cavity was filled with potting as planned. The electrical resistance and capacitance of the accelerometer was measured and found to be normal. The accelerometer was then subjected to normal calibration shocks and found to give only 10 percent of its normal output level. The unit was then X-rayed with the results shown in Figure A-19. If this X-ray is compared with the X-ray of a normal unit, such as shown on Page 45 of the Sixth Monthly Report, it is seen that the majority of the opaque "liquid" within the ceramic spherical shell leaked to the interior of the metal case. The reduced mass within the piezoelectric shell would account for the reduced output.

With the accelerometer removed, attempts were made to apply calibration signals to the signal electronics through the accelerometer connector. An intermittent electrical condition was discovered--it took twenty minutes to warm up before the applied signal would properly modulate the transmitter. The trouble was in the initial stages of the signal electronics. between the INPUT and CALIB points as identified on the schematic of Page 36 in the Seventh Monthly Report. The intermittent condition was affected by a large change in temperature of the sphere--but apparently not by hammer taps.

The transmitter frequency was normal and the 40 kc internal chopper functioned properly.

At this point in the testing sequence, it was decided that the penetrometer was no longer useful in furnishing information because of the internal intermittent condition and the damage done during disassembly. There seemed to be no way to further disassemble the unit for diagnostic tests without incurring additional damage.

A.4 TEST CONCLUSIONS

The tests reported by this document did qualify the design of many subsystems within the penetrometer. Unfortunately, the failure of the internal battery, which was probably due to misuse, prevented certain needed tests. There were some subsystems which were expected to show inadequate performance because of their development status, and this did occur. Also, there were subystem failures which had not been anticipated; fortunately, design changes were made to correct these deficiencies before another prototype model was built. The following paragraphs will describe the results, failures, and probable failure causes for each of the subsystems within the penetrometer.

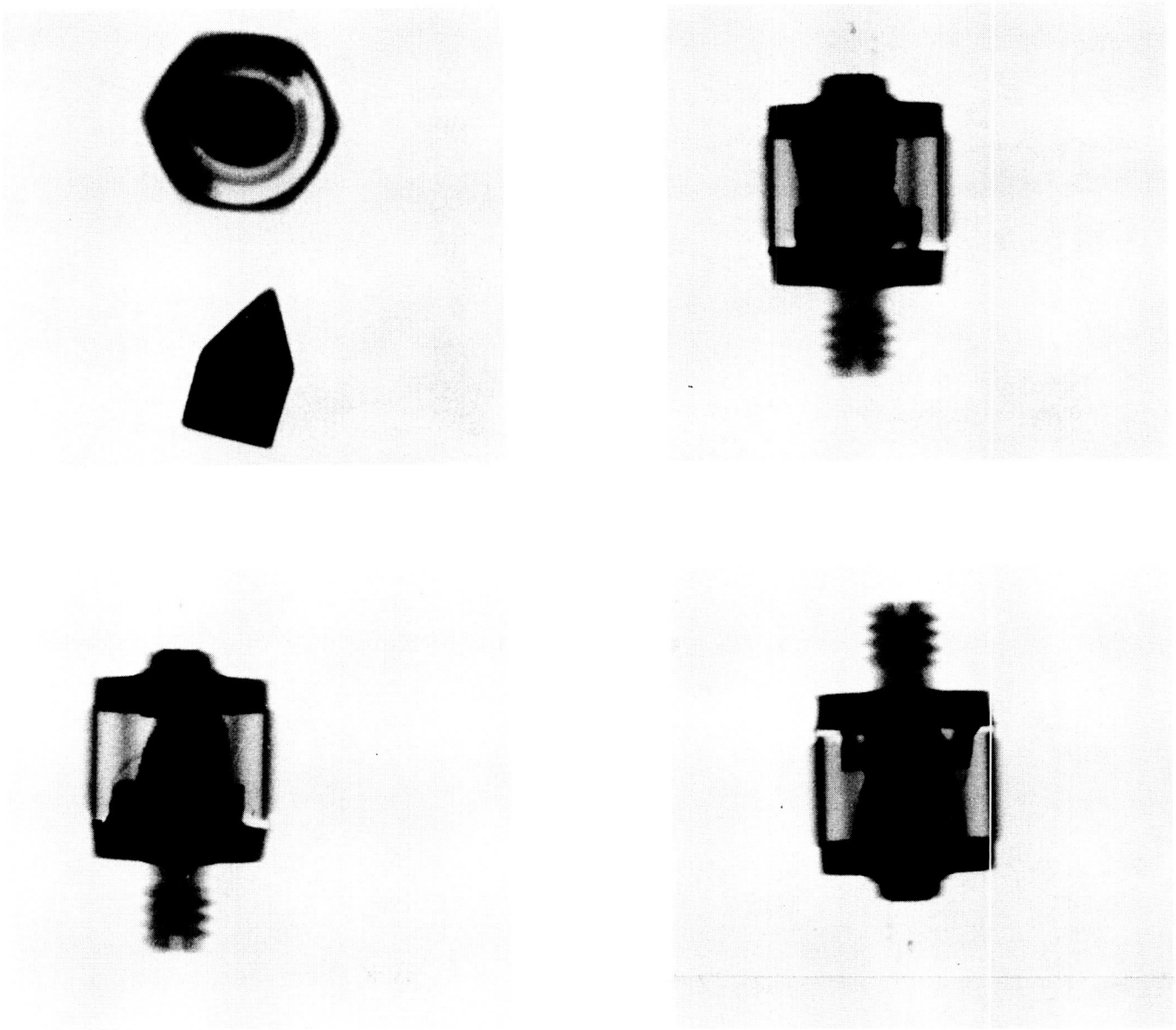

F01114U

FIGURE A-19. X-RAY VIEWS OF OMNIDIRECTIONAL ACCELEROMETER REMOVED FROM PENETROMETER

A.4.1 ANTENNA

The test results show no substantial changes in the antenna pattern due to the high velocity impact. Further, no mechanical damage to the antenna loops or their supports was noted. The crushing impact was in a quadrant of the sphere between loops so that the antenna supports were subjected to compression and shear. Therefore, the mechanical design of the antenna was judged satisfactory. An additional desirable test would be a high velocity impact directly over the antenna feed loops.

A.4.2 ACCELEROMETER

The test results indicate that the accelerometer failed some time during the test sequence by leakage of the "fluid" from the piezoelectric sphere. It is believed that this happened during initial bench testing, or possibly during assembly of the penetrometer. The failure has not been fully analyzed, but is believed due to improper sealing of the fill hole with epoxy. The cure would seem to be better assembly and inspection techniques by the vendor.

A.4.3 BATTERY

The battery failed during the tests by leakage of electrolyte and failure to retain a charge. This occurred before any real environmental extremes were experienced. There is evidence that the battery was overcharged during the penetrometer assembly procedure. The battery was charged with a Yardney charger which had excessive ac in its output. The charge limiting voltage was set by a meter which read average voltage, but the battery charged to the peak voltage. Additionally, the two sections of the battery were charged in series despite their prior discharge at different rates. The individual cells had not been selected to have equal charge capacities.

It appears that similar battery failures in the future can be avoided by:

(1) Selecting cells for similar capacities.

(2) Charging cells individually or in small groups.

(3) Carefully monitoring cell voltages during charging to avoid overcharging.

The final discharged condition of the positive battery was probably due to conduction in the test connector caused by leaking electrolyte.

A.4.4 POWER REGULATOR/TIMER

There was no evidence of power regulator/timer failure in the prototype except for the visible cracks in the glass diodes after the disassembly.

These cracks could have been caused by the disassembly actions or have been caused by the epoxy shrinking. A recommended prevention action would be to coat all glass diodes with silicone rubber before they are encapsulated with epoxy.

The observed condition of the timer not turning off predictably could have been due to noise pickup in the long leads or more likely due to conductance in the test connector from leaking electrolyte.

A.4.5 SIGNAL ELECTRONICS

Failure of the accelerometer prevented the observation of the signal electronics characteristics during most of the tests. The post disassembly findings, and the actions during two of the captive Hyge shocks, indicated some sort of intermittent, erratic condition existed in the signal electronics. Unfortunately, there were not enough external test points to fully diagnose this behavior. Therefore, it will have to be assumed that this trouble, which had not occurred on previous modules, was caused by a faulty component or an improper connection.

It is recommended that future prototypes have additional external test points for the signal electronics. It is recognized that connector limitations and impedance considerations place restrictions on such test points.

A.4.6 TRANSMITTER

The oscillator module within the transmitter was known to have poor shock and temperature characteristics when the penetrometer was assembled. The module used thin brass walls and all components were completely encapsulated. The improved oscillator modules were not available at time of assembly.

The oscillator did not meet either shock or temperature stability requirements. In captive Hyge tests, an acceleration of 1000 g produced at least a 40 kc frequency transient at the output frequency of 435 Mc. The transmitter output frequency varied considerably with temperature and always drifted about 170 kc in the first two minutes of operation. These were not unknown problems and consequently they were being separately analyzed and solved. The transmitter did not exhibit any permanent changes due to shock and no unsuspected troubles were encountered.

A.4.7 STRUCTURE

The metal structure passed the severe impact test satisfactorily. No permanent deformation of the structure was observed. As previously mentioned, the balsa impact limiter was not well bonded to the outside of the metal sphere, but this in no way caused trouble. However, it is recommended that the metal surface be treated differently in future models to enhance the adhesion of the epoxy.

A.4.8 IMPACT LIMITER AND COVER

This particular penetrometer model had the fiberglass cover, but not the thin mylar covering. The mylar covering is mainly for a moisture seal in vacuum and was not needed in these tests.

The depth of balsa crushing experienced in the impact test agreed closely with the predicted value. There was no acceleration measurement obtained within the sphere during the impact, but it is presumed by analogy that the deceleration was limited to 7000 g. There was no evidence of payload movement, or cannon-balling, within the limiter. Small voids were noted in the glue joint between limiter halves but these were not considered serious. In general, the impact limiter design appeared successful.

APPENDIX B

TEST REPORT FOR PENETROMETER PROTOTYPE NO. 2

B.1 INTRODUCTION

This report describes the test results for the Penetrometer Prototype No. 2, the second complete penetrometer to be subjected to environmental and functional tests. As in the previous tests of Prototype No. 1, tests were performed in accordance with a general test procedure. Variations and modifications of the test procedures and sequences were necessary, however, because of an unfortunate incident in the final assembly of the test item.

During the installation of the impact limiter on Prototype No. 2 penetrometer, both umbilical plugs and an aluminum tube used to protect the umbilical plug from being encapsulated were inadvertently encapsulated in the limiter. The silicone grease liberally applied to prevent any such bonding completely failed in this function. This has never happened before in much prior usage, and no explanation has yet been found.

Although some limited drop testing could have been accomplished with the probes left in, there was the danger of permanent circuit or battery damage due to shorted external leads and a probability of unreliable connections due to the silicone grease in the umbilical connectors. The decision was made to attempt to remove the umbilical plugs and the aluminum protective tube. The round battery umbilical was removed without incident. When removing the aluminum tube surrounding the square umbilical plug, the teflon insulation on the wires remained bonded to the tube, leaving bare wires at the umbilical plug down at the bottom of the probe hole. This plug contained wires for the trigger input, +17V, -3.3V, calibration signal, and external power. Although utmost care was taken

to prevent shorting when these wires were cut, the extremely small pin spacing on the plug make this very difficult. It is believed that the drain of the second stage MOS-FET was shorted to +17 volts through the calibration lead. This device was found to be defective following signal electronics disassembly.

The following paragraphs describe the subsequent test sequence and results obtained, in the order performed, with general conclusions drawn from the results.

B.2 TEST SEQUENCE

B.2.1 BENCH CHECKOUT

Bench tests were scheduled employing the assembled penetrometer in conjunction with standard laboratory test equipment and a single data relay receiving channel. A turn-on transient test, linearity test and a qualitative standard "tapping" acceleration test were the principal tests in this category. The penetrometer was operated using external power and rf carrier reception obtained via an auxiliary antenna.

a. Turn-On Transient Test. Operating with external power and Prototype No. 2 at essentially room temperature, temperature and frequency stability checks were made by monitoring the rf and data channel outputs. Temperature and rf frequency measurements were obtained and are shown in Figures B-1 and B-2. The basic test setup is also shown in Figure B-2. A data channel output was not obtained at this point because of the observed rf carrier frequency difference, i.e., the penetrometer transmitter frequency was approximately 432.4 MHz while the relay receiver channel was fixed-tuned to 432.0 MHz.

Because of the basic frequency offset, attributed to epoxy dielectric constant changes over a long cure time, the relay receiver channel was modified to accept an external local oscillator signal to provide a flexible tuning capability for subsequent testing.

b. Linearity Test. A dc calibration level was injected at the signal electronics test point via the umbilical connector to measure overall linearity of the penetrometer relay receiver and AM demodulator channel. The test point in the case of Prototype No. 2 provided connection to the drain of the second stage MOS-FET, i.e., pin 1 of Q3 (2N3609), and was a revision from that employed in the Prototype No. 1 design (see 7th Monthly Progress Report, MPR 65-136). No output was observed in response to a variation in the input stimulus. A small residual 40 KHz subcarrier modulation signal level was observed at the output of the relay receiver FM discriminator, however, and was noted to be approximately 5 to 10 percent of full-scale channel deviation (i.e., $\pm$ 160 KHz). It was concluded that a malfunction within

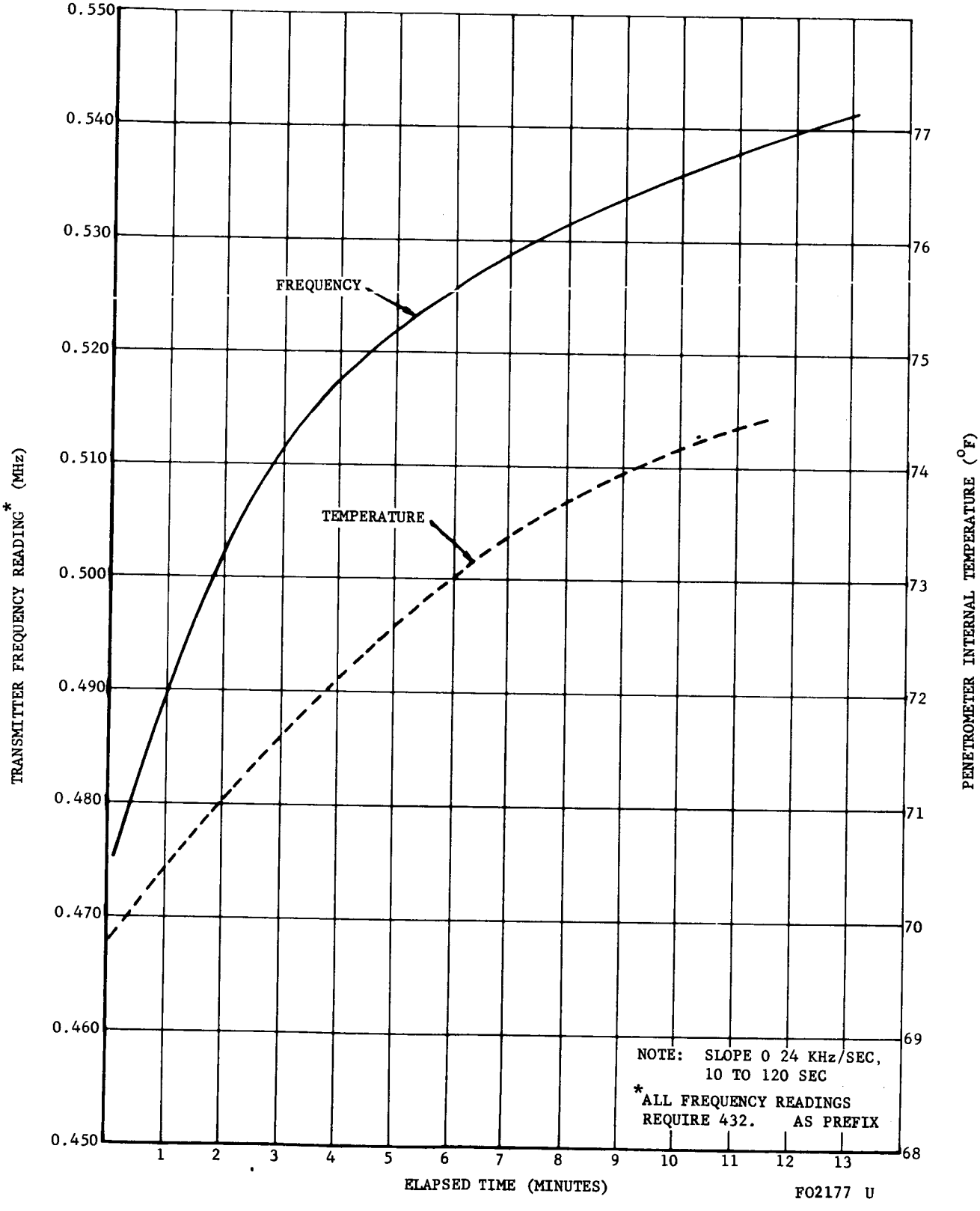

FIGURE B-1. PENETROMETER PROTOTYPE NO. 2 TURN-ON TRANSIENT RESULTS

PENETROMETER PROTOTYPE NO. 2 TURN-ON TRANSIENT TEST

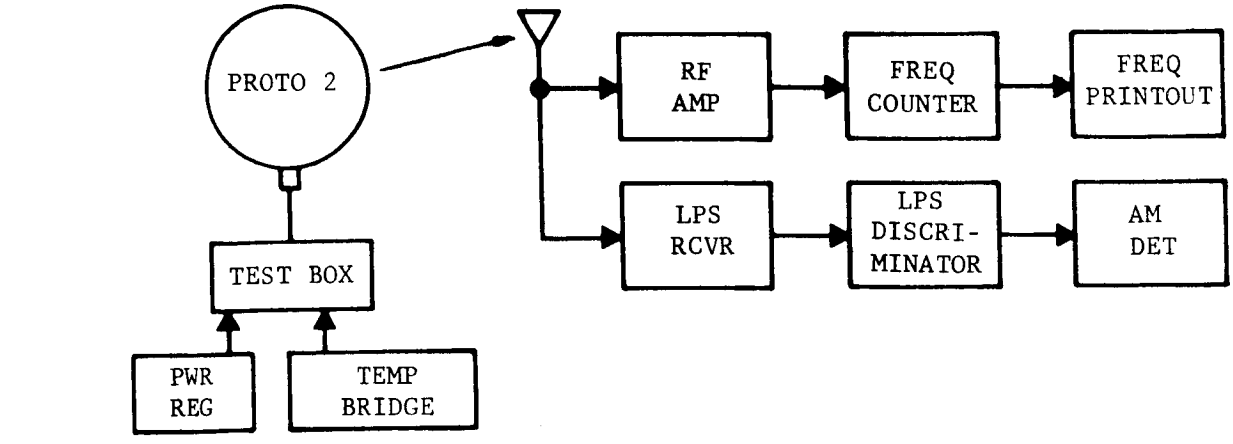

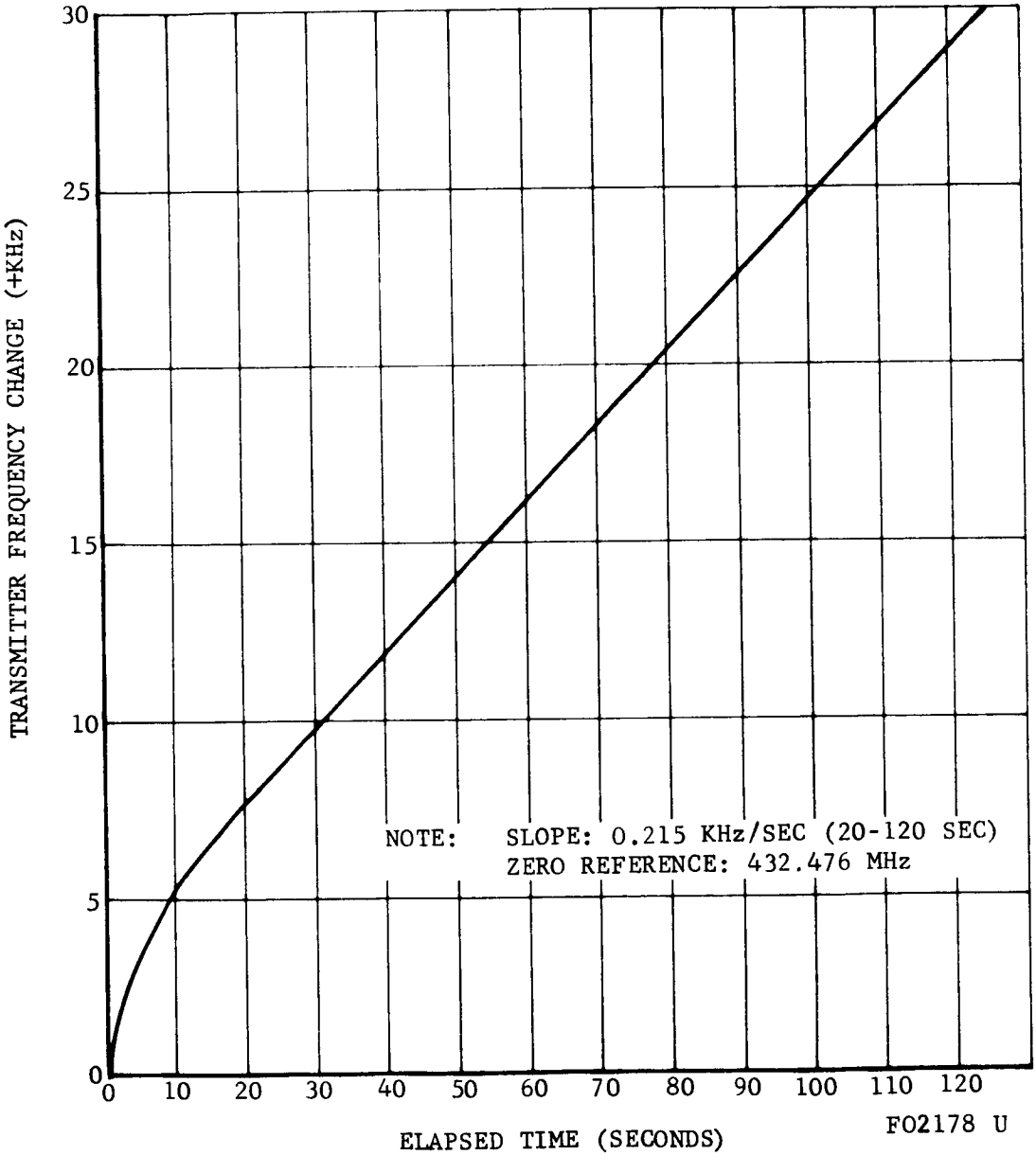

FIGURE B-2. TRANSMITTER FREQUENCY VERSUS TIME AFTER TURN-ON

the signal electronics module had made impossible further tests requiring operation of the signal electronics. Revisions were made in the subsequent test sequence, therefore, to eliminate tests where the penetrometer had to measure acceleration.

c. Tapping Test. The tapping test was employed prior to reaching the aforementioned decision to alter the test sequence. By means of this test, operation of the accelerometer and signal electronics up to the test point was tested. No output was observed when shocking the penetrometer with a mallet.

B.2.2 POWER OUTPUT REFERENCE

A measurement of relative radiated field strength was made, as in Prototype No. 1 tests, to use as a later comparison for power output. The penetrometer was placed in an enclosure of rf absorbing material while the field strength was measured at one known location. The receiving dipole was rotated about its axis to obtain both minimum and maximum indications of field strength. The test setup and results are shown in Figure B-3. This measurement was made using external power.

B.2.3 CHARGE BATTERY

The next step before proceeding to Hyge captive shock testing was to recharge the battery. During previous final assembly checks, one set of four-cells (18 to 24 volts) was observed to be low. Recharge at this point ensured peak battery performance going into the captive tests. Table B.1 shows the pre- and post-charge no-load terminal voltages observed.

B.2.4 HYGE CAPTIVE ACCELERATION AND VIBRATION TESTS

The captive acceleration and vibration tests were physically arranged as in the Prototype No. 1 testing (see 8th Monthly Progress Report, MPR 65-156). A variation in the umbilical cabling operation was incorporated with the penetrometer operating on internal power during all dynamic Hyge testing. Tests were therefore programmed to occur within the 15 second timer-controlled operating period.

The acquisition of penetrometer acceleration data was not possible during these tests because of previously reported problems apparently occurring in the signal electronics.

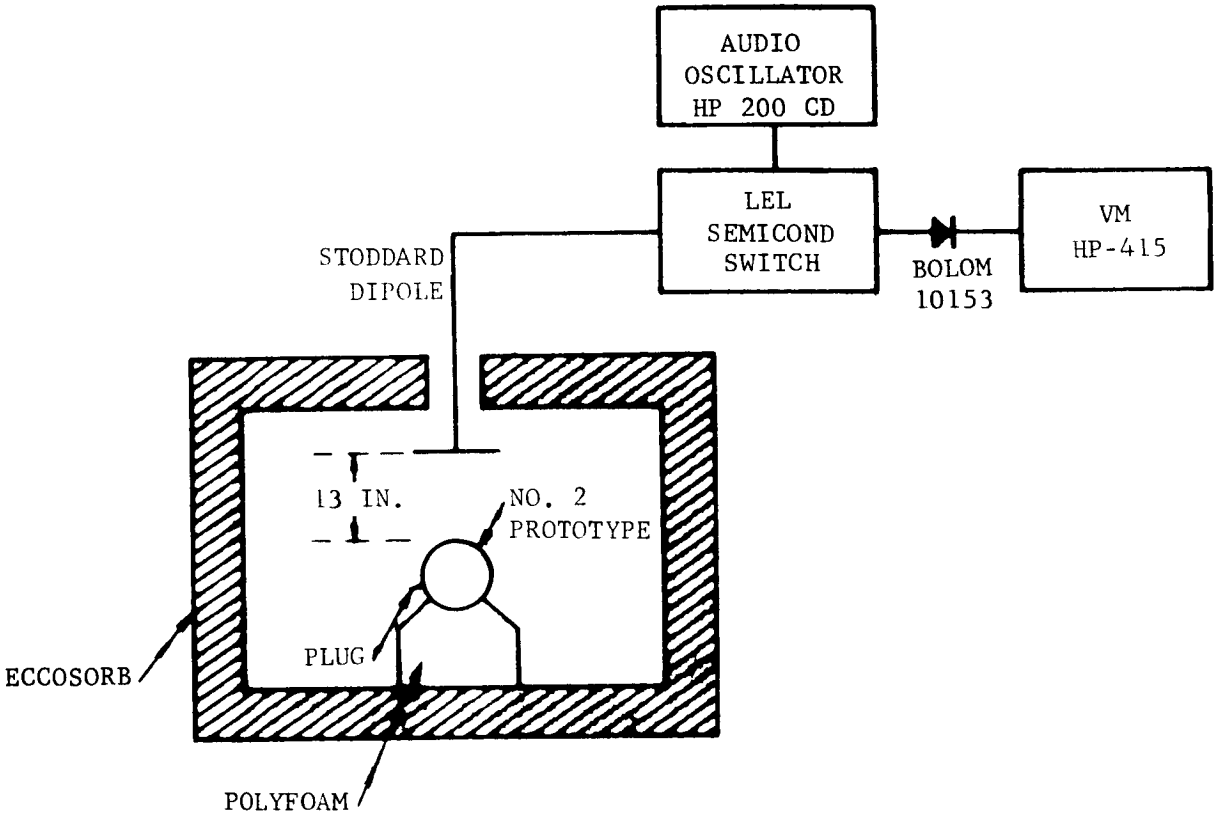

CONDITION	MAXIMUM READING	MINIMUM READING	TOTAL FIELD
BEFORE IMPACT 1/18/66	- 0.5 db	- 1.5 db	0 db (REF)
AFTER IMPACT 1/21/66	- 1.0 db	- 2.5 db	- 1.4 db

F02179 U

FIGURE B-3. POWER OUTPUT REFERENCE MEASUREMENT FOR PENETROMETER PROTOTYPE NO. 2

TABLE B.1

PROTOTYPE NO. 2 BATTERY DATA

Recorder No.	Cell Group Identification		No-Load Voltage dc Pre-Charge	No-Load Voltage dc Post-Charge
1	+24 to +31.5 v	5 cells	8.3	8.7
6	+18 to +24 v	4 cells	4.4	7.2
3	+12 to +18 v	4 cells	6.5	7.4
4	+6 to +12 v	4 cells	6.6	7.3
5	0 to +6 v	4 cells	6.6	7.4
7	0 to -6 v	4 cells	6.6	7.3

The radiated signal from the penetrometer was received via an auxiliary antenna to a primary FM receiver to furnish FM carrier monitor signals for the oscillograph recorder. With the signal electronics inoperative, no AM data were anticipated. RF frequency measurements were made at various stages in the tests. The output from a reference accelerometer on the Hyge fixture was also recorded. The overall test setup is shown in Figure B-4.

An initial captive test was run with acceleration applied along the polar axis utilizing the LPS relay receiver, with an external local oscillator signal furnished by an HP 608C signal generator, as the sole receiving element. Erroneous indications (following the shock pulse) were observed in the data traces which were later found to be attributed to the external local oscillator test equipment seismic shock sensitivity. The valid information obtained was therefore restricted to pre- and post-run frequency measurements and is shown in Table B.2. The second test was a repeat of the first with a substitute FM receiver, the AN/FRW-3 Collins (crystal controlled), utilized as the primary receiving element. The record of this test is shown in Figure B-5. The acceleration along the polar axis consisted of a 440 g pulse followed by a peak 1070 g deceleration. The maximum carrier frequency transient was about 10 KHz. Frequency measurements taken before and after are shown in Table B.2.

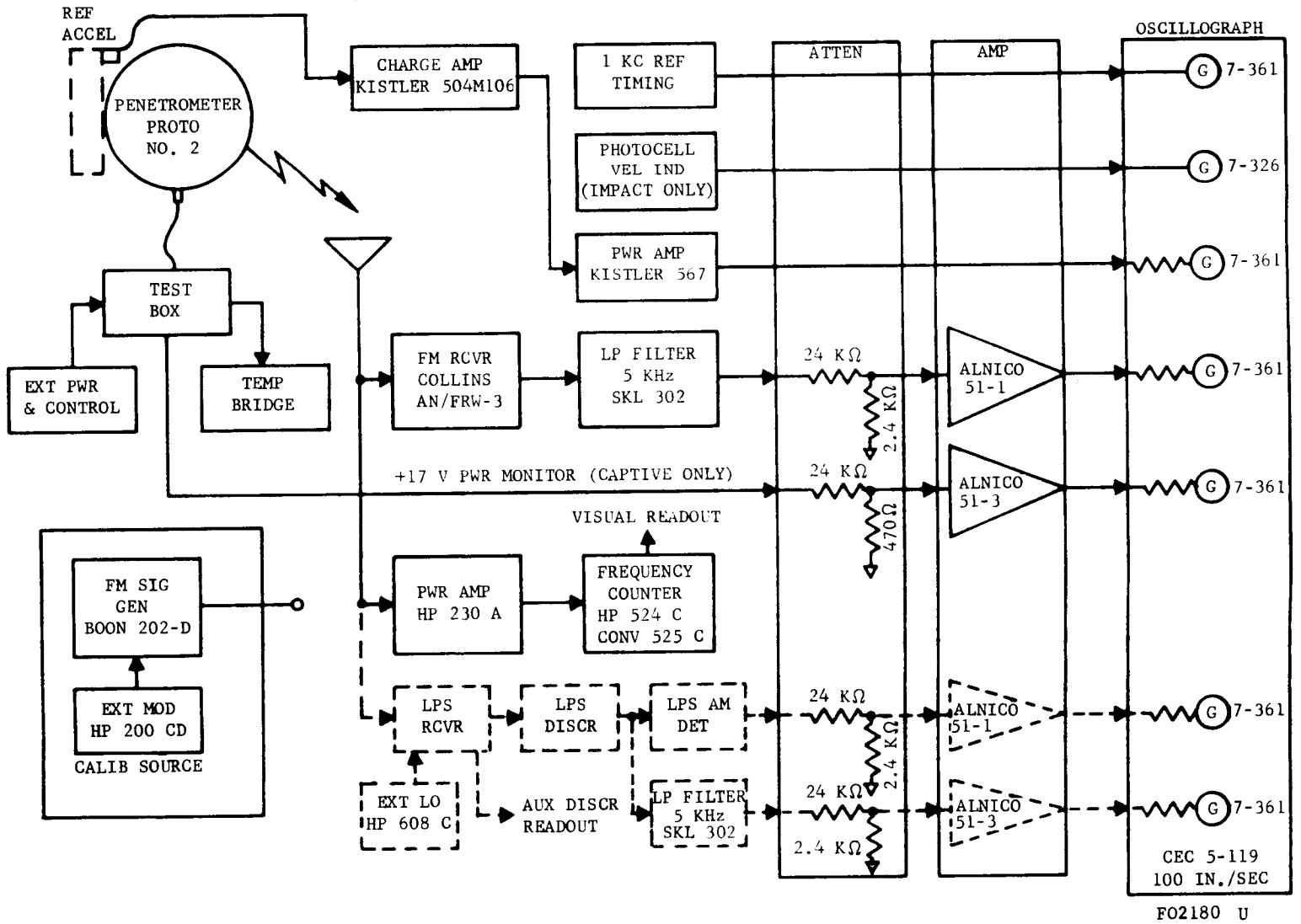

FIGURE B-4. PENETROMETER PROTOTYPE NO. 2 HYGE CAPTIVE AND IMPACT TEST SETUP

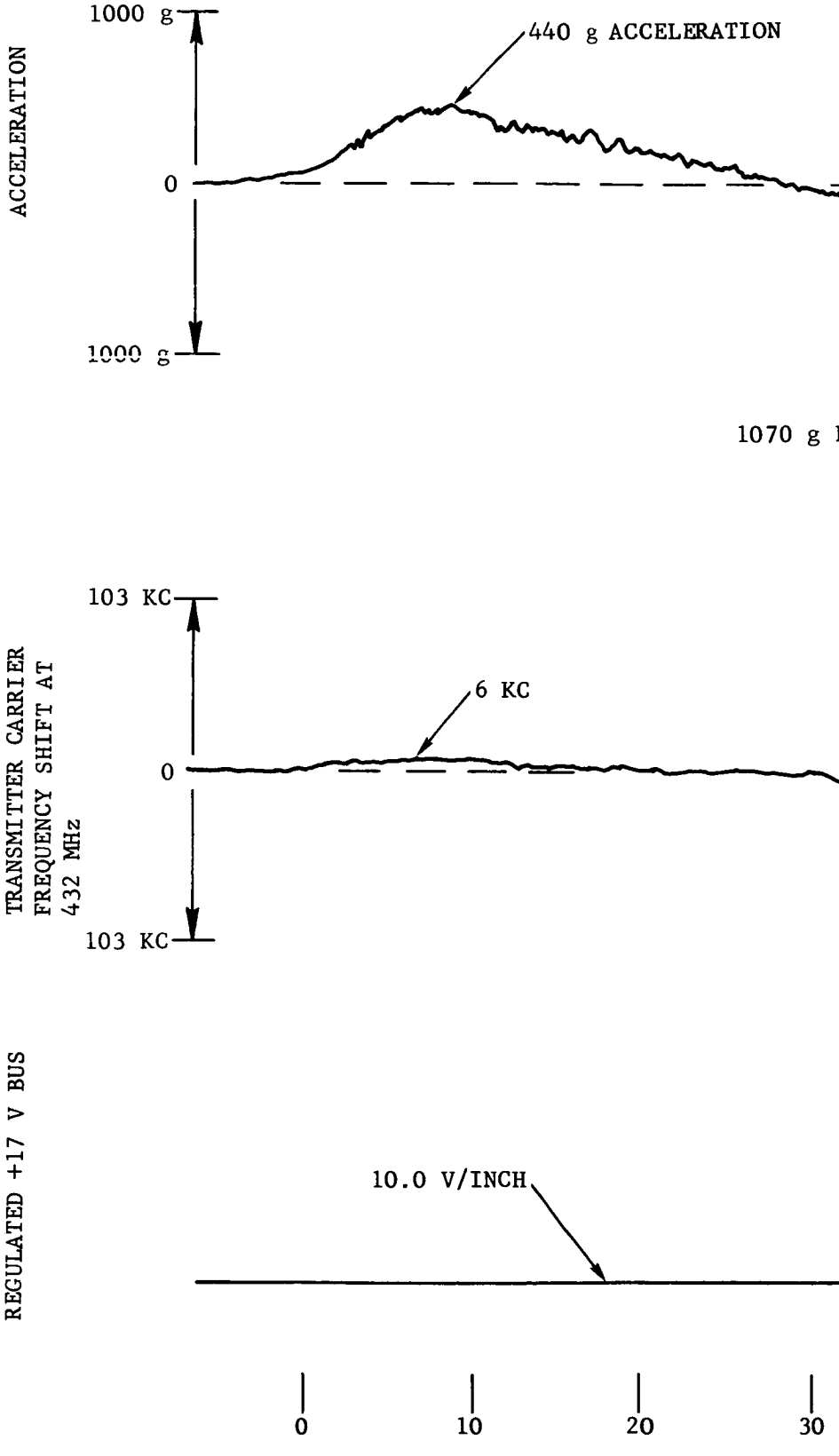
ACCELERATION
1000 g
0
1000 g
440 g ACCELERATION
1070 g
TRANSMITTER CARRIER FREQUENCY SHIFT AT 432 MHz
103 KC
0
103 KC
6 KC
REGULATED +17 V BUS
10.0 V/INCH
0
10
20
30

B-9-1

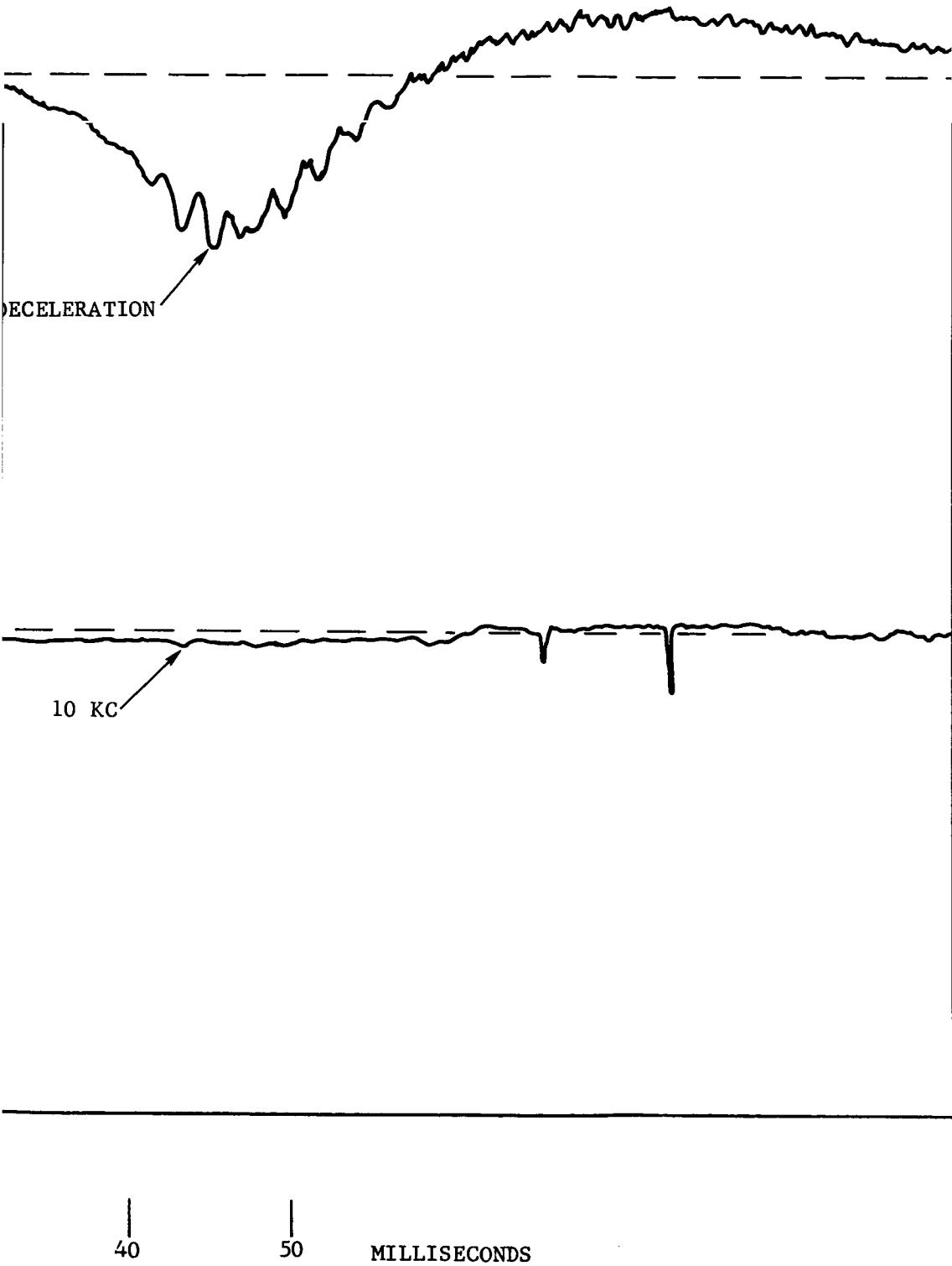
DECELERATION
10 KC
40
50
MILLISECONDS

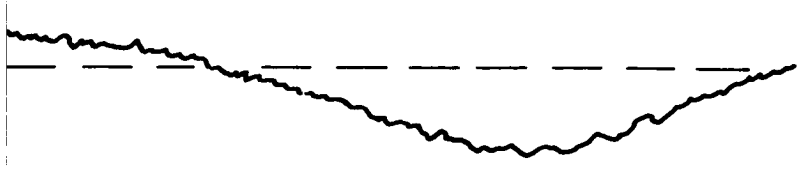

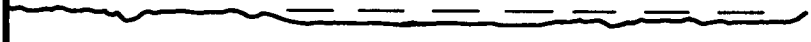

FO2181 U

FIGURE B-5. TEST RECORD FOR THE NO. 2 PROTOTYPE PENETROMETER IN THE POLAR AXIS CAPTIVE HYGE SHOT

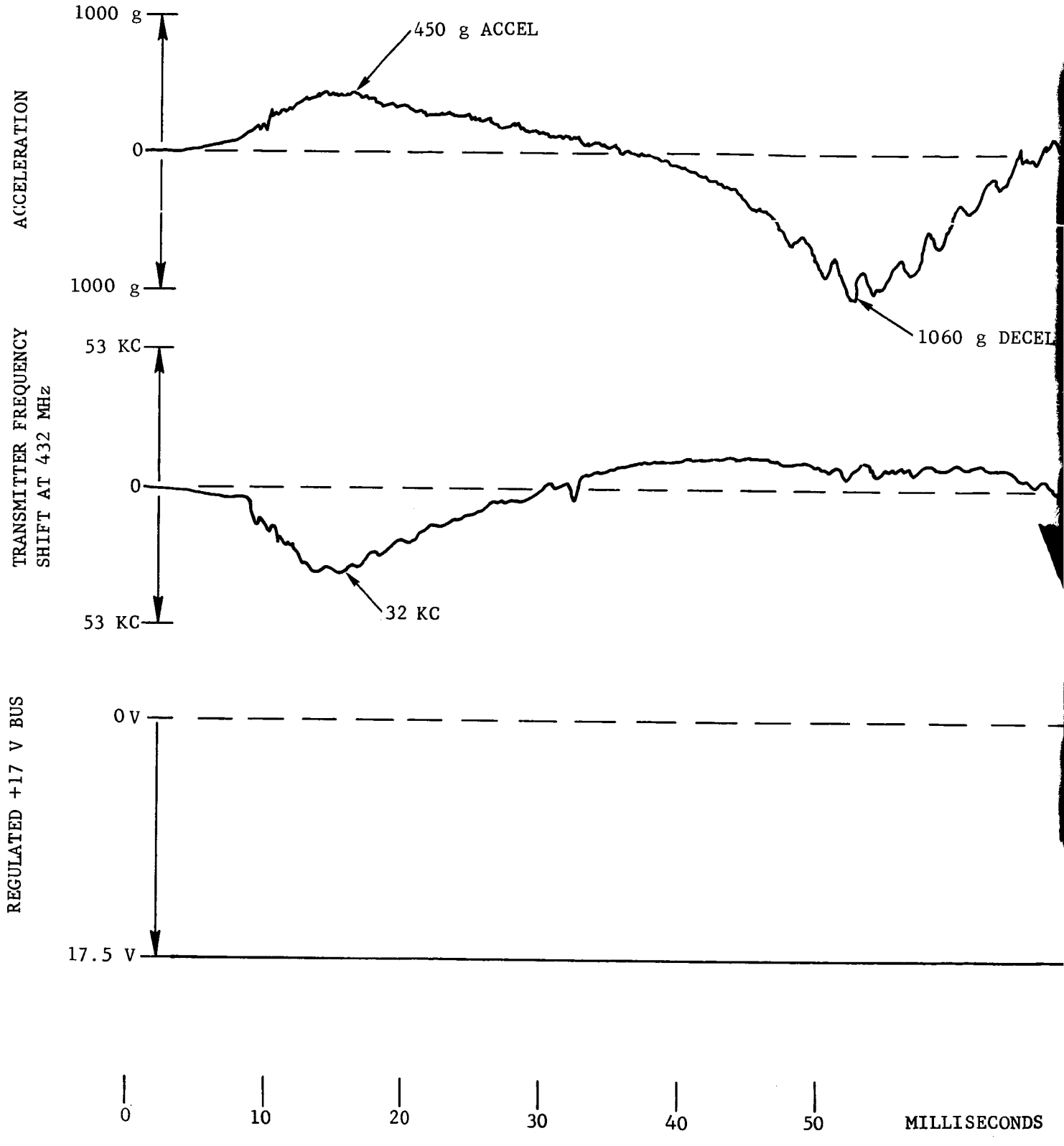
ACCELERATION
1000 g
0
1000 g
450 g ACCEL
1060 g DECEL
TRANSMITTER FREQUENCY SHIFT AT 432 MHz
53 KC
0
53 KC
32 KC
REGULATED +17 V BUS
0 V
17.5 V
0
10
20
30
40
50
MILLISECONDS

B-10-1

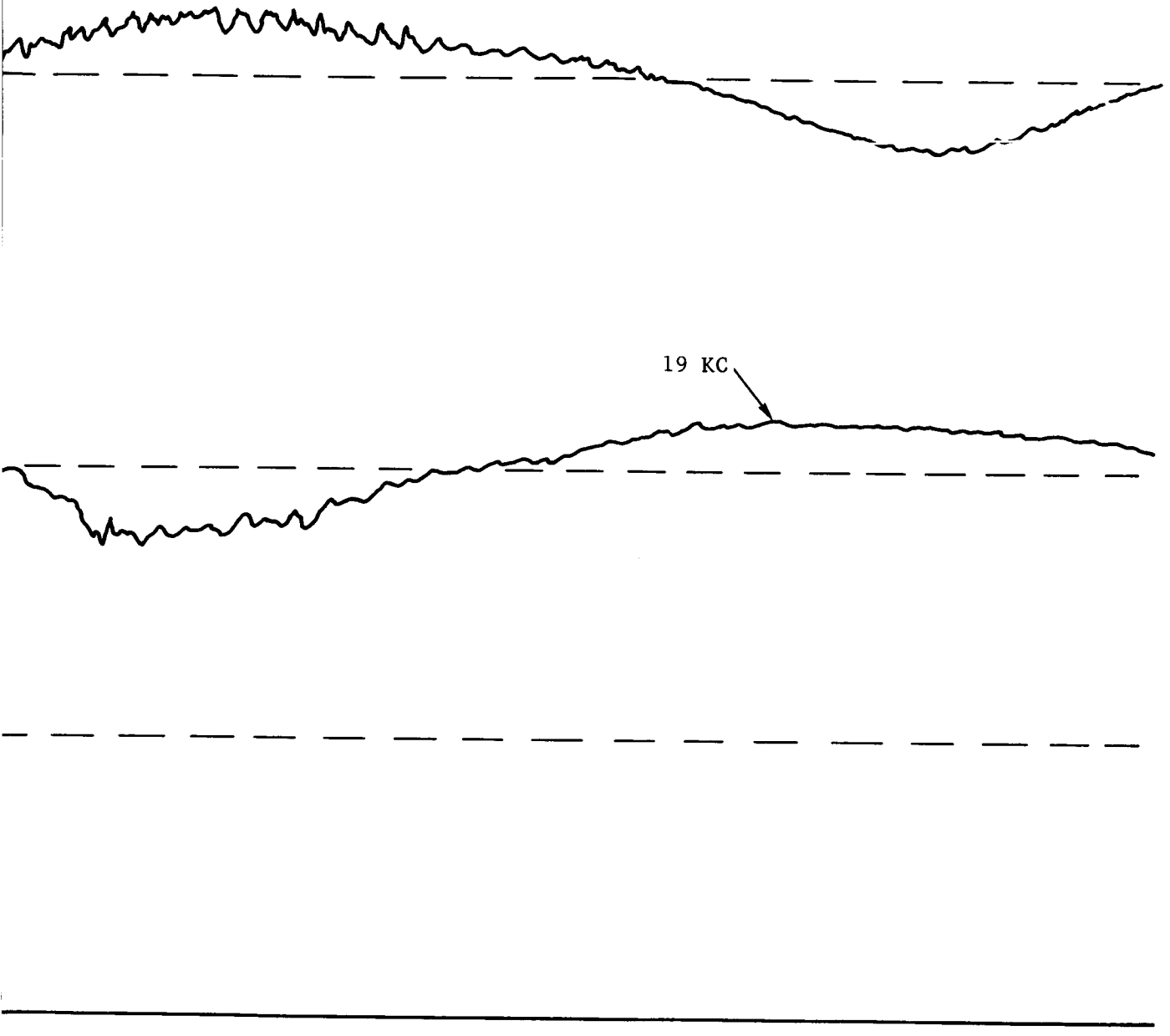

F02182 U

FIGURE B-6. TEST RECORD FOR THE NO. 2 PROTOTYPE PENETROMETER IN THE EQUATORIAL PLANE CAPTIVE HYGE SHOT

2

TABLE B.2

HYGE TESTS - RF FREQUENCY MEASUREMENTS
(PROTOTYPE NO. 2)

		Frequency MHz			
Time	Power Source	Test 1 Captive	Test 2 Captive	Test 3 Captive	Hyge Impact
Pre-run	External	432.420	432.402	432.418	432.404
Pre-run	Internal	432.397	432.364	432.371	---
Post-run	Internal	---	432.288	---	---
Post-run	External	432.366	432.406	---	432.420

For the second test, the umbilical cable was left in the penetrometer so that the regulated +17 volt supply from the internal battery could be monitored during the shock. Figure B-5 shows no variation in this voltage during the test.

A third test was staged with the penetrometer oriented in the Hyge fixture so the acceleration axis was in the plane of the penetrometer equator. An acceleration profile essentially the same as that applied in the previous tests was obtained. The test record is shown in Figure B-6. The initial peak acceleration applied was 450 g followed by a peak 1060 g deceleration pulse. The observed peak carrier frequency shifts were noted as 32 KHz and 19 KHz. The +17 vdc monitor demonstrated a satisfactory performance level which was maintained throughout test duration. The rf frequency checks made as shown in Table B.2. There were no anomalies observed during this test period.

B.2.5 ANTENNA PATTERN

A revision in the test schedule resulted in the antenna pattern test following the initial Hyge captive test. Chronologically, this placed it between captive tests 1 and 2. The pattern was measured at the Aeronutronic antenna range site with a spinning dipole in the standard method previously employed for Prototype No. 1 and development tests. Figure B-7 is the measured pattern in the polar plane with the penetrometer operating on external power. Polarization axial ratio is exhibited in the small pattern peaks and results from the spinning dipole measurement method. The pattern shows the desired omnidirectional characteristics. The bonding of the balsa impact limiter and the initial Hyge captive test did not degrade the pattern.

NOTES: PATTERN IN POLAR PLANE TAKEN
WITH EXTERNAL POWER AFTER
CAPTIVE HYGE TEST

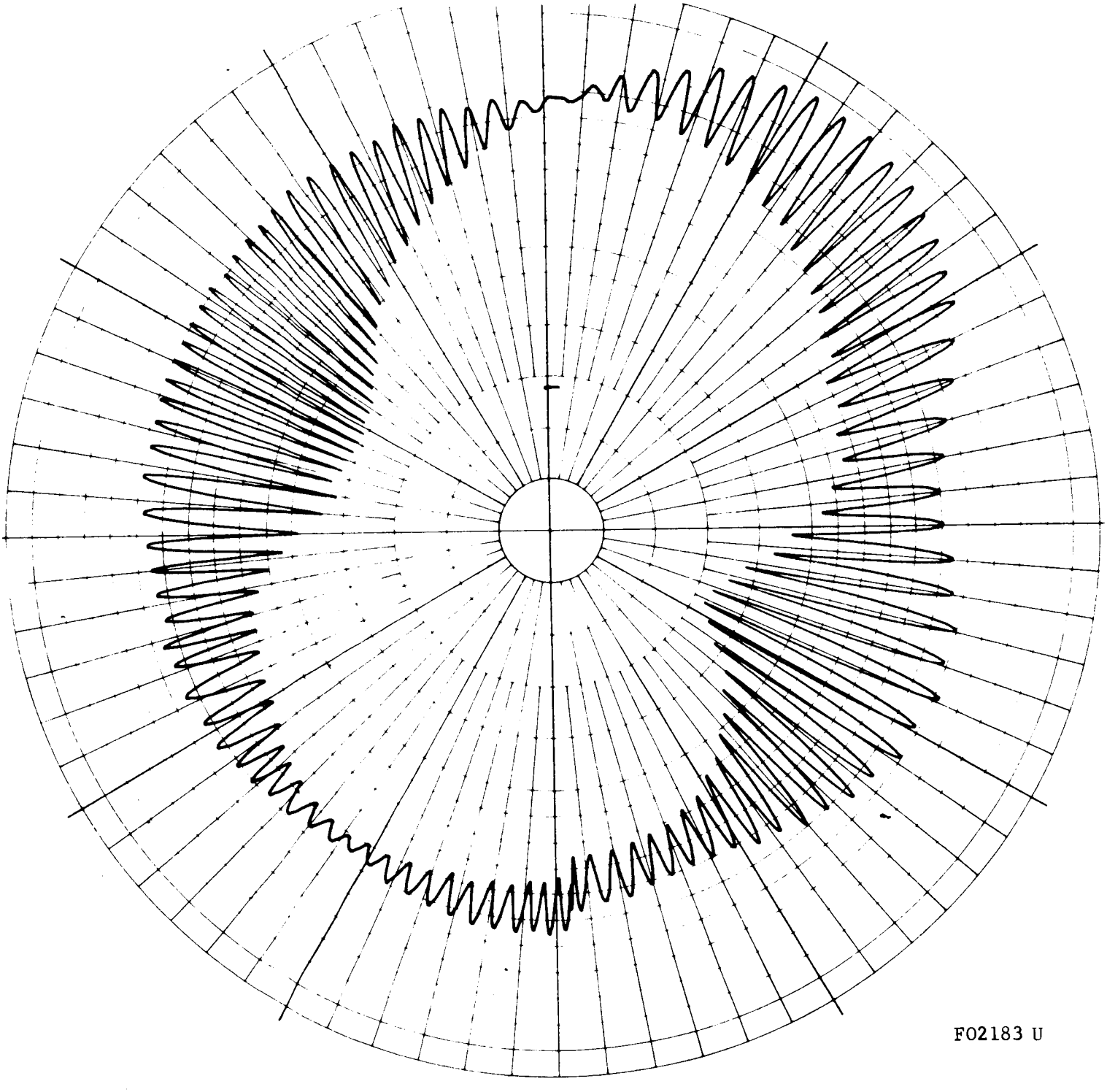

F02183 U

FIGURE B-7. PRE-IMPACT ANTENNA PATTERN FOR PENETROMETER PROTOTYPE NO. 2

B.2.6 HYGE IMPACT TEST

Following the Hyge captive tests was the "free ball" Hyge impact test in which the penetrometer was thrown at 198 ft/sec against a rigid concrete steel target. In this test the penetrometer was taped into a hemispherical cup on the end of the Hyge ram. As in the captive tests, internal power was employed with pre- and post-test external power and special monitoring furnished via the umbilical cable. Velocity of the penetrometer was measured by a photo-cell trap near the impact block. The umbilical connector was pulled out seven seconds before firing, and therefore, internal voltage was not monitored.

Figure B-8 is the oscillograph record tracing of this test. The penetrometer was thrown with the antenna feed loop forward. During free flight the ball rolled about 20 degrees and hit at a velocity of 198 ft/sec. The imprint of the impact on the target was 6-3/4 inches in diameter, indicating a crush depth of about 1-5/8 inches into the balsa limiter. The observed peak carrier frequency shift was 48 KHz occurring during about a 3/4 millisecond impact. This is very close to the design objective of 45 KHz, and is well within the allowable shift. This amount of limiter crushing is identical to that observed in Prototype No. 1 tests. Upon switching to internal power, carrier frequency drift was noted to be higher than normal. The battery pack was adjudged low and checked that way in the post checks. Good SNR performance, however, was observed in the noise-free detection of the carrier.

B.2.7 POST IMPACT TESTS

a. Battery Checks. Post-test battery checks resulted in no-load battery voltage levels of 7.8, 4.4, 6.3, 6.2, and 6.35 volts, respectively. Upon comparison with the pre-test results of Table B.1, the low voltage groups of cells was again shown to be low in capacity.

b. Antenna Pattern. The antenna pattern measurement was repeated. Figure B-9 shows the measured results. Again the pattern depicts the desired omnidirectional characteristics, showing no degradation as a result of the severe Hyge testing.

c. Power Output Reference. The power output reference check was repeated with the results shown in Figure B-3. Relatively little change was observed between pre- and post-test results.

B.3 DISASSEMBLY INVESTIGATION

Following the Hyge impact, the impact limiter and antenna were removed. The top hemispherical dome was cut off in thin sections in a lathe. A hot air gun and probe were used to remove the silica-loaded epoxy

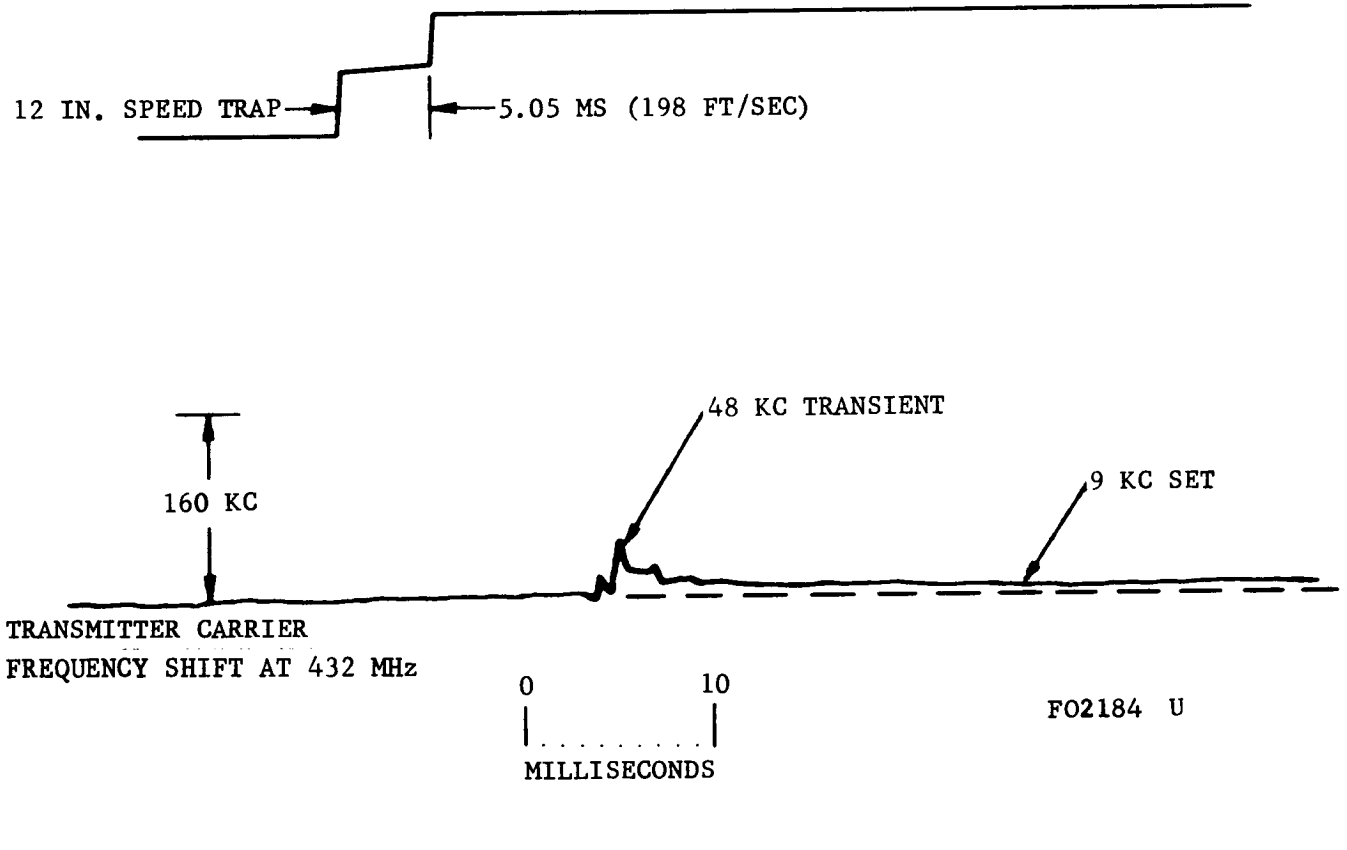

FIGURE B-8. TEST RECORD FOR THE PROTOTYPE NO. 2 HYGE IMPACT AGAINST A RIGID SURFACE

NOTES: PATTERN IN POLAR PLANE TAKEN
WITH EXTERNAL POWER AFTER IMPACT
AT 198 FT/SEC AGAINST RIGID SURFACE

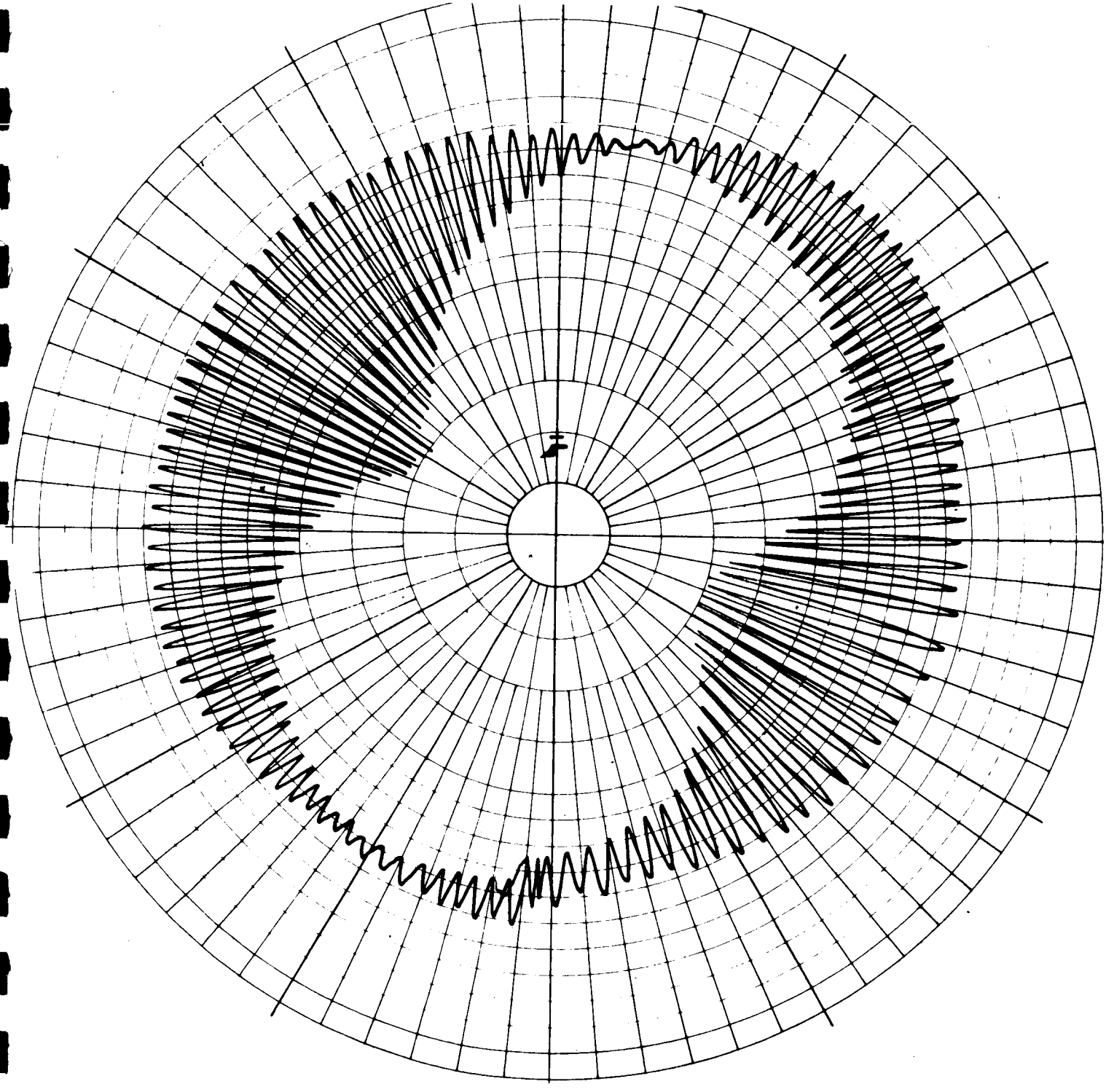

F02185 U

FIGURE B-9. POST-IMPACT ANTENNA PATTERN FOR PENETROMETER PROTOTYPE NO. 2

surrounding signal electronics interconnection wires. This allowed use of a milling machine to remove the signal electronics protective cover, after which the two boards were separated by clipping interconnection posts. Both signal electronics boards were removed intact and bench tested. These tests verified the vailure of the second stage MOS-FET.

The preceding disassembly operations allowed access to the modulation input terminal of the transmitter. Tests showed that 40 KHz signals applied to this terminal would modulate the transmitter in a normal manner. Therefore, it was concluded that the penetrometer Prototype No. 2 was suitable for rebuilding by replacing the signal electronics module and the other removed hardware. This reconditioning of Prototype No. 2 was initiated in parallel with the buildup of Prototype No. 3.

B.4 CONCLUSIONS AND TEST RESULTS

Certain conclusions and observations may be made as a result of the test findings. The difficulty in freeing the probes following limiter bond, with the subsequent shorting failure of the signal electronics module, impaired the evaluation and test of a complete penetrometer assembly. It was possible, however, to gain test data on all other operating subassemblies. The design improvements arising from Prototype No. 1 testing resulted in an improved prototype model which minimized previous deficiencies. Obviously, some final assembly problems occurred which will be eliminated in Prototype No. 3 by design changes. The following paragraphs denote conclusions and/or observations made, according to subassemblies.

B.4.1 ANTENNA

The electrical and mechanical integrity of the antenna subassembly was again demonstrated by the results of the Penetrometer Prototype No. 2 testing. The effect of a high velocity impact in the vicinity of the antenna feed loop was satisfactorily evaluated. No degradation in omnidirectional characteristics was noted.

B.4.2 ACCELEROMETER AND SIGNAL ELECTRONICS

Failure of signal electronics operation prevented the evaluation of the accelerometer and signal electronics subassemblies. However, the signal electronics did not fail due to shock or faulty construction. As explained before, it is believed that the signal amplifier was accidentally shorted to a battery voltage while attempting to remove the umbilical connector which had been erroneously epoxied in the impact limiter.

B.4.3 BATTERY AND POWER REGULATOR/TIMER

Battery operation was satisfactory except for the degradation in performance of the 18 to 24 volt cell grouping. This did not hamper the testing of Prototype No. 2 described herein. It certainly contributed to the low capacity performance noted at the conclusion of the final Hyge test. The power supply regulator and timer were found to operate satisfactorily throughout Prototype No. 2 testing. More than ten cycles of timer controlled operating periods were obtained successfully during testing. Active monitoring of the +17 volt power regulator during captive tests 2 and 3 showed no adverse effects from low level shocks.

Degradation in battery performance actually was observed prior to Prototype No. 2 system tests, i.e., during hammer testing operations. Probably one cell in the 18 to 24 volt cell grouping is under voltage. Charging operations resulted in bringing the cell group up to acceptable performance levels for the few cycles required in the test sequence.

B.4.4 TRANSMITTER

The important observation made in Prototype No. 2 tests regarding transmitter performance is the fact that only a 48 KHz frequency transient occurred at Hyge impact. The transmitter, as in Prototype No. 1 tests, did not exhibit any permanent changes due to shock and no basic problems were encountered.

Data taken in the initial turn-on transient test depicts the temperature and frequency stability characteristic for a completely assembled penetrometer for a specific set of conditions (see Figures B-1 and B-2). Additional testing of complete penetrometer assemblies is required before any final conclusions are reached regarding overall temperature and frequency stability characteristics. For example, repeated test runs for varied (soak temperatures) initial conditions would yield a more complete performance picture over the anticipated operational temperature regime.

APPENDIX C

TEST REPORT FOR (REFURBISHED) PROTOTYPE NO. 2

C.1 INTRODUCTION

This appendix describes the test results for the refurbished Penetrometer Prototype No. 2. Complete functional operation of an omnidirectional penetrometer was achieved during this test sequence.

As reported in Appendix B, a malfunction in the signal electronics second-stage MOS-FET of the original Prototype No. 2 prevented operation of the acceleration sensing function. The refurbishing operation, therefore, consisted of removing the limiter, the antenna and antenna spacers, and machining off the structure upper hemisphere to gain access to the signal electronics assembly. The signal electronics failure was attributed to the additional handling and rework operations that were required in the process of removing the umbilical connectors which had been inadvertently potted into the limiter during the original final assembly sequence. The signal electronics assembly was successfully replaced and Prototype No. 2 reassembled, incorporating design changes scheduled for Prototype No. 3.

In an effort to minimize further delays, the test sequence was modified to expedite the acquisition of impact test data. The following sections describe the test sequence employed and the results obtained, in the order performed; general conclusions are drawn from the results.

C.2 TEST SEQUENCE

C.2.1 BENCH CHECKOUT

Bench tests were run employing the refurbished penetrometer in conjunction with standard laboratory test equipment and a modified data relay receiving channel. The modification allowed use of an external local oscillator signal to permit 432.4 MHz rf frequency reception. A turn-on transient test, linearity, and a qualitative standard tapping test were identified as the principal tests in this category. The penetrometer was operated using external power, and rf carrier reception was effected via an auxiliary antenna.

a. Turn-On Transient Test. Operating with external power and Prototype No. 2 at essentially room temperature, temperature and frequency stability checks were made by monitoring the rf and data channel outputs. Temperature and rf frequency measurements were obtained and are shown in Figure C-1. The basic test setup is also shown in Figure C-1. A data channel output was also obtained and is shown in Figure C-2. Results denoted an output voltage variation encompassing a 30-second duration but not exceeding 2.7 percent of data channel bandwidth, or about 30 g, based upon Hyge captive calibration data. The initial transient decay was missed, as the recorder start followed the actual turn-on by a few seconds.

b. Linearity Test. An ac 500 Hz sine wave calibration signal was applied at the signal electronics test point, and an output was obtained through the overall relay receiver and AM demodulator channel. Operation was observed to be excessively noisy, and incremental input voltage steps did not produce satisfactory output data. Subsequent checks revealed the problem to be the combination of high signal levels with large deviations causing a blocking of the LPS receiver. Linearity data were not obtained at this time, and a decision was made to continue testing with careful monitoring of signal strength into the LPS receiver while also employing an auxiliary receiver, the AN/FRW-3 Collins receiver. The tapping test was not attempted at this time.

C.2.2 CHARGE BATTERY

Before proceeding into the field test impacts, the penetrometer battery was recharged. As reported in the earlier Prototype No. 2 tests, one set of four cells (18 - 24) was observed to be low. Table C.1 shows the post-charge and interim-post-test no-load voltage readings; that is, the interim period involved three cycles of internal power.

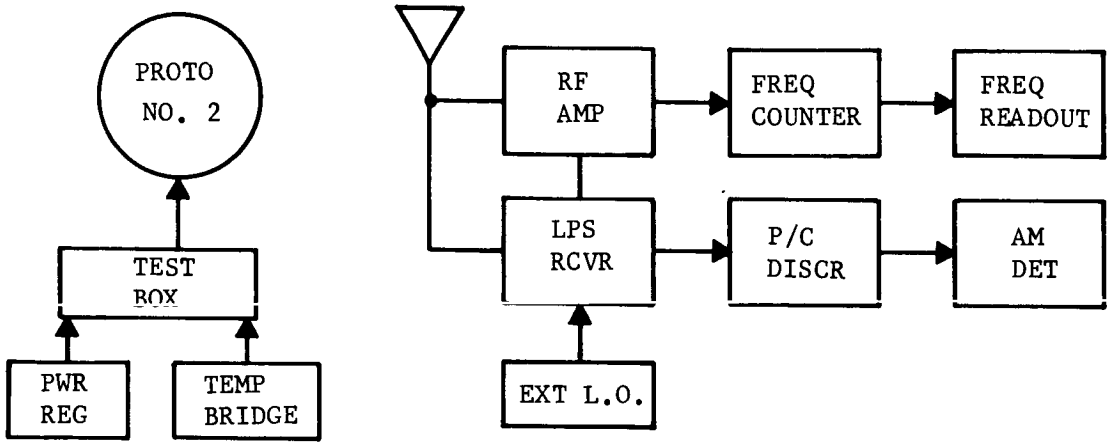

TEST SET-UP - BLOCK DIAGRAM

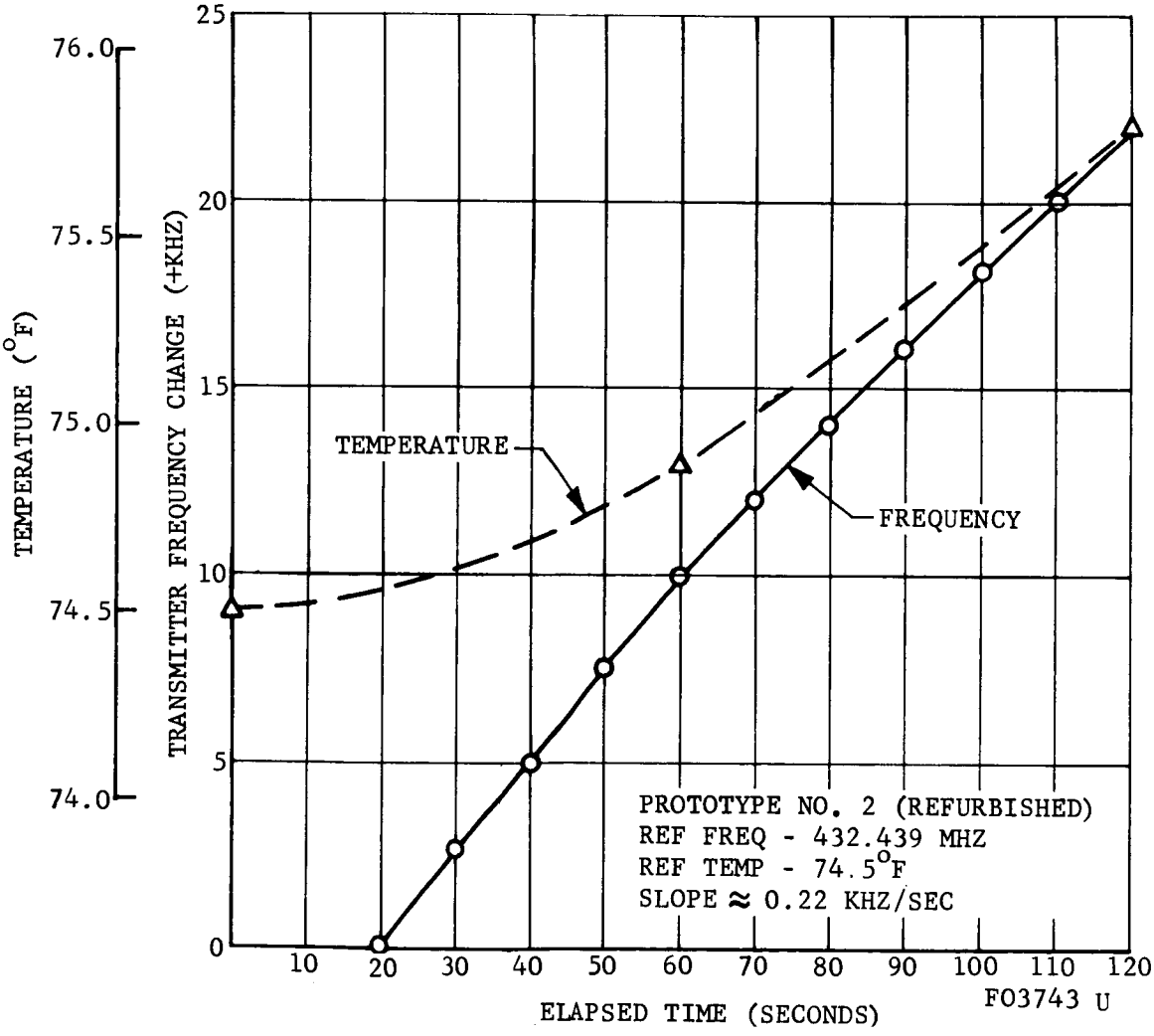

FIGURE C-1. TURN-ON TRANSIENT TEST PROTOTYPE 2

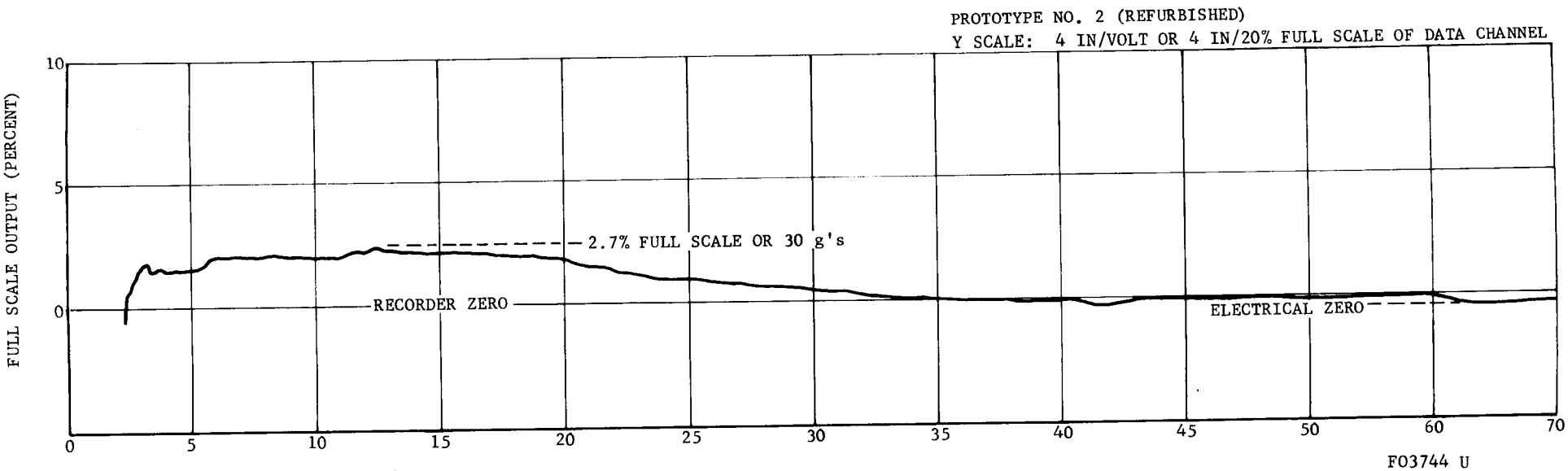

FIGURE C-2. TURN-ON TRANSIENT TEST - AM DETECTOR OUTPUT

TABLE C.1

PROTOTYPE NO. 2 BATTERY DATA

Cell Identification (volts)	No-Load Voltage - dc Post Charge	Post Interim Test
24 to 31.5	7.9	7.9
18 to 24	5.2	4.8
12 to 18	6.2	6.2
6 to 12	6.2	6.2
0 to 6	6.25	6.3
0 to -6	6.4	6.4

C.2.3 FIELD TEST IMPACTS

Four field test impacts were conducted into Nevada 120-2 sand at nominal test velocities of 20, 50, and 85 ft/sec. In each case, the penetrometer was operated on internal power, and impact data were obtained via the 432.4 MHz UHF radio penetrometer-to-data relay channel link.

The tests were conducted at the LPS impact research test site using the MDI accelerator. The target material was conditioned prior to each impact by aeration with dry nitrogen gas at 400 psig for 1 minute. A 20-minute period was allowed for settling of the target material prior to impact. Impact speed was determined from photoelectric speed trap data, including corrections for the static 1-g earth accelerating field acting on the specimen while it was in the speed trap.

The penetrometer was operated on external power through its umbilical connector until 7 seconds prior to firing, at which time removal of the umbilical connector was executed, leaving the penetrometer on internal power. Figure C-3 shows the test setup. Data were recorded on direct readout oscillograph paper at 100 ips. High-frequency response in the data channels was limited by the recorder galvanometers to 3 KHz. All pertinent test results are listed in the succeeding tables. Figures C-4 through C-7 are tracings of the analog data. References to acceleration derived from the penetrometer subcarrier information were obtained from the transfer function (Figure C-8). Tables C.2 and C.3 indicate the tabulated impact results and rf frequency checks obtained during the tests.

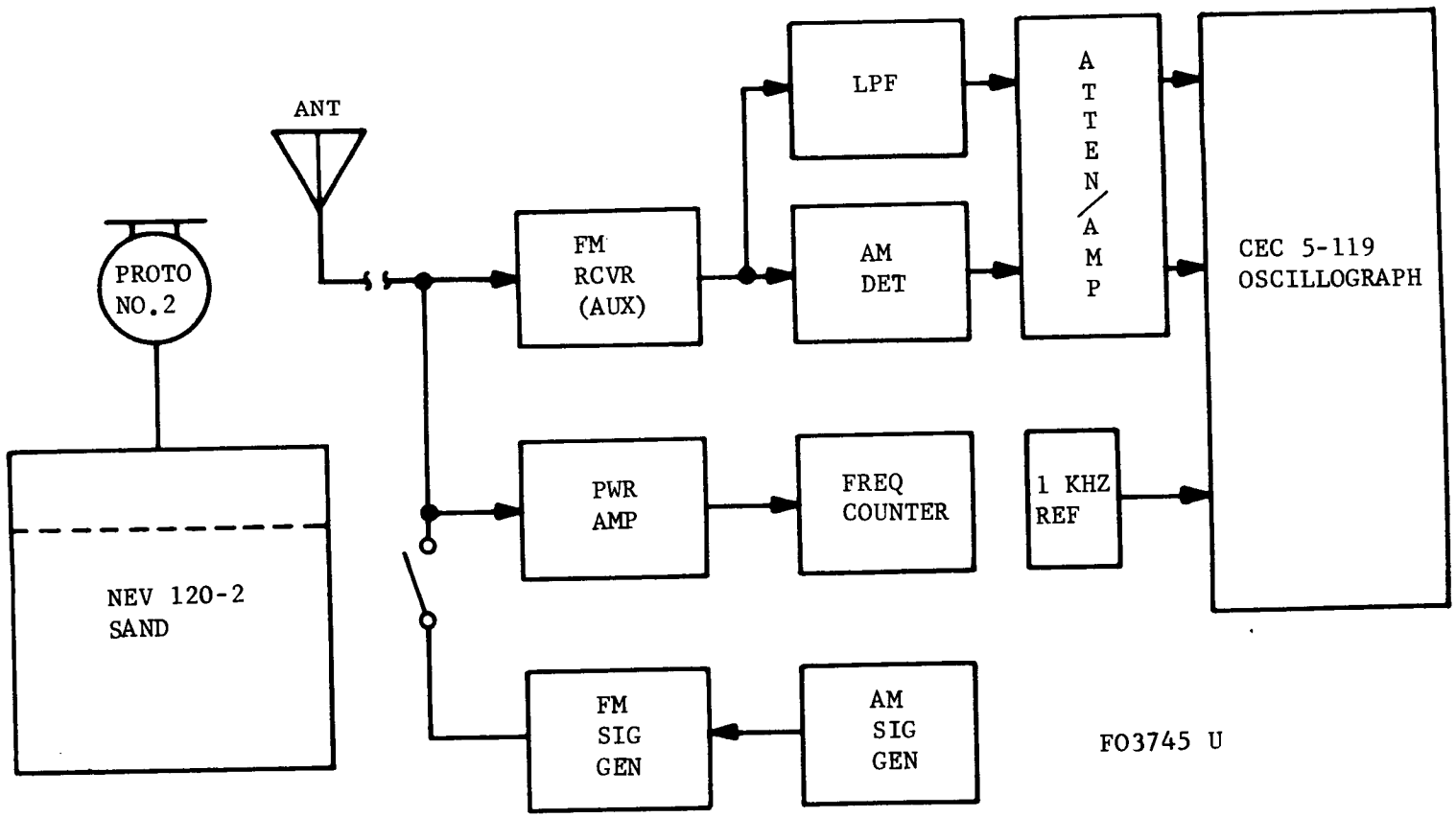

FIGURE C-3. FIELD TEST IMPACT - TEST SET-UP

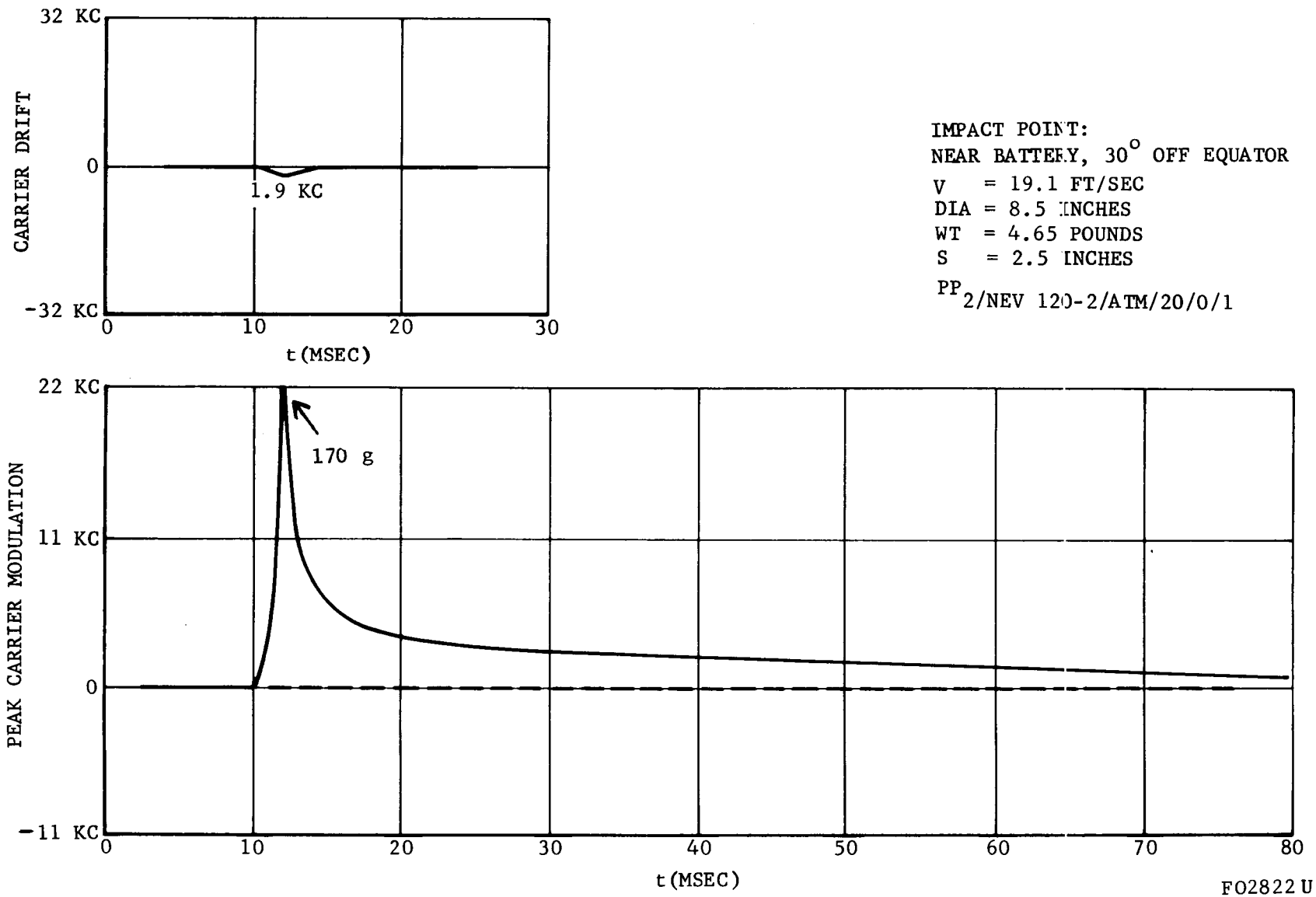

FIGURE C-4. PENETROMETER PROTOTYPE NO. 2, FIELD TEST NO. 1, TELEMETERED DATA

IMPACT POINT: DOUBLER AT EQUATOR

V = 51 FT/SEC
DIA = 8.5 INCHES
WT = 4.65 POUNDS
S = 4.0 INCHES
PP_2/NEV120-2/ATM/50/0/3

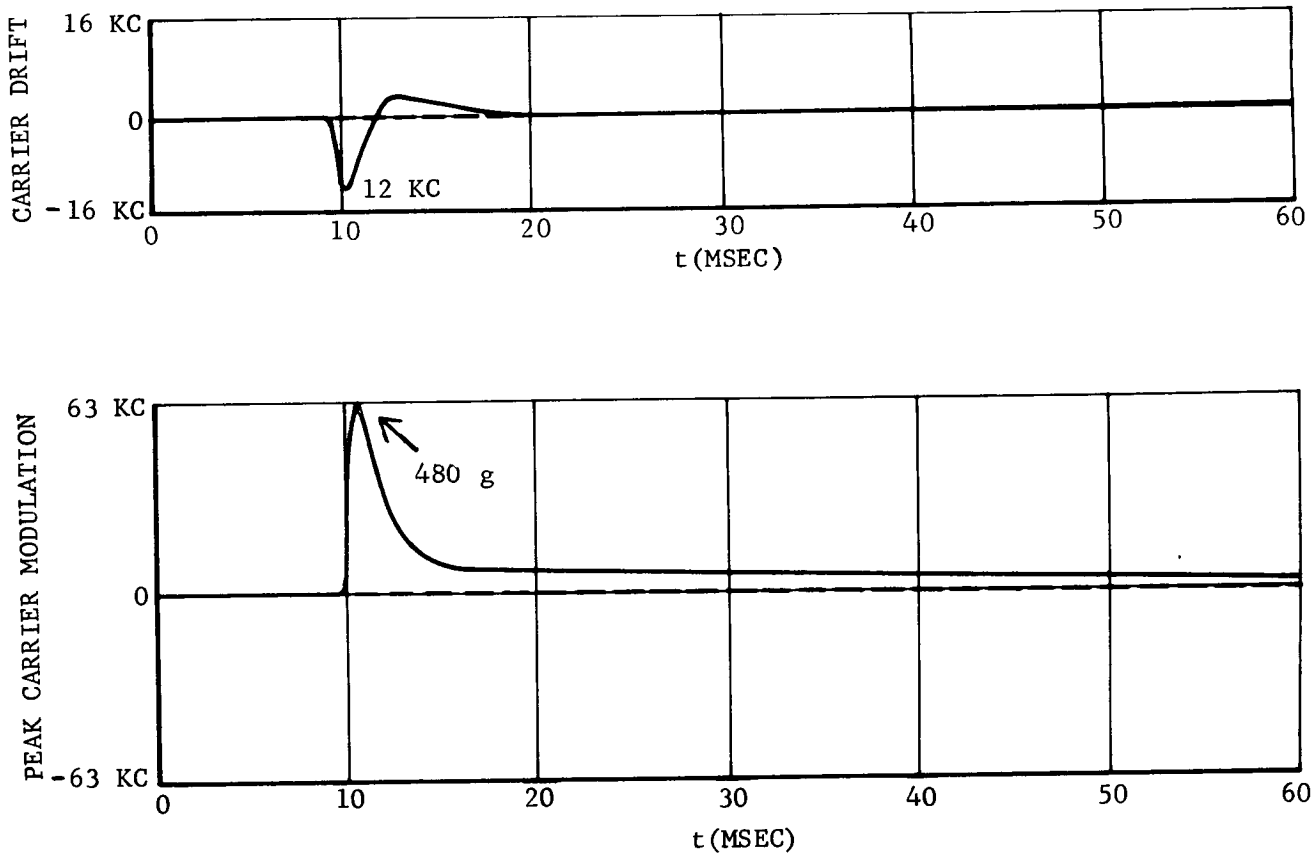

FIGURE C-5. PENETROMETER PROTOTYPE NO. 2, FIELD TEST NO. 2, TELEMETERED DATA

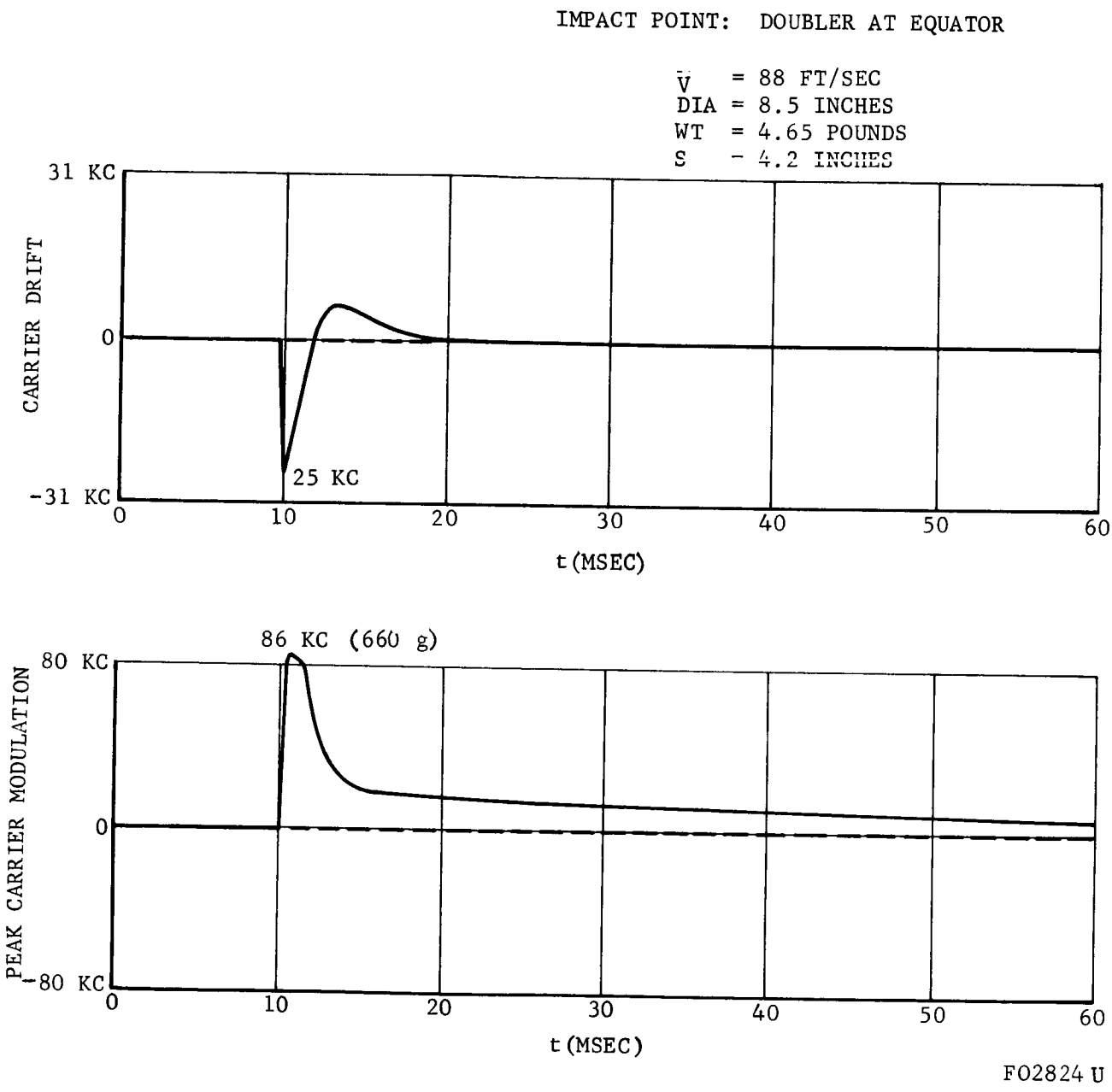

FIGURE C-6. PENETROMETER PROTOTYPE NO. 2, FIELD TEST NO.3, TELEMETERED DATA

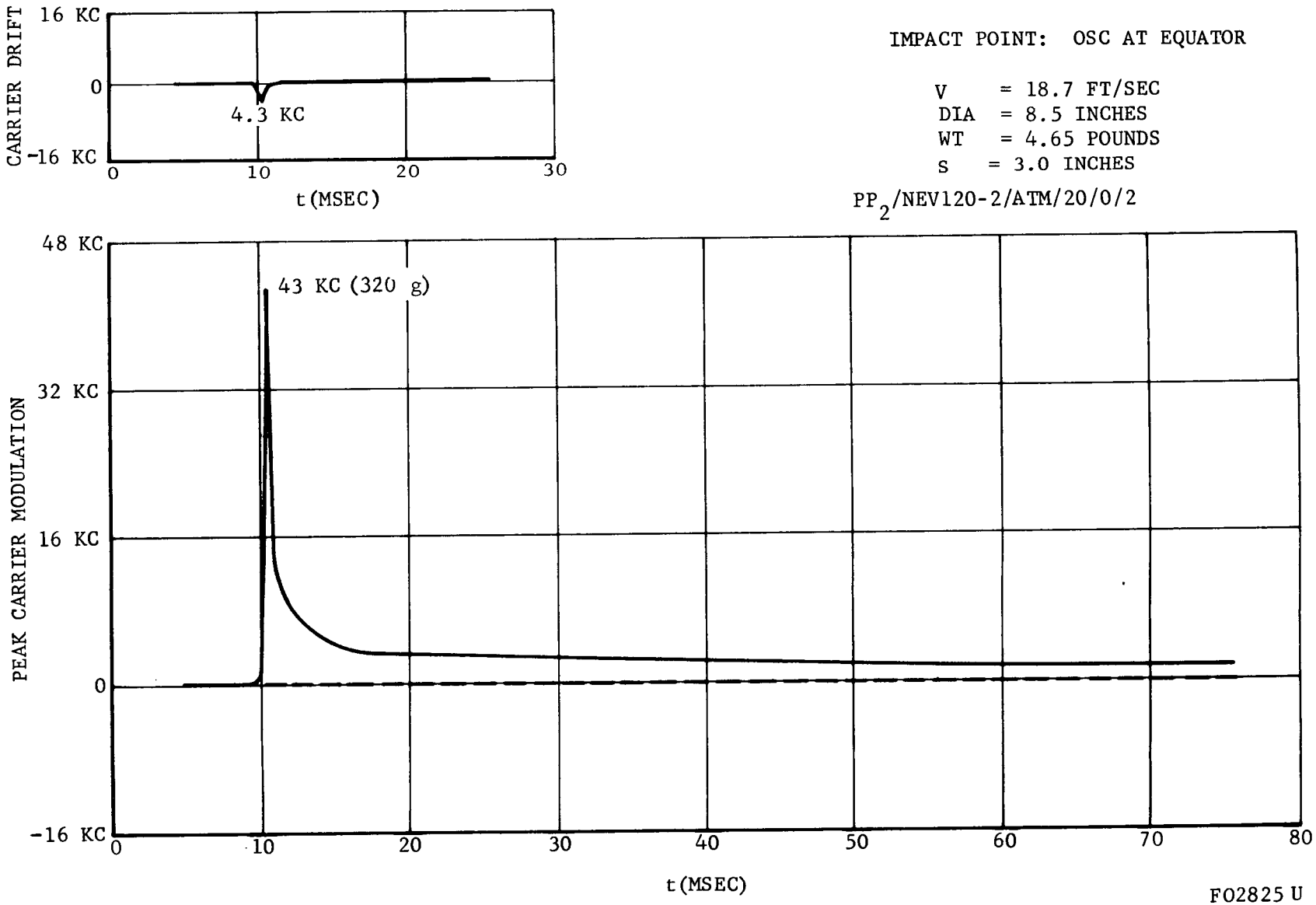

FIGURE C-7. PENETROMETER PROTOTYPE NO. 2, FIELD TEST NO. 4, TELEMETERED DATA

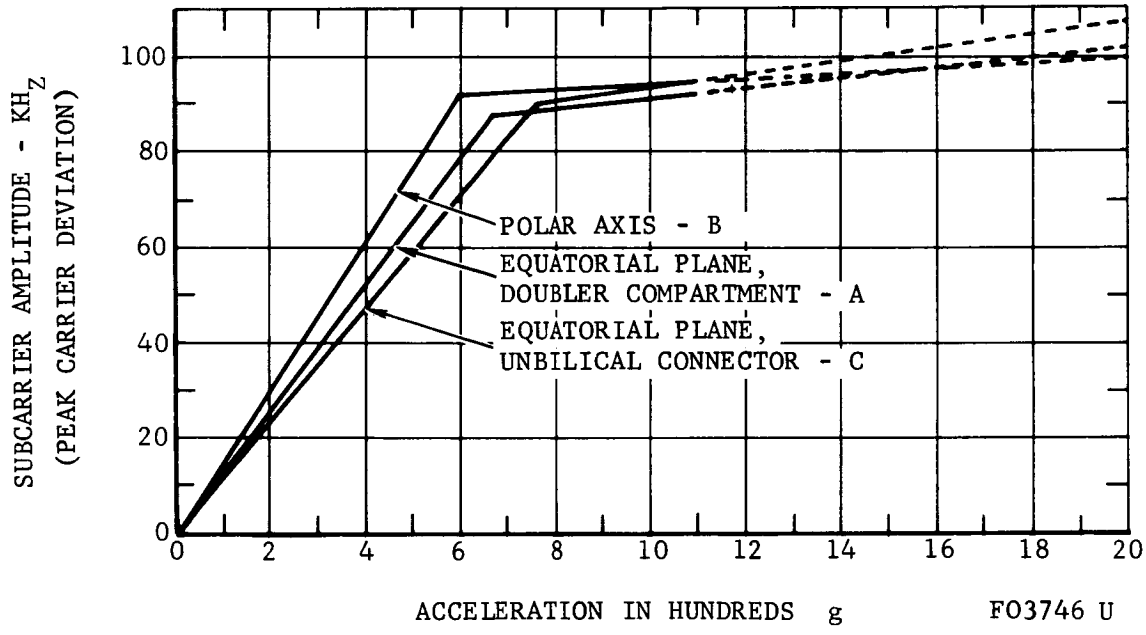

FIGURE C-8. LPS PROTOTYPE NO. 2 MULTIPLE PLOT UNIAXIS SENSITIVITY TRANSFER FUNCTION BY REF. ACCELEROMETER

TABLE C.2

FIELD TEST DATA - IMPACT RESULTS

Field Test No.	Velocity (ft/sec)	Accelerator Fire Pressure (psig)	Accelerator Cushion Pressure (psig)	Sub-carrier (kc)	Peak Carrier FM (kc)	Derived Peak Acceler-ation (g)	Depth of Penetra-tion (in.)
1	19.1	157	100	22	1.9	170	2.5
4	18.7	157	100	43	4.3	330	3.0
2	51	235	100	63	12	480	4.0
3	88	340	100	86	25	660	4.2

TABLE C.3

FIELD TEST DATA - RF FREQUENCY CHECKS

Time	Power	RF Frequency Data (MHz) Test 1	Test 2	Test 3	Test 4
Pre-Run	External	432.442	432.440	432.427	-
Pre-Run	External	-	432.405	432.448	-
Pre-Run (-1 sec)	Internal	-	432.400	432.406	432.381
Post-Run	Internal	-	432.396	432.399	432.373

C.2.4 BATTERY CHARGE

Following the Field Test Impacts and prior to the hyge captive calibrations, the penetrometer battery was recharged to typical post-charge levels. Table C.4 shows the pre-charge, typical post-charge and post-test (three cycles of internal power) no-load voltage readings.

TABLE C.4

PROTOTYPE NO. 2 - BATTERY DATA

Cell Identification (volts)	No-Load Voltage, dc		
	Pre-charge	Typical Post Charge	Post (Captive) Test
24 to 31.5	7.7	8.7	7.8
18 to 24	4.6	7.2	4.4
12 to 18	6.25	7.4	6.3
6 to 12	6.25	7.3	6.3
0 to 6	6.25	7.4	6.35
0 to -6	6.3	7.3	6.4

C.2.5 HYGE CAPTIVE CALIBRATION TEST

Prototype Penetrometer No. 2 was subjected to high-velocity, transient shock motions along three orthogonal axes using the Aeronutronic Hyge facility. The penetrometer was held captive in a fixture on the end of the accelerator ram. A Kistler 808A accelerometer was used on the captive fixture to provide reference acceleration data.

External power and control signals were applied to the penetrometer through its umbilical connector, which was released 7 seconds prior to firing the Hyge. Penetrometer data were obtained via rf link, as was done in the earlier field tests.

All dynamic data were recorded on direct readout oscillograph paper at 100 ips. The frequency response of each channel was limited to 3 KHz by the recorder galvanometer. Hyge fire-pressure and cushion-pressure were 1150 psig and 115 psig respectively for all tests.

The data were reduced by comparing the penetrometer subcarrier demodulator output amplitude to the reference accelerometer signal at corresponding time points for acceleration values in the range of 0 to +450 g to -1100 g. Figure C-8 shows the three transfer functions on one graph for easy comparison.

Table C.5 lists rf frequency checks made before and after the individual calibration runs.

TABLE C.5

RF FREQUENCY CHECKS - HYGE CALIBRATION

Time	Power	Frequency MHz Test A	Test B	Test C
Pre-Run	External	432.379	432.388	432.405
Pre-Run	Internal	432.354	432.344	432.344
Post-Run	Internal	432.321	-	-

C.2.6 PENETROMETER ELECTRICAL CALIBRATION

Laboratory tests were conducted to investigate the electrical calibration difficulties encountered during the earlier bench tests. The receiver blocking problem was eliminated as a factor by careful adjustment (attenuation) of signal input levels into the LPS receivers during any and all subsequent tests. An auxiliary FM receiver, the AN/FRW-3 (Collins), which possesses a wide input signal dynamic range capability, was also employed as an alternate receiver during tests.

Electrical calibrations were made for several types of waveforms, for example, full-sine, half-sine, and triangular. Since signal electronics is unidirectional, it responds only to the positive-going portion of an applied waveform. It was verified on a scope presentation that use of a 500 Hz full sine wave yielded results approximately the same as for a half-sine of equivalent period. The plot of Figure C-9 shows results of two different type calibrations. The oscillograph readout data were obtained prior to the Hyge captive test, while the pulse-type oscilloscope-derived data were obtained a week later. The former utilized a 500 Hz full sine wave into the penetrometer test point, while the latter input signal was a 1 ms half-sine pulse with a long duty cycle. The knee of the compression point occurs at about 320 g. Figure C-8 of the Hyge calibration run shows the knee to be about 680 g. The electrical and actual g calibrations appeared to differ, therefore, by about a factor of 2. No immediate explanation of this difference was found. It should be noted that the electrical calibration test point occurs following a unity gain differential amplifier input stage and signal attenuator circuit in the signal electronics. The omni-accelerometer works into the unity gain input stage. Some form of loading or reduction in sensitivity of this segment of the acceleration-sensing function could account for the stated difference.

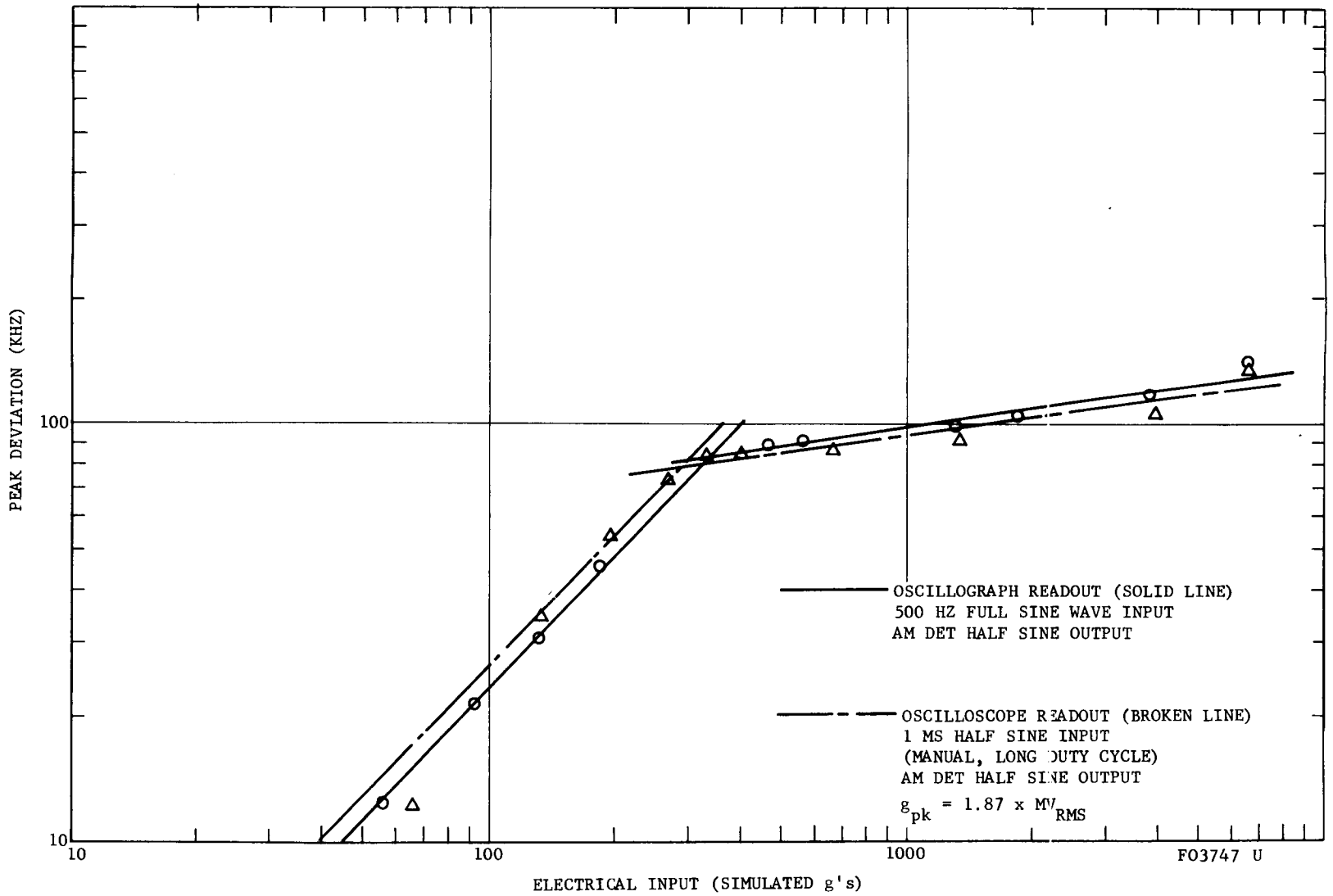

FIGURE C-9. PROTOTYPE NO. 2 SYSTEM (ELECTRICAL) CALIBRATION

The exact cause will have to be determined at a later date; meanwhile, the "real" or actual g calibration versus peak deviation will be employed in all subsequent data interpretations.

C.2.7 ANTENNA PATTERN AND FIELD STRENGTH

To document antenna pattern data for the refurbished Prototype No. 2, a pattern was taken and is shown in Figure C-10. No pre-test patterns were made because of various scheduling problems affecting the conduct of tests. Relative field strength readings were similarly taken only once. The minimum and maximum relative power output readings taken were -10.5 db and -8.5 db, respectively. The total field relative to Prototype No. 1 total field data was noted to be -7.0 db.

C.2.8 FIELD TEST HYGE IMPACT

Prior to the "free ball" Hyge impact, the penetrometer battery was recharged to the typical post-charge no-load voltage levels. For the subsequent rigid impact test, Prototype No. 2 was thrown against a reinforced concrete block with a steel cover plate using the Hyge facility to throw the projectile. Data were obtained and recorded in the same manner as in the calibration tests described above.

The impact speed was 198 ft/sec, resulting in a balsa limiter crush depth of 1-9/16 inch. Figure C-11 illustrates the data recording and test setup information. Figure C-12 is a tracing of the recorded penetrometer data at impact. Applying the transfer function of Figure C-8 to the subcarrier modulation data of Figure C-12 shows a peak shock during the impact of only 2400 g. The mechanism of the erroneous result is not known, nor is it known why the 70 percent zero-shift occurred.

C.2.9 POST-IMPACT CHECKS

Operation of the penetrometer was satisfactorily checked for basic electrical performance integrity following the rigid impact test. Subsequent laboratory checks resulted in the linearity and frequency response data shown in the plots of Figures C-13 and C-14, respectively.

The linearity or calibration data are seen to have the knee at about 320 g, which agrees with the pre-impact test data shown in Figure C-9. However, differences in peak deviation at the corresponding knee points may be noted and are attributed to the difference in readout. Figure C-13, derived at the discriminator output, is about 25 percent higher than the data derived at the demodulator output. This type of readout performance has been observed in the resulting test data. Upon correlating both sets of electrical calibration data and comparing them to actual g (captive Hyge) calibration, which are read out in identical terms (that is, at the AM demodulator output), there still exists the approximate factor-of-2 difference between electrical and actual g calibration data.

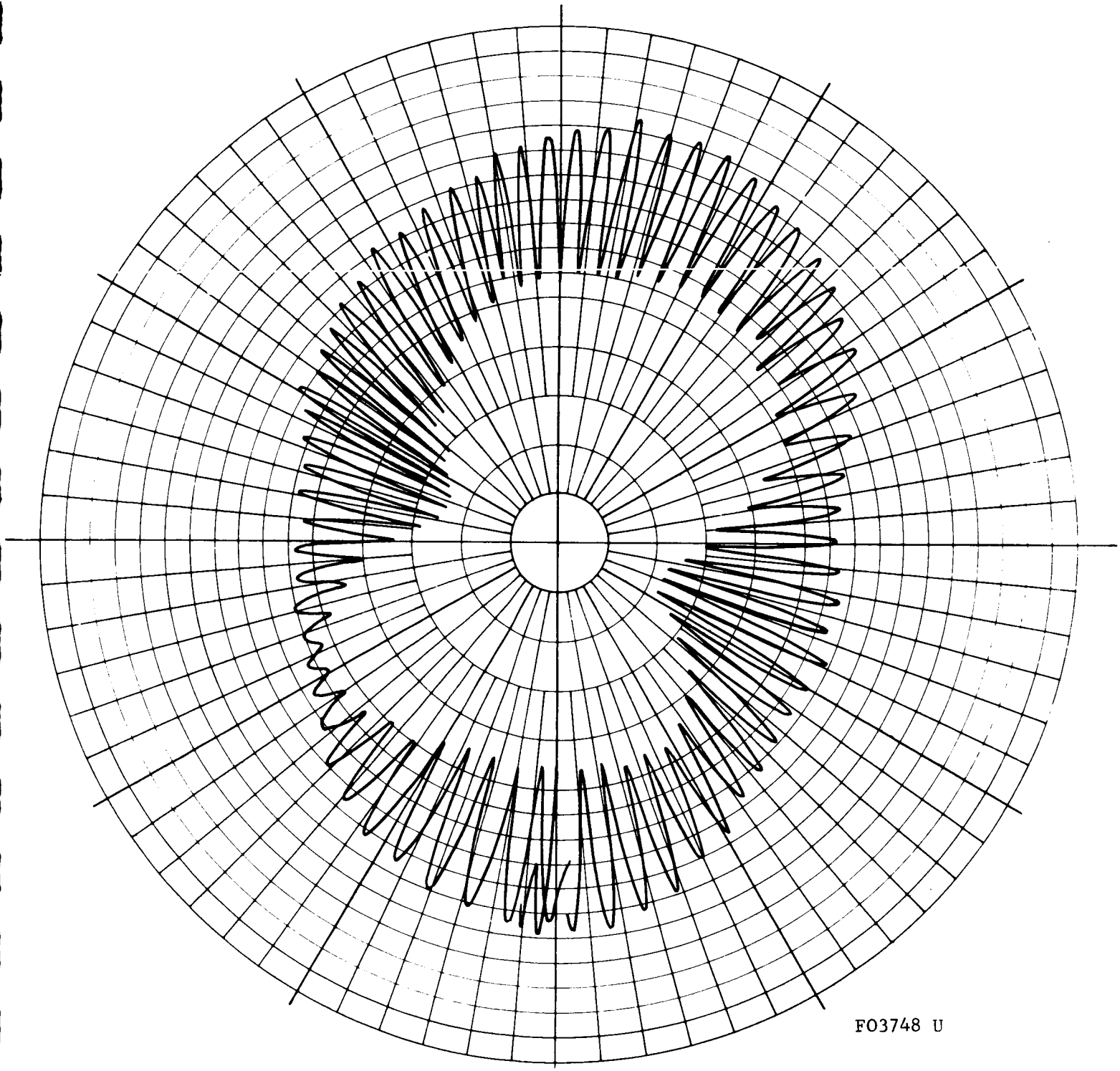

NOTES: REFURBISHED PENETROMETER
POLAR PLANE
POST CAPTIVE HYGE/PREHYGE RIGID IMPACT

FIGURE C-10. PROTOTYPE NUMBER 2 ANTENNA PATTERN

OSCILLOGRAPH TRACES (CEC 5-119) (PER FIG. 3 OF TEST PROCEDURE)

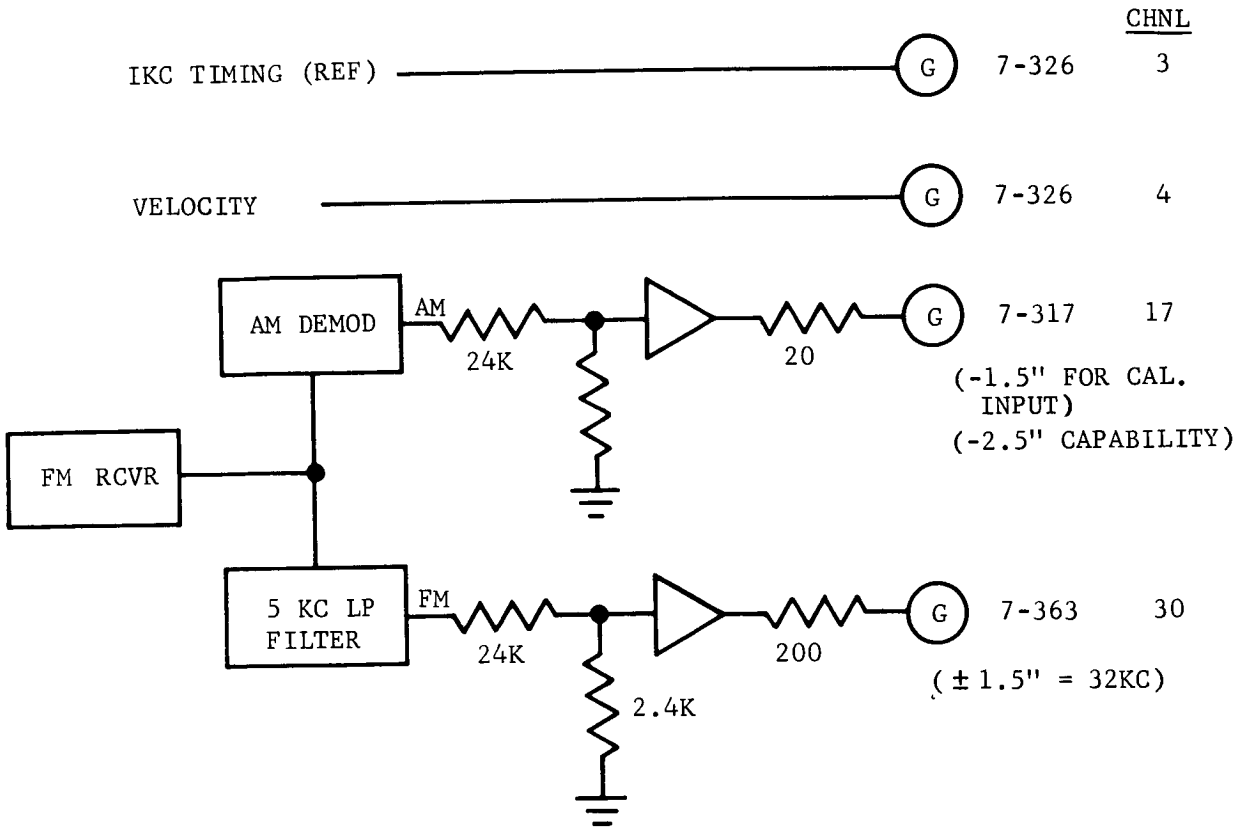

(a) INSTRUMENTATION

PROJECTILE: WT. = 4.72 LB, DIA = 8.49" PROTOTYPE NO. 2 (REFURBISHED)
HYGE PRESSURES: P_f = 800psi, Pc = 80 psi
RECORDED IMPACT VELOCITY: 5.07 MS = 198 fps

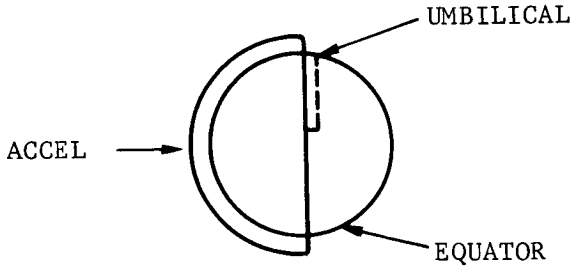

FO3749 U

(b) IMPACT TEST INITIAL CONDITIONS

FIGURE C-11. HYGE RIGID IMPACT - TEST SET UP

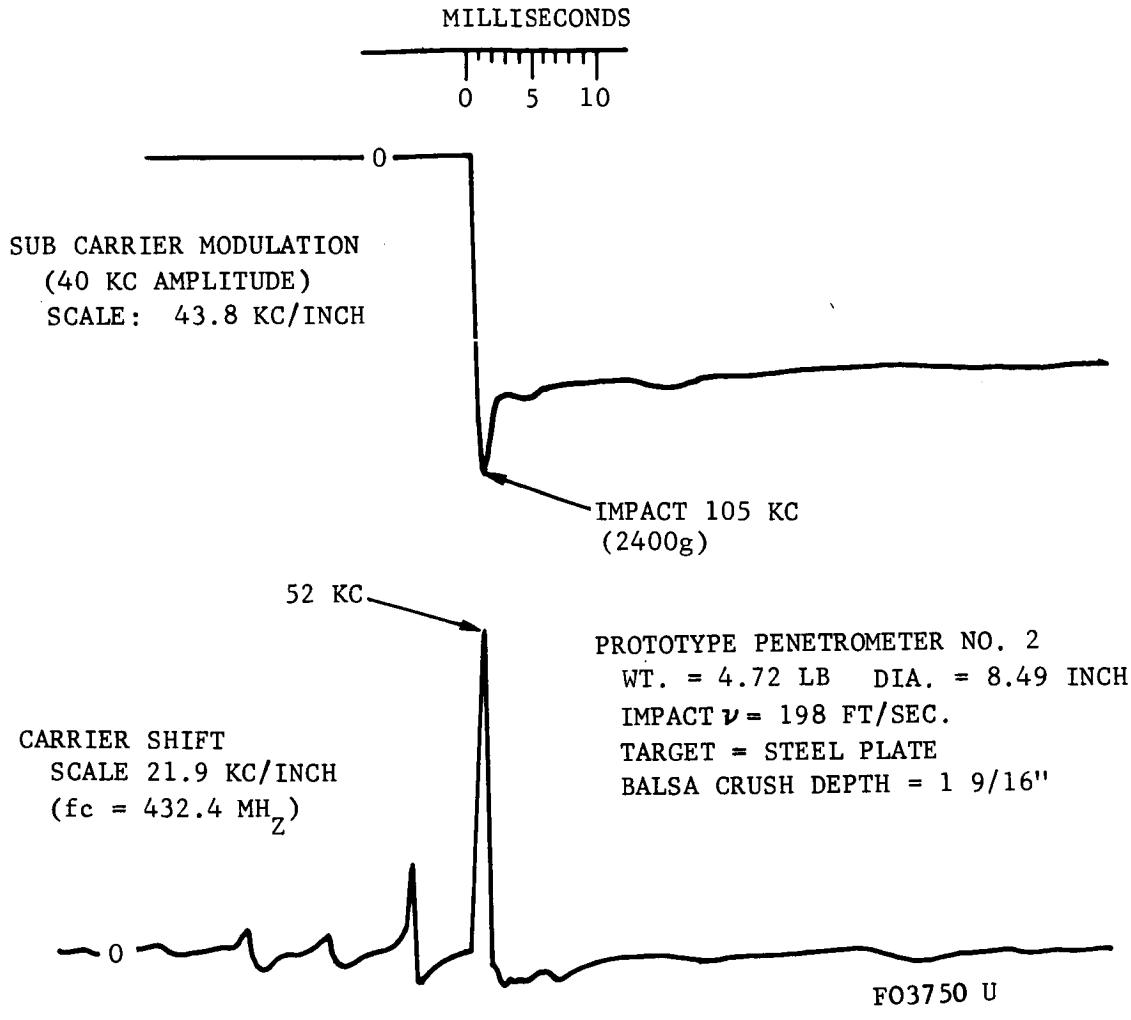

FIGURE C-12. HYGE RIGID IMPACT TEST DATA

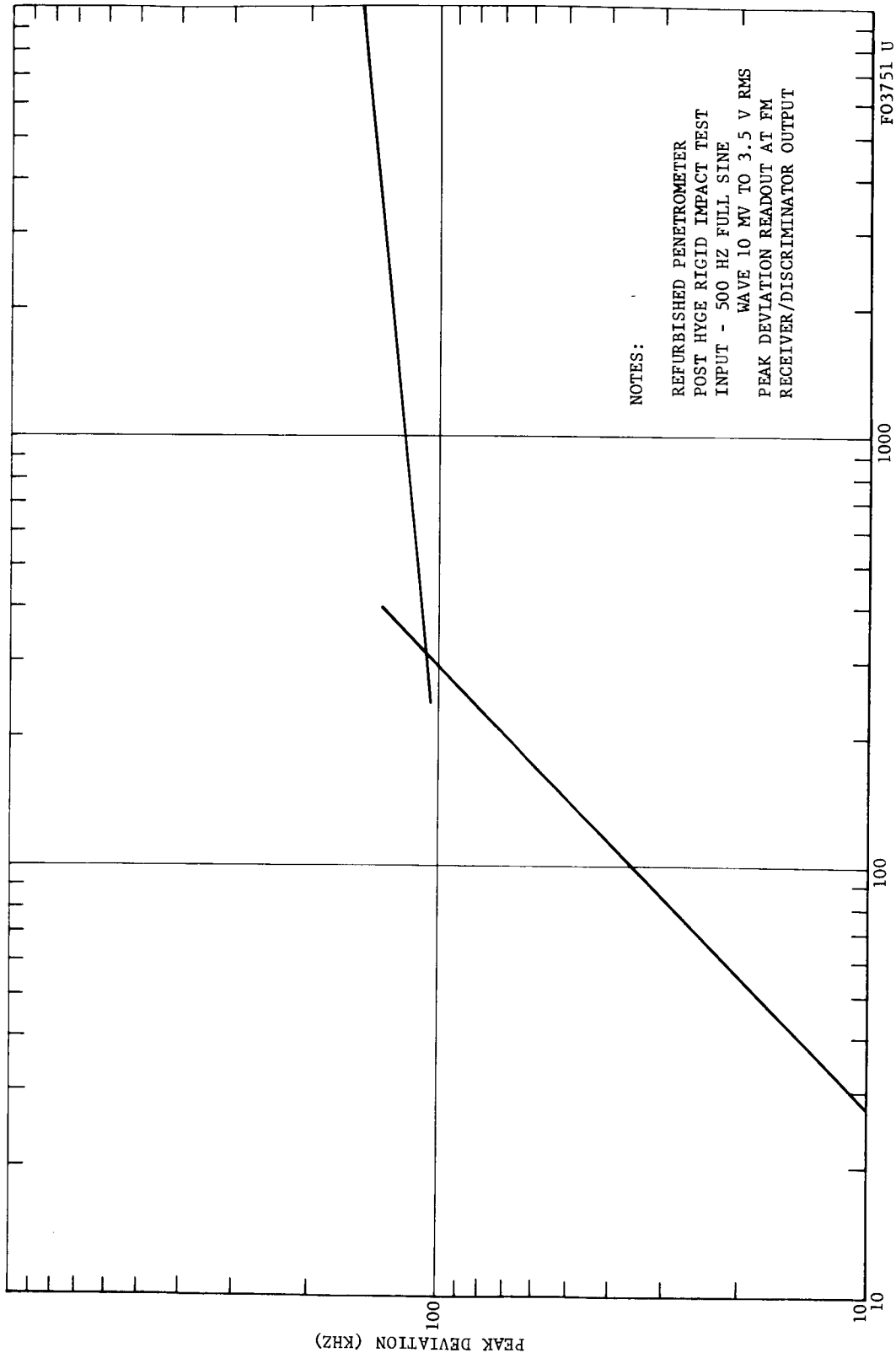

FIGURE C-13. PROTOTYPE NO. 2 ELECTRICAL CALIBRATION

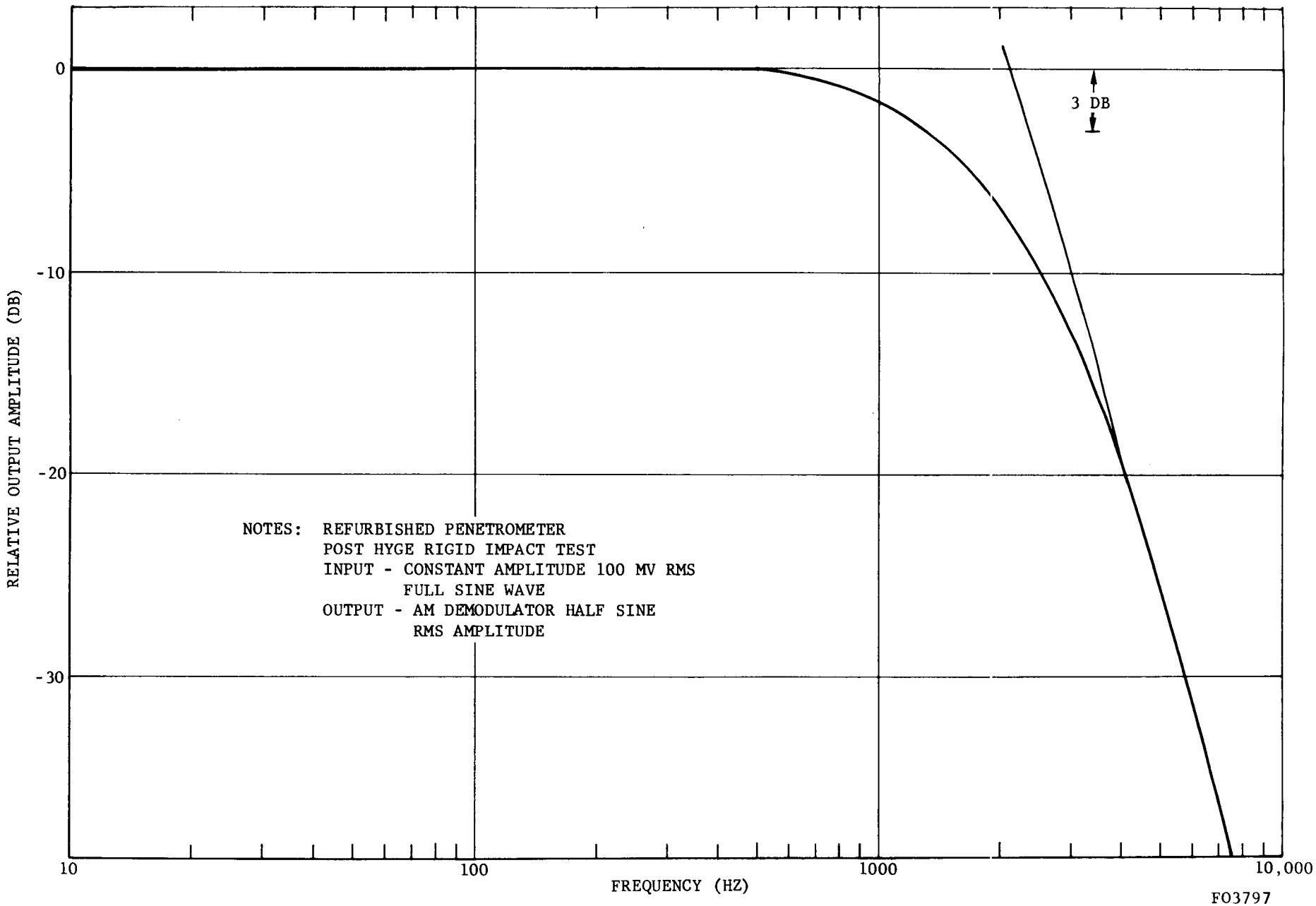

FIGURE C-14. PROTOTYPE NO. 2 FREQUENCY RESPONSE

C.3 CONCLUSIONS AND TEST RESULTS

A milestone was reached by achieving complete functional operation of an omnidirectional penetrometer in this series of tests. Extensive testing could be carried out in accordance with a written general test procedure. Numerous low-velocity impact testing was performed as part of controlled field tests and multiple drop system tests. The results of the tests completed were generally very satisfactory with few anomalies observed. The principal anomalies observed were in the area of system calibration, that is, resolving electrical calibrations with actual physical g (acceleration) inputs, and of Hyge rigid impact performance. The calibration problem is believed to be one of refinement or improvement of the entire calibration approach. The rigid impact test, which indicated g levels much lower than anticipated, constituted information not previously encountered. Further investigation and testing of improved calibration techniques are currently underway as part of a work extension authorized under the present contract. Results are expected to provide answers to the stated anomalies. An account of other conclusions and/or observations derived from the variety of tests reported herein is presented according to assemblies in the succeeding paragraphs.

C.3.1 ANTENNA

The electrical and mechanical integrity of the antenna assembly was maintained as a result of the extensive testing performed on the refurbished model of Prototype No. 2. The pattern of Figure C-10 depicts the basic antenna performance characteristics and exhibits only a minor degradation from that which is typical. This was primarily because usual antenna final tuning procedures could not be performed on the reworked prototype.

C.3.2 ACCELEROMETER AND SIGNAL ELECTRONICS

Satisfactory functional operation of the accelerometer and signal electronics was demonstrated in the numerous tests and under a variety of operating shock environments. As stated previously and in the detailed test results, both a calibration and rigid impact performance anomaly existed. Further investigation of these anomalies was recommended and is scheduled to be carried out in the subsequent work extension. The turn-on transient characteristic of the signal electronics appeared allowable over the interval observed, although improvement would be sought in subsequent development.

The multiple plot of individual uniaxis sensitivity of Figure C-8 depicts the omnidirectional sensitivity observed during Hyge captive test calibrations. The variation is illustrated by examining the high sensitivity portion below the knee. A variation of about $\pm$10 percent about a mean

value of 0.133 KHz/g is seen to exist. This is presumably due to the accelerometer, since electrical scaling checks of the associated electronics did not appear to exhibit this same characteristic.

C.3.3 BATTERY AND POWER REGULATOR/TIMER

The battery and power regulator/timer performed satisfactorily, and no additional significant degradation developed over that previously reported for the original Prototype No. 2 configuration. It should be noted that the battery and power regulator/timer are, of course, the same assemblies employed in the original Prototype No. 2. Some degradation in charge retention was observed, but frequent recharge cycles brought the battery up to acceptable performance levels for the test sequences employed herein.

C.3.4 TRANSMITTER

Transmitter shock sensitivity under Hyge rigid impact was commensurate with that observed in the previous tests on the "original" prototype. This constituted an indication of repeatability. No permanent changes because of shock were observed in this repeat test. Data taken in the turn-on transient tests depicting temperature and frequency stability characteristic agreed essentially with that previously observed. Frequency stability was within the revised transmitter performance drift characteristic.

APPENDIX D

TEST REPORT FOR PROTOTYPE NO. 3

D.1 INTRODUCTION

This report describes the test results for the Lunar Penetrometer Prototype No. 3. Complete functional operation of an omnidirectional penetrometer was achieved as demonstrated by the test results reported herein. This third prototype model represents the last of an initial series of three prototypes designed and developed as part of NASA contract NASI-4923. Appendices A, B, and C discuss the results obtained in tests of Prototypes No. 1 and 2.

Prototype No. 3 is the second completely functional omnidirectional penetrometer successfully developed. The complete test sequence identified in the testing of the preceding prototypes was shortened to facilitate the completion of multiple penetrometer tests, which were aimed at demonstrating overall system functional operation. The principal tests completed on Prototype No. 3, therefore, were the bench tests of linearity and frequency response, antenna pattern and relative output power checks, and Hyge captive g calibration in three axes. It should be noted that additional functional drop tests performed as part of an interim, extension of the initial contract, demonstrated very satisfactory operation and repeatability for a series of low-velocity impacts.

D.2 TEST SEQUENCE

D.2.1 BENCH CHECKOUT

Bench tests were conducted using Prototype No. 3 in conjunction with standard laboratory test equipment and a data relay receiving channel.

The auxiliary FM receiver, the Collins AN/FRW-3, was used in place of the LPS receivers which were being integrated into the Data Relay for use in the subsequent multiple drop system functional tests. Prototype No. 3 was operating at a standard assigned penetrometer frequency of 438.0 MHz.

a. Turn-On Transient Test. Operating with external power and Prototype No. 3 at room temperature, rf frequency and data channel stability checks were made. The results obtained are shown in Figure D-1 and D-2. The basic test setup is also shown in these illustrations. The data channel output depicts the turn-on transient dying out in several seconds and a slower perturbation reaching an equivalent 28.5 g value before decaying to the observed channel residual level.

b. Linearity and Frequency Response. An ac electrical calibration was injected at the signal electronics test point via the umbilical connector to measure overall linearity of the penetrometer via an FM receiver and AM demodulator channel. The overall frequency response characteristics of the same channel elements were also obtained. Figures D-3 and D-4 show the linearity and frequency response characteristics respectively.

D.2.2 ANTENNA PATTERN AND RELATIVE OUTPUT POWER

The antenna pattern of Figure D-5 was measured in the polar plane with a spinning dipole in the standard method previously described in Appendix A. The Penetrometer Prototype No. 3 was operated on external power for this test. Polarization axial ratio is exhibited in the varying peaks which result from the spinning dipole measurement technique.

A measurement of relative field strength was also made. For this check the penetrometer is in the standard test enclosure of rf absorbing material, and field strength is measured at one location. Both minimum and maximum readings are noted by means of rotating a receiving dipole about its axis. Readings of -11.5 db and -10.0 db were observed, respectively. The total field is -8.2 db relative to that obtained for Prototype No. 1.

D.2.3 HYGE CAPTIVE CALIBRATION TEST

An original attempt to calibrate the penetrometer was thwarted when a failure in the Hyge ram test fixture attachment occurred. The fixture containing the penetrometer broke loose from the ram during the test and ricocheted around the inner walls of the Hyge chamber. The penetrometer remained operating throughout its timed cycle and incurred only slight damage to the limiter and outer cover. Following rework of the fixture and some patchwork on Prototype No. 3, the test was successfully completed.

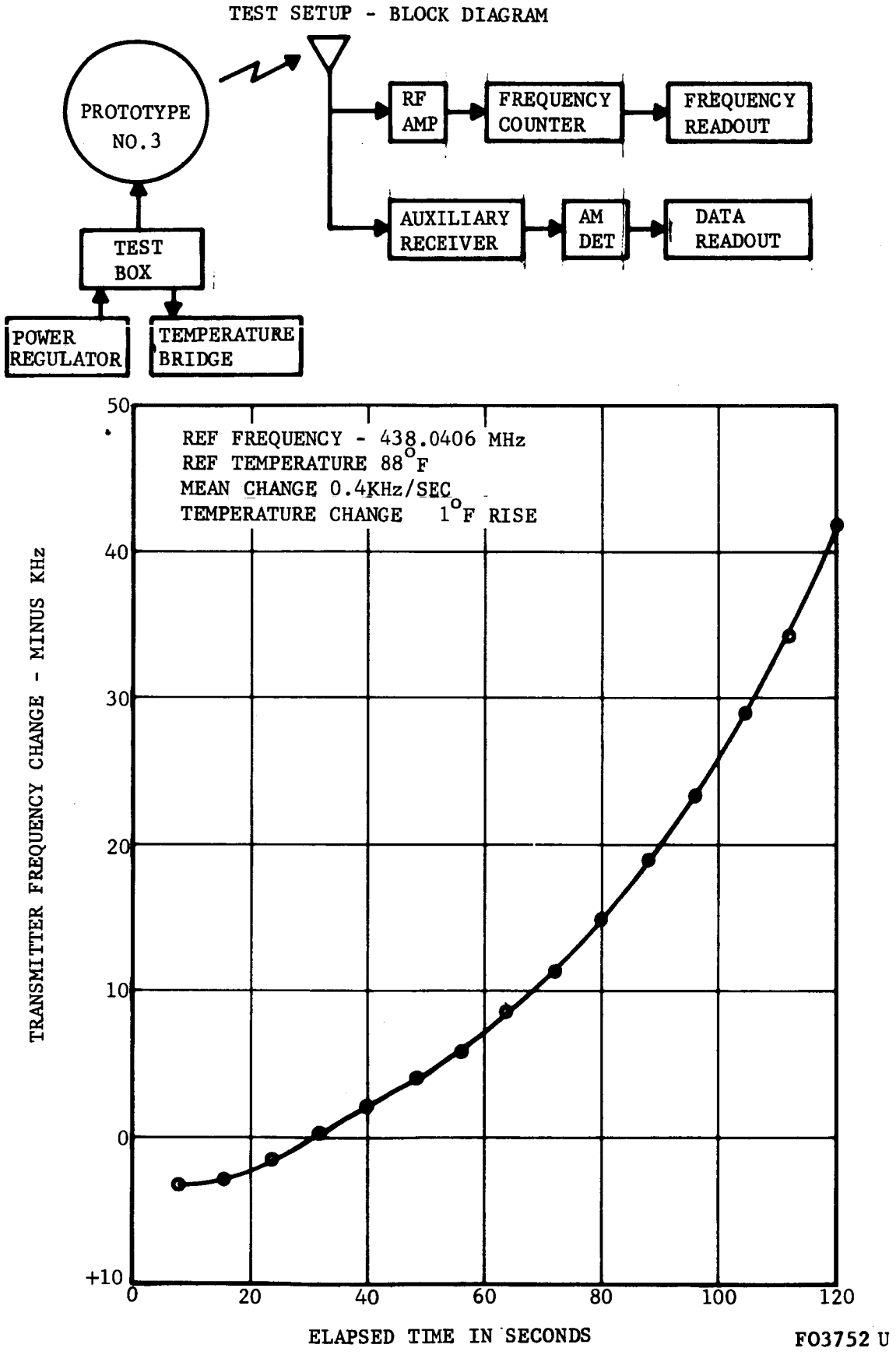

FIGURE D-1. TURN-ON TRANSIENT TEST PROTOTYPE NO. 3

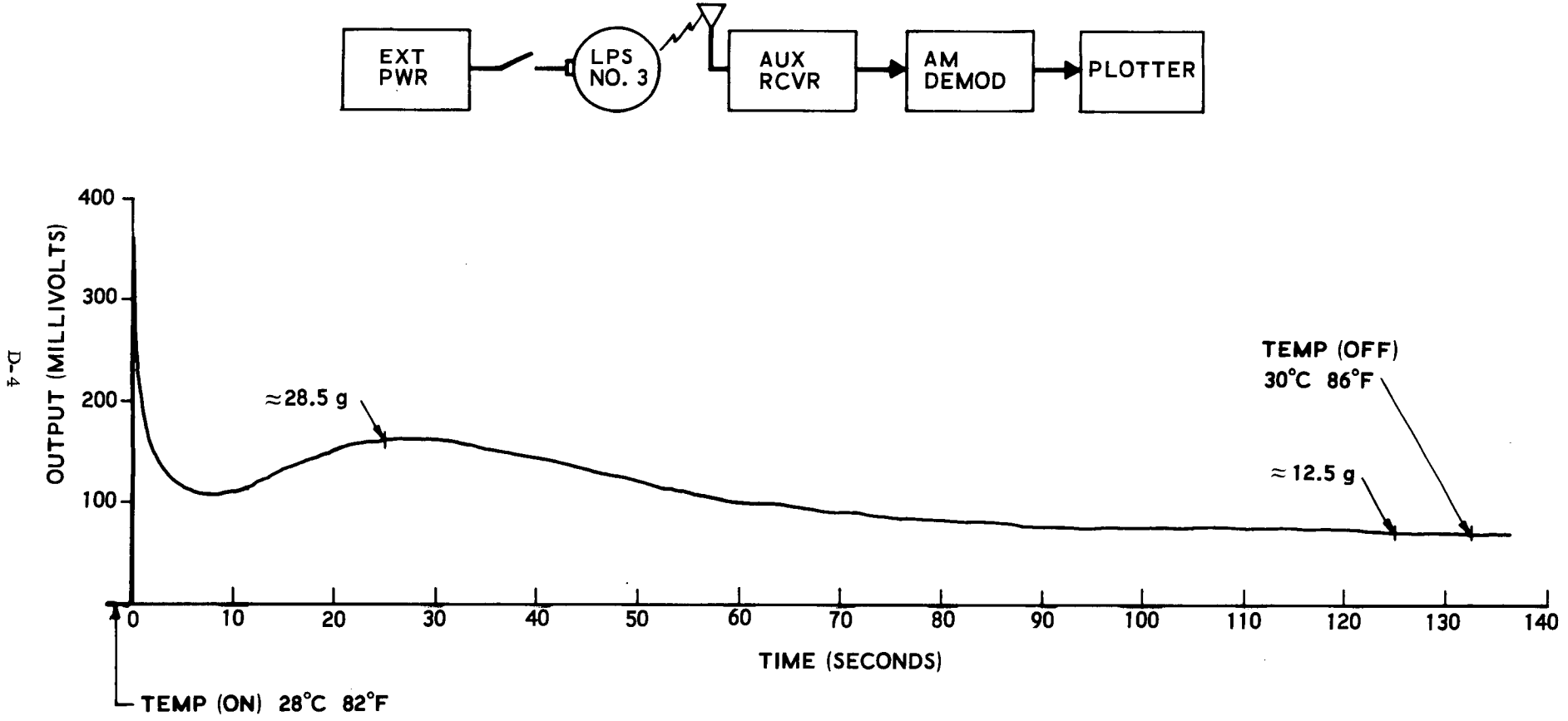

FIGURE D-2. PROTOTYPE NO. 3 TURN-ON TRANSIENT TEST

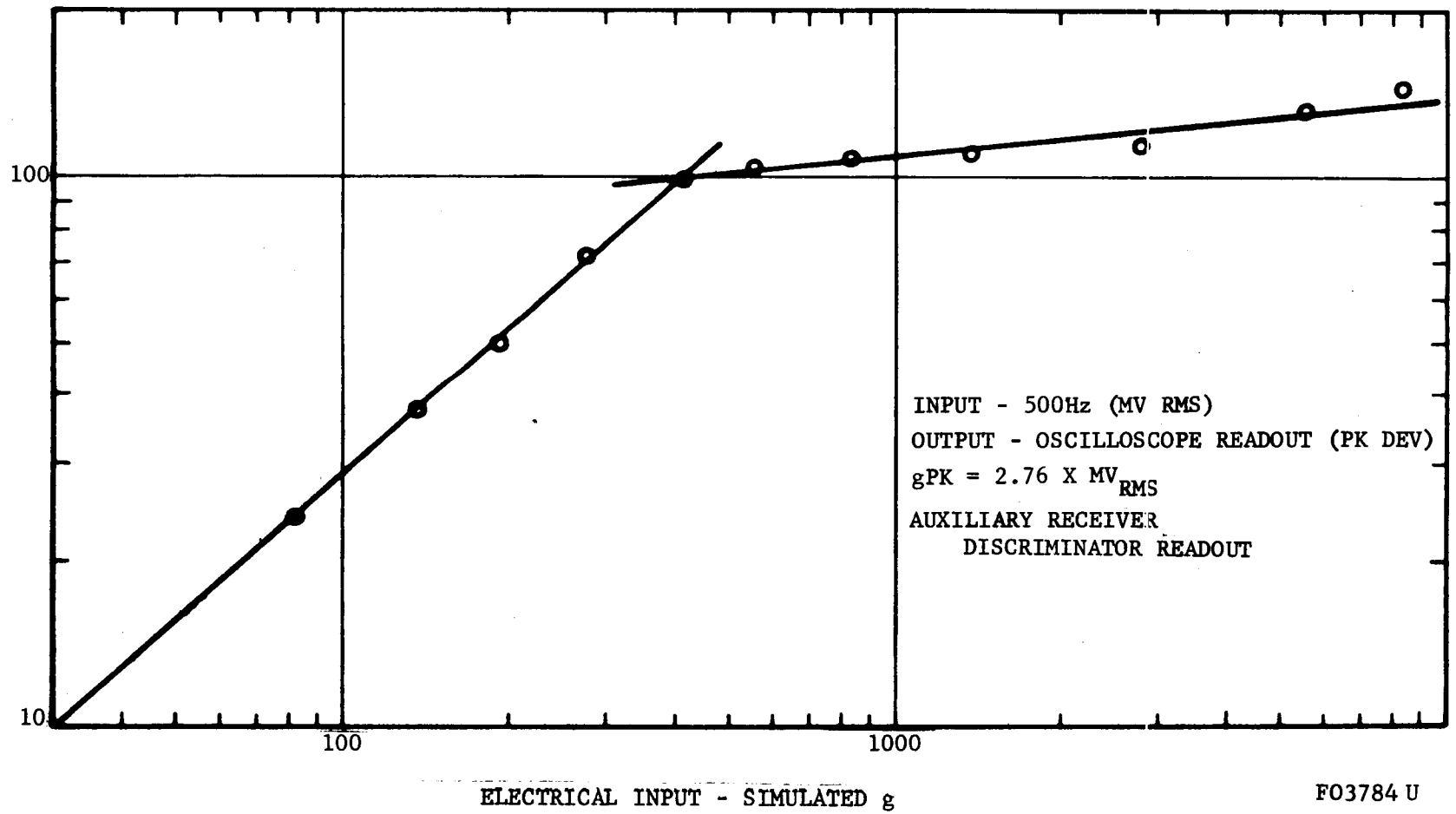

FIGURE D-3. PROTOTYPE NO. 3 SYSTEM (ELECTRICAL) CALIBRATION

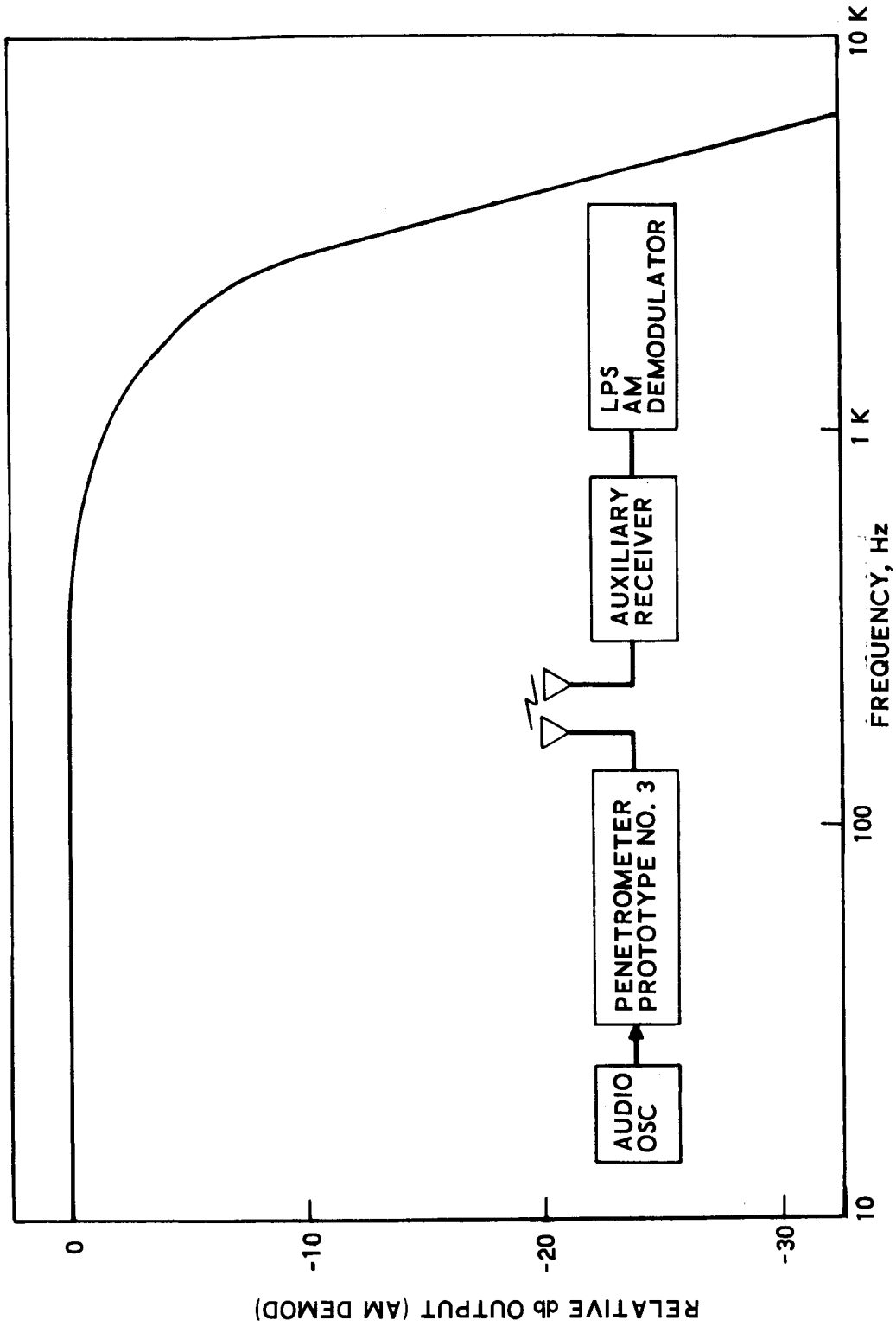

FIGURE D-4. PENETROMETER PROTOTYPE NO. 3 SYSTEM FREQUENCY RESPONSE

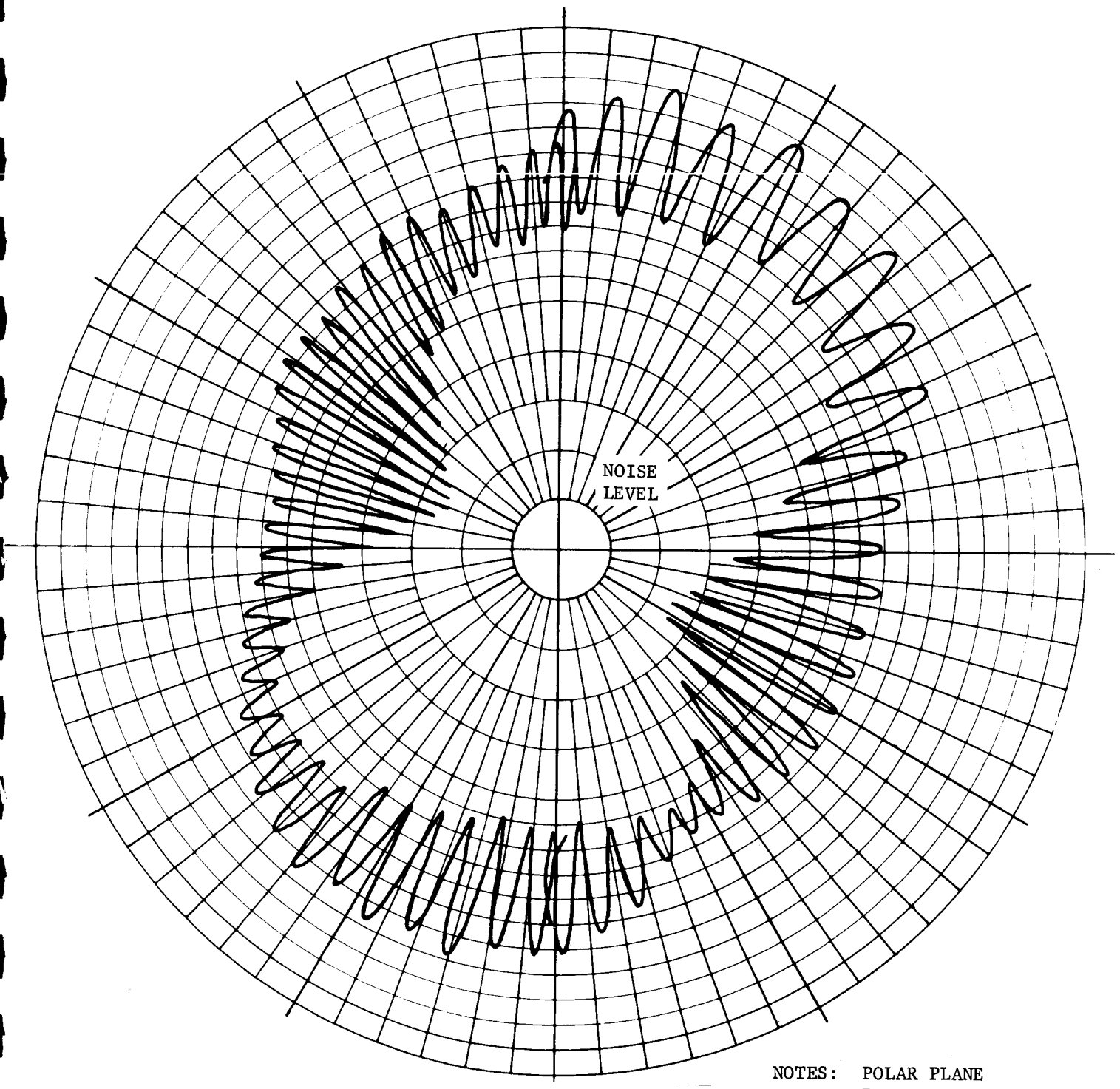

NOTES: POLAR PLANE
PRE-HYGE CALIBRATION

FIGURE D-5 PROTOTYPE NO. 3 ANTENNA PATTERN

Hyge captive shock tests were completed in each of the penetrometer three major axes. External power and control signals were applied through the umbilical connector, which was released 7 seconds prior to firing, leaving the penetrometer on internal power during the actual test cycle.

The primary recorded data consisted of reference acceleration data from a Kistler 808A accelerometer mounted on the holding fixture and AM demodulated penetrometer output signal data obtained via the uhf telemetry rf link. Also obtained were rf frequency readings before and after each test cycle. Table D.1 shows the frequency data.

TABLE D.1

HYGE TESTS - RF FREQUENCY MEASUREMENTS

		Prototype No. 3 Frequency, MHz		
Time	Power	Test 1	Test 2	Test 3
Prerun	External	438.059	438.030	438.026
Prerun	Internal	438.041	437.965	438.045

Figure D-6 is a reproduction of the data recording obtained in the first test. To illustrate the data reduction technique employed, the graphical analysis construction lines are depicted. The basic data traces were read at eight points corresponding to peak acceleration values. The average of the ratios of subcarrier amplitude to acceleration (i.e., KHz/g) was taken as the slope of the penetrometer transfer function between zero and the compression point. The slope of the transfer function in the data compression range was taken as the ratio $\Delta f/\Delta g$ indicated in Figure D-6. Table D.2 shows the mean values of scale factors obtained in a reduction of the Hyge data.

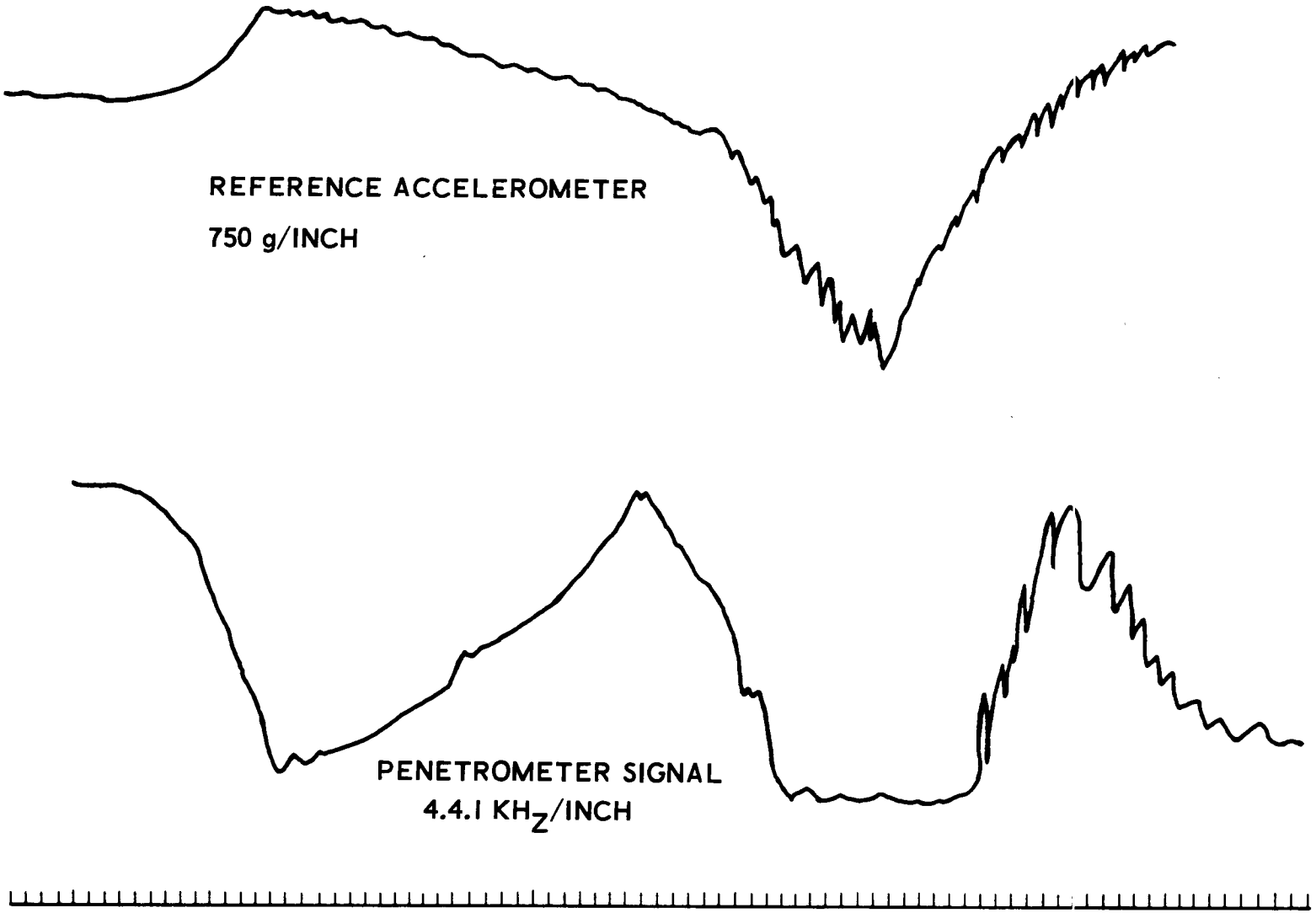

FIGURE D-6. DYNAMIC CALIBRATION TEST DATA FOR PROTOTYPE NO. 3 PENETROMETER

TABLE D.2

PROTOTYPE NO. 3 - TRANSFER FUNCTION DATA

Test	Mean Value Scale Factor, KHz/g	
	High Sensitivity	Low Sensitivity
1	0.174	0.0078
2	0.170	0.0078
3	0.174	0.0083

Figures D-7 through D-9 show the transfer functions thus obtained for tests 1 through 3 (i.e., axes 1 through 3), respectively. Figure D-10 shows the composite triaxial calibration data for Prototype No. 3. The Hyge instrumentation test setup is shown in Figure D-11.

D.3 CONCLUSIONS AND TEST RESULTS

Complete functional operation of an omnidirectional penetrometer prototype design was demonstrated by the test results reported herein. Prototype No. 3 is the second completely functional omnidirectional penetrometer successfully developed. On the basis of the test results described herein, certain conclusions and observations may be made. They are presented in the following paragraphs, according to major assemblies.

D.3.1 ANTENNA

The electrical and mechanical integrity of the antenna assembly was maintained throughout the series of tests completed.

D.3.2 ACCELEROMETER AND SIGNAL ELECTRONICS

Satisfactory functional operation of the accelerometer and signal electronics was demonstrated by virtue of the tests performed herein. Numerous low-velocity impact tests, performed as part of an interim work extension but not reported herein, also demonstrated very satisfactory operation and repeatability. Turn-on transient data depict satisfactory initial decay times of several seconds and exhibit a slower perturbation with excursions similar to that observed in Prototype No. 2 data.

Electrical calibration data (Figure D-3) taken during bench tests was found to differ from the Hyge captive calibration data (Figure D-10) by a factor of better than 1.5, the discrepancy between electrical and physical transfer functions occurring in a manner similar to that observed for Prototype No. 2. Excellent omnidirectional sensitivity was observed in Prototype No. 3 as evidenced in the composite plot of Figure D-10 .

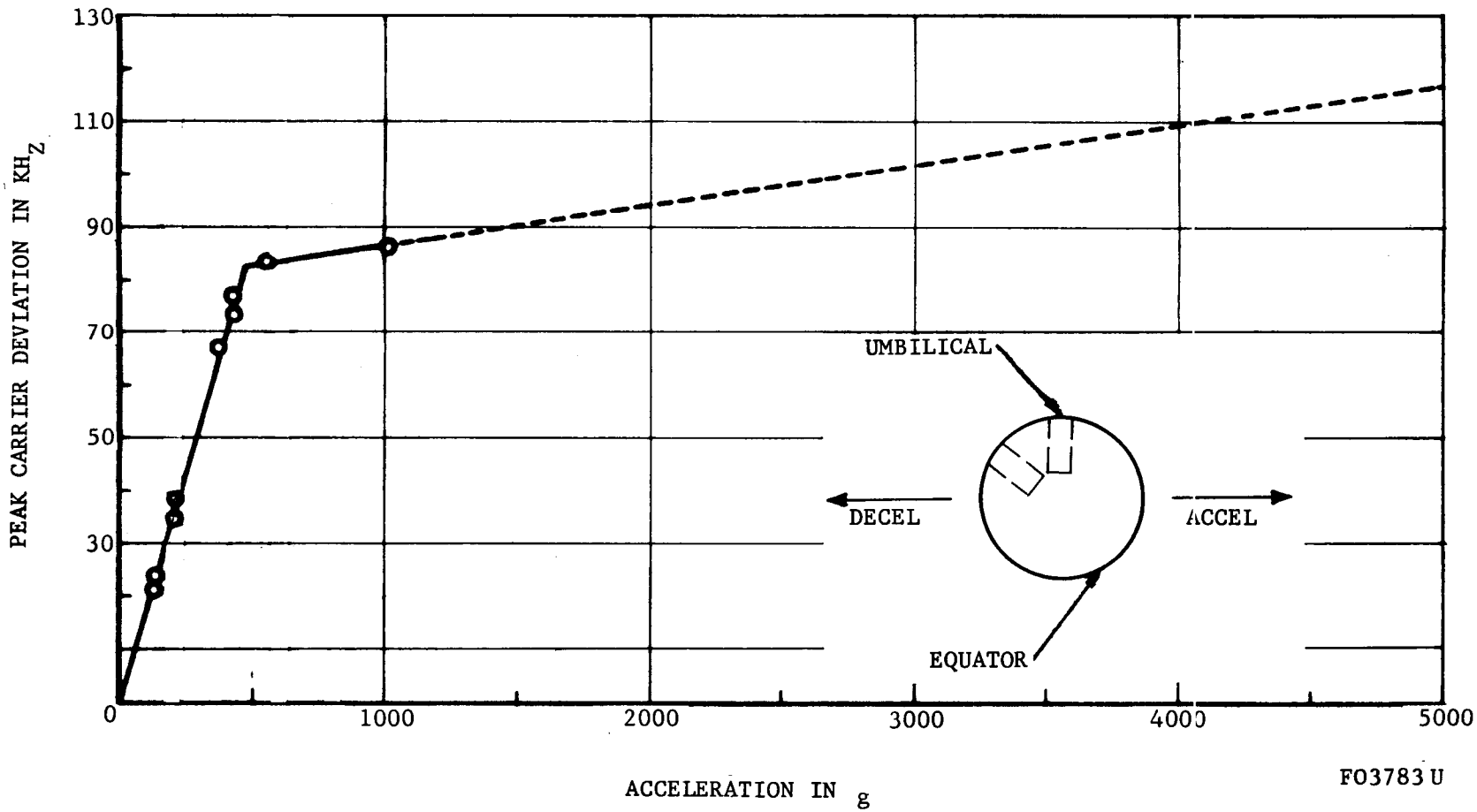

FIGURE D-7. LPS PROTOTYPE NO. 3 CALIBRATION - HYGE TEST NO. 1

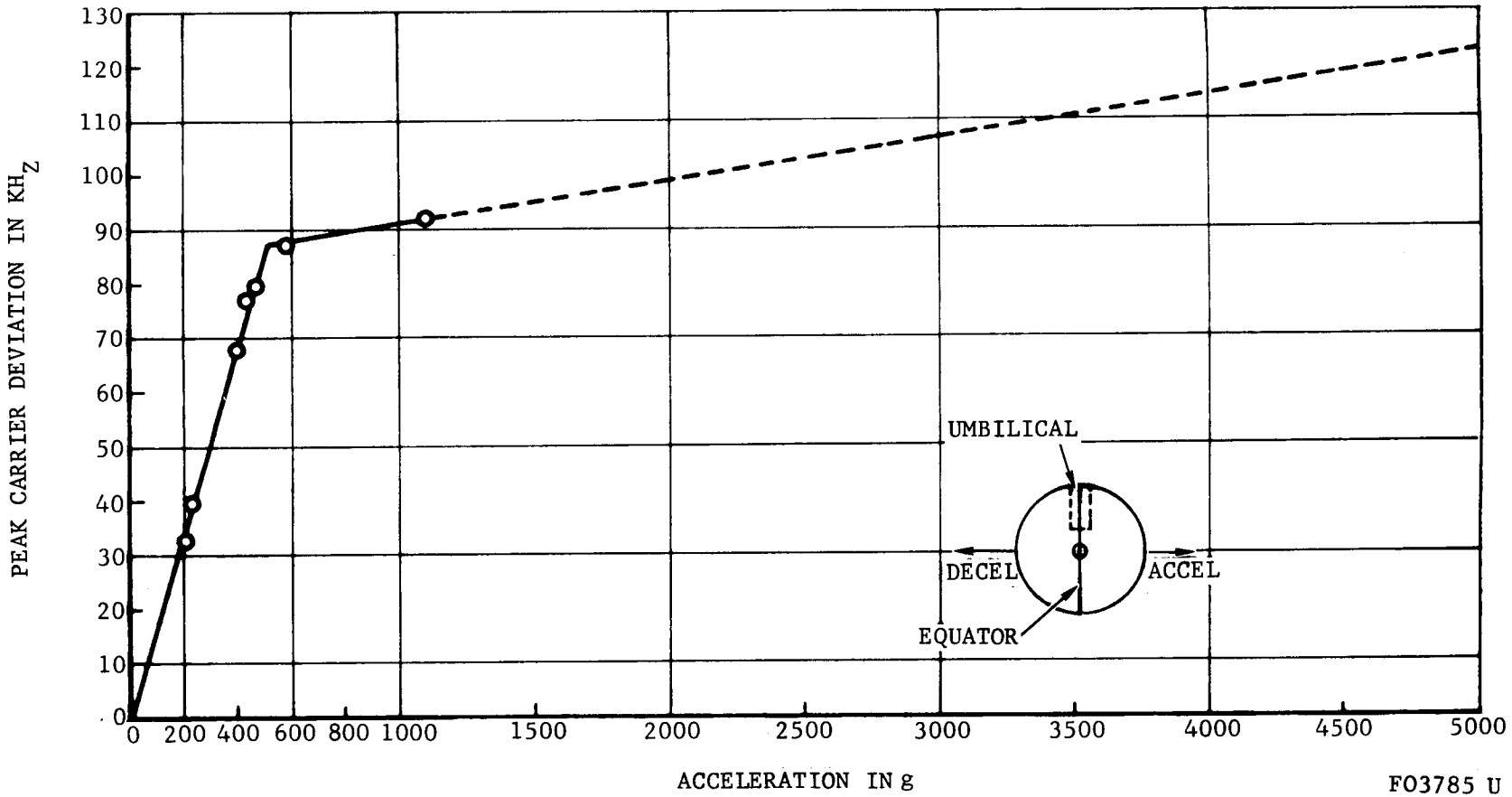

FIGURE D-8. LPS PROTOTYPE NO. 3 CALBRATION - HYGE TEST NO. 2

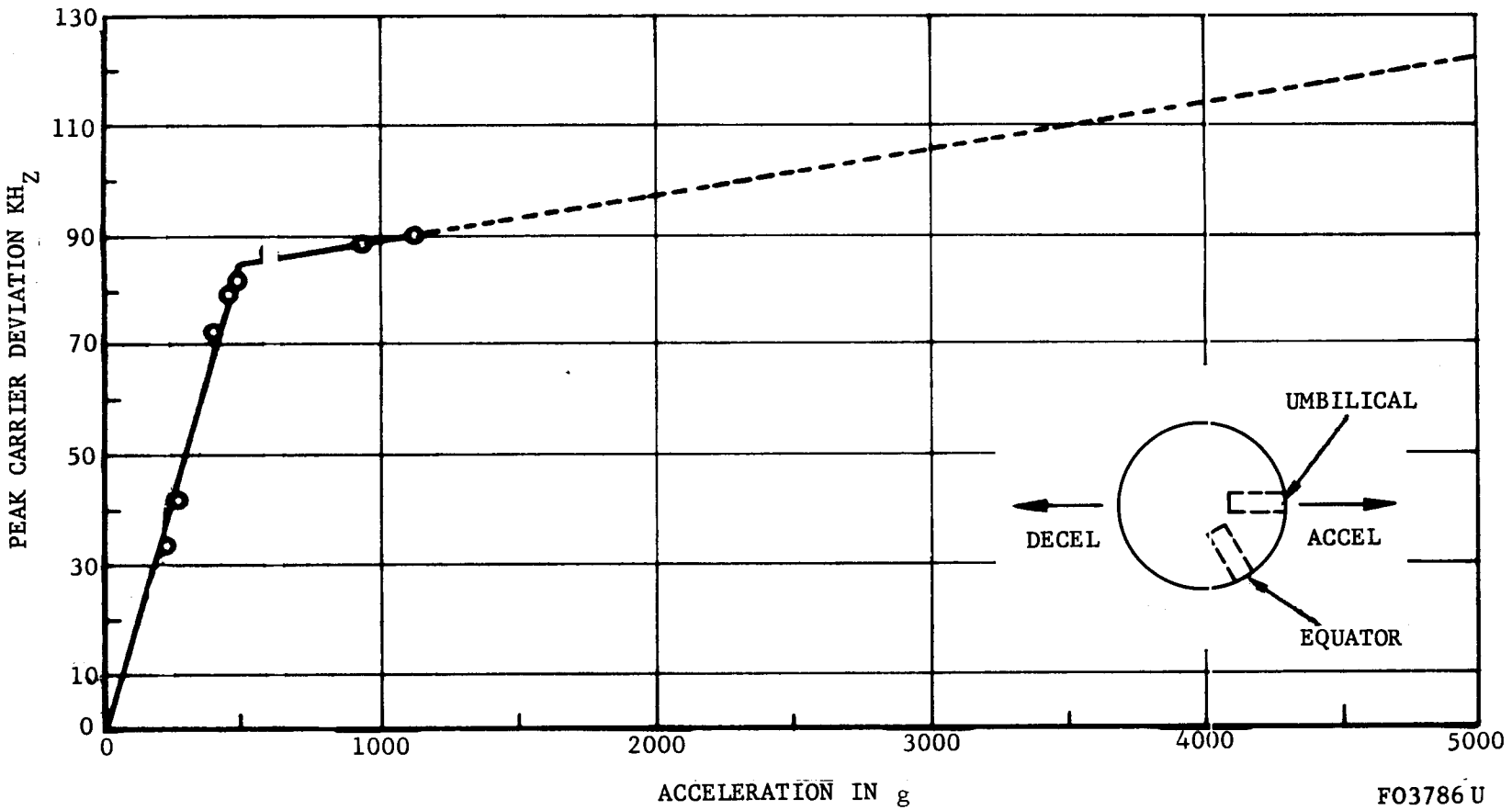

FIGURE D-9. LPS PROTOTYPE NO. 3 CALIBRATION - HYGE TEST NO. 3

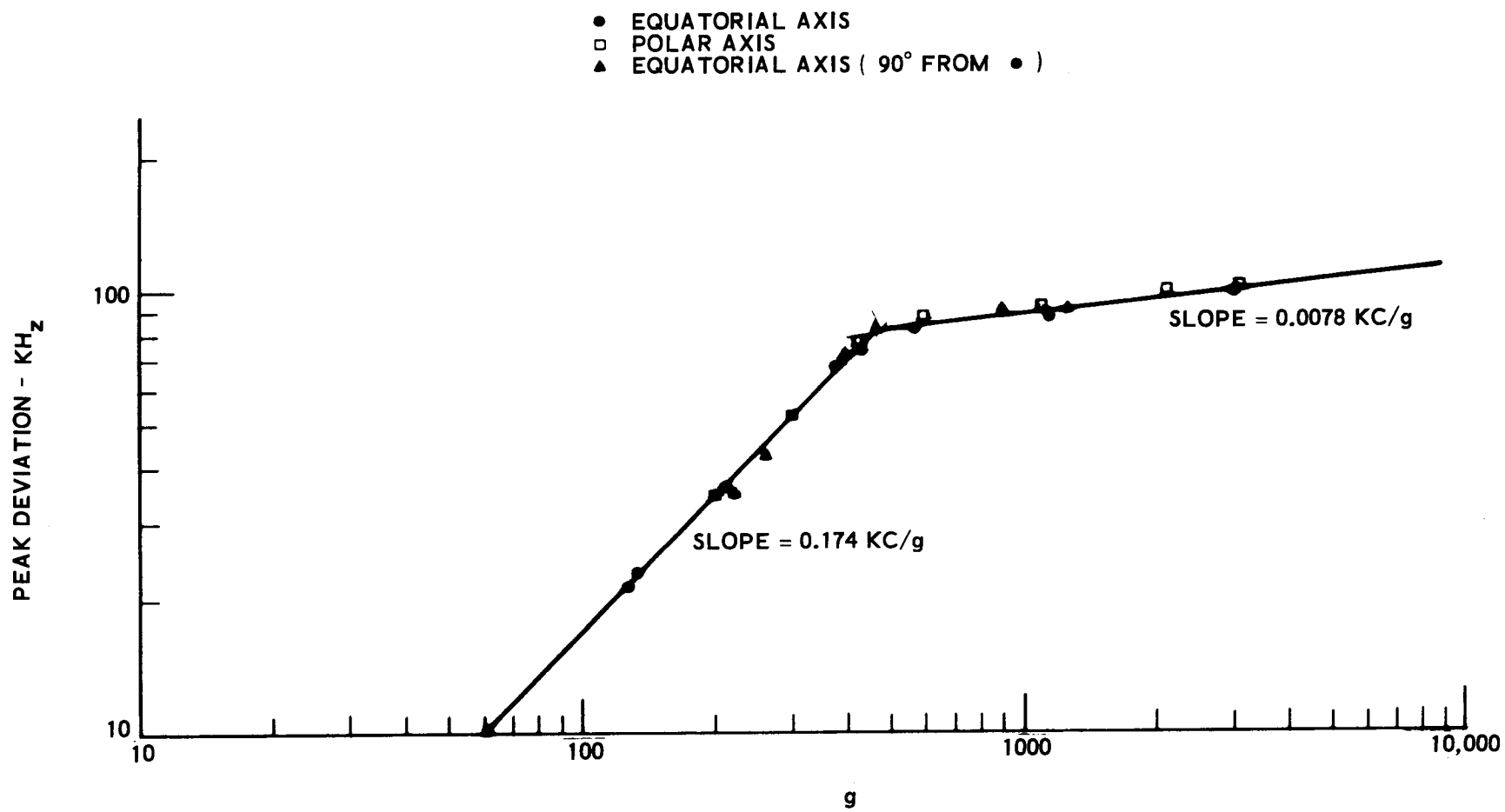

FIGURE D-10. PROTOTYPE PENETROMETER NO. 3 THREE AXIS HYGE CALIBRATION

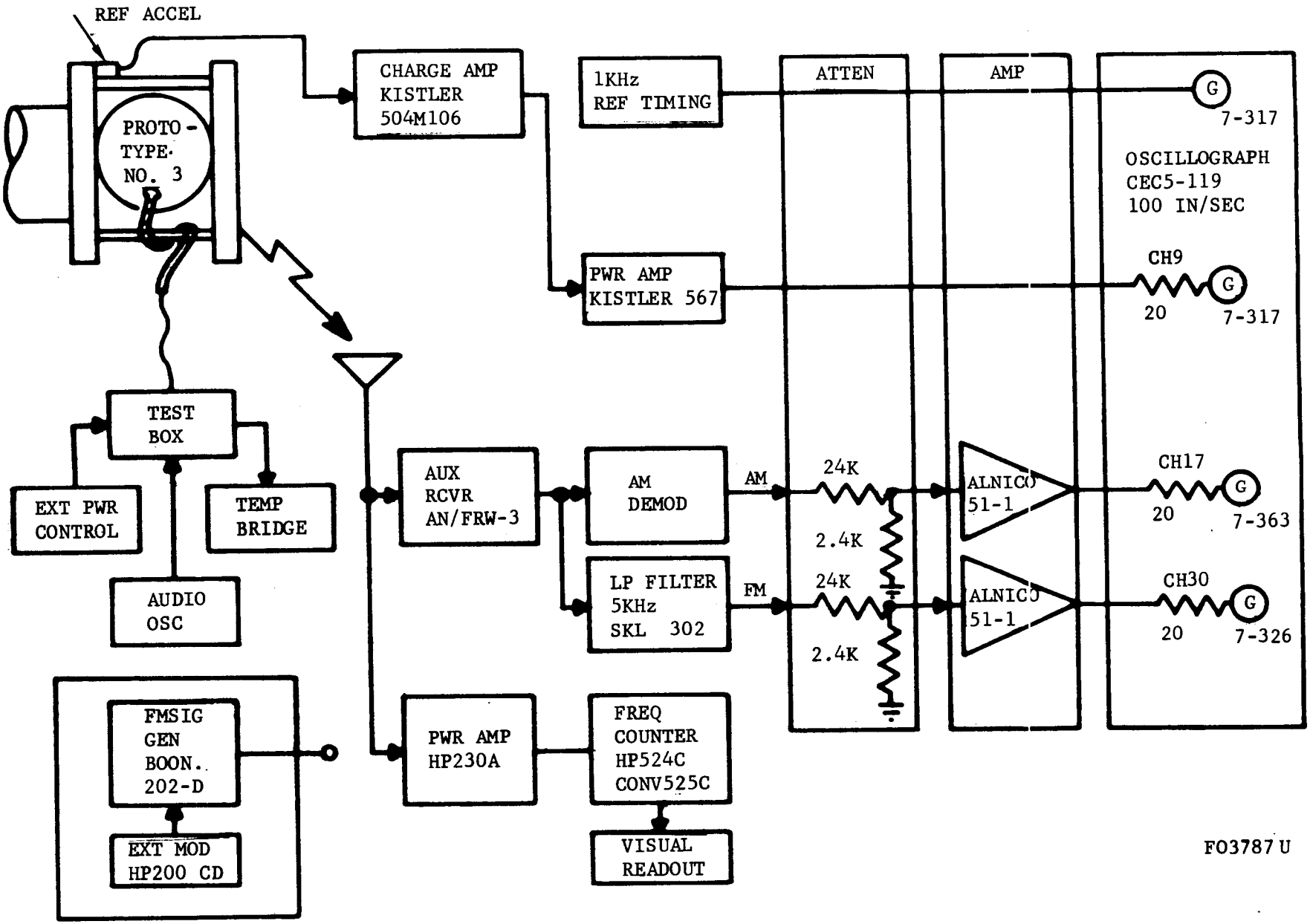

FIGURE D-11. PROTOTYPE NO. 3 - HYGE CALIBRATION TEST SETUP

D.3.3 BATTERY AND POWER REGULATOR/TIMER

The battery and power regulator/timer performed satisfactorily during all testing reported herein. No degradation in characteristics was observed during or following the numerous low-velocity impact tests conducted in the follow-on work period.

D.3.4 TRANSMITTER

Transmitter performance was very satisfactory during all testing described herein. Operation at the design frequency of 438.0 MHz was achieved and maintained with temperature and frequency stability characteristics remaining within latest performance requirements.

APPENDIX E

RECEIVER SPURIOUS RESPONSE ANALYSIS

E.1 PRESENT FUNCTIONAL MODEL RECEIVER (1st IF = 60 MHz)

Table E.1 indicates the various operating frequencies in the receiving system. Note that the spurious response ratio of Mixer No. 1 ranges from 0.861 to 0.867. Figure E-1 shows that the nearest spurs are 6A - 5B, 7B - 8A, and 7A - 6B. These spurs are examined in detail below:

A = 372 MHz to 393 MHz	B = 432 MHz to 453 MHz
6A = 2232 to 2358 MHz	5B = 2160 to 2265 MHz
7A = 2604 to 2751 MHz	6B = 2592 to 2718 MHz
8A = 2976 to 3144 MHz	7B = 3024 to 3171 MHz

6A - 5B = 72 to 93 MHz

7B - 8A = 48 to 27 MHz

7A - 6B = 12 to 33 MHz

Not only are these spurs 11th order and higher, but they are far removed from the IF passband. This provides excellent spurious response performance.

TABLE E.1

FUNCTIONAL MODEL RECEIVER FREQUENCY ANALYSIS

Channel		1st IF	1st LO	1st Image	Spurious Response Ratio	Adjacent Channel Local Oscillator Spurious Responses (IF = 60 MHz)
No.	Frequency					
1	432 MHz	60 MHz	372 MHz	312 MHz	0.861	20(375-372) = 60 10(378-372) = 60 5(384-372) = 60 4(387-372) = 60
2	435 MHz	60 MHz	375 MHz	315 MHz	0.862	20(378-375) = 60 20(375-372) = 60 10(381-375) = 60 5(387-375) = 60 4(390-375) = 60
3	438 MHz	60 MHz	378 MHz	318 MHz	0.863	20(381-378) = 60 20(378-375) = 60 10(384-378) = 60 10(378-372) = 60 5(390-378) = 60 4(393-378) = 60
4	441 MHz	60 MHz	381 MHz	321 MHz	0.863	20(384-381) = 60 20(381-378) = 60 10(387-381) = 60 10(381-375) = 60 5(393-381) = 60
5	444 MHz	60 MHz	384 MHz	324 MHz	0.865	20(387-384) = 60 20(384-381) = 60 10(390-384) = 60 10(384-378) = 60 5(384-372) = 60
6	447 MHz	60 MHz	387 MHz	327 MHz	0.865	20(390-387) = 60 20(387-384) = 60 10(393-387) = 60 10(387-381) = 60 5(387-375) = 60 4(387-372) = 60
7	450 MHz	60 MHz	390 MHz	330 MHz	0.866	20(393-390) = 60 20(390-387) = 60 10(390-384) = 60 5(390-378) = 60 4(390-375) = 60
8	453 MHz	60 MHz	393 MHz	333 MHz	0.867	20(393-390) = 60 10(393-387) = 60 5(393-381) = 60 4(393-378) = 60

A/B		ORDER														
		1	2	3	4	5	6	7	8	9	10	11	12	13	14	15
	0.000	B	B±A	B±2A	B±3A	B±4A	B±5A	B±6A	B±7A	B±8A	B±9A	B±10A	B±11A	B±12A	B±13A	B±14A
1/16	0.063															15A
1/15	0.067														14A	
1/14	0.072													13A		
1/13	0.077												12A			
1/12	0.083											11A				2B-13A
1/11	0.091										10A				2B-12A	
1/10	0.100									9A				2B-11A		
1/9	0.111								8A				2B-10A			
1/8	0.125							7A				2B-9A				
2/15	0.133															14A-B
1/7	0.143						6A				2B-8A				13A-B	
2/13	0.154													12A-B		
1/6	0.167					5A				2B-7A			11A-B			
2/11	0.182											10A-B				3B-12A
1/5	0.200				4A				2B-6A		9A-B				3B-11A	
3/14	0.214															13A-2B
2/9	0.222									8A-B				3B-10A		
3/13	0.231														12A-2B	
1/4	0.250			3A				2B-5A	7A-B				3B-9A	11A-2B		
3/11	0.273												10A-2B			
2/7	0.286							6A-B				3B-8A				
3/10	0.300											9A-2B				4B-11A
4/13	0.308															12A-3B
1/3	0.333		2A				2B-4A 5A-B				3B-7A 8A-2B				4B-10A 11A-3B	
4/11	0.364													10A-3B		
3/8	0.375									7A-2B				4B-9A		
2/5	0.400					4A-B				3B-6A			9A-3B			
5/12	0.416															11A-4B
3/7	0.429								6A-2B				4B-8A			
4/9	0.445											8A-3B				5B-10A
5/11	0.455														10A-4B	
1/2	0.500	A			3A-B	2B-3A		5A-2B	3B-5A		7A-3B	4B-7A		9A-4B	5B-9A	
6/11	0.545															10A-5B
5/9	0.555												8A-4B			
4/7	0.571									6A-3B				5B-8A		
3/5	0.600						4A-2B				4B-6A				9A-5B	
5/8	0.625											7A-4B				6B-9A
2/3	0.667			2A-B				3B-4A	5A-3B				5B-7A	8A-5B		
7/10	0.700															9A-6B
5/7	0.715										6A-4B				6B-8A	
3/4	0.750					3A-2B				4B-5A			7A-5B			
7/9	0.778														8A-6B	
4/5	0.800							4A-3B				5B-6A				
5/6	0.833									5A-4B				6B-7A		
6/7	0.856											6A-5B				7B-8A
7/8	0.875													7A-6B		
	1.000				2B-2A		3B-3A		4B-4A		5B-5A		6B-6A		7B-7A	

FIGURE E-1. MIXER CHART. OUTPUT FREQUENCY - B-A

Repeating the above analysis for Mixer No. 2 shows that the spurious response ratio is 0.850. Referring again to Figure E-1, the nearest spurs are 5A - 4B, 6B - 7A, 6A - 5B, and 7B - 8A. These spurs are examined in detail below:

A = 51 MHz	B = 60 MHz
5A = 255 MHz	4B = 240 MHz
6A = 306 MHz	5B = 300 MHz
7A = 357 MHz	6B = 360 MHz
8A = 408 MHz	7B = 420 MHz

5A - 4B = 15 MHz

6B - 7A = 3 MHz

6A - 5B = 6 MHz

7B - 8A = 12 MHz

The nearest spur here is 11th order and relatively far removed from the second IF center frequency of 9 MHz. Also note that harmonics of the 51 MHz second local oscillator fall completely out of the input frequency band of 432 to 453 MHz. This again provides good spurious response performance. Images are also far removed.

It has been assumed here that the local oscillator is a pure fundamental frequency. The first local oscillator is the result of a fundamental oscillator in the 124 to 131 MHz range multiplied up to the desired 372 to 392 MHz range. Harmonics of these fundamental frequencies can and often do cause additional spurious responses. The performance specifications define different frequency usage in first and second local oscillators and IF's such that all possibilities of this type are eliminated.

E.2 FLIGHT MODEL RECEIVER (1st IF = 120 MHz)

Table E.2 indicates the various operating frequencies in the proposed receiving system. (See Performance Specifications.) Note that the spurious response ratio of Mixer No. 1 ranges from 0.722 to 0.735. Figure E-1 shows that the nearest spurs are 6A - 4B, 6B - 8A, 3A -2B, 4B - 5A, and 7A - 5B. These spurs are examined in detail below:

A = 312 MHz to 333 MHz	B = 432 MHz to 453 MHz
3A = 936 to 999	2B = 864 to 906

TABLE E.2

FLIGHT MODEL RECEIVER FREQUENCY ANALYSIS

Channel						
No.	Frequency	1st IF	1st LO	1st Image	Spurious Response Ratio	Adjacent Channel Local Oscillator Spurious Responses (IF = 120 MHz)
1	432 MHz	120 MHz	312 MHz	192 MHz	0.722	40(315-312) = 120 20(318-312) = 120 10(324-312) = 120 8(327-312) = 120
2	435 MHz	120 MHz	315 MHz	195 MHz	0.724	40(318-315) = 120 40(315-312) = 120 20(321-315) = 120 10(327-315) = 120 8(330-315) = 120
3	438 MHz	120 MHz	318 MHz	198 MHz	0.726	40(321-318) = 120 40(318-315) = 120 20(324-318) = 120 20(318-312) = 120 10(330-318) = 120 8(333-318) = 120
4	441 MHz	120 MHz	321 MHz	201 MHz	0.728	40(324-321) = 120 40(321-318) = 120 20(327-321) = 120 20(321-315) = 120 10(333-321) = 120
5	444 MHz	120 MHz	324 MHz	204 MHz	0.730	40(327-324) = 120 40(324-321) = 120 20(330-324) = 120 20(324-318) = 120 10(324-312) = 120
6	447 MHz	120 MHz	327 MHz	207 MHz	0.731	40(330-327) = 120 40(327-324) = 120 20(333-327) = 120 20(327-321) = 120 10(327-315) = 120 8(327-312) = 120
7	450 MHz	120 MHz	330 MHz	210 MHz	0.733	40(333-330) = 120 40(330-327) = 120 20(330-324) = 120 10(330-318) = 120 8(330-315) = 120
8	453 MHz	120 MHz	333 MHz	213 MHz	0.735	40(333-330) = 120 20(333-327) = 120 10(333-321) = 120 8(333-318) = 120

5A = 1560 to 1665 MHz

6A = 1872 to 1998 MHz

7A = 2184 to 2331 MHz

8A = 2496 to 2664 MHz

4B = 1728 to 1812 MHz

5B = 2160 to 2265 MHz

6B = 2592 to 2718 MHz

6A - 4B = 144 to 186 MHz

6B - 8A = 96 to 54 MHz

3A - 2B = 72 to 93 MHz

4B - 5A = 168 to 147 MHz

7A - 5B = 24 to 66 MHz

These spurs are far removed from the passband, thus providing excellent spurious response performance.

Repeating the above analysis for Mixer No. 2 shows that the spurious response ratio here is 0.791. Referring again to Figure E-1, the nearest spurs are 8A - 6B, 4A - 3B, and 5B - 6A. These spurs are examined in detail below:

A = 95 MHz

4A = 380 MHz

6A = 570 MHz

8A = 760 MHz

B = 120 MHz

3B = 360 MHz

5B = 600 MHz

6B = 720 MHz

8A - 6B = 40 MHz

4A - 3B = 20 MHz

5B - 6A = 30 MHz

These spurs are far removed from the second IF center frequency of 25 MHz. The second IF bandpass filter also has very sharp skirts for setting the bandpass characteristics of the receiver. Also note that harmonics of the 95 MHz second local oscillator fall completely out of the input frequency band of 432 to 453 MHz. This again provides good spurious response performance. Images are also far removed.

It has been assumed again that the local oscillator is a pure fundamental frequency. The first local oscillator is the result of a fundamental oscillator in the 156 to 166.5 MHz range multiplied (doubled) up to the desired 312 to 333 MHz range. Harmonics of this fundamental oscillator can in no way cause spurs like those experienced in Paragraph 6.2.1 of the final report.

Since excellent mixer spurious response performance has been proved, it would appear as though the worst interference is caused by harmonics of adjacent local oscillator signals at the mixers as shown in Tables E.1 and E.2. This defines the filtering requirement of the receiver preselector, power divider, and power lines to ensure adequate attenuation of adjacent local oscillators. Since the noise power at the first mixer input is approximately -95 dbm, shielding in the order of 100 db is provided.

APPENDIX F

LUNAR PENETROMETER/APOLLO COMMAND AND SERVICE MODULE - INTERFACE STUDY

F.1 SCOPE

The intent of this study is to define the communication system characteristics of the Apollo Block II Command and Service (CSM) and recommend the best penetrometer/CSM system interface. The primary criterion of this interface is that it must enable adequate CSM reception, storage, and subsequent transmission to earth of the penetrometer data with minimum impact upon the existing CSM communication system design consistent within overall weight, volume, and prime power constraints. Figure F-1 illustrates the penetrometer/data relay/CSM/Earth communication interface under consideration.

F.2 APOLLO BLOCK II CSM COMMUNICATION SYSTEM

A block diagram of the Block II CSM communication system is given in Figure F-2. Since only Block II missions are lunar, this study is directed toward the Block II CSM communication system design.

The Block II design is rather well definitized. References (1) and (2) define the parameters of each CSM communication mode. The normal in-flight CSM rf communication links are illustrated in Figure F-3. The recovery communication modes are illustrated in Figure F-4.

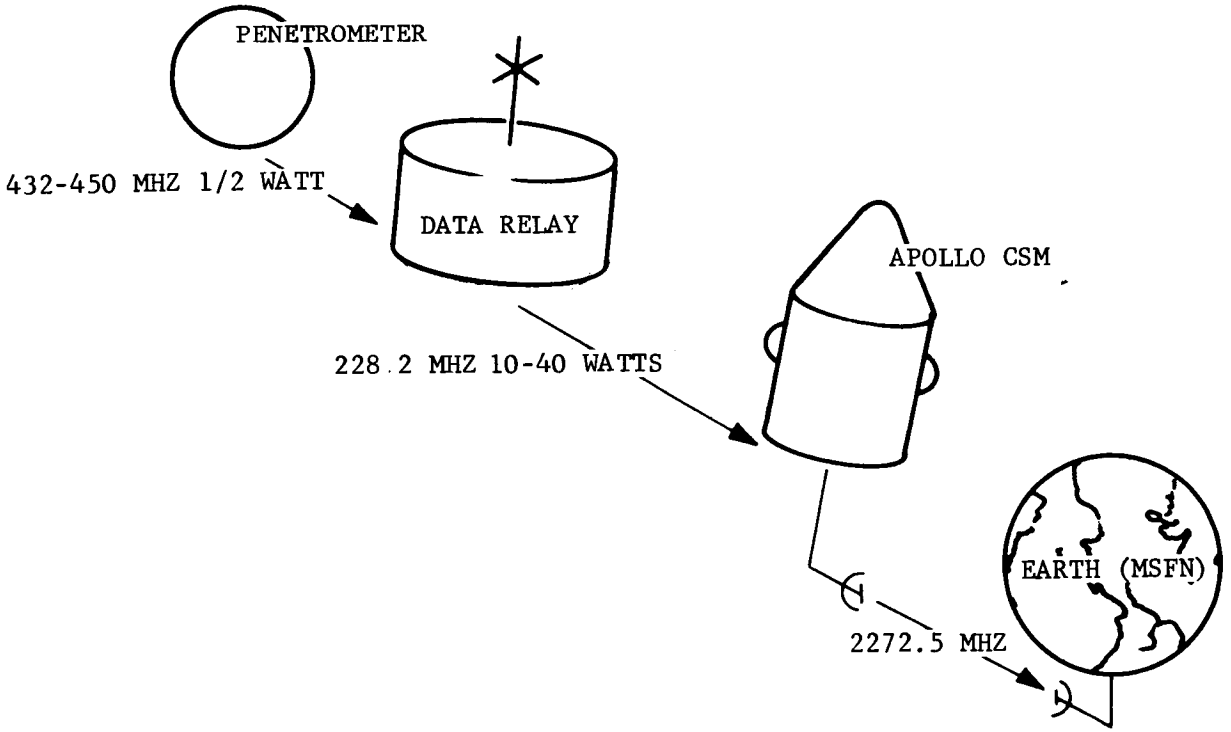

FIGURE F-1. LUNAR PENETROMETER SYSTEM DATA RELAY CONFIGURATION

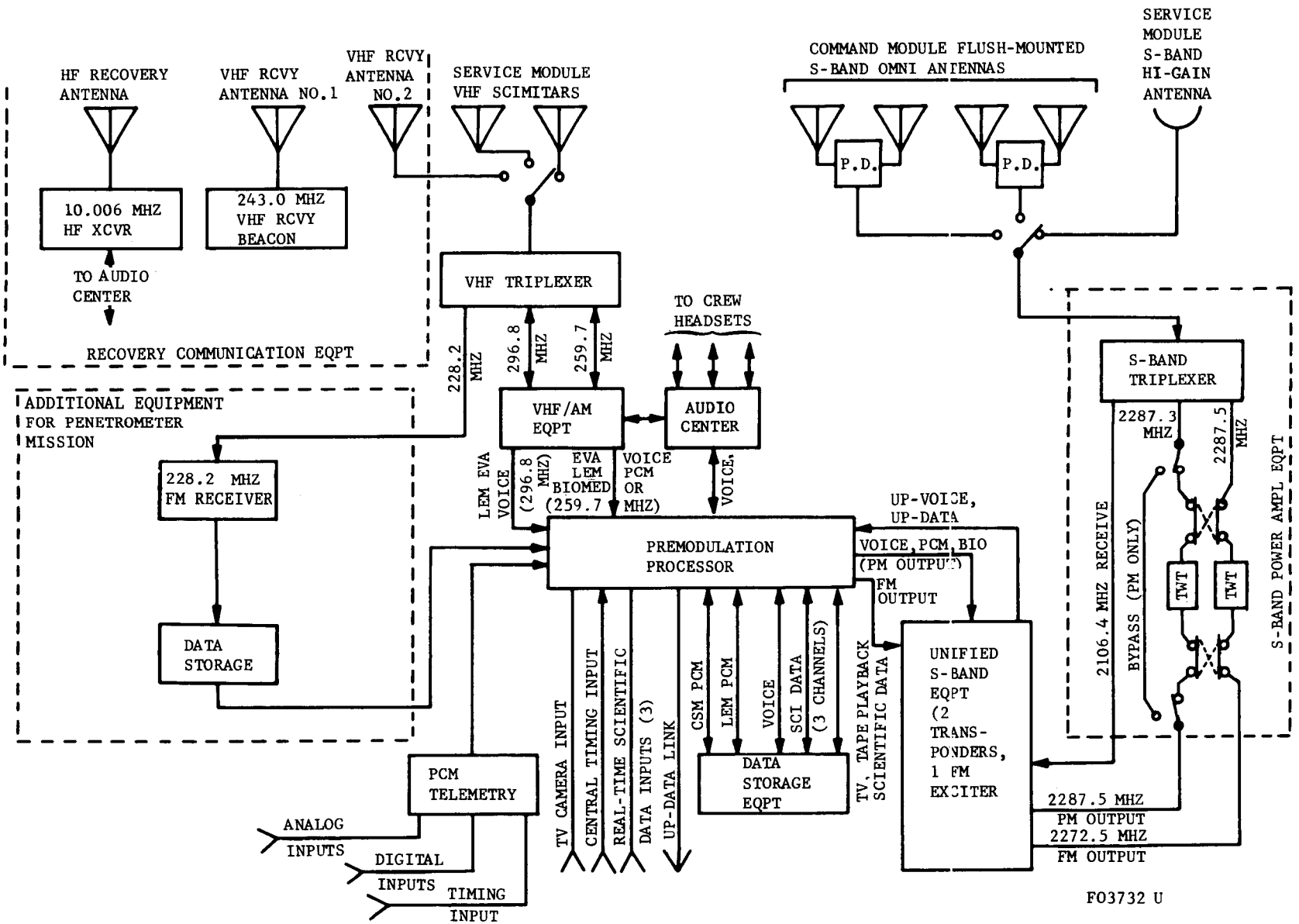

FIGURE F-2. BLOCK II APOLLO CSM COMMUNICATION SYSTEM BLOCK DIAGRAM

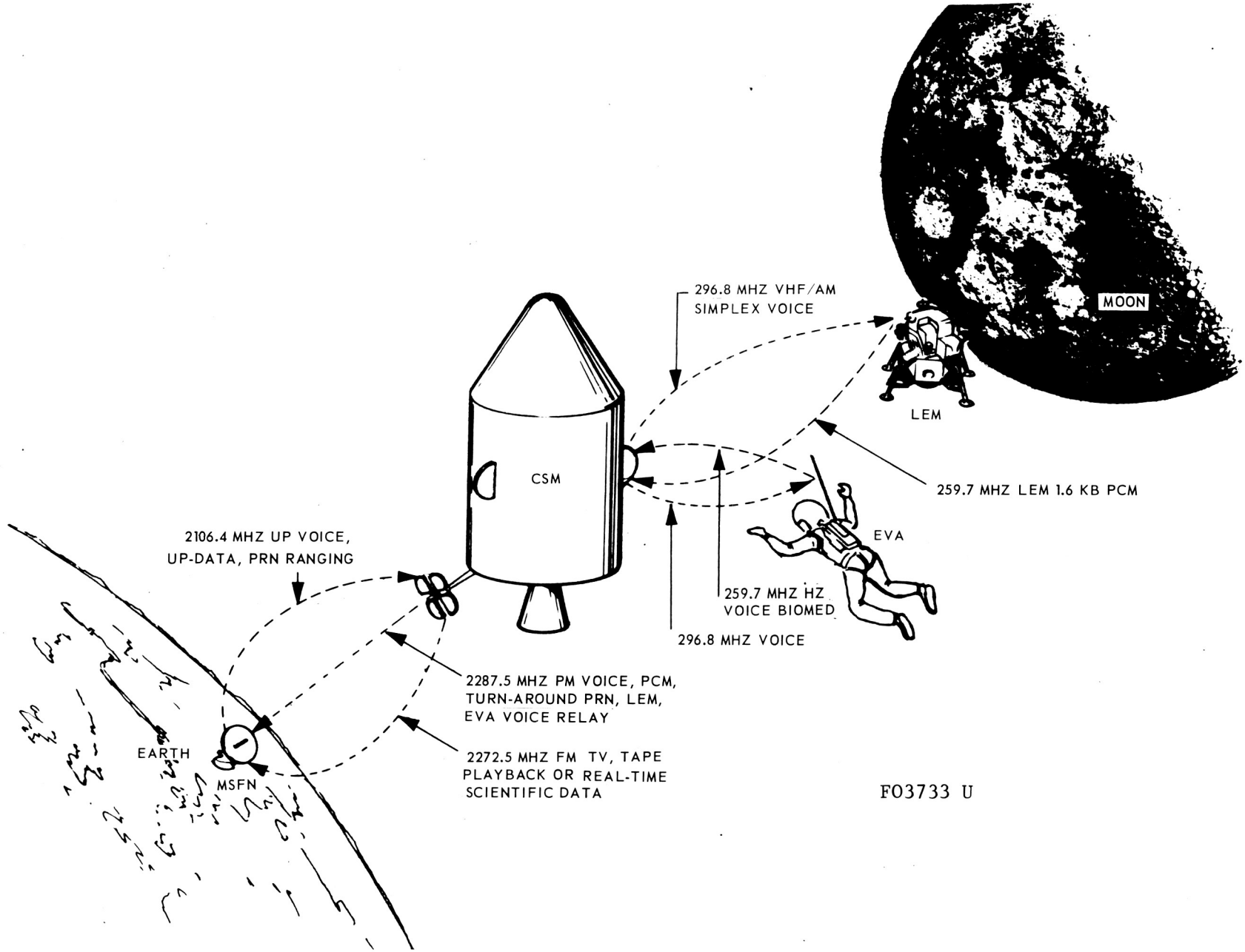

FIGURE F-3. CSM BLOCK II NORMAL INFLIGHT COMMUNICATION LINKS

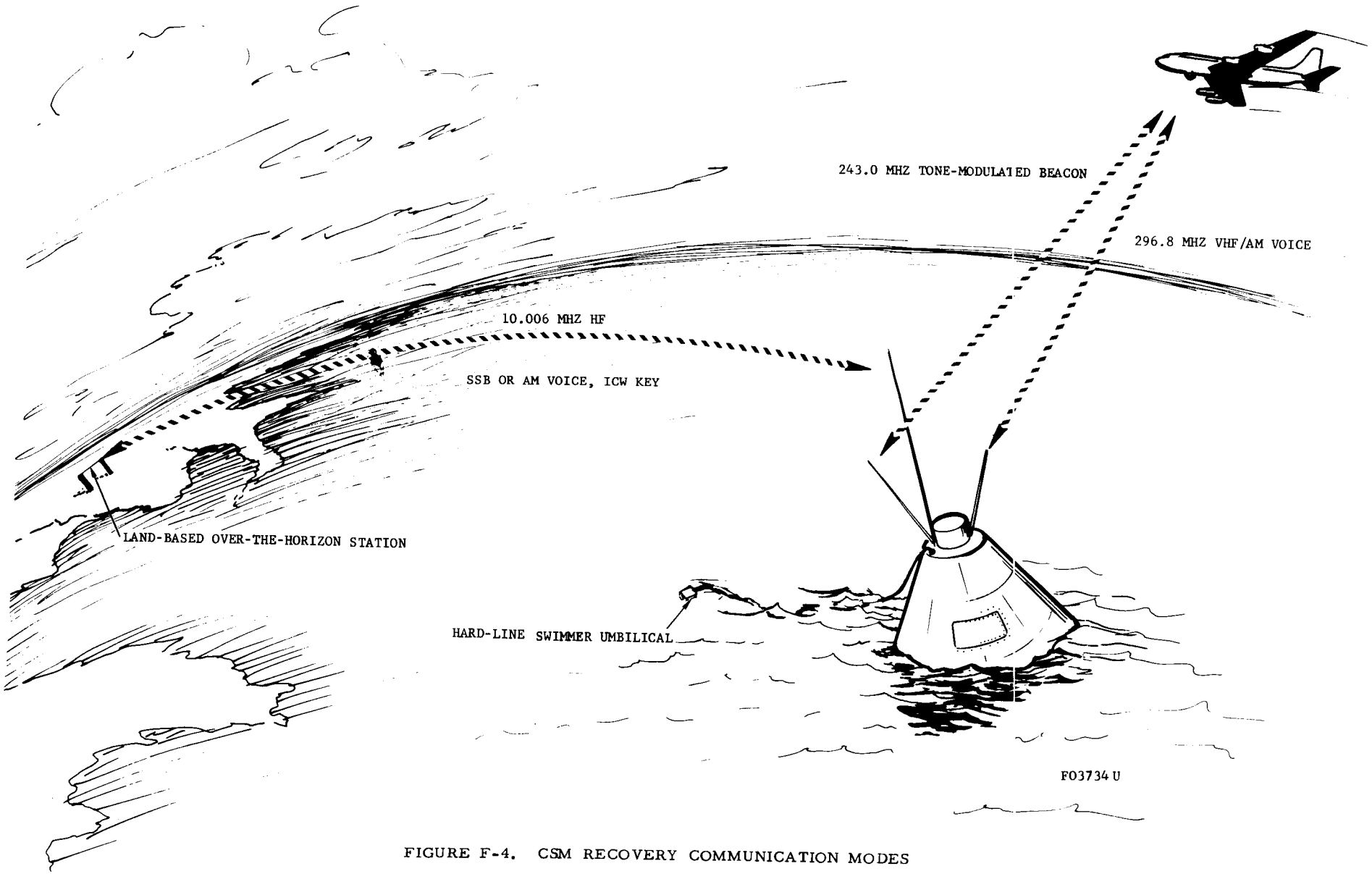

FIGURE F-4. CSM RECOVERY COMMUNICATION MODES

F.2.1 CSM S-BAND COMMUNICATION LINKS

As illustrated in Figure F-3, the primary link between the CSM and the Manned Space Flight Network (MSFN) is the unified S-band system. The S-band system utilizes coherent phase modulated two-way transmissions for doppler tracking, pseudo-random noise (PRN) ranging, and voice and data transmission. The up-link MSFN-to-CSM communication link consists of a 2106.4 MHz carrier, phase modulated by up-voice and up-data subcarriers, and the wideband PRN ranging signal. Figure F-5 illustrates the frequency spectra of the various up-link and down-link CSM-MSFN S-band communication modes. This up-link carrier is detected by a modulation restrictive tracking loop. A down-link carrier frequency is generated at a precise 240/221 ratio of the received up-link carrier frequency. This down-link carrier is then phase modulated by PCM telemetry and down-voice subcarriers, and by the turned-around PRN ranging signal.

The down-voice subcarrier may be modulated not only by the output from the crew's mikes but also by voice (from the LEM) or voice and biomed data (from and extra-vehicular astronaut (EVA)) received via the CSM VHF/AM rf links.

In addition to the coherent two-way S-band link, the CSM has an additional 2272.5 MHz FM transmitter for transmitting TV, stored data, or real-time scientific data. It is anticipated that lunar penetrometer data would be relayed to the MSFN via this transmitter.

The CSM 2106.4 MHz S-band receiver could possibly be utilized for reception of the penetrometer data. However, transponder acquisition problems, circuit margins at S-band, and operational constraints make this transmission mode appear to be much less feasible than a VHF penetrometer-CSM transmission link.

F.2.2 CSM VHF COMMUNICATION LINKS

The CSM VHF in-flight communication links, illustrated in Figure F-3, utilizes two VHF/AM transmitter-receivers packaged in a single unit and coupled to either of two service-module (SM) mounted VHF scimitars through a VHF triplexer and rf switch. These transmitter-receivers may be operated either simplex or duplex in any combination. The receiver IF bandwidths are 70 kHz at the 6 db points. The detected output is flat to approximately 13 kHz. The 259.7 MHz receiver may be utilized to receive from an EVA baseband voice and seven telemetry subcarriers ranging in frequency from 4 to 12.7 kHz. This composite voice and biomed signal is relayed in real time to the MSFN via the down-voice S-band subcarrier.

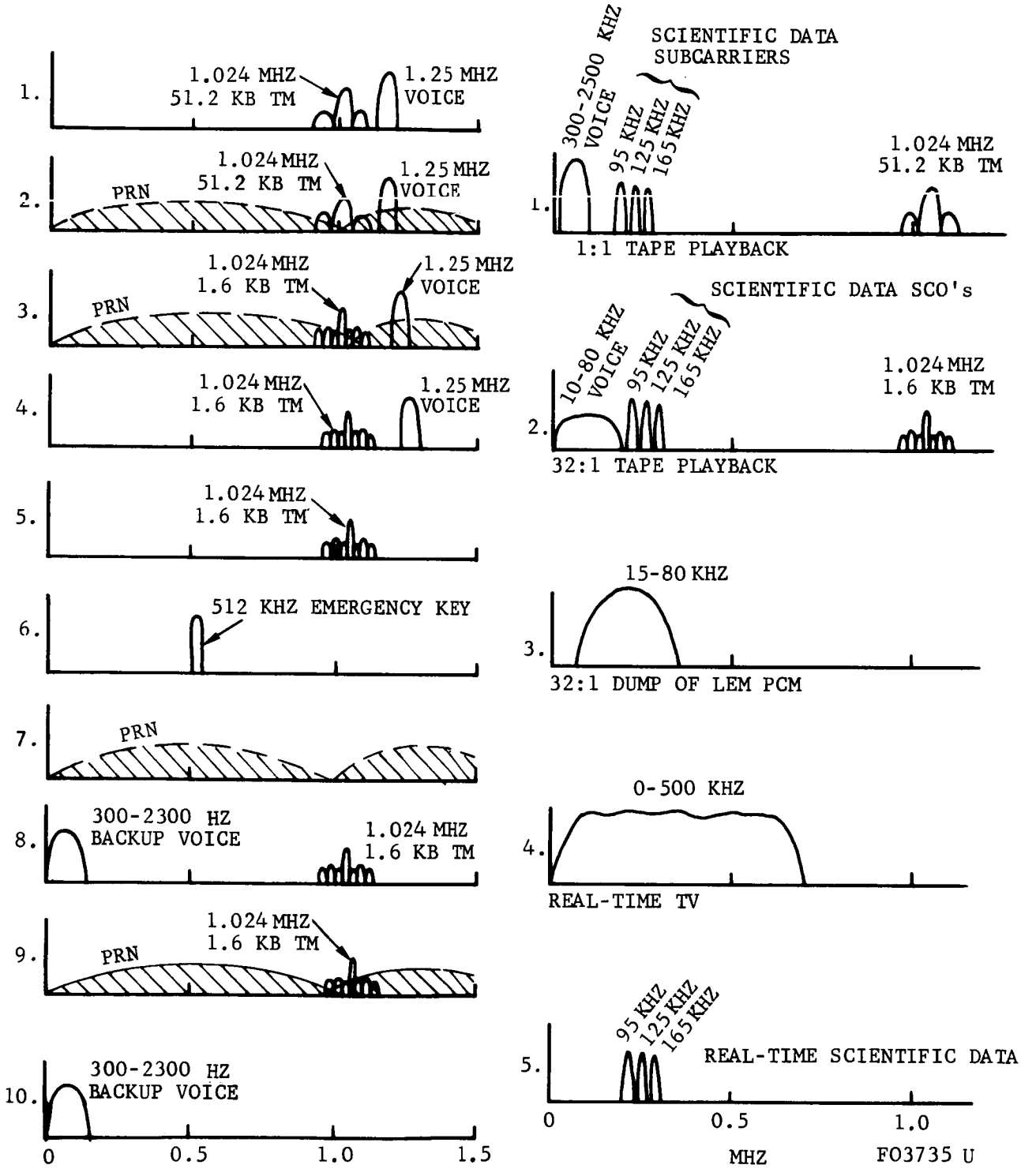

FIGURE F-5. CSM S-BAND DOWN LINK TRANSMISSION COMBINATIONS
(UPPER SIDEBAND FREQUENCY SPECTRA SHOWN)

The 259.7 MHz receiver is also used to receive 1.6 KBPS "split-phase" telemetry data from LEM during LEM descent and ascent mission phases. This telemetry, which occupies a 600 to 2800 Hz frequency spectrum, is recorded by the CSM Data Storage Equipment (DSE) for later playback to the MSFN via the S-band FM transmitter.

The VHF/AM receivers are of conventional solid-state design with a noise figure of approximately 6 db. The transmitters, however, use a unique modulation technique. The voice input from the crew or MSFN (via up-link S-band) is infinitely clipped. The resulting square wave type waveform then keys the class C transmitter on and off at an approximate 50 percent duty cycle. During the "on" period the transmitter emits 10 watts peak, with essentially no power emitted during the "off" period. The average transmitter output power is thus approximately 5 watts. This transmitter design results both in high prime power efficiency and in higher signal margins due to the heavy speech clipping.

F.2.3 COMMAND MODULE RECOVERY COMMUNICATIONS

The VHF/AM transmitter receiver equipment is also utilized during CM recovery for line-of-sight 296.8 MHz simplex communications with recovery aircraft. During this phase, a separate CM-mounted VHF pop-up antenna, which erects upon main parachute deployment, is utilized.

Two additional rf links are provided during recovery. A 243 MHz VHF recovery beacon is transmitted via a separate CM pop-up VHF antenna to enable direction finding by recovery aircraft. A 10.006 MHz SSB/AM HF transceiver and erectable antenna are also provided for over-the-horizon communications. Use of this HF transceiver for the penetrometer-CSM data link is not feasible due to the limited (3 kHz) post-detection bandwidth and the lack of an HF antenna which can be deployed in flight.

F.3 BLOCK II CSM COMMUNICATION EQUIPMENT CHARACTERISTICS

The overall communication links and their functions were described in the previous paragraph. In this paragraph, the salient equipment parameters of interest are presented. The communications equipment can be categorized into three groups; the S-band equipments, VHF/AM rf equipments (including antennas), and the data handling, processing, and storage equipment. Since use of the recovery communications equipment does not appear to be feasible for the penetrometer/CSM link, the detailed recovery equipment characteristics will not be presented.

F.3.1 DATA HANDLING, PROCESSING, AND STORAGE EQUIPMENT

The primary components of this group are the PCM telemetry equipment, the data storage equipment (DSE), and the pre-modulation processor (PMP). In addition, a central timing unit is provided for master synchronization of CSM subsystems, an audio center unit provides the necessary processing for crew audio communications, and a digital up-data link receives and executes ground-originated commands via a 70 kHz subcarrier on the S-band up-link.

a. PCM Telemetry Equipment. This equipment gathers various analog and digital inputs from spacecraft sensors and converts them into a serial digital output for transmission, storage, or preflight spacecraft checkout.

Two output data rates are available. A high bit rate, 51.2 KBPS output, is utilized for close monitoring of all spacecraft subsystems' performance during preflight checkout and for analysis of in-flight performance during critical mission phases. A reduced 1.6 KBPS rate is provided for nominal monitoring of spacecraft status during quiescent mission phases, for recording when out of sight of an MSFN station, or when CSM-to-MSFN rf signal margins are inadequate for the high bit rate transmission. The highest sampling rate of an individual analog channel is 200 samples/second. Therefore, it is unlikely that the PCM telemetry equipment can be utilized for relay of penetrometer data. A simplified block diagram of the PCM telemetry functional flow is given in Figure F-6.

b. Data Storage Equipment (DSE). The DSE is utilized for recording data during critical mission phases or whenever the CSM is beyond LOS of the MSFN. The CSM PCM telemetry is recorded digitally, using 5 digital tracks. Five analog tracks are provided for recording and playback of voice, LEM PCM, and three channels of scientific data. The capability is provided for adding four additional analog channels on an as-required basis by plugging in the necessary record and playback electronics.

Two recording speeds are utilized. The speeds are governed by the bit rate of recorded CSM PCM. Low bit rate PCM is recorded at 3-3/4 inches per second (ips); high bit rate PCM at 15 ips. A bit rate sensing circuit during playback automatically selects a 120 ips playback speed for low bit rate PCM and a 15 ips speed for high bit rate. Hence, the record and playback tape speeds for all tracks, including analog, are governed by the recorded PCM bit rate.

The record bandwidths of the analog tracks are dependent upon the recording speed. The overall record-through-playback frequency response at 15 ips is 50 to 25,000 Hz. The frequency response at a 3-3/4 ips record speed is 12.5 to 6250 Hz.

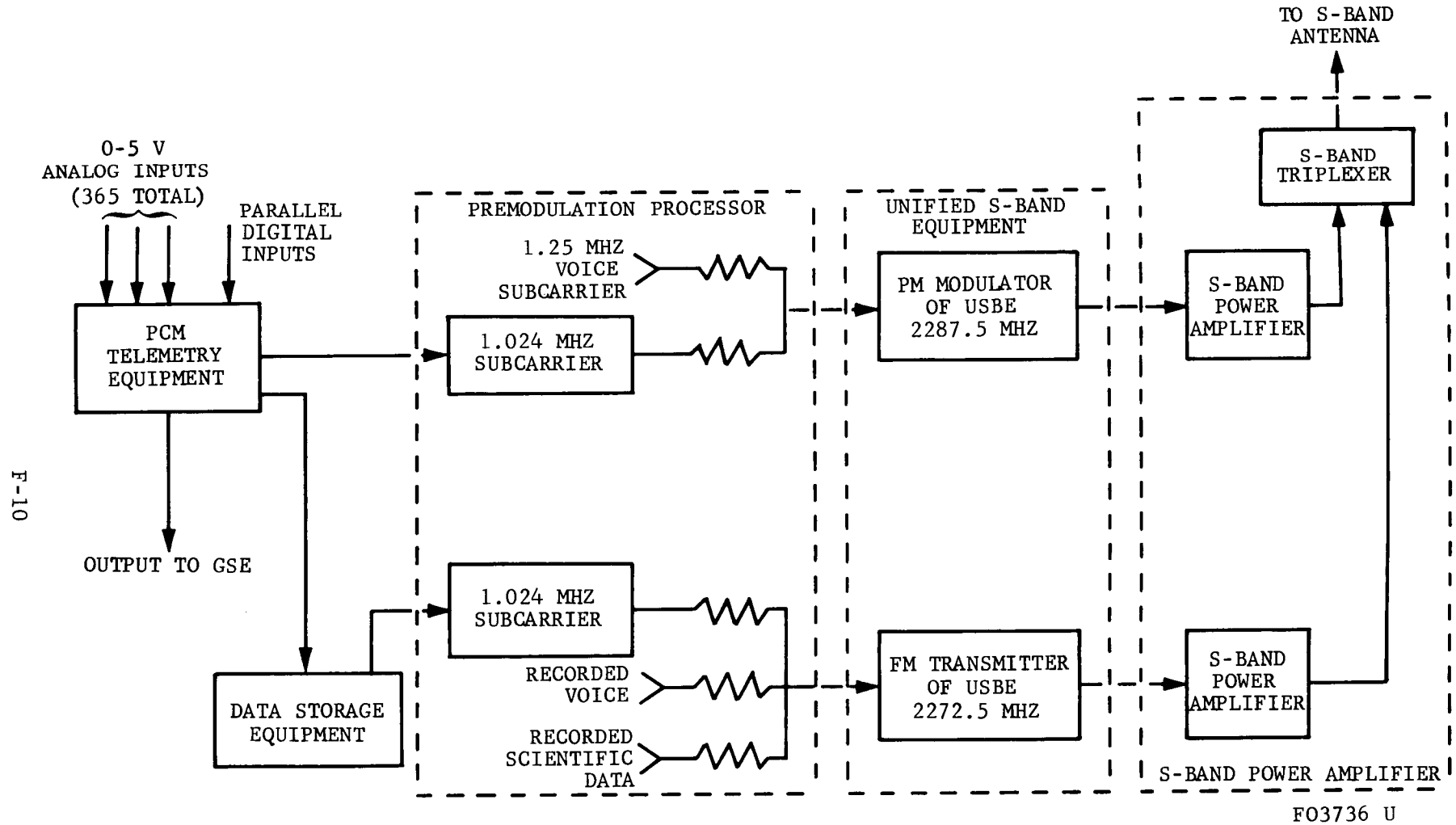

FIGURE F-6. CSM PCM TELEMETRY FUNCTIONAL FLOW DIAGRAM

An analog signal recorded at the 3-3/4 ips speed is multiplied in frequency by a 32:1 factor upon playback because of the high playback speed of 120 ips.

c. Premodulation Processor (PMP). The PMP provides the switching, processing, subcarrier modulation, and subcarrier demodulation functions for the CSM-MSFN S-band links and the MSFN-CSM-EVA and MSFN-CSM-LEM relay communications links. Figure F-7 presents the block diagram of the PMP.

(1) Up-link Voice and Data Demodulation. The PMP demodulates the frequency-modulated up-link 30 kHz voice and 70 kHz up-data subcarriers and routes the detected outputs to the Audio Center and the up-data-link equipments, respectively. In case of a filure of the 30 kHz voice discriminator, a switching function permits the 70 kHz subcarrier to be used as a backup for up-link voice.

(2) Down-link Voice and PCM. Down-link S-band voice and PCM are modulated on 1.25 and 1.024 MHz subcarriers, respectively. The subcarriers are summed through a mixing network and the resulting output presented to the unified S-band equipment where it phase modulates the 2287.5 MHz carrier. When LEM voice or EVA voice and biomed (7 telemetry subcarriers ranging in frequency from 4 to 12.7 kHz) are to be relayed to the MSFN, the VHF/AM receiver output level is adjusted to the proper modulating level and summed with voice from the Audio Center. This composite signal then modulates the 1.25 MHz voice subcarrier.

(3) Television. When TV transmission is selected, the video input from the TV camera is dc-coupled through the PMP to the 2272.5 MHz FM transmitter. The video input from the TV camera has a dc to 500 kHz bandwidth. The input level ranges from 0.3 to 2.3 volts. A 1.3-volt bias is placed upon the FM transmitter during TV transmission to keep the output frequency spectrum centered about the nominal 2272.5 MHz center frequency.

(4) Real-time Scientific Data. Three subcarriers are provided for scientific data transmission via the FM transmitter. By switching inputs, these subcarriers can transmit either real-time or stored data (see Figure F-8). The frequency response capabilities for the subcarriers are:

Subcarrier (kHz)	Frequency Response (Hz)
95	0 to 2850
125	0 to 3750
165	0 to 4950

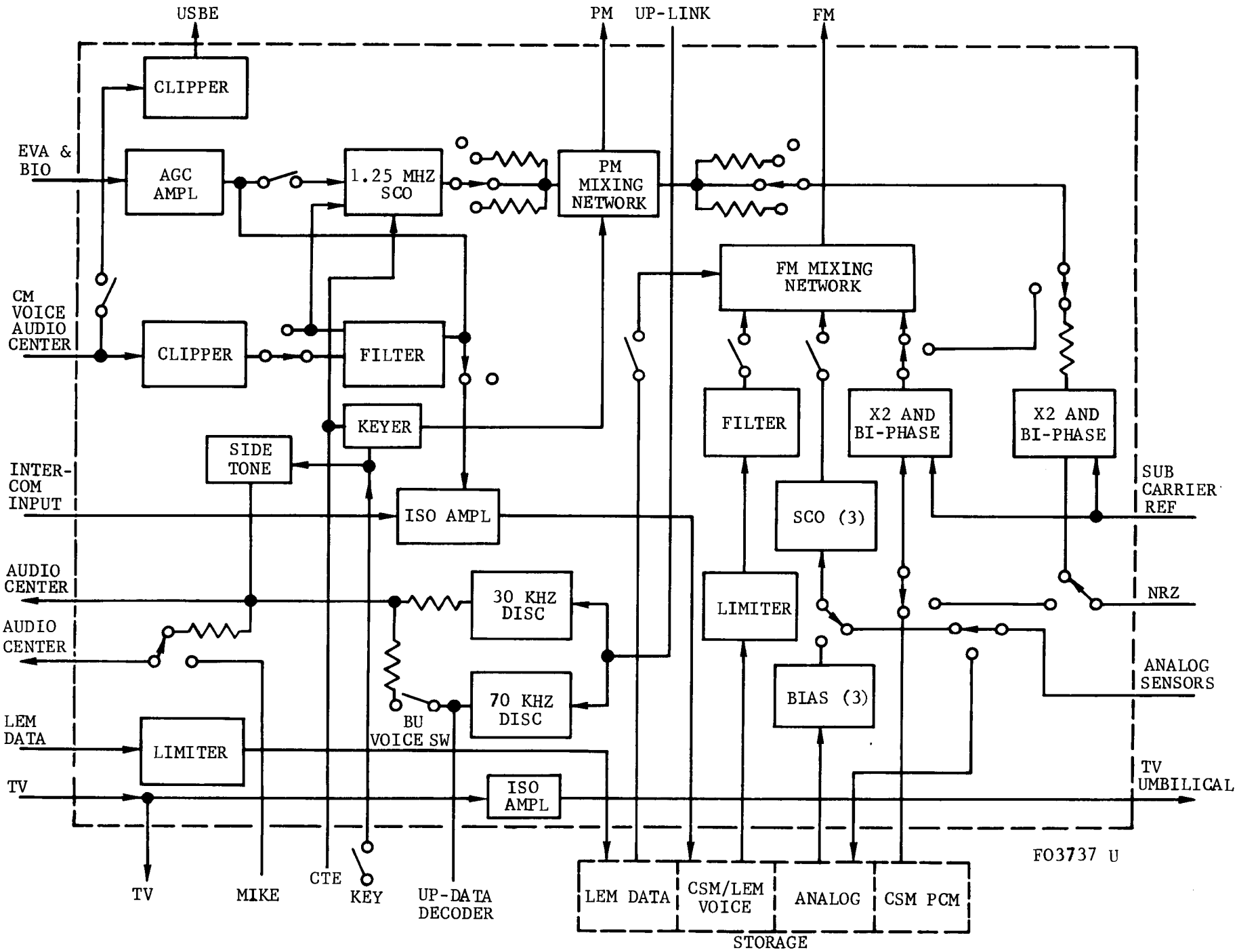

FIGURE F-7. CSM PREMODULATION PROCESSOR - BLOCK DIAGRAM

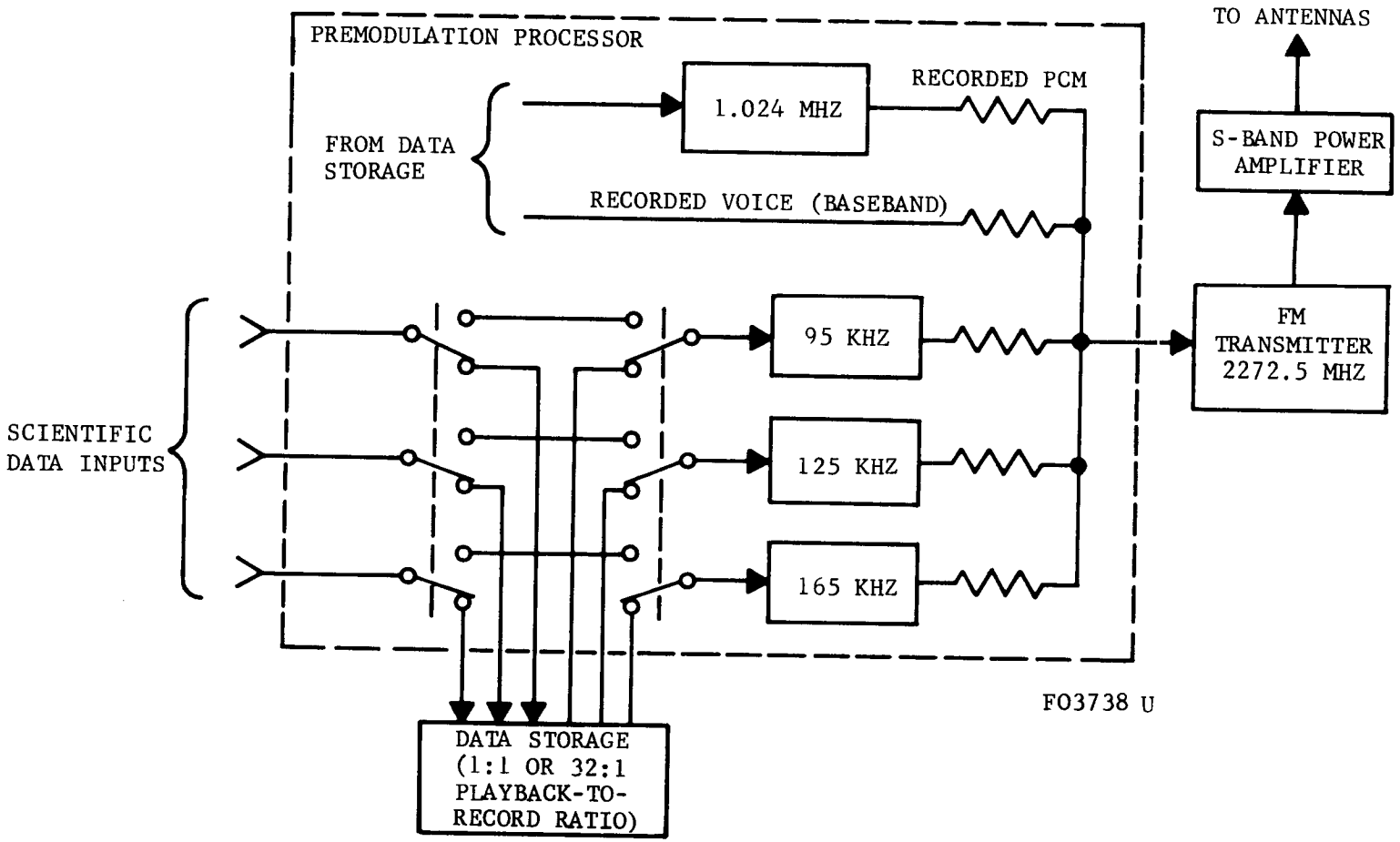

FIGURE F-8. CSM FUNCTIONAL FLOW DIAGRAM FOR THE 3 SCIENTIFIC DATA CHANNELS

(5) CSM Data Playback. When this transmission mode is selected, recorded voice, CSM PCM telemetry, and the three channels of recorded scientific data are all transmitted simultaneously via the FM transmitter. The playback PCM bi-phase modulates a second 1.024 MHz subcarrier. The three channels of scientific data modulate the 95 kHz, 125 kHz, and 165 kHz data subcarriers. The baseband voice and the subcarriers are summed through mixing networks and the composite output presented to the FM transmitter modulator.

The upper frequency response of the three scientific data subcarriers for recorded and real-time scientific data is the same. Since data recorded at 3-3/4 ips gets multiplied in frequency by a 32:1 ratio, the prerecording frequency response for such data must be reduced to 1/32 of the allowable response for real-time scientific data.

(6) LEM PCM Data Playback. When this data playback mode is selected, the DSE is played back at 120 ips and the single LEM PCM channel is routed to the FM transmitter by the PMP.

(7) Other PMP Functions. A 512 kHz emergency key subcarrier permits emergency down-link communications in case of a loss of both the S-band power amplifier and the high-gain antenna. This subcarrier output to the S-band PM modulator is gated on and off at the keying rate.

A back-up voice mode is provided for other potential conditions where rf signal levels are inadequate for normal down-voice communications. When this mode is selected, the voice from the Audio Center is heavily clipped and applied at baseband to the PM modulator.

A switching function is provided within the PMP to enable use of the second 1.024 MHz PCM subcarrier, which is normally used for transmission of CSM recorded PCM, as a backup for real-time PCM transmission, should a failure disable the primary real-time PCM subcarrier.

The PMP performs the combining of the audio signals from the Audio Center intercom bus and the VHF/AM receivers. The composite output is then routed to the DSE for recording and later playback to the MSFN.

The necessary switching for enabling use of the CSM as a voice relay between the MSFN and LEM or EVA is accomplished in the PMP.

The baseband frequency spectra of the various S-band up-link and down-link transmission combinations which can be selected via the PMP are illustrated in Figure F-5.

F.3.2 S-BAND RF EQUIPMENT

The S-band rf equipment consists of three major components: the unified S-band equipment (USBE), the S-band power amplifier equipment (S-band PA), and the S-band antenna system.

a. Unified S-band Equipment. The USBE consists of 2 switchably redundant PM transponders and an FM transmitter, all packaged in a single unit.

(1) Transponder. The transponder receiver has a 12 db noise figure. Two detectors are utilized: a 700 Hz $2B_{LO}$ carrier tracking loop, and a wideband modulation detector. The transponder can accommodate input modulation bandwidths of up to $\pm$1.5 MHz. The frequency stability, when unlocked to a reference, is 42 kHz, i.e., to be assured of quick receiver lockup, the incoming frequency must be swept over this range from the assigned 2106.40625 MHz receiver frequency.

The output from the wideband modulation detector is routed to two places: to the PMP for demodulation of the 70 kHz up-data and 30 kHz up-voice subcarriers, and also back to the transponder PM modulator for retransmission of the two-way PRN ranging signal, if required.

The transmitter portion of the transponder derives its output frequency (nominally 2287.5 MHz) in a precise 240/221 transmit/receive ratio to the received frequency from the receiver VCO when the receiver is firmly locked to an up-link signal. This coherent 240/221 frequency ratio enables the MSFN to obtain highly accurate two-way doppler data. When the receiver is unlocked, the frequence reference for the transmitter is automatically switched to an auxiliary crystal oscillator. This switchover in reference is required since, otherwise, incoming receiver noise modulating the unlocked receiver VCO would create excessive phase jitter and make it difficult or impossible for the MSFN to lock up on the CSM-transmitted carrier.

The transponder carrier output level is approximately 1/4 watt. If desired, this level can be amplified to either 5 or 20 watts by means of a TWT amplifier in the S-band PA. If signal margins permit, the TWT amplifier can be bypassed and the transmitter output connected directly to the S-band triplexer (also located physically in the S-band PA). Including internal switching and triplexer losses, the net output levels for the PM carrier at the S-band PA/antenna interface are 11.2, 2.8, and 0.125 watts for high-ower TWT, low-power TWT, and bypass operation, respectively.

(2) FM Transmitter. The 2272.5 MHz FM transmitter is relatively independent of the redundant PM transponders. It is designed to accept modulating frequencies up to 500 kHz and be capable of peak carrier deviations up to 3 MHz. It accepts either unipolar dc coupled inputs or ac inputs. The FM transmitter output to the S-band PA can be amplified at either of two power levels by means of a second TWT amplifier to yield a net S-band PA output for this transmitter of either 10.0 or 2.5 watts. This transmitter output does not have the TWT bypass capability as does the 2287.5 MHz PM output.

b. S-band Power Amplifier. This equipment essentially consists of two independent TWT amplifiers (including power supplies), coax switches, and an S-band triplexer (see Figure F-9). The 2106.4 MHz up-link signal is routed directly to the USBE transponder receiver input. The 2287.5 MHz PM carrier may be routed to a TWT for amplification, or, by the bypass provision, connected directly to its triplexer input port. No bypass provision exists for the 2272.5 MHz FM carrier. Each TWT amplifier can be operated independently. For reliability either TWT may operate with either down-link carrier input.

c. S-band Antennas. Two antenna systems are provided, omni and high-gain. The location of these antennas, as well as the VHF Scimitars, are shown in Figure F-10. The S-band omni antennas are flush-mounted cavities spaced at approximately 90-degree intervals around the base of the command module. They are presently fed in 180-degree separated pairs. The crew can remotely select, via a coax switch, either omni pair or the high gain antenna. It is anticipated that the later CSM's used on lunar missions will have the capability for the crew to select individually any of the four omni antennas.

The high gain antenna is located at the base of the service module. It is stowed and cannot be used until the CSM and LEM complete the initial docking maneuver subsequent to translunar injection. Three transmitting bandwidths are provided for use at various ranges. The narrow bandwidth for use at lunar distance is 4.6 degrees; the on-axis antenna gain for this beamwidth is 27.4 db. The estimated circuit losses between the S-band PA and the high gain antenna are approximately 6.5 db, including antenna switch and VSWR losses. High gain antenna pointing is accomplished automatically with an rf angle track pointing system. Worst-case antenna pointing losses should be no more than 0.4 db.

The omni antennas in the current paired configuration yielded a predicted gain of minus 3 db or higher over 80 percent of the sphere. Individual switching between the four omnis should increase this gain to approximately 0 db or higher for the same coverage factor. The circuit losses from the S-band PA to the omni antennas are approximately 5 db.

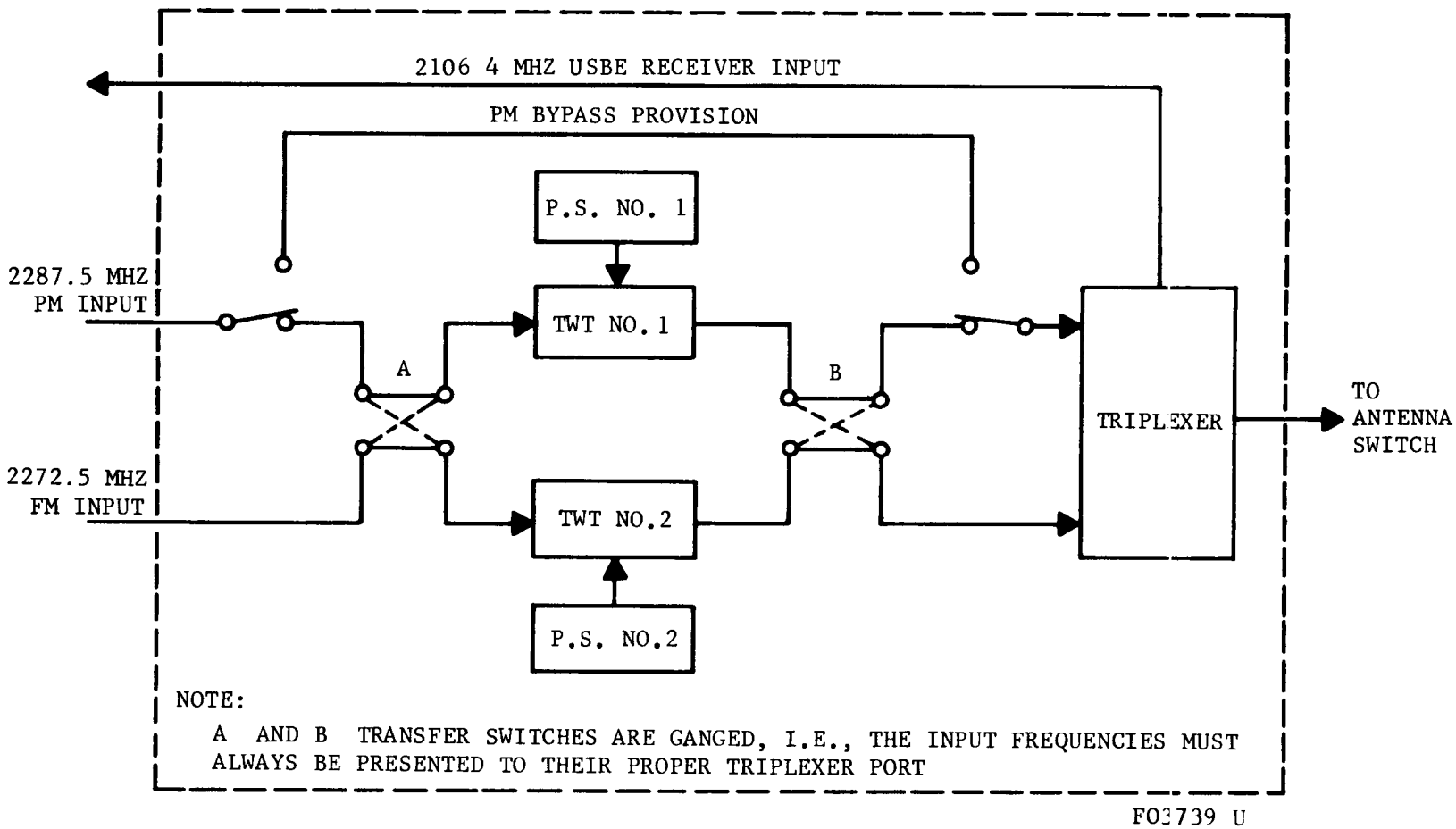

FIGURE F-9. CSM S-BAND POWER AMPLIFIER BLOCK DIAGRAM

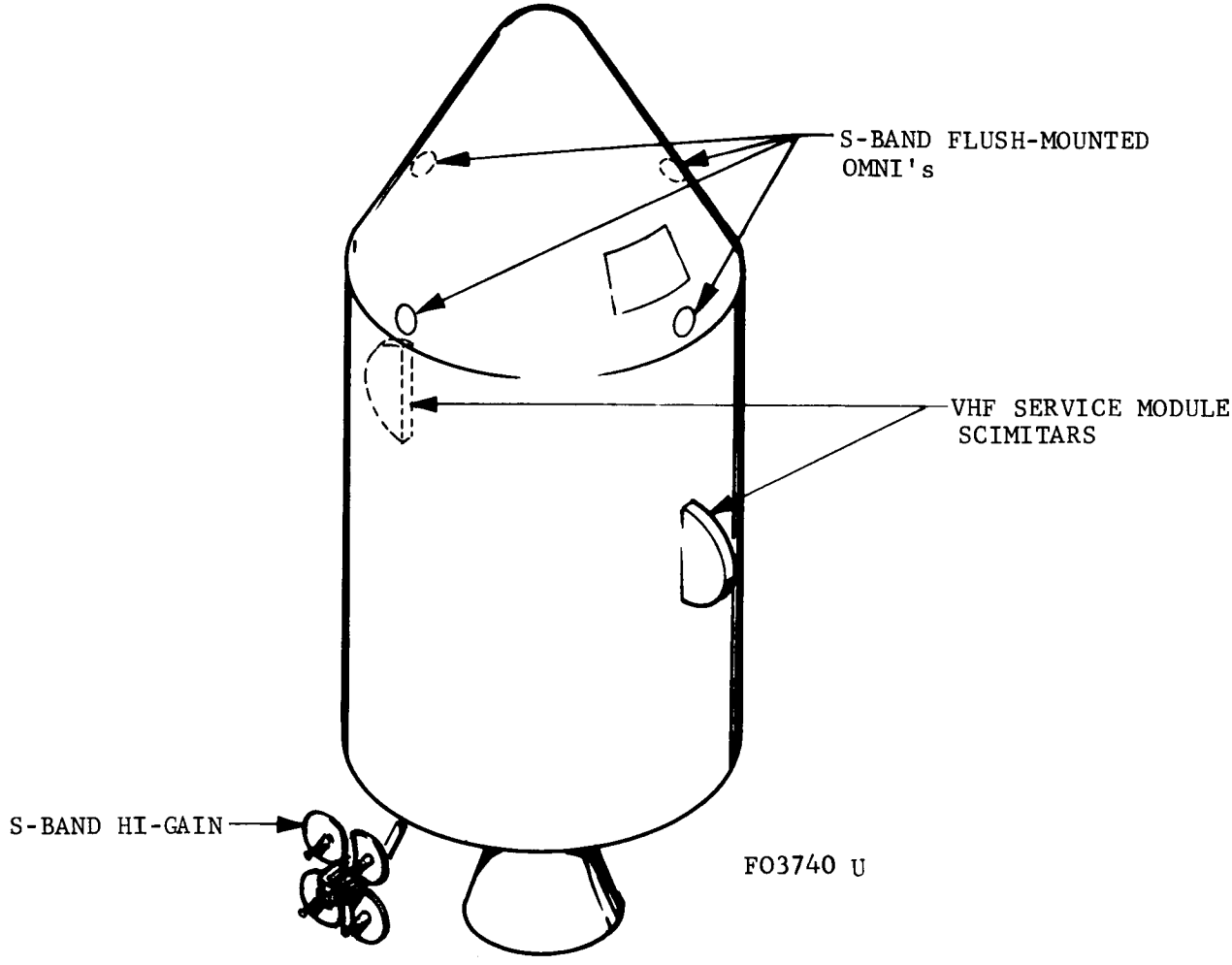

FIGURE F-10. BLOCK II CSM INFLIGHT ANTENNAS

F.3.3 VHF RF EQUIPMENT

The inflight VHF rf equipment consists of the two VHF/AM transmitter-receivers described previously, a VHF triplexer, and two service module mounted VHF scimitar antennas connected to the triplexer through a coax switch.

a. VHF Triplexer. The VHF triplexer multiplexes the 296.8 MHz and 259.7 MHz VHF/AM frequencies and a spare 228.2 MHz port to the scimitar antennas. The 228.2 MHz port is available for R&D or scientific purposes. The triplexer insertion loss is approximately 1.5 db for each port. The co-channel isolation is greater than 40 db.

Losses between the VHF triplexer and the scimitar antennas are approximately 2.6 db, including cable, connector, switch, and VSWR losses.

b. VHF Scimitar Antennas. Figure F-11 illustrates the location of the antennas on the service module. Typical approximate antenna patterns for the scimitars are shown in Figure F-12. It is anticipated that CSM attitude constraints can be utilized if required during the short time interval required for data relay/CSM data transmission. Hence, CSM scimitar antenna gain for a data relay/CSM transmission link should be minus 3 db or higher. The scimitars are linearly polarized; hence, if the penetrometer relay unit uses circularly polarized transmitting antennas, the polarization loss should not be much greater than 3 db.

If CSM attitude constraints cannot be exercised for the duration of the data relay/CSM data transmission, more information concerning the scimitar antennas must be obtained to assure the adequacy of the data relay/CSM transmission system design. Specifically, the following information is required:

(1) Definition of antenna locations relative to pattern plots given in Reference (4).

(2) Pattern plots to account for other polarization components, i.e., LHC (RHC is given in Reference (4)).

A summary of the pertinent CSM equipment specifications is given in Table F.1.

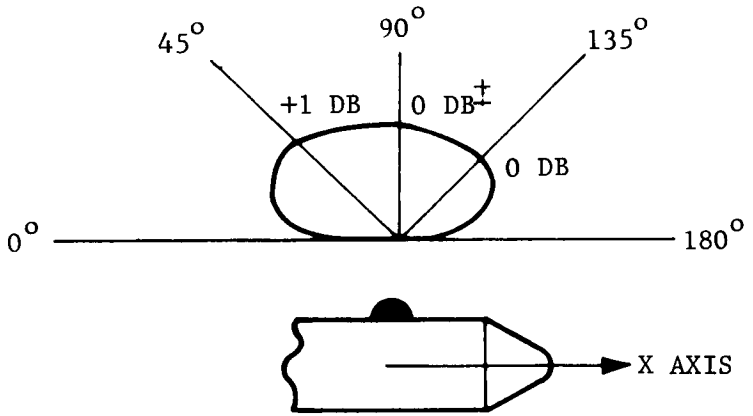

± RELATIVE TO LINEAR POLARIZATION

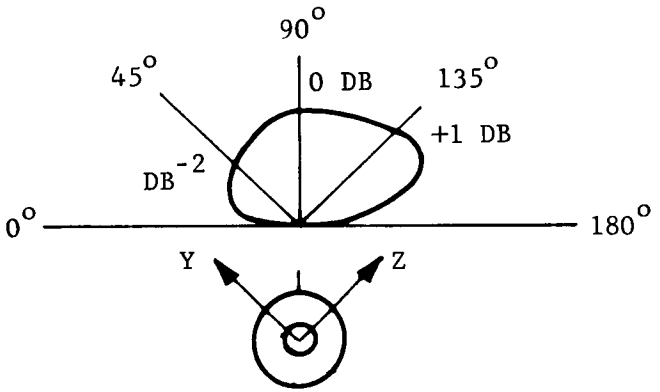

FO3741 U

FIGURE F-11. BLOCK II CSM VHF SCIMITAR ANTENNA COVERAGE

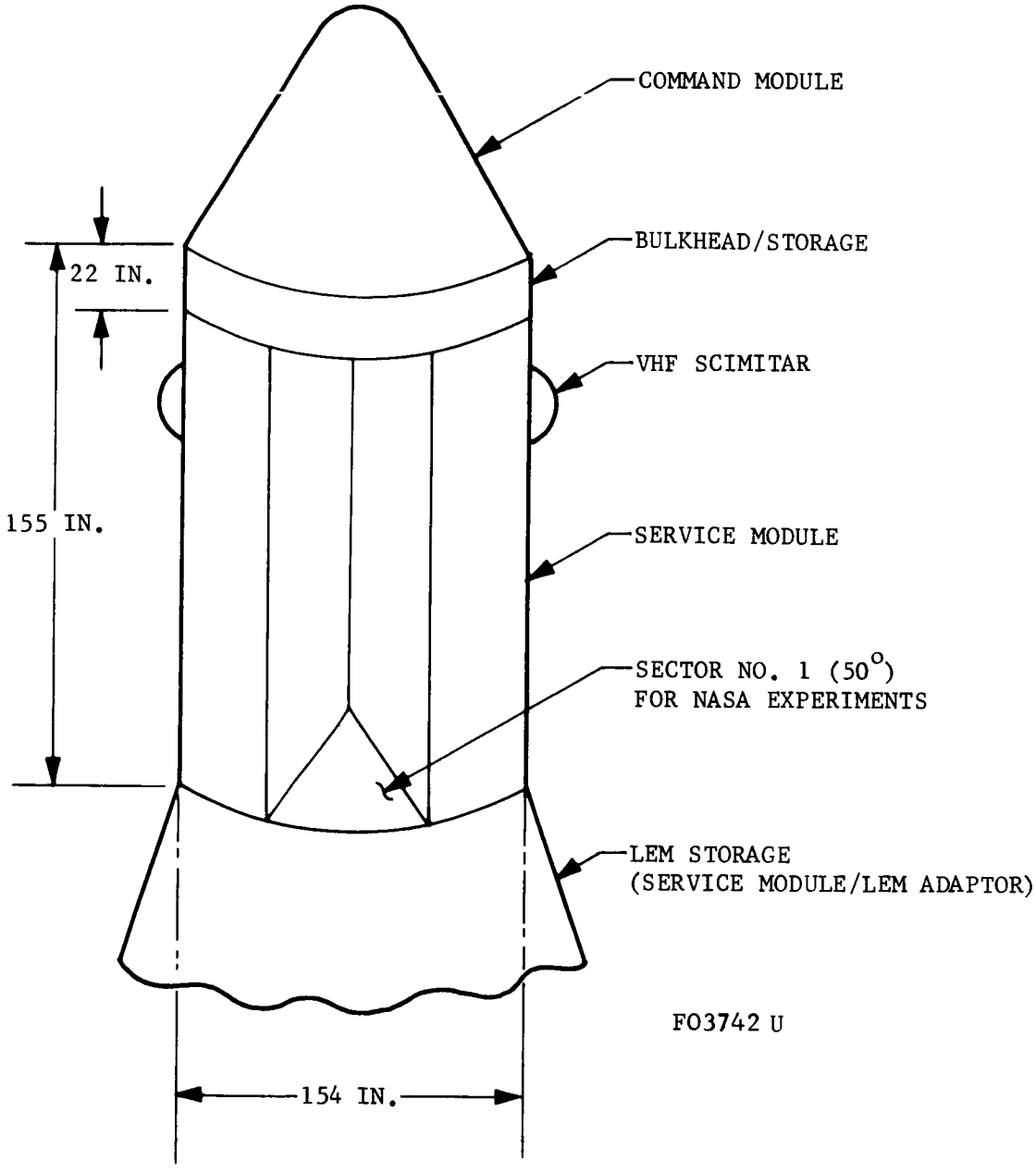

FIGURE F-12. APOLLO CSM MECHANICAL CONFIGURATION

TABLE F.1

APOLLO CSM COMMUNICATION EQUIPMENT SUMMARY

1. VHM/AM Transmitter-Receiver Equipment

Transmit frequencies	296.8, 259.7 MHz
Receive frequencies	296.8, 259.7 MHz
Frequency stability	
Transmit	±0.003 percent
Receive	±0.002 percent
Receiver noise figure	6 db
IF bandwidth (6 db)	70 KHz
Audio output response	300 to 13,000 KHz
Supplier	RCA

2. Unified S-Band Equipment (Supplier - Motorola)

a. PM Receiver Characteristics (2106.40625 MHz)

Noise figure	11 db
Tracking threshold	-127 dbm
VCO stability	±0.002 percent
Wideband modulation frequency response	300 Hz to 1.5 MHz
Carrier loop bandwidth	700 Hz ($2B_{LO}$)
Loop gain	5.3×10^6

b. PM Transmitter Characteristics

Frequency (in lock)	240/221 x received freq
Frequency (out of lock)	2287.5 MHz ± 0.002 percent
Frequency response	300 Hz to 1.5 MHz
Output power	250-400 mw
Modulation sensitivity	1 radian/volt
Maximum deviation	4 radians

c. FM Transmitter

Frequency	2272.5 MHz
Frequency stability	± 455 KHz
Modulation sensitivity	1 MHz/volt
Frequency response	0 to 500 KHz
Maximum frequency deviation	3 MHz
Input impedance	95 ohms

TABLE F.1 (Continued)

3. S-Band Power Amplifier

Receive channel insertion loss	1.5 db
PM output levels (2287.5 Mc)	2.8, 11.2, 0.125 watts
FM output levels (2272.5 Mc)	10.0, 2.5 watts
Supplier	Collins

4. VHF Triplexer

Outputs	
Transmitter - Receiver #1	296.8 MHz
Transmitter - Receiver #2	259.7 MHz
Spare Port	228.2 MHz
Co-channel isolation	40 db minimum
Insertion loss	1.5 db maximum
VSWR	1.5 : 1 maximum
Output bandwidths	1 Mc minimum

5. VHF In-flight Antenna System

Type	2 broadband scimitars on Service Module, selected individually by coax switching
Frequency Range	225 to 450 MHz
Coverage	Figure 4-10
Losses	2.6 db from VHF triplexer to either antenna

6. PCM Telemetry Equipment

Outputs	2 formats; 51.2 KBPS or 1.6 KBPS NRZ PCM
Inputs, 51.2 KBPS format	
0 to 5 v analog, 8 bits/sample inputs	
200 S/S channels	4
100 S/S channels	16
50 S/S channels	15
10 S/S channels	180
1 S/S channel	150
Parallel digital, 8 bits/sample inputs	
200 S/S channels	2
50 S/S channels	1
10 S/S channels	310
Parallel digital, 32 bits/sample inputs	
50 S/S channels	1

TABLE F.1 (Continued)

Serial digital, 8 bits/sample inputs	
50 S/S	1
Inputs, 1.6 KBPS output format	
0 to 5 v analog, 1 S/S	100
Serial digital, 40 bits/sample, 10 S/S	1
Parallel digital, 8 bits/sample, 10 S/S	1
Parallel digital, 32 bits/sample, 1 S/S	1
Parallel digital, 8 bits/sample, 1 S/S	31
Supplier	Radiation, Inc.

7. Data Storage Equipment

Number digital tracks	5
Number analog tracks	5*
Normal record speed	15 ips
Reduced record speed	3.75 ips
Analog frequency response (±4 db relative to 1 KHz)	
15 ips record	50 Hz to 25 KHz
3.75 ips record	12.5 Hz to 6.25 KHz
Digital rate response	
14 ips record	51.2 KBS
3.75 ips record	1.6 KBS
Playback time	
120 ips	3.75 min
15 ips	30 min
Input impedance	100 k ohms
Output impedance	600 ohms
Supplier	Leach

8. Premodulation Processor, Inputs for S-Band Transmission

a. Crew voice (from Audio Center)

Bandwidth	300 to 3000 Hz
Clipping level	Normal voice, 12 db; Backup voice, 24 db
Input impedance	600 ohms
Modulation technique	
Normal voice	FM on 1.25 MHz subcarrier, then output to PM S-band transmitter
Backup voice	Direct baseband output to PM S-band transmitter

*Capability exists to add 4 additional tracks on an as-required plug-in basis.

TABLE F.1 (Continued)

b. PCM	
Bit rate	51.2 KBPS or 1.6 KBPS, crew selectable
Modulation technique	PSK's 1.024 MHz subcarrier
Modulation output	To PM S-band transmitter
c. TV	
Bandwidth	0 to 500 KHz
Impedance	95 ohms, dc coupled
Level	0.3 to 1.3 volts
d. Real-time scientific data (3 channels)	
Bandwidth	0 to 2850 Hz (95 KHz SCO) 0 to 3750 Hz (125 KHz SCO) 0 to 4950 Hz (165 KHz SCO)
Input impedances	300 k ohms minimum
Source impedances	1 k ohm maximum
Input level	0 to +5 volts peak
Modulation technique	FM on 95, 125, 165 KHz subcarriers
Modulation output	To FM S-band transmitter
e. Recorded voice (from DSE)	
Input bandwidth	300 to 80,000 Hz
Input level	Maximum of 6.3 v pp
Input impedance	10 k ohms minimum
Source impedance	600 ohms
Modulation output	To FM S-band transmitter
f. Recorded CSM PCM	
Bit rate	51.2 KBPS
Modulation technique	PSK of separate 1.024 MHz SCO
Modulation output	To FM S-band transmitter
g. Recorded scientific data (3 channels)	
Input impedance	10,000 ohms minimum
Source impedance	600
Input level	Maximum of 8 v pp
Modulation technique	Inputs FM the 95, 125, 165 KHz SCO's (real-time inputs are switched out)
Output	To FM S-band transmitter

TABLE F.1 (Continued)

h. Recorded LEM PCM	
Input impedance	10 k ohms minimum, balanced
Source impedance	600 ohms
Frequency response	15,000 to 90,000 Hz (within 1 db of peak response)
Modulation technique	Baseband output to FM transmitter
Supplier	Collins Radio

F.4 PENETROMETER/CSM INTERFACE

The desired interface between the existing CSM and required penetrometer equipments is a minimum power, weight, and size package requiring little or no modification to the CSM equipment. Ideally, the existing VHF antennas, AM voice and biomed receiver, and tape recorder would all be utilized. However, the anticipated penetrometer data characteristics and bandwidth requirements (300 to 500 kc) make utilizing all of these equipments impractical. The VHF AM receiver is limited to a predetection bandwidth (6 db) of 70 kc. In addition, the demodulation techniques used are not compatible to the penetrometer accuracy requirements. The existing data storage system is limited to an upper frequency response of 25 kc. Two receivers may be necessary if diversity combination of the penetrometer data is performed at the ground rather than in the relay satellite.

Providing space for necessary penetrometer data reception and storage equipment does not present a problem at this time. Space is available in the CSM bulkhead area. Also, one sector (see Figure F-12) of the service module has been allocated to NASA experiments. If this is not adequate, there is further space available in the LEM storage area.

F.5 RECOMMENDED CONFIGURATION

Because of the high data rate requirements of the penetrometer system, separate reception and data storage equipments are recommended. The proposed configuration is indicated in Figure F-2. One or two wideband FM receivers would be utilized, depending upon where the diversity combination is performed.

The penetrometer data can be transmitted in digital or analog form via the unified S-band system. Since the incoming penetrometer signal is in analog form, digitizing in the relay or CSM would be necessary prior to earth transmission over the S-band link in digital form. The digital system would have the advantage of increased accuracy, assuming sufficiently high sampling rates and quantization resolution are employed. The data storage equipment would utilize tape or core memory.

The least additional equipment is required if the incoming data on subcarriers are stored in a magnetic tape recorder directly (without demodulation). Later, upon tape playback, the subcarrier signals are applied directly to the FM modulator in FM mode 5 (see Figure 5). This method of handling the data in the CSM is preferred because it is the most simple and direct, and the accuracy attainable of approximately 2 percent is commensurate with the overall system. Specifications for the required equipment are given in Table F.2.

TABLE F.2

CSM PENETROMETER DATA RECEIVING EQUIPMENT SPECIFICATIONS

1. CSM Receiver

Modulation	FM
Input Frequency (Nominal)	228.2 MHz
Noise Figure	3 db
Dynamic Range	60 db
Lo Stability	$\pm$0.002%
Image Rejection	60 db
First IF	50 MHz
Second IF	10 MHz
IF Bandwidth	300 kHz
Input Impedance	50 Ohms
Input VSWR	1.3 Max
Output Impedance	600 Ohms
Output Level (50 kc Deviation)	4 volts p-p
Input Voltage	18 to 30 vdc
Input Power	2.5 watts
Size	1.8 by 6 by 6 in.
Weight	4.0 lb

2. CSM Penetrometer Data Storage Equipment

Type	Tape Recorder
Channels	2 Analog*
Record Response (Each Channel)	300 Hz to 125 kHz
Record Speed	30 ips
Record Time	10 min
Tape Length	150 ft
Playback Speeds	60 ips, 3.75 ips
S/N (30, 60 ips)	32 db
S/N (3.75 ips)	28 db
Distortion	1% max, 3rd harmonic
Input Sensitivity	0.5 to 5 vrms
Input Impedance	100 k ohms
Output Level	5 v p-p
Output Impedance	600 Ohms
Input Voltage	24 to 32 vdc
Input Power	33 watts
Size	4 by 4 by 5 in.
Weight	5.6 lb

*One channel not required if only one FM receiver is used.

F.6 REFERENCES

1. NAA Specification MC 901-0712, Apollo CSM Block II Communication and Data Subsystem Procurement Specification, dated 19 April 1965.

2. NAA Document SID 64-1613, CSM-MSFN Signal Performance and Interface Specification - Block II, Revised 22 February 1965.

3. NAA Document MH01-13002-414, EVA/CSM VHF/AM Communications Circuit Margin ICD, Block II, dated 9 September 1965.

4. NAA TM 65-2, Coberage Factors for Non-Flush Mounted VHF Antennas on the Service Module, Block II, dated 8 January 1964.

5. Collins Radio Specification 514-0037, Equipment Specification for the Premodulation Processor Equipment of the Apollo Communications and Data Subsystem, Revision C, dated 19 October 1965.

APPENDIX G

MODULATION METHODS STUDIES

G.1 INTRODUCTION

A study of modulation methods is presented, based on sinusoidal modulation, resulting in expressions depicting penetrometer to data relay communication system performance above threshold. Mean output signal-to-noise power ratios (SNR) are obtained for AM, FM, AM/FM, and FM/FM systems based upon the following assumptions:

(1) Signal power much greater than noise power.

(2) Single frequency sinusoidal modulation of full scale signal amplitude.

(3) Signal power assessed with noise assumed absent and noise power in absence of signal (unmodulated carrier present).

(4) Identical input carrier power and noise spectral density applied to each system.

(5) All powers were derived relative to unity loads.

G.2 AMPLITUDE MODULATION (AM)

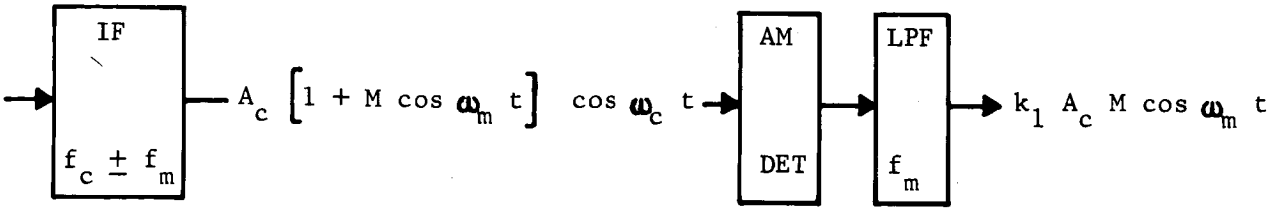

given

AM carrier at detector input as noted, no noise

A_c is the unmodulated carrier amplitude at same point

AM carrier at detector and LPF output is as noted where

k_1 is the constant of proportionality of DET/LPF and M is the modulation factor.

then

Mean output signal power across unity load impedance is

$$S_o = \left(k_1 A_c M\right)^2 \frac{1}{T} \int_0^T \cos^2 \omega_m t \, dt \qquad (1)$$

$$S_o = 1/2 \, k_1^2 A_c^2 M^2 \qquad (2)$$

Since mean value of unmodulated carrier power is $S_c = 1/2 \, A_c^2$, we can rewrite Equation (2) as

$$S_o = k_1^2 M^2 S_c \qquad (3)$$

The input noise power in a 2 f_m bandwidth is

$$N_c = \Phi \, 2 f_m \qquad (4)$$

where

Φ = noise power spectral density and is a constant.

The detected noise power is of the form

$$\frac{k_1^2 A_n^2}{2}$$

i.e., $k_1 A_n \cos \omega_n t$ and the output noise power is

$$N_o = k_1^2 \bullet 2 f_m = k_1^2 N_c \quad (5)$$

Taking SNR_o at the output of the baseband detector, we get

$$SNR_o = \frac{k_1^2 M^2 S_c}{k_1^2 N_c} \quad (6)$$

$$\therefore SNR_o = M^2 SNR_i \quad (7)$$

where

SNR_i = the input carrier-to-noise ratio in a 2 f_m bandwidth

Based on the assumed fullscale applied amplitude, M = 1 then

$$\boxed{SNR_o = SNR_i} \quad (8)$$

G.3 FREQUENCY MODULATION (FM)

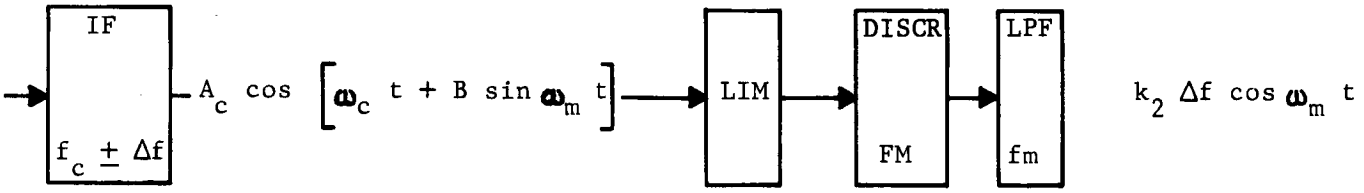

given

FM carrier input to limiter as noted, no noise

A_c is unmodulated carrier amplitude at same point

then

$S_c = 1/2 A_c^2$ independent of modulation (9)

$N_c = \bullet 2 f_m$ input noise power over 2 f_m bandwidth (10)

Mean output noise power of data channel is obtained by summing noise power contributions within $\pm f_m$ bandwidth

$$N_o = 2 \int_o^{fm} \Phi \frac{k_2}{A_c} f^2 \, df = \frac{2 \Phi f_m^3}{3} \left(\frac{k_2}{A_c}\right)^2 \tag{11}$$

where

k_2 = discriminator constant

$$N_o = \frac{2 \Phi f_m k_2^2 f_m^2}{1/2 A_c^2 6} = \frac{N_c k_2^2 f_m^2}{S_c 6} \tag{12}$$

Mean output signal power in the discriminator baseband is

$$S_o = \frac{k_2^2 (\Delta f)^2}{2} \tag{13}$$

The output SNR_o is obtained ratioing Equations (13) and (12)

$$SNR_o = \frac{1/2 \, k_2^2 (\Delta f)^2}{\frac{N_c k_2^2 f_m^2}{S_c 6}} = 3\left(\frac{\Delta f}{f_m}\right)^2 \frac{S_c}{N_c} \tag{14}$$

$$\therefore SNR_o = 3 \beta^2 SNR_i \tag{15}$$

where

$SNR_i = SNR/2 f_m$

and

$\beta = \frac{\Delta f}{f_m}$ (deviation ratio)

or

$$\boxed{SNR_o = 3\left(\frac{\Delta f}{f_m}\right)^2 SNR_i} \tag{15}$$

G.4 AMPLITUDE MODULATION/FREQUENCY MODULATION (AM/FM)

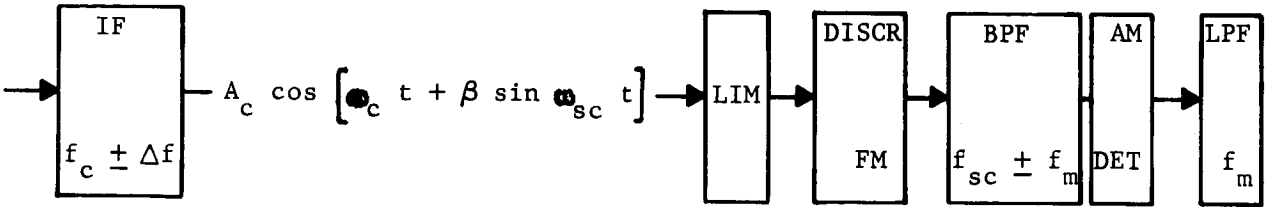

given

$$\beta = \frac{\Delta\omega}{\omega_m} = \frac{\Delta f}{f_m} \quad ; \quad \Delta f \propto A_{sc} (1 + M \cos \omega_m t)$$

FM carrier at input to limiter as noted, assuming no noise

A_c is unmodulated carrier amplitude

$A_{sc} (1 + M \cos \omega_m t) \cos \omega_{sc} t$ is the AM subcarrier

then

$$S_c = 1/2 \, A_c^2 \quad \text{carrier power independent of modulation} \qquad (16)$$

$$N_c = \Phi \, 2 f_m \quad \text{input noise power in } 2 f_m \text{ bandwidth} \qquad (18)$$

$$N_d = 2 \int_{f_1}^{f_2} \Phi \left(\frac{k_2}{A_c} \right)^2 f^2 \, df \quad \text{is input noise power to AM detector} \qquad (18)$$

where

$$f_1 = f_{sc} - f_m$$

and

$$f_2 = f_{sc} + f_m$$

k_2 = discriminator/BPF proportionality constant

Φ = noise power spectral density, constant.

$$N_d = 2\left(\frac{k_2}{A_c}\right)^2 \bullet \frac{f_2^3 - f_1^3}{3} = 2\left(\frac{k_2}{A_c}\right)^2 2 \bullet f_m \left(\frac{3 f_{sc}^2 + f_m^2}{3}\right) \quad (19)$$

Since $f_{sc} > f_m$ we can simplify Equation (19) into

$$N_d = \frac{k_2^2}{1/2\ A_c^2} 2 \bullet f_m f_{sc}^2 = \frac{N_c}{S_c} k_2^2 f_{sc}^2 \quad (20)$$

and as in the AM case, the detector output noise power is

$$N_o = \frac{N_c}{S_c} k_1^2 k_2^2 f_{sc}^2 \quad (21)$$

For the FM operation, the instantaneous frequency, $\omega = d\theta/dt$, now θ, from our expression for the FM carrier is $\omega_c t + \beta \sin \omega_{sc} t$. Thus $\omega = \omega_c + \beta\omega_{sc} \cos \omega_{sc} t$, which simplifier to $\omega = \omega_c + \Delta\omega \cos \omega_{sc} t$. The discriminator output is proportional to $\Delta\omega$; i.e., instantaneous frequency deviation is $\omega - \omega_c$. Therefore, we can say

$$E_o(t) = k_2 \Delta f \cos \omega_{sc} t \quad , \quad k_2 = \text{discriminator constant V/cps} \quad (22)$$

But $\Delta f \alpha A_{sc} (1 + M \cos \omega_m t)$, from that essumed given (23)

$$\Delta f \alpha = k_3 A_{sc} (1 + M \cos \omega_m t) \quad (24)$$

where

k_3 = proportionality constant cps/V

Therefore, the discriminator output may be written

$$E_o(t) = k_2 \left[k_3 A_{sc} (1 + M \cos \omega_m t)\right] \cos \omega_{sc} t \quad (25)$$

AM subcarrier i.e., subcarrier + 2 side bands, $M/2 \cos (\omega_{sc} \pm \omega_m) t$

and the output signal after the detector and LPF is

$$E_o(t) = k_1 k_2 k_3 A_{sc} M \cos \omega_m t \quad (26)$$

where

k_1 = proportionality constant of detector and LPF.

The mean signal power out may be obtained by

$$S_o = \left(k_1 k_2 k_3 A_{sc} M\right)^2 \frac{1}{T} \int_0^T \cos^2 \omega_m t \, dt \tag{27}$$

And taking S_o/N_o ratio using Equations (21) and (27), we get

$$\frac{S_o}{N_o} = 1/2 \frac{\left(k_1 k_2 k_3 A_{sc} M\right)^2}{\frac{N_c}{S_c} k_1^2 k_2^2 f_{sc}^2} = 1/2 \left(\frac{k_3^2 A_{sc}^2 M^2}{f_{sc}^2}\right) SNR_c \tag{28}$$

rewriting

$$SNR_o = 1/2 \frac{k_3^2 A_{sc}^2 M^2}{f_{sc}^2} SNR_i/2 f_m \tag{29}$$

and since we can say $(k_3 A_{sc} M)^2 = (\Delta f)^2$

$$\therefore \boxed{SNR_o = 1/2 \left(\frac{\Delta f}{f_{sc}}\right)^2 SNR_i} \tag{30}$$

G.5 FREQUENCY MODULATION/FREQUENCY MODULATION (FM/FM)

FM/FM is examined on the basis of certain assumed LPS constraints pertaining to carrier level performance plus certain assumed subcarrier constraints. One shortcoming is absence of specific subcarrier frequency instability allowances; however, satisfactory performance estimates are possible for frequency tolerance of ≤ 6 percent f_{sc}.

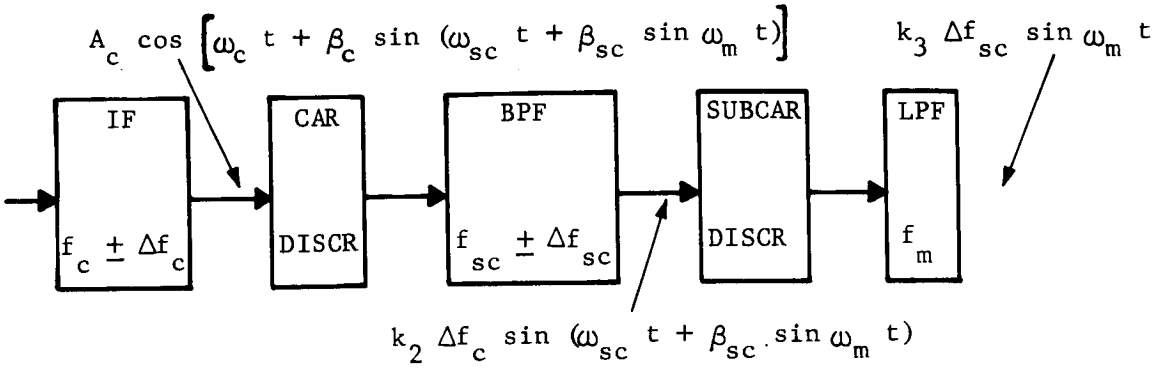

given

$$\beta_c = \frac{\Delta f_c}{f_{sc}} = \frac{160 \text{ kc}}{40 \text{ kc}} = 4 \; ; \qquad \beta_{sc} = \frac{\Delta f_{sc}}{f_m} = \frac{3 \text{ kc}}{2 \text{ kc}} = 1.5 \; ;$$

$B_{if} = 700$ kc

$B_{sc} = 16$ kc

FM carrier at input to carrier discriminator as noted, no noise

A_c is the unmodulated carrier amplitude at same point

then

Mean input signal power, independent of modulation is

$$S_c = 1/2 \, A_c^2 \tag{31}$$

The input noise power in a $2 f_m$ bandwidth is

$$N_c = \bullet \, 2 f_m \tag{32}$$

where

$\bullet$ = noise spectral density.

Noise power output of carrier discriminator and BPF is

$$N_{o_{cd}} = 2 \int_{f_1}^{f_2} \bullet \left(\frac{k_2}{A_c}\right)^2 f^2 \, df \tag{33}$$

where

$$f_1 = f_{sc} - 2.7\,\Delta f_{sc} = f_{sc} - 4\,f_m$$

$$f_2 = f_{sc} + 2.7\,\Delta f_{sc} = f_{sc} + 4\,f_m$$

k_2 = discriminator constant*

Solving Equation (33) we get

$$N_{o_{dc}} = 2\,\Phi\left(\frac{k_2}{A_c}\right)^2 \frac{f_2^3 - f_1^3}{3} = 2\left(\frac{k_2}{A_c}\right)^2 \frac{\left(f_2 - f_1\right)\left(f_1^2 + f_2^2 + f_1 f_2\right)}{3} \tag{34}$$

$$N_{o_{cd}} = 2\,\Phi\left(\frac{k_2}{A_c}\right)^2 (5.4\,\Delta f_{sc}) \left[\frac{3 f_{sc}^2 + (2.7\,\Delta f_{sc})^2}{3}\right] \tag{35}$$

or

$$N_{o_{cd}} = 2\,\Phi\left(\frac{k_2}{A_c}\right)^2 8 f_m \left[\frac{3 f_{sc}^2 + (4 f_m)^2}{3}\right] \tag{36}$$

By noting $f_{sc} > f_m$ in out assumed case, we can approximate

$$N_{o_{cd}} = \frac{k_2^2\,\Phi\,2 f_m\,4 f_{sc}^2}{1/2\,A_c^2} \tag{37}$$

$$N_{o_{cd}} = k_2^2\,4\,f_{sc}^2\,\frac{N_c}{S_c} \tag{38}$$

by recalling Equations (31) and (32) above.

Now, the mean output signal power of the carrier discriminator and BPF is

$$S_{o_{cd}} = \frac{k_2^2\,(\Delta f_c)^2}{2} \tag{39}$$

*Note: The bandwidth assignments conform to general TM practice. e.g., for $\beta_c = 4$, B_{if} (required) = 3.6 Δf_c + other frequency shift tolerances, similarly $\beta_{sc} = 1.5$ $\therefore$ B_{sc} (required) = 5.3 Δf_{sc}. The above values for f_1 and f_2 are therefore in terms of Δf_{sc} and f_m for convenience of subsequent interpretation.

By ratioing the $S_{o_{cd}}$ to $N_{o_{cd}}$ we get

$$\frac{S_{o_{cd}}}{N_{o_{cd}}} = \frac{1/2\ k_2^2\ (\Delta f_c)^2\ S_c}{k_2^2\ 4\ f_{sc}^2\ N_c}$$

which simplifies to

$$\frac{S_{o_{cd}}}{N_{o_{cd}}} = \frac{1}{8}\left(\frac{\Delta f_c}{f_{sc}}\right)^2 \frac{S_c}{N_c} \tag{40}$$

To solve for the final output signal-to-noise ratio out of the subcarrier discriminator, we note for the typical FM case that

$$SNR_o = 3\ \beta^2\ SNR_B\ \frac{B}{2\ f_m} \tag{41}$$

where

SNR_B = SNR in the input bandwidth

B = input bandwidth

f_m = baseband (or data bandwidth).

In our case the

$$SNR_B = \frac{S_{o_{cd}}}{N_{o_{cd}}}$$

and

$$\frac{B}{2\ f_m} = \frac{8\ f_m}{2\ f_m} = 4$$

$$\therefore\ SNR_o = 3\left(\frac{\Delta f_{sc}}{f_m}\right)^2 \frac{S_{o_{cd}}}{N_{o_{cd}}}\ (4) \tag{42}$$

$$SNR_o = 3\left(\frac{\Delta f_{sc}}{f_m}\right)^2 \left(\frac{\Delta f_c}{f_{sc}}\right)^2 \frac{1}{8} \frac{S_c}{N_c} \quad (4) \qquad (43)$$

Simplifying Equation (43) we get

$$SNR_o = \frac{3}{2}\left(\frac{\Delta f_{sc}}{f_m}\right)^2 \left(\frac{\Delta f_c}{f_{sc}}\right)^2 \frac{S_c}{N_c} \qquad (44)$$

or

$$\boxed{SNR_o = 3/2\ \beta_{sc}^2\ \beta_c^2\ SNR_i} \qquad (45)$$

where

SNR_i = SNR in a 2 f_m bandwidth.

G.6 SUMMARY

The following table depicts the resulting expressions.

Modulation Method	SNR_o	Explanation
AM	SNR_i	f_c {carrier frequency deviation
FM	$3\left(\frac{\Delta f_c}{f_m}\right)^2 SNR_i$	f_m {maximum data baseband frequency
AM/FM	$\frac{1}{2}\left(\frac{\Delta f_c}{f_{sc}}\right)^2 SNR_i$	Δf_{sc} {subcarrier frequency deviation
FM/FM	$\frac{3}{2}\left(\frac{\Delta f_c}{f_{sc}}\right)^2 \left(\frac{\Delta f_{sc}}{f_m}\right)^2 SNR_i$	f_{sc} {subcarrier frequency

A general comparison of moculation methods may be derived from the above; however, additional parametric analyses are required to obtain a more detailed assessment of modulation methods for the penetrometer application. A simple variation or change in the affected parameters may imply a different overall system configuration.

APPENDIX H

FM FEEDBACK DEMODULATION

H.1 INTRODUCTION

The Frequency Modulation Feedback (FMFB) principle has been analyzed and a general comparison of FMFB and conventional discriminator performance has been made. Exact Signal-to-Noise ratio (SNR) performance improvement achievable for each of several possible penetrometer modulation methods has not been determined. The results of this study, however, imply that about a 7 db SNR improvement can be realized independent of modulation index.

While the feedback discriminator performs the same function as a standard discriminator in that both devices demodulate frequency-modulated signals, the feedback discriminator has a lower closed loop threshold than the standard discriminator. This threshold lowering is the most important advantage obtainable through using a feedback discriminator.

A designer can use this threshold lowering to his advantage in several ways. For example, he can reduce the amount of required transmitted power and thus realize power and weight. On the other hand, he can transmit the same power, increasing link margin. He can also increase the modulation index while keeping the transmitted power constant, and the quality of the demodulated signal improves.

H.2 A QUALITATIVE DESCRIPTION OF FEEDBACK DISCRIMINATORS

Before proceeding with a detailed discussion of feedback discriminators, it seems advisable to qualitatively discuss their operation.

For this discussion, refer to the block diagram of feedback discriminator, Figure H-1. The feedback discriminator employs a mixer, an IF amplifier with a bandpass filter, a frequency detector (discriminator), a low pass filter, and a voltage-controlled oscillator (VCO). An FM signal is applied to the mixer at the input terminal, and the demodulated baseband is obtained at either point W or point C.

An input signal mixes with an output signal from the VCO and the resultant signal, which is an FM signal, feeds into the IF amplifier. The IF center frequency equals the difference between the input carrier frequency and the VCO center frequency.

The purpose of the IF amplifier is to provide sufficient voltage to the discriminator to enable it to operate in a linear manner. An IF bandpass filter attenuates noise outside the bandwidth of the IF signal. A standard discriminator then demodulates the FM signal, and the resulting demodulated baseband passes through a low pass filter for further noise attenuation.

The output of the low pass filter is applied to the VCO. Since voltage changes at the VCO input manifest themselves as frequency changes at the VCO output, the VCO is essentially a frequency modulator. The modulation index of the VCO output is a function of the loop gain, while the baseband is an estimate of the input signal. Moreover, two FM signals then beat together in the mixer, and since the phase components subtract in the mixing process, the equivalent modulation index of the signal at the output of the mixer decreases.

This modulation index reduction reduces the number of sidebands needed to convey the information. Consequently, the IF bandpass filter can be narrower than if no feedback were employed. This reduction in noise bandwidth seen by the discriminator accounts for the threshold reduction achievable with a feedback discriminator.

In the analysis of feedback discriminators, much of the effort has been directed to developing the idealized situation in which the loop has only two poles (one pole is contributed by the IF filter and the other pole is produced by the low pass filter). Although a two-pole loop constitutes an optimum design from the standpoint of time-response and stability, a physically realizable design will have more than two poles as well as delay. The effect of the additional poles and delay is to introduce excess phase shift which lowers the threshold.

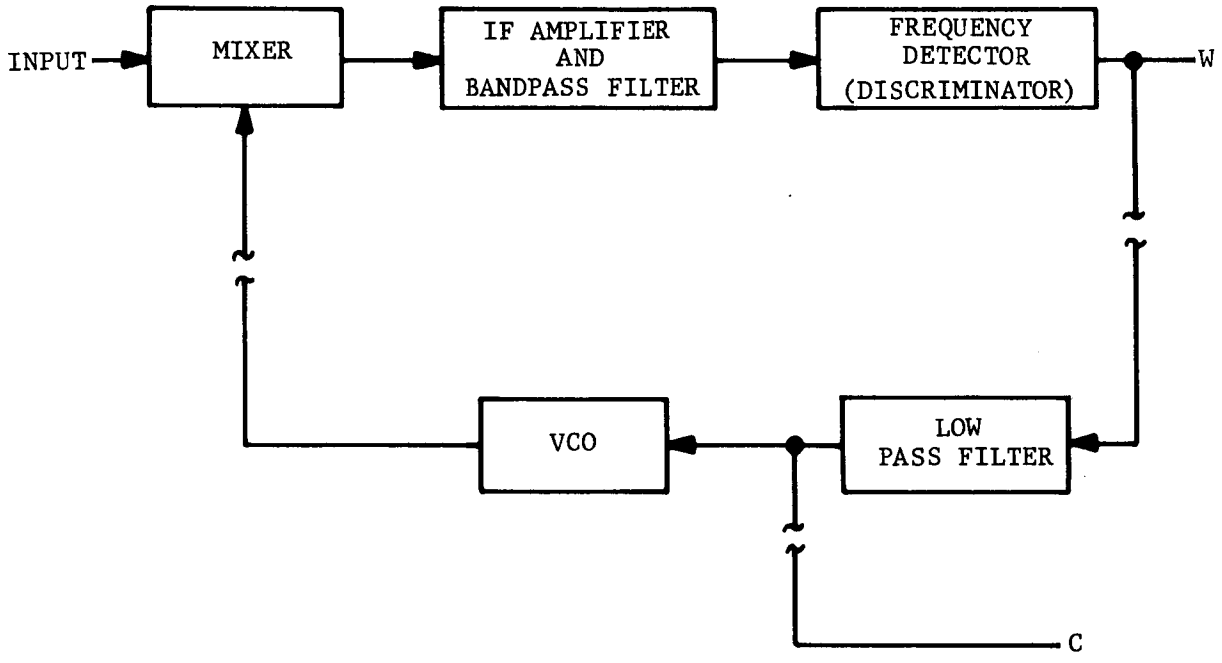

FO3791 U

FIGURE H-1. BLOCK DIAGRAM OF A FEEDBACK DISCRIMINATOR

H.3 LINEAR EQUIVALENT MODEL

The first step in analyzing feedback discriminators is the reduction of the loop parameters to their "linear equivalent" forms. The "linearization" process can be circumvented in the analysis of feedback discriminators (for example, in carrying out the analytical development using differential equations), but "linearization" greatly simplifies the work entailed in analyzing and designing feedback discriminators.

The "linearization" process is defined here as being the reduction of loop parameters to S-plane or Laplace polynomials when the input to the loop is considered as being frequency.

The loop components prior to "linearization" are shown in Figure H-2. At the VCO output, E_2 is the maximum VCO voltage amplitude; $\omega_2/2\pi$ is the VCO center frequency; ϕ is the VCO estimate of the input signal phase; and θ_2 is a phase term encompassing noise jitter as well as all VCO phase components not contained in $\omega_2 t$ and ϕ. At the input to the loop, A_c is the maximum voltage amplitude of the signal; $\omega_c/2\pi$ is the carrier frequency; ϕ_1 is the phase of the information; and ϕ_n is the noise phase contribution. The equivalent frequency input can be found through differentiating the input phase:

$$F_{in} = \frac{\omega_c + \frac{d\phi_1}{dt} + \frac{d\phi_n}{dt}}{2\pi} \qquad \text{(H.1)}$$

With sinusoidal modulation, the Laplace transform of Equation (H.1) is

$$F_1(s) = \frac{\omega_c}{2\pi s} + \frac{f_d\ \omega_m}{s^2 + \omega_m^2} + \frac{1}{2\pi} \cdot \frac{A_n}{A_c} \cdot \frac{\omega^2}{s^2 + \omega^2} \qquad \text{(H.2)}$$

where

f_d = carrier frequency deviation

$\omega_m/2\pi$ = modulation frequency

A_n = maximum incremental noise voltage amplitude

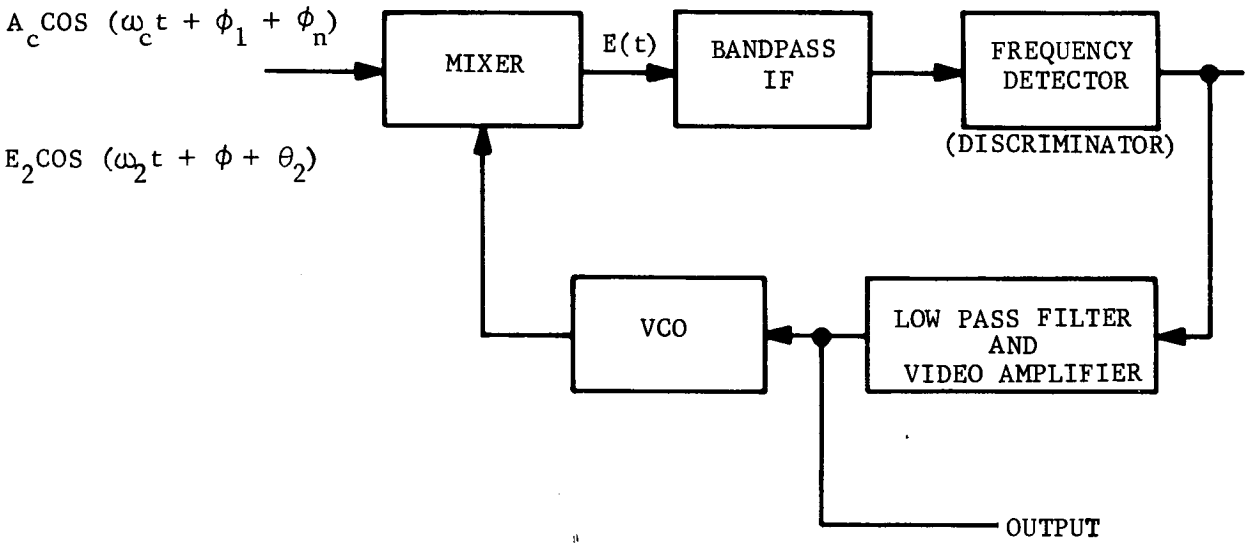

FO3792 U

FIGURE H-2. BLOCK DIAGRAM OF A FEEDBACK DISCRIMINATOR SHOWING THE INPUT VOLTAGE AND THE VCO OUTPUT VOLTAGE

The mixer, shown in Figure H-2 multiplies input voltage by VCO output voltage. Therefore, input and VCO frequency components subtract and add, but the resulting addition component is neglected because a bandpass filter centered at $\omega_o = \omega_c - \omega_2$ follows the mixer. The subtraction component is known as frequency error.

Before discussing "linearization" of the bandpass filter, the discriminator will be considered. While a discriminator generally has an S-curve response (i.e., output voltage amplitude versus input frequency), generally, the transfer characteristic is approximately linear throughout an operating range about the center frequency. The discriminator center frequency is $\omega_o/2\pi$, the IF center frequency: at $\omega_o/2\pi$, the discriminator output voltage is zero, but the discriminator output voltage is K_d volts when

$$\frac{\omega_i - \omega_o}{2\pi} = 1$$

Hence, the discriminator transfer function is K_d in the linear range.

As far as the band filter is concerned, it converts to an equivalent low pass function, defined as $G_a(s)$, through a transformation from bandpass to low pass. In this transformation, the IF or bandpass filter center frequency translates from $\frac{\omega_o}{2\pi}$ to zero. For example, if the IF bandwidth is 2b rad/sec, and if the filter is a single-pole filter;

$$G_a(s) = \frac{b}{s + b} \qquad (H.3)$$

Notice that the bandwidth decreases a factor of two by the transformation.

A low pass filter and a video amplifier follow the discriminator in the loop. The function of $G_b(s)$ is defined so that it encompasses these two quantities. If the low pass filter is a simple 6 db/octave roll-off filter, and if the video amplifier has a voltage gain of K_f, then

$$G_b(s) = \frac{K_f a}{s+a} \qquad (H.4)$$

A VCO changes its output frequency of oscillation as a function of its input voltage. In the feedback discriminator circuit, assume that the oscillator frequency is directly proportional to the transfer function of the VCO, which is K_V.

Now that the loop components have been "linearized," a composite model can be constructed, and this model appears in Figure H-3. For this model, $G_a(s)$ and $G_b(s)$ assume the values denoted by Equations (H-3) and (H-4), respectively. The model, shown in Figure H-3, furnishes a basis for understanding much of the analysis in the following sections. However, a different model will be used for the actual loop to be designed.

Two points worth stressing are: (1) All noise bandwidths are doublesided because a two-sided noise spectrum is used; and (2) the input to the loop goes through a limiting process before reaching the loop. Limiting eliminates amplitude variations.

H.4 TRANSFER FUNCTIONS

In view of the analytical necessity of being able to express loop response in terms of input stimuli, this section presents loop transfer functions in terms of an equivalent frequency input.

Figure H-4 shows the transfer function for $[H(S)/R(S)]$. Assume a normalizing excess phase shift, ϕ_b, in terms of phase shift (rad) per baseband bandwidth (rad/sec) so that a factor of $\exp\left\{-\frac{S\phi_b}{\omega_m}\right\}$ is multiplied by the gain function. For example, the open loop transfer function is

$$\frac{H(S)}{E(S)} = K_d K_v \exp\left\{\frac{-S\phi_b}{\omega_m}\right\} G_a(S)\, G_b(S).$$

Ideally, an open transfer loop transfer function is desired which maintains full feedback over most of the baseband, while still having a minimum noise bandwidth. A two pole loop with such characteristics has a Butterworth transfer function as shown below:

$$\frac{C(S)}{E(S)} = \frac{1}{S^2 + \sqrt{2}\,\omega_m S + \omega_m^2} \qquad \text{(H.5)}$$

However, the excess phase causes the loop to be underdamped and possibly even unstable. To offset this, a zero is introduced into the loop. In order to maintain loop operational flexibility, it is desirable to be able to vary the IF transfer function $G_b(S)$ and the open loop transfer function $G_a(S)$ independently. This can be done if $G_a(S)$ contains a zero to cancel the pole of $G_b(S)$.* Thus,

*Here (a) and (b) are defined so that the zero is at ω_{ma} and the pole at ω_{mb}.

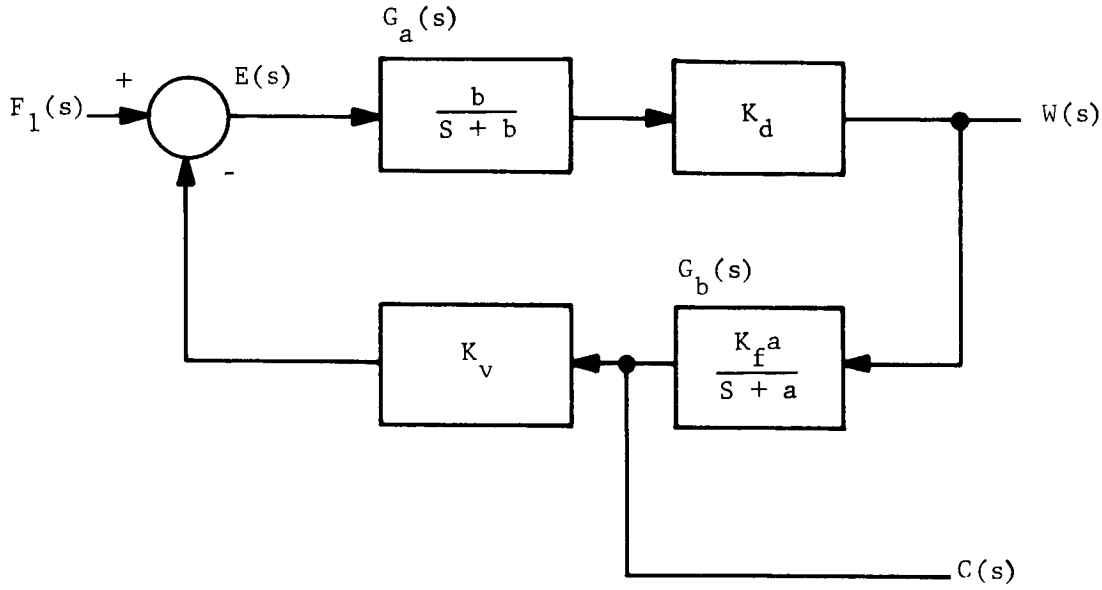

FO3793 U

FIGURE H-3. "LINEARIZED" EQUIVALENT MODEL OF A FEEDBACK DISCRIMINATOR

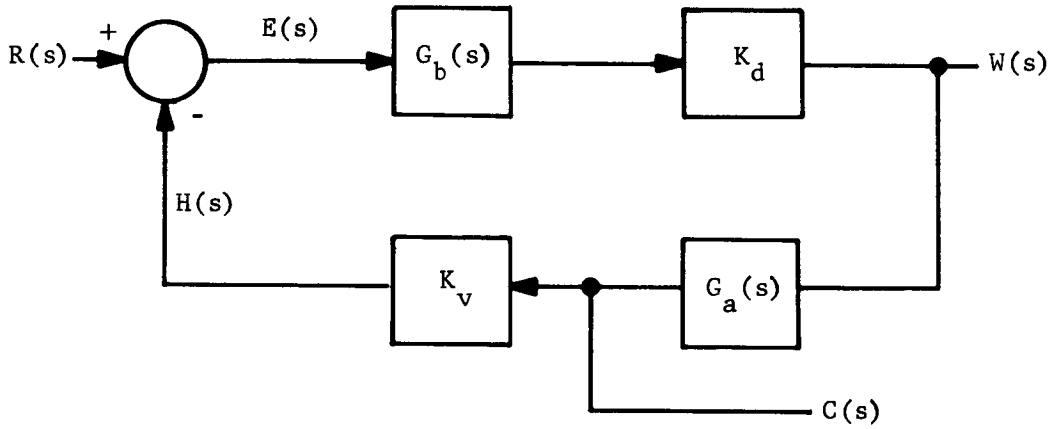

FO3804 U

FIGURE H-4. BLOCK DIAGRAM ILLUSTRATING POINTS IN THE LOOP FOR WHICH TRANSFER FUNCTIONS HAVE BEEN DETERMINED

$$\frac{H(S)}{W(S)} = \frac{K_v(S + a\,\omega_m)\quad (S + b\,\omega_m)\,\omega_m}{S^2 + \sqrt{2}\,\omega_m\ S + \omega_m^2} \tag{H.6}$$

and from (H-6),

$$\frac{H(S)}{E(S)} = \frac{\omega_m K_f K_v K_d (S+a\omega_m) \exp\left\{\frac{-S\,\phi_b}{\omega_m}\right\}}{S^2 + \sqrt{2}\,\omega_m\ S + \omega_m^2} \tag{H.7}$$

where

K_v= VCO gain constant (rad/sec/volt)
K_d= discriminator gain constant (volt/rad/sec)
K_f= filter gain constant

From (H.7), the closed loop transfer function is

$$\frac{H(S)}{R(S)} = \frac{\omega_m\ K(S+a\omega_m)\ \exp\left\{\frac{-S\,\phi_b}{\omega_m}\right\}}{S^2 + \omega_m S\sqrt{2 + K}\ \exp\left\{\frac{-S\,\phi_b}{\omega_m}\right\} + \omega_m^2\ \left(1 + Ka\ \exp\left\{\frac{-S\phi_b}{\omega_m}\right\}\right.} \tag{H.8}$$

where

$K \triangleq K_f K_d K_v$.

Equation (H.8) gives the closed loop transfer function. Equation (H.8) can be used to find the loop noise bandwidth (see paragraph H.5) and to ascertain stability.

H.5 LOOP DESIGN

The first step in designing the system is to find the threshold relationships. A feedback discriminator has essentially two thresholds: the open loop threshold, which is the threshold of the standard discriminator in the loop; and the closed loop threshold. If the open loop threshold is reached prior to the closed loop threshold, then the IF SNR determines the threshold of the loop. However, if the closed loop threshold is reached first, then the closed loop threshold alone sets the threshold of the loop.

The threshold of the discriminator is defined as the lowest value of input SNR, with fixed IF noise bandwidth and modulation frequency, for which the following formula gives the output SNR

$$\rho_o = \frac{3}{2} \beta_{RF}^2 \frac{B_{NIF}}{f_m} \rho_i \qquad \text{(H.9)}$$

where

B_{NIF} = IF noise bandwidth, low pass equivalent (cps)

f_m = modulation frequency (cps)

ρ_i = SNR input

β_{RF} = modulation index

Equation (H.9) relies upon having a post-detection filter of bandwidth f_m following the loop.

Moreover, if the discriminator in the loop reaches its threshold prior to the point at which the closed loop threshold is reached, then the threshold of the loop is

$$\rho_{iT} \left\{B_{n\ell}\right\} = \rho_{DT} \left(\frac{B_{NIF}}{B_{n\ell}}\right)$$

where

ρ_{iT} = input SNR at threshold
ρ_{DT} = discriminator SNR threshold
$B_{n\ell}$ = closed loop noise bandwidth (Hz)

Since $B_{NIF} < B_{n\ell}$, it is obvious from the above equation that the loop realizes some degree of threshold improvement. However, a greater threshold improvement results from reaching the closed loop threshold first. The following equation, defined in noise bandwidth $B_{n\ell}$, gives the closed loop threshold:

$$\rho_{iT} \approx 4.8 \left(\frac{F-1}{F}\right)^2 \qquad \text{(H.10)}$$

where

$$F = 1 + K_v K_d K_f.$$

To ensure that the open loop threshold is not reached prior to the point at which the closed loop threshold is reached, the SNR at the discriminator input must be above its threshold when the loop input SNR equals to the closed loop threshold SNR. At the closed loop threshold, the discriminator input SNR is

$$\rho_{iD} = \rho_{iT} \frac{B_{n\ell}}{B_{NIF}} \qquad \text{(H.11)}$$

where
ρ_{iD} = discriminator input SNR.

Substituting the right side of Equation (H.10) for ρ_{iT} into Equation (H.11)

$$\rho_{iD} \approx 4.8 \left(\frac{F-1}{F}\right)^2 \frac{B_{n\ell}}{B_{NIF}} \qquad \text{(H.12)}$$

For example, suppose a carrier is being modulated by a 1 MHz wave with a modulation index of 10. Then the ratio of B_{NIF}/f_m is equal to 24, and the threshold of an ordinary discriminator is about 13db. But, using a feedback discriminator with F = 10, the threshold from Equation (H.10) is 3.92 or 5.94 db. Moreover, since $B_{n\ell}$ is smaller than the 24 MHz input noise bandwidth, a further threshold enhancement results. Equation (H.13) expresses total threshold improvement as follows:

$$\zeta = 13 - 5.94 + 10 \log_{10} \frac{24 \text{ Mc}}{B_{n\ell}}$$

where

ζ = threshold improvement factor in db.

The threshold is expressed in twice the baseband bandwidth by multiplying Equation (H.10) by $B_{n\ell}/2f_m$:

$$\rho_{iT} \left\{2f_m\right\} = 4.8 \left(\frac{F-1}{F}\right)^2 \frac{B_{n\ell}}{2f_m} \qquad \text{(H.13)}$$

where

f_m = baseband bandwidth (Hz)

Moreover, the noise bandwidth, $B_{n\ell}$, in terms of the loop parameters is as follows:

$$B_{n\ell} = \frac{1}{2\pi H_m^2} \int_{-\infty}^{\infty} \left|\frac{H(j\omega)}{R(j\omega)}\right| d\omega \qquad \text{(H.14)}$$

where

H_m = maximum absolute value of $\frac{H(j\omega)}{R(j\omega)}$

$\frac{H(j\omega)}{R(j\omega)}$ = the transfer function of the VCO output.

As shown in Paragraph H.4, (a) has to be large enough to offset the effect of the excess phase shift. The design equations are quite complicated, and a graphical design approach is the most feasible.

The first of the design graphs (Figure H-5) shows a plot of (b) and (a) versus F (the design curves come from L.H. Enloe)[1]. Thus, for a given F, the filter constants can be found. Figure H-6 contains a plot of F versus ρ_{iT} and β versus ρ_{iT} for various values of excess phase shift. For a given value of β, the value of ρ_{iT} is found on the solid wave for a value of ϕ. Then, keeping the threshold constant, the corresponding value of F is found. Here, ρ_{iT} is the loop threshold in twice the baseband.

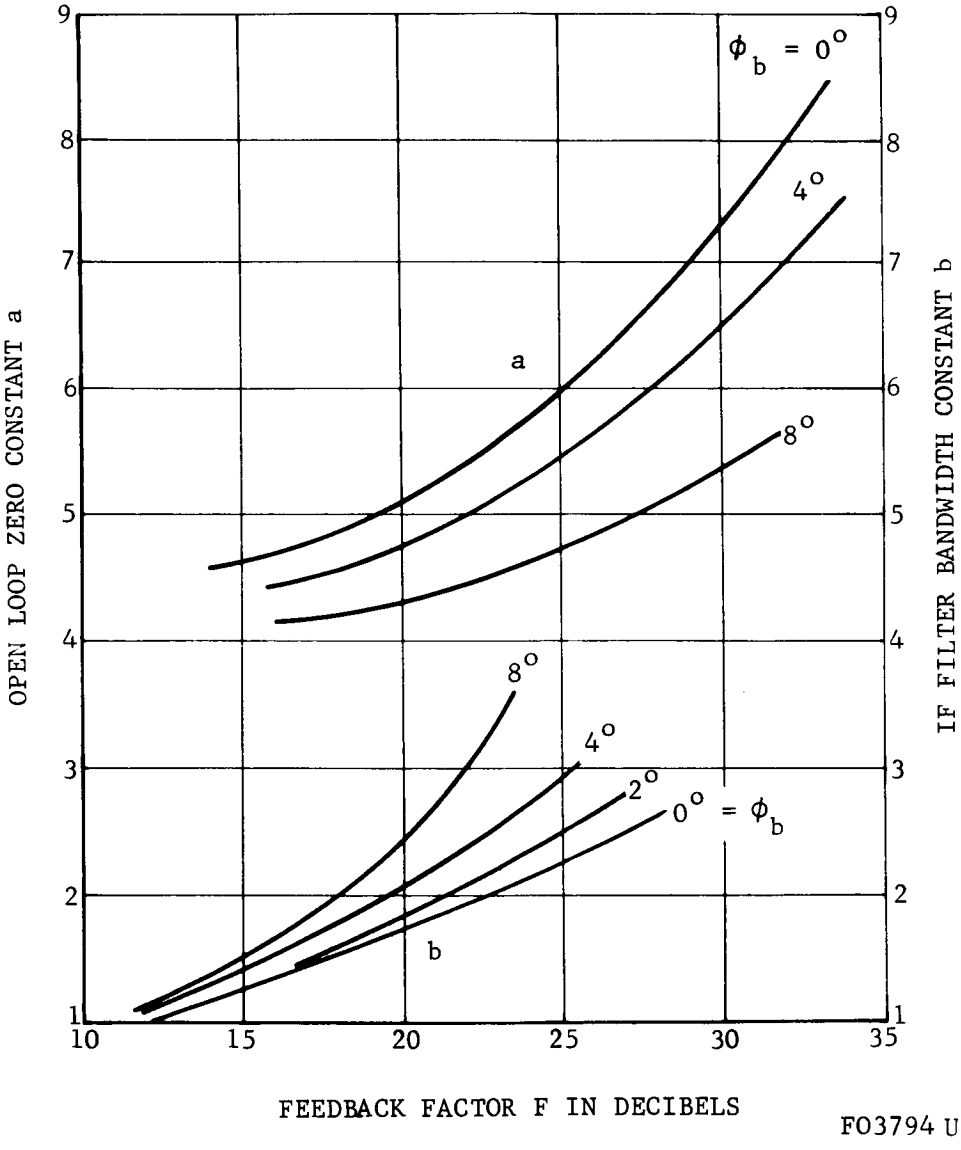

FO3794 U

FIGURE H-5. OPEN-LOOP ZERO CONSTANT "a" AND IF FILTER BANDWIDTH CONSTANT "b" PLOTTED VERSUS THE FEEDBACK FACTOR F. THE VALUE FOR F IS DETERMINED FROM FIGURE H-6.

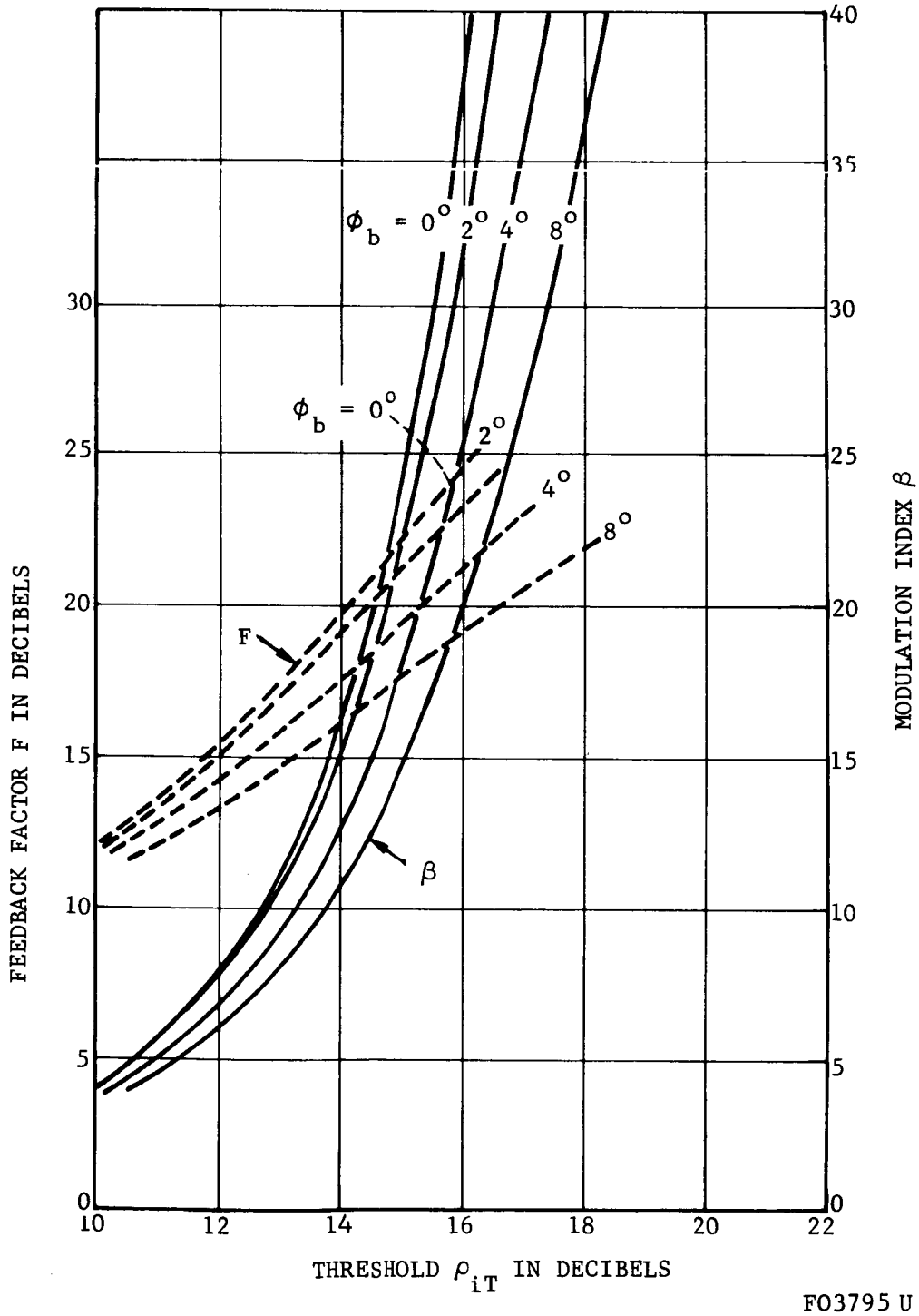

FIGURE H-6. FEEDBACK FACTOR F AND MODULATION INDEX β PLOTTED VERSUS THE THRESHOLD

To compare the FMFB discriminator with the conventional discriminator, the threshold SNR versus modulation index is plotted (Figure H-7). Here, the threshold SNR is taken in the RF bandwidth; Carson's rule is used to make the conversion. The threshold of the conventional discriminator can be assumed to be a constant 10db. (For comparative purposes, this assumption is not unreasonable and the loop excess phase shift can be assumed to be 4 degrees.)

---

[1] Enloe, L.H., "Synthesis of Frequency Feedback Demodulators," National Electronic Conference, pp. 477-497; Sept., 1962.

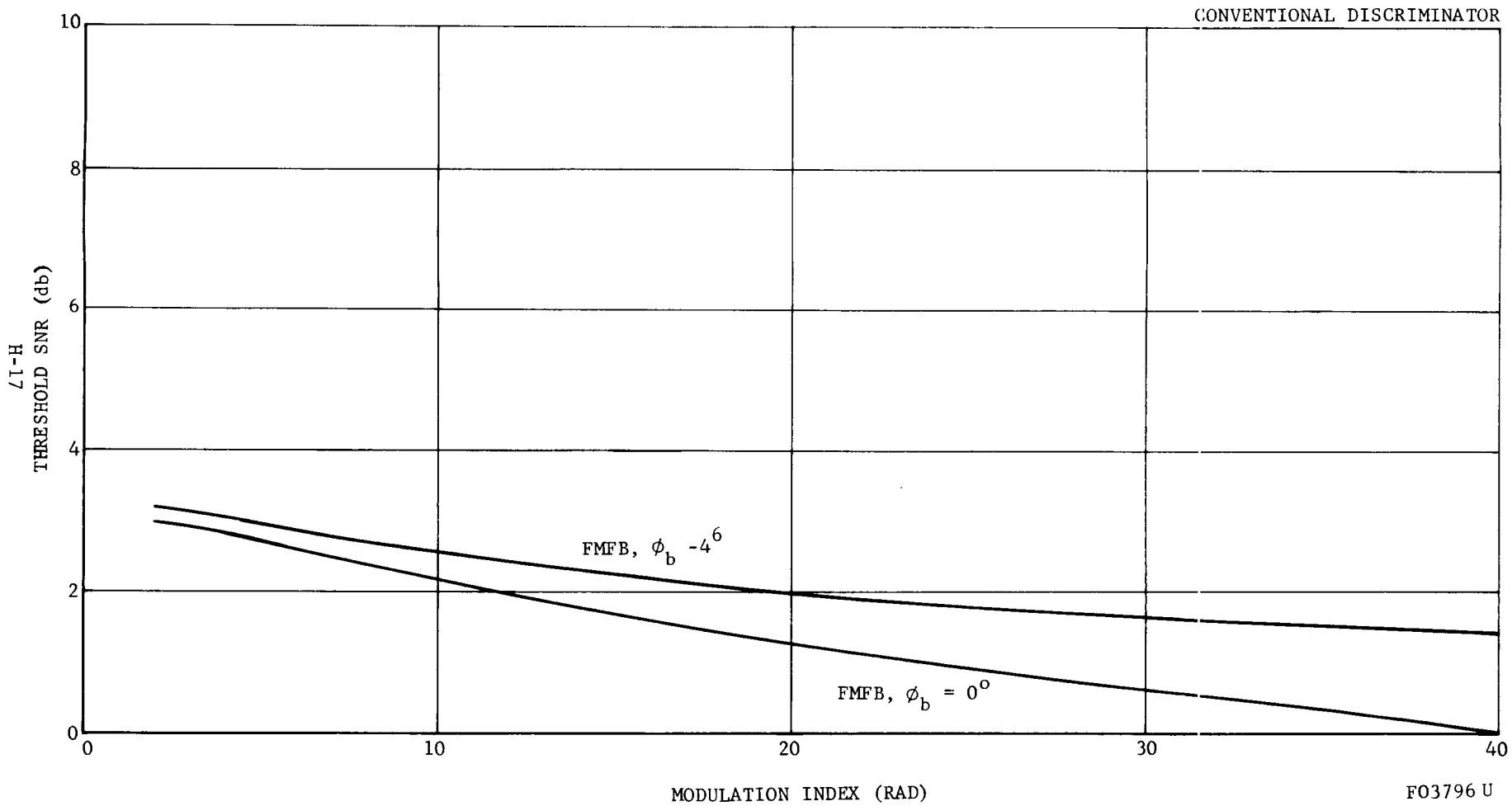

FIGURE H-7. THRESHOLD SNR PLOTS VERSUS MODULATION INDEX

APPENDIX J

RADIATION VULNERABILITY OF MOS-FET DEVICES FOR A TYPICAL LUNAR MISSION

J.1 INTRODUCTION

This appendix summarizes the findings of a brief investigation of the possible radiation damage that a MOS-FET device may experience during a typical lunar mission, i.e., passage through the van Allen belts, followed by passage through the average cosmic ray background of solar space; also including the possibility of encountering a solar flare.

J.2 TYPE AND INTENSITY OF RADIATION ENVIRONMENT

The types of primary radiations considered relevant to this brief study are:

(1) Electrons of van Allen belts.

(2) Protons of van Allen belts.

(3) Cosmic radiation comprised of protons, α-particles, gamma and X-radiation, and other heavy nuclei.

(4) Protons of solar flares.

J.2.1 VAN ALLEN BELTS

The van Allen belts are usually considered as two concentric toroidal belts: the inner belt extends from about 600 km to 10^4 km altitude (above the equator) and is sometimes called the proton belt, since it includes

most of the protons, but also some of the electrons; however, the latter extend to much greater distances from the earth, reaching maximum intensity at about 23,000 km. The intensity of radiation in the belts and the position of contour lines within the belts vary somewhat on a daily basis. The particle density represents a balance between the integrated accumulation (from cosmic background solar flares, and atomic weapons), and depletion caused by leakage to the earth and into space, and recombinations.

The peak intensity of electrons is approximately:

10^{11} electrons/cm^2 sec on an "excited" day

2×10^8 electrons/cm^2 sec on an "quiet" day

These electrons have energies ranging from about 0.1 Mev to about 0.7 Mev. The time-integrated spectrum (elect/cm^2 Mev) for a typical earth exit on a lunar mission follows an energy dependence E^{-n} over this range, where $n \approx 6$.

The proton peak intensity (average day) is on the order of 10^4 protons/cm^2 sec at an altitude of about 3600 km. The proton energies range from about 10 Mev to 600 Mev. The energy dependence of the proton spectrum is

$$N(E) \sim E^{-72}, \quad 10 \text{ Mev} < E < 80 \text{ Mev}$$

$$\sim e^{-E/170}, \quad 80 \text{ Mev} < E < 700 \text{ Mev}.$$

J.2.2 COSMIC RADIATION

The cosmic radiation originates outside the solar system. The particle energies are extremely high - up to 10^{20} ev. The chief constituents are protons, but there is a significant fraction of α-particles (~15%), and lesser amounts of heavier nuclei. The differential energy spectrum of the proton component is given as

$$n(E) = \frac{0.3}{E^{2.5}} \quad \frac{\text{protons}}{\text{cm}^2 \text{ sec sterad Gev}},$$

for $E > 10$ Gev. (One Gev = 10^9 ev)

These fluxes are, of course, extremely low compared to the fluxes of the trapped radiation within the van Allen belts. The dosages associated with the cosmic background will be seen (Paragraph J.3) to be negligible in comparison with that associated with the van Allen belts for a lunar (unmanned) mission, even though much less time is spent in the latter. In solar space, a much more significant environment is that of the solar flares, discussed in the following paragraph.

J.2.3 SOLAR FLARES

Solar flares are bursts of nuclei, predominantly protons, emitted from the sun during magnetic storms. There is a high degree of correlation between the frequency of such flares and the 11 year sunspot cycle, which has a maximum in about 1969. During the most recent maximum in the sunspot activity (July 1957 through December 1958), there were a total of 6762 flares, of which 41 where Class 3 or 3+, those of maximum intensity. This averages out to about 2.3 per month of the more intense flares. Each such flare may have a duration of from 2 to 3 hours to to 2 to 3 days. Advance predictability of their occurrence is low, at least on the time scale of a lunar mission.

The energy spectrum of the protons in a typical Class 3+ flare is

$$\frac{dN}{dE} = 2.6 \times 10^{8} E^{-2.86} \text{ protons/cm}^2 \text{ sec Mev},$$

where 10 Mev $< E <$ 1000 Mev. This amounts to a total flux of protons (integrating over the indicated energy range) of

$$N \cong 2 \times 10^{6} \text{ protons/cm}^2 \text{ sec}$$

It is beyond the scope of this study to dwell in more detail on the relative probabilities of the flare occurrence, intensity and spectral variation. In Paragraph J.4, it will be seen that the dosage associated with such a flare as the one just described is fairly severe, but not definitely intolerable (for unmanned vehicles).

J.3 ABSORPTION MECHANISMS AND SECONDARY RADIATION

When a charged particle impinges on a solid (or liquid or gas), it exchanges energy with the nuclei and electrons of the medium by means of either elastic or inelastic collisions. Electrons may be stripped from the atoms (ionization) or raised to existed states; nuclei may be displaced from lattice sites; emission of radiation may (or may not) accompany the collisions with the nuclei (bremsstrahlung); the incident particles may simply exchange energy elastically with the nuclei, conserving momentum (nuclear back scattering); or a number of less probable reactions may occur, such as nuclear excitation and Ramsauer effect.

The relative effectiveness of each of the possible energy-loss mechanisms depends on the atomic number and ionization potentials of the medium and on the velocity and mass of the incident particle. In the case of lunar mission environments, involving 0.1 to 0.7 Mev electrons and 30 to 1000 Mev protons, it is found that the overwhelming mechanisms of energy loss is the ionization process; however, the disposition of the balance of energy loss by the less effective mechanism varies greatly, depending upon whether the

particles are protons or electrons. These secondary mechanisms, while usually negligible in accounting for the total energy loss of the incident particle, are important in determining the final state of the medium, and the amount of secondary radiation emitted, after primary irradiation. A realization of the latter effects is especially important in view of the fact that there is a tendency among the experimentalists to characterize their irradiation experiments simply by the rad dosage administered to the sample or device. A rad is a measure of the energy per unit mass absorbed by the medium (1 rad = erg/gm). However, in many cases, the dosage is not necessarily indicative of the permanent damage suffered by a device, as will be demonstrated in the following paragraph.

J.3.1 ELECTRON INTERACTIONS

The predominance of ionization in stopping electrons is exemplified in Table J.1, which shows the cross section per aluminum atom for incident 0.1 Mev and 0.5 Mev electrons. The cross sections are in units of barns/atom (1 barn = 10^{-24} cm^2).

TABLE J.1

Energy Loss Mechanism	Cross Section (barns/atom) 0.1 Mev electrons	0.5 Mev electrons
Ionization	1950	4280
Nuclear Back Scattering	470	75
Scattering by Atomic Electrons	290	50
Bremsstrahlung	3.3	1+

The secondary particulate products of the first three processes listed in Table J.1 are lower energy electrons, many of which, however, still have sufficient energy to produce further ionization. Thus, the electrons continue to degrade in energy until, ultimately, the energy is equilibrated by means of excitation photons, lattice vibrations (heat), and leakage of excess charge. As the electron energy becomes very low, they tend to wander about, some of them straggling on to fairly great distances before leaking off, or becoming attached. It is difficult to define a true range for electrons for two reasons: (1) the straggling process cross sections follow essentially different energy dependences than ionization processes by fast electrons, and (2) the collisions of the fast electrons are erratic in energy exchange and consequently in direction. However, it is possible

to define a "practical" or extrapolated range which accounts for practically all the energy. In aluminum, it is found that ranges of 0.1 and 0.5 Mev electrons are approximately as shown in Table J.2.

TABLE J.2

Energy (Mev)	Range (gm/cm^2)	Range (cm)
0.1	0.015	0.0055
0.5	0.20	0.074

The results shown in Tables J.1 and J.2 indicate that it is not difficult to shield against the bulk of the electron energy. Furthermore, the greater part of the damage is transient in most materials. Exceptions are (1) the possibility of affecting the cross-linking and general electronic structure of polymeric materials, (2) the possibility of charge build-up in systems having insulated regions that prevent the charge from leaking off, (3) the possiblity of "breaking down" insulation, or potential barriers in components which have voltage applied across them, or (4) propagating large signals through electronic equipment which is turned on and has a large gain factor.

The bremsstrahlung (X rays and gamma rays), although not involving a very large fraction of the total energy, is much more penetrating than the primary electrons. The mean free path of a 200 Kev X-ray in aluminum is about 10 gm/cm^2. Thus, prolonged orbiting within the van Allen belt would make for a difficult shielding problem.

There is very little displacement damage associated with electrons. The small mass of the electron, relative to the mass of the nucleus, requires a high threshold energy for the reaction in order for momentum to be conserved.

J.3.2 PROTON INTERACTIONS

As is the case with incident electrons, the predominant energy exchange is in the ionization process. The concept of range is more applicable to the stopping of protons, primarly because they are sufficiently massive to travel in a more or less straight line, and because they lose their energy rapidly near the end of their paths. For proton energies up to about 500 Mev, the deposition profile is characterized by a fairly uniform energy loss rate over half the range, losing in the process from 1/4 to 1/2 the energy, followed by a steeply increasing loss rate over the second-half-range. Table J.3 shows, for protons incident on aluminum, the range (cm),

the energy loss rate over the first half-range (Mev/cm), and dosage in the first half-range (rad/proton/cm^2).

TABLE J.3

Incident Proton Energy (Mev)	Range in Aluminum (cm)	Energy Loss Rate (1st Half-Range) (Mev/cm)	Dosage in First Half-Range (Rad/proton/cm^2)
4	0.01	200	1.2×10^{-6}
10	0.06	100	6.0×10^{-7}
20	0.23	65	3.9×10^{-7}
40	0.80	30	1.8×10^{-7}
100	4.4	17	1.0×10^{-7}
200	24.0	9	5.4×10^{-8}

Table J.3 indicates that there would be no severe problem in shielding against protons of up to about 50 Mev, but very difficult for high energies.

The bremsstrahlung energy associated with the incident protons is very low, in fact, negligible. However, there is bremsstrahlung associated with the secondary electrons produced in the ionization process. No calculation of this effect is made here, as a fairly detailed spectrum of the electrons would be required.

Contrary to the case of incident electrons, the protons are sufficiently massive and energetic to produce a significant number of displaced atoms. The efficiency of this process depends on (1) the maximum amount of energy, Em, that can be transferred, which is determined by the principle of conservation of momentum and depends on the masses of the incident particle and the struck nuclei, and on the kinetic energy of the incident particle, (2) the Wigner energy, Ed, which is related to the amount of energy required to remove the struck nucleus from the lattice, (3) the cross section of the interaction, which depends on Ed, Em, on the atomic numbers of the incident particles and the nucleus, on the velocity of the incident particle, and on the reduced mass of the system.

In addition to the displaced atoms produced directly by the incident particle, which are designated primary displaced atoms, the primaries, themselves, may produce additional secondary displacements. The number of such secondaries for a given target material has been calculated by

Harrison and Seitz, and depends on Ed, the Wigner energy, and on the spectrum of excess energy delivered to the primary displaced atoms. By making some rather crude assumptions concerning the excess energy spectrum, the total number of displaced atoms per unit volume per incident proton/cm^2 may be estimated, as a function of incident proton energy. The results are shown in Table J.4.

TABLE J.4

Incident Proton Energy (Mev)	No. of Displaced Atoms/cm^3 per Proton/cm^2 Incident
10	260
20	140
40	73
100	31
200	16.5

In Table J.4, the tabulated values in the right column are equivalent to the number of displaced atoms per centimeter of path of each proton. To get the total number formed, it is necessary to multiply by the path length. Thus, the lower energy protons produce more displaced atoms per centimeter of path, but the greater range of the higher energy particles produce more displacements provided the medium is thick enough. (Actually, the number per unit path length near the end of the range is greater than indicated in the table.)

To sum up this paragraph, the following points are noted:

(1) Both electrons and protons lose most of their energy by ionization; this energy loss is characterizable by the rad dosage.

(2) Incident electrons produce bremsstrahlung directly, while protons do not; however, the secondary electrons ionized by the protons may contribute to bremsstrahlung.

(3) Displaced atoms which may cause <u>permanent</u> damage to semiconducting materials, are created by protons, but not by electrons. This effect is <u>not</u> characterizable by the rad dosage unless the dosage is delivered by the same or similar massive charged particles.

J.4 DOSAGE ESTIMATES

To calculate accurately the dosages and atomic displacements in a lunar vehicle, it would be necessary to perform integrations over the energy spectra of the particles, over the time-space variables of the van Allen belt contours as determined by the trajectory, and over the stopping-power formulae peculiar to the incident particles and medium for each of the possible reactions. For media situated on the interior, it would be further necessary to modify the environment in accordance with the shielding and nature of the secondary radiation and particulate reaction products produced.

Needless to say, such a calculation, even as accurately as would, in principle, be possible, has never been done. An approximation, utilizing a computer program, has been carried out, for the case of a lunar mission, by R.A. Miller and C. Cranford, of General Dynamics Nuclear Aerospace Research Facility (hereafter abbreviated GD). The GD calculations are carried out for a medium in the vehicle situated behind 2 gm/cm^2 of aluminum. The vehicle was assumed to experience the following environment:

(1) 0.82 hr through the heart of the proton belt.

(2) 3.4 hr through the electron belt.

(3) 55 hr through a Class 3 flare.

Before summarizing their results, it may be of interest to perform a few crude calculations using the data of Paragraphs J.2 and J.3:

(1) <u>van Allen Electrons</u>

Assume 10^8 electrons/cm^2 sec, 0.5 Mev electrons

Time in belt = 1.2×10^4 sec

Range in Al = 0.2 gm/cm^2

These assumptions lead to a dosage of $\sim 5 \times 10^4$ rad (averaged over a depth equal to the 0.2 gm/cm^2 range).

(2) <u>van Allen Protons</u>

Assume 10^4 proton/cm^2 sec, 20 Mev protons

Time in belt = 3×10^3 sec

Range in Al = 0.62 gm/cm^2

Dosage $\approx$ 16 rad (over 0.6 gm/cm^2)

(3) Solar Flare

Assume 2×10^6 proton/cm^2 sec, 100 Mev protons

Time in flare = 2×10^5 sec

Energy loss rate = 17 Mev/cm

Dosage $\approx 4 \times 10^4$ rad (over 5 to 10 gm/cm^2)

Displaced atoms = 1.2×10^{13}/cm^3

The GD calculations for the same trajectory yielded the following dosages in rads from the various sources. (Recall that this calculation assumes 2gm/cm^2 Al shielding)

Radiation Component	Dose (rads)
van Allen electrons	14
van Allen protons	0.3
Cosmic protons	0.062
Other heavy particles	0.035
Solar flare protons	2.2×10^4

It should be noted that the 2 gm/cm^2 Al shielding has effected a significant reduction (factor of 3×10^3) in the electron dosage, and that the van Allen proton dosage has been decreased by a smaller factor. (Not too much confidence should be placed on this comparison, because of the crudity of the hand calculations.)

The solar flare protons were not apparently affected significantly by the shielding. Actually, an additional amount of shielding, in this case, might increase the dosage if the thickness should happen to correlate with the mean range of the protons.

GD also carried out a supplementary calculation to determine shielding effectiveness against the solar flare protons. They showed, for example, that an additional 6 gm/cm^2 (2.2 cm) of Al, followed by 10 gm/cm^2 ($\approx$ 7 cm) of polyethylene would reduce the dosage to about 300 rads. This is a reduction of about a factor of 100, but the severe weight penalty may be taken as an indication of the difficulty in shielding.

The number of displaced atoms computed for the assumed mission ($\sim 10^{13}$/cm^3) may be a significant permanent damage mechanism in semi-conducting materials, but is not expected to be damaging to materials such as fuzed quartz, used as an insulator.

J.5 RESUME OF RADIATION EXPERIMENTS ON MOSFET DEVISES

A very brief search of recent literature on the subject of radiation damage to MOSFET devices revealed four similar experiments. The first was performed by F. Gordon of Army Signal R&D Lab, Fort Monmouth, N.J. (hereafter designated the Signal R&D experiment); the second, third and fourth were conducted by H.L. Hughes and R.R. Giroux of NRL (designated the NRL experiments).

In all experiments, a number of p-channel and n-channel MOSFET devices were exposed to γ-radiation from a Co^{60} source. Total dosages administered were 10^6 rad in the NRL experiment and 0.5×10^6 rad in the SIGNAL R&D experiment. In addition, the SIGNAL R&D workers exposed similar devices to fluxes of 2 Mev electrons in amounts of 10^{11}, 10^{12}, 10^{13}, and 10^{14} electrons/cm^2

In the NRL experiments it was found that changes in bulk semiconductivity were negligible. However, in before and after measurements, they found changes in channel conductance (at fixed gate voltage), a factor of 650 decrease for p-channel and a factor of 15 decrease for n-channel. They reported a change in g_m (transconductance), as a result of the decrease in drain current concomitant to the channel conductance change, but also an intrinsic change at fixed drain current. They noted little permanent degradation in gate leakage current. Table J.5 shows their results for 5 n-channel, and 6 p-channel devices.

TABLE J.5

		Leakage Current ($\mu\mu$ amp)		Fixed Gate Voltage g_m (μmhos)		Fixed Drain Current g_m (μmhos)	
Type	Unit	Before	After	Before	After	Before	After
n-Channel	1	1.0	1.0	600	200	450	200
	2	1.0	0.2	500	160	400	160
	3	3.1	5.0	600	30	400	20
	4	2.5	0.15	750	40	400	60
	5	2.0	3.0	1400	200	375	120
p-Channel	1	0.01	0.01	1500	600	800	600
	2	0.01	0.01	1300	35	500	N.M.
	3	0.015	0.01	1700	100	600	N.M.
	4	0.01	0.01	1700	900	1000	900
	5	0.01	0.03	1025	425	1100	600
	6	0.01	0.01	1250	725	750	725

(3) Solar Flare

Assume 2×10^6 proton/cm^2 sec, 100 Mev protons

Time in flare = 2×10^5 sec

Energy loss rate = 17 Mev/cm

Dosage $\approx 4 \times 10^4$ rad (over 5 to 10 gm/cm^2)

Displaced atoms = 1.2×10^{13}/cm^3

The GD calculations for the same trajectory yielded the following dosages in rads from the various sources. (Recall that this calculation assumes 2gm/cm^2 Al shielding)

Radiation Component	Dose (rads)
van Allen electrons	14
van Allen protons	0.3
Cosmic protons	0.062
Other heavy particles	0.035
Solar flare protons	2.2×10^4

It should be noted that the 2 gm/cm^2 Al shielding has effected a significant reduction(factor of 3×10^3) in the electron dosage, and that the van Allen proton dosage has been decreased by a smaller factor. (Not too much confidence should be placed on this comparison, because of the crudity of the hand calculations.)

The solar flare protons were not apparently affected significantly by the shielding. Actually, an additional amount of shielding, in this case, might increase the dosage if the thickness should happen to correlate with the mean range of the protons.

GD also carried out a supplementary calculation to determine shielding effectiveness against the solar flare protons. They showed, for example, that an additional 6 gm/cm^2 (2.2 cm) of Al, followed by 10 gm/cm^2 ($\approx$ 7 cm) of polyethylene would reduce the dosage to about 300 rads. This is a reduction of about a factor of 100, but the severe weight penalty may be taken as an indication of the difficulty in shielding.

The number of displaced atoms computed for the assumed mission ($\sim 10^{13}$/cm^3) may be a significant permanent damage mechanism in semi-conducting materials, but is not expected to be damaging to materials such as fuzed quartz, used as an insulator.

J.5 RESUME OF RADIATION EXPERIMENTS ON MOSFET DEVISES

A very brief search of recent literature on the subject of radiation damage to MOSFET devices revealed four similar experiments. The first was performed by F. Gordon of Army Signal R&D Lab, Fort Monmouth, N.J. (hereafter designated the Signal R&D experiment); the second, third and fourth were conducted by H.L. Hughes and R.R. Giroux of NRL (designated the NRL experiments).

In all experiments, a number of p-channel and n-channel MOSFET devices were exposed to γ-radiation from a Co^{60} source. Total dosages administered were 10^6 rad in the NRL experiment and 0.5×10^6 rad in the SIGNAL R&D experiment. In addition, the SIGNAL R&D workers exposed similar devices to fluxes of 2 Mev electrons in amounts of 10^{11}, 10^{12}, 10^{13}, and 10^{14} electrons/cm^2

In the NRL experiments it was found that changes in bulk semiconductivity were negligible. However, in before and after measurements, they found changes in channel conductance (at fixed gate voltage), a factor of 650 decrease for p-channel and a factor of 15 decrease for n-channel. They reported a change in g_m (transconductance), as a result of the decrease in drain current concomitant to the channel conductance change, but also an intrinsic change at fixed drain current. They noted little permanent degradation in gate leakage current. Table J.5 shows their results for 5 n-channel, and 6 p-channel devices.

TABLE J.5

		Leakage Current ($\mu\mu$ amp)		Fixed Gate Voltage g_m (μmhos)		Fixed Drain Current g_m (μmhos)	
Type	Unit	Before	After	Before	After	Before	After
n-Channel	1	1.0	1.0	600	200	450	200
	2	1.0	0.2	500	160	400	160
	3	3.1	5.0	600	30	400	20
	4	2.5	0.15	750	40	400	60
	5	2.0	3.0	1400	200	375	120
p-Channel	1	0.01	0.01	1500	600	800	600
	2	0.01	0.01	1300	35	500	N.M.
	3	0.015	0.01	1700	100	600	N.M.
	4	0.01	0.01	1700	900	1000	900
	5	0.01	0.03	1025	425	1100	600
	6	0.01	0.01	1250	725	750	725

The NRL group further reported that matched pairs of devices were damaged equally up to a dosage of 2×10^5 rad, with noticeable changes occurring after only 60 rad. Beyond 2×10^5 rad, the matched nature of the devices began to fall off.

The general tendency of the SIGNAL R&D results seems somewhat at variance with the NRL results. The former reported no definite tendency in the change in slope of the drain current-gate voltage characteristics. Thus, if the transconductance, g_m, is defined as $\partial I_p / \partial V_G$, then no trend was discovered. They did, however, report changes in the "dc" transconductance, i.e., the ratio I_p/V_G. They reported large changes, up to a factor of 10^4 increase, in the drain leakage, and factors of 2 to 3 increase in gate threshold voltage. In their electron beam experiments, no definite trend in gm change was observed. Certain changes in gate threshold voltage were detected, which they represented as an improvement. Further experimentation in this area was suggested. Highes in Reference 1 and 2 concludes that the major contribution to surface contamination is a positive space charge buildup in the silico-dioxide film. In Reference 3, Hughes concludes that certain circuit configurations, such as differential amplifiers allow the use of n-channel MOSFET's (in the depletion mode) with a minimum of radiation sensitivity.

J.6 RELEVANCE OF EXPERIMENTAL IRRADIATION AS SIMULATION OF ACTUAL ENVIRONMENTS

A substantial effort in the past has been made to establish the equivalence of changes in macroscopic properties of various components and devices in radiation environments that are characterised only by the total rad dosage administered. To a very great extent, this equivalence has been demonstrated for most conventional devices when exposed to electron beam, X ray sources, and γ ray sources. The equivalence is less well established for neutrons, protons, and other heavy particle beams. The basic reason for this is that the photon and electron beam irradiation is primarily effective in producing only ionization effects (ultimately), while the heavy particles produce displacement damage as well.

---

[1] Hughes, H. L., "Surface Effects of Space Radiation on Silicon Devices," IEEE Transactions on Nuclear Science, December 1965.

[2] Hughes, H. L., "Radiation Effects on MOS Devices," Paper presented at Third Navy Microelectronics Conference, Monterey, California, April 1965.

[3] Hughes, H. L., Giroux, R. A., "Space Radiation versus MOS Devices and Circuits," Paper presented at 12th East Coast Conference on Aerospace and Navigational Electronics, Baltimore, Maryland, October 1965.

Ionization effects are predominantly transient in nature, and the permanent effects obtained are not at all well understood. To a degree, the permanent effects are specific to the particular device; the degree of damage is related to the function of the component, and to the particular circuit involved.

Probably, the most significant long-lasting effect in non-polymeric materials is the accumulation of charge on surfaces, particularly in devices where exceptionally high impedances to ground are involved. For this reason, it is advisable, if possible, to arrange for irradiation of circuits which simulate closely the operational circuits contemplated. If sufficient care is taken in this regard, there is every reason to believe that equivalence assumptions are justified for the ionization effects.

Atomic displacement effects are the major cause of damage in semiconducting materials, and may lead to gross changes in the bulk conductivity of transistors and diodes. There is a good correlation between measured changes in properties and the number of displaced atoms/cm^3, based on parametric variations in flux levels for other identical, monochromatic beams of particles. Extrapolation of results to other particles or energies is not straightforward, however, for several reasons: (1) energetic electrons (>1 Mev) tend to produce a (relatively small) number of more or less isolated displacements, while heavier particles tend to produce clusters of displaced atoms, (2) the theory of displacement probability is not particularly well developed, so that the energy dependence is both complicated and uncertain in many materials, and (3) annealing effects are possible, and are even less well understood.

In summary, two points are worthy of mention in connection with the applicability of the Co^{60} γ-ray experimentation to the question of MOSFET behavior in lunar mission environment:

(1) The Co^{60} radiation very likely does not simulate adequately the possible displacement damage that may be expected in the proton environments. This damage could be expected to have an effect on the semiconducting properties of the device (g_m, etc.) rather than on the high impedance fuzed silica layer.

(2) The ionization effects measured probably simulate those for any MOSFET device which is used in circuits similar to those of the experiment, but there is a possibility that the isolated (from ground) branch of the device could be peculiarly sensitive to charge accumulation. The changes noted in the transconductance are believed to be generally applicable.

J.7 CONCLUSIONS

The data at hand do not provide conclusive evidence concerning the vulnerability of MOSFET devices to the radiation that may be encountered in a lunar mission. If it were to be assumed that solar flares could be avoided, then the calculated dosage administered to interior components of a vehicle with even very modest shielding capacity would appear to be of negligible importance. This conclusion assumes that prolonged orbiting within the van Allen belts is avoided.

The rad dosage associated with the simulated mission described in Paragraph J.3, involving passage through an intense flare, may be sufficient to cause alarm. The flare environment is admittedly more intense than the average flare that might be expected. A judicious consideration of the likelihood of encountering such a flare, in the light of the parameter variations obtained in the experiments described in Paragraph J.4, which involved a dosage level approximately two orders of magnitude greqter than that calculated from the flare, may indicate whether further concern is warranted. Any facility capable of providing the necessary dosages may be utilized to simulate the ionization effects on the actual circuitry contemplated.

There is some basis for concern that the displacement damage accompanying the high energy protons may not have been adequately simulated in the Co^{60} experiments. There are available two possible procedures for obtaining additional displacement data should it be felt to be warranted: (1) a neutron source, as from a reactor, may be utilized to induce equivalent numbers of displaced atoms within a device, and the data may be correlated with proton displacement calculations, or (2) a direct beam of protons of, for example, 6 to 10 Mev protons (as from a van de Graaf facility) may be used.

BIBLIOGRAPHY

The following references were utilized in preparing this memo:

1. The Atomic Nucleus, R. D. Evans, McGraw-Hill Book Co., Inc., N.Y., 1955.

2. R. A. Miller and W. Crawford, "A Procedure for Calculating Radiation Exposure on Space Missions," a report issued by General Dynamics Nuclear Aerospace Research Facility, Fort Worth, Texas, A. F. Contract No. AF 33(657)-7201.

3. ASTM Special Technical Publication No. 363, "Space Radiation Effects," publ. by ASTM, Philadelphia, June 23, 1963.

4. F. Gordon, "Radiation Damage Effects to MOS-FET, a memorandum issued by Army Signal Res. and Dev. Lab., Ft. Monmouth, N. J., Dec. 3, 1964.

5. H. L. Hughes and R. R. Giroux, "Space Radiation Affects MOS FETS," Electronics 37, Dec. 1964.

6. REIC Report No. 37, "The Space-Radiation Environment and Its Interactions with Matter," Radiation Effects Information Center, Battelle Memorial Institute, Columbus, Ohio, Jan. 15, 1965.

7. H. L. Hughes, "Surface Effects of Space Radiation on Silicon Devices," IEEE Transactions on Nuclear Science, December 1965.

8. H. L. Hughes "Radiation Effects on MDS Devices," Paper presented at Third Navy Microelectronics Conference, Monterey, Calif, April 1965.

9. H. L. Hughes, R. D. Giroux, "Space Radiation Versus MDS Devices and Circuits," Paper presented at 12th Conference by Aerospace & Navigational Electronics, Oct. 1965, Baltimore, Md.

APPENDIX K

BUFFER AMPLIFIER CONNECTION COMPARISONS

A direct comparison of the common base and common emitter connections is presented below.

The T equivalent circuit for the common base connection is

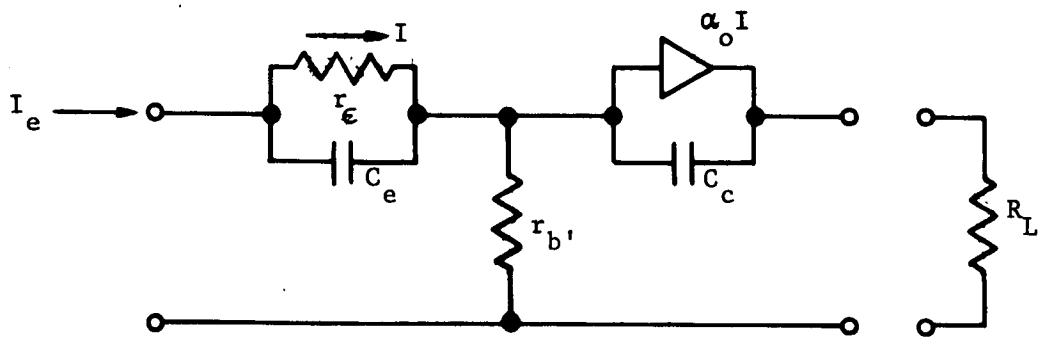

where:

$r_\epsilon = \frac{26}{I_e}$

$C_e = \frac{1}{r_\epsilon W_t}$

$r_{b'}$ = intrinsic base resistance

It is assumed that the collector circuit is tuned to resonance and can be represented as a pure resistance, R_L. The current through $r_{b'}$ can be written

$$I_{r_{b'}} = I(1 - \alpha) + S\ C_e(Ve - V_{b'}) + S\ C_c\ (Vc - V_{b'})$$

$$V_e - V_{b'} = \frac{Ie}{C_e} \frac{1}{s + \frac{1}{r_\epsilon\ C_e}}$$

If the voltage gain is large,

$$Vc - V_{b'} \cong Vc$$

If $Xc_c \gg R_L$,

$$Vc = \alpha_o\ I\ R_L$$

Assuming $\alpha_o \cong 1$, the equation is rewritten

$$I_{r_{b'}} = \frac{s\ I_e}{s + \frac{1}{r_\epsilon\ C_e}} + S\ I\ R_L\ C_c$$

$$I = \frac{V_e - V_{b'}}{r_\epsilon} = \frac{Ie}{r_\epsilon\ Ce} \frac{1}{s + \frac{1}{r_\epsilon\ Ce}}$$

Define $W_L = \frac{1}{R_L\ C_c}$,

$$I_{r_{b'}} = \frac{s\ I_e \left(1 + \frac{W_t}{W_L}\right)}{s + W_t}$$

The voltage across $r_{b'}$ is

$$V_{b'} = I_{r_{b'}} r_{b'}$$

The equivalent impedance at $r_{b'}$ is thus

$$Z_{b'} = \frac{V_{b'}}{I_e} = \frac{s\, r_{b'} \left(1 + \frac{W_t}{W_L}\right)}{s + W_t}$$

This has the form of the impedance of a shunt R - L circuit, where

$$Z = \frac{s\, R}{s + \frac{R}{L}}$$

It is evident that the common base circuit can be redrawn as

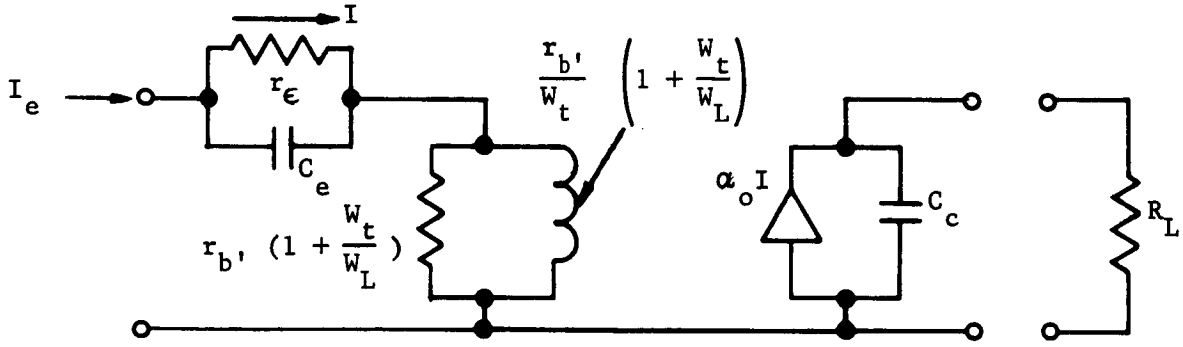

If $W < \frac{W_t}{2}$, the circuit can be redrawn as

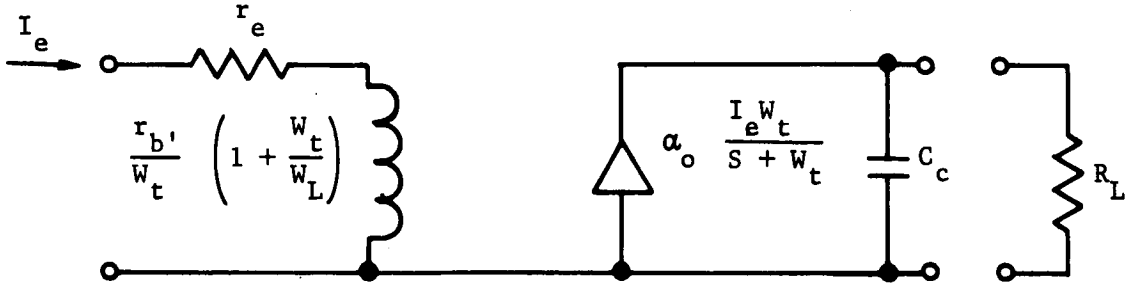

The percentage variation in the input inductance is

$$\% = \frac{100\ W_t}{W_L} = 100\ W_t\ R_L C_c$$

The high frequency common emitter equivalent circuit is well known to be

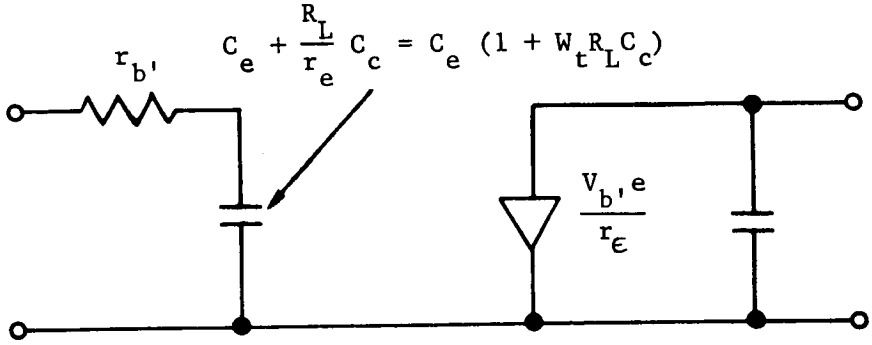

The percentage variation in input reactance is again

$$\% = 100\ W_t\ R_L\ C_c$$

It can be seen that the two connections are equivalent. For additional isolation, either circuit must be neutralized. Since common base neutralization is in general more difficult and requires dissipating input power in a resistor, the common emitter circuit seems to be the logical choice for this application since it may be neutralized if necessary.